Luminescence Spectroscopy of Strontium and Barium atoms isolated in Low Temperature Solids – an experimental and theoretical study

A Thesis submitted by

Barry Davis, B.Sc. (Hons.)

to the **Maynooth University** in fulfilment of the

requirements for the Degree of Doctor of Philosophy

Based on research carried out in the

Low Temperature Laboratory,

Department of Chemistry,

Maynooth University.

Research Supervisor: Dr. John G. McCaffrey

Head of Department: Dr. John Stephens

Maynooth,   January, 2016
Co. Kildare,
Ireland.

Table of Contents

Declaration

This thesis has not been submitted before, in whole or in part, to this or any other University for any degree, and is, except where otherwise stated, the original work of the author.

Barry Davis

_____

Acknowledgements

Firstly, I would like to sincerely thank my supervisor, Dr. John Mc Caffrey, for his constant help, advice and support over the years. His enthusiasm for my research project was a tremendous source of motivation and encouragement. I could not have asked for a better mentor during my Ph.D. study. Thank You.

To my lab colleague, Chris (Chiggy, El Chig, Chiggington Bear, The Chiggy Badger, Chig Fondle, The Shoe Thief, and so forth…): I'm sure it would sound more dignified if I suggested that we spent our time having stimulating conversions about ab initio methods or matrix-isolation. Truth be told, we were too busy enjoying cups of tea (over 6500 cups in your case – a modest estimate!) and getting up to mischief. Honestly, you made working those long hours a breeze – we'll get around to that breakfast/trap-filling machine soon! Cheers Chig.

To the Gents, Chris (Him again?), Ross (Rod Walker) and Adam (Alan Carpet): I simply want to say thank you for your friendship over the last four and a half years. When the work weighed me down, you were always good for an 'auld' Indian, a movie, and maybe even a Rebel Red. It has been a pleasure.

A special word of thanks to Jack (Hey!?), Michelle (I think she likes wine!), Ruth (mermaids are real!), Andrew (always good for a finger of whiskey!), Justine (Jacinta – which way is Spain?), Alice (thanks for being such a sound landlady!) and Jessica (Chriiiiiiiiis!): thank you for the friendship, fun and great memories. To all of the Post Grads in the Chemistry Department, past and present: Ula, Mark G., Harlei, Alba, John K., Finno (don't mind them, Chig), Michelle D., Caroline, Keeley, Andrea, Saidhbhe, Karen, Gama, Emer, Michelle K., Muhib, Mark K., Anthony, Matt, Big Jim Welsh, Ursula, Niamh, John M., Niall, Joey, Susan, Connor, Haixin, Rob, Lorna, Roisín and Foxy, to name but a few! Thanks for the lunchtime banter, tasty cakes and brilliant nights out.

I would also like to thank the academic staff and technicians of the Chemistry Department. In particular, I am grateful to Dr. Ken Maddock for ordering any materials I required, with minimal fuss. I am forever indebted to fellow Laois man, Noel Williams - I can't praise him enough. Whether it was to fix a vital piece of equipment or simply to have a chat (usually about the state of Laois hurling/football), Noel was always available and willing. He is a gentleman, and a true genius.

A special mention to the Laois gang, the originals: Barry (eile), Keith, Patrick and Eoghan. Is it just me or do all of the Brennan's Days roll into one? To Shane – we'll never

forget the night a Hurrishane struck Maynooth! Honestly cousin, you've been an amazing friend. Games night?

To my Belcotton family, Marguerite, Dónal, Patrick, Emily, Evanna and Riti: I am very grateful for the support and kindness you've shown me over the years. I especially thank Marguerite for her delicious cooking and baking – much of this thesis was founded on those meals, which always arrived in generous, 'Mog-sized' portions. I also thank Riti, who is solely responsible for Chapter V – he was collecting his ball while I was collecting my thoughts.

To my family, Emma, Thomas, Sarah, Lisa, Ada, Alan, Anthony, Jenna, Kate, Karen, Daniel, Chloe and Jack: I couldn't have asked for a more supportive and caring family. I don't know where I'd be without you.

Dedications

To my Parents, Liam and Adrienne: I will never forget all that you've done for me. You are the epitome of kindness and selflessness – never were any of us left wanting. Everything good in my life is a direct result of the example you set for me, the values you instilled in me and the love that you showed me. Simply put, ye are the best people I know. I love you both and dedicate my thesis to you.

To my beautiful girlfriend, Mairéad (Rú): You have filled my life with so much love, friendship, fun and happiness. I could not have done this without the confidence and encouragement you gave me. I love you and dedicate my thesis to you.

Finally, it is hard to believe how quickly your life can change. In April 2016, a true gentleman left this world. Tom, you provided me with a loving home and were an incredible source of support and happiness in my life. I am inspired by the dignity, courage and selflessness you showed in the face of death – indeed, you were more worried about how your illness was affecting everyone else than your own wellbeing. In one of our final conversations, you were imagining the world without you and how life would eventually go on. Life does go on, Tom, but we will never forget you. Thank you for everything. I dedicate my thesis to the memory of Tom Davis.

Abstract

This thesis presents an experimental and theoretical study of the alkaline earth atoms, strontium and barium, isolated in rare gas matrices (argon, krypton and xenon) at cryogenic temperatures. These solid-state M/RG (M = Sr and Ba; RG = Ar, Kr and Xe) samples are extensively characterised using time-integrated (steady-state) and time-resolved spectroscopic techniques. The primary goal of this work is to develop the spectroscopy of matrix-isolated Group II metals and augment the ongoing research of the Maynooth Group, which focuses on S metal atom – rare gas systems. Moreover, the literature on the spectroscopy of matrix-isolated Sr or Ba is quite sparse and the limited number of reports that do exist contain inaccuracies, which are in need of clarification and amendment.

M/RG samples deposited at 10 K, under conditions of low metal loading, consist of well-isolated metals atoms. Conversely, matrices formed at elevated temperature contain a higher yield of metal clusters. Absorption spectra recorded of M/RG solids condensed onto a 'warm' sample window reveal the presence of additional non-atomic features – these are attributed to metal dimers based on the low metal fluxes employed during deposition. Further characterisation of the Group II diatomics was accomplished using steady-state and time-resolved luminescence spectroscopy. The luminescence produced with excitation of the metal dimer absorption bands reveals very different behaviour for Sr_2/RG and Ba_2/RG. Resonance fluorescence with a lifetime of 15 ns is observed for the lowest energy transition of Sr_2. In contrast, the lowest energy transition of Ba_2 is completely quenched – this behaviour is consistent with the absence of vibrational structure on the near-IR absorption band of Ba_2, indicating that a lifetime broadening effect exists on this molecular transition. Moreover, the excitation/emission features identified in the visible spectral region (580 – 680 nm) for matrix-isolated Ba_2, likely originate from molecular states of the dimer, which dissociate to atomic asymptotes existing above the (6s6p) $^1P_1$ level of the atom.

The $(nsnp)\ ^1P \leftarrow (ns^2)\ ^1S$ resonance transitions, which occur in the visible spectral region, are used to compare the isolation conditions of these two metal atom systems. Complex and structured absorption bands were recorded for both Sr and Ba in all three hosts, even after extensive sample annealing. Thus, these alkaline earth atoms occupy a myriad of thermally stable sites in solid Ar, Kr and Xe matrices. As a

result, each M/RG solid exhibits numerous (nsnp) ^{1}P emission bands and two dimensional – excitation and emission (2D-EE) spectra are required to fully unravel the luminescence. The excitation spectra extracted from the 2D-EE scans allow the complex absorption bands to be resolved into site-specific features. Both metal atom systems display a variety of excitation patterns, ranging from the classic Jahn-Teller threefold split, to asymmetric threefold (2+1) patterns and broad, unstructured bands. It is therefore concluded that the isolation of Sr and Ba atoms in rare gas solids occurs in cubo-octahedral, crystalline (*fcc*) sites on one hand and in non-crystalline sites on the other.

To assist the interpretation of the site occupancy, novel ground state potential energy curves are computed for the 1:1 M·RG complexes (M=Ca, Sr, Ba and RG = Ar, Kr, Xe), using the empirical Tang-Toennies (TT) and *ab initio* CCSD(T) methods. The spectroscopic constants obtained from both approaches were in agreement. Long bond lengths (> 5 Å) and shallow bound regions (<142 cm^{-1}) were revealed for the nine M·RG diatomics. Although the TT model is computationally inexpensive and accurately describes the long range, attractive portion of the potential energy curves, the poor performance of this function at describing the inner repulsive walls precludes the use of this method in analysing the M/RG matrix systems. Thus, the site occupancy was interpreted using only the *ab initio* results. A comparison of the M·RG (coupled-cluster) and RG$_2$ potential energy curves allowed for comments to be made regarding the occupancy of the alkaline earth atoms within cubic sites of the *fcc* rare gas lattices. Combining the theoretical analysis with the site-specific (nsnp) ^{1}P$_1$ excitation spectra recorded in annealed matrices yielded tentative site assignments. In summary, the 'blue' sites of isolation are tentatively assigned to tetra-vacancies (TVs) and the 'green' sites to hexa-vacancies (HVs). The 'violet' and 'R1' trapping sites produce an asymmetric threefold (2+1) pattern in absorption/excitation, inferring a non-isotropic environment removes the degeneracy of the excited (nsnp) ^{1}P state. Accordingly, these sites are proposed as cylindrically shaped voids (CV).

The atomic (nsnp) ^{1}P$_1$ luminescence recorded in RG matrices reveals contrasting behaviour for Sr and Ba atoms. Only resonance (6s6p) ^{1}P$_1$ → (6s^2) ^{1}S$_0$ emission was observed for Ba/RG solids – scans made out to 900 nm (the limit of our detection system) do not reveal any lower energy features. Conversely, the luminescence of Sr/RG solids is richer as emissions arising from the (5s5p) ^{1}P$_1$, (5s4d) ^{1}D$_2$, (5s4d) ^{3}D$_1$ and (5s5p) ^{3}P$_1$ excited states of Sr are identified. In addition, the ^{1}D$_2$

state of atomic Sr can be readily accessed in absorption, therefore allowing investigation of the (5s4d) $^1D_2$ luminescence. For both metal atom systems, state assignments were made based on the observed spectral (location and bandwidth) and temporal characteristics. For example, the resonance (nsnp) $^1P_1$ emission bands exhibit nanosecond radiative lifetimes (< 10 ns). In contrast, the $^3D_1$ and $^3P_1$ emission features of Sr exhibit microsecond radiative lifetimes (> 1 μs). The results presented in this thesis demonstrate that the site of isolation critically governs the excited state guest/host interactions and the photophysical properties observed. However, temperature studies also reveal the existence of a host dependence. As a result, it is proposed that intersystem crossings occur in both metal atom systems and the efficiency of these processes are greatest in solid Xe due to the external heavy atom effect. For Ba, it is suggested that a $^1P_1 \rightarrow {}^3P_2$ relaxation pathway competes with the resonance fluorescence and is most active in Xe at elevated temperatures. Similarly, it is proposed that non-radiative $^1P_1$, $^1D_2 \rightarrow {}^3D_J$ transitions strongly influence the luminescence of atomic Sr in RG solids, even at low temperature (10 K).

Chapter I

Introduction

I.1   Matrix-Isolation – history, development and overview

The term 'matrix-isolation' refers to an experimental technique whereby a reactive or unstable species is trapped in an excess of some inert host material (the matrix). The matrix is usually condensed onto a window or in an optical cell held at cryogenic temperatures, which facilitates characterisation by conventional spectroscopic means. At such low temperatures, diffusion is very limited and most chemical reactions are arrested as the guest species are isolated from each other. Moreover, the spectra recorded for molecules are often less complex and more resolved because only the lower electronic and vibrational quantum states are populated and rotational motion is quenched.

The origin of the matrix-isolation technique can be traced back to Norwegian physicist, Lars Vegard, who performed low temperature experiments designed to recreate the conditions of the upper atmosphere. Vegard wished to identify the cause of the aurora borealis, particularly the striking green line at 557.7 nm. He proposed that the intense green colour arose from electrically charged nitrogen, which was condensed onto dust particles at high altitude. In 1924, at Heike Kamerlingh Onnes's famous cryogenic laboratory in Leiden, Vegard set about proving his hypothesis. Here, he deposited nitrogen onto a copper plate that was cooled with liquid hydrogen and subsequently bombarded the thin film with high-voltage cathode rays. To his delight, the layer of nitrogen became "brilliantly luminous with green colour", when the cathode potential was raised above 500 volts. Vegard was convinced that he had solved the mystery of the auroral lines. However, his claim was later disputed by Canadian physicists, McLennan and Shrum[1], who conclusively assigned the auroral line to a forbidden $^1S \leftrightarrow {}^1D$ transition of atomic oxygen. Nonetheless, Vegard's experiments represent the first known spectroscopic studies conducted using low temperature solids.

It wasn't until the 1940s that an optically transparent material was purposefully doped with a molecule of interest for spectroscopic study. At the University of California, Berkeley, G.N. Lewis and co-workers[2,3] showed that low temperature organic glasses, such as ether–pentane–alcohol (EPA), were convenient media for

trapping and characterising transient, reactive intermediates. Typically, the precursor molecule was mixed with EPA and the solution was cooled to 90 K in a quartz Dewar, forming a rigid glass. Free radicals could then be generated by photolysis or radiolysis of the solid. In the years that followed, many unsuccessful attempts were made at trapping reactive species using more elaborate experimental techniques. In the mid-1950s, Norman and Porter subsequently returned to the method introduced by Lewis *et al.*, realising that this was probably the best way to study atoms and molecules which exist 'fleetingly' in the gas phase. They recorded the optical spectra of a wide range of reactive radicals and atoms, which were prepared by photolysis in rigid hydrocarbon glasses, at 77 K[4,5].

Around the same time (early 1950s), George Pimentel[6] was interested in molecules that were not on "the chemical shelf". He attempted to characterise these extremely reactive molecules in flames using infra-red (IR) spectroscopy, but became frustrated because he couldn't achieve concentrations high enough to obtain accurate absorption measurements. Together with his postdoctoral student, Eric Whittle, Pimentel decided the best approach was to quickly trap the short-lived molecules in a solid inert gas at cryogenic temperatures[7], so that they could conduct 'leisurely' spectroscopic studies. This was the inception of the 'modern' version of the technique – Pimentel's group is credited with coining the phrase 'matrix-isolation'. In contrast to Norman and Porter's experiment, Pimentel adopted the rare gases (RG's) as solid hosts and the matrices were formed by spraying a gas mixture of the matrix and active species onto a surface cold enough to allow rapid solidification. Thus, reactive intermediates did not have to be generated *in situ*. Prototype experiments[8,9] were successful only after the development of reliable low-temperature cells, and a systematic study of the effects of concentration, deposition conditions and temperature on the isolation efficiency and matrix stability. In 1958, this effort was rewarded by the first IR detection of matrix-isolated HNO[10], and was soon followed by the detection of the HCO[11] radical.

In Pimentel's time, conducting matrix experiments required a degree of adventurousness because it involved the handling of liquid hydrogen or helium in open Dewar vessels. However, since then, cryostats have undergone many phases of improvement and are commercially available. Indeed, closed-cycle cryostats or 'displexes' are at the heart of the modern matrix experiment and temperatures as low as 10 K can be readily reached at a sample substrate. Surfaces at low temperatures must be kept out of contact with the ambient environment. This is achieved by a vacuum

shroud that surrounds the two expander stages of the displex and the sample substrate. High vacuum (10^{-8} mbar) is maintained in the matrix rig to ensure sample purity and to avoid collisional heat transfer. Matrix-isolated samples can be prepared by deposition of a gaseous host/guest pre-mixture, provided the guest is sufficiently volatile. In many cases, the species of interest is not volatile (metal atoms) and must be co-deposited with the host gas following controlled vapourisation. This is usually accomplished by resistive heating, laser ablation or 'sputtering' by electron bombardment of the bulk material. In order to achieve complete isolation and supress reactions between the guest species, large host to guest ratios of between 10^4 and 10^5 are normally employed.

For over twenty years, a large portion of the work conducted by Dr. McCaffrey's group at Maynooth has focused on the luminescence spectroscopy of metal atoms isolated in solid rare gases. A range of metals have now been examined, including Mg[19-21], Zn[22,23], Cd[24], Hg[25], Mn[26,27], Na[28] and most recently, Eu[29]. These atoms are characterised by spherically symmetric (S) ground states and exhibit strong nsnp $\leftarrow$ ns type transitions in absorption and emission. Coupled with theoretical simulations[22,28,30], these luminescence studies have considerably advanced the understanding of the ground and excited state interactions occurring between the guest metal atom and rare gas host. Many exciting and often quite unexpected results have been documented – such as the observation of very sharp excitation and emission features arising due to crystal field splitting of the D states of Mn, induced by the rare gas lattice[26,27], or the facile production and stabilisation of singly charge Eu cations[31] in solid Ar, Kr and Xe. As a natural progression, this body of research is now extended to include the alkaline earth atoms, Sr and Ba, both of which exhibit (ns^2) ^{1}S$_0$ ground

Although matrix-isolation was created for the purpose of trapping free radicals and transient molecules, over the years the range of species studied using this technique has broadened quite considerably. The extensive study of matrix-isolated metal atoms was pioneered by McCarty and Robinson, who in 1959, presented the absorption spectra of Hg and Na atoms isolated in Ar, Kr and Xe matrices[12]. Soon afterwards, Schnepp developed a high temperature furnace attachment, which allowed metal atoms with higher melting points, like Mg and Mn, to be vaporised and thus isolated in a RG solid[13,14]. Since then, a plethora of studies have appeared concerning the spectroscopy of matrix-isolated metal atoms[15-18].

state terms ($n = 5$ for Sr and 6 for Ba). As will be discussed ahead, these metal-rare gas (M/RG) systems are not well studied and the existing literature needs clarification.

I.2   Rare gas (RG) hosts

Many of the qualities that make the rare gases (RG = Ne, Ar, Kr and Xe) ideal matrix hosts derive from their ground state $n\mathrm{s}^2n\mathrm{p}^6$ electronic configuration, which consists of fully occupied s and p subshells. This arrangement is known as 'the stable octet' because it is very difficult to remove an electron from the valence orbitals. As a consequence, the rare gas solids are very inert and can be used to isolate reactive species. Moreover, RG matrices are optically transparent from the far infra-red to the vacuum ultraviolet and the trapped species may be characterised using many spectroscopic techniques. For example, the UV/Vis absorption spectra recorded of guest metal atoms, such as Sr or Ba, are free from interfering bands due to the host lattice. RG atoms exhibit high ionisation thresholds[32] and, as a result, the first strong resonance $n\mathrm{s}^2n\mathrm{p}^6 \rightarrow n\mathrm{s}^2n\mathrm{p}^5(n+1)\mathrm{s}^1$ absorptions do not occur until the vacuum UV region (see Table I.1).

Table I.1   **Wavelength positions of the first resonance $[n\mathrm{s}^2n\mathrm{p}^6 \rightarrow n\mathrm{s}^2n\mathrm{p}^5(n+1)\mathrm{s}^1]$ transitions of the rare gases. It is noteworthy that these gas phase values will be slightly shifted when the RG atoms condense into a solid[33].**

Rare Gas	Wavelength (nm)
Ne[34]	74.4
Ar[35]	106.7
Kr[36]	123.6
Xe[34]	150 .0

The closed shell configuration of the RG atoms gives rise to a $^1\mathrm{S}_0$ ground state term. If this spherically symmetric charge distribution was rigid, then the interaction between noble gas atoms would be zero and they could not condense into a solid upon cooling[37]. However, the rare gases are not 'ideal' and weak interactions may arise between the atoms due to small quantum mechanical fluctuations in their electron densities. Although no permanent dipole moment exists, the atoms can induce dipole moments in each other, creating a weak, attractive interaction at certain internuclear

separations. This is called the van der Waals or London interaction[38] and it is responsible for the condensation of the RG's. A consequence of these weak forces is that the rare gases exhibit low melting points[a] and cryogenic temperatures are required to form solids.

It is known from X-ray diffraction experiments[39] that the most commonly used matrix materials (Ne, Ar, Kr and Xe) crystallise into a face centred cubic (*fcc*) structure, when sufficiently cooled. In this simple close packing arrangement, the van der Waals forces (vdW) are maximised by each atom achieving the highest possible coordination number, i.e., the largest number of nearest neighbours[37]. A unit cell of the *fcc* structure is presented in Figure I.1 and shows the fourteen lattice points, eight of which are positioned at the corner of the cell, while the remaining six occupy the centres of the cubic faces.

Face Centred Cubic (*fcc*) unit cell

a = lattice parameter
R = nearest neighbour distance
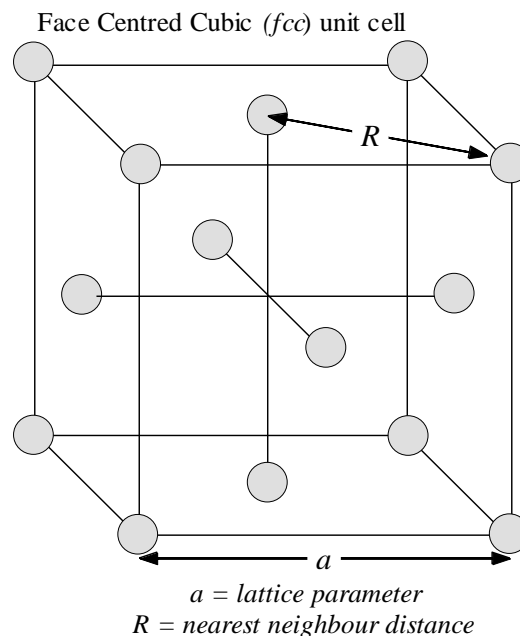
Figure I.1   **One unit of a face centred cubic (*fcc*) crystal lattice structure. This structure is adopted by the rare gas when sufficiently cooled. The lattice parameter, *a*, and the nearest neighbour distance, *R*, are displayed.**

These lattice points coincide with the RG atom's centre of mass. In an *fcc* crystal, each atom has twelve equidistant nearest neighbours arranged in a structure exhibiting cubo-octahedral symmetry, and the nearest neighbour distance, *R*, is given by Equation I.1.

---

[a] The melting point temperatures[32] of Ne, Ar, Kr and Xe are 24.6, 83.8, 115.8 and 161.4 K respectively.

$$R = \left(\frac{a}{\sqrt{2}}\right) = 0.707a \qquad\qquad \text{Eq. (I.1)}$$

where a is the lattice parameter. There are six next nearest neighbours located at a distance of one lattice parameter (a) away[37]. The lattice parameters[40] of the solid rare gases, Ne to Xe, are listed in Table I.2.

Table I.2   **Lattice parameter (a) and site sizes for the solid rare-gas hosts in a fcc unit cell. All distances are quoted in angstroms (Å) and were computed using the equations provided in the text. For the T_d and I_{oh} sites, the values in brackets represent the nearest neighbour distances.**

RG Solid	Lat. Param. (a) / CO(Å)[40]	T_d (Å)	I_{oh} (Å)	SV (Å)	TV (Å)	HV (Å)
Ne	4.462	0.709 (1.578)	1.307 (2.231)	3.155	3.699	3.864
Ar	5.312	0.844 (1.878)	1.556 (2.655)	3.756	4.404	4.598
Kr	5.644	0.897 (1.996)	1.653 (2.882)	3.991	4.679	4.884
Xe	6.131	0.974 (2.168)	1.796 (3.065)	4.335	5.083	5.308

The manner in which the rare gases are cooled determines the type of solid formed. A single fcc crystal, free from any defects, can only be prepared under special conditions. Simmons and co-workers[41-44] showed that such crystals could be formed by slow cooling from the liquid phase, using a well annealed 'seed' layer to initiate growth. Although 'perfect' crystals provide accurate structural information, such as the lattice parameter (a), they are rarely used as hosts because of their extreme reluctance to accept most guests – only very small atoms, such as hydrogen, are accommodated without disruption to the lattice. Rare gas matrices, on the other hand, are commonly prepared under non-equilibrium conditions and can readily accept large guest atoms or molecules. The matrix samples presented in this study were formed by rapid co-condensation of the vaporised guest metal with the desired RG host[b]. Matrices prepared in this fashion have been characterised with a variety of techniques, ranging from x-ray and neutron diffraction and scattering[45-47], to refractive index and adsorption capacity measurements[48-50] (using hydrogen as the adsorbate). These experiments reveal that vapour deposited solids are not completely crystalline or amorphous, rather,

---

[b] A detailed description of the M/RG (M = Sr, Ba; RG = Ar, Kr and Xe) sample preparation methods will be provided in Chapter II.

they are more accurately described as an ensemble of *fcc* microcrystalline grains, which are randomly orientated with respect to each other. These grains are separated by disordered regions called 'grain boundaries'. A schematic representation of a grain boundary (GB) is shown in Figure I.2.
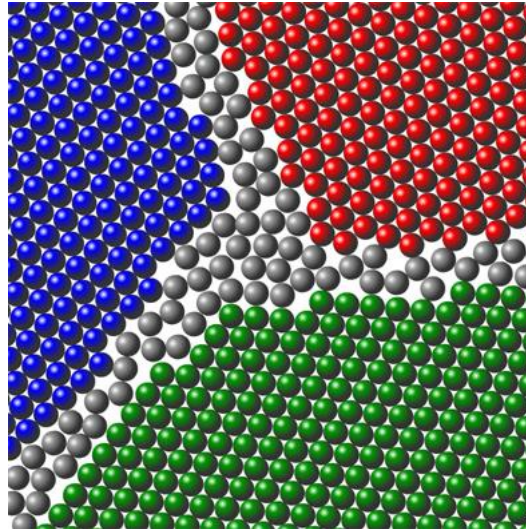
Figure I.2 **Schematic representation of a vapour deposited rare gas solid. The three *fcc* microcrystalline grains are depicted by the blue, green and red atoms. These grains are randomly orientated with respect to each other. The disordered 'grain boundary' region is represented by the grey atoms.**

In general, it was found that fast cooling and slow deposition leads to: 1. a very 'open' structure, with large GB voids and 2. imperfect *fcc* grains containing defects, such as vacancies and dislocations. Conversely, denser or more crystalline matrices, similar to those formed from the liquid phase, can be achieved by depositing at higher temperatures and/or matrix annealing[48]. The latter involves gently heating and re-cooling the sample to allow organisation of the lattice into its regular packing structure. Sr and Ba atoms exist in spherically symmetric ground states – similar to the rare gases. The regularly packed *fcc* lattice allows consideration of the possible sites of isolation for spherical ground state atoms within a microcrystalline grain. There exists six types of vacancies capable of accommodating a spherical guest atom, the size of each is displayed in Table I.2. Three of these sites are presented in Figure I.3, using a two layer space filled representation of a face centred cubic unit cell.

Lattice Parameter (*a*)
Substitutional Site or Single Vacancy (SV)
Octahedral Interstitial Site (I_{oh} Int.)
Tetrahedral Interstitial Site (T_d Int.)
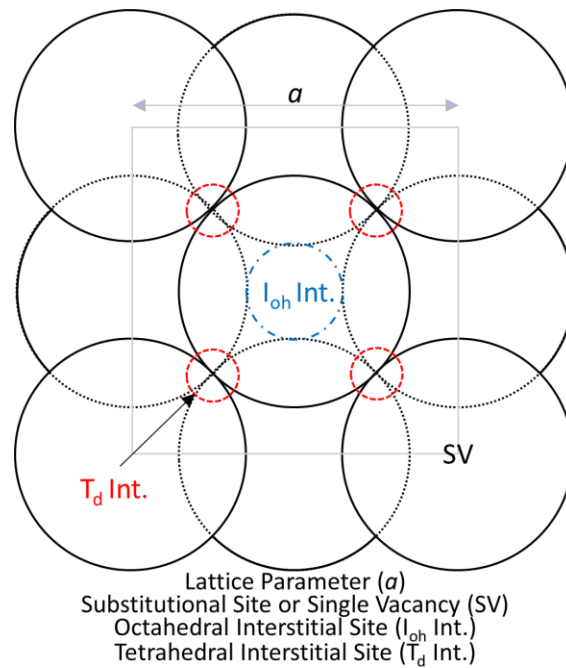
Figure I.3   **A two layer space filled representation of a *fcc* unit cell, highlighting both interstitial sites (I_{Oh} Int. and I_{Td} Int.) and the single vacancy (SV).**

Interstitial Sites

While there are countless ways of arranging identical spheres, the face centred cubic (*fcc*) and hexagonal close packed (*hcp*) structures make the most efficient use of space. The fraction of the total volume occupied by the spheres is 0.74 for both structures. Thus, in an *fcc* rare gas crystal, the host atoms occupy only 74 % of the total volume[51], leaving 26 % unoccupied where a small guest species may reside. This empty space gives rise to two distinct trapping sites which are intrinsic to the *fcc* crystal, they are: 1. the tetrahedral interstitial (T_d Int.) site and 2. the octahedral interstitial (O_h Int.) site.

The tetrahedral interstitial (T_d Int.) site is represented by the smallest circles in Figure I.3. Each *fcc* unit cell contains eight T_d Int. vacancies, four of which are shown in this figure. These sites are often referred to as tetrahedral holes as the vacancy is located at the centre of four rare gas atoms, forming a regular tetrahedron. Tetrahedral interstitial sites are extremely small and may only accommodate spheres of less than one quarter the diameter of the host atom[51]. Their diameter can be calculated using Equation I.2, where *sv* is the size of a single vacancy lattice site.

$$T_d = \left(\frac{\sqrt{3}}{\sqrt{2}} - 1 \right) sv \qquad \text{Eq. (I.2)}$$

The octahedral interstitial (I_{oh} Int.) site is a vacancy located at the centre of the *fcc* unit cell. A small sphere/atom isolated at this location has six nearest neighbours, arranged in a structure exhibiting octahedral symmetry. This site's size and position is displayed in the centre of Figure I.3. It can only accommodate spheres smaller than one half the diameter of the host atom[51]. The diameter of this vacancy can be calculated using Equation I.3:

$$I_{oh} = a - sv \qquad \text{Eq. (I.3)}$$

However, when assessing the site occupancy of a guest metal atom in the interstitial sites, it is more appropriate to compare the M·RG diatomic bond lengths to the internuclear separation of neighbouring atoms as opposed to the site diameter. The nearest neighbour distances for the tetrahedral ($nn\cdot T_d$) and octahedral ($nn\cdot I_{oh}$) interstitial sites are given by Equations I.4 and I.5, respectively. In addition, these values are listed in brackets in Table I.2. In these equations, *sv* is the diameter of a single vacancy site and *a* is the lattice parameter.

$$nn \cdot T_d = \frac{sv}{2} \qquad \text{Eq. (I.4)}$$

$$nn \cdot I_{oh} = \frac{a}{2} \qquad \text{Eq. (I.5)}$$

The interstitial sites are very small in size and cannot accommodate most dopant atoms. Hydrogen is the only neutral atom which has been convincingly shown to occupy such vacancies of the *fcc* rare gas (RG = Ar, Kr and Xe) crystal.[52,53]. On the other hand, charged species such as metal cations, may occupy interstitial sites. Indeed, recent MP2[31] and CCSD(T)[54] calculations of the 1:1 Eu$^+$·RG ground state potential energy curves revealed short equilibrium bond lengths (3.3 – 3.5 Å) for these singly-charged complexes. A comparison of these bond lengths with the nearest neighbour distances of the interstitial sites suggested that Eu$^+$ cations could be accommodated in I_{oh} sites of the RG lattice, especially Xe. Conversely, metal atoms which exhibit

relatively large van der Waals (vdW) radii, such as Sr and Ba[55,56], are not expected to reside in these intrinsic voids.

Single Substitutional or Single Vacancy Site (SV)

The next largest site available involves the removal of a single RG atom. The diameter (*sv*) of the single vacancy site can be computed from the lattice parameter using Equation I.1, i.e. *sv = R*. These sites are represented by the largest circles in Figure I.3 and their centres coincide with the *fcc* unit cell lattice points. In general, guest atoms exhibiting a van der Waals radius less than or equal to that of the rare gas atom will be accommodated in a single substitutional site[16].

Multi-Substitutional Sites

The vdW radii of the rare gas atoms are reported[55] as 1.88, 2.02 and 2.16 Å for Ar, Kr and Xe, respectively. The alkaline earths[55,56] exhibit significantly larger radii of 2.5 and 2.7 Å, for Sr and Ba respectively.
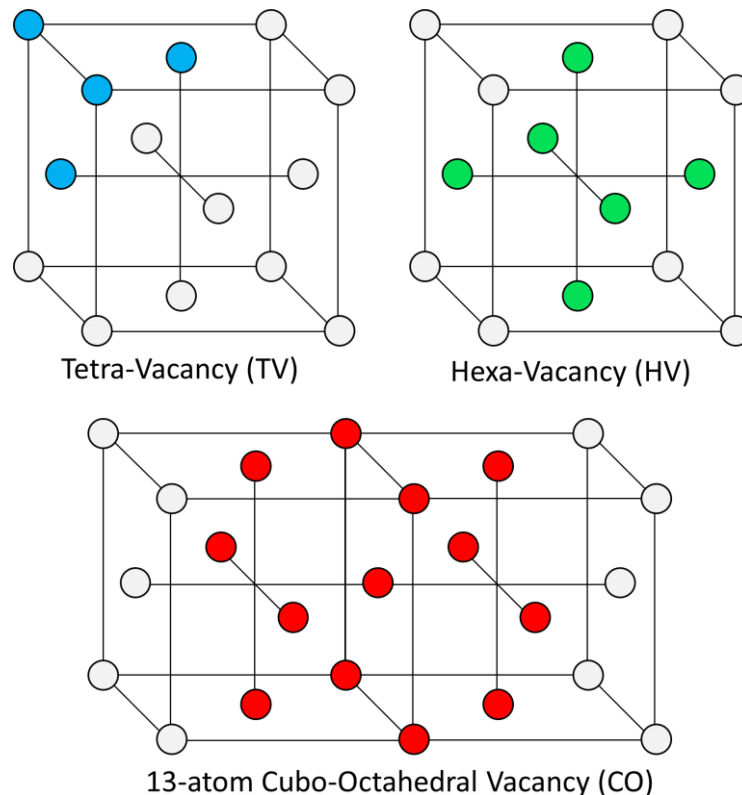

Figure I.4   *Fcc* **unit cells providing a visual representation of the rare gas atoms removed for the three types of multi-substitutional sites discussed in the text. Note that the diameters of the RG atoms are not to scale – they have been significantly reduced to facilitate a cleaner illustration.**

Even in Xe, which has the largest lattice parameter, the occupation of a single vacancy site may not occur owing to this size mismatch. Thus, larger voids, where more than one RG atom has been removed must be considered. Given the spherically symmetric nature of the ground states of Sr and Ba, a preference for sites of high symmetry is expected. The three smallest multi-atom vacancies that exist are illustrated in Figure I.4, and will now be discussed.

The tetra-vacancy (TV) site shares a common centre with the tetrahedral interstitial site and is generated by the removal of the four rare gas atoms arranged in a regular tetrahedron around this central point. The rare gas atoms removed are highlighted in blue in the top left of Figure I.4. The diameter of this vacancy can be computed from the lattice parameter using Equation I.6:

$$tv = \frac{\sqrt{11}}{4a}$$
Eq. (I.6)

A hexa-vacancy (HV) site corresponds to the removal of six rare gas atoms surrounding an octahedral interstitial site, as shown in the top right of Figure I.4. Thus, this site is characterised by octahedral symmetry and its centre coincides with the centre of an I_{oh} Int. vacancy. The diameter of a hexa-vacancy can be calculated using Equation I.7:

$$hv = \frac{\sqrt{3}}{2}a$$
Eq. (I.7)

The largest crystalline site of high symmetry considered in this study is the 13-atom cubo-octahedral vacancy (CO), which is created by the removal of a central rare gas atom and its twelve nearest neighbours. For a given RG host, the diameter of the CO site is equivalent to the lattice parameter (a). An illustration of the RG atoms removed from the *fcc* lattice to produce this vacancy is provided in the bottom of Figure I.4.

The possibility of grain boundary (GB) trapping cannot be excluded for metal atoms like Sr or Ba, which, as previously discussed, are characterised by large vdW radii. Indeed, molecular dynamics simulations conducted by Gervais and co-workers[57] revealed that the comparably large alkali metal atoms, Na and K, prefer to occupy

smaller cavities at grain boundaries rather than larger vacancies within the *fcc* grain. This arises because the removal of a large number of atoms to generate the bigger HV and CO sites (6 and 13 atoms respectively) destabilises the host due to the loss of lattice atom-atom interactions. However, grain boundaries offer more free volume than the bulk crystal and, as a result, many possible geometric arrangements exist. Unlike the regularly packed *fcc* crystal, it is therefore very difficult to identify the most likely trapping sites for a given guest, without the use of molecular dynamics simulations.

I.3   Matrix effects

The matrix-isolation technique was initially invented to provide an inert/non-interacting environment for transient or very reactive guest species. However, it was promptly realized that rare-gas matrices are not really inert, but can perturb, in some cases quite considerably, the isolated species and their spectra. Atoms in particular, are much more sensitive to the immediate environment than diatomic or polyatomic molecules. The relatively high degeneracies which occur in atomic levels would, for example, be removed by a trapping site with symmetry lower than the full rotation group $O(3)$[58]. Thus, the electronic transitions between these levels can be used as a sensitive probe of the solid state surroundings. Four important consequences of matrix embedding will now be discussed. Three of these pertain directly to electronic transitions of the atom within the solid, they are: 1. matrix shift, 2. Stokes shift and 3. the dynamic Jahn-Teller effect. The fourth is the observation of multiple, spectrally distinct trapping sites which can lead to broad and complex absorption profiles, and numerous emission features for a single electronic transition of the matrix-isolated metal atom.

I.3.I   Matrix shift

The electronic absorptions of a metal atom, embedded in a rare gas solid, do not occur at the same energy as in the gas phase. A frequency shift known as a 'matrix shift' is often observed and can be quite pronounced, particularly for P ← S type transitions[20,28]. The matrix shift (Δv_{abs}) is calculated using Equation I.8:

$$\Delta v_{abs} = v_{matrix} - v_{gas\ phase} \qquad \text{Eq. (I.8)}$$

where v_{matrix} and $v_{gas\,phase}$ correspond to the frequency (in cm^{-1}) of the transition, measured in a matrix and in the gas phase, respectively. The Franck-Condon (FC) principle plays an important role in understanding the nature of optical transitions of atoms in RG solids. According to this principle, the absorption of a photon is an instantaneous process during which the nuclei are enormously heavy as compared to the electrons. The electronic transition occurs on a time scale that is short compared to nuclear motion, so the transition probability can be calculated at a fixed nuclear position.

Consider a spherical ground state metal atom isolated in the SV site of a rare gas lattice, at low temperature (T ~ 10 K). The guest atom and the local RG environment are in an equilibrium/minimum energy configuration. According to the FC principle, the redistribution of electron density associated with an P ← S type transition occurs without a change in the positions of the surrounding RG atoms. The excited state is effectively larger than the ground state and a repulsive interaction arises between the occupied p orbital of the metal and the host. A result of this confinement is the deformation[59] of the p orbital which ensues to minimise overlap with the RG cores. This causes the excited state to be raised in energy with respect to that of the gas phase/free atom. The scenario just described is illustrated in the left-hand side of Figure I.5, with representative ground and excited state potentials for the metal-rare gas system. The repulsive interaction in the excited state is manifested as a shift in the equilibrium position of the excited state potential, with respect to that of the ground state. Although the 'vertical' transition begins from the lowest energy vibrational level of the ground state ($E_0(v_0)$), it terminates at a higher vibrational level of the excited state ($E_1(v_n)$). In this case, a matrix blue-shift would be observed in absorption.

In general, the matrix shift is a sum of two independent effects[16]: 1. short range repulsive interactions which decrease when the vacancy radius increases and 2. long range attractive interactions which increase with increasing host polarisability. The addition of both effects implies a better stabilisation of the excited guest atom in larger, more polarisable hosts. Therefore, in Xe matrices, absorptions of a given site type are often shifted to lower energy (red-shift) than the gas phase, while in Ar and Kr, matrix shifts to higher energy (blue-shift) are observed.

Solid state, matrix-isolated   Gas Phase
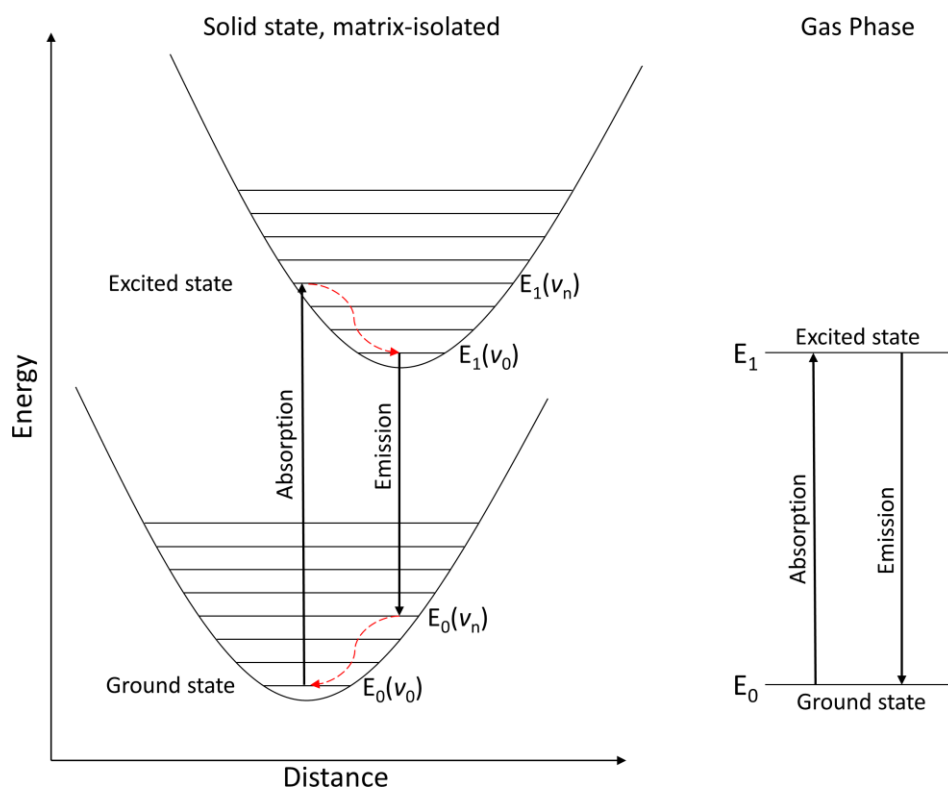
Figure I.5   **Right of figure: $E_{abs} = E_{em}$ for the metal atom in the gas phase. Left of figure: when embedded in a matrix, short range repulsive interactions with the host shift the excited state M-RG potential energy surface causing an increase in the absorption energy and also a Stokes shift between absorption and emission.**

I.3.II   Stokes shift

Figure I.5 (right) presents a schematic for an electronic transition of a gas phase atom. When a photon of sufficient energy impinges on the atom, absorption occurs from the ground state E_0 to the excited state E_1, corresponding to a transition energy $\Delta E_{1,0} = E_1 - E_0$. Following a finite period of time, the excited state decays via radiative emission back to the initial state. Absorption and emission occurs between the same two levels or states, hence the transition energies for both processes are equal, i.e., $\Delta E_{1,0}\,(Abs.) = \Delta E_{1,0}\,(Em.)$. Therefore, the emission and absorption lines spectrally coincide for the atom in the gas phase. In contrast, electronic transitions of matrix-isolated atoms exhibit a shift between the absorption and emission band maxima. This frequency difference is known as a Stokes shift and, like the matrix shift, arises due to the presence of the surrounding matrix cage. Its magnitude depends on the nature of the electronic transition.

The introduction of the luminescent centre (the atom) to a crystalline solid (RG) results in a Stokes' shift as $\Delta E_{1,0}\,(Abs.) > \Delta E_{1,0}(Em.)$. The difference in energy between

absorption and emission processes arises due to the interaction of the metal centre with lattice phonons in both the ground, E_0, and excited, E_1, states. Inspection of the left-hand side of Figure I.5 shows that a 'vertical' transition prepares the excited centre in a Frank-Condon configuration ($E_1(v_n)$) which does not correspond to the excited state minimum. Consequently, a fast non-radiative relaxation (red, curved arrow) must occur to the lowest energy phonon level, v_0, of the E_1 excited state. This relaxation process involves radiation of phonons, which are a characteristic of the lattice vibrational mode[60]. Almost all of the vibrational energy in the excited centre is lost by energy exchange with the phonon reservoir (i.e., the host lattice), producing heat in the system. Following this, the excited state decays via radiative emission back to the ground state potential energy surface.

$$\Delta E_{1,0}(Em.) = E_1(v_0) - E_0(v_n) \qquad \text{Eq. (I.9)}$$

However, FC considerations dictate that the higher energy phonon/vibrational levels of the ground state ($E_0(v_n)$) are populated from this electronic transition, and a second non-radiative relaxation must occur to return the system back to the ground state, $E_0(v_0)$. As a result, the emission energy $\Delta E_{1,0}(Em.)$ is given by Equation I.9 and the Stokes shift observed is the sum of the non-radiative energies occurring in both the ground and excited states.

I.3.III Dynamic Jahn-Teller effect

The absorption spectra recorded of matrix-isolated metals atoms undergoing P $\leftarrow$ S transitions often show a threefold split pattern. Such a characteristic bandshape can be attributed to the removal of the degeneracy associated with the three p (x, y and z) orbitals of the excited state. However, the exact mechanism of this effect was the source of much debate, over many years. Threefold split bands were observed, even in the earliest matrix studies conducted by McCarty and Robinson[12] on Na and Hg, and by Schnepp[13] on Mg and Mn atoms. At this stage, the explanations put forth were speculative. On the one hand, McCarthy and Robinson considered these M/RG systems to be "loosely coupled molecules in orbitally degenerate states", and as such, the Jahn-Teller[61] (JT) effect requires that the local lattice of the guest atom distorts to remove this degeneracy. On the other hand, Schnepp proposed that the threefold split was

caused by "an asymmetric crystal field perturbation on the trapped atom in the excited P state". Schnepp later presented calculations of the covalent and dispersion interactions between an excited (P state) Mg atom[14] and a single substitutional site of an *fcc* Ar lattice. It was tentatively concluded that the absorption triplet corresponded to a crystal field (CF) splitting, arising from the presence of an adjacent Ar vacancy, which removed the octahedral (O_h) symmetry of the site.

Although the JT[12] and CF[13,14,62] effects were the two main contentions, over the years alternate explanations for the threefold splitting pattern were also considered. After conducting systematic concentration studies on the Li/RG (RG = Ar, Kr and Xe) systems, Andrews and Pimentel[63] proposed that non-nearest neighbour, metal-metal interactions, were likely contributors to the observed absorption bandwidth and shape. In addition, Dudley and Ryan (1973) recorded absorption spectra of the P ← S transition of atomic Hg, which was isolated in RG matrices containing varying amounts of impurity gases, such as oxygen and nitrogen. They noticed that the relative intensities of each triplet peak varied as a function of impurity gas concentration and an assignment to three distinct trapping environments for atomic Hg was made.

In 1979, Schatz[64] and co-workers conducted a combined magnetic circular dichroism (MCD)/absorption study, focusing on the resonance $(3s5p)\ ^1P_1 \leftarrow (3s^2)\ ^1S_0$ transition of atomic Mg in the solid RG's. Three main conclusions emerged from this study: 1. The threefold splitting pattern arose from a <u>single</u> trapping site. 2. The orbital angular momentum of the $(3s3p)\ ^1P_1$ excited state is significantly quenched in all four RG matrices (RG = Ne, Ar, Kr and Xe), due to mixing of the Mg 3p orbitals with the orbitals of surrounding RG atoms. 3. A moment analysis, assuming octahedral site symmetry, revealed that a dominant non-cubic (Jahn-Teller active) mode contributed to the absorption bandwidth in the three hosts (Ar, Kr, Xe), where the characteristic threefold split pattern was observed. A Jahn-Teller explanation of this splitting, via $T_1 \times t_{2g}$ coupling, was thus proposed for Mg/RG. Soon afterwards, the MCD/absorption technique was extended to Li/RG solids[65]. This study showed that the Jahn-Teller effect was responsible for the P ← S threefold splitting pattern and, significantly, that simple CF models could not simultaneously account for both the absorption and MCD spectra observed. Finally, Rose *et al.*[66] (1986) recorded MCD and absorption spectra of Li/Xe and Na/Xe over a range of temperatures. A theoretical/lineshape analysis of these results by O'Brien and coworkers[67] demonstrated, conclusively, that the characteristic threefold split pattern was a consequence of a strong Jahn-Teller effect.
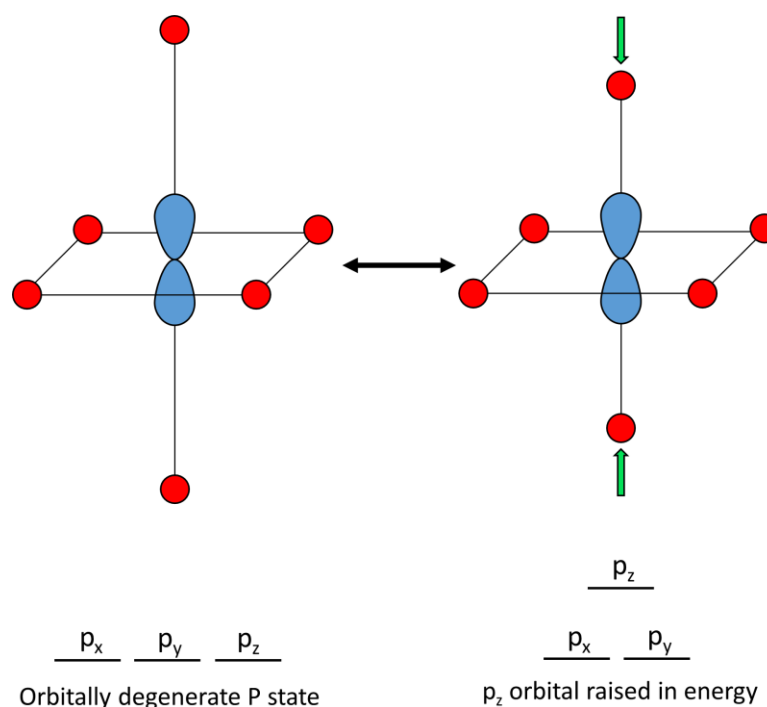
Figure I.6   **A representation of Jahn-Teller distortion of an electronically degenerate P state in the RG lattices. The distortion shown here lowers the symmetry of the RG environment from O_h to D_{4h}. Thus, the p_z orbital is raised in energy with respect to p_x and p_y. At least one more vibration must occur to remove the degeneracy associated with p_x and p_y, thereby producing a threefold split band in absorption.**

It is now widely accepted in the matrix-isolation community that JT effects are the source of the threefold splitting on $P \leftarrow S$ absorptions of metal atoms embedded in the RG's. The JT effect may be defined[61,68] as follows: for an electronically degenerate state in a site of high symmetry, distortion occurs to lower the symmetry and remove the degeneracy, thereby reducing the overall energy of the system. This is known as the 'dynamic Jahn-Teller effect' when there are several different structural distortions that are separated by small energy barriers[58]. An illustration of one of these distortions/vibrations is provided in Figure I.6. In the specific case of atomic Sr or Ba, we are dealing with a triply degenerate P (p_x, p_y, p_z) state, isolated in a highly symmetric, spherical site. Vibrations of the host lattice could lower the symmetry and remove the degeneracy, resulting in a threefold absorption band.

I.3.IV   Multiple metal atom trapping sites

As the M/RG vapour condenses into a solid at low temperatures, metal atoms will exhibit a preference for certain sites of isolation within the RG host. To a large extent,

the site occupancy is controlled by the vdW radius of the dopant atom and the sizes of the vacancies available in the host. As was discussed in Section I.2, the van der Waals radii[55,56] of Sr and Ba are quite large compared to those of the RG atoms, which suggests that these metal atoms will likely reside in multi-atom vacancies. Assuming that embedding occurs within an *fcc* grain, a more accurate approach would be to compare the sizes of the available sites (Table I.2) with experimentally determined 1:1 metal-rare gas (M·RG) ground state equilibrium bond lengths[69]. However, these values are currently not available for M = Sr and Ba. Thus, a portion of the work presented in this thesis (Chapter VI) is directed at obtaining high quality ground state interaction potentials for the M·RG (M = Ca, Sr and Ba: RG = Ar, Kr and Xe) diatomics, using empirical (Tang-Toennies[70,71]) and *ab initio* (CCSD(T)[72]) methods. With these calculated bond lengths, an assessment can be made regarding the site occupancy of Sr or Ba atoms in a RG lattice, and this greatly aids the interpretation of the absorption and luminescence observed for each M/RG system[27].

The simplest situation arises when the ground state M·RG bond length is smaller than the size of a single vacancy site in a given host. This criteria is usually only met in solid Xe. Due to the larger site sizes available, but also for rigidity reasons, Xe is known to be the most efficient rare gas matrix for the isolation of atomic species. The rigidity is directly related to the magnitude of the RG·RG diatomic dissociation energy (D_e) – these values are presented in Table I.3. For instance, metal atoms which exhibit a small vdW radius, such as Cd[24] or Hg[25], have been shown to occupy only single substitutional sites in annealed Xe matrices. Thus, the P ← S transitions recorded of these M/Xe systems are characterised by a single Jahn-Teller threefold-split band in absorption. Conversely, when the ground state M·RG bond length is larger than the size of the single vacancy, multiple site occupancy ensues – in other words, the metal atoms reside in more than one type of cavity. This usually occurs in the lighter RG solids and, as a consequence, the P ← S absorption profiles are broader and multi-featured due to contributions from more than one site. Typically, excitation spectra recorded of the site-specific emission bands are required to de-convolute these complex absorption profiles. Indeed, this was necessary for many of the metal atoms studied by the Maynooth Group, such as Eu[73]. Owing to the size of Sr and Ba, multiple site occupancy is expected within the rare gas solids.

Table I.3   **The lattice parameters (*a*) for the RG solids and the ground state bond lengths (*R_e*) for the RG dimers given in angstrom units. The dissociation energies (*D_e*) for the RG dimers are presented in wavenumber units.**

RG Solid	Lat. Param. (*a*) [40]	RG·RG	R_e (Å)	D_e (cm^{-1})
Ne	4.462	Ne·Ne[74]	3.091	29.4
Ar	5.312	Ar·Ar[75]	3.756	99.5
Kr	5.644	Kr·Kr[75]	4.017	138.4
Xe	6.131	Xe·Xe[75]	4.363	196.2

I.4   Spectroscopy of Sr/RG and Ba/RG solids

The literature on the spectroscopy of matrix-isolated Ba is quite limited – a surprising situation considering the direct connection between rare gas matrix work and studies probing the behaviour of atomic Ba in a variety of environments, including He-nanodroplets[76,77], solid and liquid helium[78] and large rare gas clusters[79-81]. A wealth of data has been accumulated from these related systems yielding insights, for example, into the excited P states forming bubbles in liquid helium or size exclusion effects forcing surface attachment on Ar clusters. Further compounding the lack of published work, the limited literature that does exist on matrix–isolated atomic Ba is in error in several regards. Thus, the original article published by Balling and Wright[82] (B&W) in 1985 as a comprehensive study of the absorption and emission spectra of Ba isolated in the three rare gas hosts Ar, Kr and Xe, is in fact restricted to results obtained in Ar. It turns out that the Ba/Kr spectra presented by B&W[82] are, as will be revealed in Chapter III of this thesis, actually annealed Ba/Ar data. Yet this article states, no effects were observed in "warm-up" (annealing) experiments. The same authors also reported that emission was not observed in the Ba/Xe system, speculating that the formation of a Ba—Xe chemical bond precluded the isolation of atomic Ba in this host.

Very recently, a study by Fairbank and coworkers[83], done as part of the nEXO project [PRL 109, 032505 (2012)] to determine the fundamental characteristics (mass) of neutrinos, demonstrated that emission does in fact occur in the Ba/Xe system. In this work, both neutral and singly ionised Ba atoms were deposited with Ar and Xe. Thus, the analysis presented was complicated as the authors had to contend with the possible presence of two distinct matrix-isolated species. In addition, the absorption and emission band assignments did not factor in the inherent contamination present in

Ba sources – its fellow Group II member, Sr. In this thesis, it will be shown that matrix-isolated Sr can contribute significantly to the absorption spectroscopy of Ba/RG samples. To address these basic deficiencies and resolve the evident complexities in the Ba/RG systems, a systematic study of both matrix-isolated Ba and Sr has been undertaken in the three hosts Ar, Kr and Xe. Moreover, the spectroscopy of Sr isolated in the solid RG's is itself worthy of a full investigation and will therefore be presented in detail alongside Ba.

Reviewing the literature reveals that the Sr/RG systems are also not well documented – only a few contributions exist. In 1976, Miller *et al*[84] recorded the absorption spectra of Mg, Ca, Sr and Ba isolated in Ar and Kr matrices. Their primary goal was to investigate the Group II, homonuclear and mixed heteronuclear, metal dimers. Consequently, the atomic spectra presented are all fully absorbing in the region of the dominant $(nsnp)$ $^1P_1 \leftarrow (ns^2)$ $^1S_0$ transition and cannot be used to extract information on the site occupancy of the metal atom. Soon afterwards, the emission spectrum of Sr_2 isolated in Ar, Kr and Xe matrices was recorded with laser excitation[85] (Kr^+ laser line at 676.4 nm). This study also briefly mentions the observation of emission bands in the region of both the $(5s5p)$ $^1P_1$ and $(5s5p)$ $^3P_1$ atomic states of Sr. In 1980, a more informative matrix MCD and absorption study was published, again by Miller *et al*[86], on Mg, Ca and Sr atoms isolated in Ne, Ar and Kr matrices and represents the first real attempt to examine the site occupancy of Sr. Overall, the spectra recorded for these alkaline earth atoms were difficult to interpret due to complex, overlapping absorption bands associated with guest occupancy in multiple sites of isolation.

I.5   Thesis layout

The results collected in this study are structured in the following manner. In Chapter III, a comparison of the UV/Vis absorption spectra recorded for both M/RG systems is presented. The main goals of this chapter are: 1. address the issue of the Sr contamination in Ba/RG samples and 2. identify the sample deposition parameters, which provide the most atomic M/RG samples, free from any additional species, such as impurity atoms and/or metal clusters ($M_{x>1}$). As was previously mentioned, the alkaline earth atoms exist in an $(ns)^2$ ground state electronic configuration, with $n = 5$

and 6 for Sr and Ba respectively. Thus, strong resonance $(nsnp)$ $^1P_1 \leftarrow (ns^2)$ $^1S_0$ transitions are observed in absorption and used to probe the local RG environment of the guest atom. Inspection of Figure I.7 reveals that these transitions occur in roughly the same energy region[34] for both metal atoms.
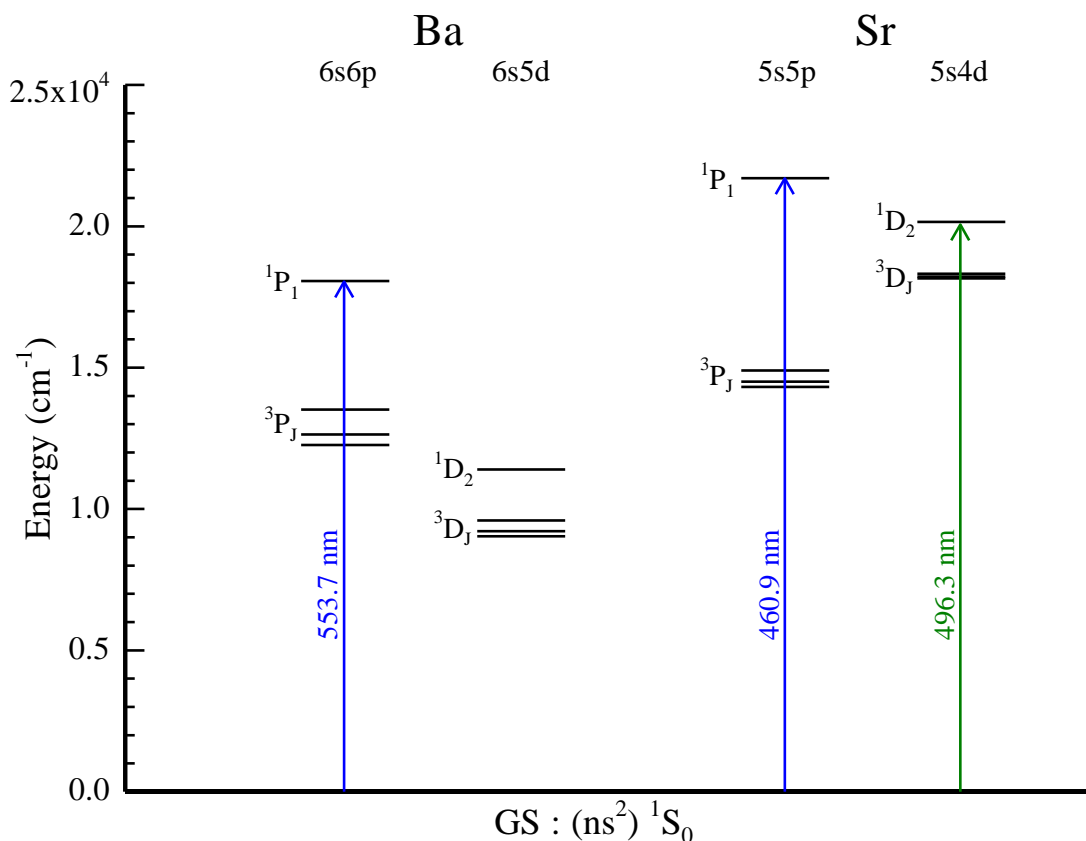

Figure I.7   **An energy diagram showing the levels of the alkaline earth metal atoms Ba and Sr which exist below 25,000 cm^{-1}. The resonance transitions of the two metal atoms occur in the visible/ near-UV spectral regions as indicated by the wavelengths specified. As can be seen, Sr exhibits D levels close to the resonance $^1P_1$ level. A parity-forbidden transition from the ground state to the (5s4d) $^1D_2$ excited state is shown by the vertical green arrow. In contrast the D states are lower than the ^3P in Ba, with the $^3D_1$ state the metastable level.**

Further scrutiny of Figure I.7 shows that the ordering of the lowest excited states is quite different for Sr and Ba. For Ba, the D states lie lower in energy than the ^3P_J manifolds and the $^3D_1$ state is the metastable level. In contrast, the $^1D_2$ and ^3D_J excited states of Sr are situated between the $^1P_1$ and ^3P_J manifolds, with $^3P_0$ being the metastable level. Moreover, the energy separation (1549 cm^{-1}) between the $^1D_2$ and $^1P_1$ levels is relatively small. This has profound consequences on the luminescence observed in the solid state because, when promoted the $^1P_1$ excited state, the matrix-isolated Sr atom has more relaxation pathways available than Ba. Thus, Sr/RG systems

exhibit emission bands associated with a multitude of excited states ($^1P_1$, $^1D_2$, ^3D_J and ^3P_J). In contrast, the luminescence of Ba/RG systems is simpler as only resonance (6s6p) $^1P_1 \rightarrow$ (6s^2) $^1S_0$ emission is observed in this study. Accordingly, the luminescence of the Ba/RG solids is presented first, in Chapter IV, and Chapter V is dedicated to the Sr/RG matrices. As resonance (nsnp) $^1P_1 \rightarrow$ (ns^2) $^1S_0$ emission is common to both metal atom systems, these results are presented in a similar fashion for each luminescence chapter:

1. An overview of the (nsnp) $^1P_1$ state fluorescence is provided with two dimensional – excitation and emission (2D-EE) spectra. These plots allow for changes to the entire luminescence to be easily tracked.

2. Excitation traces extracted from these 2D-EE spectra are used to resolve multiple site occupancies, which are convoluted in the (nsnp) $^1P_1$ absorption spectra. This is an essential step in analysing the site occupancy of these large metal atoms.

3. Steady-state emission scans are presented for each unique trapping site, as are temporal decay profiles obtained with pulsed-laser excitation. Moreover, temporal and spectral scans are recorded over a range of temperatures to identify the radiative lifetimes and investigate the possibility of non-radiative decay processes competing with the resonance fluorescence.

In Chapter V, after presenting the (5s5p) $^1P_1$ state fluorescence of Sr/RG matrices, full range emission scans are employed to identify bands arising from the lower lying excited states ($^1D_2$, ^3D_J and ^3P_J), which are produced indirectly with (5s5p) $^1P_1$ irradiation. The features observed are firstly attributed to a specific site of isolation, with the aid of 2D-EE spectra. Following this, assignment to a particular electronic transition is made based on the spectral (location and bandwidth) and temporal characteristics. In addition, the temperature dependences are reported to gain insight into the excited state dynamics leading to the observed emission bands. The parity-forbidden (5s5p) $^1D_2 \leftarrow$ (5s^2) $^1S_0$ transition of atomic Sr is not easy to observe in the gas phase, but is made allowed by a combination of the matrix environment and the small $^1P_1 - {}^1D_2$ energy separation (see Figure I.7). Therefore, the luminescence produced with (5s5p) $^1D_2$ excitation is also presented in Chapter V – the Sr/RG systems offer an

excellent opportunity to compare the interactions of two spatially different excited states (P and D) with a rare gas cage.

In Chapter VI, ground state 1:1 M·RG (M=Ca, Sr and Ba; RG = Ar, Kr and Xe) interaction potentials are modelled with the Tang-Toennies function[70] and computed using the *ab initio* CCSD(T) approach. A simple comparison of the M·RG and RG_2 potential energy curves (PECs) allows for comments to be made regarding the occupancy of Sr and Ba atoms within cubic sites of an *fcc* rare gas lattice. Combining this theoretical approach with a comparison of the site-specific excitation spectra, recorded for the alkaline earths in annealed rare gas matrices, permits tentative site assignments to be made. This global approach has proven successful in a previous M/Ne study from our group[20], where the sites occupied by atomic Mg, Zn and Cd were analysed in solid neon.

All of the experimental data reported in this thesis was recorded in the Low Temperature Laboratory in the Department of Chemistry, Maynooth University, Maynooth, Co. Kildare, Ireland. The details and specifications of the experimental apparatus and spectroscopic set-ups used to achieve these results are presented in Chapter II. In addition, the *ab initio* computations were implemented on a PC workstation (AMD64 quad-core 2.8 GHz processor) which was also located in the Department of Chemistry at Maynooth University.

References

[1]   J. McLennan, and G. Shrum, Proceedings of the Royal Society of London. Series A, Containing Papers of a Mathematical and Physical Character, 501 (1925).

[2]   G. N. Lewis, D. Lipkin, and T. T. Magel, J. Am. Chem. Soc. **63**, 3005 (1941).

[3]   G. N. Lewis, and D. Lipkin, J. Am. Chem. Soc. **64**, 2801 (1942).

[4]   I. Norman, and G. Porter, in *Proceedings of the Royal Society of London A: Mathematical, Physical and Engineering Sciences* (The Royal Society, 1955), pp. 399.

[5]   I. Norman, and G. Porter, Nature **174**, 508 (1954).

[6]   D. Ridgway, J. Chem. Educ. **51**, 224 (1974).

[7]   C. B. MOORE, Biographical Memoirs **90**, 275 (2009).

[8]   E. Whittle, D. A. Dows, and G. C. Pimentel, J. Chem. Phys. **22**, 1943 (1954).

[9]   E. D. Becker, and G. C. Pimentel, J. Chem. Phys. **25**, 224 (1956).

[10]   H. W. Brown, and G. C. Pimentel, J. Chem. Phys. **29**, 883 (1958).

[11]   G. E. Ewing, W. E. Thompson, and G. C. Pimentel, J. Chem. Phys. **32**, 927 (1960).

[12]   M. McCarty Jr, and G. W. Robinson, Mol. Phys. **2**, 415 (1959).

[13]   O. Schnepp, J. Phys. Chem. Solids **17**, 188 (1961).

[14]   M. Brith, and O. Schnepp, J. Chem. Phys. **39**, 2714 (1963).

[15]   B. Meyer, Berichte der Bunsengesellschaft für physikalische Chemie **82**, 24 (1978).

[16]   C. Crepin-Gilbert, and A. Tramer, Int. Rev. Phys. Chem. **18**, 485 (1999).

[17]   D. W. Ochsner, D. W. Ball, and Z. H. Kafafi, (1998).

[18]   D. W. Ball, L. Fredin, Z. H. Kafafi, R. H. Hauge, and J. L. Margrave, *A Bibliography of matrix isolation spectroscopy: 1954-1985* (Rice University Press, 1988).

[19]   J. G. McCaffrey, and G. A. Ozin, J. Chem. Phys. **101**, 10354 (1994).

[20]   B. Healy, P. Kerins, and J. G. McCaffrey, Low Temp. Phys. **38**, 679 (2012).

[21]   P. Kerins, B. Healy, and J. G. McCaffrey, Low Temperature Physics **26**, 756 (2000).

[22]   J. G. McCaffrey, and P. N. Kerins, J. Chem. Phys. **106**, 7885 (1997).

[23]   V. A. Bracken, P. Gürtler, and J. G. McCaffrey, J. Chem. Phys. **107**, 5290 (1997).

[24]   B. Healy, and J. G. McCaffrey, J. Chem. Phys. **110**, 3903 (1999).

[25]   M. A. Collier, and J. G. McCaffrey, J. Chem. Phys. **119**, 11878 (2003).

[26]   M. A. Collier, M. C. Ryan, and J. G. McCaffrey, J. Chem. Phys. **123**, 044508 (2005).

[27]   M. A. Collier, O. Byrne, C. Murray, and J. G. McCaffrey, J. Chem. Phys. **132**, 164512 (2010).

[28]   M. Ryan, M. Collier, P. d. Pujo, C. Crépin, and J. G. McCaffrey, J. Phys. Chem. A **114**, 3011 (2009).

[29]   O. Byrne, and J. G. McCaffrey, J. Chem. Phys. **135**, 024507 (2011).

[30]   M. A. Collier, and J. G. McCaffrey, J. Chem. Phys. **119**, 11888 (2003).

[31]   O. Byrne, B. Davis, and J. G. McCaffrey, J. Chem. Phys. **142**, 054307 (2015).

[32]   W. M. Haynes, *CRC handbook of chemistry and physics* (CRC press, 2014).

[33]   J. C. Phillips, Phys. Rev. **136**, A1714 (1964).

34   A. Kramida, Y. Ralchenko, J. Reader, and NIST ASD Team. NIST Atomic Spectra Database (ver. 5.2). Available at: http://physics.nist.gov/asd [2015, October]. National Institute of Standards and Technology, Gaithersburg, MD.

35   G. M. Lawrence, Phys. Rev. **175**, 40 (1968).

36   K. Yoshino, and Y. Tanaka, J. Opt. Soc. Am. **69**, 159 (1979).

37   C. Kittel, *Introduction to Solid State Physics* (John Wiley & Sons Inc., 1996), Ed. 7th.

38   J. S. Rowlinson, *Cohesion: a scientific history of intermolecular forces* (Cambridge University Press, 2002).

39   G. L. Pollack, Rev. Mod. Phys. **36**, 748 (1964).

40   H. E. Hallam, *Vibrational Spectroscopy of Trapped Species* (Wiley - Interscicnce, New York, 1973).

41   O. Peterson, D. Batchelder, and R. Simmons, Phys. Rev. **150**, 703 (1966).

42   O. Peterson, D. Batchelder, and R. Simmons, J. Appl. Phys. **36**, 2682 (1965).

43   D. Losee, and R. Simmons, Phys. Rev. **172**, 944 (1968).

44   D. Batchelder, D. Losee, and R. Simmons, Phys. Rev. **162**, 767 (1967).

45   W. Langel, W. Schuller, E. Knözinger, H. W. Fleger, and H. Lauter, J. Chem. Phys. **89**, 1741 (1988).

46   W. Langel, A. Becker, H.-W. Fleger, and E. Knözinger, J. Mol. Struct. **297**, 407 (1993).

47   E. Knözinger, W. Schuller, and W. Langel, Faraday Discussions of the Chemical Society **86**, 285 (1988).

48   W. Schulze, and D. M. Kolb, Journal of the Chemical Society, Faraday Transactions 2: Molecular and Chemical Physics **70**, 1098 (1974).

49   H. Abe, and W. Schulze, Chem. Phys. **41**, 257 (1979).

50   Y. Haas, and U. Samuni, Prog. React. Kinet. **23**, 211 (1998).

51   S. Cradock, and A. J. Hinchcliffe, *Matrix Isolation, A technique for the study of reactive inorganic species* (Cambridge University Press, 1975).

52   S. N. Foner, E. L. Cochran, V. A. Bowers, and C. K. Jen, J. Chem. Phys. **32**, 963 (1960).

53   R. Alimi, R. Gerber, and V. Apkarian, J. Chem. Phys. **89**, 174 (1988).

54   A. A. Buchachenko, and L. A. Viehland, J. Chem. Phys. **140**, 114309 (2014).

55   M. Mantina, A. C. Chamberlin, R. Valero, C. J. Cramer, and D. G. Truhlar, The Journal of Physical Chemistry A **113**, 5806 (2009).

56   S. S. Batsanov, Inorg. Mater. **37**, 871 (2001).

57   E. Jacquet, D. Zanuttini, J. Douady, E. Giglio, and B. Gervais, J. Chem. Phys. **135**, 174503 (2011).

58   T. Wolfram, and Ş. Ellialtıoğlu, *Applications of group theory to atoms, molecules, and solids* (Cambridge University Press, 2014).

59   D. Zanuttini, J. Douady, E. Jacquet, E. Giglio, and B. Gervais, J. Chem. Phys. **133**, 174503 (2010).

60   V. Ter-Mikirtychev, and V. Ter-Mikirtychev, Fundamentals of Fiber Lasers and Fiber Amplifiers, 7 (2014).

61   H. A. Jahn, and E. Teller, in *Proceedings of the Royal Society of London A: Mathematical, Physical and Engineering Sciences* (The Royal Society, 1937), pp. 220.

62   S. L. Kupferman, and F. Pipkin, Phys. Rev. **166**, 207 (1968).

63   L. Andrews, and G. C. Pimentel, J. Chem. Phys. **47**, 2905 (1967).

64   R. L. Mowery, J. C. Miller, E. R. Krausz, P. N. Schatz, S. M. Jacobs, and L. Andrews, J. Chem. Phys. **70**, 3920 (1979).

65   P. Lund, D. Smith, S. Jacobs, and P. Schatz, The Journal of Physical Chemistry **88**, 31 (1984).

66   J. Rose, D. Smith, B. Williamson, P. Schatz, and M. O'Brien, The Journal of Physical Chemistry **90**, 2608 (1986).

67   M. O'Brien, J. Chem. Phys. **82**, 3870 (1985).

68   H. Jahn, in *Proc. Roy. Soc.(London) A*1938), p. 117.

69   M. A. Collier, and J. G. McCaffrey, J. Chem. Phys. **122**, 54503 (2005).

70   G. P. Yin, P. Li, and K. T. Tang, J. Chem. Phys. **132**, 074303 (2010).

71   K. T. Tang, and J. P. Toennies, J. Chem. Phys. **118**, 4976 (2003).

72   F. Jensen, *Introduction to computational chemistry* (John Wiley & Sons, 2013).

73   O. Byrne, and J. G. McCaffrey, J. Chem. Phys. **134**, 124501 (2011).

74   R. A. Aziz, and M. Slaman, Chem. Phys. **130**, 187 (1989).

75   J. G. Kaup, and W. Breckenridge, The Journal of Physical Chemistry **99**, 13701 (1995).

76   E. Loginov, and M. Drabbels, J. Chem. Phys. **136**, 154302 (2012).

77   X. Zhang, and M. Drabbels, J. Chem. Phys. **137**, 051102 (2012).

78   V. Lebedev, P. Moroshkin, and A. Weis, Phys. Rev. A **84**(2011).

79   J. Visticot *et al.*, J. Chem. Phys. **100**, 158 (1994).

80   M. Briant, M. A. Gaveau, and J. M. Mestdagh, J. Chem. Phys. **133**, 034306 (2010).

81   A. Masson, L. Poisson, M. A. Gaveau, B. Soep, J. M. Mestdagh, V. Mazet, and F. Spiegelman, J. Chem. Phys. **133**, 054307 (2010).

82   L. Balling, and J. Wright, J. Chem. Phys. **83**, 2614 (1985).

83   E. X. O. C. n *et al.*, Phys. Rev. A **91**, 022505 (2015).

84   J. C. Miller, B. S. Ault, and L. Andrews, J. Chem. Phys. **67**, 2478 (1977).

85   J. C. Miller, and L. Andrews, J. Chem. Phys. **69**, 936 (1978).

86   J. C. Miller, R. L. Mowery, E. R. Krausz, S. M. Jacobs, H. W. Kim, P. N. Schatz, and L. Andrews, J. Chem. Phys. **74**, 6349 (1981).

Chapter II
Experimental

II.1   Introduction

As described in Chapter I, the term 'matrix-isolation' encompasses a range of techniques where guest atoms or molecules are trapped in rigid host materials[1]. However, the experimental method used in this work specifically relates to George Pimentel's approach: the species of interest is mixed with a large excess of an inert (mostly) host gas and condensed on a surface that is sufficiently cold to assure rapid solidification of the material[2]. In this project, Ba or Sr vapour was generated and co-condensed with the rare gases (RG = Ar, Kr and Xe) onto a spectroscopic window, held at cryogenic temperatures. This chapter describes, in detail, the experimental set-up used to form and spectroscopically characterise the matrix-isolated M/RG (M = Sr, Ba) samples, and is arranged as follows. Firstly, the matrix-isolation apparatus employed to achieve high vacuum and low temperatures is presented. Secondly, an account is given of the dedicated gas-handling system (GHS). Thirdly, the two methods used for metal vapourisation are described and an outline of a typical sample deposition is provided. Finally, the steady-state and time-resolved spectroscopic apparatus used to characterise each M/RG sample is described.

II.2   Matrix-isolation apparatus

A schematic of the matrix-isolation apparatus used in this work is presented in Figure II.1. Vacuum of less than 1×10^{-7} mbar was attained inside the sample chamber with a Speedivac oil diffusion pump backed by an Edwards rotary pump[3]. The pressure was monitored with an Alcatel Penning Gauge (Model CF2P). An Edwards quarter-swing butterfly valve allowed the sample chamber to be isolated from the pumping system – a convenient arrangement when opening the system to atmosphere and/or purging with nitrogen. A liquid nitrogen cold trap positioned on top of the diffusion pump prevented back streaming of hot oil vapour towards the sample window when it was cooled. The specifications of the components required to achieve high vacuum in the matrix-isolation rig are given in Table II.1.
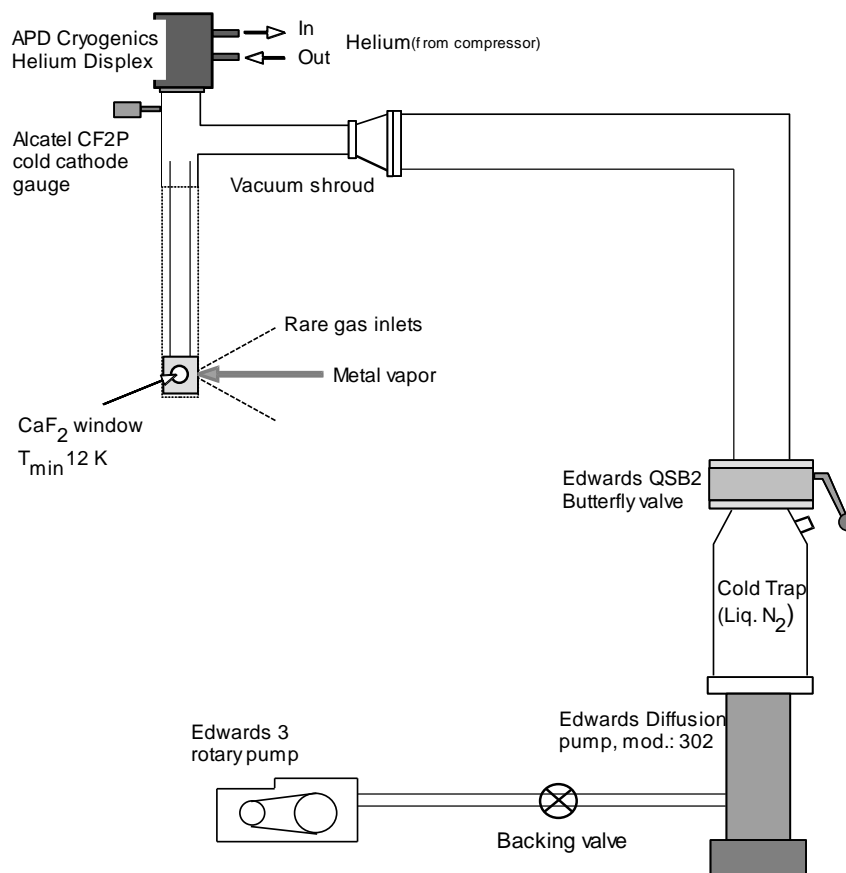
Figure II.1   An overview of the matrix-isolation apparatus used in this work.

Table II.1   Details of the components which comprised the pumping system.

Component	Manufacturer	Model/Part number
Quarter-Swing butterfly valve	Edwards	QSB2
Rotary Vacuum Pump	Edwards	RV3
Oil Vapour Diffusion Pump	Edwards	E02

Cryogenic temperatures were achieved with an APD expander[4] which was operated by a helium compressor[5]. The water-cooled, rotary compressor delivers high pressure ($260 - 265$ psi) and high purity (99.995 %) helium gas to the expander through a flexible and braided stainless steel supply line. The expander is a two-staged refrigerator that operates on the Gifford-McMahon cycle[6]. The cooling process is derived from the expansion of the high pressure helium. A rotating valve disc in the expander controls the intake (high pressure), expansion and exhaust (low pressure) of gaseous helium and runs at a frequency of 50 Hz. The low pressure helium is then

passed back to the compressor where it is purified and prepared for re-use – a closed cycle system. The specifications of the cryogenic refrigeration system are presented in Table II.2.

Table II.2 **Details of the components necessary to achieve and monitor low temperatures (~10K) at the sample window.**

Component	Manufacturer	Model/Part number
Expander[4]	APD Cryogenics	DE-202
Helium compressor[5]	APD Cryogenics	HC-2D
Refrigerator[7]	APD Cryogenics	DMX-1AE
Silicon diode[8]	Scientific Instruments	SI-410A diode
Digital Temperature Controller[8]	Scientific Instruments	SI-9600-1

The two-stage refrigerator sat inside a vacuum shroud which was custom built and supplied by APD cryogenics, as shown in Figure II.2. The pumping system described above, created a vacuum envelope which allowed low temperatures to be reached and provided a suitable and clean environment for matrix-isolation. Calcium fluoride (CaF_2) was the chosen substrate material, upon which matrix-isolated samples were deposited. In addition to a high transmission over a wide spectral range (130 - 9000 nm), these windows are also chemically inert, non-hydroscopic and quite durable. The CaF_2 spectroscopic window was situated at the base of the shroud and attached to the second stage of the refrigeration system. A copper holder secured the window in place and an indium wire seal ensured good thermal contact between the two. A custom built radiation shield surrounded the sample substrate and the second stage of the refrigerating unit. This allowed for a base temperature of 10 K to be achieved at the window. Cool down of the sample window usually took $60 - 70$ minutes. Following this process, the pressure inside the matrix rig was typically measured to be below 3 x 10^{-8} mbar – a result of cryopumping.

Accurate knowledge of the CaF_2 window and matrix temperature was very important in this study. For example, emission scans and excited state lifetime measurements were usually made over a range of temperatures to identify radiative lifetimes and access the contribution of non-radiative feeding steps to the overall decay process. The temperature was measured with a Scientific Instruments 9600-1 silicon diode which was fastened to the copper holder. In addition, a dedicated heater[8] was

also mounted to holder, allowing the CaF$_2$ window to be warmed above base temperatures. The uncertainty associated with the measurement of temperature is specified as $\pm$ 0.5 K from 1.5 –to 35 K, and $\pm$ 1.0 K from 35 –to 300 K[8]. To ensure that the CaF$_2$ window and M/RG sample were in thermal equilibrium, a 'settling' time of at least five minutes was observed every time the temperature was changed.
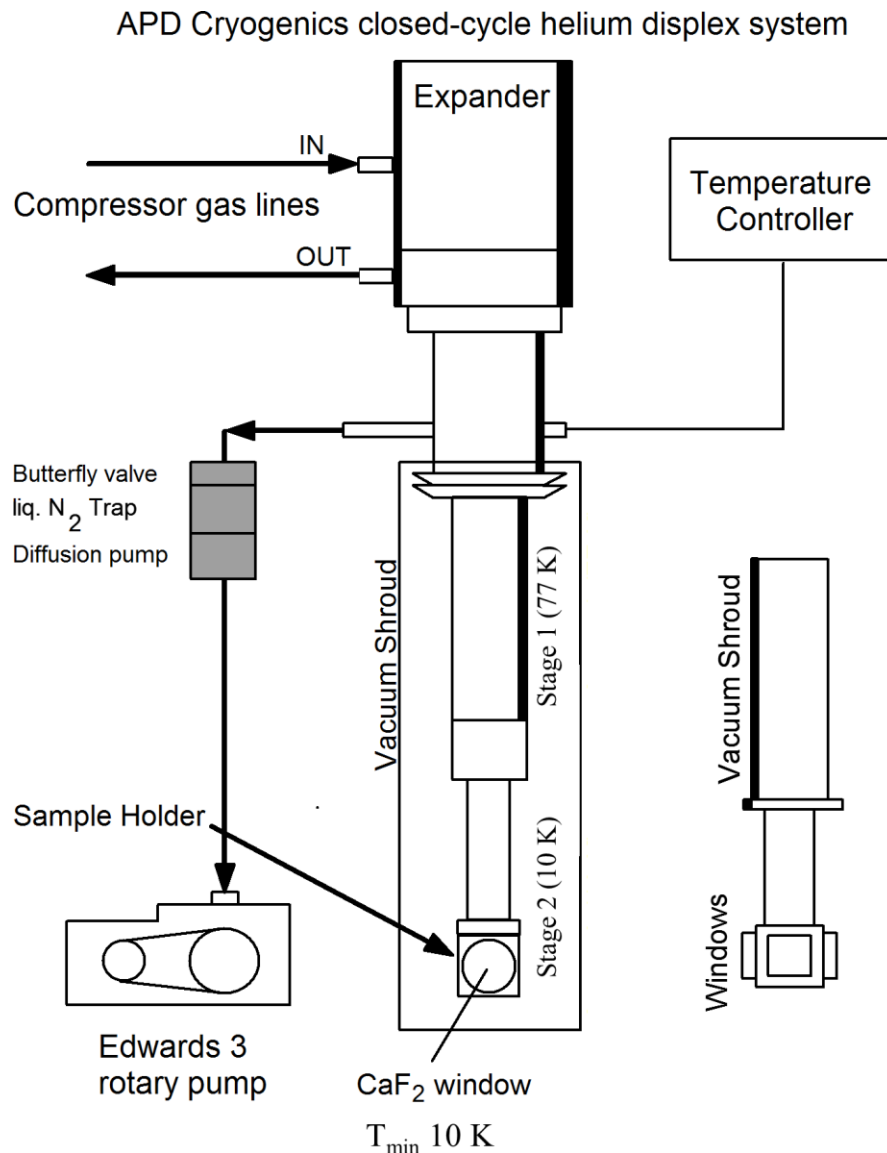

Figure II.2 **APD Helium displex showing the two-staged refrigeration set-up. A vacuum shroud surrounds the expander and sample window.**

A plan view of the sample compartment is illustrated in Figure II.3. Three faces of the chamber cube were covered by a one inch diameter optical window. The sample window was free to rotate by 360^0 to allow for transmittance scans directly through the

sample or excitation/emission scans recorded monitoring emission perpendicular to the excitation source. The fourth face allowed for a metal vapour source and host gas inlets to be attached. The bottom of the cube consisted of a blank cover. The immediate connections to the five faces of the sample compartment were sealed with Viton® O-rings.

Plan of vacuum shroud
surrounding optical sample holder
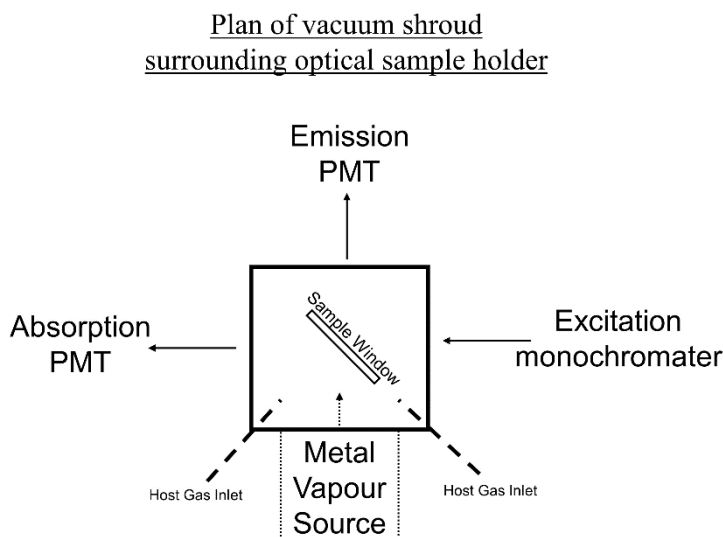
Figure II.3   **Plan view of the sample compartment.**

II.3   Gas-Handling system (GHS)

The matrix gases used in this study were prepared in a separate, high vacuum gas handling chamber. This set-up ensured that the host gases were kept pure and allowed gas mixtures to be prepared without interfering with the sample chamber. A schematic of this set-up is presented in Figure II.4 and a list of the individual components is given in Table II.3. Vacuum in the low 10^{-8} mbar range was achieved by a Pfeiffer Balzer turbo-molecular (TPU-180H) pump[9], backed by an Edwards high vacuum rotary pump[10] (E2M-18). The rotary pump was positioned below the turbo pump to limit backstreaming of its lubricating oil. The GHS vacuum was monitored with an ionization gauge[11], combined with a Granville-Phillips (GP) controller[12] (model 307). The pressure of host gas present in the system before, during and after sample deposition was monitored by two baratron gauges (Tylan General: CDLD-11 and CDLD-31) which were sensitive in the ranges 0 - 10 and 0 - 1000 Torr respectively[13]. A Granville-Phillips variable leak valve[11] (Model 203) allowed for the controlled admittance of the host gas into the sample chamber. Thus, the rate of host gas flow

during a sample deposition could be accurately controlled. The host gases employed in this work to isolate Sr and Ba are listed in Table II.4.
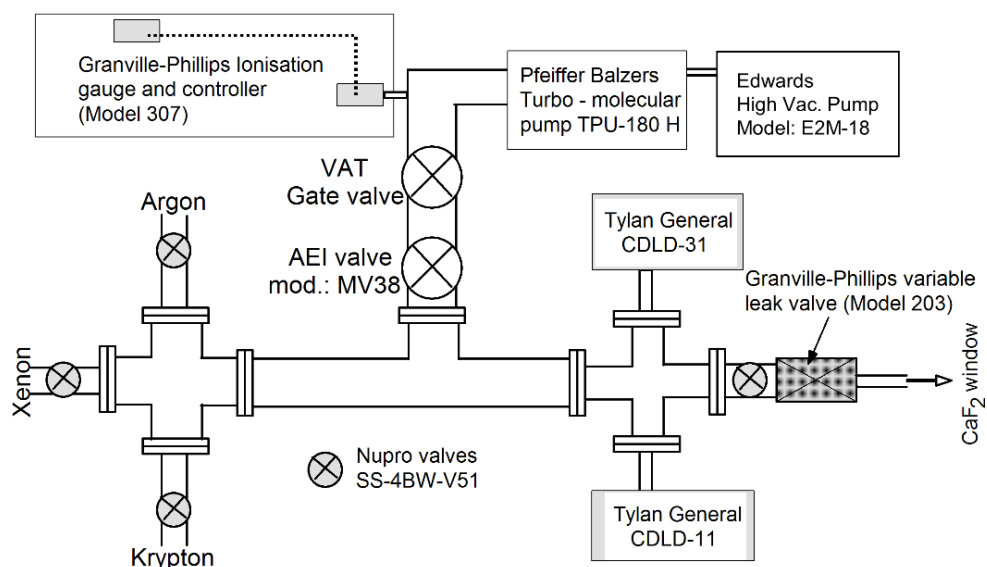

Figure II.4   **The dedicated Gas Handling System.**

Table II.3   **Details of the components which comprise the gas handling system (GHS).**

Component	Manufacturer	Model/Part number
Turbo-molecular pump[9]	Pfeiffer	TPU-180H
Rotary pump[10]	Edwards	E2M-18
Control unit[12]	Granville-Phillips	307
Ionisation gauge[12]	Granville-Phillips	274043
Baratron gauge (0-10 Torr)[13]	Tylan General	CDLD-11
Baratron gauge (0-1000 Torr)[13]	Tylan General	CDLD-31
Variable leak valve[11]	Granville-Phillips	203

Table II.4   **Matrix host gases, suppliers and purity. Mp represents the melting point of each gas, in unit of Kelvin.**

Host Gas	Purity	Supplier	M_P (K)[14]
Ar (Ar)	99.998 %	BOC Gases	83.79
Kr (Kr)	99.998 %	Linde Gases	115.79
Xe (Xe)	99.999 %	CK Special Gases	161.41

II.4   M/RG sample preparation

Solid M/RG (M = Ba, Sr; RG = Ar, Kr and Xe) samples were formed by co-condensing metal vapour with the host gases onto a CaF_2 substrate. The window temperature ranged from 10 K (base) up to approximately one quarter of the melting point of the host gas, depending on the desired sample characteristics. For instance, depositing at elevated temperatures can lead to simpler atomic isolation as the matrix solid would be more densely packed or crystalline, and the occupation of thermally unstable trapping sites is reduced. However this comes with a caveat. A higher window temperature means the metal atoms are more mobile on the surface of the forming matrix and hence more likely to encounter each other and form clusters. A key aspect of this work was to investigate the conditions yielding the most atomic M/RG samples, with the least number of sites for the atom.

Two methods of metal vaporisation were employed. The first was with electron bombardment of Ba or Sr pieces held in a Mo crucible, as used in most of our previous metal atom investigations[15,16]. The second method involved resistive heating of a metal dispenser. Thermal vaporisation was used in an attempt to preclude charged species, such as Ba cations being deposited in the samples. Chapter III describes in detail the sample characterisation of both Ba/RG and Sr/RG systems and the need for two distinct techniques for generating metal vapour. Both methods are now discussed individually.

II.4.I   Electron bombardment

Vapourisation via electron bombardment was achieved with an ultra-high vacuum Omicron (EFM3) electron gun, the details of which can be examined in Figures II.5, II.6 and Table II.5. The metal pieces (either Ba or Sr, see Table II.5) were loaded into a molybdenum (Mo) crucible[17]. While the crucible was held at a high voltage (500 – 700 V), a current was passed through a tungsten filament that was situated a few millimetres away. The voltage differential across both components causes electrons from the filament to be accelerated towards the crucible and hence metal source. The bombarding electron beam (e-beam) induces an acute temperature rise localised onto a small spot on the surface of the metal pieces. Given the right crucible voltage and filament current, the temperature of this spot exceeds the melting and boiling points of the metal[14] (see Table II.5) producing a stream of vaporised material.
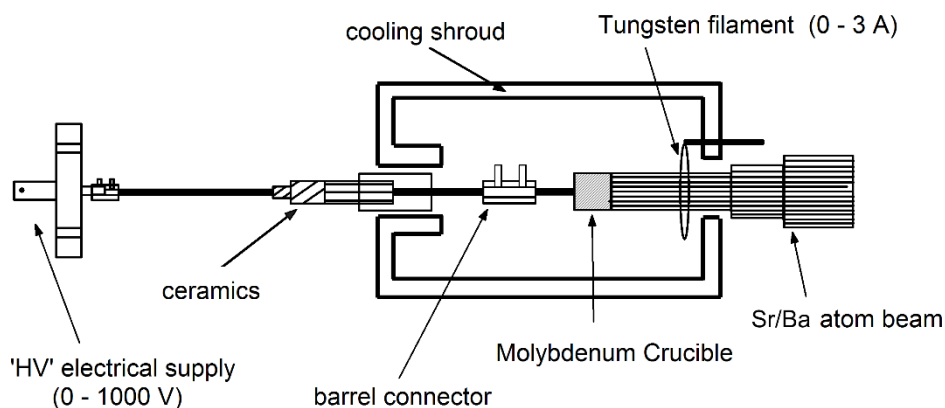
Figure II.5   **A representation of the Mo crucible and the interior of the evaporation cell.**
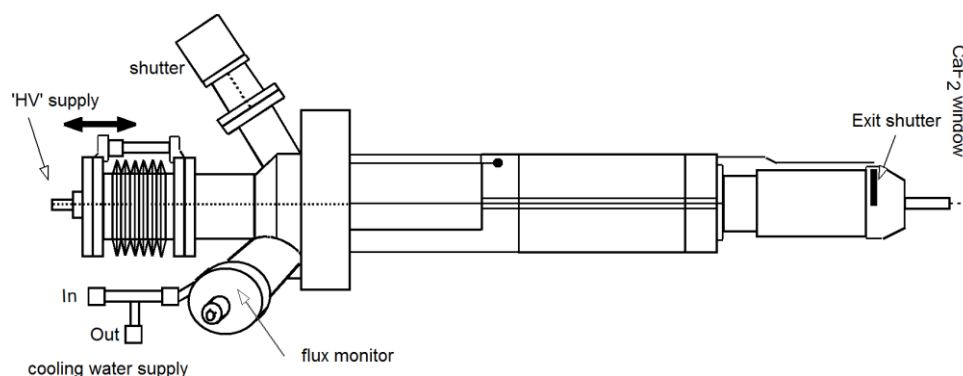

Figure II.6   **A schematic of the Omicron EFM3 electron gun and integrated flux monitor.**

The beam exit column contained an ion collector which served as integrated flux monitor. At a given filament current and e-beam energy, the ion flux measured is directly proportional to the flux of evaporated atoms. The flux monitor can therefore provide a real-time measurement of the amount of metal being vaporised and deposited in a given sample. However, as irregular sized pieces of metal were used in this work, the flux observed was dependent on the crucible packing, and was not consistent between samples because reproducible loading was not possible. Therefore, the flux monitored during sample deposition served only as a guide. Ultimately, the exact quantity of metal in a given sample was measured via absorption spectroscopy following sample deposition. An exit shutter positioned between the crucible and sample window controlled the admittance of metal vapour during the deposition process. The metal flux could therefore be stabilised with the shutter closed prior to co-condensation with the host gas.

As Ba and Sr readily form metal oxides in air, a number of steps were taken to minimise contamination during each crucible re-fill. A preparative step involved gentle filing of the metal surface in the crucible before loading onto the vacuum chamber which was purged with gaseous nitrogen. The EFM evaporator has a convenient rear-loading feature which enables crucibles to be quickly re-filled without detaching the whole unit from the matrix rig. Once under vacuum, the evaporant was degassed prior to sample deposition. This was done in two stages. Firstly, the tungsten filament was outgassed by slowly increasing the current without high voltage on the crucible. Secondly, any contaminants or metal oxides were removed from surface of the bulk metal by vaporising the metal (as described above) with the exit shutter closed. Outgassing was completed when a stable metal flux could be maintained without a noticeable pressure rise in the sample chamber.

Table II.5   **Details of the components comprising the electron bombardment vaporisation method. The melting/boiling point (M_p/B_p) of each metal is given in unit of Kelvin.**

Item	Manufacturer	Model/Item number	Details
Electron gun[18]	Omicron	UHV EFM3	I_{fil}: $0 - 2.5$ A
Crucible[17]	Omicron	B000432-S	Outer diameter: 8.0 mm Inner diameter: 6.0mm Capacity 250 mm^3 T_{max}: 2473 K
Ba	Sigma-Aldrich	403334-10G	99 % purity M_p/B_p[14]: 1000/2170 K
Sr	Sigma-Aldrich	343730-10G	99 % purity M_p/B_p[14]: 1050/1655 K

II.4.II   Thermal vaporisation

A gentler vapourisation method was achieved with resistive heating of a metal dispenser. Ba and Sr getters were purchased from Alvatec[19] and modified to facilitate attachment to our matrix-isolation rig. The dispensers are specially produced under high vacuum conditions. They consist of a small stainless steel tube which is sealed by a pressed indium layer. The bulk metal resides in an inert Ar atmosphere and is free of any adsorbed contaminants or oxides.

The dispenser was mounted on a high vacuum electrical feedthrough which was attached to the front face of the sample chamber with a CF flange[20]. A cylindrical stainless steel radiation shield and cap (attached to the base of the feedthrough) surrounded the dispenser. An aperture (5 mm in diameter) in the centre of the cap allowed the metal vapour to escape in the direction of the sample window with minimal radiative heating. The whole unit was positioned such that the centre of the dispenser was aligned with the centre of the CaF_2 window. A schematic of this set-up is presented in Figure II.7 and the specifications are given in Table II.6.
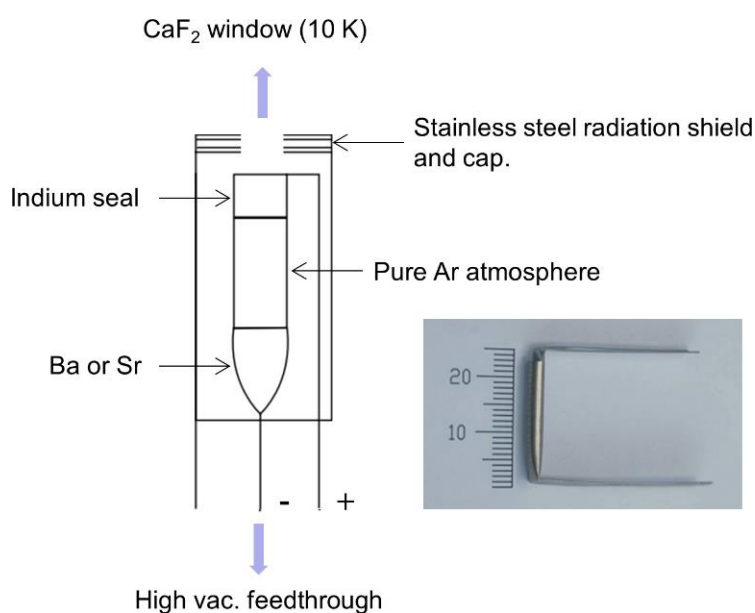
Figure II.7   **A schematic of the metal dispenser and stainless steel housing.**

Table II.6   **Details of the components comprising the thermal vaporisation method.**

Metal dispenser	Manufacturer	Model	Details
Ba[19]	Alvatec	AS-3-Ba-50-C	Diameter: 3 mm Capacity: 50 mg
Sr[19]	Alvatec	AS-3-Sr-50-C	Diameter: 3 mm Capacity: 50 mg

Once mounted under high vacuum, the dispenser was heated with a variac controlled electrical supply. Initial heating involved applying a low current (2-3 A) to melt the indium seal on the top of the dispenser. Ar gas, used as an inert environment in the compartment, was thereby released exposing the metal to vacuum. Higher

currents (~ 6 A) were used for outgassing and ultimately to sublimate Ba or Sr and produce a metal beam.

II.4.III Sample deposition

The deposition procedure employed for the two methods of metal vaporisation varied slightly. Both will now be briefly outlined. With electron bombardment, the metal vaporisation rate was firstly allowed to stabilise with the exit shutter closed. The flux was monitored with the control unit of the electron gun. Stabilisation of the metal beam typically took 15 – 20 minutes. When a stable metal flux had been achieved, a base layer of pure rare gas was deposited for 5 minutes to limit metal aggregation and contamination of the window between samples. Then the shutter of the electron gun was opened allowing metal vapour into the sample chamber to be co-condensed with the host gas of interest.
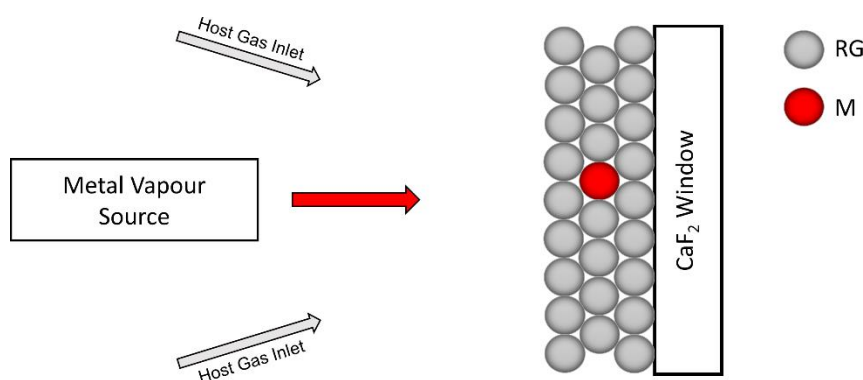
Figure II.8   A representation of a matrix-isolated M/RG sample during deposition.

With the thermal method, the ideal metal vaporisation current was found by trial and error, with the Alcatel Penning Gauge of the matrix rig indicating the amount of metal evaporating. This endeavour was also aided by the Alvatec[19] manual which provides a current activation region for each metal dispenser. Initially, the current of the dispenser was slowly increased to just below the determined activation threshold. This was done with the matrix window orientated for transmittance, the radiation shield therefore prevented any material being deposited during warm-up. An initial layer of pure host gas was deposited for five minutes. The getter current was then increased

above the threshold value. This essentially acted as an 'on switch' for the metal beam which was subsequently co-condensed with the host gas onto the CaF_2 window.

Samples were deposited for a period of 20 minutes with both the metal and rare gas flowing. Following this, a cap layer of pure RG was deposited for five minutes without any metal. The total deposition time was 30 minutes, with the host gas flowing at a rate of 8-10 mmol/hr. Continuity between samples was achieved by using the same rare gas flows and metal fluxes/currents. The sample thickness and the M:RG ratios were achieved by controlling the two factors which govern the deposition rate. They are 1) the backing pressure in the GHS and 2) the flow rate selected by the Granville-Phillips variable leak valve.

II.5   Luminescence measurements

Steady-state and time-resolved UV/Vis luminescence spectroscopy was used in this work to probe the deposited M/RG thin films. The optical arrangement of each spectroscopic experiment will now be described in detail.

II.5.I   Steady-state luminescence

A schematic of the time-integrated, steady-state luminescence arrangement is presented in Figure II.9. Steady-state scans were obtained either with a deuterium lamp (UV, 180–400 nm range) or a tungsten lamp (UV–Vis, 300–900 nm range). The excitation wavelength was selected using a 0.3 m focal length monochromator[21] (Acton Research Corporation, model SpectraPro-300i) containing a 1200 grooves/mm diffraction grating blazed at 300 nm. Transmittance spectra were recorded directly through the matrix sample using a Hamamatsu R928 PMT detector[22]. The transmitted light was focused onto the PMT by means of a quartz focusing lens positioned between the sample window and photomultiplier tube.

$$OD = -\log_{10} \frac{I_{sample}}{I_{blank}}$$ Eq. (II.1)

An absorption spectrum was obtained by rationing the doped sample transmittance (I_{sample}) spectrum with the corresponding, pure RG, blank transmittance spectrum

(I_{blank}). The absorbance, measured in units of optical density (OD), can be computed using the Beer-Lambert law (Equation II.1). This model assumes the same sample thickness for the M/RG thin film and the corresponding RG blank.
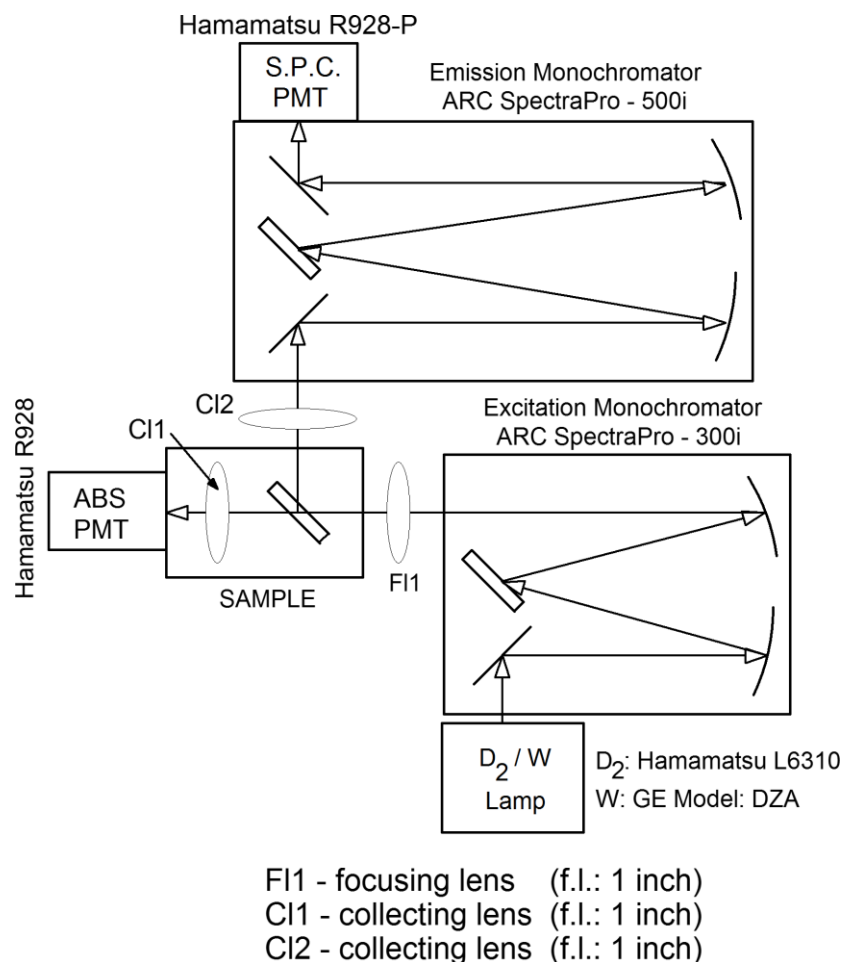

Figure II.9 **Plan-view of the UV/Vis Luminescence set-up used to record steady-state, time-integrated spectra.**

Excitation and emission spectra were recorded perpendicular to the sample window with an Acton Research 0.5 m SP500i monochromator[23] fitted with three gratings: a 1200 g/mm and a 150 g/mm, both blazed at 300 nm and a 600 g/mm grating blazed at 500 nm. Two separate detectors were mounted on the SP500i: 1) A Hamamatsu R928P PMT[22] maintained at $-20°C$ in a Products for Research (Photocool, S600) cooled housing[24] and 2) an intensified, time-gated charge coupled device (iCCD) detector[25] (Andor Technologies, model iStar DH720) held at -15°C by an integrated Peltier cooling system. A swing mirror in the SP500i allowed the emitted radiation to reach the detector of choice. For steady-state scans, the PMT was operated in photon

counting mode by relaying its signal via an amplifier/discriminator module[26] to the ARC NCL data acquisition and controller unit. The CCD could also record time-integrated spectra by switching to the continuous-wave mode of operation. In this case, the Andor iStar software and card (CCI-010), mounted on a PC, controlled the SP-500i monochromator and selected the emission region of interest.

Table II.7   **Specifications of the Acton Research Corporation (ARC) Spectra-Pro 300i and 500i monochromators. The * indicates that the specifications refer to the 1200 grooves/mm gratings.**

ARC Monochromator	SpectraPro-300i[21]	SpectraPro-500i[23]
Focal length (mm)	300	500
Wavelength range (nm)	180 nm – far infrared	180 nm – far infrared
Gratings (grooves/mm) / Blaze (nm)	1200/300	1200/300
		600/500
		150/300
Resolution (nm)*	0.1 @ 435.8 nm	0.05 @ 435.8 nm
Dispersion (nm)*	2.7	1.7
Accuracy (nm)*	± 0.2	± 0.2

Table II.8   **Details of the photomultiplier tubes used to record steady state spectra. The R928P has lower electronic noise and was therefore used to record emission/excitation spectra.**

Hamamatsu PMT	R298[22]	R298P[22]
Ranger (nm)	185 - 900	185 - 900
Peak wavelength (nm)	400	400
Photo-cathode material	Multialkali	Multialkali
Window material	UV glass	UV glass

Emission spectra were recorded by selecting the excitation wavelength with the 300i monochromator and monitoring the emission region of interest with the detector of choice. Similarly, excitation spectra were obtained by scanning the SP-300i and selecting a particular emission wavelength with the SP-500i monochromator. An excitation spectrum plots the emission intensity as a function of the excitation wavelength. These spectra therefore allow broad and complex absorption bands to be deconvoluted into components which are specific to the chosen emission band.

2D-fluorescence spectra were acquired (with a continuous wave lamp source) by scanning the SP-300i excitation monochromator across the wavelength region of interest, whilst simultaneously monitoring an entire emission region with the iCCD. The iCCD software, Andor, stores this information as a series of emission slices. The data collected actually comprised three dimensions: emission (x-axis), excitation (y-axis) and intensity (z-axis). Calibration of the excitation axis was achieved by dividing the number of these emission slices by the total range scanned in excitation (in nm). A spectroscopic analysis package (OPUS-5.5) allowed the scans to be calibrated and presented as two dimensional – excitation and emission (2D-EE) contour plots, where the contour spacing indicated the intensity of the luminescence. The 2D-EE technique has two main advantages over normal emission/excitation spectroscopy, they are:

1. Easier visualisation and interpretation of an entire luminescence spectral region.
2. Greater efficiency – a vertical slice (y) through a contour plot yields an excitation spectrum, while a horizontal slice (x) yields an emission spectrum.

2D scans were also recorded with a Nd:YAG laser (described below) as the excitation source. High resolution laser excitation and emission spectra could therefore be extracted by taking the appropriate slices through the plot.

Both the SP-300i and SP-500i monochromators were calibrated using a Hg emission lamp. For example, a comparison of the spectra recorded (~ 578 nm) with each of the three gratings of the SP-500i is presented in Figure II.10. These data are overlaid on the known[27] gas phase emission values of atomic Hg, highlighting the accuracy of the calibration. At most, the Hg emission wavelengths measured using either the SP300i or SP500i monochromator deviated from the values quoted on the NIST website[27] by approximately 6 cm^{-1} – the maximum deviation occurred in the UV region (λ < 300 nm). As such, the main source of error in the measurement of wavelength is the uncertainty related to the scanning of either monochromator, which is specified as $\pm$ 0.2 nm[21,23].
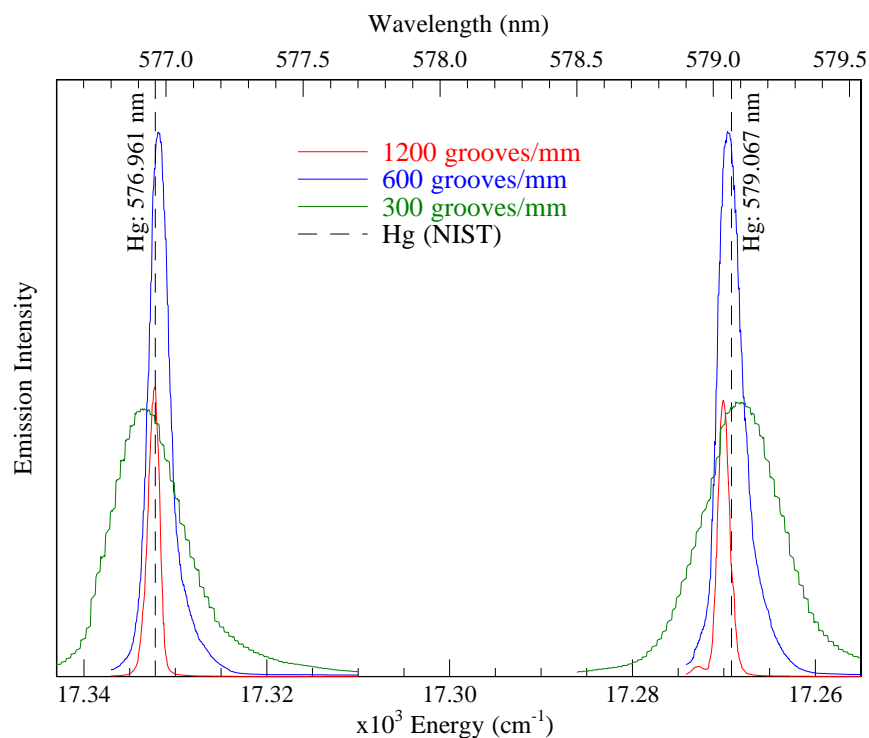
Figure II.10   **Calibration of the SP-500i emission monochromator was achieved using a Hg lamp. Spectra recorded with the three gratings of the monochromator are shown in colour and are compared to the known values[27] of the visible Hg emission lines (dashed vertical lines).**

II.5.II   Time-resolved luminescence

Luminescence spectra were also recorded with pulsed laser excitation using a Nd:YAG[28] (Quantel YG 980E-10) operating at a frequency of 10 Hz. The second (532 nm) or third (355 nm) harmonic of the YAG pumped a dye laser[29] (Quantel TDL-90), producing tuneable laser radiation. A schematic of this optical arrangement is shown in Figure II.11 and the specifications of the laser source are given in Table II.9. Table II.10 provides details of the organic dyes[30] used in this study to photo-excite Sr or Ba atoms. The UV absorption bands of atomic Ba were accessed by frequency mixing the fundamental of the YAG (1064 nm) with the doubled output of the dye laser using DCM as the dye material. A KDP (Potassium Dihydrogen phosphate) crystal (Quantel MCC1) was used to frequency double and mix while a quartz (Quantel QCC2) crystal was used to compensate for the walk of the resultant beam. A Pellin-Broca prism separated the final UV output from the dye and YAG beams. Typical laser fluences in the range $2 - 6 \ \mu J/mm^2$ were recorded at the sample window with a Molectron power-max 500 A meter and PM10V1 head. These fluences were obtained using only the

oscillator and pre-amplifier of the dye laser and could vary depending on the dye material and excitation wavelength selected.
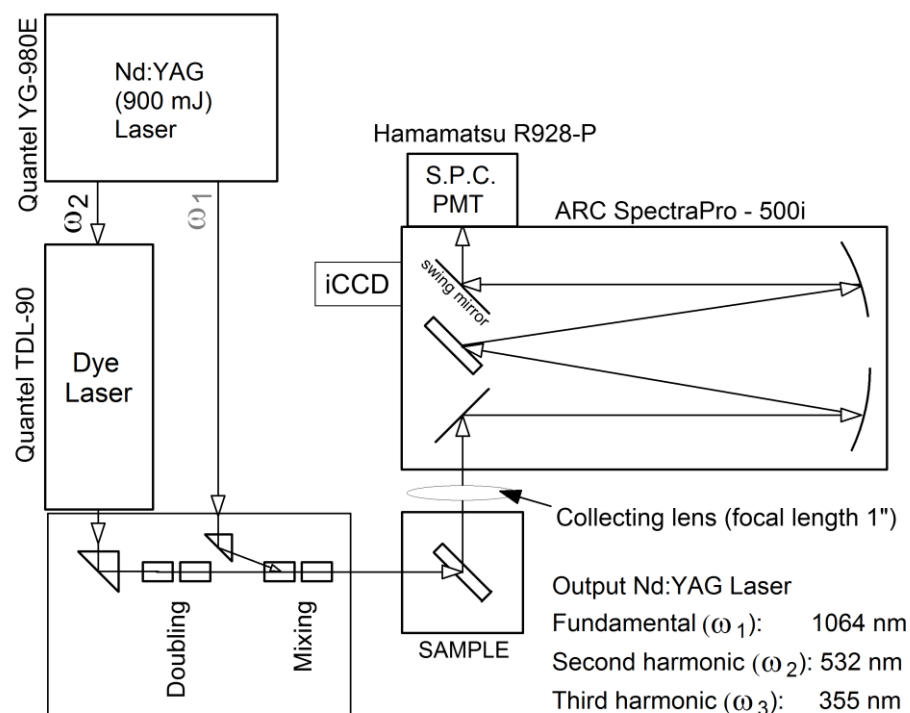

Figure II.11   **Plan-view of the optical set-up used to record time-resolved spectra. The transmittance PMT was removed to allow the pulsed laser radiation to reach the M/RG sample.**

Table II.9   **Specifications of the Quantel laser set-up**

Pump Laser System	Nd:YAG, Quantel YG 980E
Gain medium	Neodymium-doped crystal (Yttrium - Aluminium – Garnet)
Repetition rate (Hz)	10
Energy (mJ) @ 1064, 532, 355 nm	650, 280, 135
Pulse duration (ns) @ 1064	6
Flash-lamps	SFL 611.09N/RX
Flash-lamp Voltage (V)	1640
Q-Switch pre pulse (ns)	500
Flash-lamp / Q-Switch delay (μs)	242
Dye Laser System	**Quantel TDL-90**
Tuning range (nm)	220 - 750
Linewidth (cm^{-1}) @ 560 nm	0.08

Table II.10   **Spectral characteristics of the dye materials used in this study. All were dissolved in ethanol and made by Radiant Dyes. The values quoted were recorded in ethanol and were obtained from the Exciton manual[30]. These dyes were pumped by the * = 3rd (355 nm) and # = 2nd (532 nm) harmonics of the Nd:YAG laser.**

Dye Material	Absorption Maximum (nm)	Fluorescence Maximum (nm)	Range (nm)
Coumarin 440* $C_{10}H_9NO_2$	354	430	429 - 460 (λ_{max} = 441 nm)
Coumarin 460* $C_{14}H_{17}NO_2$	373	445	442 - 479 (λ_{max} = 460 nm)
Coumarin 480* $C_{16}H_{17}NO_2$	390	473	452 - 500 (λ_{max} = 480 nm)
Coumarin 500* $C_{12}H_{10}F_3NO_2$	392	495	485 - 530 (λ_{max} = 500 nm)
Coumarin 540A* $C_{16}H_{14}F_3NO_2$	423	530	523 - 586 (λ_{max} = 543 nm)
Rhodamine 6G# $C_{28}H_{31}N_2O_3Cl$	530	560	559 - 576 (λ_{max} = 566 nm)
DCM# $C_{19}H_{17}N_3O$	481	644	610 - 660 (λ_{max} = 627 nm)
LDS 698# $C_{19}H_{23}ClO_4$	476	668	667 - 720 (λ_{max} = 692 nm)

The temporal characteristics of the observed emission bands were recorded by coupling of the pulsed laser output with a time gated sensor. For shorter, nanosecond decay times, the time-gated iCCD sensor was used – this consists of a CCD camera connected to a gated image intensifier. The image intensifier is an evacuated tube comprising a photocathode, microchannel plate (MCP) and phosphor screen. The photocathode is coated on the surface of the input window. When a photon strikes the window, a photoelectron is emitted, which is then drawn towards the MCP by an electric field. The MCP is a thin disk (~ 1 mm thick) of honeycombed glass. A high potential applied across it enables the photoelectron to accelerate down one of the channels in the disc. When the photoelectron has sufficient energy, it dislodges secondary electrons from the channel walls. These electrons, in turn, undergo

acceleration which results in a cascade of electrons exiting the MCP. The degree of electron multiplication depends on the gain voltage applied across the MCP, which can be controlled in the camera.
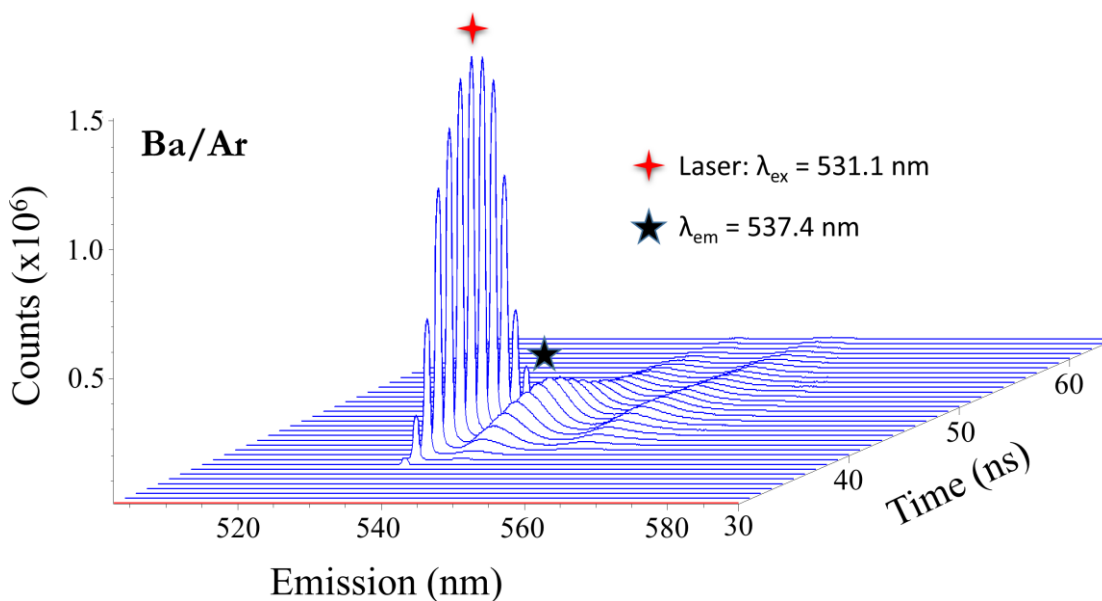

Figure II.12   A time-resolved emission spectrum (TRES) recorded by exciting the $^1P_1 \leftarrow {}^1S_0$ transition of atomic Ba in solid Ar.

As well as amplifying, the image intensifier can be rapidly switched on and off, permitting it to be used as a very fast shutter. Triggering the device with the pulsed output of the Nd:YAG laser allowed time-resolved emission spectra to be recorded. Individual time-gated spectra were obtained by setting a small gate width and stepping this in time. Combining these temporal slices produced a time-resolved emission spectrum (TRES) – an example of a TRES is shown in Figure II.12. The Andor software allowed for a slice to be taken through the TRES at a particular emission wavelength, yielding a data set of emission intensity versus time.

Longer lifetimes (> 1 µs) were recorded with the R928P PMT employing the multi-channel scalar (MCS) technique[31]. In contrast to analog techniques, each detector pulse represents the detection of an individual photon. The number of pulses, rather than the signal amplitude, provides the measure of the light intensity at the input of the detector. In our set-up, the signal from the R928P PMT was amplified by an Ortec (Model VT120) fast-timing preamplifier[32] and relayed to an Ortec (Model 584) constant-fraction discriminator (CFD)[33], which limited electronic noise. The output of the CFD was simultaneously passed to an Ortec (Model 661) ratemeter[34] and to a 2 GHz multi-channel scalar (Fast ComTec, Model 7886)[35]. Again, the Q-switch pre pulse

of the YAG provided the start for the multi-channel scalar. When the binwidth of the MCS is set to one (minimum value), each time channel corresponds to a 500 ps dwell time. The temporal resolution of this arrangement has been determined to be approximately 500 ns, limited largely by the poor pulse-pair resolution of the R928P PMT when high intensity, low repetition laser excitation is used.

The MCS technique was primarily used to gain information on the long-lived excited states of atomic Sr isolated in the rare gas solids. Decay times for the lowest energy emission bands of this atom typically ranged from $1 - 1500$ µs. For each scan, the set binwidth and sweep range were optimised to match the decay time being recorded. For example, if the decay time was ~ 1500 µs, a binwidth of 64 bits and a sweep range of 200960 channels was adopted. In this case the total sweep time would be 6430 µs, thus allowing a wide enough window to ensure the entire decay event had been observed.

II.5.III Decay curve fitting and error analysis

Single or multi-exponential decay functions were fitted to the long-lived (< 1 µs) decay curves (recorded using the MCS technique) in order to extract excited state lifetime values. These non-linear least-squares fits (NLSFIT) were implemented using the data analysis and plotting program, Genplot. In brief, the NLSFIT algorithm[36] takes a function and a set of variables upon which the function depends. The numeric value of each of these variables is then modified and the variance between the function and the data is determined (i.e. the chi-square value, χ^2). Using the change in the variance, a new guess is made for each of the variables, iterating through the parameter space until a sufficiently good minimum is located. Genplot then prints out the standard deviation (σ) associated with each variable – these σ values are estimated from the curvature of the correction matrix, yielding an error bar for each parameter, which will result in a doubling of χ^2. Thus, the uncertainties associated with the long-lived, phosphorescent lifetimes (τ) are provided in the figure captions of each temporal scan (see Chapter V). These statistical values should be of high quality, since each decay curves recorded using the MCS technique involves the accumulation of over 200,000 data/time channels – each scan typically lasted between one and two hours.

Single or multi-exponential decay functions were also fitted to the nanosecond decay curves, which were obtained by taking a slice through the TRES, as describe in the previous section. In contrast to the long-lived decays, the NSLFIT algorithm could not be used to model the nanosecond temporal profiles because the function required to fit these decay curves was more complex, and involved a re-convolution with the time profile of the laser. Thus, trial fits were used in lieu of a non-linear least-squares analysis. These fits were generally performed over four orders of magnitude (in intensity) to ensure that the extracted lifetime values were accurate. An estimate for the uncertainty associated with the nanosecond lifetimes was computed manually. This was achieved by analysing the decay curves recorded for the 537.4 and 549.9 nm fluorescence bands of Ba/Ar. A range of τ values were obtained for each emission by collecting data from a number of Ba/Ar samples. These samples used were deposited under similar conditions, annealed to the same temperature and exhibited the same absorption optical density. From the statistical analysis conducted, an average standard deviation (σ_{av}) of ± 0.1 ns was computed. This represents an estimate of the uncertainty associated with the nanosecond decay times reported in this thesis.

II.5.IV Lineshape fitting and error analysis

As will be shown in Chapters IV and V, the site-specific absorption/excitation bands recorded for Sr/RG and Ba/RG are complex and multi-featured. To identify all of the components, and to gain further insights into the photophysical properties of these solids, lineshape fits were often conducted. The components of a given excitation band were represented by Gaussian functions – a valid approximation considering the strong electron-phonon coupling that occurs in the ground and excited states of these metal atom systems[37,38]. A Gaussian function, $f(x)$, is described by Equation II.2:

$$f(x) = Ae^{-\frac{(x-M)^2}{2S^2}}$$

Eq. (II.2)

In this formula, A is the height, M is the position and S is the width of the curve. The NLSFIT algorithm was also used to perform each lineshape analysis. Accordingly, for all of the fits presented in Chapters IV and V, the uncertainty (σ) relating to the position of each Gaussian curve is provided in the figure captions.

References

[1]   T. Bally, *Matrix isolation.* (John Wiley & Sons: Hoboken, NJ, 2004).

[2]   E. Whittle, D. A. Dows, and G. C. Pimentel, J. Chem. Phys. **22**, 1943 (1954).

[3]   Edwards, *Rotary Vacuum Pumps E2M2, E1M5/E2M5, E1M8/E2M8.* (Edwards High Vacuum, 1983).

[4]   *DE-202 Expander Technical Manual.* (APD Cryogenics Inc., May 1989 (257519A)).

[5]   *Helium Compressor HC-2D Technical Manual.* (APD Cyrogenics Inc., Jan 1992 (256685A)).

[6]   W. E. Gifford, in *Adv. Cryog. Eng.*, edited by K. D. Timmerhaus (Springer US, 1966), pp. 152.

[7]   *Laboratory interface components Technical manual, Models WMX, DMX, HMX, FMX.* (APD Cryogenics Inc., Aug, 1990 (257692A)).

[8]   *Instructions Manual, Series 9600 microprocessor - based digital temperature indicators/controllers manual #A090-145.* (Scientific Instruments Inc., March 6th, 1990).

[9]   Balzers, *Operating Instructions Manual, Turbo-molecular pump (TPU 180H).* Ed. 3.

[10] Edwards, *Instructions Manual, E1M18 and E2M18 Rotary Vacuum Pumps.* (Edwards, High Vacuum, 2011).

[11] Granville-Phillips, *203 Variable Leak Valve, Technical Manual.* (1993).

[12] Granville-Phillips, *307 Vacuum Gauge Controller Technical Manual.* (1993).

[13] *Technical Sheets, Capacitance Diaphragm Gauges CDL Series.* (Tylan General).

[14] D. R. Lide, *CRC Handbook of Chemistry and Physics* (2010), Ed. 90th.

[15] O. Byrne, and J. G. McCaffrey, J. Chem. Phys. **134**, 124501 (2011).

[16] M. A. Collier, and J. G. McCaffrey, J. Chem. Phys. **122**, 54503 (2005).

[17] Omicron, *EFM Evaporators, 'Ultra-Pure submonolayer and multilayer thin film growth'.* (2015).

[18] Omicron, *Instruments for Surface Science, Instruction Manual UHV Evaporator EFM3/4.* (Version 2.0, May 1996).

[19] Alvatec, *Alvasources, 'Chromate-free metal vapour sources'.* (March, 2015).

[20] *Feedthroughs - electrical and optical* (Carburn-MDC Europe Limited, UHV CF Flange, Model DN40CF).

[21] *Operating Instructions SpectraPro - 300i.* (Acton Research Corporation, SP - 300i, Manual Rev. 997.1).

[22] Hamamatsu, *Data Sheet, Photomultiplier Tubes R928, R955*.

[23] *SpectraPro -500i.* (Acton Research Corporation, 500i Manual V1097.1).

[24] *Photocool Series Power Supply, Instruction Manual.* (Products for Research, Inc., Model PC177CE009 for R928).

[25] *Intensified and Gated CCD Cameras.* (Andor Technology, Model DH720, June 2003).

[26] *Photomultiplier Amplifier-Discriminator Type AD 6, DS_AD6.* (Electron Tubes Limited, Issue 1, Feb. 1997).

[27] A. Kramida, Y. Ralchenko, J. Reader, and NIST ASD Team. NIST Atomic Spectra Database (ver. 5.2). Available at: http://physics.nist.gov/asd [2015, October]. National Institute of Standards and Technology, Gaithersburg, MD.

[28] Quantel, *Instructions Manual QUANTEL YG 980 Q-switched Nd:YAG laser.* (Doc. 980, Version 1, anglaise PM/DT, 12.05.97).

29   Quantel, *TDL-90, Instructions Manual.* (Issue 1).
30   Exciton Catalogue. Available at: http://www.exciton.com/laserdyeslist.html [24 July 2015].
31   W. Becker, *Advanced Time-Correlated Single Photon Counting* (Springer, 2005).
32   Ortec, *Model VT120, Fast Timing Pre-Amplifier: Operating and Service Manual.* (Part No. 760360, Revision B).
33   Ortec, *Model 584, Constant - Fraction Discrimintor: Operation and Service Manual.* (Part No. 733550, Revision B).
34   Perkin-Elmer, *Model 661 Ratemeter: Operation and Service Manual* (EG&G Ortec, Part No. 740380, Revision B).
35   *Model 7886, 2 Ghz Fast Multiscalar: User Manual.* (Fast ComTec GmbH, Version 2.1, Aug. 1998).
36   P. R. Bevington, and D. K. Robinson, *Data reduction and error analysis for the physical sciences* (McGraw-Hill, 2003).
37   C. W. Struck, and W. H. Fonger, *Understanding luminescence spectra and efficiency using Wp and related functions* (Springer-Verlag, 1991).
38   K. Huang, and A. Rhys, Proceedings of the Royal Society of London A: Mathematical, Physical and Engineering Sciences **204**, 406 (1950).

Chapter III
M/RG Absorption Spectroscopy and Sample Characterisation

III.1   Introduction

As discussed in Chapter I, the existing work on the absorption spectroscopy of matrix-isolated Sr and Ba is quite convoluted. Therefore, significant effort will be dedicated in this Chapter to the characterisation of the M/RG (M = Sr, Ba; RG = Ar, Kr and Xe) samples. Firstly, the issue of the Sr contamination present in Ba/RG samples will be addressed and the absorption bands associated with each metal atom will be assigned. A method of minimising the Sr impurity in Ba/RG samples will also be outlined. Secondly, for each M/RG system, the deposition parameters of 1) metal flux/concentration and 2) window temperature will be systematically varied with the aim of discriminating absorption bands associated with the atom versus bands that result from metal dimers or higher metal aggregates. Finally, the steady-state and time-resolved luminescence of Sr_2 and Ba_2 will be presented, forming a more complete characterisation of these Group II dimers.

Following identification of the 'ideal' deposition procedure, the absorption spectroscopy of the most atomic M/RG samples will be presented. As the metal atoms are trapped at very low temperature (~ 10 K), the transitions observed in absorption originate from their spherically symmetric, $(ns^2)^1S_0$, ground states.   Inspection of the energy level diagram of atomic Sr and Ba (Figure I.7, Chapter I) shows that the fully-allowed $(nsnp)$ $^1P_1 \leftarrow (ns^2)$ $^1S_0$ transition should therefore dominate the spectroscopy. It is well known that matrix absorption spectra recorded of P $\leftarrow$ S type transitions possess a characteristic three-fold splitting pattern. This structure has been attributed[1,2] to Jahn-Teller coupling in the degenerate P excited state, and as a result, the isolation of these metal atoms has been inferred to occur, preferentially, in sites of high (cubo-octahedral) symmetry. In this Chapter, matrix annealing will be used to remove any thermally unstable sites of isolation for the metal atom. The $(nsnp)$ $^1P_1$ absorption profiles will then be analysed in an attempt to identify the number of thermally stable sites occupied by Sr and Ba in each host solid.

III.2 Ba/RG sample characterisation

The absorption spectroscopy of matrix-isolated Ba is complex for a number of reasons:

1. Weak absorption bands appear to the blue of the resonant Ba (6s6p) $^1P_1 \leftarrow$ (6s^2) $^1S_0$ line when a relatively high e-gun filament current is used to vaporise Ba during sample formation. Their spectral location at ~ 460 nm suggests that they result from the isolation of singly-ionised cationic Ba[3].

2. Absorption features associated with Ba aggregates occur in the region of the (6s6p) $^1P_1 \leftarrow$ (6s^2) $^1S_0$ atomic transition, some of which spectrally coincide with the atomic absorption bands.

3. A substantial mismatch exists between the Ba·RG and RG·RG diatomic bond lengths (see Chapter VI). This discrepancy is manifested experimentally by the observation of broad, multi-featured atomic absorption bands which result from the atom residing in a number of distinct environments or sites within each RG solid.

Each of these issues will be addressed in turn. Firstly, the origins of the higher energy features will be investigated. As Ba cation is a possible candidate, the deposition procedure is modified by replacing the energetic e-gun with a gentler thermal vaporisation source. Secondly, concentration and temperature studies are employed to identify absorption bands which may be attributed to Ba aggregates, specifically Ba dimer (Ba$_2$). A detailed characterisation of the dimer is then achieved with steady-state and time-resolved luminescence techniques. Excitation spectra recorded of the dimer emission provides further discrimination between the atom and dimer absorption bands. Finally, the most atomic Ba/RG samples will be presented and analysed in Section III.3.

III.2.I Initial Ba/RG samples

The first matrix absorption spectra recorded for samples prepared by co-depositing Ba vapour with Ar and Xe at 10 K are shown by the black traces in Figure III.1, in the range 400 to 650 nm. In addition to the strong (6s6p) $^1P_1 \leftarrow$ (6s^2)$^1S_0$ resonance transition of Ba at approx. 550 nm, a number of bands are also located at 460 nm.

Because of their spectral positions, these bands were thought initially to be Ba ions isolated on deposition, and the suspicion was that the atomic cation was being generated in the e-bombardment source used.
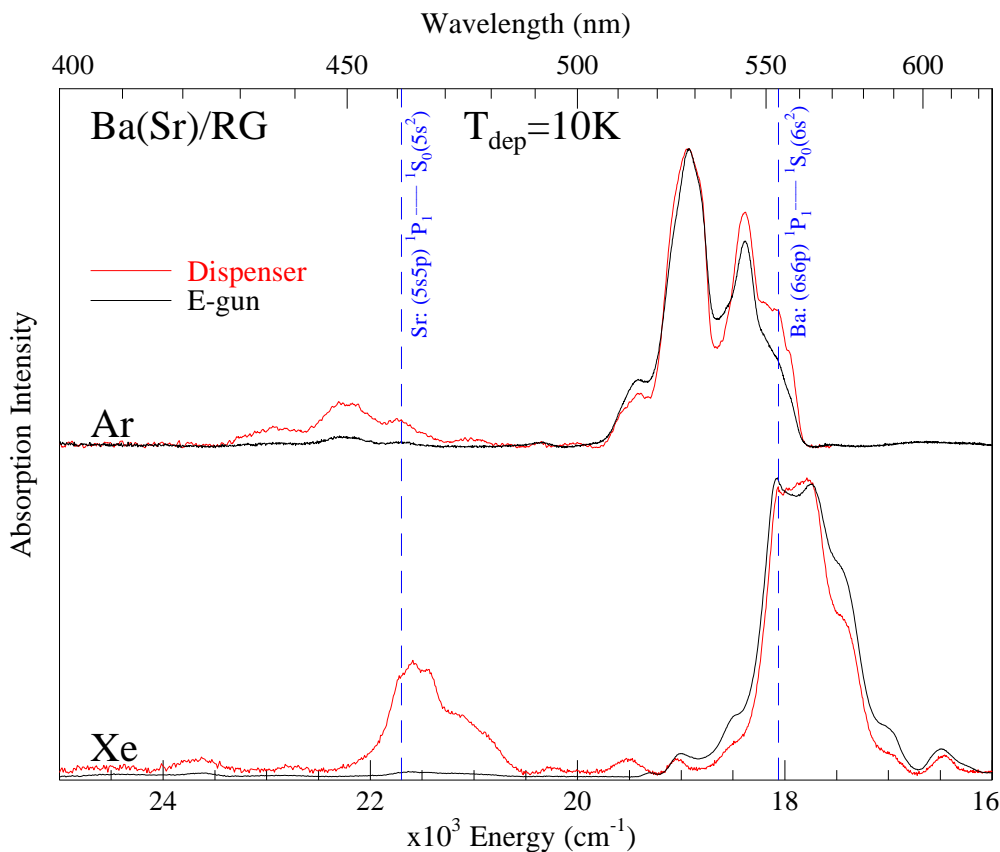

Figure III.1 **Absorption spectra recorded for Ba/Ar and Ba/Xe samples at 10 K in the UV visible spectral region. The solid black traces were recorded for samples formed from electron-bombardment, while the red traces show the result of using the thermal dispenser. As revealed by the indicated transitions, significant amounts of atomic Sr are present in both matrices. The comparison further shows the greater extent of the Sr contamination in the samples formed from thermal deposits.**

To investigate this possibility, the Ba dispenser described in the methods section, (Alvatec, Alvasource AE-3-Ba-50C) was used instead of the e-gun for metal vaporisation. The absorption spectra recorded of samples deposited using this thermal source are presented as red traces in Figure III.1. A cursory inspection of Figure III.1 reveals that the samples formed using the dispenser actually contain more Ba "ions" than those formed using the electron bombardment (e-gun) source. Because of this nonsensical finding, obtained with a low energy thermal source, checks were made of the Ba metal being used - only to make a rather surprising discovery.
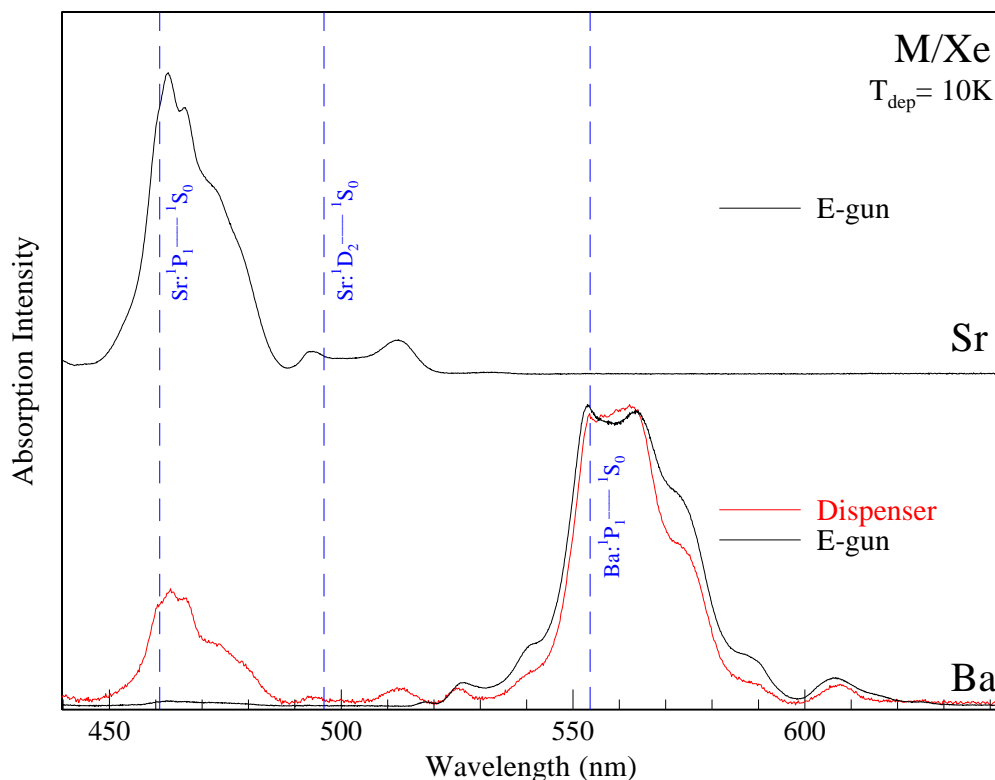
Figure III.2 **Absorption spectra recorded for Sr/Xe and Ba/Xe samples at 10 K in the visible spectral region. The solid black traces were recorded for samples formed from electron-bombardment, the red trace shows the result of using the thermal dispenser. A comparison of the pure Sr/Xe e-gun sample (top trace) with both Ba/Xe samples definitively shows that the higher energy features are in fact matrix-isolated atomic Sr.**

It turns out that Sr is a small (~ 0.8 %) but persistent impurity in Ba metal[4]. Having a similar melting point (1050 K) to Ba but with a much lower boiling point (1655 vs. 2170 K)[5], Sr vaporises much more readily. The large boiling point difference exaggerates, as evidenced by the Xe scans shown in Figure III.1, the extent of Sr contamination in "Ba" samples formed as thermal deposits far above its impurity level. Figure III.2 presents a comparison of the Ba/Xe absorption spectra obtained using both vapourisation methods (bottom panel) with the spectrum of a pure Sr/Xe sample, formed using the e-gun (top panel). This comparison clearly demonstrates that the blue absorption bands, observed in the Ba/RG dispenser samples (and in the e-gun samples to a lesser extent), originate from matrix-isolated atomic Sr.

Knowing that Sr is inherently present in sources of Ba metal, a systematic study of the vaporisation conditions was conducted to minimise the amount of Sr deposited in the Ba/RG matrix samples. The study revealed that the presence of the Sr impurity is considerably smaller with the bombardment source. In contrast to the dispenser

source, which melts the entire volume of the Ba metal, the electron-beam only melts a spot on the surface of the metal. Thus, samples deposited with the e-gun were found to contain much less Sr, suggesting that the Sr contamination can be depleted in the local area (spot) of the bulk Ba metal heated by the e-beam. This depletion could be completed during the 15 - 20 minute warm-up time required to stabilise the metal flux. Provided the metal flux was kept small during the deposition (with a low e-beam current), Ba/RG samples largely free of Sr could be formed with e-bombardment. The presence of a Sr impurity has also been observed for Ba isolated in liquid helium and solid He matrices[6], as well as in the recent study in Ar and Xe matrices[7].

In order to properly characterise the spectroscopy of the Ba/RG samples, we have also investigated the spectroscopy of matrix-isolated Sr. Accordingly, the absorption spectra recorded of pure Sr/RG samples are presented in Sections III.4 and III.5. The results obtained for the 'purest' Ba/RG samples, formed following the procedure previously outlined, will now be presented.

III.2.II Ba/RG concentration studies

A concentration study for the isolation of Ba in Ar is presented in Figure III.3. Traces a), b) and c) were recorded for samples deposited at 19 K with high, medium and low metal fluxes respectively. Trace d) represents a 10 K/low flux deposition, which contains predominantly isolated Ba atoms. The spectra presented in Figure III.3 reveal a number of important trends regarding the isolation conditions of the metal. Firstly there is a steady increase in intensity of the absorption features labelled I – III, centred at 747.4, 568.5 and 491.5 nm respectively, with respect to the atomic features present in the 10 K spectrum (trace d). Secondly, the nature of the bands in the vicinity of the resonance atomic (6s6p) $^1P_1 \leftarrow$ (6s^2) $^1S_0$ transition (c. 550 nm) get progressively broader and more complex with increasing concentration. Thirdly, and in stark contrast to the 550 nm region, the pair of absorption bands present in the near-UV region (at approx. 320 nm) change very little with increasing metal loading from the high dilution, low temperature sample shown in trace d). Each of these three characteristics will be analysed in turn.
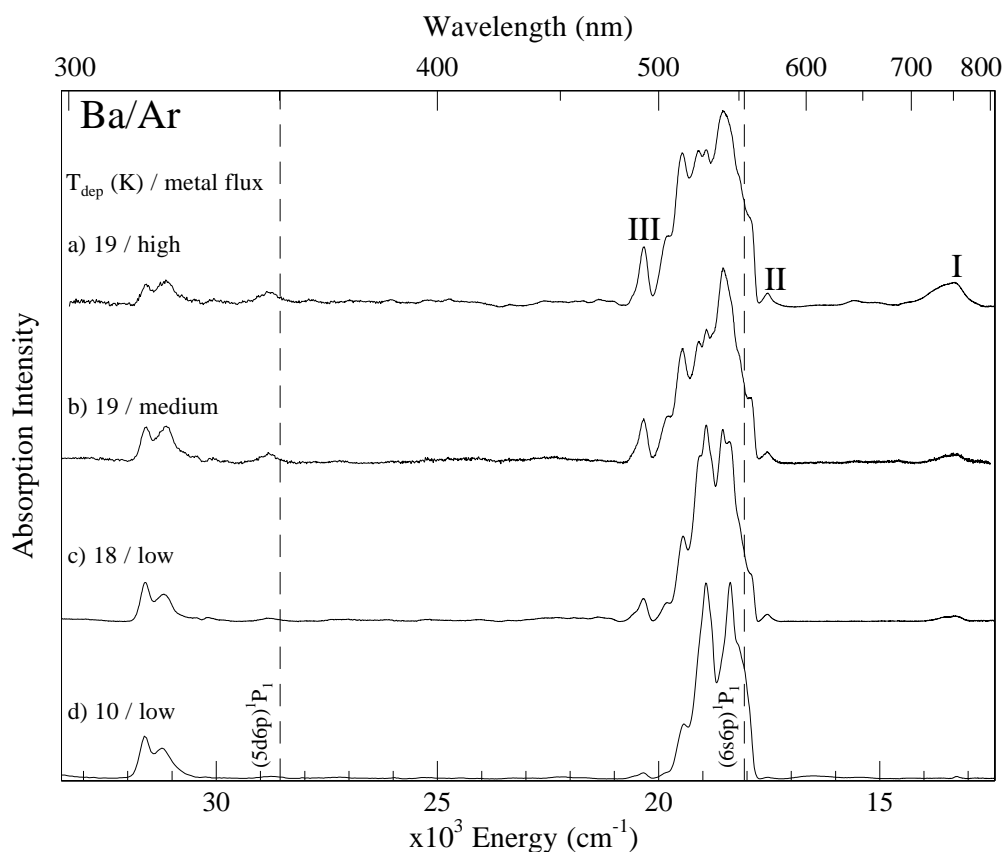
Figure III.3   **Normalised UV/Vis absorption spectra recorded following co-condensation of Ba vapour and Ar. Window temperatures of $T_w = 10$ and 19 K were employed during deposition. The four spectra shown detail the changes in the relative intensities of the absorption bands that occur with 1) increasing deposition temperature and 2) increasing metal loadings. The gas phase positions of the intense (6s6p) $^1P_1$ and (5d6p) $^1P_1$ atomic states are shown as dashed vertical lines.**

Normalising each spectrum to peak III at 491.5 nm, demonstrates that a constant intensity ratio of the bands I-III is maintained throughout. Combining this behaviour with the growth patterns described above indicates that these absorptions belong to the same species. As all three features are present, albeit extremely weakly, in the low temperature sample (d), a tentative assignment to Ba dimer (Ba_2) is made. Support for this assignment comes from a resonant, two-photon ionization (R2PI) study of Ba_2[8]. With the R2PI technique, an excitation spectrum of Ba_2 was obtained which consisted of a group of 12 vibrational bands in the 740 – 764 nm region. This series was assigned to the $(2)^1\Sigma_u^+ \leftarrow X\ (1)^1\Sigma_g^+$ transition of Ba dimer, with the aid of Ba_2 potential energy curves, computed by Lebeault *et al*[8]. Although unstructured, the broad feature (band I) at 747.4 nm in Ar is thereby attributed to this molecular transition.
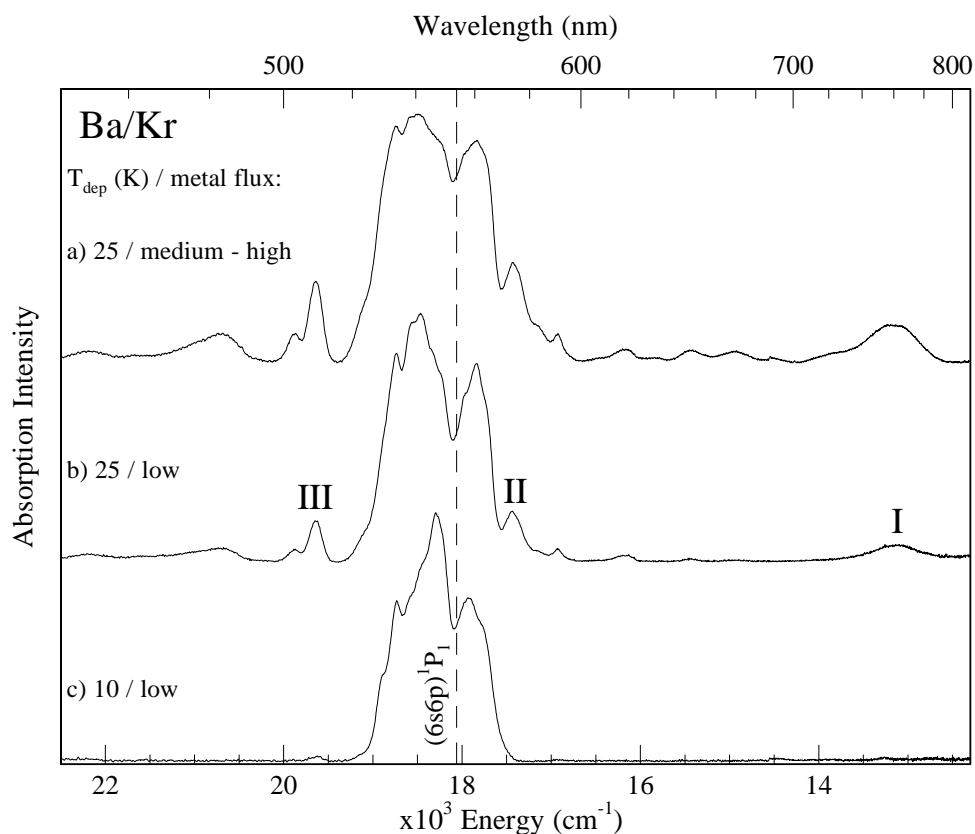
Figure III.4   **Normalised absorption spectra recorded following co-condensation of Ba vapour with $T_w = 10$ and 25 K. The effects of increasing metal loadings and deposition temperature can be observed. The gas phase position of the intense (6s6p) $^1P_1$ atomic state is shown as a dashed vertical line.**

A similar concentration study is presented for the Ba/Kr system in Figure III.4. Traces a) and b) were recorded following deposition at 25 K with a medium-high and a low metal flux respectively. Trace c) represents a low flux/10 K deposit and illustrates the high degree of atomic isolation achieved for Ba/Kr in this investigation. The bands labelled I, II and III first appear in the low flux/25 K deposit and are observed to increase in intensity with a higher metal loading. As with Ba/Ar, these bands are associated with transitions of Ba$_2$. The lowest energy band (I) located spectrally at 760.6 nm is tentatively assigned to the $(2)^1\Sigma_u^+ \leftarrow X (1)^1\Sigma_g^+$ transition of Ba dimer. In contrast to Ba/Ar, the formation of Ba dimer in solid Kr was more difficult to achieve. In particular, samples deposited at 10 K with increased metal loading showed very little change relative to the intense (6s6p) $^1P_1 \leftarrow (6s^2)\ ^1S_0$ transition of the atom. Indeed, only when the (6s6p) $^1P_1$ band became saturated could these additional 'satellite' absorptions be discerned. A more fruitful method of generating Ba dimer was to simply increase the window temperature, as illustrated in Figure III.4.
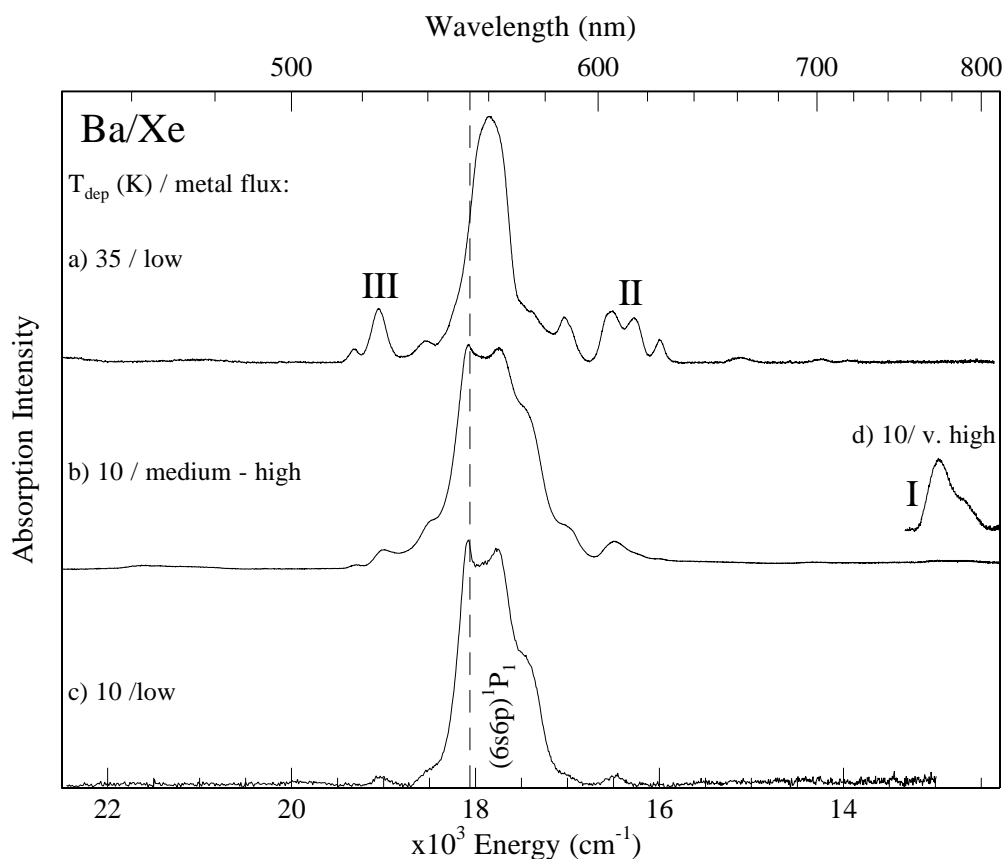
Figure III.5   **Normalised absorption spectra recorded following co-condensation of Ba vapour with Xe at $T_w = 10$ and 35 K. The effects of increasing metal loadings and deposition temperature can be observed. The noise in trace c) is due to a weak absorption strength at low metal concentrations. The gas phase position of the $(6s6p)^1P_1$ atomic state is shown as a dashed vertical line.**

A concentration study for Ba/Xe is shown in Figure III.5. Analysis of this system is slightly more challenging than the previous two. The lowest energy feature (labelled I) which was attributed to a transition of Ba_2 in Ar and Kr is far weaker in Xe and cannot be directly related to bands II and III by an analysis of the peak growth patterns. However, a band could be observed at 772.2 nm from a sample deposited at 10 K with a very large metal flux, as illustrated by trace d). Note that the rest of this spectrum was not presented as the $(6s6p)$ $^1P_1$ band was fully absorbing. Comparing trace a) and b) shows that the features at 524.6, 588.6, 606.2 and 614.3 nm become more pronounced at a higher deposition temperature and are therefore tentatively assigned as Ba dimer. Trace b) is representative of a typical absorption spectrum recorded of Ba/Xe when deposited at 10 K. As with Kr, increasing the metal flux does not drastically alter the composition of a 10 K deposit. However, employing a very high metal flux during sample formation does lead to significant changes in absorption

and these samples are always characterised by a fully absorbing (6s6p) $^1P_1$ atomic band. Surprisingly, Ba/Xe is the most complex of the three systems, with the persistence of the weak 'satellite' absorptions in 500 - 620 nm range. In an attempt to completely remove these bands, absorption spectra were recorded of Ba/Xe samples which were formed at 10 K, with a low metal flux, as shown in trace c). In spite of the noisier baseline, it can be seen that the aforementioned features have been markedly reduced, but again are not fully removed. As such, the weakly absorbing features shown in the trace c) are assigned to atomic Ba.

Unfortunately, it appears that the absorptions of Ba_2 spectrally coincide with these atomic bands, as evidenced by the 'growth' of the features labelled II and III in trace a). Fortuitously, a comparison with the Sr/Xe system supports the atomic assignment in low flux/low temperature samples. For instance, highly atomic deposits of Sr/Xe also exhibit similarly weak fringe absorption bands, especially to the blue (430 – 450 nm) of the dominant (5s5p) $^1P_1 \leftarrow$ (5s^2) $^1S_0$ profile (see Figure III.16). In contrast to Ba_2/Xe, the absorptions of Sr_2 in Xe are further removed from the atomic region, allowing for a confident atomic assignment to be made. Perhaps depositing at 10 K is too far from the critical temperature (T_c) of solid Xe which occurs at 40 K[9] (T_c of Kr is 29 K). Therefore, samples formed at 10 K contain "porous" layers which may allow the formation of many distinct trapping sites for Sr and Ba atoms during deposition – the observed absorption bands are possibly associated with the occupation of such thermally labile vacancies.

In summary, UV/Vis absorption spectroscopy has been used to investigate the composition of Ba/RG samples formed under conditions where the deposition temperature and metal loading are varied. The parameters necessary to achieve optimal atomic isolation in each RG host have been found and a number of absorption bands have been attributed to Ba_2. These molecular attributions are collected in Table III.1. During the course of recording the luminescence of atomic Ba (Chapter IV) in each host solid, it was observed that excitation of the Ba_2/RG absorptions produced red emission bands, which were spectrally distinct from the atomic luminescence. Thus, the luminescence of Ba_2 isolated in the RG solids will now be presented and discussed. To the best of my knowledge, the luminescence of matrix-isolated Ba dimer has not appeared in any studies to date.

Table III.1   **Spectral positions of the absorption features attributed to Ba dimer isolated in the solid RG's on deposition. Peak values are given in wavelength (λ, nm) and wavenumber (ν, cm^{-1}).**

Ba$_2$ /RG	Band	λ (nm)	ν (cm^{-1})
Ar	I	747.4	13380
	II	568.5	17590
	III	491.5	20346
Kr	I	760.6	13148
	II	573.3	17443
		583.1	17150
		590.6	16932
	III	508.8	19654
Xe	I	771.8	12957
	II	588.6	16989
		606.2	16496
		614.3	16279
	III	524.6	19062

III.2.III Ba$_2$/RG emission

The Ba/RG concentration studies shown in Figure III.3 – III.5 reveal that non-atomic absorption bands overlap the resonance (6s6p) $^1P_1 \leftarrow$ (6s^2) $^1S_0$ atomic region, with increasing metal loading. To extract these bands, excitation spectra were recorded for the relatively weak, red-shifted emission they produce in each host. The emission spectra, shown by the red solid traces in Figure III.6, have band maxima centred at 580.9, 617.4 and 676.8 nm in Ar, Kr and Xe respectively. The corresponding excitation spectra, recorded monitoring each of the aforementioned emission wavelengths, are represented by the solid blue traces. Excitation profiles recorded in Kr and Xe show a clear resemblance and allow for a definitive connection to be made with partly resolved features present in the absorption spectra (grey traces). For Kr (Xe), the absorption/excitation bands at 508.8 (524.6), 562.8 (588.6), 579.4 and 589.6 (606.2) nm share a common emission and are therefore associated with the same molecular species, Ba$_2$. The excitation spectrum of Ba$_2$ recorded in Ar appears simpler, consisting of one intense band centred at 568.5 nm and a broad wing extending up to 500 nm. The Ba$_2$/Kr system results shown in Figure III.6 demonstrate the advantage of excitation spectroscopy over absorption alone. For instance the band located at 562.8 nm was a

barely evident shoulder on the intense atomic $^1P_1 \leftarrow {}^1S_0$ absorption, but has been fully resolved and is clearly identified in the excitation scans.
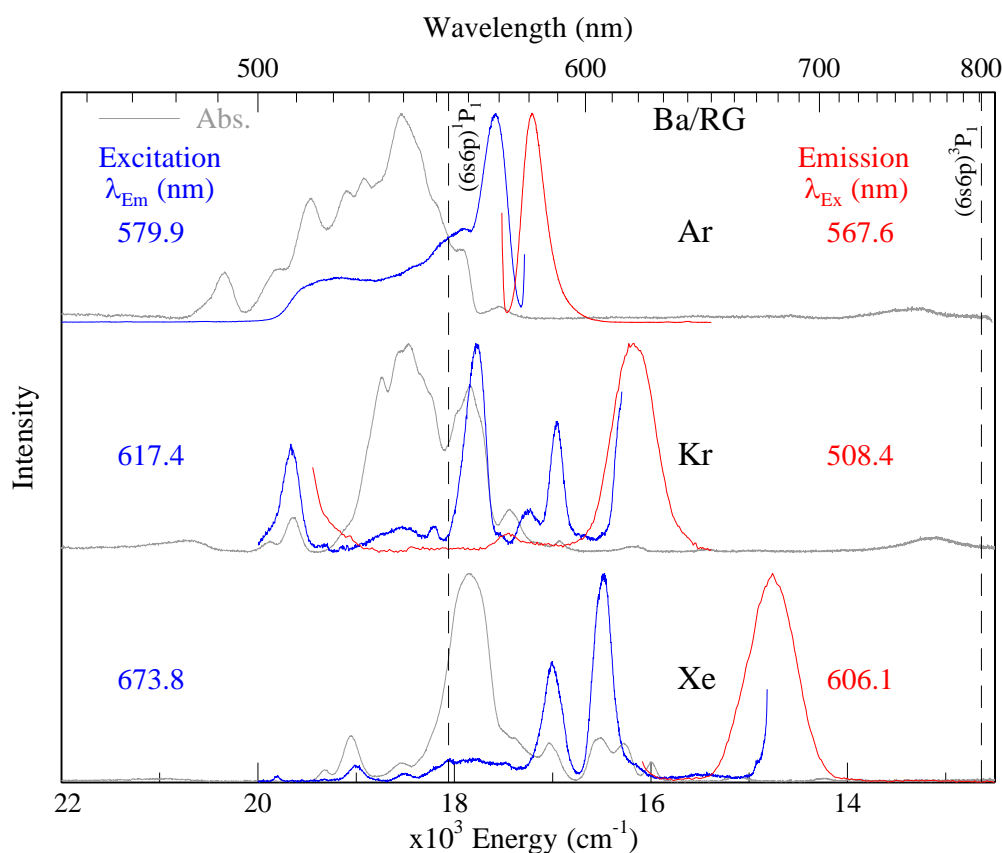

Figure III.6   **Absorption (grey), excitation (blue) and emission (red) spectra recorded of Ba₂ isolated in Ar, Kr and Xe following deposition at 19, 25 and 35 K respectively. The gas phase $^1P_1 \leftarrow {}^1S_0$ transition of the atom is shown by a dashed vertical line as a reference. The magnitude of the Stokes shift is clearly increasing with the heavier, more polarizability host solids.**

The photophysical characteristics of the observed Ba₂ emission in the three rare gas hosts are collected in Table III.2. Lifetimes of 6 ns were recorded in Ar (as shown in Figure III.7) and Kr while the value in Xe is longer, in the region of 9 ns. Particularly pronounced in Table III.2, and evident in Figure III.6, is the variation of the Stokes shifts in the three rare gas solids studied – it increases by more than a factor of 4 from a value of 375 cm^{-1} in Ar to 1741 cm^{-1} in Xe, indicating a stronger interaction of the molecule with the heavier hosts. It is important to mention that the emission scans shown in Figure III.6 were made beyond 850 nm in all three RG's but no additional, lower energy dimer emission was observed in these low flux/high temperature samples. Furthermore, direct excitation of the dimer features between 720 and 800 nm also did not yield any emission out to the limit of detection at 900 nm.

Ba/Ar - Decay profile $\lambda_{Em.}$ = 579.9 nm at 10 K
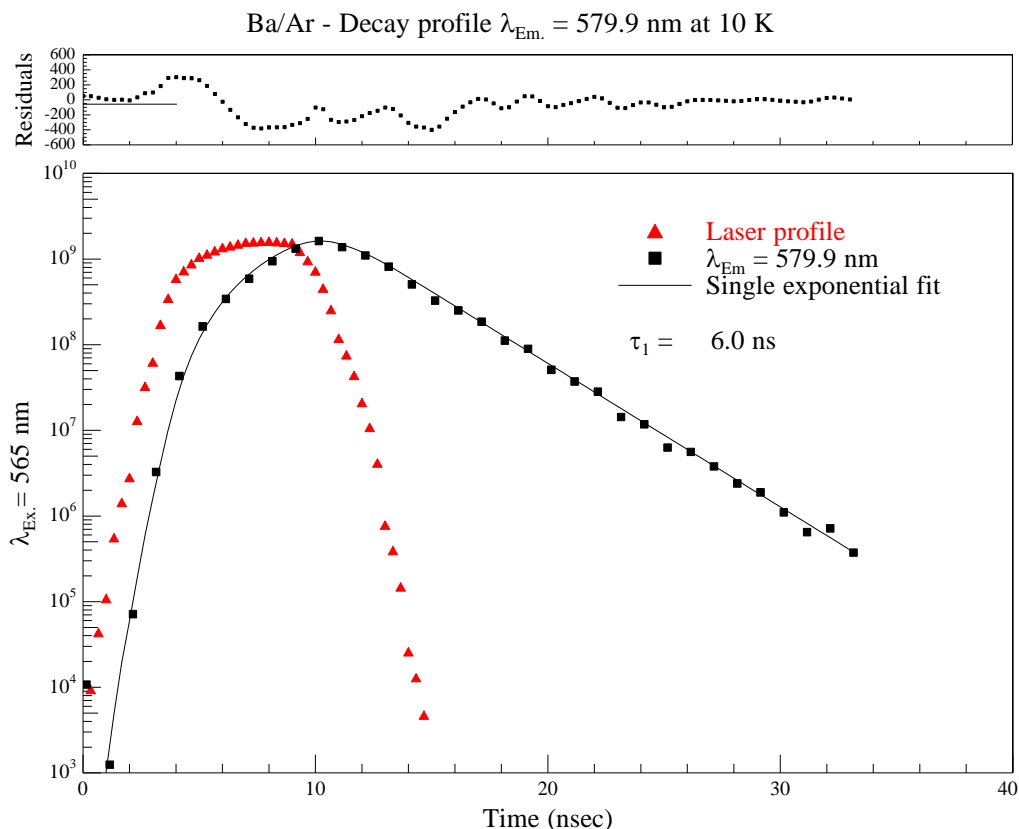
Figure III.7   **Decay profile of the Ba$_2$/Ar emission feature at ~ 580 nm, recorded at 10 K following sample deposition at 19 K with a medium-low metal flux. The decay profile is convoluted with the temporal profile of the laser excitation source at 565 nm. A single exponential function adequately fit the decay profile, as evidenced by the residuals analysis (top panel).**

Table III.2   **A summary of the photophysical characteristics extracted for the emission of Ba dimer (shown in Figure III.6) in the vicinity of the atomic resonance transition. SS is the Stokes shift between the emission and the lowest energy excitation band. From the values listed, the Stokes shift increases more than 4-fold from Ar to Xe indicating a stronger interaction of the dimer with the heavier RG hosts, especially Xe. *Note that the lifetime values in Kr and Xe were obtained indirectly with excitation of the resonance atomic transition.**

Ba$_2$/RG	Excitation Features			Emission Features			
	Component	λ (nm)	ν (cm^{-1})	λ (nm)	ν (cm^{-1})	SS (cm^{-1})	τ_{obs} (ns)
Ar	1	568.5	17590	580.9	17215	375	6
Kr	1	508.4	19670	617.4	16197	3473	6.3*
	2	562.8	17768			1571	
	3	579.4	17259			1062	
	4	589.6	16961			764	
Xe	1	524.4	19069	676.8	14775	4294	8.8*
	2	588.6	16989			2214	
	3	606.2	16496			1741	

III.3 Ba/RG atomic features

In this section, the UV/Vis absorption spectra, recorded of the most dilute Ba/RG samples are presented and analysed. Atomic transitions are assigned based on their proximity to the gas phase resonance line. Due to the relatively weak van der Waals forces responsible for the Ba-rare gas interaction (see the results of coupled-cluster calculations in Chapter VI), the energy of the solid-phase atomic transition is not expected to differ greatly from that of the free atom. The $(6s6p)\ ^1P_1 \leftarrow\ ^1S_0\ (6s^2)$ is the dominant gas phase transition of atomic Ba (out of the ground state) and occurs in the visible spectral region at 553.7 nm[3]. This transition will be used to probe the immediate RG environment of the Ba atom. Annealing effects on the $(6s6p)\ ^1P_1$ absorption profile allow identification of the thermally unstable sites of isolation for atomic Ba in the RG lattices. These thermally labile sites are created during vapour deposition at 10 K.

The complete absorption spectra recorded for the three Ba/RG matrix systems are presented in Figure III.8 for Ba isolated in samples formed at 10 K. Electron bombardment and medium/low metal fluxes were employed during these depositions to reduce the Sr contamination but also to minimise the formation of Ba metal aggregates. The UV/Vis spectra presented consist of strong bands in the vicinity of the resonance atomic $(6s6p)\ ^1P_1 \leftarrow (6s^2)\ ^1S_0$ transition of Ba, while the spectra in the near-UV region appear quite different in the three hosts studied. The bands in this region are much weaker than in the visible and cannot be associated immediately with any of the indicated atomic transitions in the gas phase (shown by the dashed vertical lines). However the analysis presented in section III.3.V will allow tentative assignments to be made.

III.3.I Ba/Ar

The UV/Vis absorption spectrum of a freshly deposited Ba/Ar sample, recorded at 10 K, is presented in the top panel of Figure III.8. Inspection of this trace reveals two main features: 1. an intense band centred at 535 nm in the visible region and 2. a less intense doublet centred at 318 nm in the UV region of spectrum. The former, dominant, absorption band is quite complex, exhibiting a series of overlapping structures at 514.2, 528.7, 543.9 and 554.0 nm. Despite the complication, assignment is straightforward based on its spectral dominance and location. Thus, this absorption band is assigned as

the solid state equivalent of the (6s6p) $^1P_1 \leftarrow$ (6s^2) $^1S_0$ transition of atomic Ba. Examination of Figure III.8 reveals that part of this absorption band overlaps with the gas phase transition energy, which is shown by a dashed vertical line.
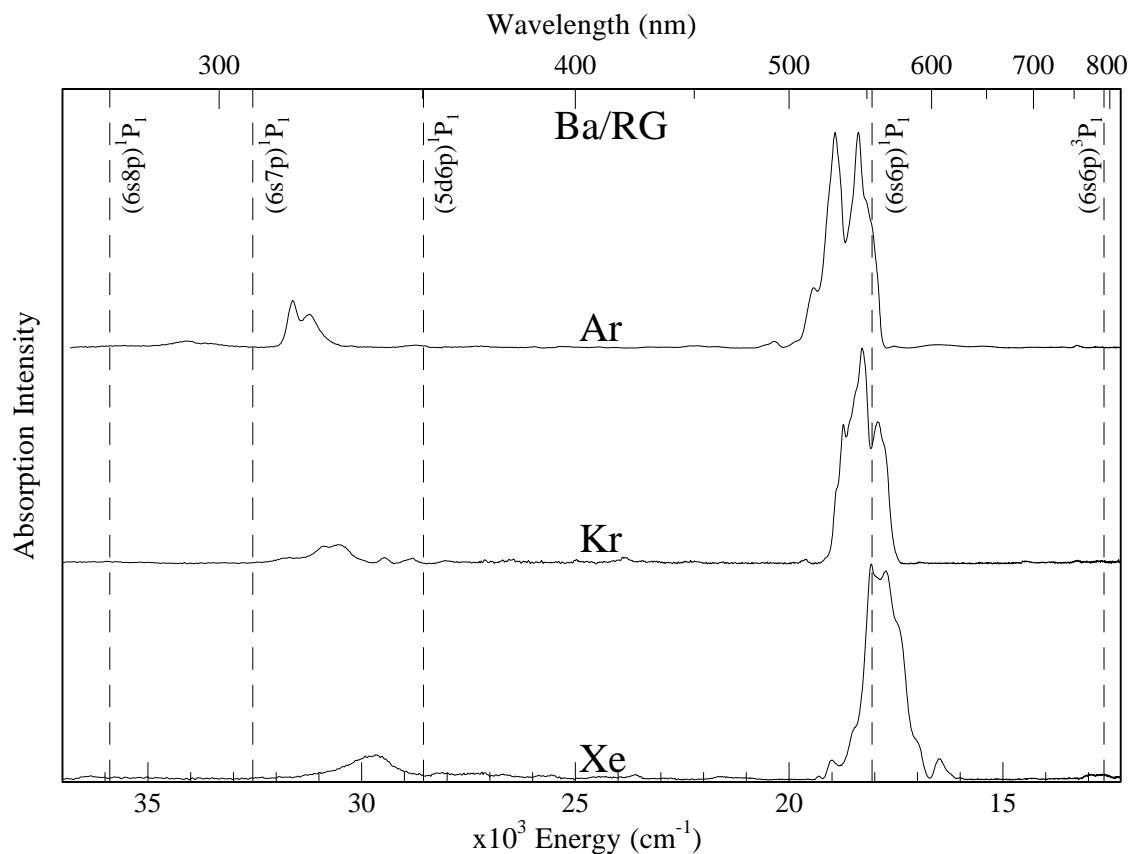

Figure III.8   **A summary of the normalised UV/Vis absorption spectra recorded following co-condensation of Ba vapour with the RG's (Ar, Kr and Xe) at 10 K. The known gas phase lines[3] of atomic Ba are overlaid for comparison and are shown as dashed vertical lines.**

Regardless of the initial deposition temperature, annealing the Ba/Ar system slowly to a temperature greater than 26 K consistently leads to the (6s6p) $^1P_1$ absorption profile depicted by the red trace in Figure III.9. Comparing the black ($T_{dep} = 10$ K) and red ($T_{an} = 30$ K) traces reveals the changes that occur in the absorption spectrum. The most striking change is the complete removal of the triplet centred at 553.6 nm. The doublet centred at 544 nm is reduced in intensity by more than a factor of three, while the absorption feature centred at 528.3 nm is enhanced and becomes dominant. A reduction in intensity is also observed for the bands at 514.2 and 524.2 nm.
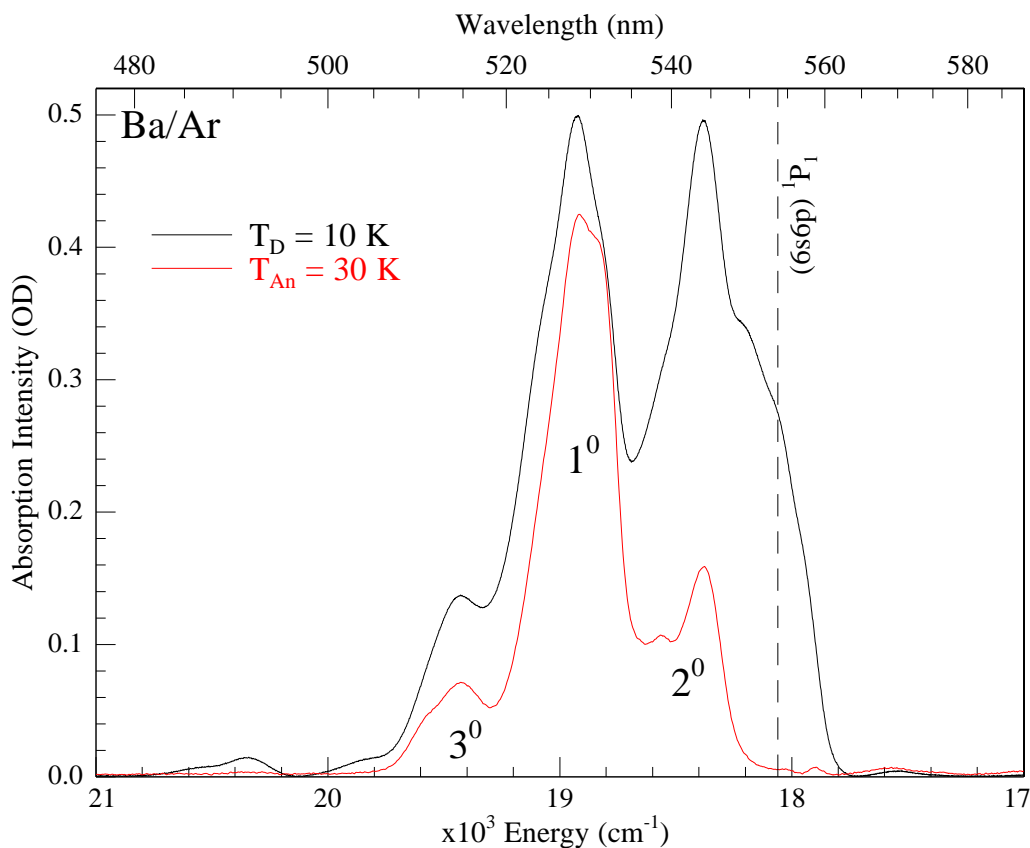
Figure III.9   **Before (black trace) and after (red trace) annealing the Ba/Ar sample to 30 K. The changes to the $^1P_1$ absorption profile result from the loss of thermally unstable sites of isolation for Ba within the Ar matrix. The spectra have not been normalised and accurately represent the changes in optical density (OD) that occur as a result of sample annealing.**

The simplification observed in absorption following annealing results from the removal of thermally unstable red sites of isolation for Ba within the Ar lattice. The remaining structured absorption feature suggests the presence of three sites of isolation for the atom. These are labelled primary (1^0), secondary (2^0) and tertiary (3^0) based on the relative amount of each, as indicated by the (6s6p) $^1P_1$ state absorption profile in Figure III.9.

III.3.II Ba/Kr

The UV/Vis absorption spectrum recorded for the Ba/Kr system following a low flux deposition at 10 K is presented by the middle trace of Figure III.8. The dominant feature in absorption is a band centred at approximately 547 nm and is assigned to the gas phase (6s6p) $^1P_1 \leftarrow$ (6s^2) $^1S_0$ transition of atomic Ba. The (6s6p) $^1P_1$ absorption profile consists peaks located at 529.1, 533.6, 537.8, 546.8, 557.8 and 562.5 nm. Weaker, UV

absorption bands are also observed and reported for the first time. These consist of a broad triplet with peaks at 315.3, 323.8, 327.6 nm and two weaker, lower energy bands at 339.4 and 346.6 nm.
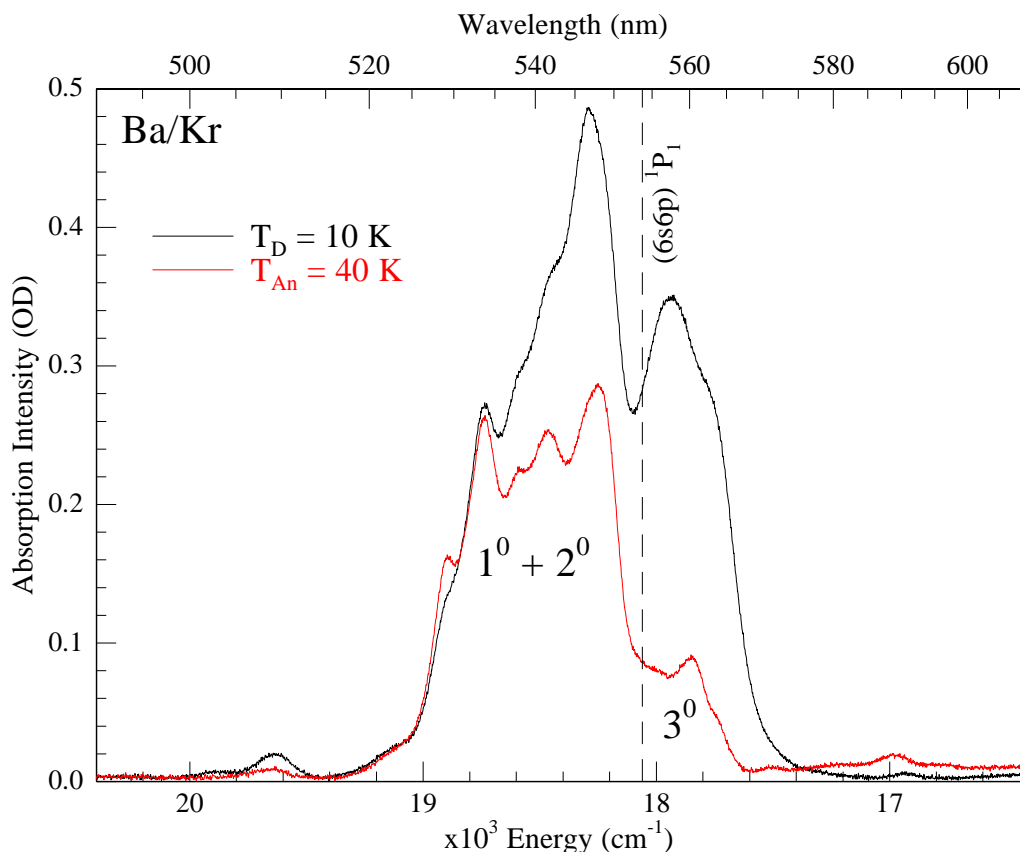

Figure III.10   **Before (black trace) and after (red trace) annealing the Ba/Kr sample to 40 K. The changes to the $^1P_1$ absorption profile reflect the loss of thermally unstable sites of isolation for Ba in solid Kr. The spectra have not been normalised and accurately represent the changes in optical density (OD) which occur as a result of sample annealing**

The effect of annealing on the (6s6p) $^1P_1$ absorption profile is shown by the red trace in Figure III.10. An unresolved, lower energy shoulder at approximately 568 nm has been completely removed. The broad red doublet, centred at 559 nm has been reduced almost by a factor of 4 and exhibits structure at 563.4, 560.2 and 555.5 nm. To the blue of the $^1P_1 \leftarrow {}^1S_0$ transition line, peaks at 548.3, 541.5 and 537.8 nm have been reduced and further resolved by the annealing process. Again, the remaining structured absorption band is suggestive of three distinct sites of isolation, with the 1^0 and 2^0 site absorptions strongly overlapping and of nearly equal intensity.

III.3.III Ba/Xe

The lowest trace of Figure III.8 presents the UV/Vis absorption spectrum recorded at 10 K, following co-condensation of Ba vapour with Xe onto a CaF_2 window, held at 10 K. Similar to the previous Ba/RG systems discussed, two main features are observed. The dominant band is centred at approximately 561 nm in the visible region. The second, less intense band is located at 337.5 nm in the UV region. The former is assigned to the gas phase $(6s6p) \, ^1P_1 \leftarrow (6s^2) \, ^1S_0$ transition of atomic Ba. Inspection of Figure III.8 reveals that the $^1P_1 \leftarrow \, ^1S_0$ absorption profile consists of multiple overlapping features with peaks at 540.5, 552.9, 557.5, 563.7, 573.7 and red shoulder at 587.6 nm.
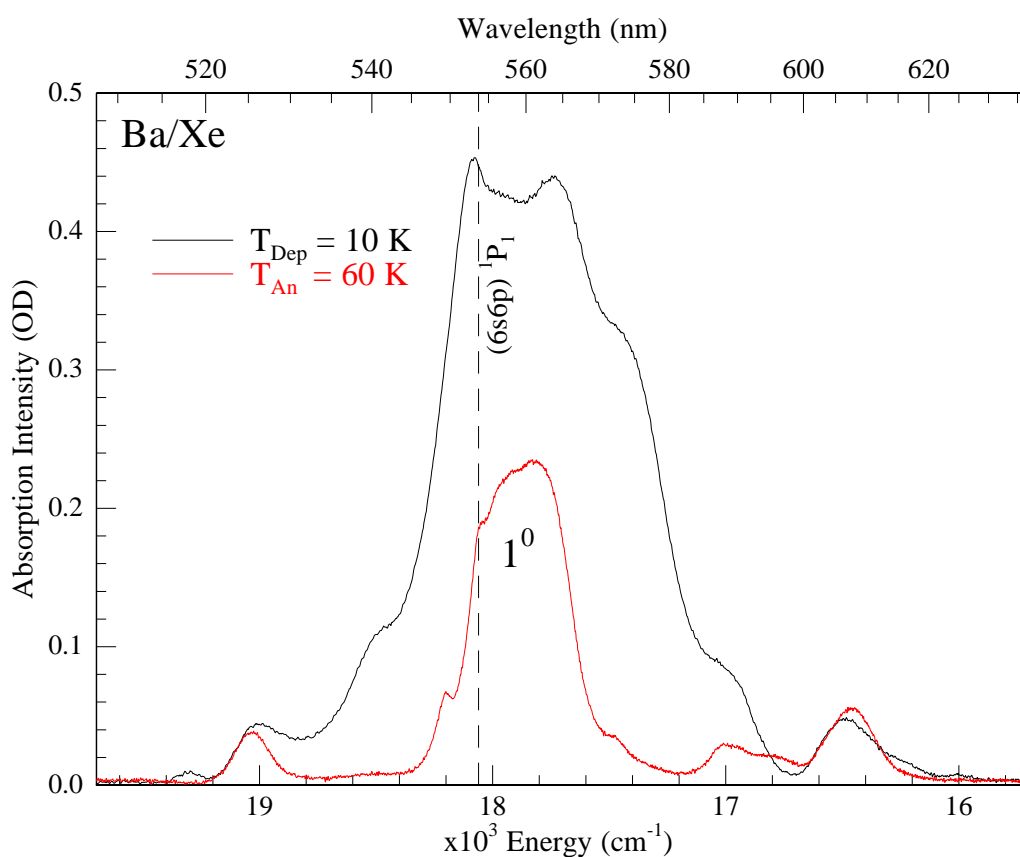
Figure III.11   **Before (black trace) and after (red trace) annealing the Ba/Xe sample to 60 K. The changes to the $^1P_1$ absorption profile reflect the loss of thermally unstable sites of isolation for the Ba atom within this host solid. Annealing results in the resolution of a Jahn-Teller threefold split centred at 557.7 nm. The spectra have not been normalised and accurately represent the changes in optical density (OD) which occur as a result of sample annealing**

Annealing the Xe matrix to 60 K greatly simplifies the spectral situation, as depicted by the red trace in Figure III.11. The bands located at 540.5, 552.9 and 573.7 nm are almost completely removed and their diminishment is attributed to the removal

of thermally unstable sites of isolation for atomic Ba within the Xe lattice. Analysing the integrated area before and after annealing shows that, over the range 515 – 640 nm, the total absorption profile has been reduced by more than a factor of three. A significant re-arrangement of the host solid has therefore occurred. Note that the features centred at 525, 589 and 606 nm correspond to well-isolated Ba_2, as described by the concentration study in Section III.2.II and the excitation spectra presented in Figure III.6.

The (6s6p) $^1P_1 \leftarrow$ (6s^2) $^1S_0$ absorption profile is characterised by a fully resolved Jahn-Teller (JT) triplet with peaks at 554.3, 557.5 and 561.0 nm and points to isolation of the atom within a highly symmetric, cubic site in solid Xe. A sharp absorption peak has also been resolved at 549.4 nm along with a broader, shoulder at 568.4 nm. Clearly a single site (1^0, see Figure III.11) of isolation dominates, however the features to the blue and red of the JT band may reflect the existence of a secondary, thermally stable site in solid Xe. The luminescence of Ba isolated in Xe will presented in Chapter IV to further investigate this possibility.

III.3.IV Ba/RG (6s6p) $^1P_1$ summary

A summary of the (6s6p) $^1P_1 \leftarrow$ (6s^2) $^1S_0$ absorption spectra recorded for Ba in the three annealed RG hosts is presented in Figure III.12. The spectral location of each individual peak is listed in Table III.3. It is clear that the (6s6p) $^1P_1$ state absorption dominates the spectroscopy of Ba/RG systems and is therefore one of the primary focuses of this investigation.
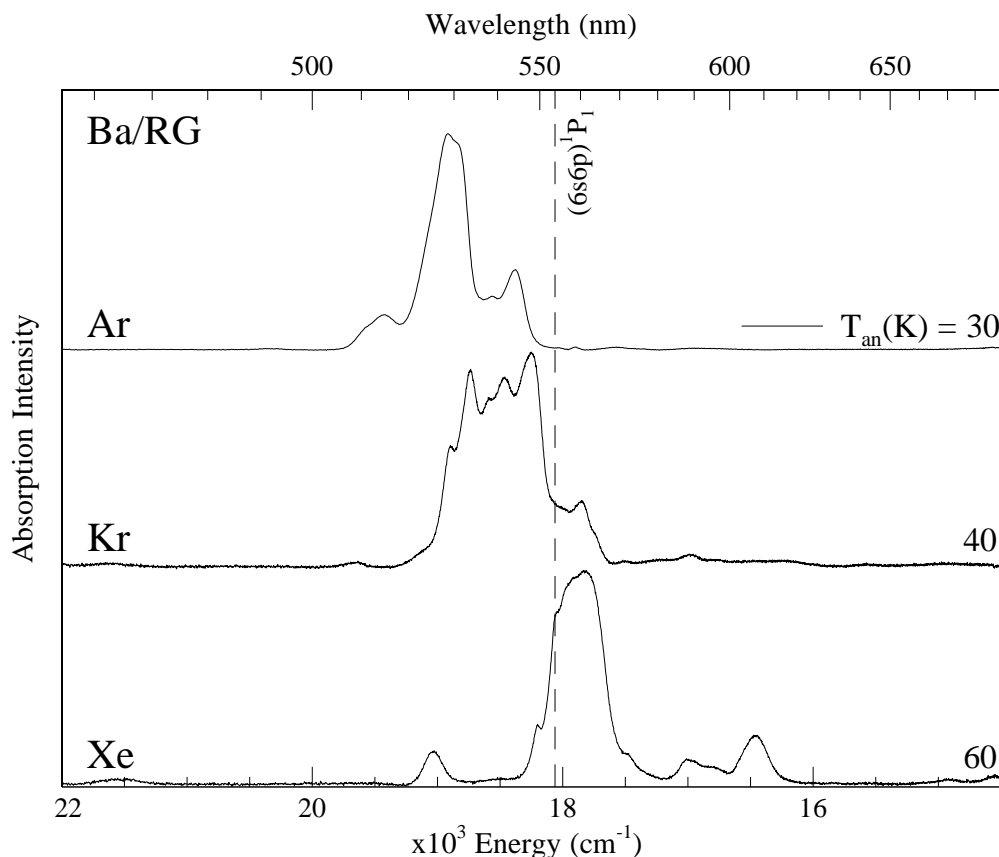
Figure III.12   **A summary of the normalised absorption spectra recorded for Ba isolated in each RG host. The spectra shown were recorded following sample annealing to 30, 40 and 60 K for Ar, Kr and Xe respectively. The gas phase position[3] of the dominant P ← S transition of the atom is denoted by a dashed vertical line.**

Taking the band centres as a reference, a progressive red shift is observed from Ar (+855 cm^{-1}), to Kr (+536 cm^{-1}) to Xe (-130 cm^{-1}) – an effect of the increasing rare gas polarizability. Annealing simplifies the spectra to an extent, with numerous absorption features being removed/reduced in each host as the thermally labile sites of the atom become de-populated. However, even after annealing, the absorption spectra are still quite complex and show that multiple thermally stable trapping sites exist for Ba within each host solid. The absorption spectra suggest the presence of three thermally stable

sites in Ar and Kr lattices and at least two in Xe. In Chapter IV, site-specific excitation spectroscopy will be used to fully unravel the complex Ba/RG absorption profiles.

Table III.3   Spectral positions of the absorption features assigned to $(6s6p)\ ^1P_1 \leftarrow\ ^1S_0\ (6s^2)$ transition of atomic Ba isolated in the solid RG's following sample annealing. δ represented the gas phase to RG matrix shift (given in units of wavenumber) calculated from the gas phase value[3] for this transition at 553.7 nm or 18060.261 cm^{-1}.

Host	Site	λ_{Abs} (nm)	ν (cm^{-1})	δ (cm^{-1})
Ar	3^0	510.7	19581	1521
		514.5	19436	1376
	1^0	524.2	19077	1016
		528.7	18915	855
		531.0	18832	772
	2^0	538.7	18563	503
		543.6	18395	334
Kr	$1^0 + 2^0$	529.1	18899	838
		533.6	18741	680
		537.8	18596	536
		541.5	18467	407
		547.0	18283	222
	3^0	555.7	17995	-65
		560.2	17851	-209
Xe	2^0	549.2	18210	149
	1^0	554.3	18041	-19
		557.7	17930	-130
		561.0	17825	-235
	2^0	568.4	17594	-466

III.3.V Ba/RG near-UV features

Near-UV absorption features have been observed for the first time for Ba isolated in the RG solids, the origins of which will now be discussed. As the bands were most prominent in Ar, analysis will begin there. An absorption doublet with peaks at 316.2 and 320.3 nm was shown in the top trace of Figure III.8. A more detailed and extensive view of this spectral region is presented in Figure III.13 revealing the presence of a weaker, higher energy doublet with peaks at 293.4 and 297.6 nm. Concentration studies conducted on the Ba/Ar system (see Figure III.3) indicate that the intensities of both doublets track the resonance atomic $(6s6p)\ ^1P_1$ absorption under all metal/Ar loadings

– provided the latter is not fully absorbing. Accordingly these bands are attributed to atomic Ba.
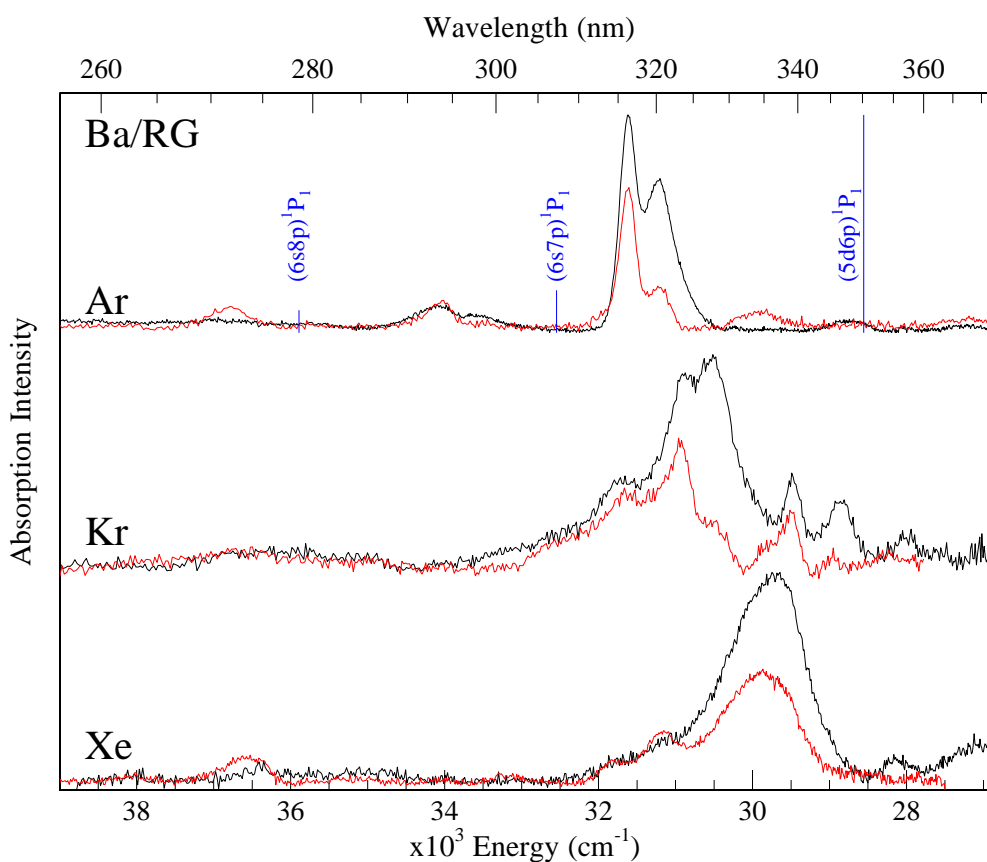
Figure III.13 **A summary of the normalised UV absorption spectra recorded for Ba isolated in all three RG hosts. The black traces represent samples freshly deposited at 10 K. The red traces show the effect of sample annealing to the 30, 40 and 60 K for Ar, Kr and Xe respectively. The gas phase position[3] of the atomic UV transitions are shown by the labelled vertical blue lines.**

The two most intense gas phase[3] atomic lines occurring in this spectral region are the $(5d6p)\ ^1P_1 \leftarrow\ ^1S_0\ (6s^2)$ transition at 350.21 nm and the $(6s7p)\ ^1P_1 \leftarrow\ ^1S_0\ (6s^2)$ transition at 307.24 nm. Their relative intensities in the gas phase are reported as 860 and 168 respectively, a ratio of approximately 5:1 as indicated by the vertical blue lines in Figure III.13.

The measured integrated areas of the two matrix absorption profiles yields a ratio of approximately 6:1, in good agreement with the gas phase value. From the intensity correspondence evident in Figure III.13, it is clear the absorption doublet centred at 318 nm arises from the $(5d6p)\ ^1P_1 \leftarrow\ ^1S_0\ (6s^2)$ transition of atomic Ba while that centred at 295 nm is the solid state equivalent of the $(6s7p)\ ^1P_1 \leftarrow\ ^1S_0\ (6s^2)$

transition with a matrix shift of +1350 cm^{-1}. The larger matrix shift of approx. +2892 cm^{-1} present on the 318 nm band in Ar is consistent with the fact it involves a two electron transition – the excited [Xe]5d6p electronic configuration is accessed from the [Xe]6s^2 ground state. The location of the (6s8p) $^1P_1$ level is not obvious in the absorption spectra recorded for freshly deposited Ar samples, however, a band arises at approx. 270 nm after annealing (red trace) which is possibly due to this transition.

The absorption bands located at 326 nm in Kr and 336 nm in Xe are assigned to the atomic (5d6p) $^1P_1 \leftarrow$ $^1S_0$ (6s^2) transition. A greater red-shift is observed on this transition in comparison to the (6s6p) $^1P_1 \leftarrow$ $^1S_0$ (6s^2) features. In Ar, Kr and Xe, the respective gas-phase-to-matrix shift is calculated (from the band centre) as approx. 2892, 2121 and 1208 cm^{-1}. It is noteworthy that the intensity of this transition appears to be reduced in Kr and Xe matrices when compared to Ar.

Table III.4   **Spectral positions of the absorption features assigned to (5d6p) $^1P_1 \leftarrow$ $^1S_0$ (6s^2) and (6s7p) $^1P_1 \leftarrow$ (6s^2) $^1S_0$ transitions of atomic Ba isolated in the solid RG's following sample annealing. δ represented the gas phase to RG matrix shift (given in units of wavenumber) calculated from the gas phase value[3] of each transition which occur respectively at 28554.221 and 32547.033 cm^{-1}.**

Host	State	λ_{Abs} (nm)	ν (cm^{-1})	δ (cm^{-1})
Ar	5d6p $^1P_1$	316.2	31626	3071
		320.3	31221	2667
	6s7p $^1P_1$	293.4	34083	1536
		297.6	33602	1055
Kr	5d6p $^1P_1$	315.5	31696	3142
		332.8	30048	1494
		327.6	30525	1971
		338.8	29516	962
Xe	5d6p $^1P_1$	314.4	31807	3252
		320.9	31162	2608
		334.4	29904	1350

However, the integrated area of each absorption profile is very similar in all three rare gas solids. The weaker intensities are compensated by broader spectral widths in Kr and Xe. In contrast to the two atomic transitions discussed, analysis of the (6s7p) $^1P_1 \leftarrow$ $^1S_0$ (6s^2) atomic transition, which was observed at approx. 295 nm for Ba/Ar, cannot be extended to all three RG's. Weakly absorbing in Ar, this transition could not be observed in the absorption spectrum of either Ba/Kr or Ba/Xe. The absorption peaks,

state assignments and matrix shifts of the annealed Ba/RG UV features are summarised in Table III.4.

III.4   Sr/RG sample characterisation

The following sections are presented in a fashion analogous to the Ba/RG investigation. Sr vapour was generated via electron bombardment and subsequently co-condensed with the RG of choice onto a CaF_2 window held at the desired temperature. Variation of two deposition parameters: metal flux and window temperature, provides a concentration study for each system. The absorption spectra of each deposit are compared to distinguish between features of the atom and the dimer. In general, interpretation of the absorption spectroscopy of Sr/RG samples is simpler than Ba/RG samples. The absorptions associated with Sr_2 do not overlap the atomic features. Moreover a characteristic vibronic structure is present on the lowest energy dimer band. As was the case for Ba_2, a more discriminating and informative analysis of Sr_2 is provided by steady-state and time-resolved luminescence measurements. The spectroscopy of the most atomic Sr/RG samples will then be presented in Section III.5.

III.4.I   Sr/RG concentration studies

As done with the matrix-isolated Ba system, a concentration study was conducted on Sr/RG samples the results of which are presented for Sr/Ar in Figure III.14. The sample with the highest metal loading, shown in trace a), presents the most complex spectrum. However, a comparison of the most dilute samples (traces c and d) reveals that many of these features can be attributed to dimer absorptions. The most prominent of these bands are indicated on trace c) with the labels I-III and are centred respectively at 405.6, 550 and 711 nm. The lowest energy dimer feature, band I, is shown on an expanded scale on the right of the figure. In contrast to the equivalent Ba_2 band (shown in Figure III.3), this transition shows resolved vibrational structure with average splittings of ~64 cm^{-1}.
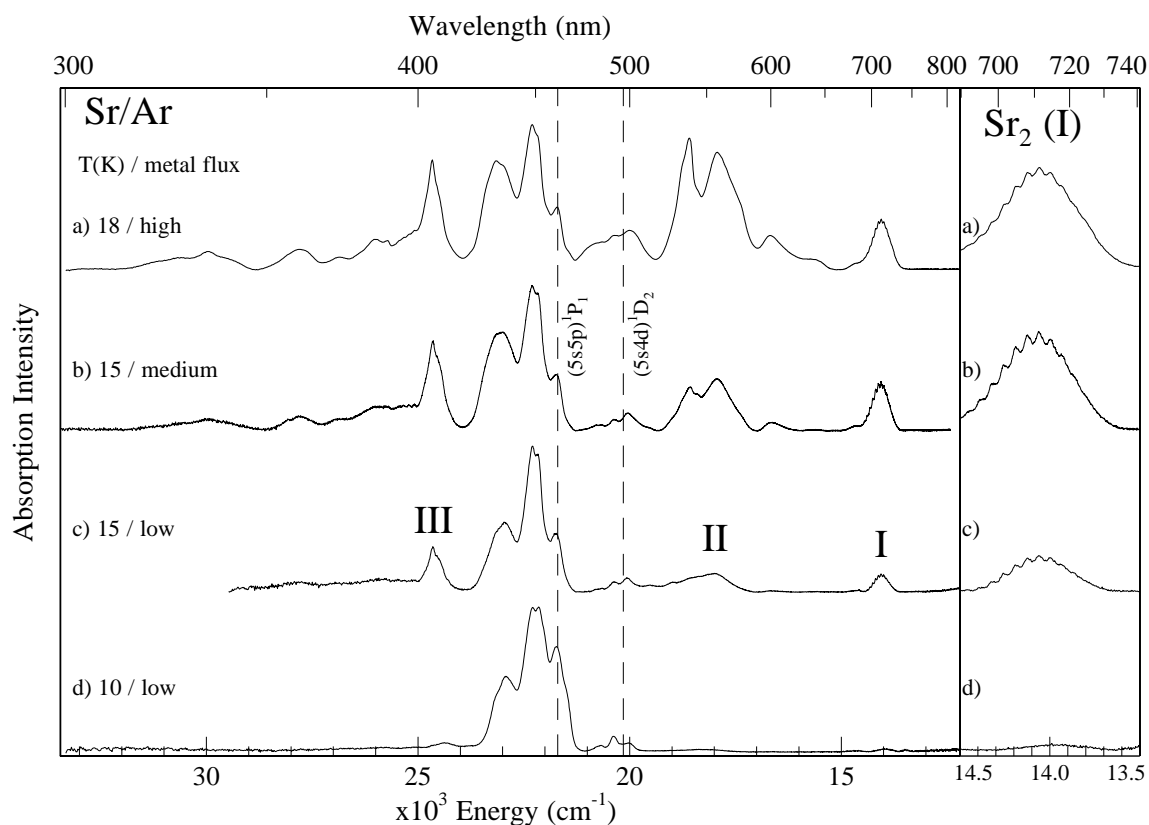
Figure III.14 Normalised UV/Vis absorption spectra recorded following co-condensation of Sr vapour with Ar at the indicated deposition temperatures. The four spectra shown detail the changes in the relative intensities of the absorption bands that occur with 1) increasing deposition temperature and 2) increasing metal loadings. The gas phase positions of the (5s5p) $^1P_1$ and (5s4d) $^1D_2$ states are shown as dashed vertical lines. The right-hand panel provides an expanded view of the Sr_2 band (labelled I) highlighting the resolved vibrational structure.

Similar to the Ba/Kr system, low temperature (10 K) Sr/Kr deposits require high metal fluxes to generate substantial amounts of Sr_2 in this host, as evidenced by trace b) of Figure III.15. However, increasing the sample window to 24 K during deposition increases the yield of aggregates, even with a low metal flux. Inspection of spectrum a) allows extraction of the bands associated with Sr dimer, these are labelled I – III and are directly related to the features observed in Ar. The low flux/ 10 K deposit contains mostly isolated Sr atoms and exhibits absorptions arising from two distinct atomic transitions (shown by dashed vertical lines) – these bands are broad and complex due to multiple site occupancy.
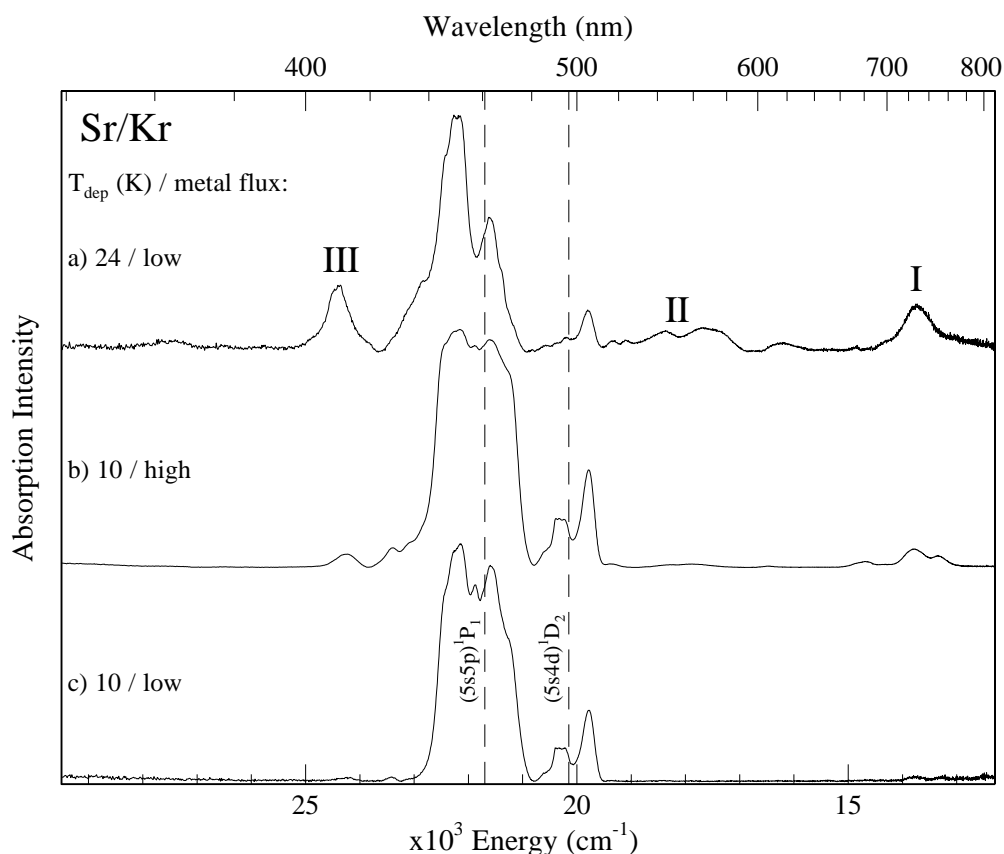
Figure III.15 Normalised absorption spectra recorded following co-condensation of Sr vapour with $T_w = 10$ and 24 K. The effects of increasing the metal loading and deposition temperature can be observed. The gas phase positions of the (5s5p) $^1P_1$ and (5s4d) $^1D_2$ states are shown as dashed vertical lines.

The absorption spectra of Sr isolated in solid Xe with varying deposition conditions (metal flux and window temperature) are presented in Figure III.16. Comparing traces b) and c), which were deposited at 10 K with a high and low metal flux respectively, shows that exclusive atomic isolation is achieved for Sr in solid Xe as both spectra are dominated by the (5s5p) $^1P_1 \leftarrow {}^1S_0$ ($5s^2$) transition[3] of the atom. However, increasing the sample window to 30 K during deposition produces a number of changes. Firstly, the atomic features are simplified and become more resolved. Secondly, two weakly absorbing bands are observed to 'grow in' at 418.4 nm and 745 nm. These are labelled I and III in association with the equivalent features observed in the other two systems. Cleary the formation of Sr_2 is limited in Xe, even with a high deposition temperature. As a consequence, the band labelled II in the previous RG hosts, is not clearly identifiable in absorption. However, excitation spectra recorded monitoring Sr_2/Xe emission will allow this band to be extracted. The luminescence of Sr_2 isolated in the RG solids will now be presented.
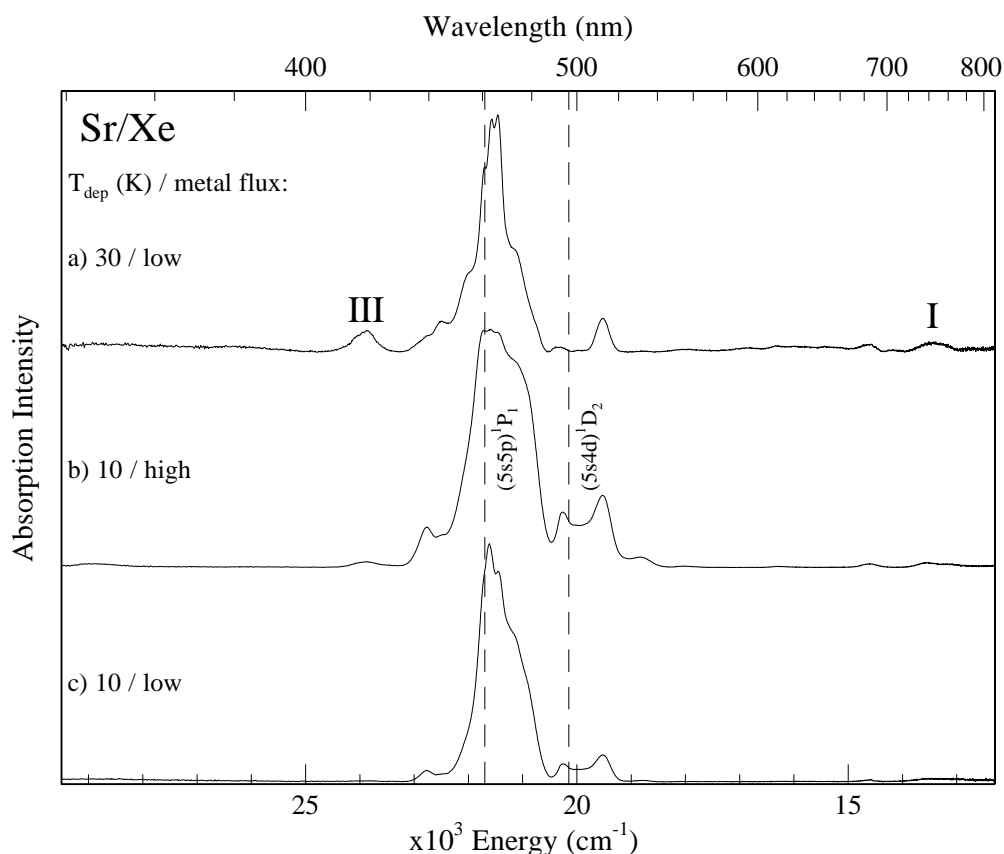
Figure III.16 Normalised absorption spectra recorded following co-condensation of Sr vapour with $T_w = 10$ and 30 K. The effects of increasing the metal loading and deposition temperature can be observed. The gas phase positions of the (5s5p) $^1P_1$ and (5s4d) $^1D_2$ states are shown as dashed vertical lines.

III.4.II Sr₂/RG emission

Sr₂/RG emission and excitation spectra are shown in Figure III.17, while the extracted photophysical parameters are collected in Table III.5. A comparison with the equivalent Ba₂ plot in Figure III.6 reveals that the diatomics of these two elements exhibit very different emission. Sr₂ clearly shows resonance emission from the lowest energy transition (band I) at approximately 780 nm, while Ba₂ produces none from this band. The lack of emission in the latter is most likely due to the density of molecular states which arise from the multitude of atomic D and P asymptotes in this region. A comparison of the atomic energy levels, provided in Figure I.7 (Chapter I), reveals the simplicity of the Sr and complexity of Ba due to the existence of the ^1D and ^3D states in the vicinity of the ^3P state.
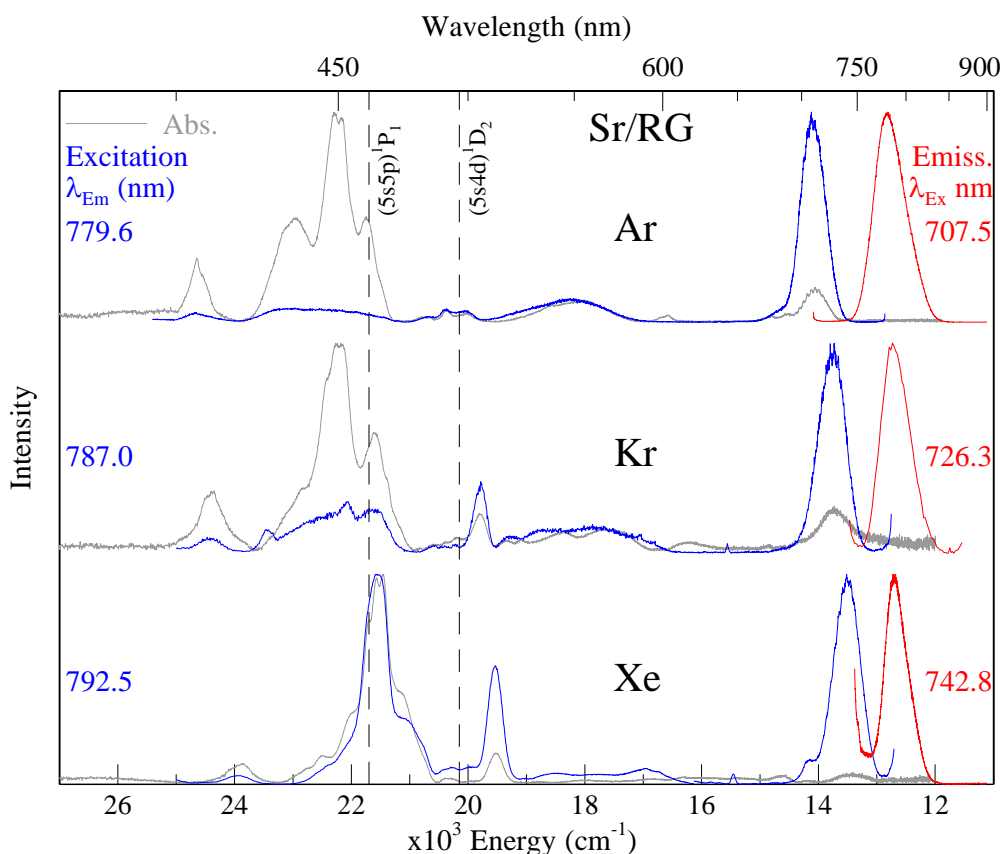
Figure III.17 Luminescence spectra recorded of the three Sr₂/RG samples which were deposited at 15, 24 and 30 K for Ar, Kr and Xe respectively. The absorption spectrum of each sample is shown in grey. Emission (shown in red) was produced with photoexcitation of the lowest energy, structured dimer band (I) in each host. Excitation spectra (shown in blue) were obtained by monitoring the resultant emission bands and were recorded across the entire spectral range, starting from 400 nm. The gas phase positions of the (5s5p) $^1P_1$ and (5s4d) $^1D_2$ atomic states of Sr are shown as dashed vertical lines.

The Ar excitation scans shown in Figure III.17 establish that band II, located at approx. 550 nm (see Figure III.14) is indeed a dimer absorption. This broad feature is more structured in the heavier two hosts with partially resolved peaks at 532.4 (539) and 563.2 (589.5) nm for Kr (Xe). Examination of the Kr and Xe excitation scans shown in Figure III.17 reveals that the atomic features are much more prominent in the heavier rare gases. This is especially evident in the Sr/Xe scans (bottom panel) and arises because efficient $^1P \rightarrow {}^3P$ intersystem crossing (ISC) produces intense atomic $^3P_1$ state emission in Xe, which coincides spectrally with the dimer emission. Details of the Sr atom emission in the solid RG's will be presented in Chapter V. In any case, the resolved vibrational structure present on the 740 nm excitation band in Sr/Xe establishes that this is indeed a dimer transition.
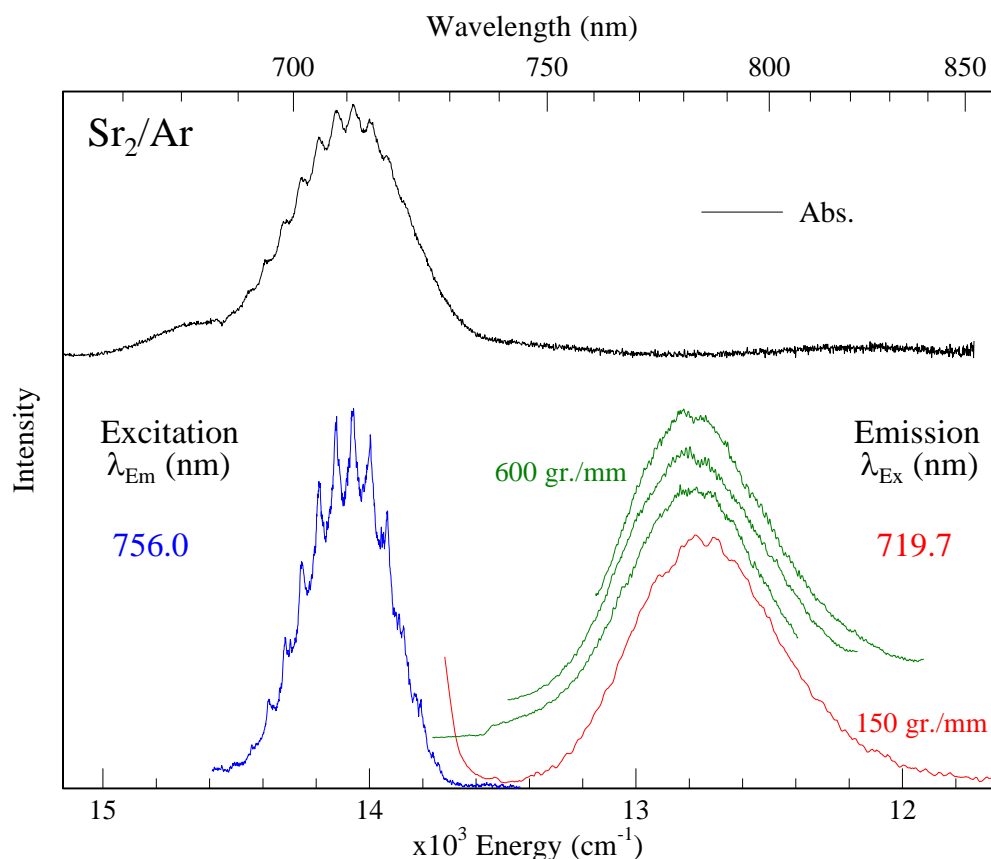
Figure III.18   **The top panel shows an absorption spectrum, recorded with a W-lamp/PMT combination, in the region of the structured Sr_2/Ar band. The lower panel presents high resolution excitation (blue) and emission spectra (green = 600 gr./mm, red = 150 gr./mm gratings) recorded with laser excitation. Slits of 0.1 mm in width were used on the emission monochromator.**

The photophysical characteristics of the Sr_2/Ar emission are summarised in Figure III.18 and the extracted data are collected in Table III.5. From a single exponential fit of recorded emission decay curve, shown on a semi-log plot in Figure III.19, a lifetime of 15.5 ns is obtained. The recorded decay curves were found to be independent of temperature up to 18 K, the highest value used, so 15.5 ns is accordingly identified as the radiative lifetime. With a lifetime of 15.5 ns, this clearly corresponds to a fully allowed molecular transition and bolsters the $^1\Sigma_u^+ \leftarrow X\ ^1\Sigma_g$ assignment previously made by Miller and Andrews[10,11], who also observed this 780 nm emission of Sr_2 in Ar matrices. The excitation scan shown in Figure III.18 was recorded by scanning the dye laser (using the LDS 698 dye) while recording the emission with the time-gated iCCD camera. The vibronic structure present on the excitation scan is more resolved than in the absorption scan (shown directly above). An average splitting of 63.7 cm^{-1} is extracted from the dye laser scan. High resolution emission scans recorded did not resolve any vibronic structure on the emission band. While there is no overlap

between the excitation and emission scans, the band origin of the molecular transition is tentatively attributed to the commencement of the emission at ~ 13500 cm^{-1}. Interestingly, a comparison of the Sr$_2$ emission data in Table III.5 with that provided in Table III.2 reveals different behaviour to that observed for Ba$_2$. In particular the Stokes shifts are small for Sr$_2$ and nearly the same in all three rare gas hosts, while those observed for Ba$_2$ are large and increase greatly in Xe.
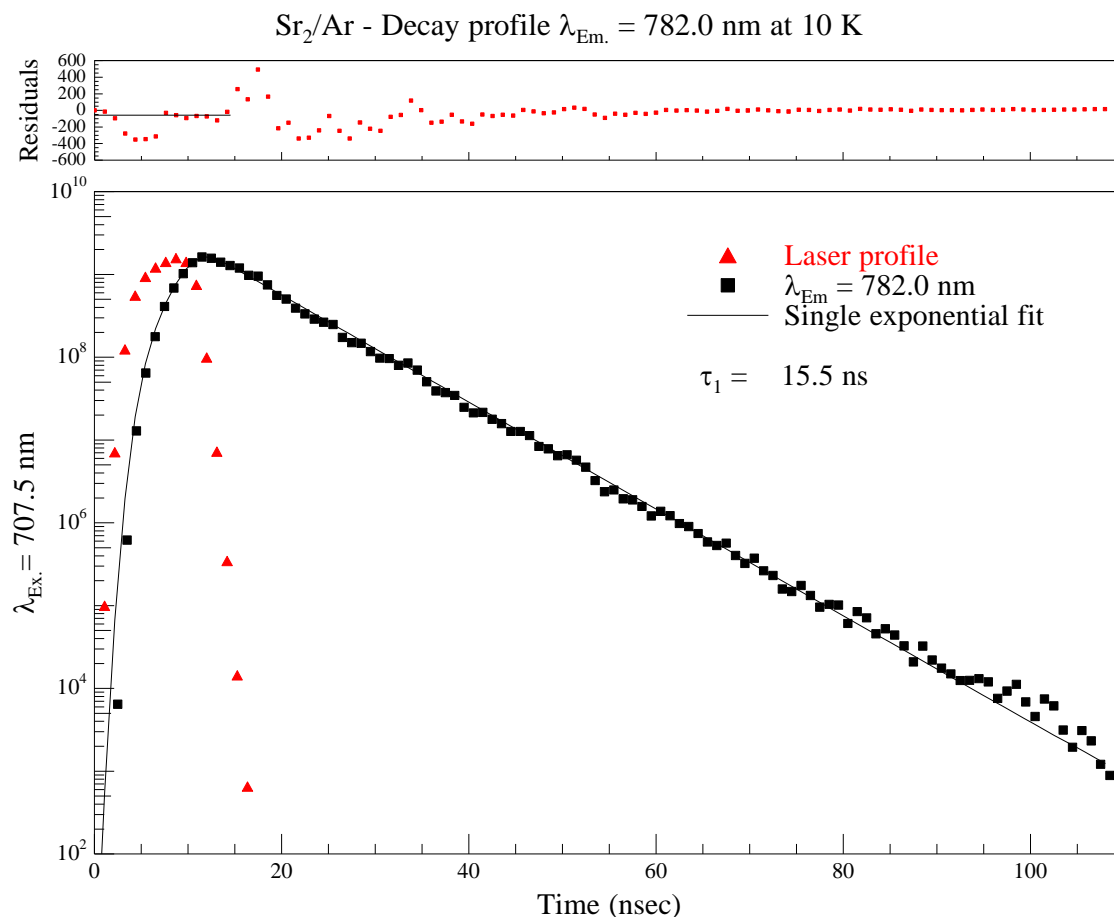

Figure III.19   **Decay profile of the Sr$_2$/Ar emission feature at ~ 780 nm, recorded at 10 K following sample deposition at 15 K with a low metal flux. The decay profile is convoluted with the temporal profile of the laser excitation source at 707.5 nm.**

Table III.5   **The photophysical characteristics of the emission of Sr dimer extracted from the spectra shown in Figure III.17. These dimer emissions occur in the vicinity of the atomic $^3P_1 \rightarrow {}^1S_0$ transition[3] at 689.4491 nm.**

Sr$_2$/RG	Excitation Features			Emission Features			
	Component	λ (nm)	ν (cm^{-1})	λ (nm)	ν (cm^{-1})	S.S (cm^{-1})	τ_{obs} (ns)
Ar	III	405.6	24655				
	II	550.0	18182				
	I	707.5	14134	779.9	12822	1312	15.5
Kr	III	409.5	24420				
	II	559.0	17889				
	I	725.4	13785	784.6	12745	1040	n/a
Xe	III	417.5	23952				
	II	567.0	17637				
	I	739.8	13517	787	12706	811	n/a

III.5 Sr/RG atomic features

Absorption spectra recorded following co-deposition of Sr vapour with the rare gases at 10 K, under conditions of low metal loading, are presented in Figure III.20. In contrast to the pure Ba/RG systems, the observed Sr features are present only in the visible spectral region from 400 - 520 nm. The dominant absorption bands are centred at 450.0 (Ar), 457.4 (Kr) and 467.7 nm (Xe). These features are assigned to the strong $(5s5p)$ $^1P_1 \leftarrow$ $^1S_0$ $(5s^2)$ transition of atomic Sr, which occurs at 460.7 nm in the gas phase[3].
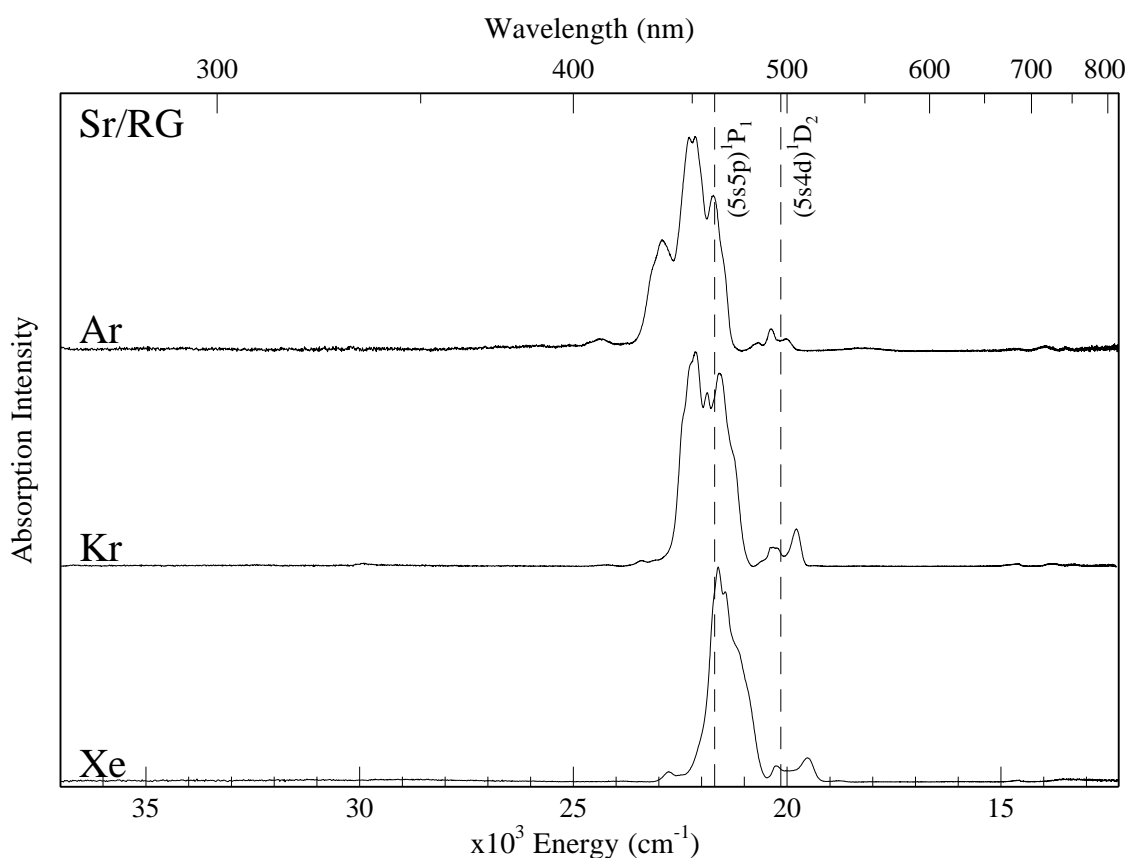
Figure III.20   **A summary of the normalised UV/Vis absorption spectra recorded following co-condensation of Sr vapour with the RG's (Ar, Kr and Xe) at 10 K. The known gas phase positions[3] of the $(5s5p)$ $^1P_1$ and $(5s4d)$ $^1D_2$ states of atomic Sr are overlaid for comparison and are shown as dashed vertical lines.**

In addition, a weaker series of absorption peaks are also observed to the red of the $^1P_1$ line. In Ar (Kr, Xe), these peaks are located at 481.9 (484.1, 492.2), 491.0 (492.2, 501.7) and 499.3 (505.4, 511.6) nm. The samples presented in Figure III.20 are highly atomic, with little or no evidence of the characteristic Sr_2 absorption around 700 nm. Therefore these weaker features are attributed to transitions of the atom. Inspection

of Figure I.7 (Chapter I) shows that the $^1D_2$ state of Sr lies energetically close to the $^1P_1$ state. Indeed, overlaying this energy value[3] (20149.685 cm^{-1}) as a dashed vertical line on the matrix absorption spectra allows for a confident assignment to be made. Thus, the strongest absorption features centred at 484.1, 492.2 and 505.4 nm in Ar, Kr and Xe respectively, are assigned to the parity-forbidden (5s4d) $^1D_2 \leftarrow$ $^1S_0$ (5s^2) transition of atomic Sr.

III.5.I Sr/Ar

An expanded view of the (5s5p) $^1P_1$ and (5s4d) $^1D_2$ absorption profiles is provided for the Sr/Ar system in Figure III.21.
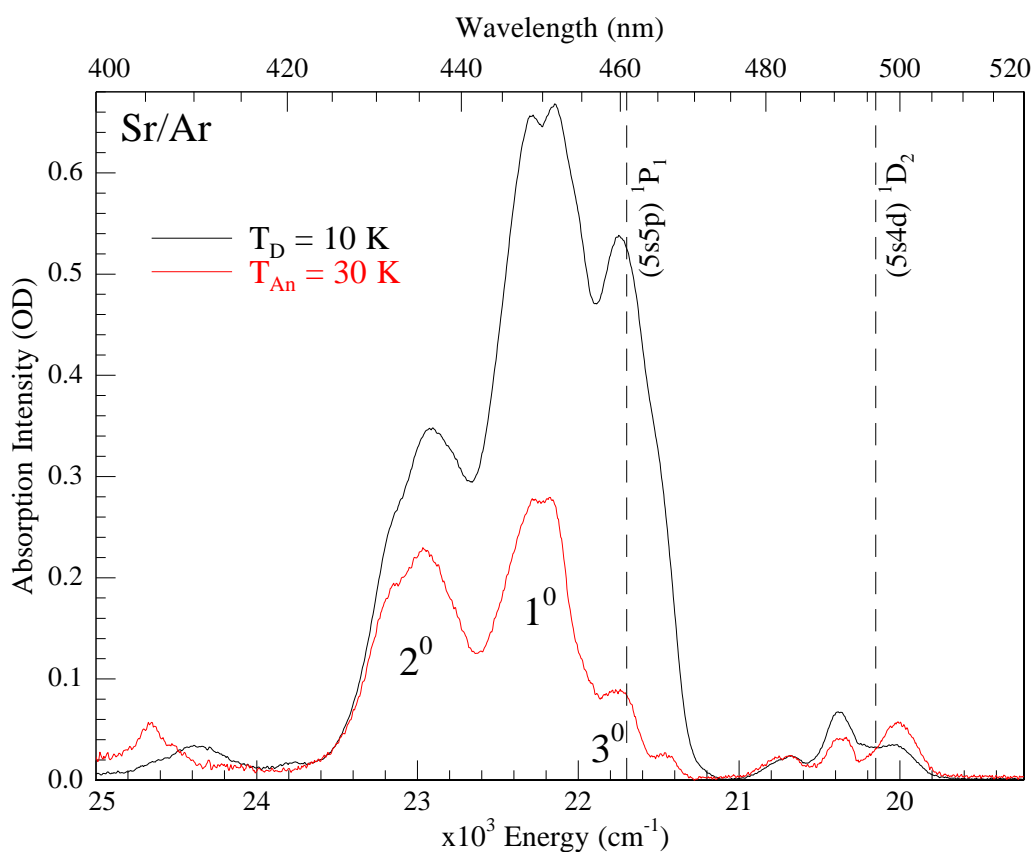
Figure III.21   **Before (black trace) and after (red trace) annealing the Sr/Ar sample to 30 K. The changes to the ^1P and ^1D absorption profiles result from the loss of thermally unstable sites of isolation for Sr in the Ar host solid. The spectra have not been normalised and accurately represent the changes in optical density (OD) which occur as a result of sample annealing.**

The (5s5p) ^1P absorption band is quite complex on deposition, as was the case for Ba/Ar, and comprises resolved features at 431.5, 435.4, 448.6, 451.0 and 459.9 nm,

with a broad shoulder at 466.1 nm. Annealing the Ar matrix slowly to 30 K significantly alters the spectrum, and this is reflected by a reduction in the integrated absorption area by almost a factor of 3 (when evaluated between 415 and 510 nm). The red features at 459.9 and 466.1 nm are reduced the most by this process. Interestingly, annealing has the opposite effect on the (5s4d) $^1D_2 \leftarrow\ ^1S_0$ (5s^2) transition, where the red feature at 499.9 nm now dominates and the bands furthest to the blue at 482.1 and 491.0 nm are diminished.

Annealing has therefore removed the thermally unstable sites of isolation for atomic Sr in solid Ar. The remaining absorption features strongly suggest the presence of three thermally stable sites for Sr in Ar. In Figure III.21, these are labelled as primary (1^0), secondary (2^0) and tertiary (3^0), based on the relative amount of each, as indicated by the (5s5p) $^1P_1$ state absorption. The 1^0 and 2^0 sites are present in almost equal amounts, with the band at 450 nm slightly more prevalent.

III.5.II Sr/Kr

The full absorption spectrum of Sr/Kr is presented in the middle of Figure III.20 and a close-up of the region of interest (420 - 520 nm) is shown in Figure III.22. On deposition, the (5s5p) $^1P_1$ and (5s4d) $^1D_2$ bands exhibit numerous overlapping features produced by the population of thermally unstable sites for the atom in Kr. Indeed, the (5s5p) $^1P_1$ profile is even more complex than for the Sr/Ar system displaying resolved structure at 445.9, 449.0, 451.6 and 457.1 nm, with a broad shoulder at 463.3 nm. Careful annealing up to 40 K partially alleviates the spectral congestion as the thermally unstable sites are removed. The resultant, annealed spectrum is shown in Figure III.22 (red trace). The lowest energy (5s5p) $^1P_1$ absorption bands are again, most amenable to change with sample annealing. This behaviour is contrasted with the (5s4d) $^1D_2$ absorption bands where the highest energy features are diminished to a greater extent. Inspection of the annealed trace reveals that, in terms of relative intensities, the (5s4d) $^1D_2$ absorption bands are a 'mirror image' of the (5s5p) $^1P_1$ features.

The annealed (5s5p) $^1P_1$ absorption profile of Sr/Kr suggests the presence of at least two thermally stable sites of isolation for the guest atom. The primary site (1^0) comprises peaks at 445.9, 449.0 and 451.6 – a characteristic Jahn-Teller threefold split, indicative of atomic isolation in a highly symmetric, cubic site of the Kr lattice. The secondary site absorption band is narrower and is centred at 462.7 nm. A shoulder to

the blue and red of the band centroid suggests an unresolved Jahn-Teller threefold split pattern. The third (3^0) site may be remnants of a thermally labile feature and will be further investigated in Chapter V with aid of the atomic Sr/Kr luminescence.
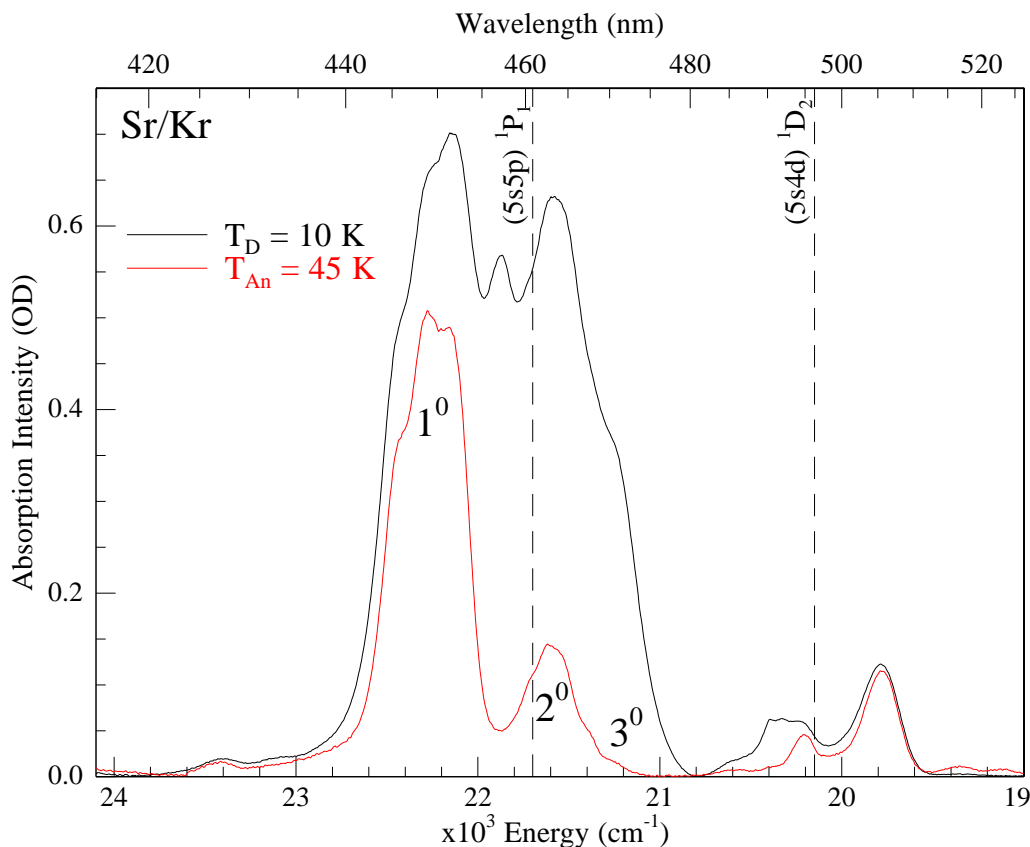

Figure III.22   **Before (black trace) and after (red trace) annealing the Sr/Kr sample to 40 K. The changes to the ^{1}P and ^{1}D absorption profiles result from the loss of thermally unstable sites of isolation for Sr in the Kr matrix. The spectra have not been normalised and accurately represent the changes in optical density (OD) which occur as a result of sample annealing.**

III.5.III   Sr/Xe

The Sr/Xe absorption spectrum is shown in the bottom of Figure III.20 (full range) and presented in greater detail in Figure III.23. On deposition at 10 K (black trace of Figure III.23), the (5s5p) $^1P_1$ profile is dominated by a triplet structure centred at 463.5 nm whereas the maximum of the (5s4d) $^1D_2$ state absorption is a band located at 512.7 nm. Annealing the Xe matrix to 60 K (red trace of Figure III.23) further simplifies the (5s5p) $^1P_1$ profile, with the complete removal of higher and lower energy shoulders, located at 453.7 and 479.2 nm respectively. In contrast, it is the higher energy bands on the (5s4d) $^1D_2$ profile at 492.2 and 501.7 which are completely removed. The total

integrated area of the absorption profile, including both (5s5p) $^1P_1$ and (5s4d) $^1D_2$ bands (evaluated over the range 430 – 520 nm), has been reduced by a factor of 6 with matrix annealing, implying significant changes occur to the Xe matrix as it is allowed to attain a more crystalline packing structure.
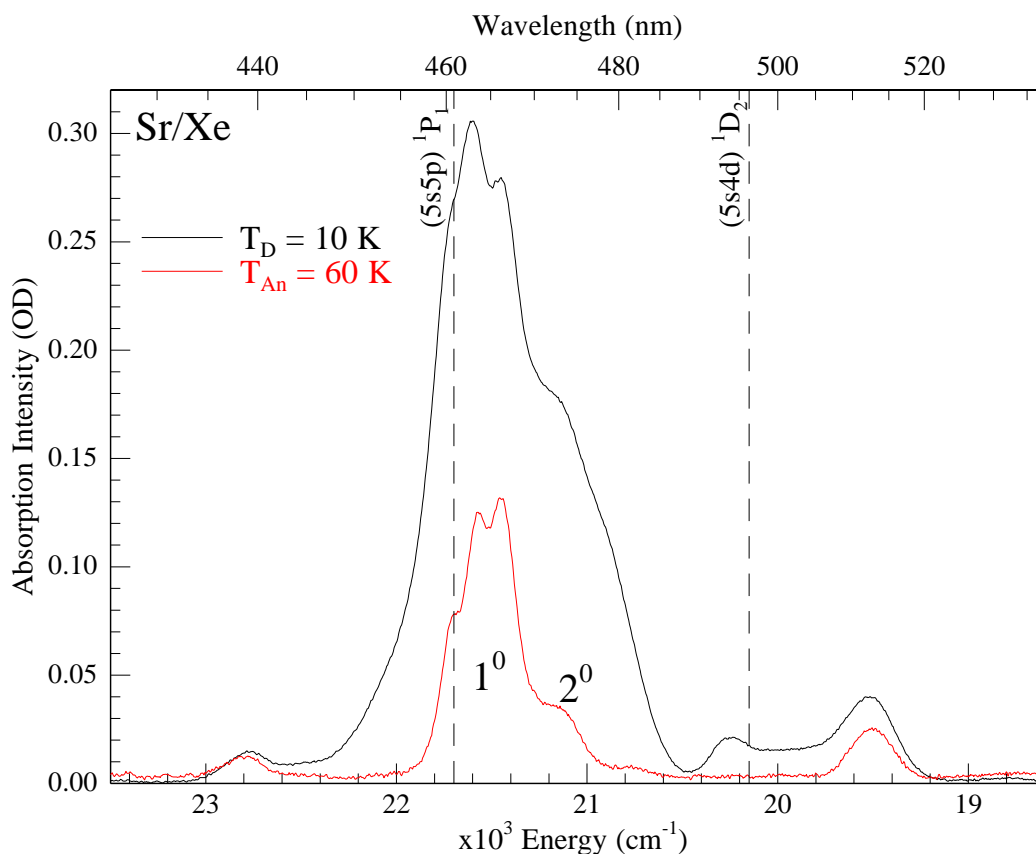
Figure III.23   **Before (black trace) and after (red trace) annealing the Sr/Xe sample to 60 K. The changes to the ^1P and ^1D absorption profiles result from the loss of thermally unstable sites of isolation for Sr. The spectra have not been normalised and accurately represent the changes in optical density (OD) which occur as a result of sample annealing.**

Two thermally stable sites of isolation exist, as evidenced by the annealed (5s5p) $^1P_1$ profile of Figure III.23. The primary site (1^0) of isolation is one of high cubic symmetry as the corresponding (5s5p) $^1P_1$ atomic absorption band is characterised by a fully resolved Jahn-Teller threefold split pattern with peaks at 460.7, 463.5 and 466.1 nm. The secondary site (2^0) appears as a lower energy shoulder and does not display any resolved structure in absorption. As was the case for Sr/Kr, the (5s4d) $^1D_2$ and (5s5p) $^1P_1$ absorption bands show a reversal in their relative intensity patterns.

III.5.IV Sr/RG summary

A summary of the visible absorption spectra recorded for Sr in the three annealed RG hosts is presented in Figure III.24. The spectral location of each resolved peak is collected in Table III.6 and assigned to either the (5s5p) $^1P_1$ or (5s4d) $^1D_2$ state of atomic Sr. Each peak is tentatively assigned to a particular site of isolation, designated as 1^0, 2^0 or 3^0 depending on the relative amounts observed in absorption. However, as with Ba, these assignments are solely based on absorption measurements and have yet to factor in the atomic luminescence, in particular high resolution excitation spectroscopy. These data will be presented in Chapter V.
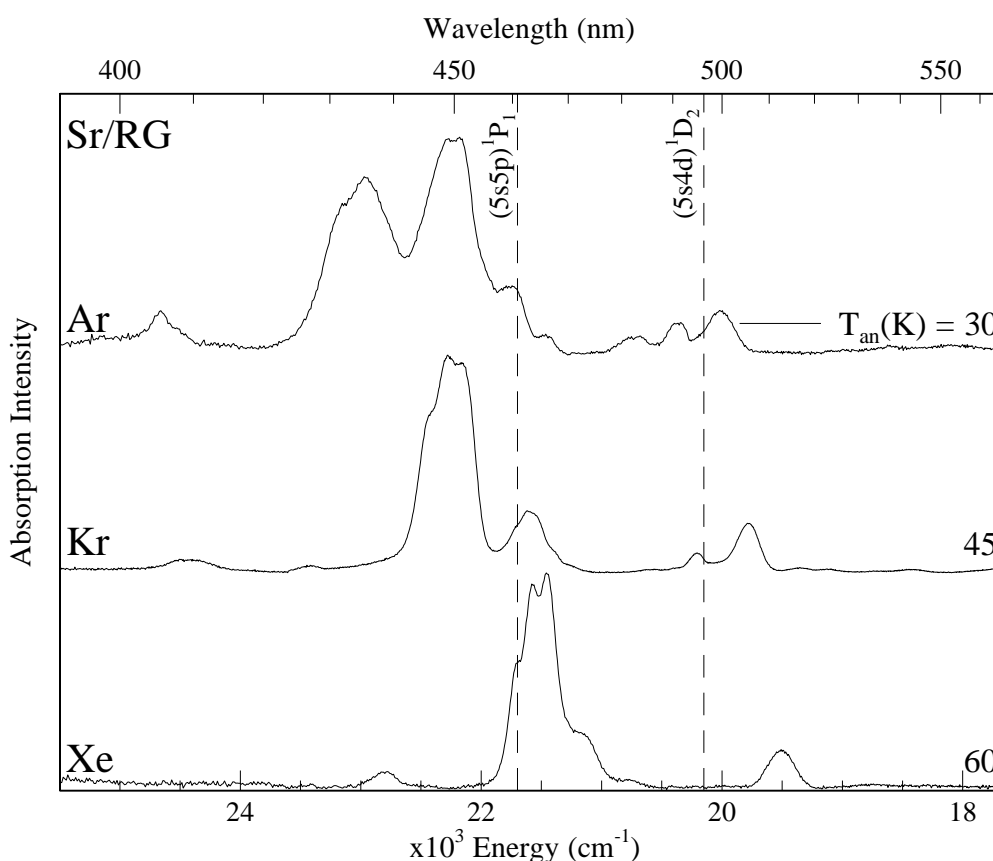
Figure III.24   **A summary of the normalised absorption spectra recorded for Sr isolated in each RG host. The spectra shown were recorded following sample annealing to 30, 45 and 60 K for Ar, Kr and Xe respectively. The gas phase positions[3] of the fully-allowed (5s5p) $^1P_1 \leftarrow {}^1S_0$ (5s^2) and parity-forbidden (5s4d) $^1D_2 \leftarrow {}^1S_0$ (5s^2) transitions of the atom are shown by the dashed vertical lines.**

Taking the centre of the highest energy (5s5p) $^1P_1$ feature as a reference, a progressive red shift is observed on the (5s5p) $^1P_1 \leftarrow {}^1S_0$ (5s^2) transition from Ar (+1269 cm^{-1}), to Kr (+573 cm^{-1}) to Xe (-123 cm^{-1}). This effect is directly related to the increase in RG

polarizability from Ar - Xe. In contrast, a smaller overall matrix red-shift is observed on the (5s4d) $^1D_2 \leftarrow {}^1S_0$ (5s^2) atomic transition of Sr. Shifts of -146 (Ar), -375 (Kr) and -645 cm^{-1}(Xe) are evaluated from the centre of the lowest energy band in each RG host.

In summary, multiple site occupancy occurs for Sr isolated in each RG solid, as was the case for Ba. The absorption spectra suggest the presence of at least three thermally stable sites in Ar and at least two in Kr and Xe matrices. In Chapter V, site-specific luminescence techniques will be used to fully unravel these complex and overlapped absorption profiles.

Table III.6   **Spectral positions of the absorption features assigned to (5s5p) $^1P_1 \leftarrow {}^1S_0$ (5s^2) and (5s4p) $^1D_2 \leftarrow {}^1S_0$ (5s^2) transitions of atomic Sr isolated in the solid RG's, following sample annealing. δ represented the gas phase to RG matrix shift (given in units of wavenumber) calculated from the gas phase value[3] of each transition.**

Host	State	Site	λ_{Abs} (nm)	ν (cm^{-1})	δ (cm^{-1})
Ar	$^1P_1$	2^0	431.5	23175	1477
			435.4	22967	1269
		1^0	448.6	22292	593
			451.0	22173	474
		3^0	459.9	21744	45
	$^1D_2$	3^0	482.1	20743	593
		2^0	491.0	20367	217
		1^0	499.9	20004	-146
Kr	$^1P_1$	1^0	445.9	22427	728
			449.0	22272	573
			451.6	22143	445
		2^0	462.7	21612	-86
		3^0	472.4	21169	-530
	$^1D_2$	3^0	485.7	20589	439
		2^0	494.9	20206	56
		1^0	505.7	19775	-375
Xe	$^1P_1$	1^0	460.7	21706	8
			463.5	21575	-123
			466.1	21455	-244
		2^0	472.9	21146	-552
	$^1D_2$	1^0	512.7	19505	-645

III.6   Discussion and conclusions

III.6.I   Metal dimer

The composition of matrix-isolated Ba and Sr samples can, as presented in Sections III.2 and III.4, vary considerably depending on the deposition conditions used. Samples can be prepared composed almost exclusively of well-isolated atoms and showing little evidence of absorption bands attributable to higher aggregates. In general, this is achieved by depositing at 10 K under conditions of low metal loading. The formation of metal dimers is shown to be quite limited in Kr and Xe matrices on deposition. High metal fluxes, resulting in fully absorbing $(nsnp)$ $^1P_1 \leftarrow (ns^2)$ $^1S_0$ atomic features, are required to yield significant amounts of M_2 (where M_2 corresponds to either Ba_2 or Sr_2) in these hosts. Both Sr and Ba possess a closed shell, ns^2, outer valence electron configuration and will therefore form only weakly bound van der Waals dimers. The most recent high level CCSDT(Q) computations[12] predict ground state binding energies (equilibrium bond lengths) of 1055 (4.663) and 1353 cm^{-1} (4.972 Å) for Sr_2 and Ba_2 respectively. The predicted Sr_2 results are in good agreement with experimentally determined values[13]. Considering these weak interaction energies, it is unlikely that the metal dimers arrive pre-formed to the growing matrix during deposition. Dimerisation must occur when the metal atoms reach the RG surface and lose their kinetic energy. The key criteria for aggregation is therefore the mobility of the guest atoms on the surface of the growing matrix.

The results of CCSD(T) calculations on the M·RG (M = Sr, Ba; RG = Ar, Kr and Xe) diatomics, which will be presented in Chapter VI, show that the binding energies more than double from M·Ar to M·Xe. Thus, the heavier, more polarizable RG atoms form a stronger bond with the guest metal atom. Because of this enhanced interaction, Sr or Ba atoms are less mobile in Kr and Xe when deposited at 10 K and hence dimer formation will be restricted. However, a warmer sample window during deposition ensures that the matrix surface is more 'cluster like' and the mobility of the guest atoms is dramatically increased. It is therefore more likely that two metal atoms will encounter one another and form a homonuclear dimer. Although the M·RG binding energies are larger for Kr and Xe, the corresponding Ba_2 and Sr_2 values are up to an order of magnitude bigger. Thus Ba or Sr will form a more stable bond with itself than with a RG atom. M_2 formation is therefore energetically more favourable, but the metal

atoms must be in close proximity for this to occur. These arguments are supported by the experimental observation that depositing on a 'warm' sample window increases the number of non-atomic absorption bands, the majority of which were attributed to isolated dimers, as they were first observed in samples formed with a low metal concentration. Deconvolution of atomic and dimer absorption bands was achieved with the aid of full range excitation spectra, which were recorded monitoring the emission of Ba_2 and Sr_2 in each RG matrix.

The lowest energy M_2 band (I), which featured mostly prominently in M/Ar samples (see Figure III.14 and Figure III.3 respectively), was assigned to a fully allowed $^1\Sigma_u^+ \leftarrow X\,^1\Sigma_g$ molecular transition. For Ba_2, the R2PI experiments of Lebeault *et al*[8] in combination with the theoretical work of Allouche *et al*[14] provides support for this assignment. Based on the theoretical determinations, it is suggested that the upper $^1\Sigma_u^+$ state of this transition dissociates adiabatically to Ba $(6s^2\,^1S)$ + Ba $(6s6p\,^1P)$ limit. In contrast to Sr_2, resolved features are not evident on this band for Ba_2. The spacing would be expected to be smaller in this case due to the increased mass of Ba compared with Sr. However, Lebeault *et al*[8] extracted an excited state vibrational frequency (ω_e') of 65.2 cm^{-1} for Ba_2 in their R2PI data, quite similar to the Sr_2 value. A similar but slightly lower value of 59 cm^{-1} was predicted from Allouche's calculation[14]. The absence of structure in the metal dimer emission bands is consistent with the low fundamental (ω_e'') frequency of 33.2 cm^{-1} identified for Ba_2 from hot bands in the R2PI work[8].

For Sr_2/Ar, direct excitation of band I produced emission at 779.9 nm (12822 cm^{-1}) with a lifetime of 15.5 ns, thereby providing experimental support for a fully-allowed $^1\Sigma_u^+ \leftarrow X\,^1\Sigma_g^+$ molecular assignment. The resolved structure evident in the top panel of Figure III.18 was found to have an average spacing of approx. 64 cm^{-1}. A laser excitation spectrum (bottom panel of Figure III.18) recorded monitoring the dimer emission at ~ 780 nm is more resolved and yields a more accurate value of 63.7 cm^{-1}. This value represents the vibrational spacing in the excited state of the dimer and is slightly smaller than the earlier absorption results of Miller *et al.*[10,11].

Examining the theoretical work of Boutassetta *et al*[15] suggests that, in contrast to Ba_2, the upper $(1)^1\Sigma_u^+$ state of Sr_2 dissociates adiabatically to Sr $(5s^2\,^1S)$ + Sr $(5d4d\,^1D)$ limit. However, recent gas phase work on Sr_2 by Stein *et al*[16] shows that this molecular state actually dissociates to the Sr $(5s^2\,^1S)$ + Sr $(5s5p\,^3P)$ asymptote due to

an avoided crossing with a higher $^3\Pi_u$ state. The authors also provide an experimentally determined T_e value (12796 cm^{-1}) between the ground and excited (1)$^1\Sigma_u^+$ state. As vibronic structure was not observed on the Sr$_2$/RG emission bands, only estimates of the band origin can be obtained. This is achieved by taking the approximate point of overlap between the emission and excitation scans (Figure III.17). The resultant estimated ν_{0-0} values are collected in Table III.7. Matrix shifts, which were calculated using the gas phase T_e value, reveal a red shift of the of the band origin in going from Ar – Xe. This effect is caused by the increasing polarizability of the heavier hosts and may also be related to the size of vacancy available to Sr$_2$. Solid Ar, with the smallest lattice parameter, exhibits the most repulsive interaction with Sr$_2$ as evidenced by the largest blue shift.

Table III.7   **Estimated band origin values for the lowest energy Sr$_2$/RG absorption band (I). These values were obtained by taking the approximate point of overlap between the emission and excitation scans which were presented in Figure III.17. The matrix shift, δ (cm^{-1}) is computed from the experimental (gas phase) T_e value of 12796 cm^{-1} for the $^1\Sigma_u^+$ – X $^1\Sigma_g$ transition of Sr$_2$.**

Sr$_2$/RG	λ_{0-0} (nm)	ν_{0-0} (cm^{-1})	δ (cm^{-1})
Ar	744.5	13432	636
Kr	756.0	13228	432
Xe	764.7	13077	281

The gas phase study of Sr$_2$ also allows a tentative assignment of band II to be made. Another fully-allowed (2)$^1\Sigma_u^+ \leftarrow$ X$^1\Sigma_g^+$ molecular state exists for Sr dimer. In this case the upper (2)$^1\Sigma_u^+$ state is related to the Sr (5s^2 ^{1}S) + Sr (5s5p ^{1}P) atomic asymptote and a T_e value of 17 358.75 cm^{-1} was recorded by Stein and co-workers[16]. Band II which was shown to be centred at 17637 cm^{-1} for Sr$_2$/Xe is indeed in the correct region for a tentative assignment to be made. Although a more definitive conclusion cannot be drawn as direct emission from this molecular state was not observed, precluding the estimation of a band origin.

The emission observed for Ba dimer and Sr dimer are quite different as a comparison of Figure III.6 and Figure III.17 reveals. Thus, the emission of Sr$_2$ occurs in the vicinity of the lowest energy absorption at c.750 nm, exhibiting resolved vibrational structure in excitation and Stokes shifts that are only weakly dependent on the matrix host. In contrast, Ba$_2$ does not produce any resonance emission with direct excitation into its lowest observed absorption band (I), which suggests that non-

radiative transitions are competing very efficiently with fluorescence. Therefore, the lack of resolved vibrational structure for Ba_2 may indicate lifetime broadening, consistent with the absence of observed fluorescence.

The contrasting behaviours can be rationalised by comparing the dissociation limits of the upper $^1\Sigma_u^+$ states involved in the transition of each metal dimer. The $^1\Sigma_u^+$ state of Ba tends to a Ba $(6s^2\ ^1S)$ + Ba $(6s6p\ ^1P)$ asymptote[8,14], whereas the $(1)^1\Sigma_u^+$ excited state of Sr_2 dissociates to a Sr $(5s^2\ ^1S)$ + Sr $(5s5p\ ^3P)$ asymptote[16]. Inspection of the energy level diagram presented in Figure I.7 (Chapter I) reveals that the (5s5p) ^3P_J manifolds of atomic Sr are the lowest energy excited states. Thus, it is reasonable to expect that the $(1)^1\Sigma_u^+$ molecular state will be the lowest energy excited state of Sr dimer. Conversely, the $^1\Sigma_u^+$ state of Ba dimer lies considerably above the ground state and will have to contend with a higher density of molecular states in its vicinity, which arise out of the lower energy ^3P, ^1D and ^3D asymptotes. The population of the $^1\Sigma_u^+$ state of Ba_2 must be non-radiative transferred to one of these lower energy molecular states and hence emission is not observed in the region (720 − 800 nm) of the dimer absorption band (1).

Moreover, the excitation/emission features that <u>are</u> observed for matrix-isolated Ba_2 must therefore correspond to a different molecular transition. The recorded lifetimes of 6 − 9 ns are again indicative of a fully allowed transition. A theoretical study of Ba_2, which examines the molecular states dissociating to atomic asymptotes above the (6s6p) $^1P_1$ level, would greatly assist the interpretation of the observed Ba_2/RG luminescence.

III.6.II Ba/RG

In this chapter, highly atomic Ba/RG samples have been interpreted via absorption spectroscopy. In each host solid, atomic bands were observed in two distinct spectral regions. The dominant absorption features occurred in the visible, centred at ~ 547 nm (in Kr) and were assigned to the (6s6p) $^1P_1 \leftarrow\ ^1S_0$ $(6s^2)$ transition of Ba. Weaker near-UV atomic bands were also identified for the first time in each host, centred at ~ 326 nm (in Kr). These were assigned to the two electron, (5d6p) $^1P_1 \leftarrow\ ^1S_0$ $(6s^2)$ atomic transition. Very weak, higher energy doublets were only observed for Ba in solid Ar,

located at ~ 295 and 270 nm and were tentatively assigned as (6s7p) $^1P_1 \leftarrow$ $^1S_0$ (6s^2) and (6s8p) $^1P_1 \leftarrow$ $^1S_0$ (6s^2) transitions of the atom, respectively.

The intense (6s6p) $^1P_1 \leftarrow$ $^1S_0$ (6s^2) absorption band was used to probe the site-occupancy of Ba in each host solid. Broad and complex (6s6p) $^1P_1$ profiles were observed on deposition, indicating that multiple sites of isolation were occupied in the RG solid. The thermal stability of the host trapping sites were assessed with matrix annealing. The absorption bands underwent significant change during this process reflecting the removal of thermally labile matrix sites for Ba, which were populated on deposition at 10 K. In general, the lowest energy Ba: (6s6p) $^1P_1$ features were most amenable to reduction/removal. Although simpler, the remaining structured absorption bands suggested the existence of multiple thermally stable sites of isolation for Ba in the solid RG's. Based on the absorption measurements, it is postulated that three thermally stable sites of isolation are present for Ba in Ar and Kr lattices, while at least two sites are present in Xe. Multiple site occupancy is not surprising for Ba. In Chapter VI, CCSD(T) calculations will highlight the considerable mismatch between the Ba-RG diatomic bond lengths and the radii of the spherically symmetric sites available to the RG lattice. The luminescence of matrix-isolated Ba will be presented in the following Chapter to provide a more detailed look at the site occupancy of Ba in the solid RG's.

As outlined in the Chapter I, very little has been published on the absorption spectroscopy of matrix-isolated Ba. Moreover, the small body of work which exists on this metal atom contains numerous errors and is in need of clarification. The earliest Ba/RG study, conducted by Balling and Wright[17], reported the (6s6p) $^1P_1$ absorption peak positions for each system, which are largely in agreement with this study. However, the transmittance trace they published for Ba/Kr is, as shown in Figure III.9, an annealed Ba/Ar scan.

Very recently (2015), the spectroscopy of Ba isolated in a solid Xe matrix has attracted attention by the nEXO Collaboration[7], as a possible way of observing the neutrinoless double beta decay (0νββ) of ^{136}Xe. This decay process produces a daughter ion, namely ^{136}Ba^{++}. The experimental concept is that following the 0νββ decay, the resultant Ba ion is frozen with some surrounding Xe onto a cold probe. Thus, detection of matrix-isolated Ba$^+$ or Ba (following neutralisation) would infer that this particular decay event has occurred. A perquisite for this concept is knowledge of the

spectroscopy of matrix-isolated Ba. Absorption and emission spectra of Ba/Xe and Ba/Ar are therefore reported by the authors. The neutral Ba/Ar and Ba/Xe (6s6p) $^1P_1$ absorption profiles they recorded are in good agreement with the spectra presented in this chapter. Although, it is suggested here that the absorption profile shown for Ba/Xe was not recorded at 10 K, as was described in their publication[7]. Higher energy bands at ~ 450 and 460 nm in Ar and Xe respectively were also observed and postulated to arise from 1) singly charged Ba cation, 2) absorptions out of 6s5d metastable states of neutral Ba or 3) matrix sites (for the neutral) with a very large shift on the (6s6p) $^1P_1 \leftarrow$ $^1S_0$ (6s^2) transition. In this chapter, it has been conclusively demonstrated these absorption features are actually due to matrix-isolated Sr, which exists as an impurity in Ba metal sources.

III.6.III Sr/RG

Similar to Ba/RG, very atomic Sr/RG samples have been deposited at 10 K and interpreted via absorption spectroscopy. Scans were made from 180 - 900 nm, however, it was observed that all of the matrix absorption bands of this metal atom occur in the visible region from 420 – 520 nm (see Figure III.20). The dominant absorption bands were (centred at 457.4 in Kr) assigned to the fully-allowed (5s5p) $^1P_1 \leftarrow$ $^1S_0$ (5s^2) transition of Sr. In contrast to Ba, a series of weaker absorption peaks were also detected (centred at 492.2 nm in Kr) to the red of the (5s5p) $^1P_1$ state absorption in each host and the concentration studies conducted in Section III.4.I confirmed their atomic nature. Assignment to the parity-forbidden (5s4d) $^1D_2 \leftarrow$ $^1S_0$ (5s^2) transition of Sr was made based on the gas phase position of the (5s4d) $^1D_2$ excited state, which lies 20149.685 cm^{-1} (496.3 nm) above the ground state.

The Sr($^1P_1$)/RG absorption profiles bear a striking resemblance to the corresponding Ba bands, indicating that Sr also occupies a multitude of sites in all three hosts, on deposition at 10 K. Annealing to a higher temperature removed the thermally unstable sites of isolation, thereby eliminating their contribution in absorption. The remaining, more resolved absorption bands are suggestive of three thermally stable sites for Sr in Ar and Kr, and at least two for Sr in Xe. The measurements recorded for Sr/Ar by Miller *et al*[2] also show three distinct components in both MCD and absorption, confirming the existence of at least three distinct sites for the atom in annealed Sr/Ar samples.

Interestingly, in the same MCD study, it was reported that the intensity pattern of (5s5p) $^1P_1$ A-terms are a 'mirror image' of the (5s4d) $^1D_2$ A-terms. The authors suggest that the highest energy $^1P_1$ absorption bands correspond to the lowest energy $^1D_2$ bands and vice versa. This behaviour has also been observed in the present study. Annealing each RG host has the effect of removing the lowest energy bands of the $^1P_1$ profile while simultaneously removing the highest energy $^1D_2$ bands. This effect is particularly pronounced for Sr/Kr, as illustrated in Figure III.22. Because both atomic transitions share a common ground state, the origin must be related to the differing shapes of the $^1P_1$ and $^1D_2$ excited state potential energy surfaces. Further investigation of this effect will be provided in Chapter V, following presentation of the luminescence of all three Sr/RG systems.

References

[1] J. Rose, D. Smith, B. E. Williamson, P. N. Schatz, and M. C. M. O'Brien, The Journal of Physical Chemistry **90**, 2608 (1986).

[2] R. L. Mowery, J. C. Miller, E. R. Krausz, P. N. Schatz, S. M. Jacobs, and L. Andrews, J. Chem. Phys. **70**, 3920 (1979).

[3] A. Kramida, Y. Ralchenko, J. Reader, and NIST ASD Team. NIST Atomic Spectra Database (ver. 5.2). Available at: http://physics.nist.gov/asd [2015, October]. National Institute of Standards and Technology, Gaithersburg, MD.

[4] R. Kresse, U. Baudis, P. Jäger, H. H. Riechers, H. Wagner, J. Winkler, and H. U. Wolf, in *Ullmann's Encyclopedia of Industrial Chemistry* (Wiley-VCH Verlag GmbH & Co. KGaA, 2000).

[5] D. R. Lide, *CRC Handbook of Chemistry and Physics* (2010), Ed. 90th.

[6] V. Lebedev, P. Moroshkin, and A. Weis, Phys. Rev. A **84**(2011).

[7] E. X. O. C. n *et al.*, Phys. Rev. A **91**, 022505 (2015).

[8] M. A. Lebeault, J. Viallon, V. V. Boutou, and J. Chevaleyre, J. Mol. Spectrosc. **192**, 179 (1998).

[9] Y. Haas, and U. Samuni, Prog. React. Kinet. **23**, 211 (1998).

[10] J. C. Miller, B. S. Ault, and L. Andrews, J. Chem. Phys. **67**, 2478 (1977).

[11] J. C. Miller, and L. Andrews, J. Chem. Phys. **69**, 936 (1978).

[12] D.-D. Yang, and F. Wang, Theor. Chem. Acc. **131**(2012).

[13] A. Stein, H. Knöckel, and E. Tiemann, Phys. Rev. A **78**, 042508 (2008).

[14] A. R. Allouche, M. Aubert-Frécon, G. Nicolas, and F. Spiegelmann, Chem. Phys. **200**, 63 (1995).

[15] N. Boutassetta, A. Allouche, and M. Aubert-Frécon, Phys. Rev. A **53**, 3845 (1996).

[16] A. Stein, H. Knöckel, and E. Tiemann, The European Physical Journal D **64**, 227 (2011).

[17] L. Balling, and J. Wright, J. Chem. Phys. **83**, 2614 (1985).

Chapter IV

Ba/RG Atomic Luminescence

IV.1   Introduction

This chapter describes the luminescence of Ba isolated in the solid rare gases Ar, Kr and Xe. The data presented were, as outlined in Chapter III, obtained from samples deposited at 10 K under conditions of low metal loading. These samples were subsequently annealed to a minimum temperature of 28, 38 and 60 K for Ar, Kr and Xe respectively. Photoexcitation of the dominant Ba/RG absorption bands produces intense emission in the visible spectral region as shown by the red traces in Figure IV.1.
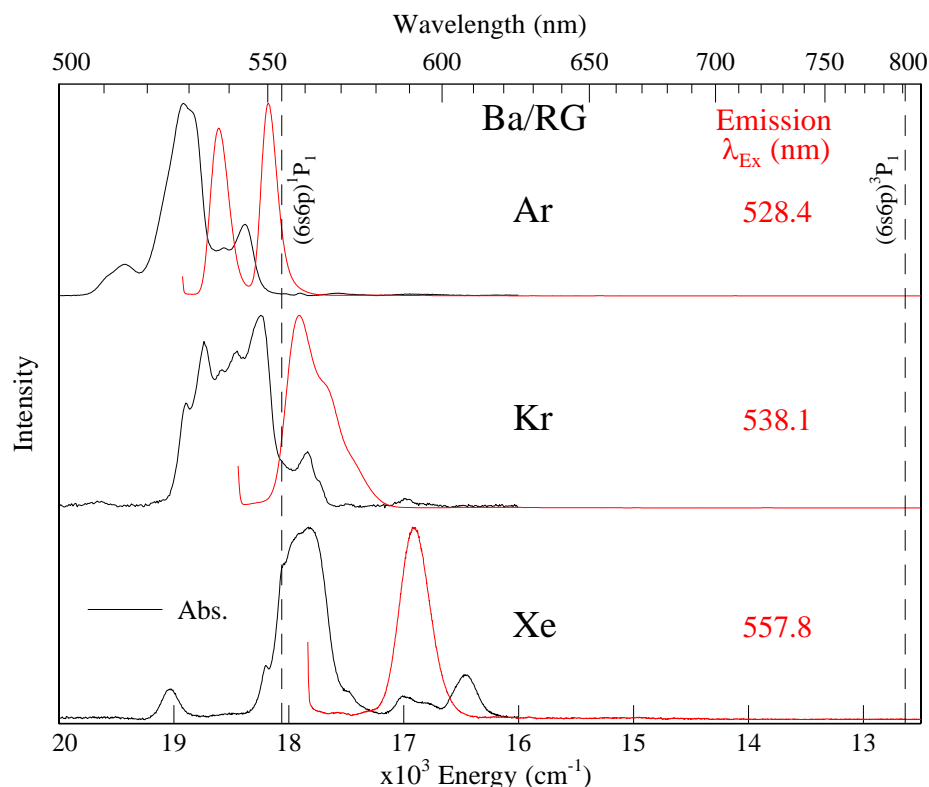
Figure IV.1   **Absorption (black) and emission (red) spectra recorded of annealed Ba/RG samples. Photo-excitation at wavelengths corresponding to the absorption band maxima produces intense emission in the region of the (6s6p) $^1P_1$ state of atomic Ba. In contrast to the luminescence of Sr/RG matrices (Chapter V), lower energy emissions, occurring in the vicinity of the ^3P_J atomic states, were not observed in this work for the Ba/RG systems.**

Based on the proximity to the gas phase line[1], the observed emission bands are assigned to the (6s6p) $^1P_1 \rightarrow$ (6s^2) $^1S_0$ transition of atomic Ba. This assignment is confirmed with

excited state lifetime measurements conducted in each solid. Scans made out to 900 nm, the limit of our detection, did not reveal any lower energy features – only resonance (6s6p) $^1P_1$ fluorescence is observed for the three Ba/RG systems. Figure IV.1 might suggest that the luminescence of Ba in these hosts is relatively straightforward. However, the more detailed examination presented in this chapter shows that situation is more challenging to interpret. As a consequence of multiple site occupancy, numerous distinct emission bands exist in each host, some of which are strongly overlapping. To resolve and identify these features, extensive use was made of two dimensional – excitation and emission (2D-EE) spectra, allowing for analysis of the site occupancy of Ba in the RG's.

The results are presented in the following manner. Firstly, a brief investigation on the effects of re-absorption is provided, using the 2D-EE luminescence of Ba/Ar as an illustrative case study. Secondly, an overview of the entire (6s6p) $^1P_1$ state luminescence of each Ba/RG (RG = Ar, Kr and Xe) system is provided with 2D-EE spectra. These plots allow for changes to the luminescence to be easily tracked, such as those that might occur with matrix annealing. Thirdly, excitation traces extracted from the 2D-EE spectra are used to de-convolute the absorption profiles into site specific features. Following this, steady-state and time-resolved emission scans are presented for each unique trapping site. Emission scans and decay profiles are also recorded at elevated temperatures to investigate the possibility of non-radiative decay processes competing with the resonance fluorescence of Ba, at a given site of isolation. Finally, a comparison of the luminescence from sites of the same type in all three of the RG's is provided, and the trends observed are highlighted and discussed.

IV.2 Re-absorption

In addition to minimising the formation of Ba clusters, employing a low metal flux produces samples with a relatively low absorption optical density (OD). The OD of a Ba/RG sample greatly affects the observable luminescence as the re-absorption of emission is a pronounced effect for these systems which exhibit strongly overlapping absorption/emission bands. 2D-EE spectra recorded in the region of the (6s6p) $^1P_1$ luminescence of Ba isolated in solid Ar are presented in Figure IV.2. The two panels represent samples deposited at 10 K, but with differing absorption coefficients.
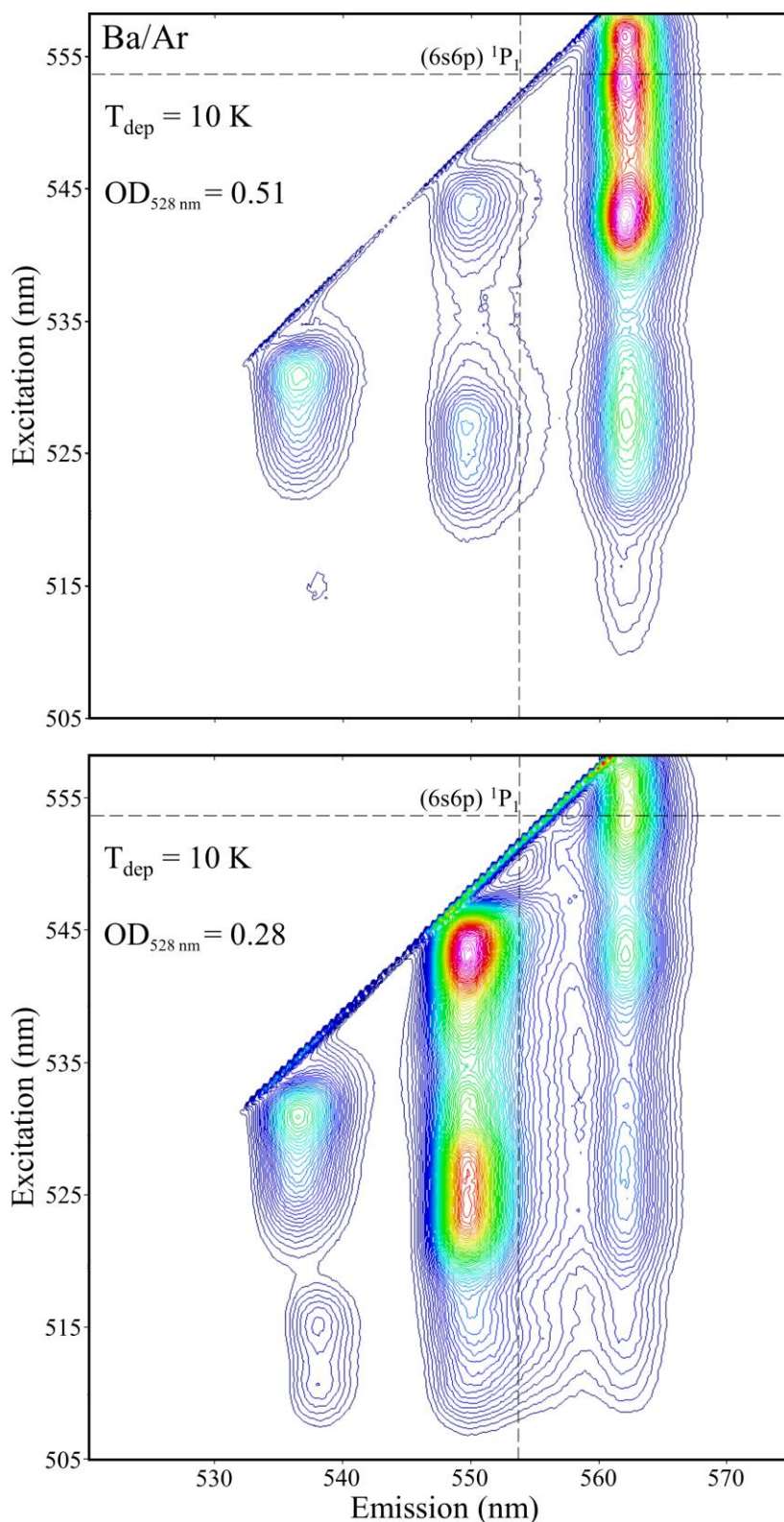
Figure IV.2 **2D-EE spectra recorded for the entire (6s6p) $^1P_1$ luminescence of Ba isolated in Ar, following sample deposition at 10 K. A horizontal slice through the plot yields an emission spectrum, whereas a vertical slice provides an excitation spectrum. The top trace depicts the luminescence originating from a sample which has an absorption optical density (OD) of 0.51 at 528 nm. The bottom spectrum corresponds to a less absorbing sample with an OD of 0.28 at 528 nm. The gas phase position[1] of the (6s6p) $^1P_1$ ← (6s^2) $^1S_0$ transition of Ba at 553.7 nm is shown, in both excitation and emission, as a dashed line.**

The top spectrum corresponds to a sample with an absorption optical density (OD) of 0.51 at 528 nm. The bottom spectrum was obtained from a less absorbing sample, which had an OD of 0.28 at 528 nm. Three emission bands are observed in both spectra, centred at approx. 537, 550 and 562 nm, however, their relative intensities vary greatly depending on the sample OD. Thus, in the more absorbing sample, the lowest energy emission feature dominates the luminescence. In contrast, the emission band at 551 nm is more intense in the less absorbing sample, and in general, the higher energy bands are more prominent and resolved. The behaviour just described is an intrinsic property of the luminescence of all Ba/RG samples due to extensively overlapped absorption/emission bands of the fully allowed atomic resonance transition.

Multiple site occupancy occurs for Ba in an Ar matrix on deposition, as was shown in Chapter III. Consequently, the (6s6p) $^1P_1$ absorption profile was observed to be broad and complex, extending over the spectral range from 505 to 562 nm. The emission bands at 537 and 551 nm occur within this region and are therefore prone to competitive re-absorption. The extent of re-absorption depends, as shown in Figure IV.2, on the optical density of the doped RG solid. If a Ba/Ar sample is strongly absorbing, the lowest energy emission band dominates, and the corresponding excitation spectrum will be more or less a continuum, spanning the entire absorption range. As each emission band corresponds to a unique site of isolation for Ba in solid Ar, information on the site occupancy of the guest metal atom would be obscured in such a case. The situation described was also observed for Ba/Kr following sample deposition at 10 K. Fortuitously, this effect is not as significant for Ba/Xe because the dominant emission features are Stokes shifted away from the atomic absorption profile and Xe contains fewer sites of isolation for atomic Ba (see Section IV.3).

The Ba/Ar emission data presented by Balling and Wright in 1985[2], comprised a single band located at ~568 nm. Clearly their samples were strongly absorbing and the authors acknowledged that the observed emission probably originated from a single site, with the intensity of the band amplified by the successive re-absorptions of higher energy emission bands. Thus, in an effort to identify all of the site-specific Ba/RG emission bands, the luminescence data presented in the following sections were obtained from samples with a low absorption strength (O.D. < 0.5). Fortunately, the deposition conditions required to achieve a high degree of atomic isolation (see Chapter III), usually result in relatively weakly absorbing samples. In addition, matrix annealing

provides further simplification as the number of absorbing and emitting sites is reduced.

IV.3   Ba/Xe

A 2D-EE spectrum recorded for the (6s6p) $^1P_1 \leftarrow$ (6s^2) $^1S_0$ transition of Ba isolated in solid Xe is presented in Figure IV.3. The 2D plot was obtained from a sample freshly deposited at 10 K, under conditions of low metal loading.
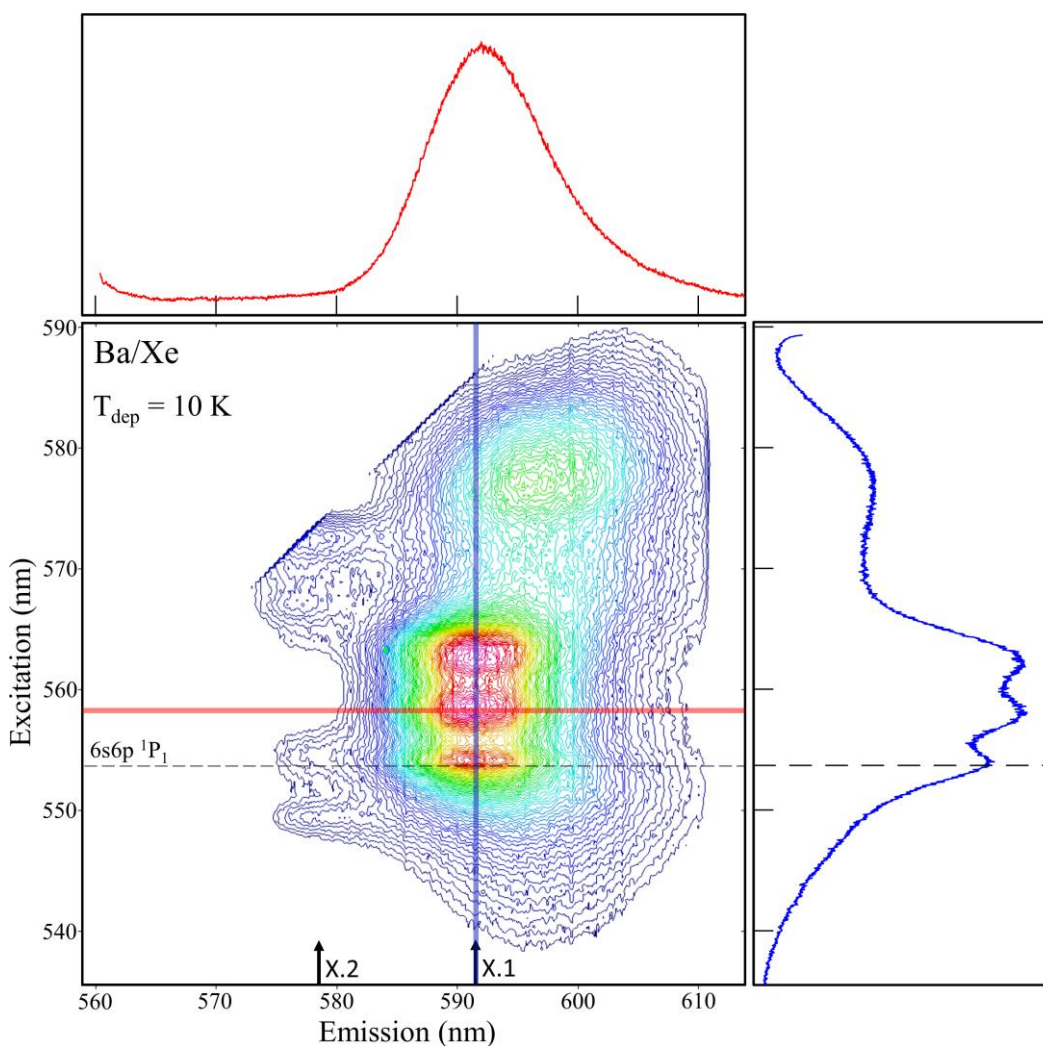
Figure IV.3   **2D-EE spectrum recorded for the entire (6s6p) $^1P_1$ luminescence of Ba isolated in Xe, following sample deposition at 10 K. A horizontal slice through the plot yields an emission spectrum (shown in red), whereas a vertical slice provides an excitation spectrum (shown in blue). The gas phase position of the (6s6p) $^1P_1 \leftarrow$ (6s^2) $^1S_0$ transition of Ba is shown, in excitation only, as a dashed horizontal line.**

The dominant feature is a band centred at 591.6/557.9 nm (emission/excitation), which exhibits a resolved threefold splitting pattern in excitation. The second most intense feature is centred at 576.7/594.7 nm and does not display resolved structure. A weaker emission exists at approx. 578 nm whose excitation intensity is divided into two bands located at 551 and 560 nm. Excitation (vertical) slices taken through the 2D-EE plot at positions X.1 and X.2 are shown overlaid on top of the absorption trace (T_{dep} = 10 K) of Figure IV.5.

Annealing the Xe host to 60 K alters the luminescence of Ba/Xe, as illustrated by the 2D-EE plot shown Figure IV.4. A cursory inspection reveals that the spectrum is much simpler, consisting of three well resolved components labelled I – III based on intensity.
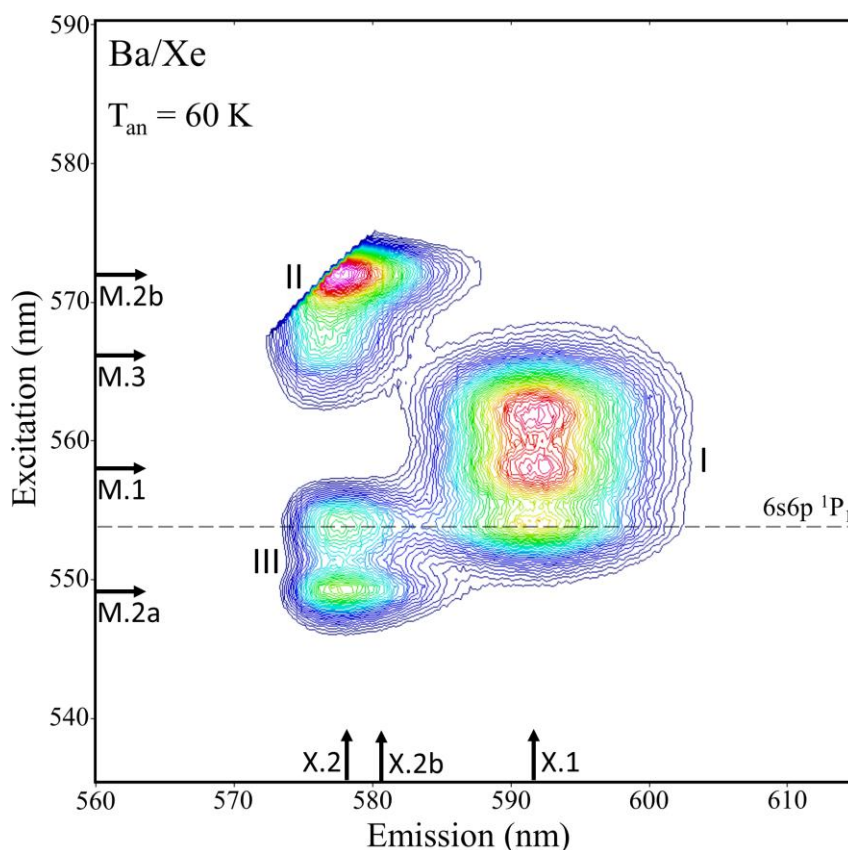
Figure IV.4   **2D-EE spectrum recorded for the (6s6p) $^1P_1$ luminescence of Ba isolated in Xe, following sample annealing to 60 K. The gas phase position[1] of the (6s6p) $^1P_1$ ← (6s^2) $^1S_0$ transition of Ba is shown, in excitation only, as a dashed horizontal line.**

The excitation spectra extracted at the indicated emission values X.1, X.2 and X.2b are presented in the lower panel of Figure IV.5 and are overlaid onto the annealed absorption profile of Ba/Xe. The excitation profile recorded of the broadest emission

band at ~591 nm (X.1) becomes much simpler following annealing. A comparison of the X.1 (blue) traces shows that the spectral location of the threefold split is unchanged. However, for the annealed trace, the red band located 576.7 nm and a broad blue wing extending to 530 nm have been completely removed. Both of these features are therefore attributable to thermally unstable sites of isolation for Ba in solid Xe. The thermally stable threefold split (band I) is a manifestation of the dynamic Jahn-Teller effect[3] and arises from the isolation of Ba in a highly symmetric site within the Xe lattice. The Jahn-Teller (JT) band directly overlaps the dominant absorption feature. The composite peaks are more resolved in excitation and occur spectrally at 553.9, 557.9 and 562.1 nm.
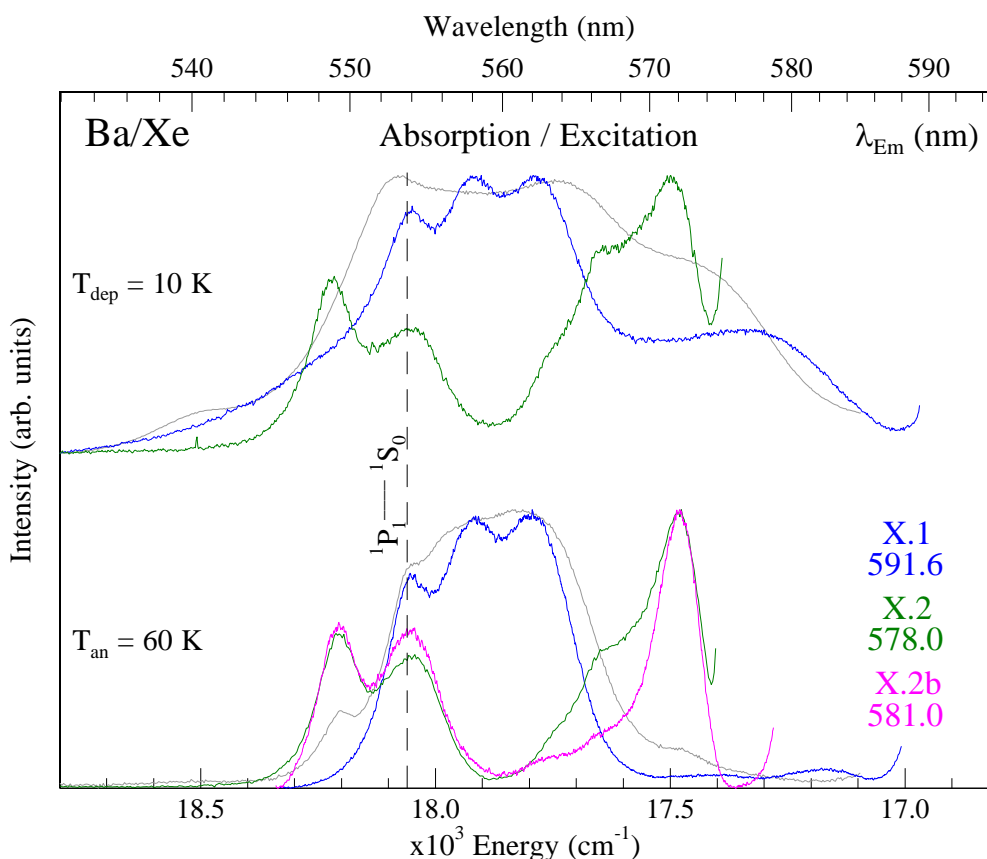
Figure IV.5   **Absorption (grey) and excitation (coloured) spectra obtained from annealed Ba/Xe samples. The excitation traces shown correspond to vertical slices through the 2D-EE spectra presented in Figures IV.3 and IV.4. The emission wavelengths selected are denoted by an X in the 2D plots.**

The effect of annealing is less pronounced for the excitation spectra recorded monitoring the emission band at 578 nm (X.2). As mentioned, this emission is split into two regions of intensity in excitation, which are labelled II and III in Figure IV.4. Band

II is characterised by a dominant component at 572 nm and extends to higher energy with less intense peaks observed at 563.4 and 566.4 nm. Band III comprises a well resolved doublet with peaks at 549.3 and 554 nm. In contrast to the characteristic threefold JT feature, this excitation profile is more challenging to interpret. The observation of five resolved components suggests that two distinct Ba trapping sites are contributing to the spectrum. This would occur if the emission bands from each site spectrally coincide. As a test, an excitation scan was obtained by taking a slice (X.2b) through the red wing of the emission at ~581 nm. The resulting spectrum, which is given by the pink trace in Figure IV.5, shows a clear connection between the doublet (band III) at 549.3 and 554 nm and the dominant component of band II at 572 nm. Accordingly, these peaks are attributed to the same site of isolation for Ba. A slice through the blue side of this emission band accentuates the peaks at 563.4 and 566.4 nm suggesting that these originate from a different matrix site.

In summary, it appears that three thermally stable sites of isolation exist for Ba/Xe. The dominant site corresponds to a well-defined JT threefold split band and is labelled as the 'blue' site of isolation. The secondary site displays an asymmetric threefold split (2+1), consisting of a pair of bands and a single band. This feature is referred to as the 'violet' site of isolation because its highest energy component at 549.3 nm is the most blue-shifted of all the absorption peaks. The minor 'green' site consists of weak, partially resolved peaks which overlap the lower energy component (band II) of the 'violet' site in excitation. The photophysical and temporal characteristics of each site will now be presented.

IV.3.I   Ba/Xe – Blue site

Emission and excitation spectra are presented in Figure IV.6 for the blue site of isolation. The excitation scan is characterised by a resolved JT threefold splitting pattern[4,5] centred at 557.8 nm, exhibiting a matrix red-shift of -133 cm^{-1} from the gas phase.
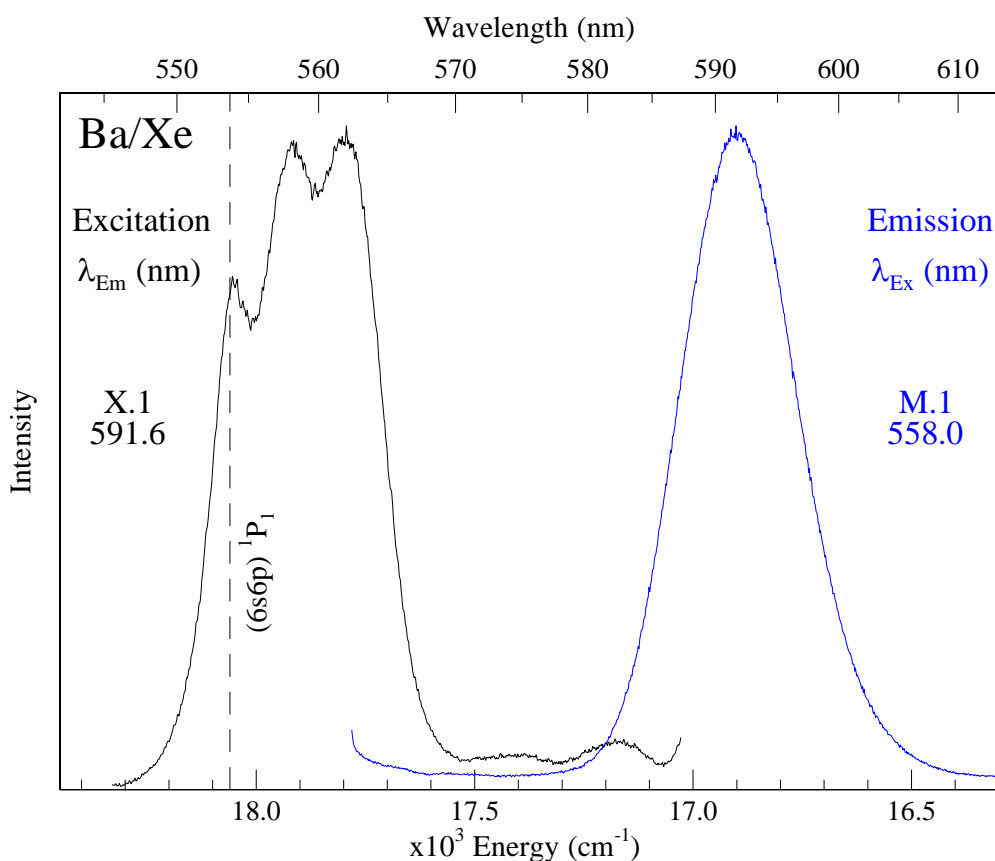
Figure IV.6   **Luminescence spectra recorded of the blue site of isolation for Ba/Xe. The lack of mirror symmetry in the excitation and emission profiles is clearly evident as the former exhibits threefold splitting while the emission band is featureless. The bandwidths of each are comparable, however the excitation profile is slightly broader.**

Photoexcitation of the central component of the JT band produces intense emission centred at 591.6 nm, corresponding to a horizontal slice through Figure IV.4 at M.1. A relatively large Stokes shift of 1018 cm^{-1} is extracted from the centre of the excitation and emission bands. A lineshape analysis for the blue site excitation profile is presented in Figure IV.52 of Appendix IV.1. Three Gaussian curves (see Equation II.2), each displaying a width (fwhm) of 144 cm^{-1}, are required to adequately fit the trace. In

contrast, the emission band requires only a single Gaussian (fit not shown), characterised by bandwidth of 311 cm^{-1}

The temporal characteristics of the blue site emission were investigated with pulsed laser excitation and iCCD detection – as described in Chapter II. A decay profile recorded at 10 K with low intensity Nd:YAG laser excitation is presented in Figure IV.7, on a semi-log plot. An excited state decay time of 3.3 ns is obtained with a single exponential function, which includes a re-convolution with the time profile of the Nd:YAG laser (red triangles). The accuracy of the trial fit is highlighted by the residuals presented in the top panel of this plot. As can be seen, the decay portion of the profile is very well reproduced.
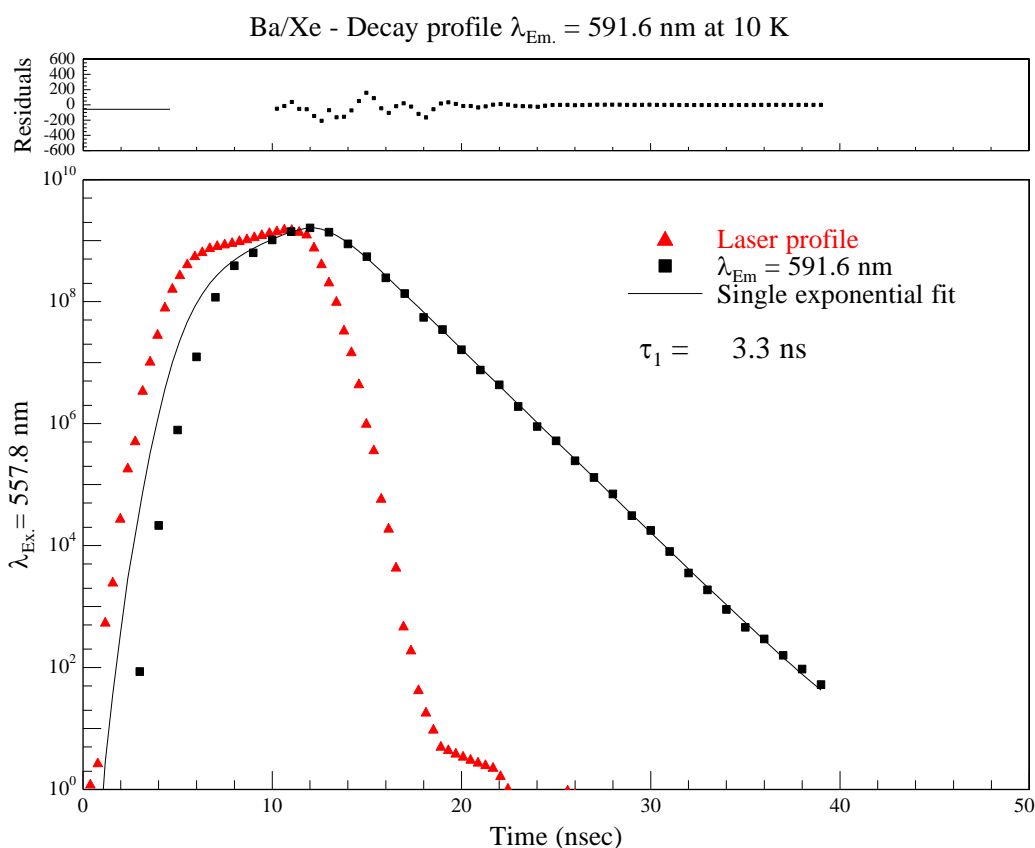
Figure IV.7   **Decay profile of the Ba/Xe blue site emission band at 591.6 nm, produced by site-selective laser excitation at 557.8 nm. An excited state decay time of 3.3 ns is obtained at 10 K with a single exponential trial function, which included a re-convolution with the time profile of the Nd:YAG laser.**

To further probe the blue site temporal characteristics, the temperature dependence of the emission decay was investigated up to 36 K. This was done to assess the contributions of non-radiative components to the overall emission. Figure IV.8 (left

panel) shows that the emission band rapidly loses intensity and becomes red-shifted with increasing sample temperature and as presented in the right panel, the extracted decay curves show significant changes over the 10 - 17 K range. Even at 10 K, a non-radiative relaxation pathway competes with the emission at this site of isolation. Thus the true radiative lifetime has not been identified for the blue site. Scans recorded out to 850 nm did not reveal the presence of any additional bands at elevated temperatures. Particular attention was given to the region of the ^3P_J states of atomic Ba, which occur in the gas phase between 740 and 815 nm.
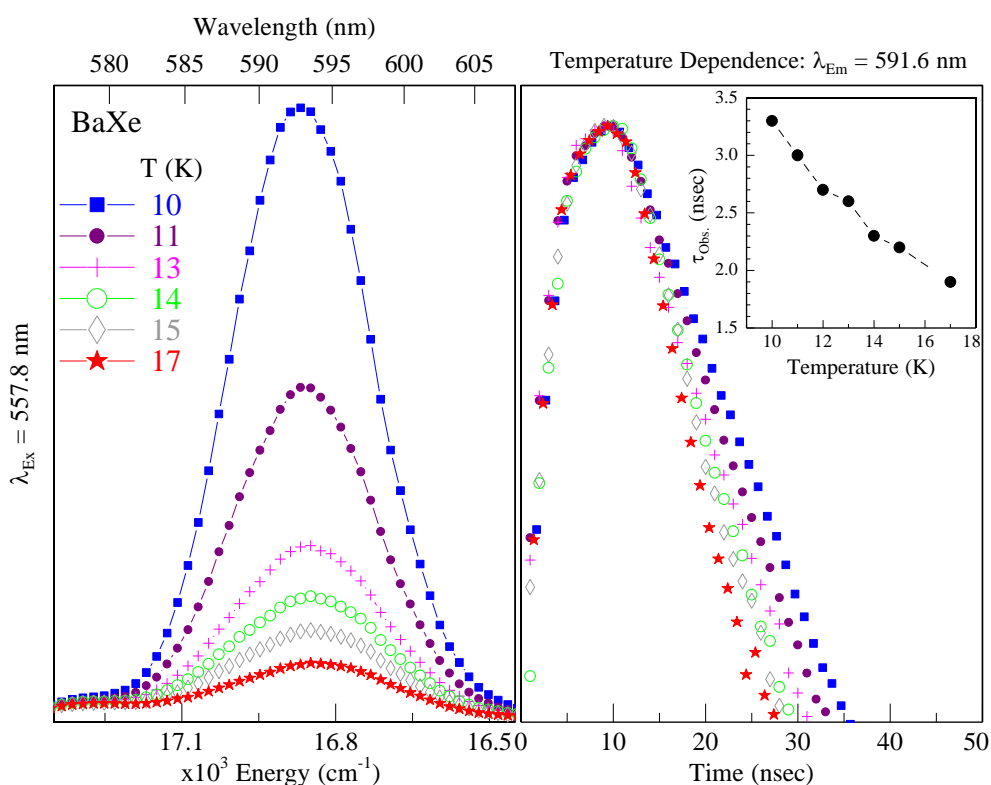
Figure IV.8   **The left panel shows the temperature dependence of the Ba/Xe blue site emission band at 591.6 nm. A progressive red-shift of the band centre occurs in conjunction with a significant decrease in the band intensity, as the sample temperature increases from 10 – 17 K. The right panel presents the temperature dependence of the corresponding decay curves.**

It is noteworthy that following the temperature study, emission scans recorded back at 10 K show that a significant and permanent loss of isolated Ba atoms occurs – this is also corroborated by absorption measurements. Thus bleaching and/or site interconversion does occur at elevated temperatures for all three Ba/RG systems even with lamp and low intensity laser irradiation (0.25 µJ/mm^2 at 558 nm, used for Ba/Xe). These effects were shown to occur for Ba/Xe[2,6] and are not directly investigated here.

Therefore the emission decay profiles will provide the most accurate indication of a non-radiative relaxation pathway for Ba, as the integrated area of the emission scans can potentially be reduced by two distinct effects.

IV.3.II Ba/Xe - Violet site

Emission and excitation spectra are presented in Figure IV.9 for the violet site of isolation. The excitation features of this site, shown on the left in this figure, occur to the blue and to the red of the Ba: $^1P_1 - {}^1S_0$ gas phase resonance line. A matrix red-shift of -578 cm^{-1} is evaluated for the dominant excitation band at 572 nm. The lowest energy peak of the pair at 553.9 nm overlaps the gas phase position displaying a very small red-shift of -6 cm^{-1}, whereas the remaining doublet peak at 549.3 nm is blue-shifted by $+145$ cm^{-1}.
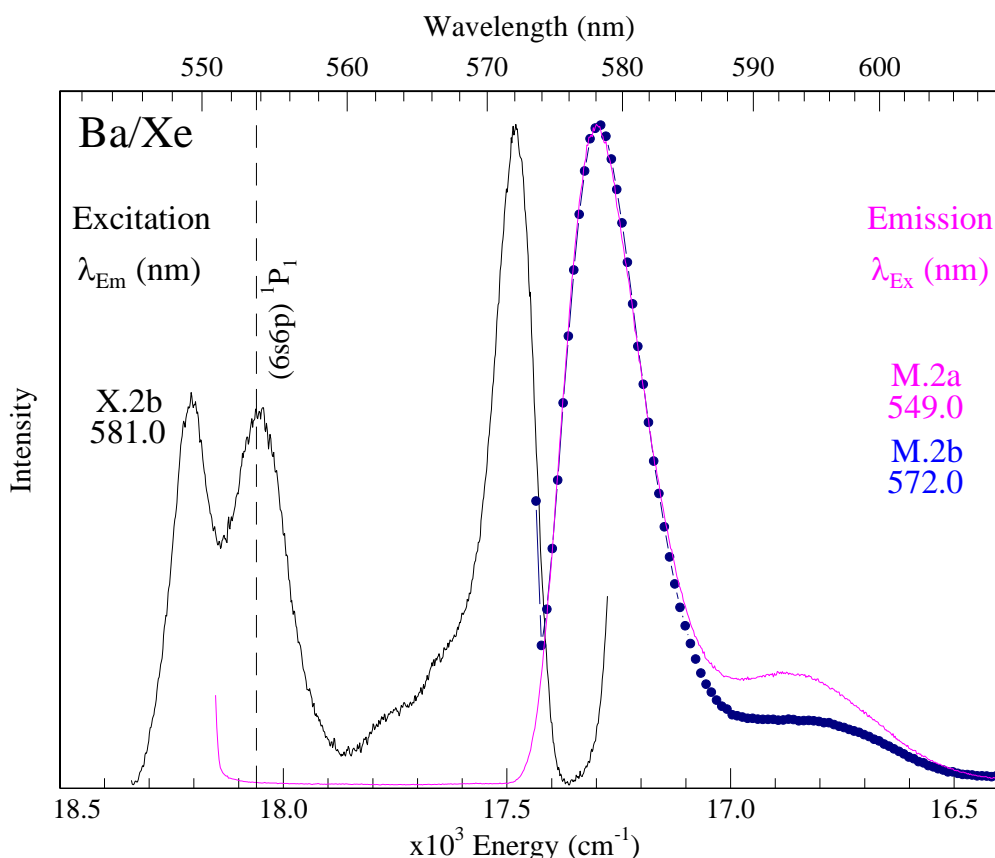
**Figure IV.9**   **Emission (coloured) and excitation (black) spectra recorded at 10 K for the violet site of isolation of Ba in solid Xe. The excitation profile was obtained by monitoring the emission at 581 nm. This was done to minimise the contribution of the green site, which emits in close proximity at 577.1 nm. The excitation scan clearly differs from that of the blue site, exhibiting a 2+1 asymmetric splitting pattern.**

A lineshape analysis of the excitation spectrum is provided in Figure IV.53 of Appendix IV.I. A total of five Gaussian curves are needed to fit the scan, two of which (shown in green) account for the minor amount of the green site features present in the spectrum. Each peak of the 2+1 structure are fitted with a single Gaussian. The highest energy component of the doublet and the lower energy singlet band are both relatively narrow, displaying bandwidths (fwhm) of 90 and 92 cm^{-1} respectively. The remaining doublet component is broader exhibiting a fwhm of 151 cm^{-1}. However this value may be skewed due to spectral overlap with the highest energy component of the blue site JT band. Photoexcitation into any of the three absorption peaks produces an emission band at 578.1 nm characterised by a bandwidth of 213 cm^{-1} and a slightly asymmetric bandshape which tails to lower energy. The emission scans shown in Figure IV.9 correspond to the horizontal slices taken at the indicated excitation values, M.2a and M.2b. The Stokes shifts evaluated from each excitation peak (high to low energy) are 907, 756 and 184 cm^{-1}.
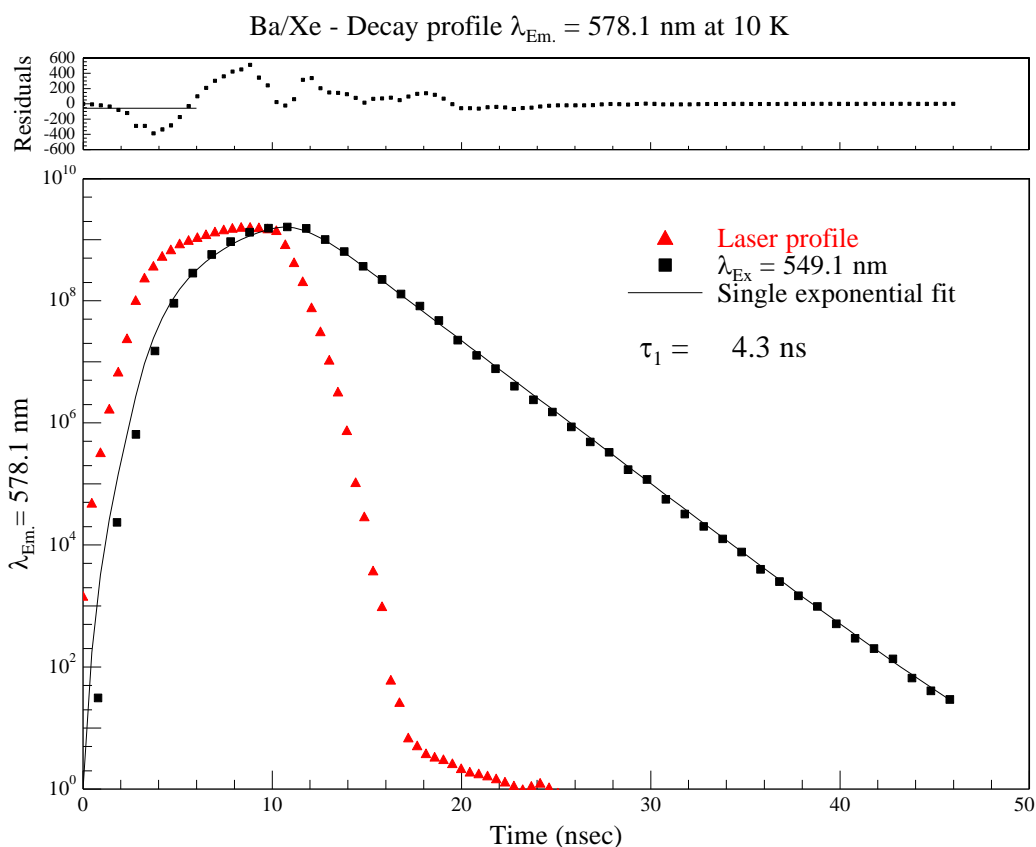

Figure IV.10   **Decay profile of the Ba/Xe violet site emission band at 578.1 nm, produced with site-selective laser excitation at 549.1 nm. An excited state decay time of 4.3 ns is obtained at 10 K with a single exponential trial function.**

A decay profile recorded at 10 K for the violet site 578.1 nm emission with laser excitation at 549.1 nm is presented in Figure IV.10. An excited state lifetime of 4.3 ns is obtained with a single exponential trial function. Decay profiles recorded with excitation of the lower energy violet site bands are very similar and yield the same lifetime values.
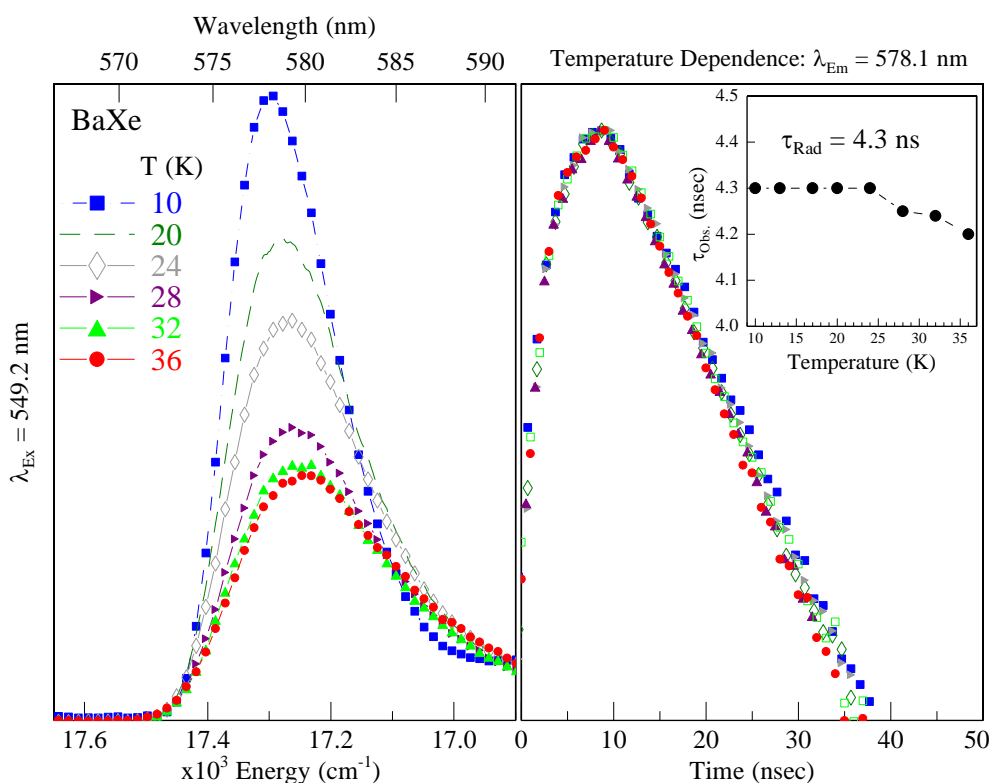
Figure IV.11 **The left panel shows the temperature dependence of the Ba/Xe violet site emission band at 578.1 nm. These were obtained with time-integrated pulsed laser excitation. A progressive red-shift of the band centre occurs in conjunction with a significant decrease in the band intensity, as the sample temperature increases from 10 – 17 K. The right panel presents the temperature dependence of the corresponding decay curves which were obtained with time-gated pulsed laser excitation.**

Spectral and temporal scans recorded for the 578.1 nm emission at elevated temperatures are presented in the left and right panels of Figure IV.11 respectively. As shown the emission loses intensity and becomes red-shifted over the temperature range investigated. Examining the right panel of this plot reveals that the corresponding decay profiles are unaffected by the sample temperature below 24 K. Thus the radiative lifetime of the violet site emission has been measured to be 4.3 ns. However, above 24 K a noticeable shortening of the observed decay time occurs. This indicates that a non-

radiative relaxation pathway competes with the fluorescence and becomes active above this temperature.

IV.3.III Ba/Xe – Green site

Figure IV.12 details the minor, green site luminescence of Ba/Xe. The excitation spectrum shown also contains the features of the violet site. For clarity, the features which are associated with the green site are highlighted in red. A matrix red-shift of -405 cm^{-1} is determined from the partially resolved band at 566.4 nm.
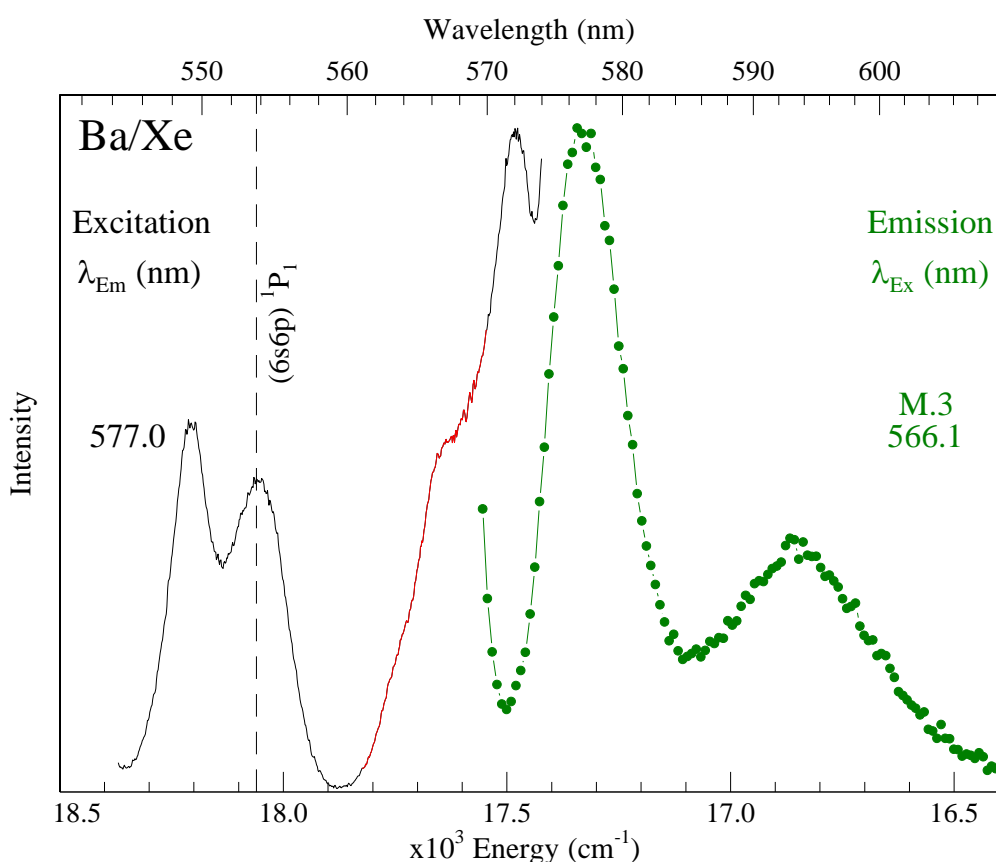
Figure IV.12   **Emission (green) and excitation (black/red) spectra recorded at 10 K for the green site of isolation of Ba in solid Xe. The excitation profile was obtained by monitoring the emission at 577 nm. The portion of the excitation trace highlighted in red corresponds to the features which are associated with the green site.**

Photoexcitation at 566 nm produces an emission band at 577.1 nm showing a bandwidth of 202 cm^{-1}, corresponding to a horizontal slice through Figure IV.4 at M.3. Thus, this emission is shown to be spectrally distinct from that of the violet site, despite both bands occurring in close proximity.
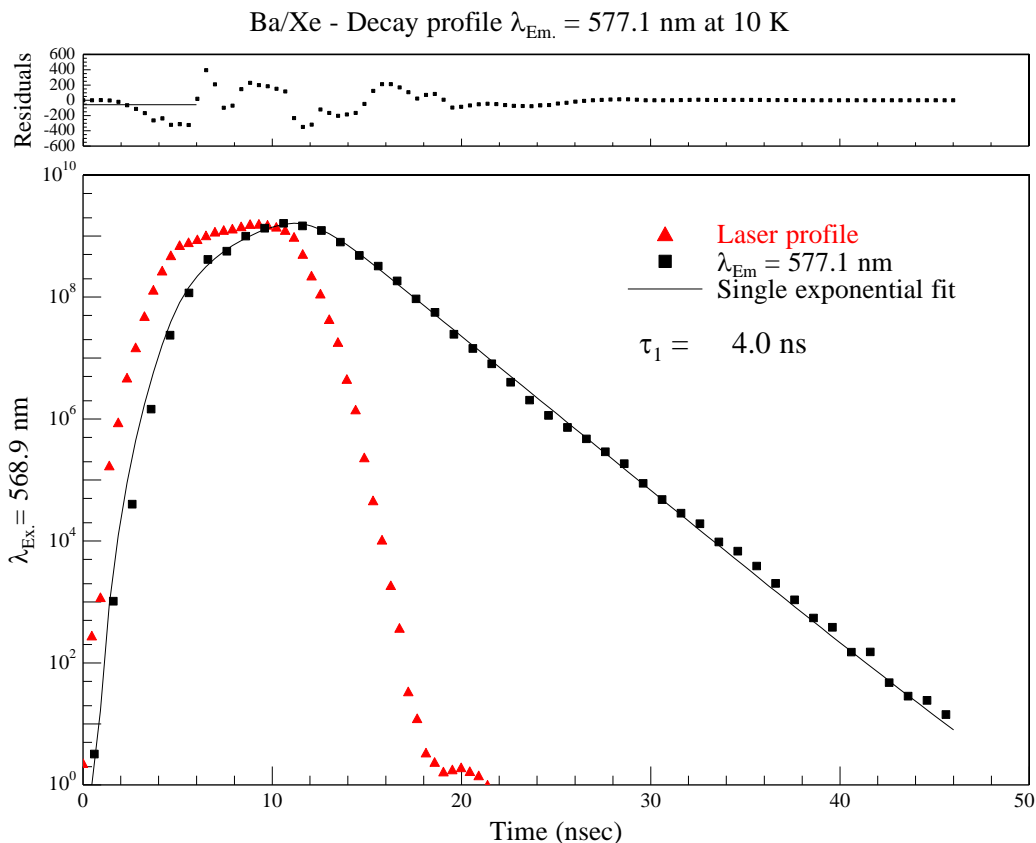
Figure IV.13 Decay profile of the Ba/Xe green site emission band at 577.1 nm, produced with site-selective laser excitation at 568.9 nm. An excited state decay time of 4.0 ns is obtained at 10 K with a single exponential trial function.

A temporal decay profile of the green site emission was obtained with laser excitation at 568.9 nm, as shown in Figure IV.13. A single exponential function provided a satisfactory fit and from this an observed lifetime of 4.0 ns was obtained, slightly shorter than that of the violet site. The temperature dependence of the spectral and temporal scans are presented in Figure IV.14. Examination of this figure illustrates that although the emission intensity decreases, the temporal profile does not change between 10 and 13 K – thus the radiative lifetime has been identified. In contrast to the violet site, the recorded lifetime of this band becomes gradually shorter at temperatures above 13 K. For instance, a value of 3.0 ns is observed at 28 K. A non-radiative process quenches the fluorescence at the green site of Ba/Xe. The activation temperature is slightly higher than that of the blue site as can be gleaned from the inset of the right panel, Figure IV.14.
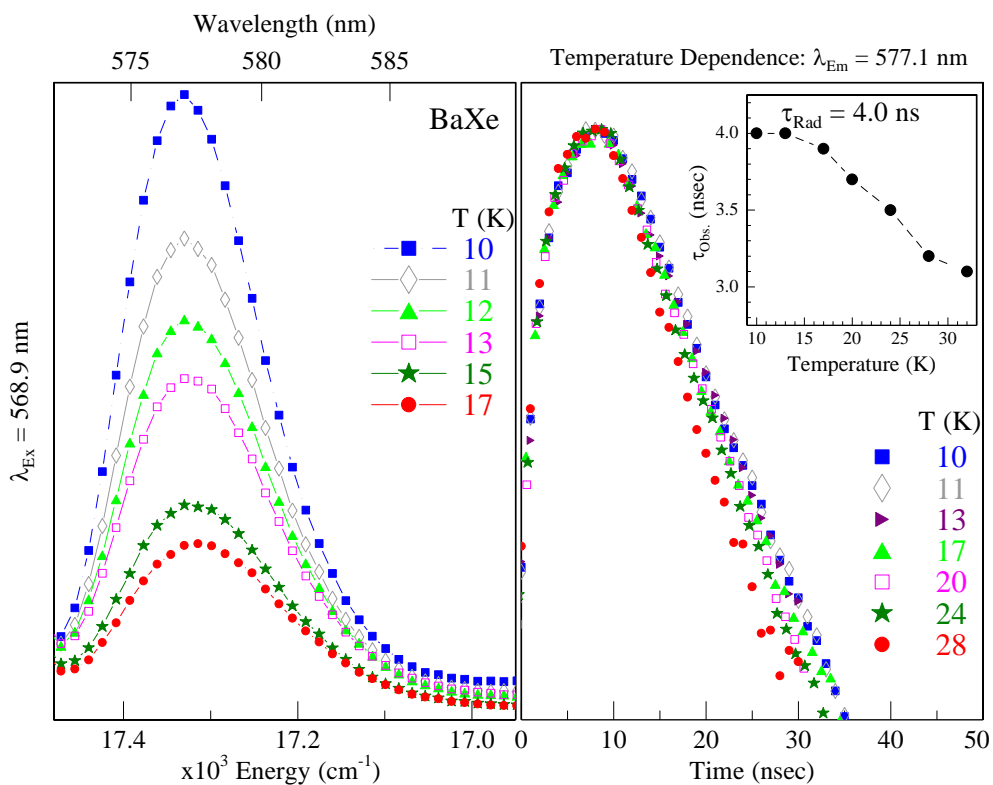
Figure IV.14   The left panel shows the temperature dependence of the Ba/Xe green site emission band at 577.1 nm. A slight red-shift of the band centre occurs in conjunction with a decrease in the band intensity, as the sample temperature increases from 10 – 17 K. The right panel presents the temperature dependence of the decay curves recorded over a wider range from 10 – 28 K.

IV.4   Ba/Kr

The 2D-EE spectrum of Ba/Kr recorded following sample deposition at 10 K is presented in Figure IV.15. The spectrum is dominated by a broad emission band centred at approx. 574 nm. The excitation spectrum of this emission feature is a continuum which spans the entire range of the $(6s6p)$ $^1P_1 \leftarrow (6s^2)$ $^1S_0$ absorption profile. As outlined in the introduction, this is an effect of re-absorption and arises because of spectral overlap between the emission band of a higher energy site with the absorption band of a lower energy site.
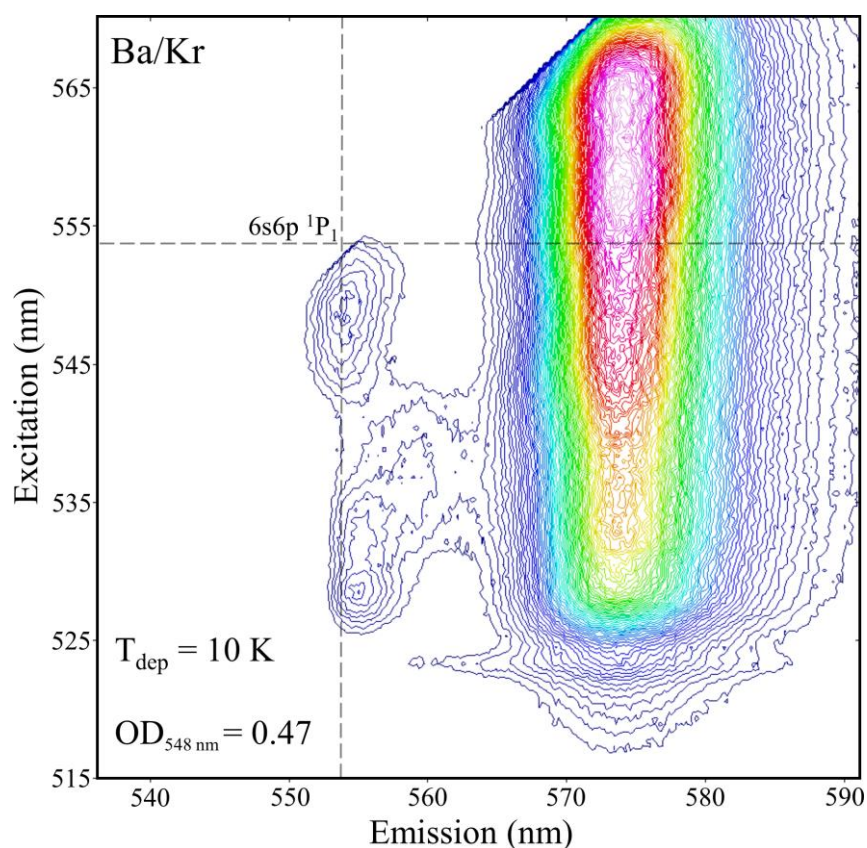

Figure IV.15   **2D-EE spectrum recorded for the $(6s6p)$ $^1P_1$ luminescence of Ba isolated in Kr, following sample deposition at 10 K. The optical density of the sample was measured as 0.47 at 548 nm. The gas phase position[1] of the $(6s6p)$ $^1P_1 \leftarrow (6s^2)$ $^1S_0$ transition of Ba is shown, in both excitation and emission, as a dashed line.**

It appears that Ba occupies a myriad of sites in solid Kr on deposition, leading to successive emission/re-absorption events – until all of the emission intensity coalesces into the lowest energy band. Even in a sample with a relatively low absorption optical density (< 0.5), re-absorption is significant and limits the amount of information discernible from the luminescence. Of course this effect can be somewhat reduced by

depositing very weakly absorbing Ba/Kr samples. However matrix annealing is a better approach. The spectral situation is much simpler because, in addition to a reduction in the optical density of the sample, the majority of the thermally unstable sites have been removed. The 2D-EE spectrum of a Ba/Kr sample annealed to 38 K, is presented in Figure IV.16. In this case the features are well resolved and can be used to extract useful information regarding the site occupancy of Ba in this host.
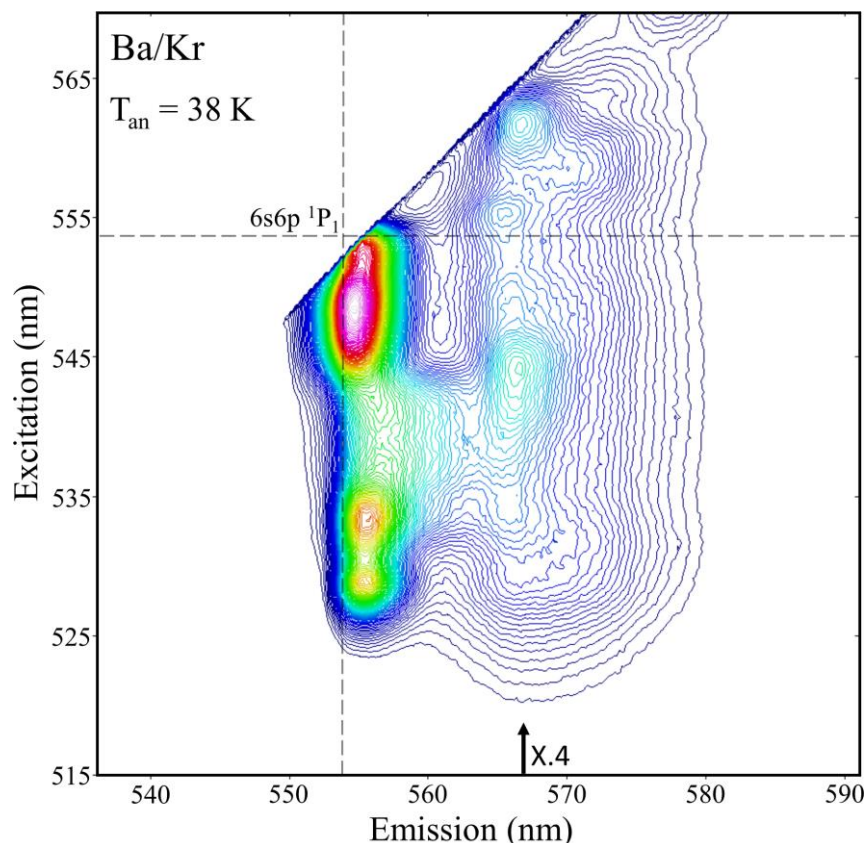
Figure IV.16   **2D-EE spectrum recorded for the (6s6p) $^1P_1$ luminescence of Ba isolated in Kr, following sample deposition at 10 K and annealing to 38 K. The gas phase position[1] of the (6s6p) $^1P_1 \leftarrow$ (6s^2) $^1S_0$ transition of Ba is shown, in both excitation and emission, as a dashed line.**

The effects of further annealing to 45 K are presented in the 2D-EE spectrum shown in Figure IV.17. A comparison of the two annealed figures reveals that the broad, relatively weak emission features between 565 and 580 nm can be completely removed leaving a spectrum which bears a resemblance to Ba/Xe, with three components labelled I − III identifiable. However, the relative intensities of bands I − III are different in Ba/Kr, reflecting the differing abundance of each trapping site in this host. It will be shown later that the spectrum recorded following annealing to 38 K is actually more like the annealed Ba/Ar system. The excitation slices X.1 − X.4 obtained

from both 2D-EE spectra are presented in Figure IV.18, overlaid onto the appropriate absorption profiles.
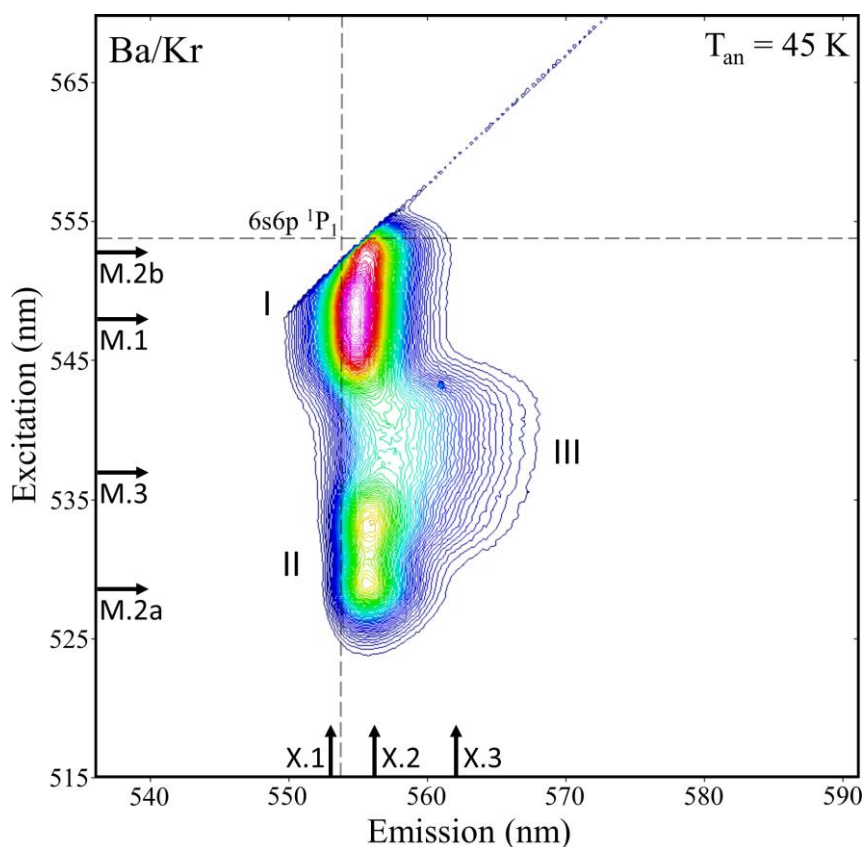
Figure IV.17   2D-EE spectrum recorded for the (6s6p) $^1P_1$ luminescence of Ba isolated in Kr, following further sample annealing to 45 K. The gas phase position[1] of the (6s6p) $^1P_1 \leftarrow$ (6s^2) $^1S_0$ transition of Ba is shown, in both emission and excitation, as a dashed line.

An excitation scan recorded for the unstable 'red' site of isolation is shown by the red trace in the upper panel of the plot. It consists of a band with two resolved components at 555.5 and 561.7 nm which are red-shifted with respect to the gas phase (6s6p) $^1P_1 \leftarrow$ (6s^2) $^1S_0$ line and a higher energy, blue-shifted band centred at 542.7 nm. The excitation spectra recorded for the three thermally stable sites are presented in the bottom of Figure IV.18. The combination of the three traces are required to reproduce all of the features present in absorption. Similar to band II of Ba/Xe, band I of Ba/Kr (Figure IV.17) actually comprises features from two distinct trapping sites. In keeping with the established labelling system, the excitation slices X.1 and X.2 extracted from the higher and lower energy sides of this feature are attributed to the green and violet sites of isolation respectively.
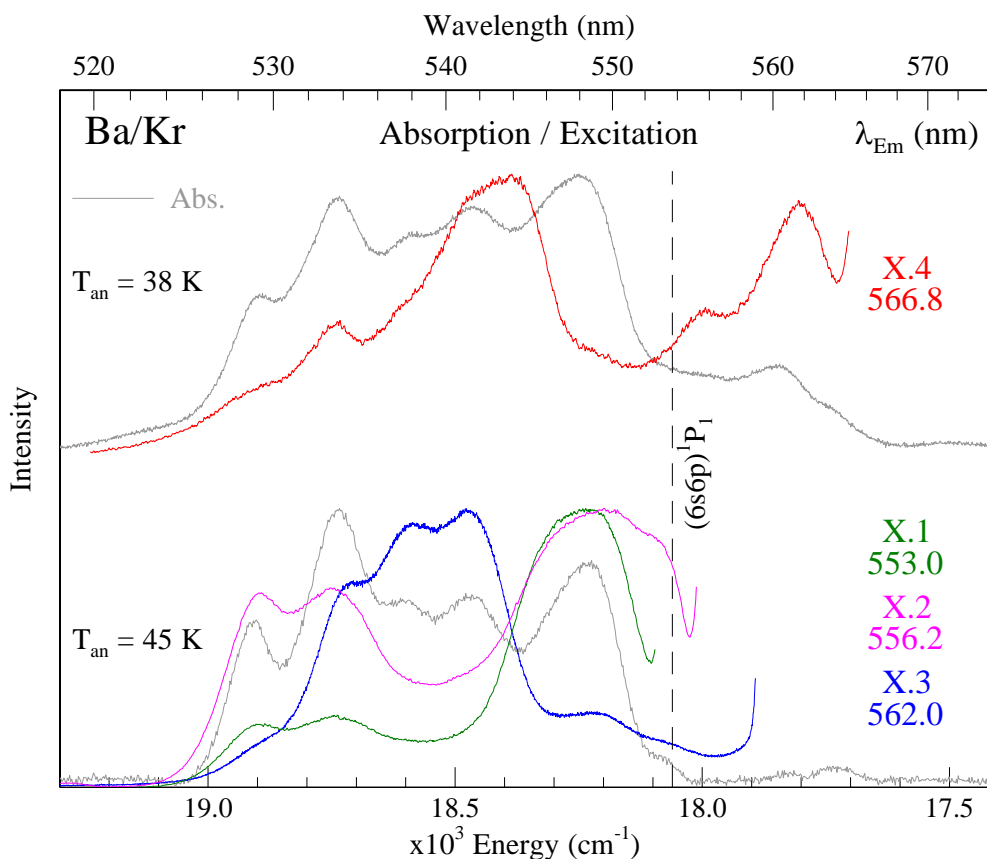
Figure IV.18   **Absorption and excitation spectra obtained with either a W lamp/ PMT combination or taken directly from the 2D-EE plots – both methods are identical and indeed interchangeable. The traces shown correspond to vertical slices through Figure IV.16 and Figure IV.17, at the wavelength indicated by an X.**

The two distinct emission bands arising from each site are located in very close spectral proximity. In contrast to Ba/Xe, the green site of isolation is now the dominant luminescent species and consists of an unstructured band centred at approx. 547 nm. The violet site spectrum exhibits a threefold asymmetric split band with a higher energy doublet at 529.1 and 533.4 nm and a lower energy singlet at 552.7 nm. However, for Kr the singlet appears as a red shoulder on the green site excitation band, owing to the greater degree of green site isolation for Ba in Kr. A slice at X.3 (562 nm in emission) in Figure IV.17 yields the blue site excitation spectrum which exhibits a fully resolved JT band with the characteristic threefold splitting pattern at 534.2, 553.8 and 541.3 nm. The photophysical and temporal properties of the three thermally stable sites of isolation for Ba/Kr will now be presented.

IV.4.I Ba/Kr - Blue site

The luminescence of the blue site of isolation for Ba/Kr is presented in Figure IV.19. Lamp excitation at 538.0 leads to emission at 557.9 nm (slice M.3, Figure IV.17) exhibiting a fwhm of 261 cm^{-1}, situated to the red of the Ba: $(6s6p)$ $^1P_1 \leftarrow (6s^2)$ $^1S_0$ line. A Stokes shift of 666 cm^{-1} is evaluated from the centres of the emission and threefold split excitation band.
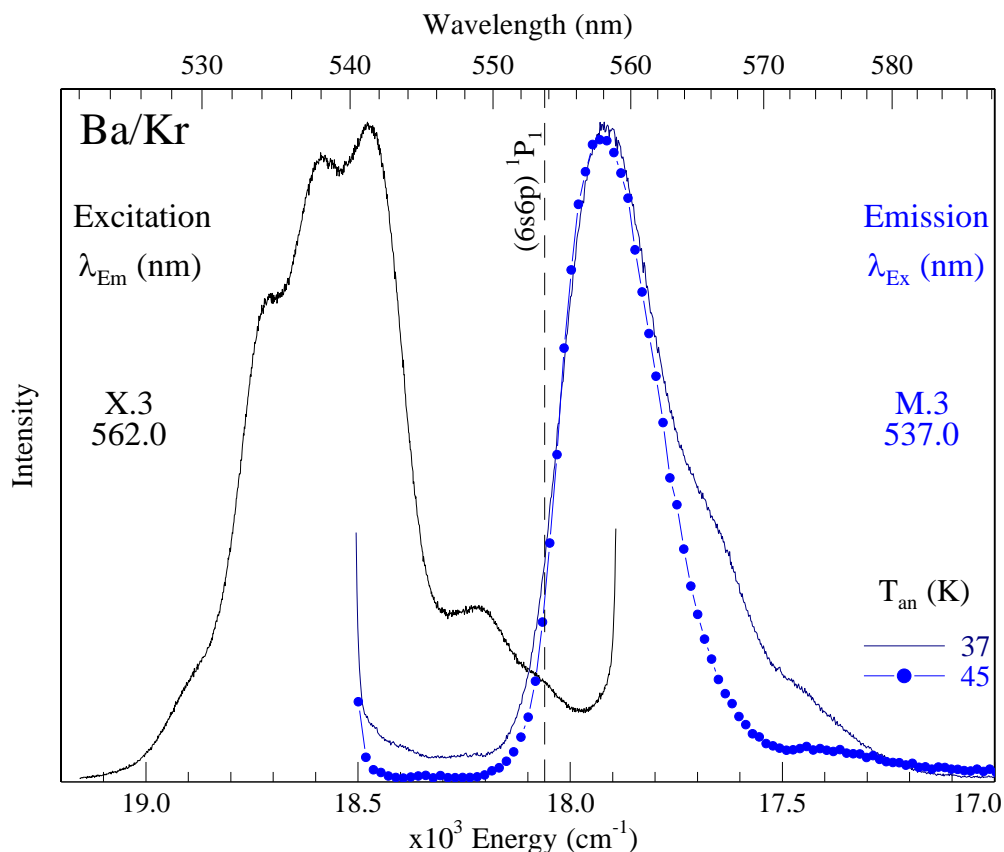
Figure IV.19   **Emission (blue) and excitation (black) spectra recorded at 10 K of the blue site of isolation for Ba in solid Kr. A comparison of the emission bands produced with excitation of the central component of the JT band, following annealing to 37 (solid trace) and 45 K (solid line and circle) is presented. The dashed vertical line represents the gas phase[1] position of the $(6s6p)$ $^1P_1 \leftarrow (6s^2)$ $^1S_0$ transition of atomic Ba.**

The excitation scan shown was obtained monitoring the emission at 562 nm to reduce the contributions from the other two sites. The entire JT band lies to the blue of the gas phase line, with a matrix shift of +531 cm^{-1}. A lineshape analysis of the threefold split excitation band is presented in Figure IV.54 of Appendix IV.I. Three Gaussian curves, each with a bandwidth of 153 cm^{-1}, are required to reproduce the bandshape.

A decay profile for the blue site emission at 557.9 nm, obtained with site-selective laser excitation at 538.0 nm, is presented in Figure IV.20 and can be adequately fit by a single exponential function with a decay time of 4.4 ns.

Ba/Kr - Decay profile $\lambda_{Em.}$ = 557.9 nm at 10 K
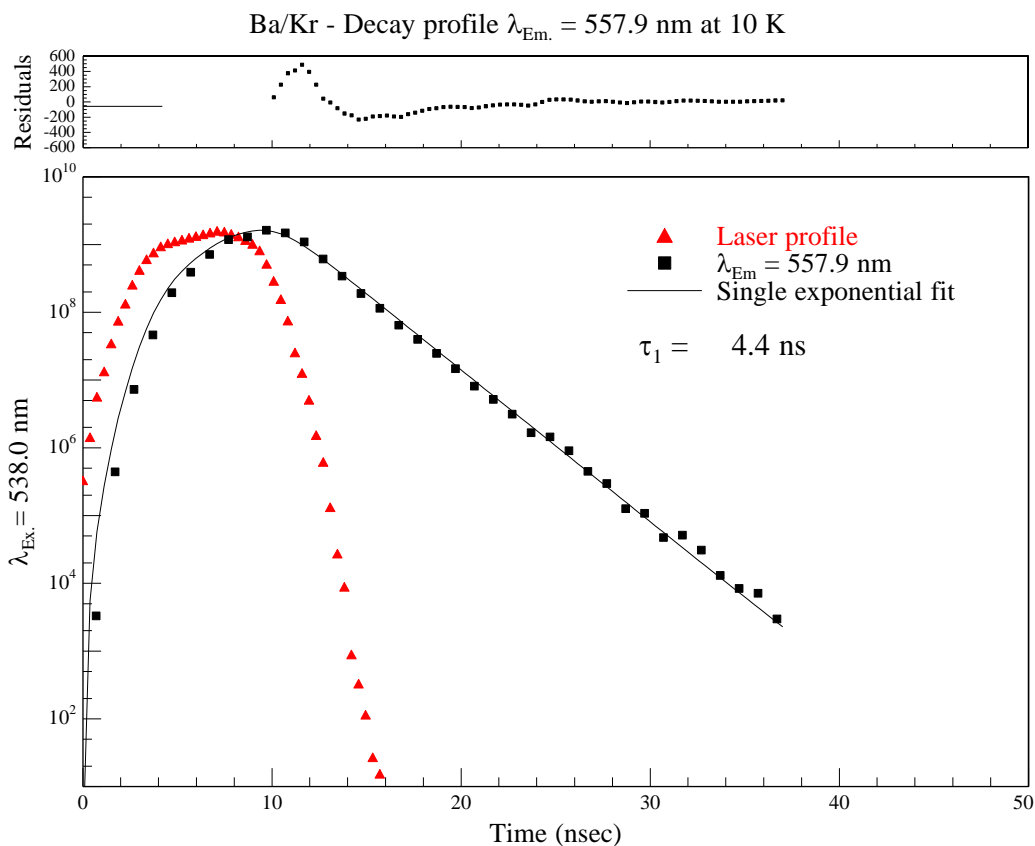
Figure IV.20   **Decay profile of the Ba/Kr blue site emission band at 557.9 nm, produced with site-selective laser excitation at 538.0 nm. An excited state decay time of 4.4 ns is obtained at 10 K with a single exponential trial function, which included a re-convolution with the time profile of the Nd:YAG laser. A residuals analysis is plotted in the top panel.**

The temperature dependence of both the emission bandshape and decay profile was investigated, the results of which are shown in the two panels of Figure IV.21. The intensity of the blue site emission gradually decreases and the band centre shows a very minor red-shift at elevated temperatures. Inspection of the right panel reveals that the decay profiles are virtually invariant to the sample temperature, at least up to 30 K. Hence, 4.4 ns is the true radiative lifetime for the excited $^1P_1$ state of atomic Ba in the blue site.
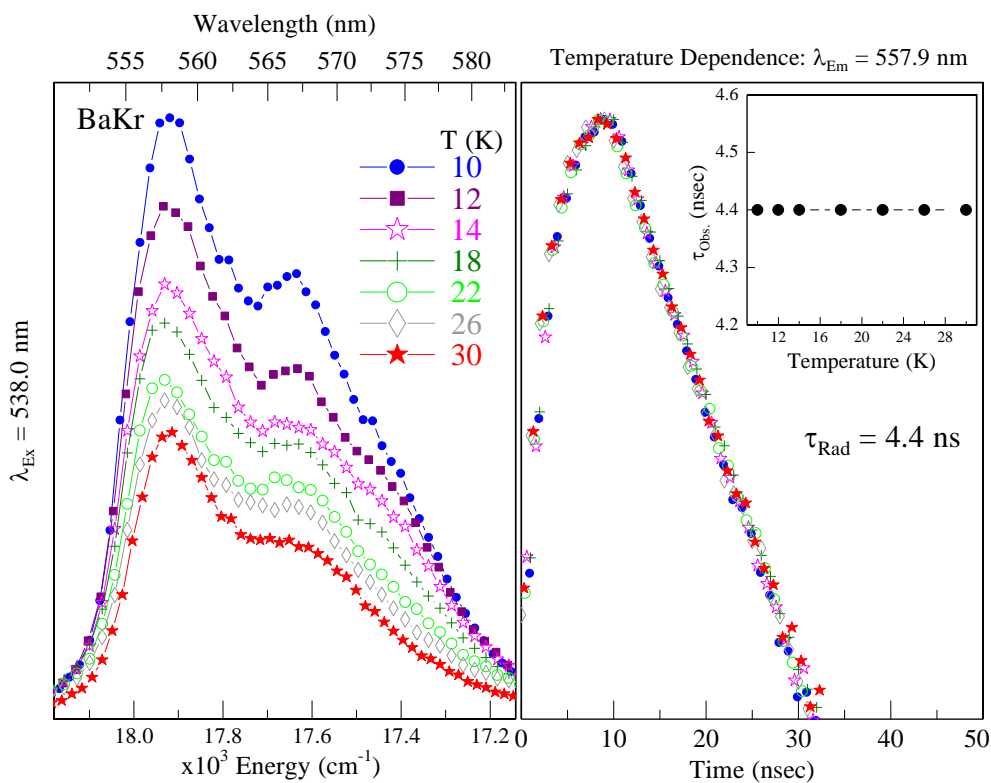
Figure IV.21   **The left panel shows the temperature dependence of the Ba/Kr blue site emission band at 557.9 nm. These decays were obtained from a Ba/Kr sample which was deposited at 10 K and annealed to 38 K, hence the observation of emission from the partially stable red site at ~567 nm. A slight red-shift of the band centre occurs in conjunction with a decrease in the band intensity, as the sample temperature increases from 10 – 30 K. The right panel presents the temperature dependence of the corresponding decay curves, which show no change over the temperature range investigated. Hence, the true radiative lifetime has been measured.**

IV.4.II Ba/Kr - Violet site

Emission and excitation spectra recorded for the Ba/Kr violet site of isolation are presented in Figure IV.22. Photoexcitation into any of the three components of the 2+1 structure produces the same emission band centred at 556.2 nm displaying a bandwidth of 129 cm^{-1}. The two excitation wavelengths selected to produce the emission shown correspond to the horizontal slices extracted from 2D-EE plot (Figure IV.17) at M.2a and M.2b.
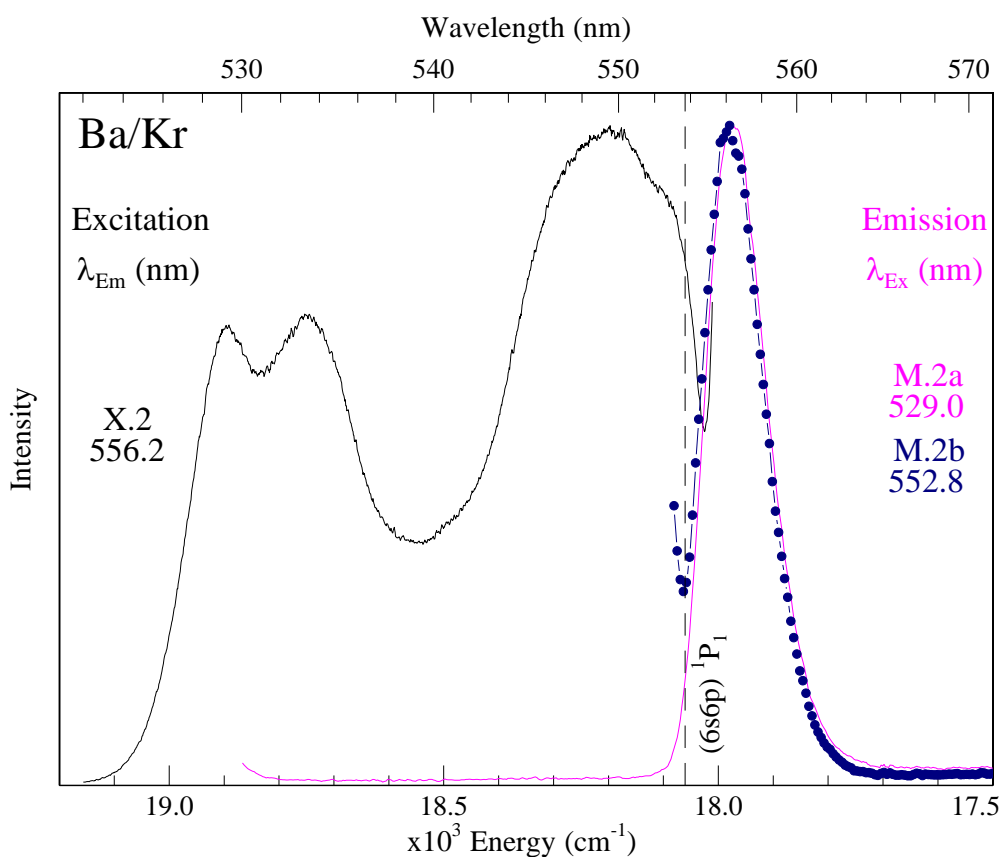
Figure IV.22 **Emission (pink/purple) and excitation (black/red) spectra recorded at 10 K of the violet site of isolation for Ba in solid Kr. The dashed vertical line represents the gas phase[1] position of the (6s6p) $^1P_1 \leftarrow$ (6s^2) $^1S_0$ transition of atomic Ba.**

Although complicated by a significant green site 'contamination', an attempt was made to fit the excitation trace in order to estimate the spectral widths of the violet site absorption bands. The result of this fit is presented in Figure IV.55 of Appendix IV.I and reveals widths of 139, 170 and 137 cm^{-1} for each component of the 2+1 feature (from higher to lower energy). In contrast to Ba/Xe, all three of the violet site bands are blue-shifted with respect to the gas phase[1] (6s6p) $^1P_1 \leftarrow$ (6s^2) $^1S_0$ line of Ba. From red to blue, the matrix shifts on each peak are determined to be +33, +687 and +840

cm^{-1}. The Stokes shifts also vary dramatically, with values of 921 and 114 cm^{-1} measured from the highest and lowest energy peaks respectively.

A decay profile was extracted from the TRES for the violet site of Ba/Kr, with site-selective laser excitation at 532 nm. A single exponential function, including a re-convolution of the laser profile, provides an excellent fit of the decay yielding an observed excited state lifetime of 4.2 ns, as presented in Figure IV.23.


Ba/Kr - Decay profile $\lambda_{Em.}$ = 556.2 nm at 10 K
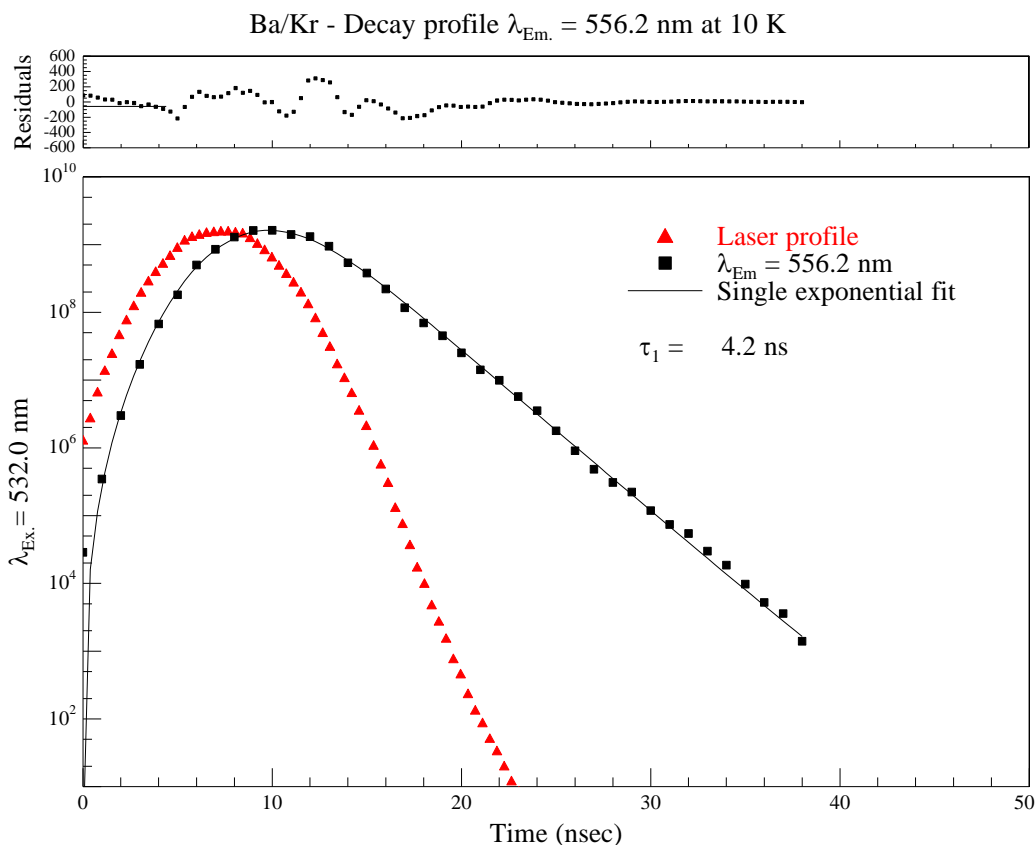
Figure IV.23 **Decay profile of the Ba/Kr violet site emission band at 556.2 nm, produced with site-selective laser excitation at 532.0 nm. An excited state decay time of 4.2 ns is obtained at 10 K with a single exponential trial function. The quality of the fit can be gleaned by examining the residuals in the top panel.**

Time-resolved emission scans were made at elevated temperatures to establish if the true radiative lifetime has been measured at 10 K. The emission centroid shifts to lower energy, becomes broader and diminishes in intensity with increasing temperature, as shown in the left panel of Figure IV.24. The band red-shift and broadening effects are reversible, however, the emission scans recorded back at 10 K reveal a permanent loss of intensity. In contrast, the decay profiles recorded in the 10 to 26 K range display no

temperature dependence indicating that the true radiative lifetime has indeed been recorded for this site. Its value is 4.2 ns.
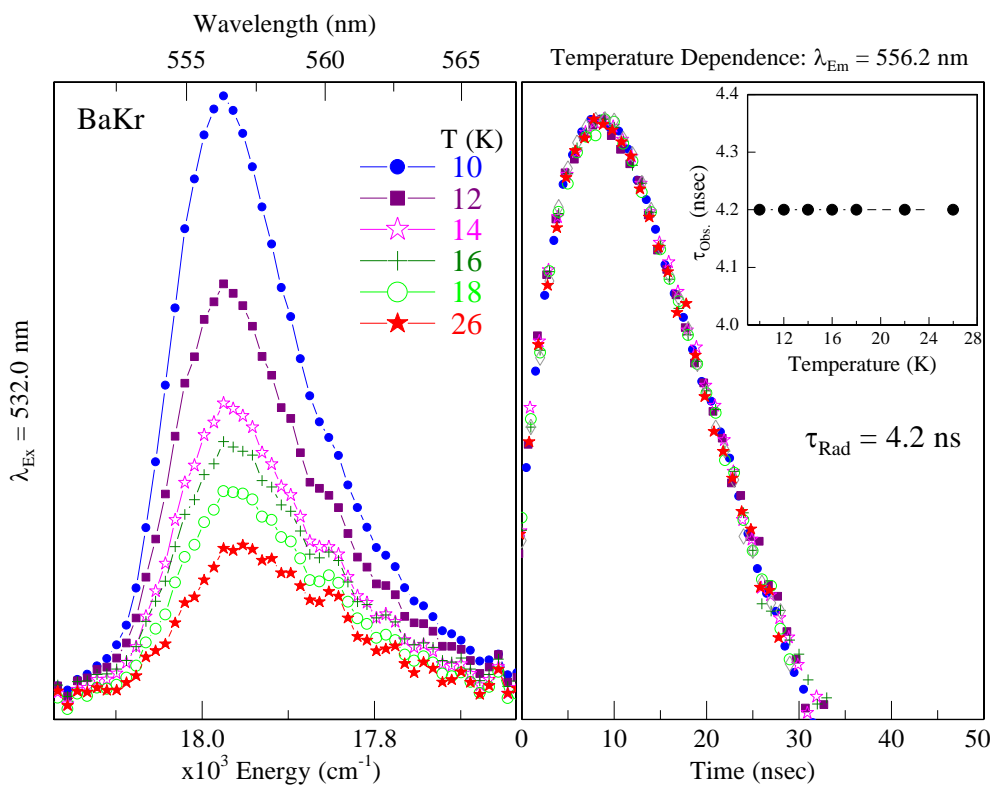

Figure IV.24   **The left panel shows the temperature dependence of the Ba/Kr violet site emission band at 556.2 nm. A progressive red-shift of the band centre occurs in conjunction with a decrease in the band intensity, as the sample temperature increases from 10 – 26 K. The right panel presents the temperature dependence of the corresponding decay curves, which show no deviation over the temperature range investigated. Hence, the true radiative lifetime has been measured.**

IV.4.III Ba/Kr - Green site

Figure IV.25 details the luminescence of the spectrally dominant green site of isolation for Ba/Kr. Steady-state lamp excitation at 548 nm produces emission at 554.9 nm which has a fwhm of 135 cm^{-1}. A Stokes shift of 234 cm^{-1} is determined from the centre of the excitation band at 547.8 nm. The excitation scan shown was obtained by monitoring a higher energy emission value of 553 nm.
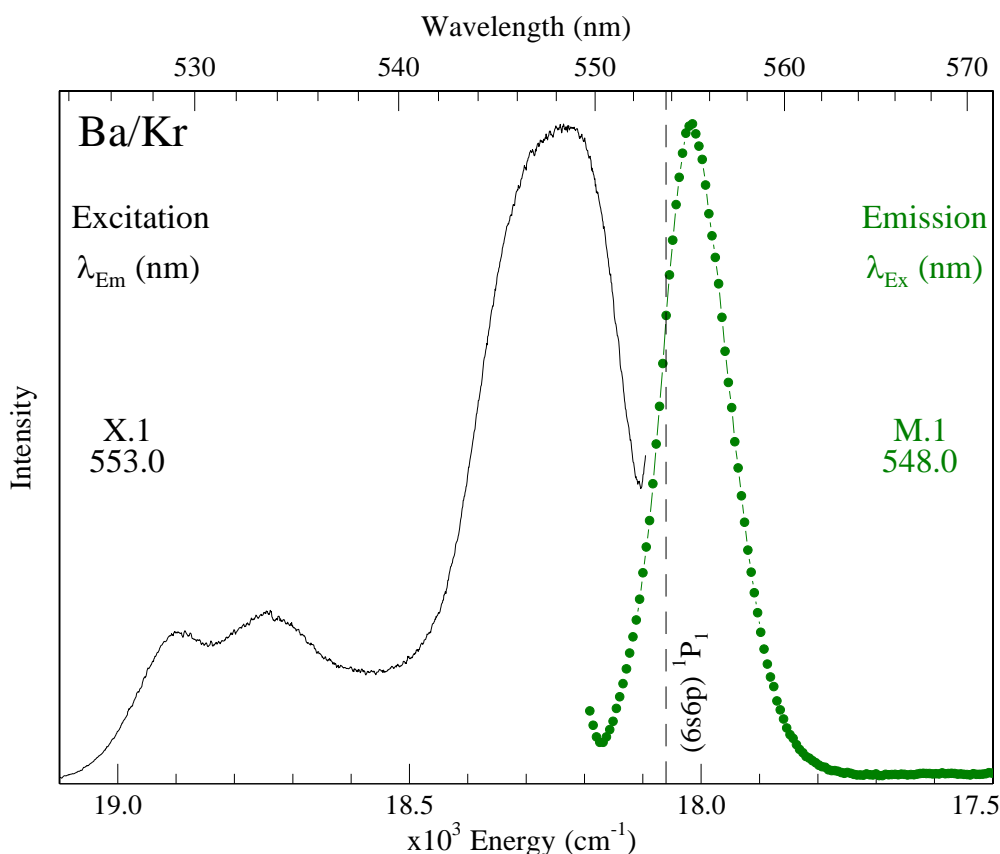
Figure IV.25   **Emission (green) and excitation (black) spectra recorded at 10 K of the green site of isolation for Ba in solid Kr. Although the emission band maximum occurs at 554.9 nm, the excitation scan shown was obtained at a shorter wavelength of 553.0 nm. This was done to minimise the features of the violet site. The dashed vertical line represents the gas phase[1] position of the (6s6p) $^1P_1 \leftarrow$ (6s^2) $^1S_0$ transition of atomic Ba.**

This was done to minimise the contribution of the violet site. The green site excitation band exhibits a width of 276 cm^{-1} and is blue-shifted by 195 cm^{-1} with respect to the gas phase resonance line. The bandshape is asymmetric, and tails to higher energies with decreasing intensity. The lineshape analysis presented in Figure IV.56 of Appendix IV.I shows that this asymmetry is accounted for by three Gaussians, each exhibiting a bandwidth of 135 cm^{-1}.

The decay profile recorded for the green site emission band at 10 K is presented in Figure IV.26. A single exponential fit with a lifetime of 4.5 ns accurately describes the decay portion of this profile.
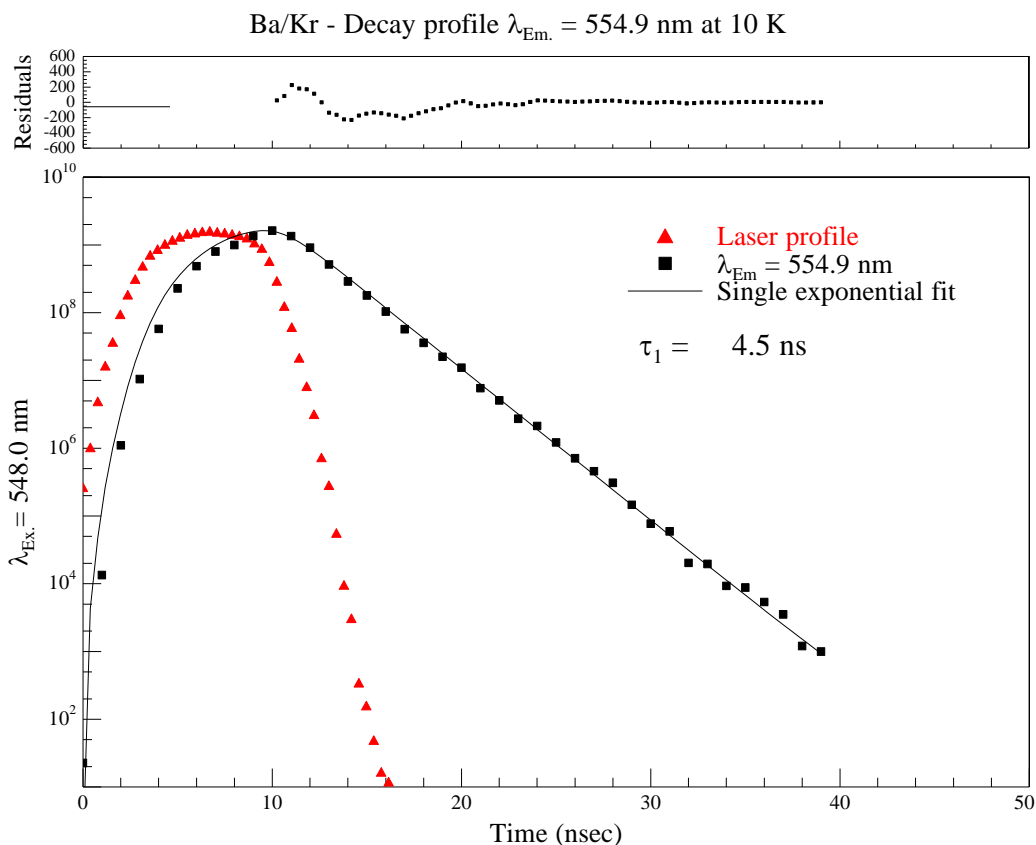

Figure IV.26   **Decay profile of the Ba/Kr green site emission band at 554.9 nm, produced with site-selective laser excitation at 548.0 nm. An excited state decay time of 4.5 ns is obtained at 10 K with a single exponential trial function.**

Time-integrated emission scans and time-resolved decay profiles were recorded over a range of temperatures, to investigate the possibility of non-radiative components contributing to the decay profile of Ba isolated at the green site in solid Kr. The results of this study are presented in Figure IV.27. The green site emission band becomes weaker in intensity, broader in width and red-shifted in position with increasing temperature (see left panel). In contrast, the decay profiles (right panel) are unaffected by the sample temperature. The 4.5 ns value observed at 10 K is therefore the true radiative lifetime for this site of isolation.
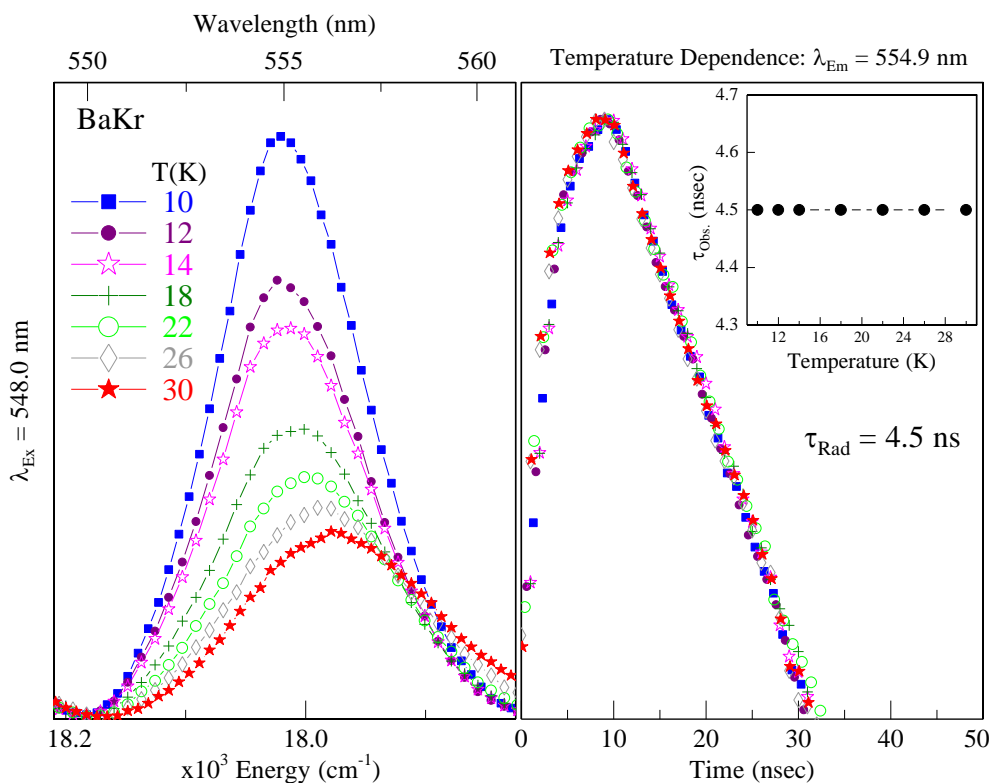
Figure IV.27 The left panel shows the temperature dependence of the Ba/Kr green site emission band at 554.9 nm. A progressive red-shift of the band centre occurs in conjunction with a decrease in the band intensity, as the sample temperature increases from 10 – 30 K. The right panel presents the temperature dependence of the corresponding decay curves, which show no deviation over the temperature range investigated. Hence, the true radiative lifetime of 4.5 ns has been measured.

IV.5   Ba/Ar

The 2D-EE spectrum of a Ba/Ar sample annealed to 28 K is presented in Figure IV.28. A comparison with equivalent plot on deposition at 10 K (see Figure IV.2) shows that the lowest energy emission band at 562 nm has been completely removed, leaving four well resolved spectral features which are labelled I – IV based on the observed intensity.
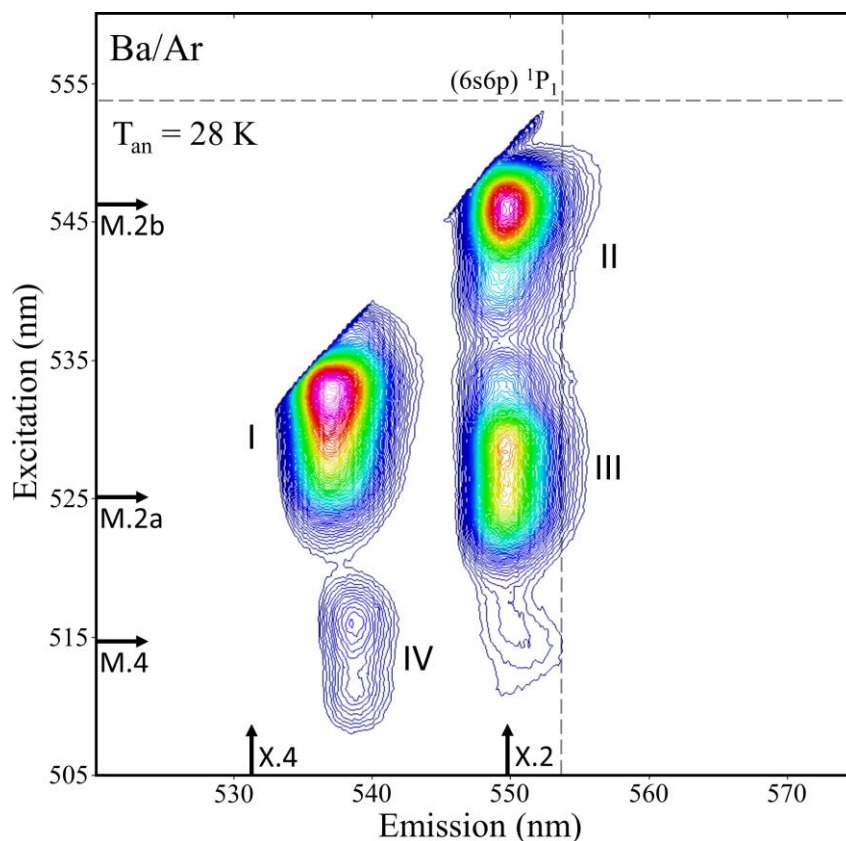

Figure IV.28   **2D-EE spectrum recorded for the entire (6s6p) $^1P_1$ luminescence of Ba isolated in Ar, following sample annealing to 28 K. The emission band at approx. 562 nm has been completely removed indicating its thermal instability.   The gas phase position[1] of the (6s6p) $^1P_1 \leftarrow$ (6s^2) $^1S_0$ transition of Ba is shown, in both excitation and emission, as a dashed vertical line.**

Further simplification of the Ba/Ar luminescence can be achieved with matrix annealing to 32 K, as shown in Figure IV.29. Bands II and III are greatly diminished by this process. However a substantial amount of the Ba/Ar sample is lost at this high temperature - only the most stable sites of isolation for Ba remain.

Excitation spectra recorded monitoring the intensity of each emission band are presented in Figure IV.30 and correspond to vertical slices taken through both annealed 2D-EE spectra (X.1 – X.4). In addition to these intense features, a very weak emission

band was found at 531.4 nm in extremely dilute Ba/RG samples (O.D. < 0.2 at 528 nm) which were deposited at higher temperatures. The excitation spectrum recorded for this emission is also presented in the top of Figure IV.30 and would corresponds to a vertical slice at X.4 as shown in Figure IV.28. However, this feature is not visible with the contour scale used in the 2D plots as the lower energy bands are far brighter emitters. Based on the polarizability assignments, which are presented ahead in Section IV.6.I, this feature will be referred to as the 'blue' site.
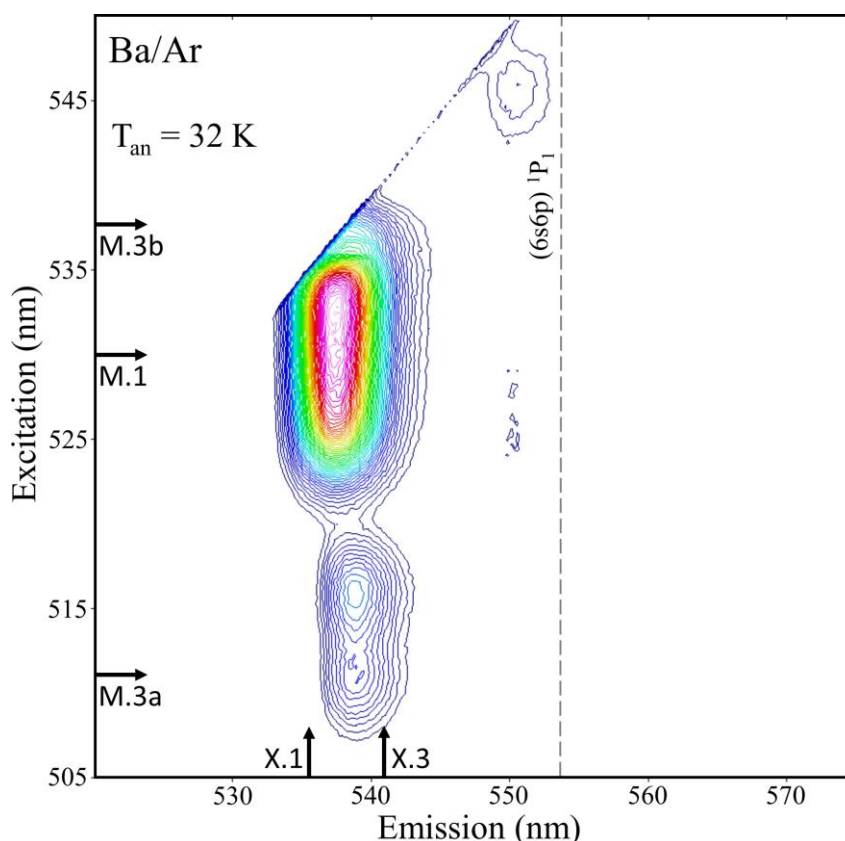
Figure IV.29   **2D-EE spectrum recorded for the entire (6s6p) $^1P_1$ luminescence of Ba isolated in Ar, following sample annealing to 32 K. The emission band at approx. 550 nm has almost been completely removed at this temperature. The gas phase position[1] of the (6s6p) $^1P_1 \leftarrow$ (6s^2) $^1S_0$ transition of Ba is shown, in both excitation and emission, as a dashed vertical line.**

The emission and excitation bands of the 'violet' and 'green' sites of isolation for Ba/Ar are strongly overlapping. However, a spectral distinction can be achieved by recording excitation spectra at the emission positions indicated in Figure IV.29 (X.1 – green site and X.3 – violet site). Inspection of Figure IV.30 reveals that the violet site excitation trace displays the now familiar asymmetric 2+1 splitting pattern. As with Ba/Kr, the lowest energy component of this structure exists as a red shoulder (~535

nm) on the green site profile. Both of these excitation traces are required to account for all of the features observed in the lower absorption trace ($T_{an} = 32$ K) of Figure IV.30.

The excitation spectrum obtained by monitoring the emission feature at 549.9 nm (X.2, Figure IV.28) is complex exhibiting intensity in two regions, which were labelled as band II and III. A cursory inspection of the 2D-EE spectrum (Figure IV.28) shows that combining both bands yields a 2+1 splitting pattern, with an intense lower energy singlet at 543.7 nm (II) connected to a higher energy doublet with peaks at 527.3 and 523.9 nm (III).
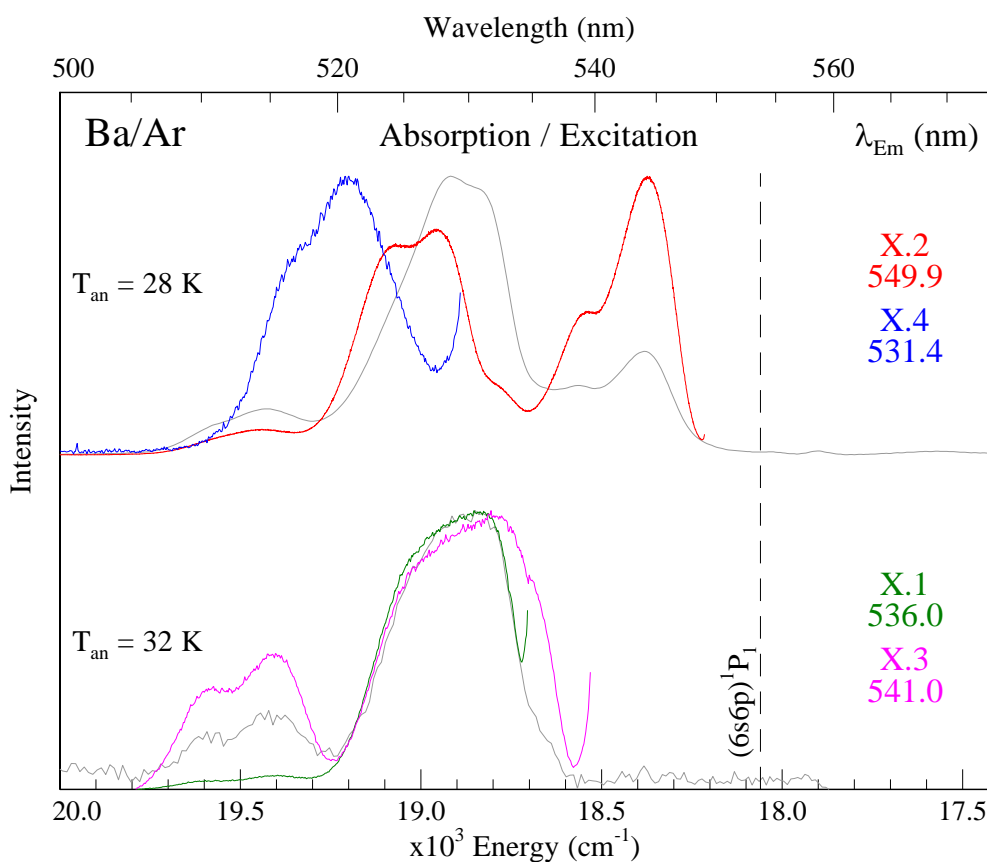

Figure IV.30   **Absorption (grey) and excitation (coloured) spectra recorded for Ba/Ar following sample annealing to 30 K. The excitation scans correlated to vertical slices through the 2D-EE plots at the emission positions labelled X.1 – X.4.**

As these two features share a common emission and are reduced in unison with annealing to 32 K, they are tentatively associated with the same matrix site, namely the 'red' site of isolation. However this analysis is hindered by the presence of a weaker shoulder at 538.8 nm on the lowest energy component and it may be that a distinct matrix site is masked by the intense singlet band. Complicating matters further, the red site profile exhibits intensity across the entire (6s6p) $^1P_1$ absorption spectrum due to

competitive re-absorption. The violet and green site intensities are 'picked up' by the red site excitation scan due to spectral overlap of the emission at 537.4 nm with a portion of the red site absorption band. To further probe these matters, the photo-physical and temporal properties of each matrix site will now be presented in detail.

IV.5.I Ba/Ar - Violet site

The luminescence of the Ba/Ar violet site is presented in Figure IV.31. As mentioned above, the excitation scan of this site displays a 2+1 splitting pattern composed of a higher energy doublet with peaks at 510.3 and 515.4 nm and a lower energy singlet at 535.0 nm. Large matrix blue-shifts of +1536, +1342 cm^{-1} and +631 cm^{-1} exist respectively for each composite peak.
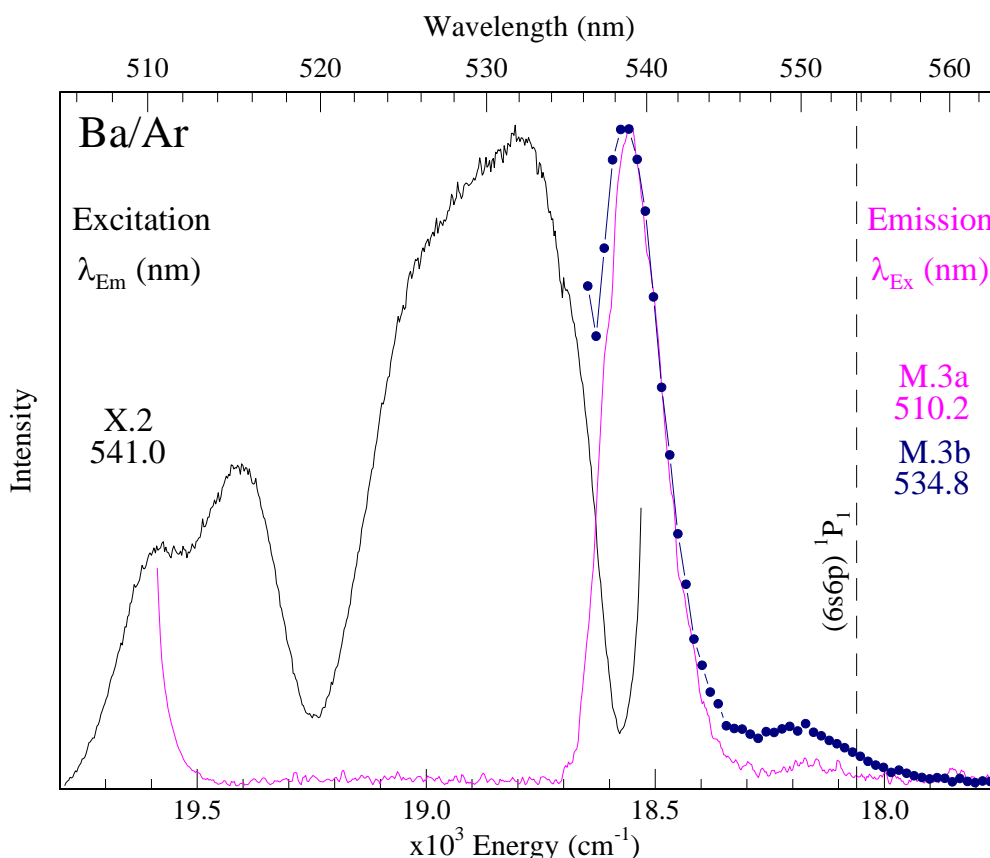

Figure IV.31   **Emission (pink/purple) and excitation (black) spectra recorded at 10 K for the Ba/Ar violet site of isolation. The dashed vertical line represents the gas phase[1] position of the (6s6p) $^1P_1 \leftarrow$ (6s^2) $^1S_0$ transition of atomic Ba.**

A lineshape analysis (see Figure IV.57, Appendix IV.I) was conducted on the excitation scan to in an attempt to ascertain the spectral widths of the three violet site

absorptions. Three Gaussian peaks, showing bandwidths of 174, 190 and 158 cm^{-1} (from blue to red), were used to fit the 2+1 structure. An emission band centred at 539.1 nm exhibiting a fwhm of 163 cm^{-1} emanates from the violet site of Ba/Ar, with photoexcitation of its absorption features. The Stokes shift depends on the excitation component chosen – values of 1047, 853 and 142 cm^{-1} are evaluated from the highest to the lowest energy absorption band respectively.


Ba/Ar - Decay profile $\lambda_{Em.}$ = 539.1 nm at 10 K

Laser profile
λ_{Em} = 539.4 nm
Single exponential fit

$\tau_1 =$ 4.5 ns
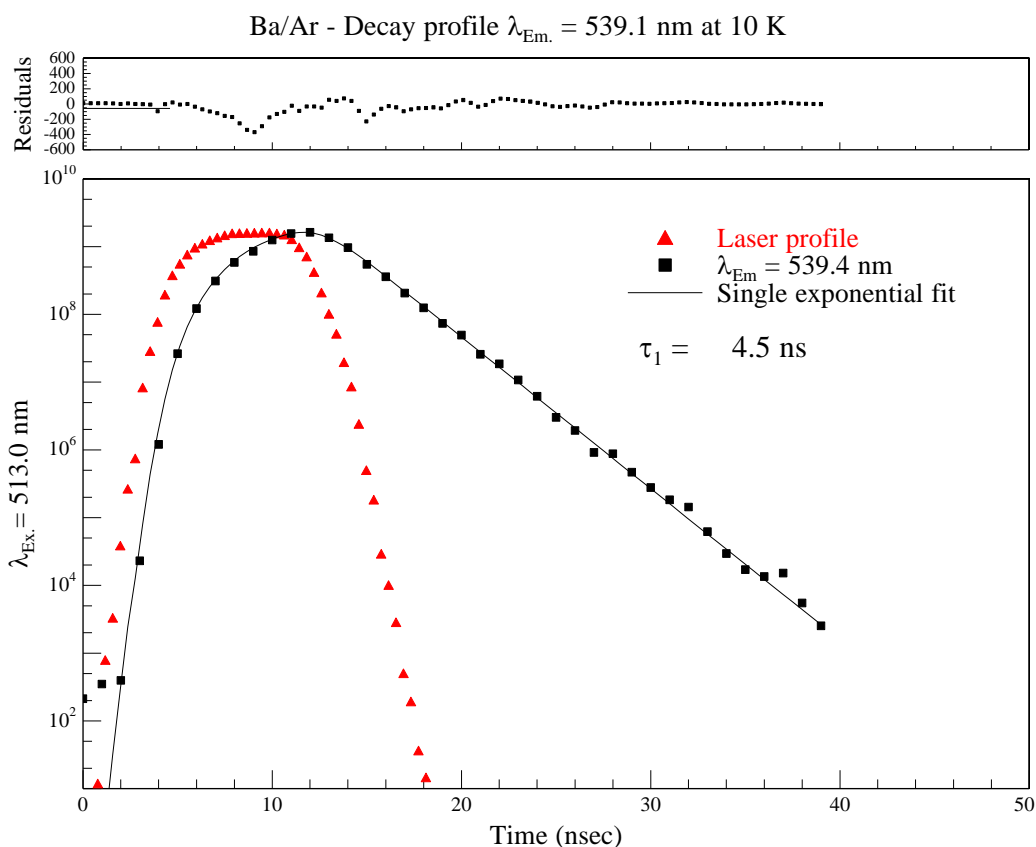
Figure IV.32 **Decay profile of the Ba/Ar violet site emission band at 539.1 nm, produced with site-selective laser excitation at 513.0 nm. An excited state decay time of 4.5 ns is obtained at 10 K with a single exponential trial function.**

The temporal profile obtained with pulsed laser excitation at 513 nm is plotted in Figure IV.32. The decay is well fit with a single exponential function yielding a lifetime value of 4.5 ns. Emission scans and temporal profiles were also recorded in the temperature range 10 − 20 K, as illustrated in Figure IV.33. The violet site emission becomes red-shifted, broader and loses intensity at higher temperatures. The temporal decay profiles exhibit no change over the investigated range, hence 4.5 ns is identified as the radiative lifetime of the (6s6p) $^1P_1 \rightarrow$ (6s^2) transition of Ba isolated in the violet site of Ar.
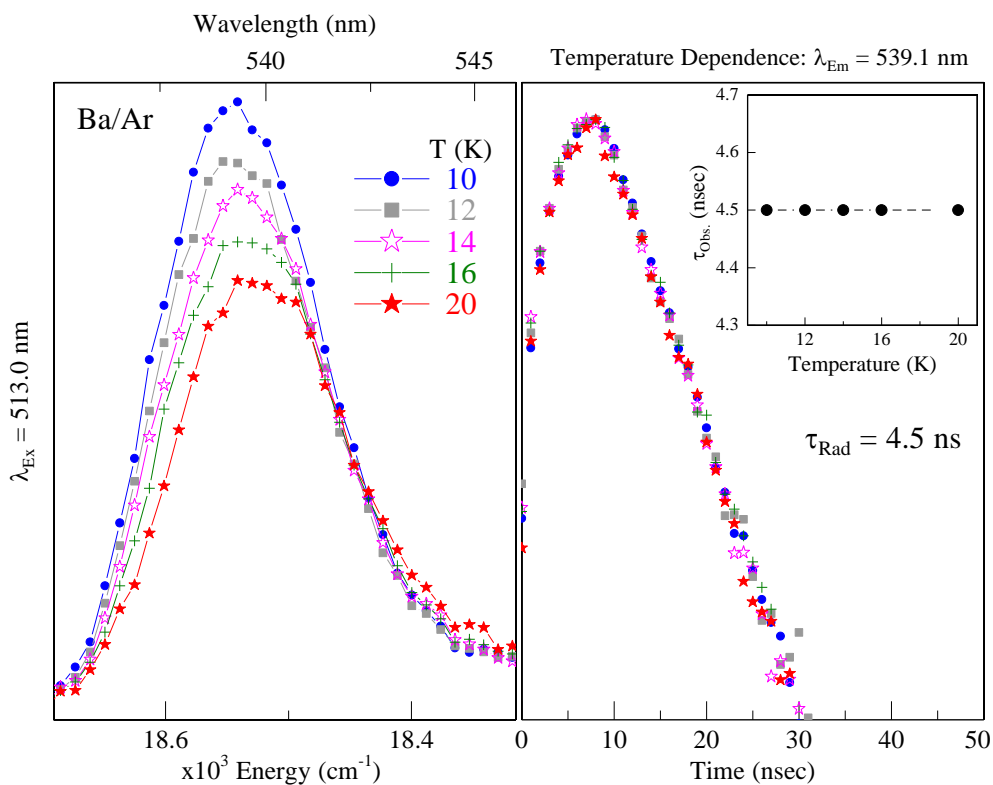
Figure IV.33   **The left panel shows the temperature dependence of the Ba/Ar violet site emission band at 539.1 nm. A red-shift of the band centre occurs in conjunction with a decrease in the band intensity, as the sample temperature increases from 10 – 20 K. The right panel presents the temperature dependence of the corresponding decay curves, which show no variation over the temperature range investigated. Hence, the true radiative lifetime has been measured.**

IV.5.II Ba/Ar - Blue site

The luminescence of Ba, isolated in the blue site in the Ar host, is shown in Figure IV.34. The excitation trace is characterised by partially resolved peaks at 516.3 and 520.6 nm with a hint of a weak shoulder at 513.0 nm. Three Gaussian curves displaying an average width of 197 cm^{-1} are required to fit the excitation spectrum, as shown in Figure IV.58 of Appendix IV.I. A matrix shift of +1308 cm^{-1} is computed from the peak at 516.3 nm.
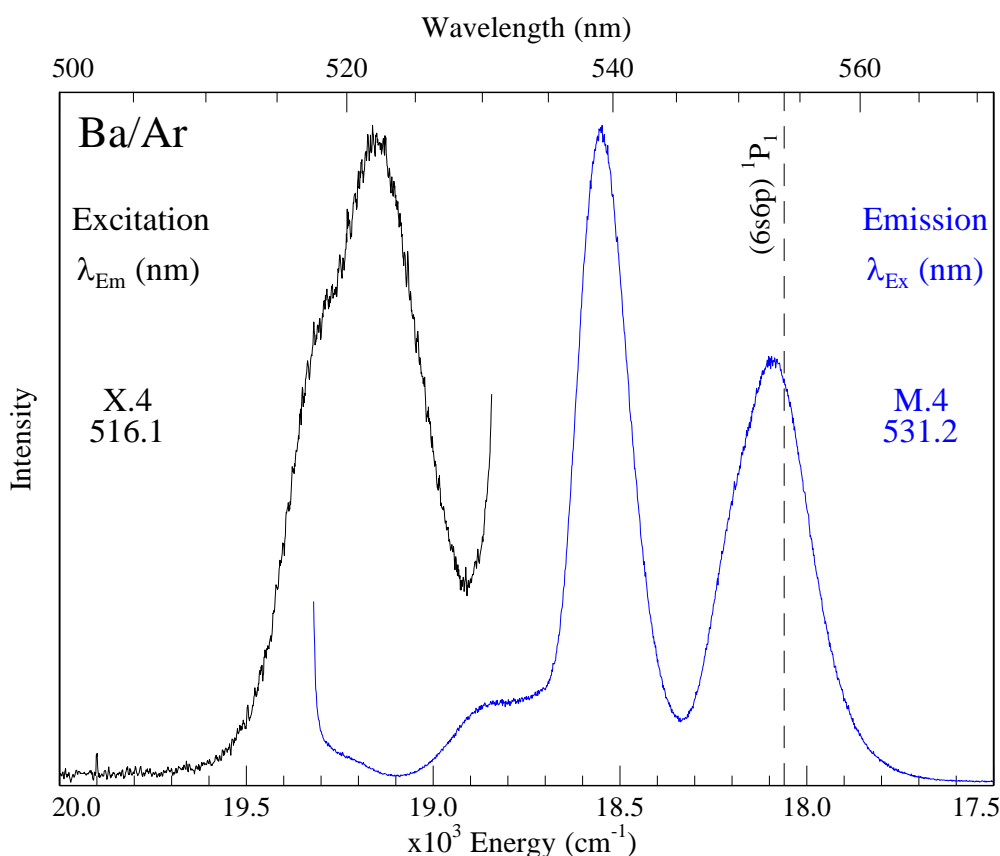

Figure IV.34   **Excitation (black) and emission (blue) spectra produced from the Ba/Ar blue site of isolation, recorded in the vicinity of the strong (6s6p) $^1P_1 \leftarrow$ (6s^2) $^1S_0$ transition of Ba.**

The emission spectrum shown in blue was obtained with excitation at 516.1 nm. Numerous bands are observed due to re-absorption. The actual blue site emission occurs at 531.2 nm, with a Stokes shift of 543 cm^{-1}, directly overlapping the strongest absorption band. Indeed, in all but the most dilute samples, this band is totally obscured.

       Obtaining an accurate decay curve was quite difficult as 1) a very weakly absorbing sample had to be formed and 2) the decay could not be fit over a large intensity range. Fortunately, an acceptable time profile was obtained with laser

excitation at 515.0 nm, as shown in Figure IV.35. A single exponential function provided a good fit and from this a decay time of 3.9 ns was extracted.
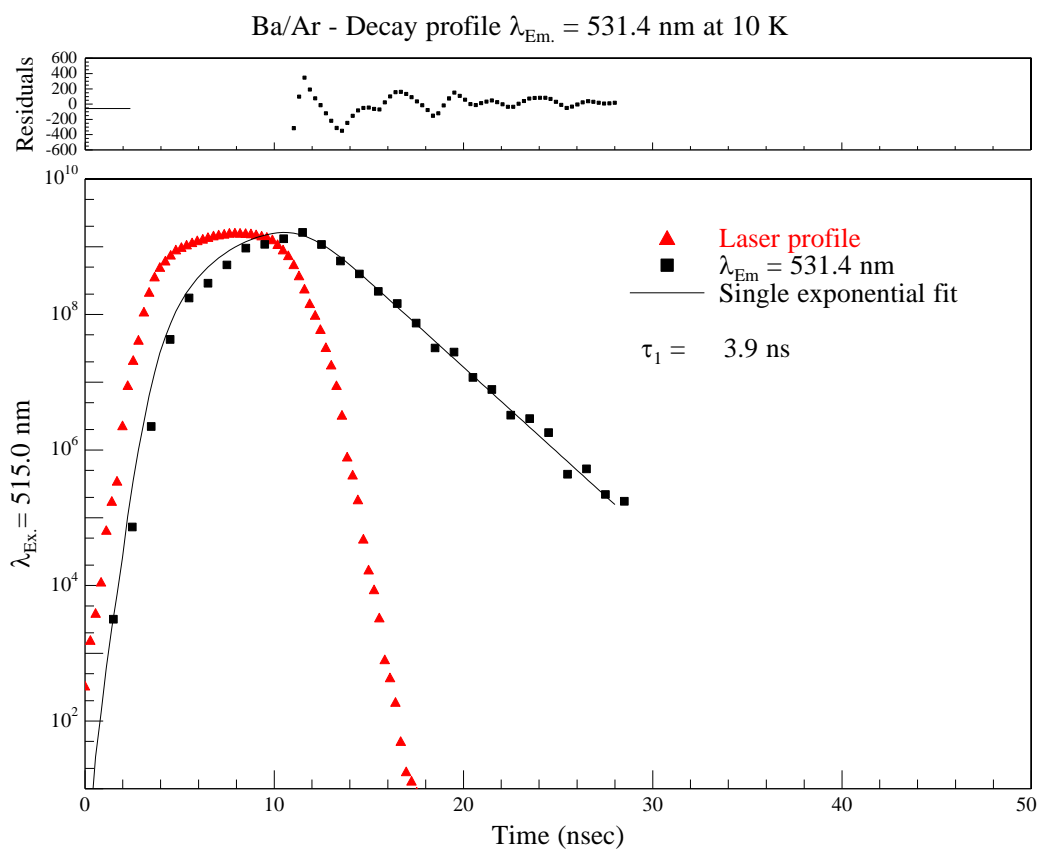

Figure IV.35   **Decay profile of the blue site emission band at 531.2 nm, produced directly with site-specific laser excitation at 515.0 nm. An excited state decay time of 3.9 ns is obtained with a single exponential trial function, which included a re-convolution with the time profile of the Nd:YAG laser.**

Due to lack of intensity, the temperature dependence of the blue site decay curves could not be accurately assessed. However, despite the noise, scans recorded up to 14 K seem to exhibit the same overall decay slope. Thus the 3.9 ns value measured at 10 K is tentatively attributed as the radiative lifetime of this emission band.

IV.5.III Ba/Ar - Green site

Emission and excitation spectra are presented in Figure IV.36 for the green site of isolation. The excitation scan for this site consists of a band centred on 528.3 nm with a spectral width of 390 cm^{-1} at half the maximum intensity (fwhm). Three Gaussian curves of equal width (177 cm^{-1}) were, as shown in Figure IV.59 of Appendix IV.I, required to reproduce the excitation band shape. A matrix blue-shift of +868 cm^{-1} is evaluated from the band centre and indicates the extent of the interaction of Ba with the Ar host in this site.
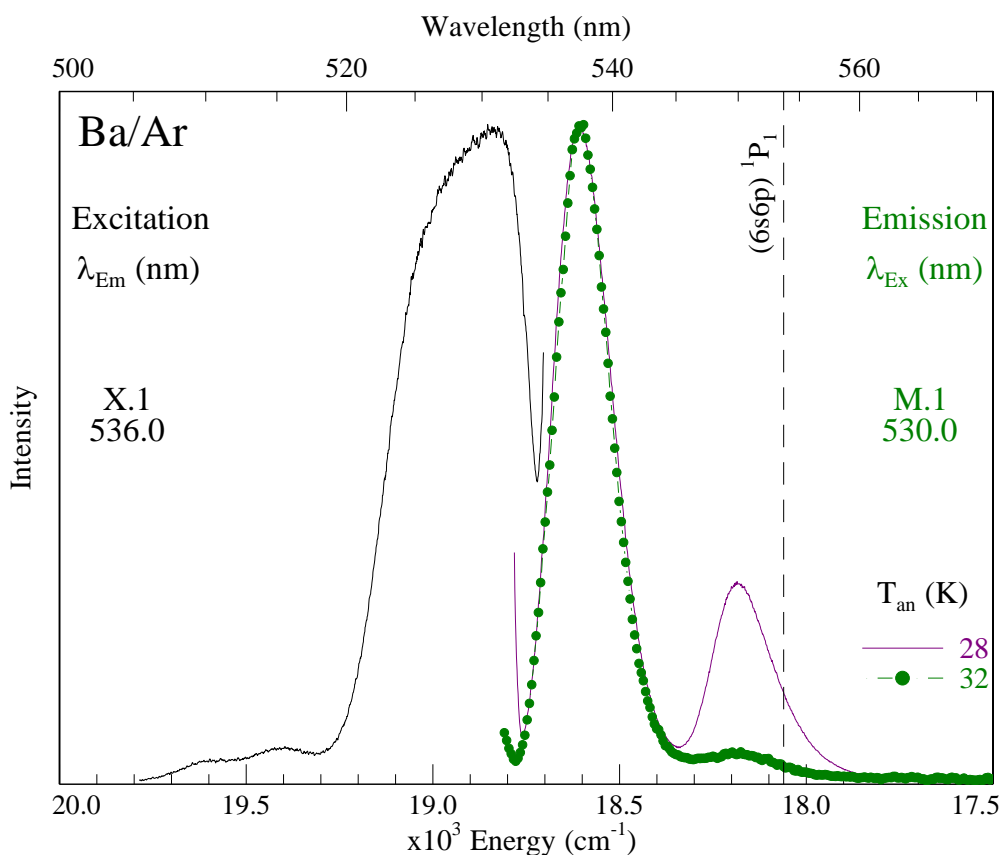
**Figure IV.36**   **Excitation (black) and emission (green/purple) spectra produced from the Ba/Ar green site of isolation, recorded in (6s6p) ^{1}P$_1$ spectral region. The emission spectra recorded following matrix annealing to 28 and 32 K are shown by the purple and green traces respectively. As can be seen, the amount of indirect red site emission produced is greatly reduced at a higher annealing temperature. This behaviour corresponds to the reduction of the red site of isolation.**

Photoexcitation of this feature produces intense green site emission at 537.4 nm, as shown in Figure IV.36, and corresponds to a horizontal slice through the 2D-EE spectrum in Figure IV.29 at M.1. A Stokes shift of 321 cm^{-1} is calculated from the centres of the emission and excitation band and a matrix blue-shift of +548 cm^{-1} is

evaluated for the emission band. The spectral width of the green site emission is smaller than that of the excitation, with a value of 183 cm^{-1}. It is noteworthy that red site emission at 549.9 nm is also produced, indirectly, with green site excitation.

A decay profile recorded at 10 K for the 537.4 nm emission band is shown in Figure IV.37. An excited state decay time of 4.3 ns is obtained with a single exponential trial function and the accuracy of the fit is highlighted by the residuals presented in the top panel.
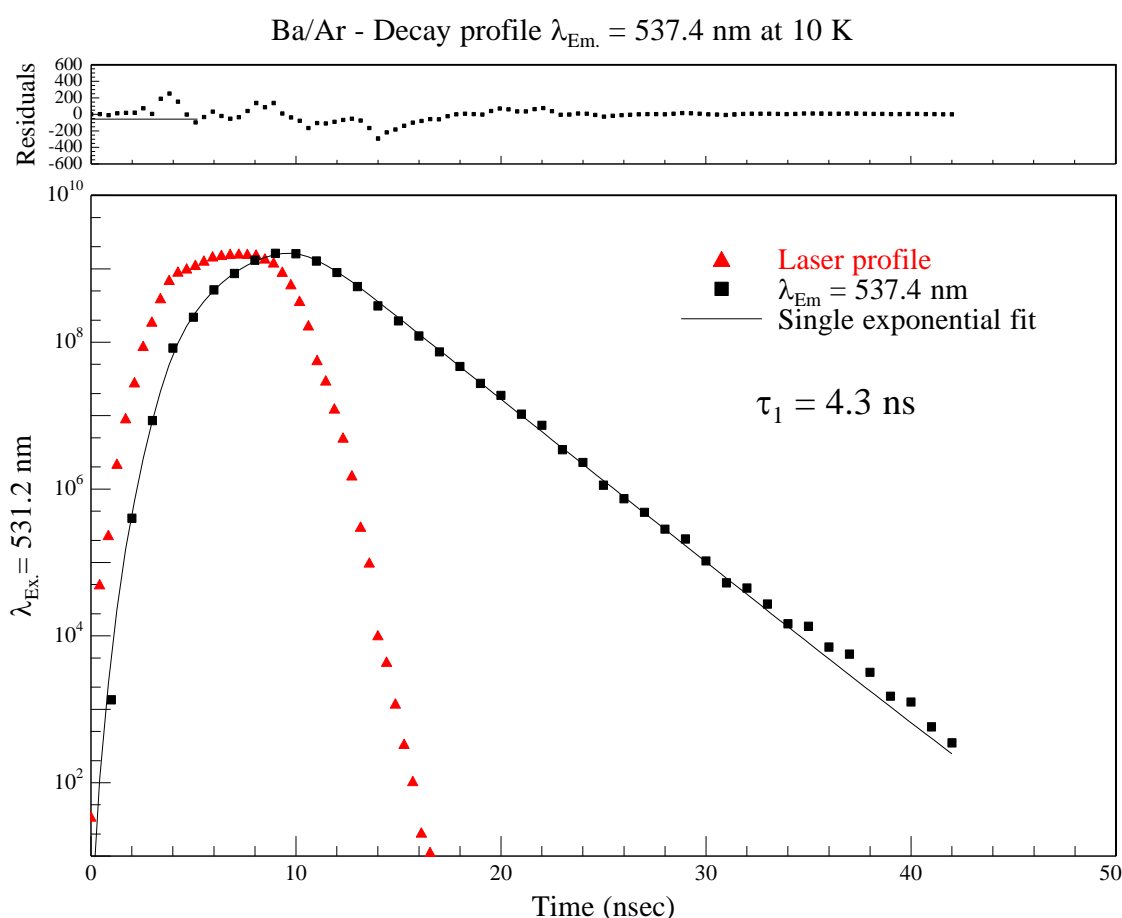

Figure IV.37 **A decay profile of the green site emission band at 537.4 nm, produced with site-specific laser excitation at 531.2 nm. An excited state decay time of 4.3 ns is obtained with a single exponential trial function.**

The temperature dependence of the green site emission was investigated to assess the contributions of non-radiative components to the overall decay, the results of which are plotted in Figure IV.38. The emission band loses intensity, broadens and becomes red-shifted with increasing temperature, as shown in the left panel. However, the extracted decay curves (right panel) show little or no change between 10 and 26 K – thus the true radiative lifetime has been identified.
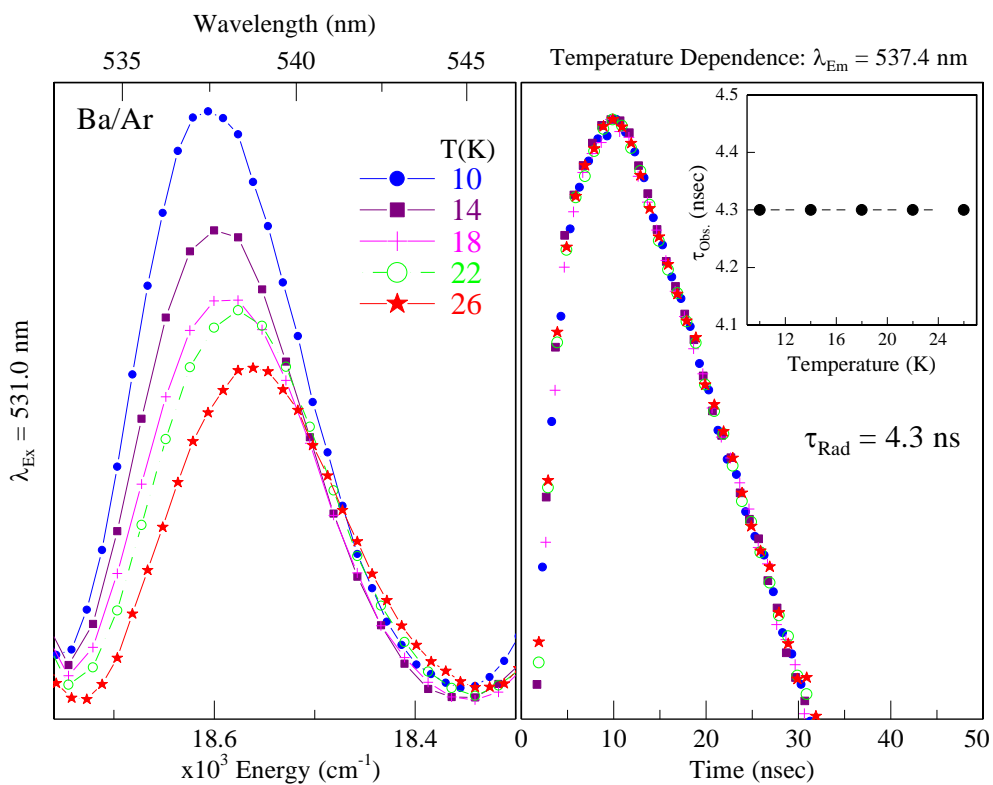
Figure IV.38 The left panel shows the temperature dependence of the green site emission band at 537.4 nm. A progressive red-shift of the band centre occurs in conjunction with a decrease in the band intensity, as the sample temperature increases from 10 – 26K. The right panel presents the temperature dependence of the corresponding decay curves. The excited state lifetime does not change between 10 and 26 K, indicating that the true radiative lifetime has been measured.

IV.5.IV Ba/Ar - Red site

The red luminescence features of Ba/Ar are presented in Figure IV.39. As mentioned earlier, the excitation profile recorded monitoring the 549.9 nm emission band is complex, generally showing several resolved features across the entire absorption region. Some of these components occur due to competitive re-absorption of the higher energy emission bands. However, given that the absorption optical density of the Ba/Ar samples presented here are low (> 0.2 at 528 nm), the re-absorbed bands are expected to be quite weak.
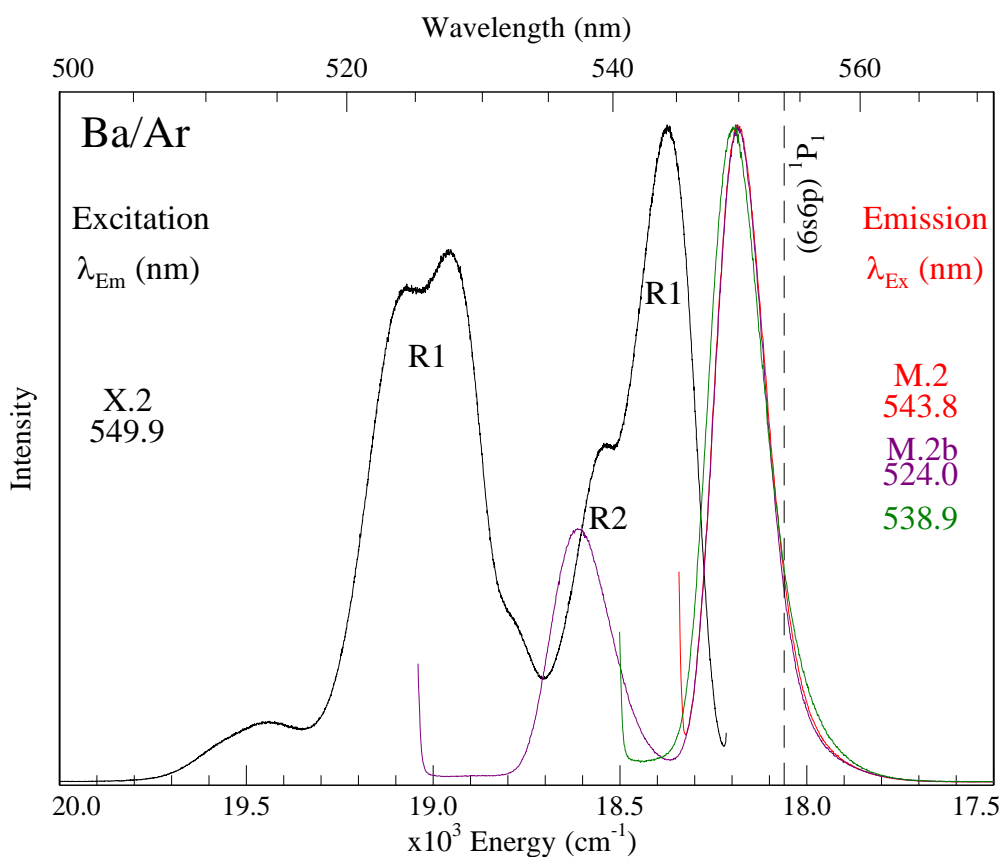

Figure IV.39   **Excitation (black) and emission (red, purple and green) spectra produced from the Ba/Ar red sites of isolation, recorded in the vicinity of the strong (6s6p) $^1P_1 \leftarrow$ (6s^2) $^1S_0$ transition of Ba. The labels R1 and R2 designate the absorption features which are tentatively associated with the two distinct sites of isolation.**

As shown in Figure IV.30, the broad band at ~513 nm corresponds to the violet site doublet and the weak shoulder at ~532 nm is due to the green site absorption band. The four remaining excitation components, namely the higher energy doublet at 523.9 and 527.7 nm (III) and the lower energy dominant band at 543.8 (II) with a blue shoulder at 538.9 nm, are proposed to be the 'real' absorption/excitation bands. The occurrence

of four components suggest that at least two matrix trapping sites contribute to the spectrum. To interpret this data, the paradigm used to explain the violet site features in all three hosts is invoked. Thus the higher energy doublet and lowest energy band are suggested to be connected to a single site of isolation of Ba in Ar, whereas the band at 538 nm represents an underlying absorption feature, associated with a distinct matrix site. Although tentative, this analysis is supported by key aspects of the recorded luminescence.

Firstly, inspection of the 2D-EE plot in Figure IV.28 reveals that the most intense excitation components obtained by monitoring the 549.9 nm emission correspond to a doublet plus singlet (2+1) structure. Moreover, analysis of this excitation trace over a number of samples shows that the intensity ratio of the peaks in the 2+1 structure is approximately constant. In contrast, the intensity of the 538 nm band can vary a good deal more. In particular, samples deposited at elevated temperatures show a marked increase in this band relative to the features of the singlet plus doublet. Finally, the emission spectra recorded by irradiation of any component of the 2+1 feature are spectrally distinct from that produced with excitation at 538 nm. Two emission traces are presented for the former in Figure IV.39, corresponding to excitation wavelengths of 524.0 (purple trace) and 543.8 nm (red trace). As can be seen, both produce an identical emission band centred at 549.9 nm displaying a fwhm of 163 cm^{-1}. In contrast, excitation at 543.8 nm (green trace) leads to an emission band centred at 549.5 nm with a larger fwhm of 176 cm^{-1}.

Based on this behaviour, the bands present in the red site excitation spectrum are tentatively assigned to two unique sites of isolation for Ba in Ar. The dominant red site shows an asymmetric splitting akin to the violet site and is designated as R1. The secondary, minor site exists as an underlying feature and is overlapped by the intense singlet band of R1. This site will be referred to as R2. A lineshape analysis was conducted on the excitation spectrum, the results of which are presented in Figure IV.60 of Appendix IV.I. The components of R1 can be fit with three Gaussians with near equal bandwidths (~148 cm^{-1}). The R2 component is accounted for with a single Gaussian displaying a bandwidth of 165 cm^{-1}.

The temporal characteristics of the red emission bands were investigated. The decays obtained with excitation at 538 and 544 nm yield identical emission lifetimes, even at elevated temperatures. It was therefore not possible to distinguish between the two sites temporally.

Ba/Ar - Decay profile $\lambda_{Em.}$ = 549.9 nm at 10 K
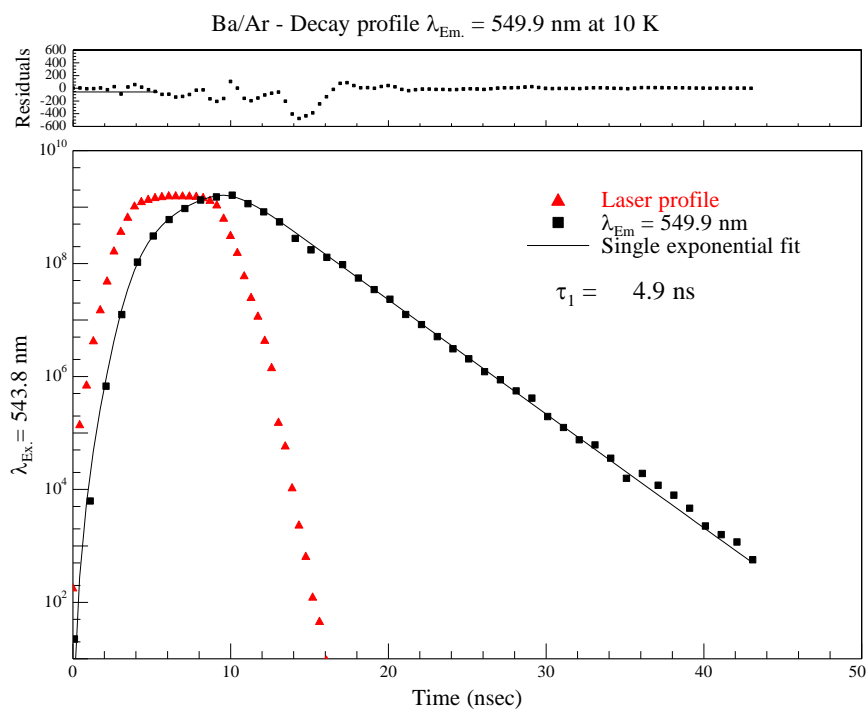
Figure IV.40   **Decay profile of the red site emission band at 549.9 nm, produced directly with site-specific laser excitation at 543.8 nm. An excited state decay time of 4.9 ns is obtained with a single exponential trial function, which included a re-convolution with the time profile of the Nd:YAG laser.**

Ba/Ar - Decay profile $\lambda_{Em.}$ = 549.9 nm at 10 K
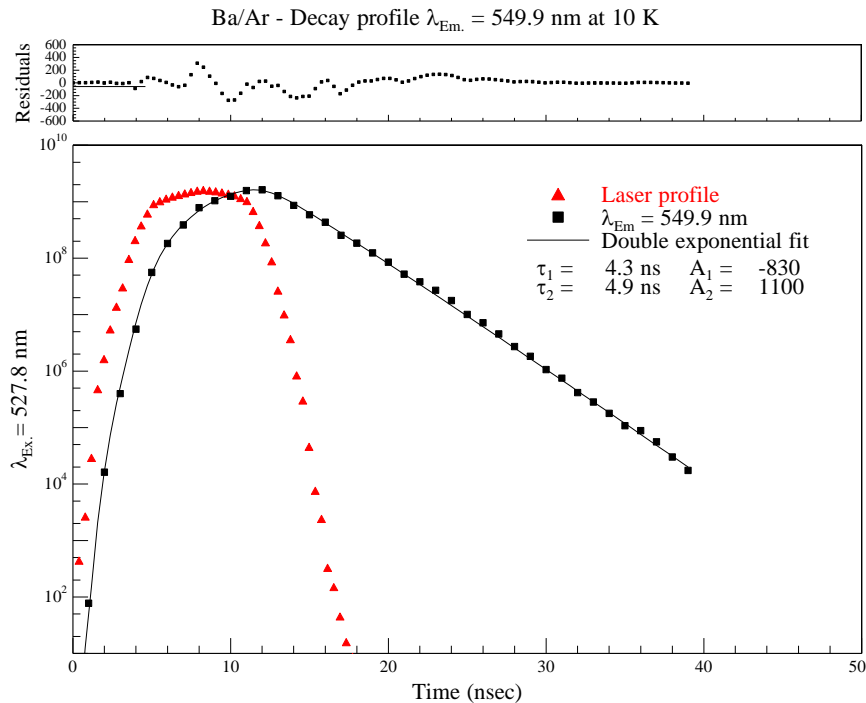
Figure IV.41   **Decay profile of the red site emission band at 549.9 nm, produced with excitation at 527.8 nm. The bulge in the centre of the decay arises due to concurrent excitation of Ba atoms in the green site of isolation. A double exponential fit is therefore required. The 4.3 ns component with a negative amplitude is a risetime feature.**

As the R1 site dominates the luminescence in this region, it is assumed that this site contributes the most to the recorded time-resolved emission spectra. The decay profiles obtained with excitation at 543.8 and 527.8 nm are presented in Figure IV.40 and Figure IV.41 respectively. Irradiation of the lowest energy band yields the simplest decay profile. As shown in Figure IV.40, a single exponential function provides a very good fit to the data, revealing a decay time of 4.9 ns. The time profile obtained with excitation at 527.8 nm is more complex and exhibits a bulge in the centre of the decay, as can be seen in Figure IV.41. This arises because the excitation wavelength used concurrently excites Ba atoms in the green site of isolation.

The greens site emission overlaps part of the red site absorption. Thus, a certain amount of the red site emission intensity comes from the re-absorbed emission of the green site. Hence a double exponential function is required to fit the decay profile. Two decay times are observed with values of 4.3 ns and 4.9 ns. The 4.9 ns component with a positive amplitude (+1100) represents the true red site emission lifetime. Whereas the shorter 4.3 ns component matches the radiative lifetime of the green site emission. The negative amplitude (-830) in this case shows that this component is a risetime. As expected, photoexcitation of the 524 nm band yields a profile with similar temporal attributes. However, a smaller risetime amplitude of -695 is observed in this case (versus a decay component with an amplitude of +1100), as the contribution of the re-absorbed green site emission is less at this excitation wavelength.

The temperature dependence of the red site emission was probed with laser excitation at 543.8 nm. The corresponding emission scans and temporal profiles are presented in the left and right panels of Figure IV.42 respectively. The red site emission of Ba/Ar exhibits no temperature dependence over the 10 – 26 K range, indicating that the radiative lifetime (4.9 ns) has been recorded.
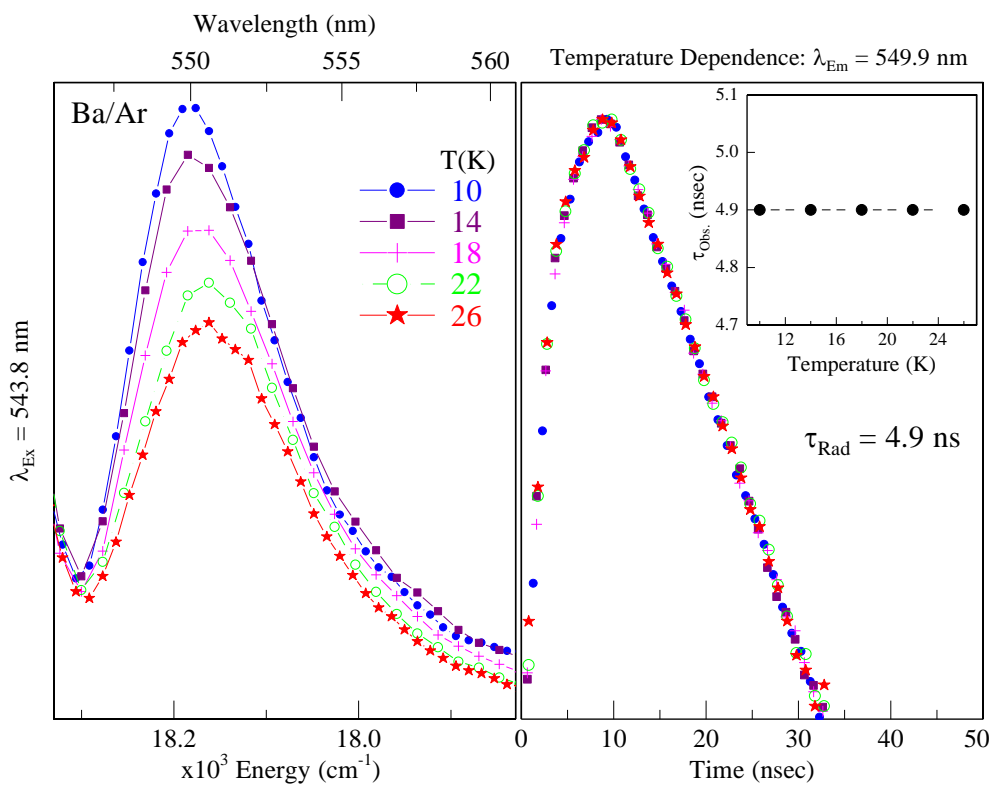
Figure IV.42   **The left panel shows the temperature dependence of the red site emission band at 549.9 nm. A progressive red-shift of the band centre occurs in conjunction with a decrease in the band intensity, as the sample temperature increases from 10 – 26K. The right panel presents the temperature dependence of the corresponding decay curves. The excited state lifetime does not change between 10 and 26 K, indicating that the true radiative lifetime has been measured.**

IV.6   Ba/RG discussion

In this section, a summary of the entire Ba/RG luminescence is presented. Firstly, the site specific excitation/absorption features identified in each RG host are connected using a simple polarizability model. Following site associations, the photophysical properties of each matrix site are collected and the trends observed across the three RG hosts are analysed. Finally, the excited state lifetimes and emission temperature dependences are compared and contrasted for each Ba/RG site of isolation.

IV.6.I   Site association

A summary of the excitation spectroscopy recorded for atomic Ba isolated in Ar, Kr and Xe is presented in Figure IV.43. The comparison shown indicates clearly that annealed Ba/Xe samples represent the simplest situation, with the occurrence of two dominant sites of isolation which were labelled as 'violet' and 'blue' in Section IV.3.
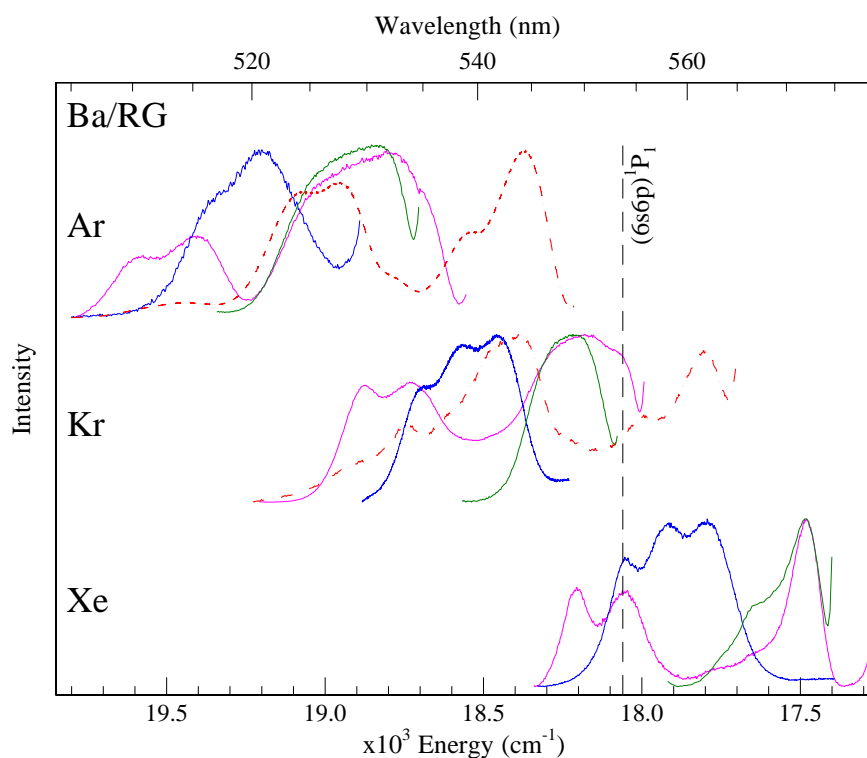

Figure IV.43 **Ba/RG site-specific excitation spectra recorded in the region of the dominant (6s6p) $^1P_1 \leftarrow$ (6s^2) $^1S_0$ transition of Ba at 10 K, following sample annealing. The spectra of Ba are complex due to the presence of numerous distinct matrix sites which overlap considerably in both emission and excitation. For clarity, some of these excitation profiles have been truncated in an attempt to remove any overlapping components. The colour of each trace represents the site of isolation. The red excitation profiles of Ar and Kr are given by dashed lines whereas solid lines are used for violet, blue and green sites.**

In addition, a minor 'green' trapping site was also identified for Ba in Xe based on the distinct emission it produces. Using the 2D-EE spectra and with a careful analysis of the unique emission bands, the excitation spectra recorded for Ba in Ar and Kr revealed features similar to those observed in Xe. Thus, in both matrices, excitation bands associated with a violet, blue and green site of isolation were observed. A fourth matrix 'red' excitation profile was also observed to be stable in Ar and unstable in Kr. Although complex, the dominant components in these excitation traces were assigned to a unique trapping site (R1) for Ba. For comparative purposes, the unstable red profile of Ba/Kr is included in the analysis.

All of the traces shown in Figure IV.43 are colour coded to match the site labelling scheme, the origin of which will now be presented. Laursen and Cartland[7] showed for Group XII metal atoms (Hg, Cd, and Zn) that the matrix shift for atomic P ← S absorptions is approximately linear when plotted against the polarizability of the RG's. This behaviour was also found for matrix-isolated atomic Na[8], Mn[4] and, more recently, atomic Eu[5]. A plot of RG polarisability versus shift from gas phase allowed association of certain site types occupied by metal atoms in the rare gas solids. For metal atoms 'trapped' in a particular site type, a linear dependence of the matrix shifts versus rare gas polarisability is expected. This model was applied to the three Ba/RG systems, the results of which are presented in Figure IV.44. The gas phase to matrix frequency shift is calculated from each of the threefold (symmetric or asymmetric) components of the blue, violet and R1 sites of isolation. As the green site excitation spectra are mostly broad and featureless, the band centres were used in lieu of resolved structure.

This analysis demonstrates a correspondence between the sites of a given 'colour' in all three hosts. For example, the dominant site in Xe, which shows a Jahn-Teller (JT) splitting, is associated with the JT band observed in Kr and the minor, partially resolved threefold split band in Ar. Thus, it is proposed that each site 'colour' represents a particular type of trapping site for atomic Ba in the rare gas solids. The details of the absorption/excitation bands unique to each site of isolation are presented in Table IV.1 for all three RG hosts. Interestingly, it is observed that the excitation components of a given site are not exactly linearly dependent on the host. For the violet, blue and green sites, the slope of the line from Ar − Kr is greater than the slope of the line from Kr − Xe. This highlights the simplicity of the polarizability model, which

does not take into account the very different interactions that occur between atomic Ba and the surrounding RG environment in the ground $^1S_0$ and excited $^1P_1$ states.
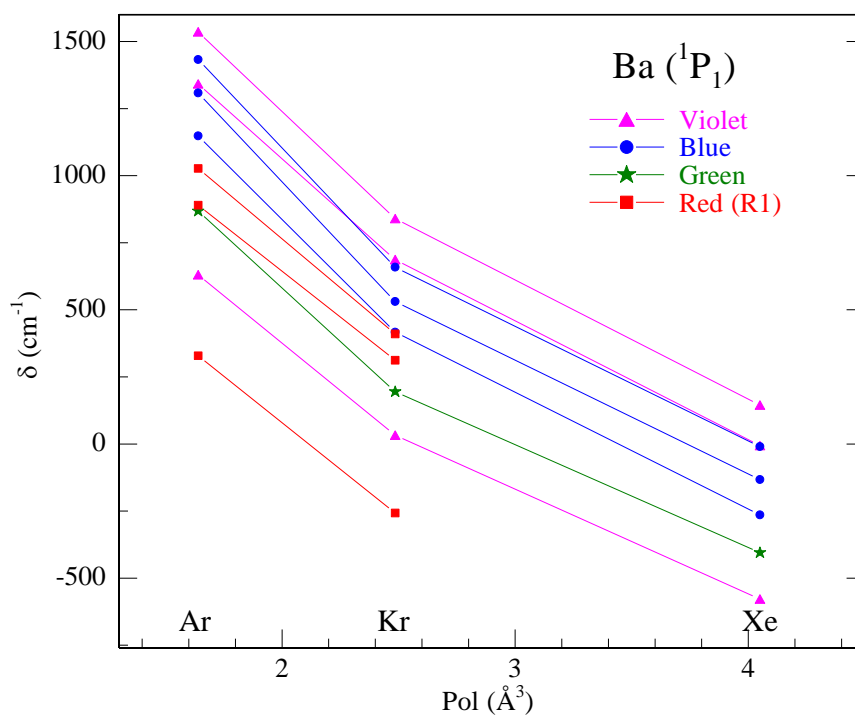

Figure IV.44   **A plot of the gas phase to Ba/RG matrix frequency shifts (δ cm^{-1}) observed for each of the components of the violet, blue, green and red sites identified for the (6s6p) $^1P_1 \leftarrow$ (6s^2) $^1S_0$ transition of atomic Ba versus the RG host polarizabilities.**

Table IV.1   **Photophysical characteristics of the Ba/RG sites of isolation as revealed by the $(6s6p)\ {}^1P_1 \leftarrow {}^1S_0\ (6s^2)$ excitation spectroscopy. δ represented the gas phase to RG matrix shift (given in units of wavenumber) calculated from the gas phase value[1] for this transition at 553.7 nm or 18060.261 cm^{-1}. *The red site in Kr was shown to be a thermally unstable site of isolation but is included to allow comparison with thermally stable red site in Ar.**

Ba/RG Site	Component	λ_{ex} (nm)	ν (cm^{-1})	δ (cm^{-1})
Ar	1	510.3	19596	1536
Violet	2	515.4	19402	1342
	3	535	18692	631
	1	513.0	19493	1433
Blue	2	516.3	19369	1308
	3	520.6	19209	1148
Green	1	528.3	18929	868
	1	523.9	19088	1027
Red	2	527.7	18950	890
	3	543.8	18389	329
Kr	1	529.1	18900	840
Violet	2	533.4	18748	687
	3	552.7	18093	33
	1	534.2	18720	659
Blue	2	537.9	18591	531
	3	541.2	18477	417
Green	1	547.8	18255	195
	1	541.4	18471	410
Red*	2	544.3	18372	312
	3	561.7	17803	-257
Xe	1	549.3	18205	145
Violet	2	553.9	18054	-6
	3	572	17483	-578
	1	554	18051	-10
Blue	2	557.8	17928	-133
	3	561.9	17797	-264
Green	1	566.4	17655	-405

IV.6.II Blue site luminescence

A summary of the Ba/RG blue site luminescence is presented in Figure IV.45. The excitation traces of Kr and Xe both show a Jahn-Teller (JT) threefold split, while the corresponding band in Ar seems to only show a resolved doublet. However, the lineshape analysis present in Figure IV.58 of Appendix IV.I reveals that a weak, higher energy band at approx. 513 nm makes up the third component of a characteristic JT pattern.
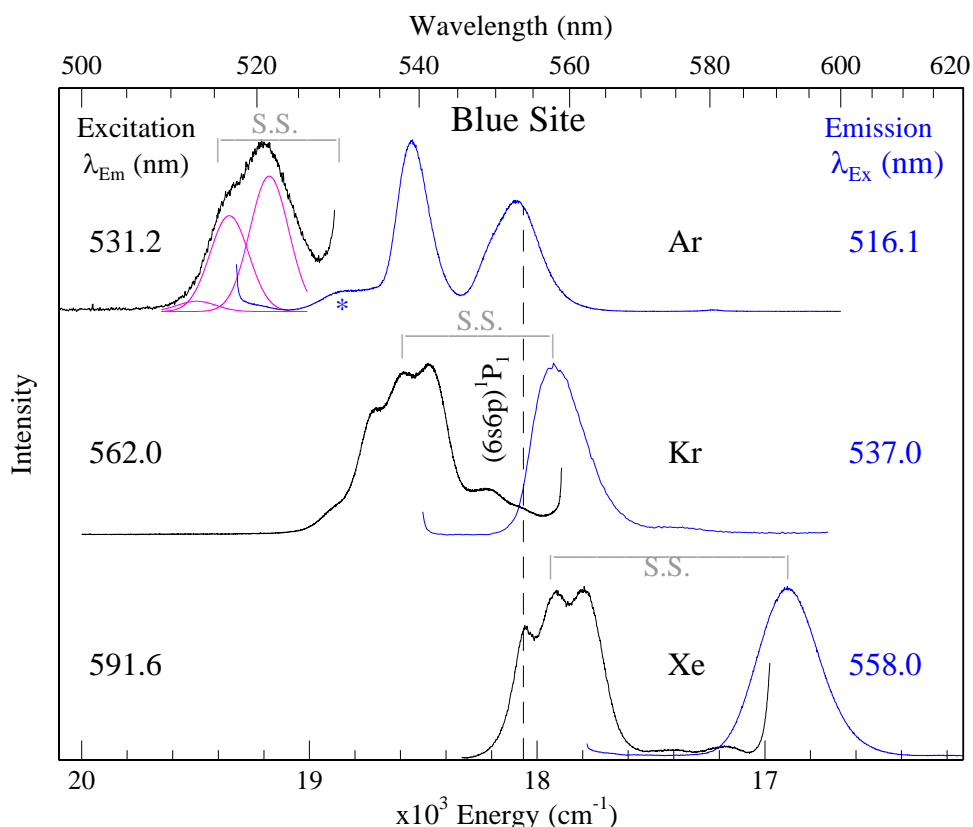

Figure IV.45　　A summary of the (6s6p) $^1P_1$ state luminescence of Ba isolated in the blue site in each RG solid. The three Gaussian curves used to fit the blue site excitation spectrum in Ar are shown by the pink solid traces. The grey horizontal lines labelled S.S. show the excitation and emission values used to calculate the blue site Stokes shifts in each host.

Based on the band splitting exhibited, the blue site of isolation must be one of high symmetry (O_h or Td), which gives rise to a dynamic Jahn-Teller distortion in the excited P state of Ba. The abundance of the blue site changes considerably depending on the host. This site is the dominant trapping environment for Ba in a Xe matrix. In contrast, blue site occupation is greatly reduced in Kr where the green and violet sites are

dominant. In Ar, this site is so weakly populated that it is difficult to detect. It seems to only form in samples deposited at higher temperatures (with a very low metal flux).

Table IV.2 **Photophysical characteristics of the Ba/RG sites of isolation as revealed by the (6s6p) $^1P_1 \rightarrow {}^1S_0$ (6s^2) emission spectroscopy. δ represented the gas phase to RG matrix shift (given in units of wavenumber) calculated from the gas phase value[1] for this transition at 553.7 nm or 18060.261 cm^{-1}. S.S. represents the Stokes shift. For the blue and green sites, this value was determined from the centre of the emission band to the centre of the excitation band. For the violet and red sites, three values are quoted which were evaluated from the centre of the emission band to each excitation component of the asymmetric threefold split. The last column, Δν, gives the full width at half maximum values for each emission band in units of wavenumber (cm^{-1}). *The spectral bandwidths of the blue site emission in Ar and the R1 site in Kr were estimated with a lineshape analysis as significant overlap with emission from other sites occurred in both cases. †Thermally unstable site of isolation.**

Ba/RG Site	λ_{ex} (nm)	λ_{em} (nm)	ν (cm^{-1})	δ (cm^{-1})	S.S. (cm^{-1})	Δν (cm^{-1})
Ar	510.3				1047	
Violet	515.4	539.1	18549	489	853	163
	535.0				142	
Blue	516.3	531.2	18825	765	543	225*
Green	528.3	537.4	18608	548	321	183
	523.9				902	
Red	527.7	549.9	18185	125	765	163
	543.8				204	
Kr	529.1				921	
Violet	533.4	556.2	17979	-81	769	129
	552.7				114	
Blue	537.9	557.9	17924	-136	666	261
Green	547.8	554.9	18021	-39	234	135
	541.4				828	
Red†	544.3	567.0	17643	-417	729	200*
	561.7				160	
Xe	549.3				907	
Violet	553.9	578.1	17298	-762	756	213
	572.0				184	
Blue	557.8	591.6	16903	-1157	1024	311
Green	566.4	577.1	17328	-732	327	202

Inspection of both Figure IV.45 and Table IV.1 shows that the expected progressive red-shift to lower energy is observed for the components of this site as one moves to a more polarisable RG host i.e. from Ar to Kr to Xe. The matrix shift is related to the strength of the short-range M-RG repulsive interaction in the excited P state and strongly depends on the size of the vacancy. For instance, the most polarizable host Xe, has the largest lattice parameter and therefore has the largest blue site radius. This leads to less confinement of the excited 6p orbital of Ba. The effects of increased host polarizability and a larger lattice vacancy contribute to yield a moderate gas-to-matrix red-shift of -133 cm^{-1} for the blue site in Xe. Contrasting this, solid Ar is the least polarizable of the three hosts and also exhibits the smallest lattice parameter. Therefore the blue site radius in Ar will be smaller than in Xe and the excited 6p orbital of Ba will be expected to experience a greater repulsive interaction. The combination of both effects yields a large gas-to-matrix blue-shift of +1308 cm^{-1} (measured from the band centre) for the blue site in Ar.

The photophysical characteristics of the site-specific fluorescence bands in the three Ba/RG systems are collected in Table IV.2. Clearly the magnitude of the blue site Stokes shift, computed from the central component of the JT band in each host, increases in going from Ar – Xe, with the value in heaviest host almost twice that measured for the lightest. In addition, the emission bandwidths (fwhm) are also shown to increase from Ar – Xe. Both of these effects indicate that the minimum of the excited Ba(^{1}P$_1$)/Xe potential energy surface is displaced, with respect to minimum of the ground state, to a greater extent when compared to Ar and Kr.

IV.6.III Green site luminescence

A summary of the luminescence specific to the green site of isolation is provided in Figure IV.46. The preference for the occupancy of atomic Ba in the green site in Ar, Kr and Xe matrices is the opposite to that of the blue site. In Ar, the green site is the dominant trapping environment for Ba. In Kr, this dominance is matched by both the violet and blue sites of isolation. In Xe, the absorption of the green site is much weaker.
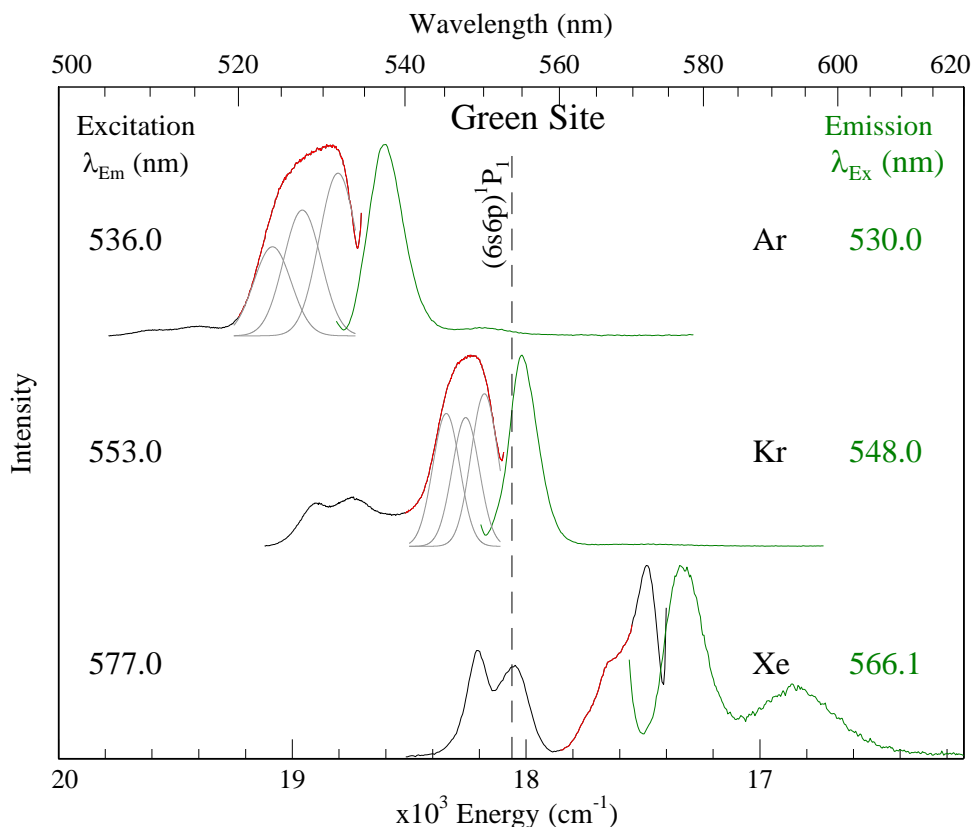

Figure IV.46   **A summary of the (6s6p) $^1P_1$ state luminescence of Ba isolated in the green site of the RG solids. The three Gaussian curves used to fit the green site excitation band in Ar and Kr are shown by the solid grey traces. For clarity, the portion of each excitation band associated with the green site of isolation is highlighted in red. Each RG matrix has been annealed to 34, 45 and 60 K for Ar, Kr and Xe respectively.**

Examination of the green site profiles (highlighted in red) in Ar and Kr reveals, in both cases, an asymmetric bandshape that tails to higher energy with decreasing intensity. As no obvious splitting patterns were observed on these bands, it is tentatively proposed that the site of occupation is isotropic (or at least not far from it), perhaps one of high (cubic) symmetry given the nature of the ground state Ba atom. Three Gaussian curves of equal width (shown in grey) were required to fit the profiles

in Ar and Kr. It may be that these bands are broadened by the dynamic Jahn-Teller effect, but the composite peaks are unresolved. If this is the case, then the green site of isolation must exhibit a larger radius than the blue site in each solid. Inspection of Table IV.1 reveals that the gas-to-matrix blue-shifts for the green site in Ar and Kr are much less than those of the blue site. In addition, the partially resolved band in Xe is more red-shifted than the corresponding blue site in this host. Thus, the confinement of the excited 6p orbitals must be less significant for Ba isolated in the green site. The matrix shifts observed therefore depend more on the RG polarizability, leading to a red-shift of the band centre with respect to absorptions of the blue site.

Inspection of Table IV.2 shows that the calculated Stokes shifts for this site are less than those recorded of the blue site in each RG host. Moreover, the magnitude of the shift does not systematically increase across the three hosts, with values of 321, 234 and 327 cm^{-1} measured for Ar, Kr and Xe – greatly contrasting the trend observed for the blue site. The green site in Kr seems to show the smallest Stokes shift and emission bandwidth out of the three systems. Overall, the emission bandwidths are noticeably narrower than those of the blue. The combination of small Stokes shifts and narrow emission bandwidths indicates that the equilibrium configuration of the Ba/green site centre is nearly the same in the ground and excited state. Thus a 'vertical' transition in absorption prepares the excited Ba atom in a Frank-Condon configuration which is relatively close to the minimum of excited state potential energy surface.

IV.6.IV Violet site luminescence

A summary of the Ba/RG violet site luminescence is provided in Figure IV.47. As with the blue and green sites, the violet excitation and emission bands all display a progressive red-shift with increasing RG polarizability. However, the splitting patterns observed on the violet site excitation profile are in stark contrast to the familiar JT pattern which was observed for the blue site.
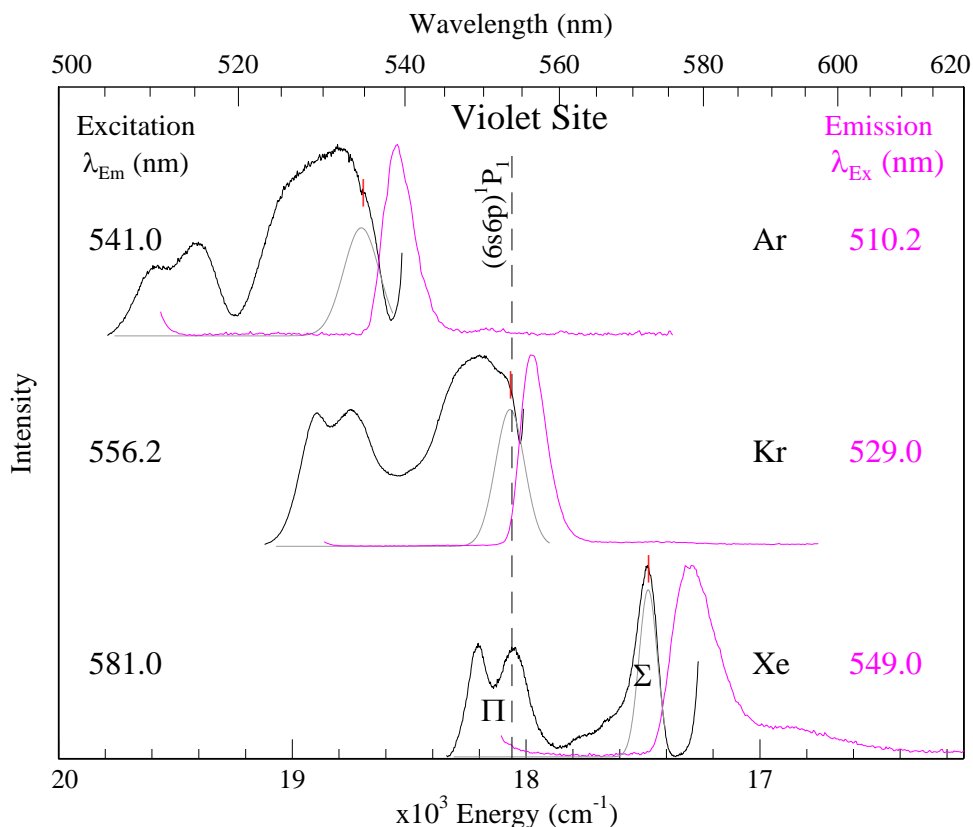

Figure IV.47   **A summary of the (6s6p) $^1P_1$ state luminescence of Ba isolated in the violet site in each RG solid. The Gaussian peaks (shown in grey) indicate the position of the lowest energy component of the asymmetric threefold split. Although the position of this band is obvious in Xe, the corresponding components in Ar and Kr are obscured by an intense green site absorption.**

The excitation profiles of the Ba/RG violet sites display an asymmetric threefold (2+1) splitting pattern, with a higher energy doublet and lower energy singlet. For Ba/Xe, each composite peak of this structure is clearly identifiable. For Ar and Kr, the higher energy doublets are also quite evident but the lowest energy band is strongly overlapped by the green site absorption spectrum. Examination of Figure IV.47 and Table IV.1 shows that this site of isolation presents two very different interactions for the Ba atom excited into its 6s6p configuration.   The splitting between the doublet and singlet

feature is substantial in each solid. Values of 794, 711 and 633 cm^{-1} are determined (from the lowest energy singlet to the centre of the doublet) in Ar, Kr and Xe respectively.

This data may be interpreted by considering the orientation of the $6p_x$, $6p_y$ and $6p_z$ orbitals of the excited Ba atom in the environment of the violet site. The interaction is anisotropic, such that two of the p orbitals (p_x and p_y) are pointing towards one or more RG atoms (Π configuration) and therefore experience a greater repulsion. It is of note that the interaction of these two orbitals is slightly different giving rise to a non-degenerate Π doublet in absorption. Contrasting this, the remaining p_z orbital, must be directed towards mostly empty space and experiences a much smaller repulsive interaction with the host atoms (Σ configuration). Thus the higher energy doublet corresponds to the more repulsive Π configuration and the lower energy singlet represents the Σ configuration. Such a Σ - Π splitting was also observed for the excited Ba(^{1}P) atom on the surface of an Ar cluster[9]. However in this case, the Π doublet was lower in energy than the Σ singlet. The $6p_z$ orbital of Ba was directed towards the Ar cluster and $6p_x$ and $6p_y$ orbitals were aligned parallel to the cluster surface, pointing towards empty space. The asymmetric threefold (2+1) splitting pattern observed for Ba in the RG solids suggests that the violet site of isolation corresponds to a cylindrical void.

In all three hosts, a non-radiative relaxation must occur to the lowest energy Σ configuration, as only a single emission band is observed. The details of the Stokes shifts computed from the violet site Π and Σ bands in each host are presented in Table IV.2. Examination of these values demonstrates that a much larger Stokes shift occurs with excitation of the Π bands – more than eight times the value of the Σ Stokes shift in the case of Kr. Thus, following excitation of an electron into one of the Π orbitals, a re-orientation occurs along the excited state surface to minimise the energy. The violet site excited state lifetime measurements conducted in Xe show the same nanosecond decay profile, regardless of the configuration excited. This signifies that the re-orientation must occur on a sub-nanosecond time scale.

IV.6.V Red site luminescence

A summary of the red site luminescence features in Ar and Kr is presented in Figure IV.48 and the photophysical characteristics are collected in Table IV.1 and Table IV.2. A detailed analysis, which included excited state lifetime measurements and the temperature dependence of these emissions bands was presented for Ba/Ar. However the same extensive study could not be provided for the equivalent bands in Kr owing to their thermal instability. Moreover, numerous distinct lower energy bands complicate the 2D-EE spectrum (Figure IV.16) of a Kr sample annealed to 38 K – indicating a multitude of partially stable sites exist. For comparative purposes the excitation profile of the brightest emission in this region is presented in the bottom of Figure IV.48.
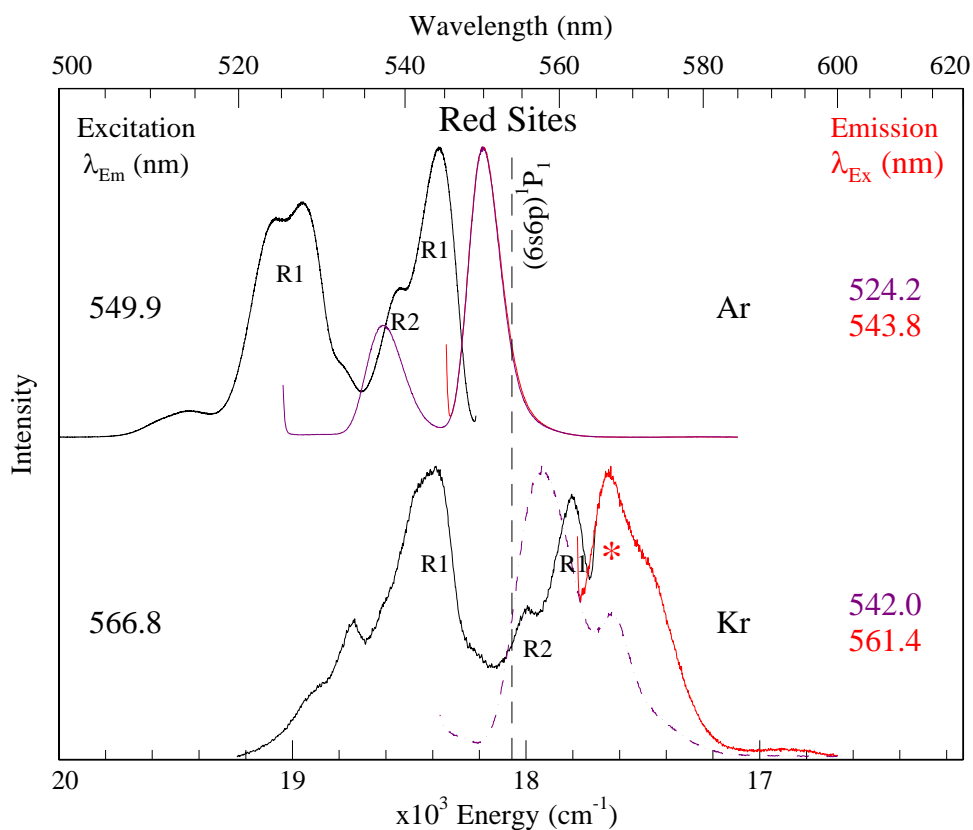

Figure IV.48   **A summary of the (6s6p) $^1P_1$ state luminescence of Ba isolated in the red site in solid Ar and Kr samples which were annealed to 28 and 38 K respectively. The red site in Kr was shown to be thermally unstable with annealing to 45 K. The same site in Ar can be removed by annealing to 34 K – with a substantial loss of the sample.**

The red site excitation profiles are proposed to be made of contributions from at least two distinct matrix sites, which are designated R1 and R2. Analysis of the

luminescence in Ar suggested that the primary contributor is a trapping site (R1) which gives rise to a 'doublet plus singlet' splitting pattern, similar to the violet site. A comparison with the thermally unstable red site profile in Kr reveals the same general features. The equivalent of the Ar higher energy doublet centred at ~543 nm is not as well resolved but does exhibit a dominant peak at 544.3 nm and a shoulder at 541.4 nm. The band at 555.8 in Kr is assigned as a secondary, minor red site (R2) based on the distinct emission produced at this excitation wavelength, as can be seen in the 2D-EE spectrum presented in Figure IV.16.

On the basis of this interpretation, the primary R1 site of isolation gives rise to two distinct interactions for the Ba atom excited into the (6s6p) $^1P_1$ state. A large splitting between the doublet and singlet feature is observed in Ar and Kr. Values of 699 and 619 cm^{-1} are determined (from the lowest energy singlet to the centre of the doublet) in Ar and Kr respectively – noticeably smaller than those obtained for the violet site. The splitting may be explained by considering the orientation of the $6p_x$, $6p_y$ and $6p_z$ orbitals of the excited Ba atom with respect to the anisotropic configuration of the surrounding RG atoms. Similar to the violet site, the higher energy doublet corresponds to the more repulsive Π configuration (p_x and p_y) and the lower energy singlet represents the Σ configuration (p_z). It is interesting to note that the extent of splitting on the Π doublet is less than that of the violet site. Combining this characteristic with a smaller overall singlet to doublet energy gap suggests a weaker interaction of the excited Ba atom at this site in comparison to the violet site. A more voluminous cylindrical site could therefore be proposed for R1. As the features of R1 are connected to a single emission band in Ar and Kr, a relaxation to the lowest energy excited (6s6p) $^1P_1$ state surface must occur in both hosts.

IV.6.VI Temporal analysis

Time-resolved emission spectra (TRES) were recorded for each Ba/RG site of isolation and the decay profiles extracted were in most cases well fitted with single exponential functions, allowing the excited state lifetimes to be determined. The observed values (τ_{obs}) are collected in Table IV.3. With the exception of the blue site in Ba/Xe, all measured values were found to be invariant over a temperature range of at least 3 K, indicating that the radiative lifetime had been identified.
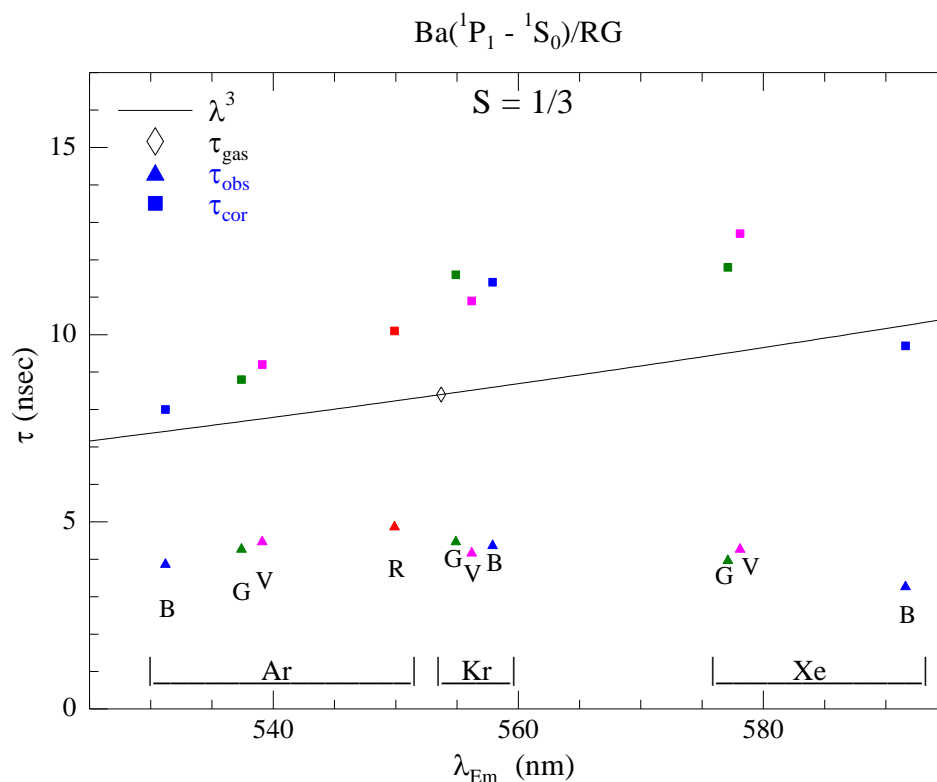

Figure IV.49 **A comparison of the lifetimes record at 10 K for the thermally stable Ba: (6s6p) $^1P_1 \rightarrow {}^1S_0$ (6s^2) emission features in Ar, Kr and Xe and a λ^3 extrapolation of the gas phase lifetime[1] for this transition of atomic Ba. The uncorrected lifetime values are given by filled triangles whereas the values corrected for the effective field of the host are denoted by the filled squares.**

The measured lifetime values are plotted in Figure IV.49 along with a λ^3 extrapolation of the gas phase[1] lifetime of 8.4 ns. This extrapolation is based on the relationship[10] between the Einstein A coefficient for the emission decay rate $A_{m,n}$ and the radiative lifetime of a level m (τ_m). It is given by Equation IV.1:

$$A_{m,n} = \left(\frac{64\pi^4}{3h\lambda^3}\right)\mu_{m,n}^2 = \frac{1}{\tau_m} \qquad \text{Eq. (IV.1)}$$

As can be seen, the directly observed matrix values (solid triangles) are all less than the gas phase extrapolation. However, in a comparison with the gas phase values, a correction must be made for the effective field of the solid, which leads to an enhancement of electronic transitions and a shortening of the observed lifetime values.

A correction[11,12] for this effect can be made using Equation IV.2. The formula is a function of the index of refraction[c], n, of the rare gas host and a 'shape' parameter, s. The latter is a depolarisation factor related to the symmetry of the site accommodating the guest atom.

$$\tau_{cor} = \tau_{obs} n \left[s(n^2 - 1) + 1 \right]^2 \qquad \text{Eq. (IV.2)}$$

For an isotropic, spherical cavity $s = 1/3$. However, this value may not be appropriate for all trapping environments of Ba in the solid RG's, i.e. the violet and red sites. The asymmetric threefold splits observed for these sites infers that the RG site accommodating the large Ba atom is anisotropic. As a test, a number of values for s were used to compute the effective field correction based on a few cavity shapes, as described by Shibuya[12]. For instance, transitions whose moments are considered to be in the longitudinal or transverse direction of a long cylindrical cavity yield values of s = 0 and ½ respectively.

Table IV.3 A summary of the observed and corrected excited state lifetimes for each site of isolation in all three RG systems. The effective field correction was made with Equation IV.2. *The decay time obtained for the blue site in Ar is only tentatively assigned as the radiative lifetime.

RG	Site	τ_{obs} (ns)	τ_{rad}?	τ_{cor} (ns): S= 0	τ_{cor} (ns): S= 1/3	τ_{cor} (ns): S= 1/2	τ_{cor} (ns): S= 1
Ar	Violet	4.5	✓	5.9	9.2	11.2	18.0
	Blue	3.9*	✓*	5.1	8.0	9.7	15.6
	Green	4.3	✓	5.7	8.8	10.7	17.2
	Red	4.9	✓	6.5	10.1	12.2	19.6
Kr	Violet	4.2	✓	6.0	10.9	13.8	24.9
	Blue	4.4	✓	6.3	11.4	14.5	26.1
	Green	4.5	✓	6.4	11.6	14.8	26.7
Xe	Violet	4.3	✓	6.4	12.7	16.6	31.6
	Blue	3.3	✗	4.9	9.7	12.7	24.2
	Green	4.0	✓	6.0	11.8	15.4	29.4

[c] Refractive index values[13] of 1.32, 1.43 and 1.49 are used for Ar, Kr and Xe respectively.

Inspection of the corrected lifetime values provided in Table IV.3 shows that the values closest to the gas phase λ^3 extrapolation (Figure IV.49) are those computed with the parameter, $s = 1/3$. However, even these show a deviation and are all systematically longer than the extrapolation, with the exception of the blue site in Ba/Xe. This model, using just the index of refraction of the solid, is probably too simplistic to take into account the various complex interactions that occur for an excited Ba atom at a given RG site and the effects such an interaction has on the oscillator strength of the transition involved. Nonetheless, short nanosecond decay times allows confident assignment of the observed Ba/RG emission bands to the $(6s6p)\ ^1P_1 \rightarrow\ ^1S_0$ $(6s^2)$ resonance fluorescence of atomic Ba.

IV.6.VII Temperature dependence

Time-integrated intensity scans and time-resolved decay profiles were recorded for each Ba/RG site-specific emission band over a range of temperatures. This was done to investigate the possibility of non-radiative relaxation pathways competing with the radiative $(6s6p)\ ^1P_1 \rightarrow\ ^1S_0\ (6s^2)$ fluorescence of Ba at a given site. Most Ba/RG emission bands show a decrease in the integrated area at higher temperatures. However, absorption and emission scans recorded back at 10 K indicate that bleaching and/or site interconversion results in a loss of signal – even with low intensity laser or lamp irradiation. Therefore two effects can lead to a decrease in the integrated area of a band over a given temperature range. However the time-resolved scans can provide a distinction, as bleaching and site interconversion should not affect the radiative lifetime of an emission band.

Of the three systems studied, the decay profiles and emission bands of Ba/Xe displayed the greatest temperature dependence. Examination of Figure IV.49 reveals that the Ba/Xe blue site lifetime is the only value lower than the gas phase λ^3 extrapolation. Even in the small 10 – 17 K range shown in Figure IV.8, the observed lifetime shortens dramatically from 3.3 – 1.8 ns. Therefore, the radiative lifetime of the blue site of isolation was not obtained at 10 K - the lowest temperature achievable in the current experimental set-up. The integrated area of the emission is also vastly reduced and cannot be accounted for by bleaching or site interconversion alone. A similar effect was observed for the green site of isolation, however the lifetime (4.0 ns) obtained at 10 K only began to shorten at temperatures above 13 K. The lifetime of the

violet site in Xe was observed as 4.3 ns at 10 K and did not shorten until temperatures of 24 K or greater were attained at the sample window. Thus the true radiative lifetimes were measured for the green and violet sites in Xe.
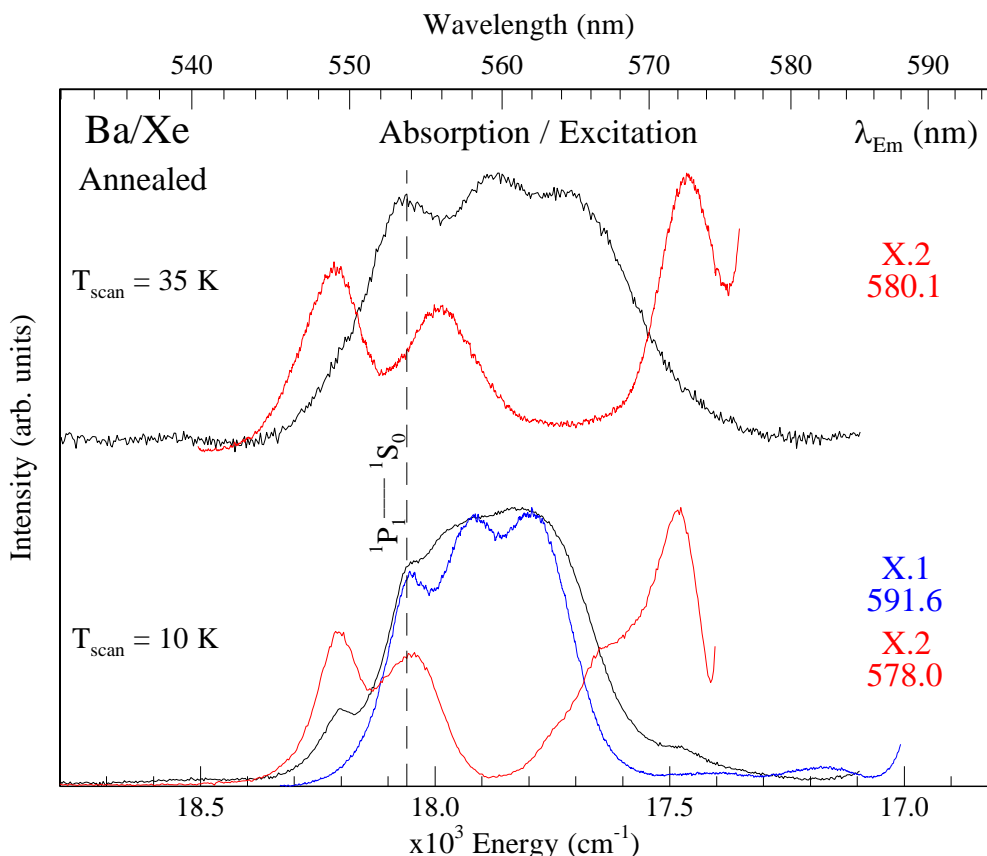

Figure IV.50   **A comparison of the absorption (black) and excitation (coloured) bands of Ba/Xe recorded at 10 K (lower traces) versus 35 K (upper traces). The blue site JT band is notably absent at 35 K in excitation as its emission intensity is all but vanished at this temperature. Contrasting this, the violet site still retains a good deal of intensity and is characterised by a 2+1 splitting pattern. All of the excitation/absorption bands are significantly broader at 35 K.**

    Figure IV.50 presents a comparison of the Ba/Xe absorption and excitation scans (X.1 and X.2 of Figure IV.4) recorded at 10 and 35 K. A striking difference between the two panels is the absence of the blue and green site excitation bands at 35 K. Indeed, the emission bands associated with these sites have all but vanished at this temperature. However the blue site excitation profile at 35 K can be obtained from absorption measurements, as shown by the black trace in the top panel of Figure IV.50. In contrast, the violet site emission band at 578.1 nm still exhibits significant intensity at 35 K, although the maximum has red-shifted to 580.1 nm. The corresponding excitation spectrum recorded at 35 K is simpler than its 10 K counterpart and exhibits

a clear 2+1 structure. It is noteworthy, that a lineshape analysis conducted on the violet site scan recorded at 35 K shows that corresponding peak widths are more equal and considerably broader than for the 10 K scan, displaying bandwidths of 143, 168 (doublet) and 146 cm^{-1} (singlet).

Thus it appears that a non-radiative relaxation process is quenching the fluorescence of Ba isolated in solid Xe. A qualitative explanation for this effect may come from the laser pump-probe investigation of the collisional deactivation of Ba (6s6p) $^1P_1$ by the rare gases (He – Xe), conducted by Breckenridge[14] *et al*. In this work the authors showed that, out of the seven possible lower lying accessible states of Ba (^3P_J, $^1D_2$ and ^3D_J), the (6s6p) $^3P_2$ state is exclusively produced by collisional deactivation of the excited (6s6p) $^1P_1$ Ba atom with a RG atom. This effect was attributed to a crossing between the attractive Ba-RG $^1\Pi$ state potential energy curve (PEC) arising from the (6s6p) $^1P_1$ atomic asymptote with the repulsive Ba-RG $^3\Sigma$ curve originating from the (6s6p) $^3P_2$ asymptote. The recent *ab initio* (configuration interaction using pseudopotentials) PECs for Ba-Xe, calculated by Abdessalem[15] and co-workers, have attempted to explain these experimental results and demonstrate a crossing between these two curves. Thus it is proposed that the non-radiative relaxation process observed for Ba/Xe matrices corresponds also to a $^1P_1 \rightarrow {}^3P_2$ inter-system crossing (ISC), as observed in the gas phase.

In order for the $^1P_1 \rightarrow {}^3P_2$ transition to be efficient, the crossing must occur below the dissociation limit of the Ba-RG $^1\Pi$ state and in the energy range accessible in a 'vertical' transition from the ground state[16]. Thus, the efficiency of such a process would depend on the interaction of the ground and excited Ba atom with the surrounding Xe environment. A qualitative comparison of the excited state PECs is shown for Ba-Xe and Ba-Ar in Figure IV.51. In contrast to Ba-Ar, the Ba-Xe $^3\Sigma$ curve crosses the bound region of the $^1\Pi$ curve. The probability of ISC is therefore greater for Xe than for Ar (and Kr). This occurs because of the external heavy atom effect – the Ba-RG $^1\Pi$ states become more bound and the $^3\Sigma$ states become more repulsive with increasing host polarizability. Extension of this analysis to Ba-RG matrices may explain why this process is so efficient in solid Xe, when compared to Ar and Kr.

It appears that the site of isolation also affects the efficiency of ISC. For the blue, green and violet sites in Xe, the activation temperatures are $\leq$ 10 K, > 13 K and > 24 K respectively. The increased efficiency of the $^1P_1 \rightarrow {}^3P_2$ transition at the blue site

is probably related to the size of the vacancy. Modelling of the Ba/Xe sites of isolation, employing accurate 1:1 Ba-Xe potential energy curves, would be required to fully understand the role the site of isolation plays in this regard.
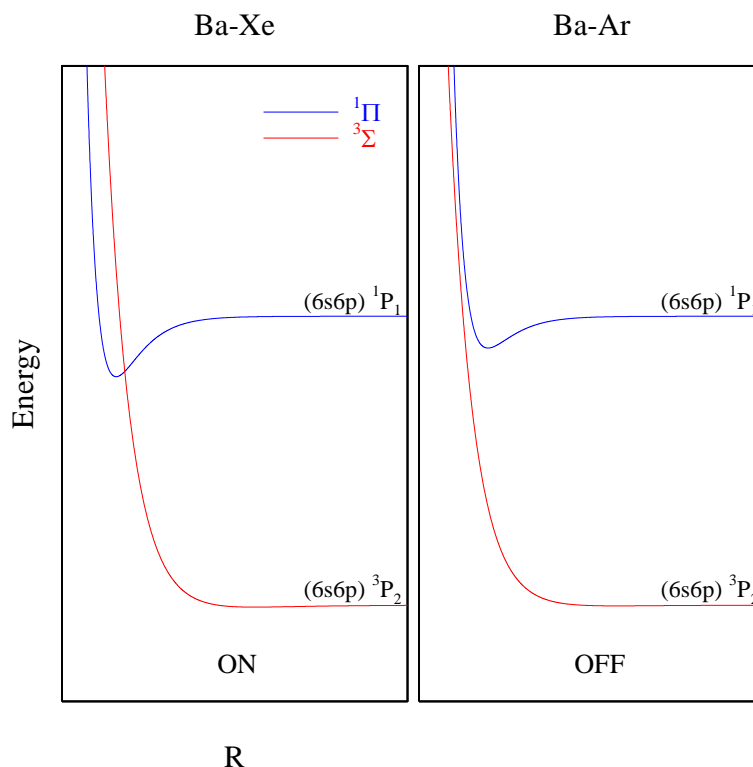

Figure IV.51 **A schematic of the Ba-RG (RG = Ar and Xe) excited state potential energy curves, which are represented by Morse functions. For Ba/Xe, the $^3\Sigma$ curve crosses the bound region of the $^1\Pi$ giving rise to efficient $^1P_1 \rightarrow {}^3P_2$ ISC. The position of this curve crossing can effectively act as a 'switch' for ISC.**

Scans recorded out to 850 nm did not reveal the presence of any additional bands for Ba/Xe emission at elevated temperatures. Thus, emission is not observed from any of the ^3P_J states which occur in the gas phase[1] between 739.9 and 815.3 nm. This indicates that further relaxation (either radiative or non-radiative) occurs to one of the lower lying potential energy curves which correlate to the $^1D_2$ and ^3D_J atomic asymptotes. If this relaxation occurs, it is possible that long-lived emission would be observed from the meta-stable $^3D_1$ level of Ba. This level occurs in the near-IR spectral region at 1107 nm, which is outside the range of our current detection system.

IV.7 Conclusions

This chapter has presented a detailed analysis of the (6s6p) $^1P_1 \rightarrow$ (6s^2) $^1S_0$ luminescence of Ba isolated in the RG solids – Ar, Kr and Xe. Based on the absorption data, it was proposed in Chapter III that three thermally stable sites of isolation exist for Ba in solid Ar and Kr and at least two sites occur in Xe. This analysis assumed a Jahn-Teller threefold split for each matrix site, as was the case for many of the other spherically symmetric M/RG systems studied by the Maynooth Group[4,5,8]. The 2D-EE spectra and excitation slices presented in this chapter reveal that the site occupancy of Ba in the RG solids is richer. Three thermally stable sites are identified in Kr and Xe and five sites exist in Ar. The revised details of the Ba/RG site-specific absorption/excitation features are collected in Table IV.1. The excitation spectra recorded display a variety of patterns, ranging from the classic Jahn-Teller threefold split to asymmetric threefold (2+1) patterns and broad, unstructured bands. Thus, experimental evidence strongly suggests that the trapping of Ba atoms in the solid RG's occurs in both cubo-octahedral, crystalline sites on one hand and in non-crystalline sites on the other.

Monte Carlo simulations conducted on Na atoms in a solid Ar[17] showed that matrix sites possessing a strong permanent axial asymmetry, such as a cylindrical vacancy, yielded a widely split 'doublet plus singlet' absorption line shape. The violet and R1 trapping sites, which give rise to the 2+1 splitting of the excited P state of Ba, must be characterised by a lower symmetry. Recent molecular dynamics simulations, conducted by Gervais *et al*[18] of the alkali atoms embedded in Ar may offer insight into such vacancies. The study revealed that the 'red' absorption bands of large atoms such as K, arise from the occupation of a number of distinct grain boundary (GB) sites in Ar. Indeed these sites were shown to be more favourable than larger vacancies in the bulk solid. The authors report that more compact GB cavities with reduced dimensionality systematically exhibit one or more peaks shifted towards higher energy. It is plausible that such a vacancy could re-produce the excitation/absorption patterns intrinsic to the occupation of a Ba atom in the violet or R1 sites. On the other hand, larger GB cavities can produce broad unstructured bands and triplet structures (not arising from a JT effect) – which could be correlated to the R2 matrix site and indeed the green site.

However, large vacancies at GB sites are known[19,20] to be quite sensitive to matrix annealing. This behaviour closely matches the relatively low annealing threshold observed for the red (R1 and R2) site features in Ar and Kr but conflicts with the high stability of the green and violet sites in all three hosts. Moreover, based on the observed matrix blue-shifts, the green and violet site cavities are expected to be smaller than those of the red site. It is therefore proposed that the green and violet sites of isolation occur in small GB sites or within the bulk crystal itself and the red excitation features (both R1 and R2) correspond to the isolation of Ba in distinct, large GB sites. In Chapter VI, the luminescence (excitation spectra) of the Sr/RG systems will be compared and contrasted with that of the Ba/RG systems. Ground state pair potentials (CCSD(T) or Tang-Toennies) will be used to provide further insight into the site occupancy of these two large metal atoms.

Finally, the temperature dependence of the excited state lifetimes was found to depend, primarily on the RG host, but also on the site of isolation. For Ba/Xe, a shortening of the site-specific emission lifetimes at elevated temperatures was attributed a $^1P_1 \rightarrow {}^3P_2$ inter-system crossing. This effect was most pronounced for the blue site of isolation, where the radiative lifetime was not identified, even at 10 K. In contrast, changes in the decay profiles were not observed in Ar and Kr over the range of temperatures assessed. The efficiency of ISC in solid Xe is proposed to arise from the external heavy atom effect[16,21].

References

1   A. Kramida, Y. Ralchenko, J. Reader, and NIST ASD Team. NIST Atomic Spectra Database (ver. 5.2). Available at: http://physics.nist.gov/asd [2015, October]. National Institute of Standards and Technology, Gaithersburg, MD.

2   L. Balling, and J. Wright, J. Chem. Phys. **83**, 2614 (1985).

3   J. Rose, D. Smith, B. E. Williamson, P. N. Schatz, and M. C. M. O'Brien, The Journal of Physical Chemistry **90**, 2608 (1986).

4   M. A. Collier, and J. G. McCaffrey, J. Chem. Phys. **122**, 54503 (2005).

5   O. Byrne, and J. G. McCaffrey, J. Chem. Phys. **134**, 124501 (2011).

6   E. X. O. C. n *et al.*, Phys. Rev. A **91**, 022505 (2015).

7   S. L. Laursen, and H. E. Cartland, J. Chem. Phys. **95**, 4751 (1991).

8   M. Ryan, M. Collier, P. d. Pujo, C. Crépin, and J. G. McCaffrey, J. Phys. Chem. A **114**, 3011 (2009).

9   J. Visticot *et al.*, J. Chem. Phys. **100**, 158 (1994).

10   K. Renk, in *Basics of Laser Physics* (Springer Berlin Heidelberg, 2012), pp. 83.

11   R. L. Fulton, J. Chem. Phys. **61**, 4141 (1974).

12   T. i. Shibuya, J. Chem. Phys. **78**, 5175 (1983).

13   *The refractive indices of Ar, Kr and Xe are 1.29, 1.28 and 1.49 recorded at 60K and λ = 488 nm from H. J. Jodl, Solid State Aspects of Matrices in The Chemistry and Physics of Matrix-Isolated Species. (North-Holland, 1989); The index of refraction used for solid Ar at 233 nm is 1.32 K at 6 K, that of Kr is 1.428 at 241 nm at 12 K. (P.Gurtler, unpublised results, 1996).*

14   W. H. Breckenridge, and C. N. Merrow, J. Chem. Phys. **88**, 2329 (1988).

15   K. Abdessalem, L. Mejrissi, N. Issaoui, B. Oujia, and F. X. Gadea, J. Phys. Chem. A **117**, 8925 (2013).

16   C. Crepin-Gilbert, and A. Tramer, Int. Rev. Phys. Chem. **18**, 485 (1999).

17   J. A. Boatz, and M. E. Fajardo, J. Chem. Phys. **101**, 3472 (1994).

18   E. Jacquet, D. Zanuttini, J. Douady, E. Giglio, and B. Gervais, J. Chem. Phys. **135**, 174503 (2011).

19   J. Douady, S. Awali, L. Poisson, B. Soep, J. M. Mestdagh, and B. Gervais, The Journal of Physical Chemistry A **119**, 6074 (2015).

20   A. Schrimpf, G. Sulzer, H. J. Stöckmann, and H. Ackermann, Zeitschrift für Physik B Condensed Matter **67**, 531 (1987).

21   W. Breckenridge, Int. Rev. Phys. Chem. **13**, 291 (1994).

Appendix IV.I

|	A	M	S
G1:	0.632	18.052	0.144
G2:	0.832	17.910	0.144
G3:	0.856	17.769	0.144
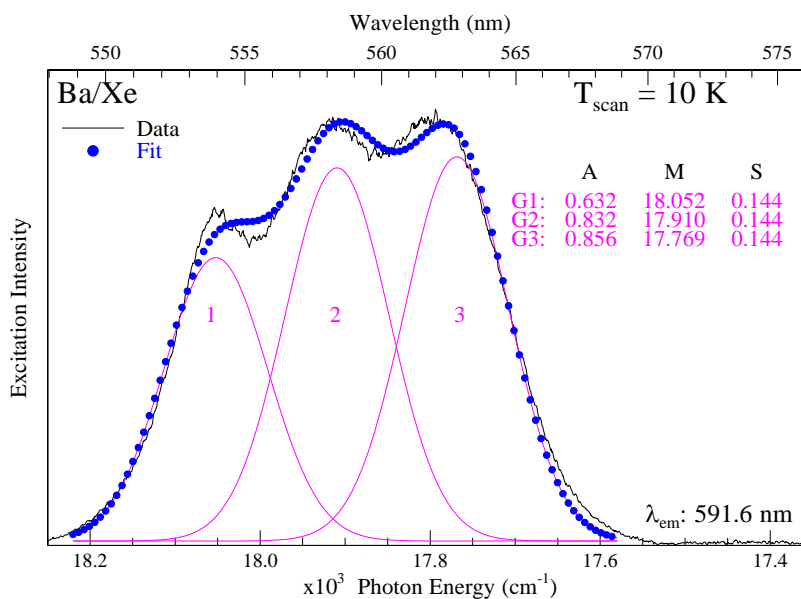
Figure IV.52   **A lineshape analysis of the blue site excitation spectrum of Ba/Xe. Three Gaussian curves (see Equation II.2) were required to provide an adequate fit of the scan. The symbols A, M and S denote the intensity, location and bandwidth of each component, where M and S are in units of 1×10^3 cm^{-1}. During the fit, the widths of each composite Gaussian curve were equal and held constant, while the intensities and positions were allowed to vary. Trial and error showed that the best overall fit (i.e. with a minimum root mean variance value) was obtained when peak widths of 144 cm^{-1} were set. The error (standard deviation) associated with each peak position is: $\sigma_{M1} = \pm 0.4$ cm^{-1}, $\sigma_{M2} = \pm 0.5$ cm^{-1} and $\sigma_{M3} = \pm 0.3$ cm^{-1}.**

|	A	M	S
G1:	0.511	18.210	0.090
G2:	0.525	18.056	0.151
G3:	0.838	17.481	0.092
G4:	0.043	17.787	0.060
G5:	0.231	17.581	0.223
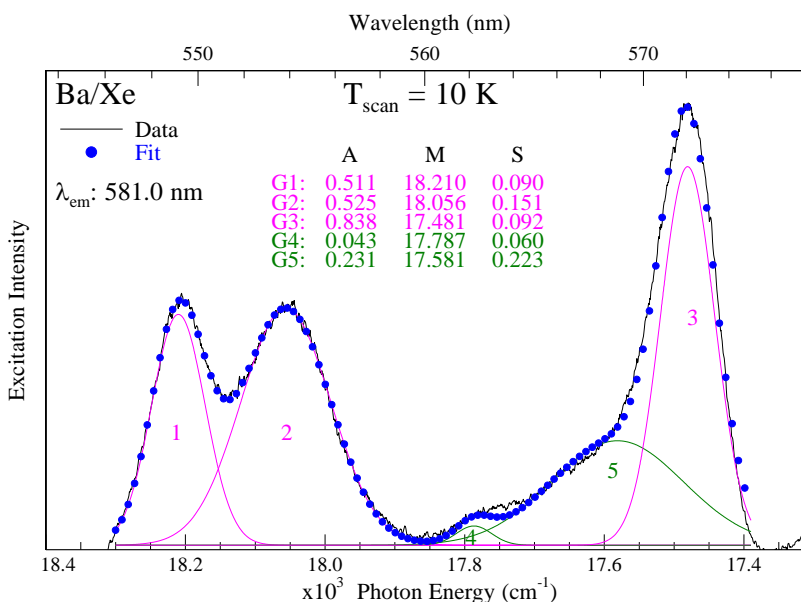
Figure IV.53   **A lineshape analysis of the violet site excitation spectrum of Ba/Xe. Five Gaussian curves were required to provide an adequate fit of the scan. During the fit, all of these parameters were allowed to vary. The two Gaussian curves shown in green (peaks 4 and 5) are required to account for a residual amount of green site picked up in the violet site scan. $\sigma_{M1} = \pm 0.9$ cm^{-1}, $\sigma_{M2} = \pm 1.1$ cm^{-1}, $\sigma_{M3} = \pm 0.5$ cm^{-1}, $\sigma_{M4} = \pm 6.9$ cm^{-1} and $\sigma_{M5} = \pm 7.0$ cm^{-1}.**
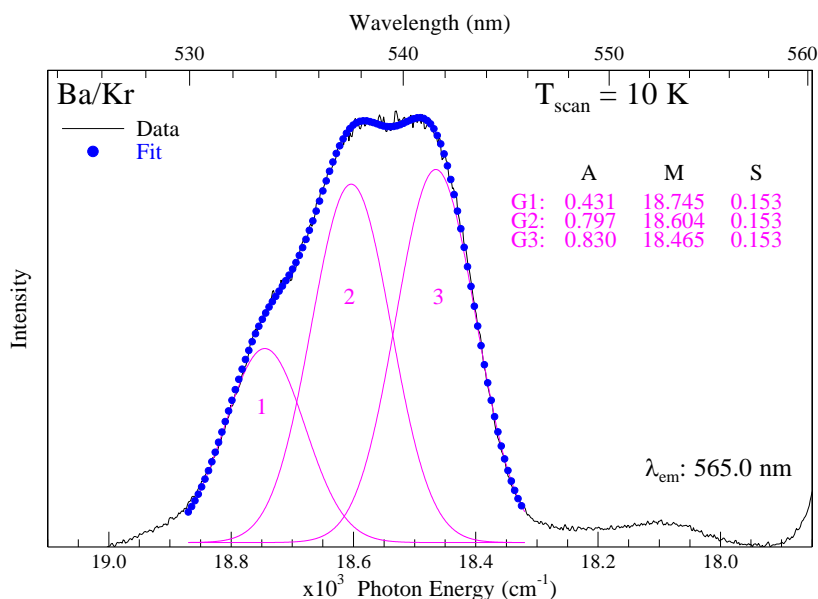
Figure IV.54 A lineshape analysis of the blue site excitation spectrum of Ba/Kr. Three Gaussian curves were required to provide an adequate fit of the scan. During the fit, the widths of each composite Gaussian curve were equal and held constant, while the intensities and positions were allowed to vary. Trial and error showed that the best overall fit was attained with peak widths of 153 cm^{-1}. The monitored emission wavelength at 566 nm was chosen to minimise contributions from the other sites. $\sigma_{M1} = \pm\ 1.9$ cm^{-1}, $\sigma_{M2} = \pm\ 1.6$ cm^{-1} and $\sigma_{M3} = \pm\ 1.0$ cm^{-1}.
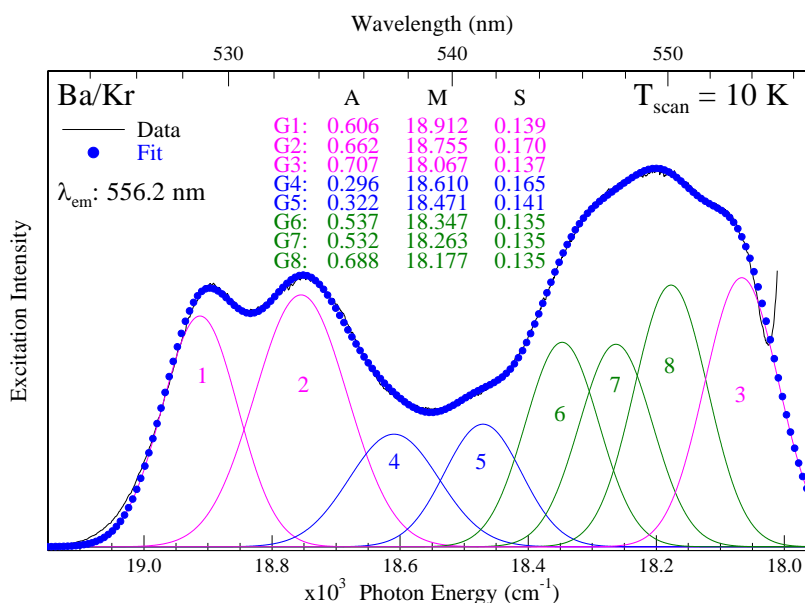
Figure IV.55 A lineshape analysis of the Ba/Kr violet site excitation spectrum. Eight Gaussian curves were required to fit this complex scan. The three Gaussian curves shown in green were taken directly from the fit of the green site in Figure IV.56, and the width and position of each was held constant. The parameters of the remaining five curves were allowed to vary. Gaussian peaks 4 and 5 account for a small amount of the blue site and peaks 1 – 3 represent the 'true' violet site absorptions. $\sigma_{M1} = \pm\ 0.4$ cm^{-1}, $\sigma_{M2} = \pm\ 0.8$ cm^{-1}, $\sigma_{M3} = \pm\ 0.3$ cm^{-1}, $\sigma_{M4} = \pm\ 2.0$ cm^{-1} and $\sigma_{M5} = \pm\ 1.1$ cm^{-1}.
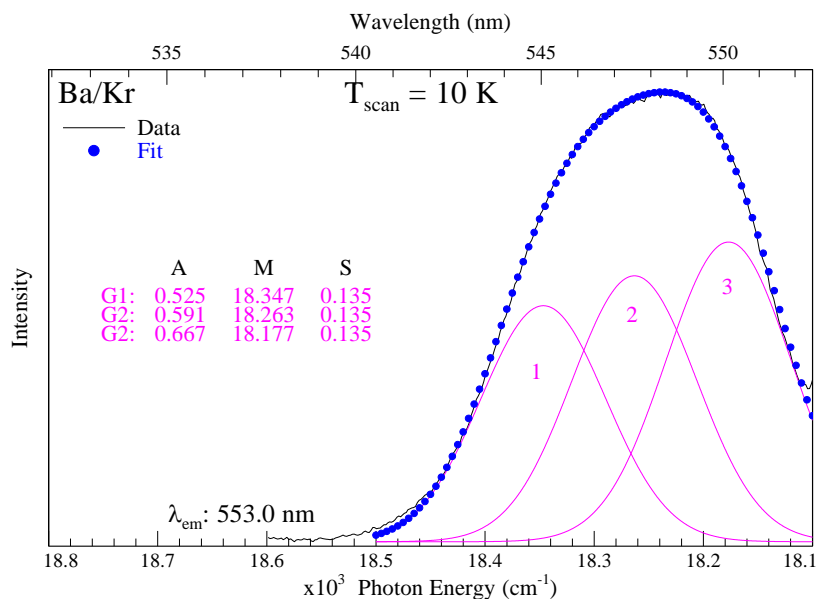
Figure IV.56   A lineshape analysis of the green site excitation spectrum of Ba/Kr. Three Gaussian curves were required to provide an adequate fit of green site absorption. During the fit, the widths of each composite Gaussian curve were equal and held constant, while the intensities and positions were allowed to vary. $\sigma_{M1} = \pm 1.5$ cm^{-1}, $\sigma_{M2} = \pm 3.2$ cm^{-1} and $\sigma_{M3} = \pm 1.3$ cm^{-1}.
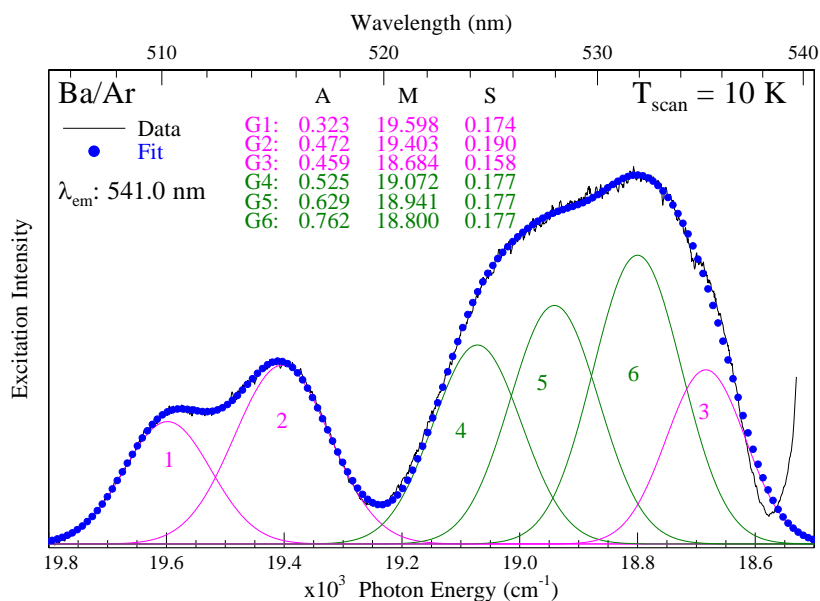
Figure IV.57   A lineshape analysis of the violet site excitation spectrum of Ba/Ar. Six Gaussian curves were required to fit this complex scan. The three Gaussian curves shown in green were taken directly from the fit of the green site in Figure IV.59, and the width and position of each was held constant. Gaussians 1 – 3 represent the 'true' violet site absorptions and all parameters of theses peaks were allowed to vary in the fit. $\sigma_{M1} = \pm 3.0$ cm^{-1}, $\sigma_{M2} = \pm 2.2$ cm^{-1} and $\sigma_{M3} = \pm 1.2$ cm^{-1}.
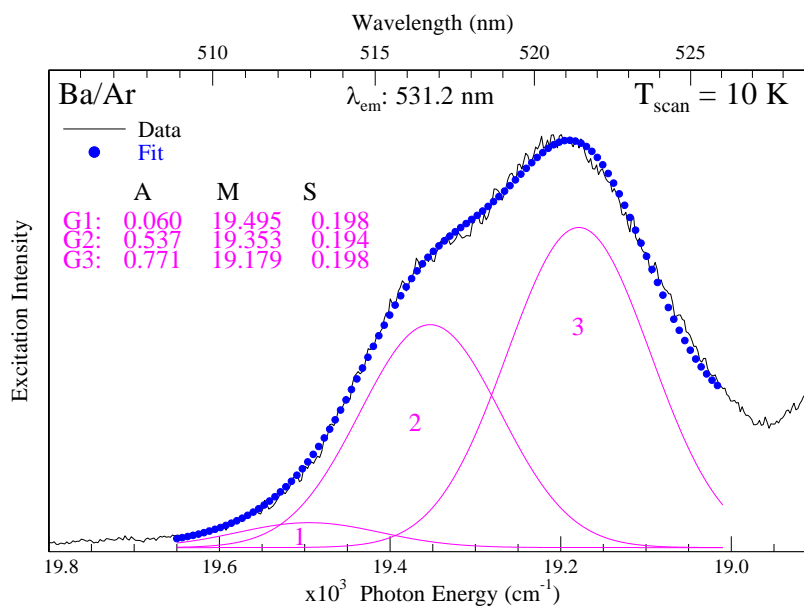
Figure IV.58 A lineshape analysis of the blue site excitation spectrum of Ba/Ar. Three Gaussian curves were required to provide an adequate fit of the data. During the fit, the width and position of peak 1 was held fixed whilst all of the remaining Gaussian parameters were allowed to vary. $\sigma_{M2} = \pm 2.0$ cm^{-1} and $\sigma_{M3} = \pm 2.8$ cm^{-1}.
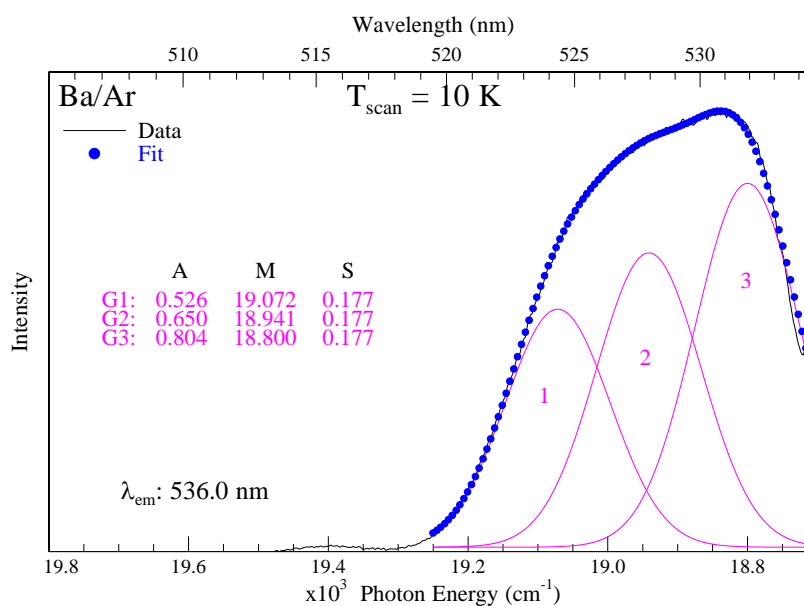

Figure IV.59 A lineshape analysis of the green site excitation spectrum of Ba/Ar. Three Gaussian curves were required to fit the data. During the fit, the width of all three Gaussian curves were held fixed whilst all of the remaining parameters were allowed to vary. $\sigma_{M1} = \pm 1.7$ cm^{-1}, $\sigma_{M2} = \pm 2.6$ cm^{-1} and $\sigma_{M3} = \pm 1.2$ cm^{-1}.
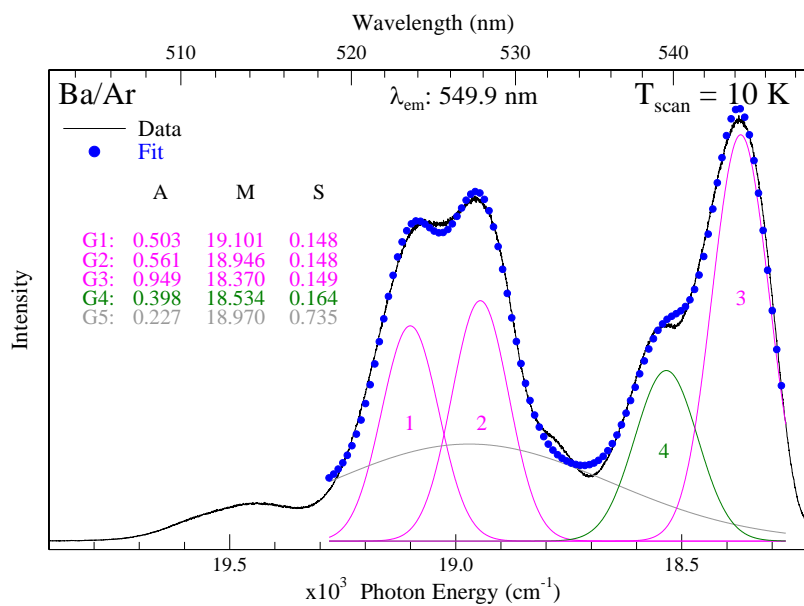
Figure IV.60 **A lineshape analysis of the red site excitation spectrum of Ba/Ar. five Gaussian curves were required to provide an adequate fit of the data. During the fit, all of these parameters were allowed to vary. The Gaussian peak shown in grey accounts for a small baseline effect present in the scan. $\sigma_{M1} = \pm\ 0.3\ \text{cm}^{-1}$, $\sigma_{M2} = \pm\ 0.3\ \text{cm}^{-1}$, $\sigma_{M3} = \pm\ 0.9\ \text{cm}^{-1}$ and $\sigma_{M4} = \pm\ 0.2\ \text{cm}^{-1}$.**

Chapter V
Sr/RG Atomic Luminescence

V.1   Introduction

The luminescence of atomic Sr isolated in the solid rare gases (RG = Ar, Kr and Xe) is presented in this Chapter. As with Ba, the spectroscopy of matrix-isolated Sr is not well documented – only a small number of experiments[1-3] have been conducted. Moreover, the existing studies are primarily concerned with the homonuclear dimer (Sr_2). While investigating the laser excited fluorescence spectrum of Sr_2 in Ar, Miller and Andrews[1] briefly reported the observation of atomic emission bands. Sharp and strong features occurred at approx. 466, 513 and 703 nm which were assigned to emission of the ^1P, ^1D and ^3P excited states, respectively. To the best of my knowledge, this is the only existing publication presenting the emission data of Sr atoms in any RG host. Consequently, the majority of the results presented in this chapter are novel.

The absorption spectra recorded of matrix-isolated Sr ($n=5$) and Ba ($n=6$) were shown in Chapter III and for both systems, the dominant features arose from the (nsnp) $^1P_1 \leftarrow (ns^2)$ $^1S_0$ transition. The (5s5p) $^1P_1$ luminescence of Sr will be presented in a similar fashion to Ba - 2D-EE spectra recorded of the resonance (5s5p) $^1P_1 \rightarrow (5s^2)$ $^1S_0$ emission features will be used extensively to characterise the sample composition and to identify the thermally stable sites of isolation. In addition to the strong resonance fluorescence, it will be shown that Sr also exhibits a number of lower energy and long-lived (< 1 µs) emissions, which are associated with the triplet states (^3D_J and ^3P_J). This is in stark contrast to Ba, where phosphorescence was not observed. Inspection of Figure I.7 (Chapter I) shows that the ordering of the lowest excited states is quite different for Sr and Ba. The metastable ^3D_J levels of Ba are situated at 9034 cm^{-1} or 1107 nm above the ground state – outside the 180 – 900 nm range of our current detection system. Conversely, the metastable ^3P_J states of Sr occur between 671 and 698 nm and are accessible in the current experimental set-up.

The absorption spectra recorded for the three Sr/RG systems exhibited a second, weaker series of visible bands which were assigned to the (5s4d) $^1D_2 \leftarrow (5s^2)$ $^1S_0$ transition of atomic Sr. This parity-forbidden transition is not easy to observe in the gas

phase, but is made allowed by a combination of the matrix environment and the small $^1P_1 - {}^1D_2$ energy separation, both of which are conducive[3] to 'intensity borrowing'. Thus, the (5s4d) $^1D_2$ excited state of Sr is readily accessed in a RG matrix. The luminescence obtained with direct excitation of the Sr/RG $^1D_2$ absorptions will therefore be presented in Section V.4.

V.2 Sr/RG (5s5p $^1P_1$) luminescence

V.2.I Sr/Xe

V.2.I.I $\lambda_{em} \approx 490$ nm

The 2D-EE spectrum of Sr/Xe, recorded following sample deposition at 10 K with a low metal flux, is presented in Figure V.1. The data was obtained by monitoring the emission bands in the 490 nm region whilst scanning the entire range of the (5s5p) $^1P_1$ absorption profile shown in Figure III.24. Inspection of Figure V.1 reveals the presence of four distinct features, which are labelled I – IV.
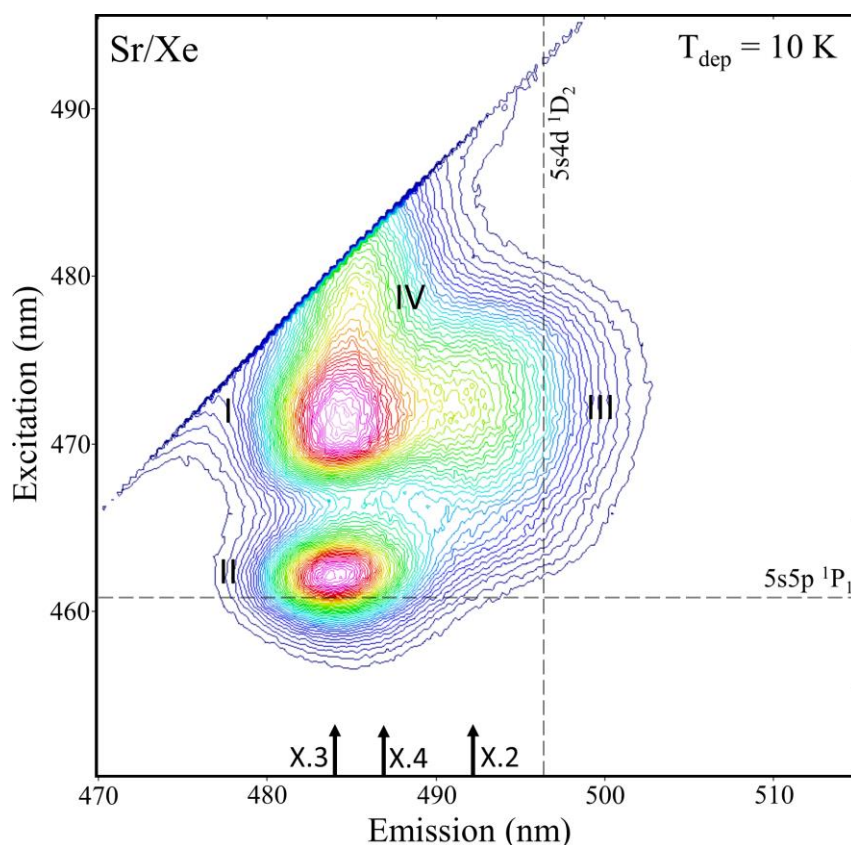

Figure V.1 **2D-EE spectrum recorded following sample deposition at 10 K. The optical density (OD) of this sample was measured to be 0.3 at 460 nm. A horizontal slice through the plot yields an emission spectrum, whereas a vertical slice provides an excitation spectrum. The gas phase position[4] of the resonance (5s5p) $^1P_1 \leftarrow$ (5s^2) $^1S_0$ transition of Sr is shown in excitation, represented by a dashed horizontal line. Whereas the (5s4d) $^1D_2 \leftarrow$ (5s^2) $^1S_0$ transition is shown as a vertical line intersecting the emission axis.**

The dominant bands, I and II, are distinct in excitation but share a common emission wavelength and are therefore attributed to a single trapping site for Sr. In contrast,

features III and IV are distinct in both emission and excitation. These bands arise from the occupation of two unique sites of isolation. The excitation slices X.2 – X.4 are shown overlaid onto the absorption spectrum in Figure V.3. Annealing the Xe matrix to 60 K greatly simplifies the luminescence, as evident in Figure I.1. Features I, II (one site) and IV are completely removed, revealing that these two matrix sites are thermally unstable. The annealed 2D-EE spectrum exhibits a dominant band (I), centred at 492.1/469.7 nm (emission /excitation)[a]. In addition, a very weak feature (II) centred at 482.2/463.3 nm becomes visible.
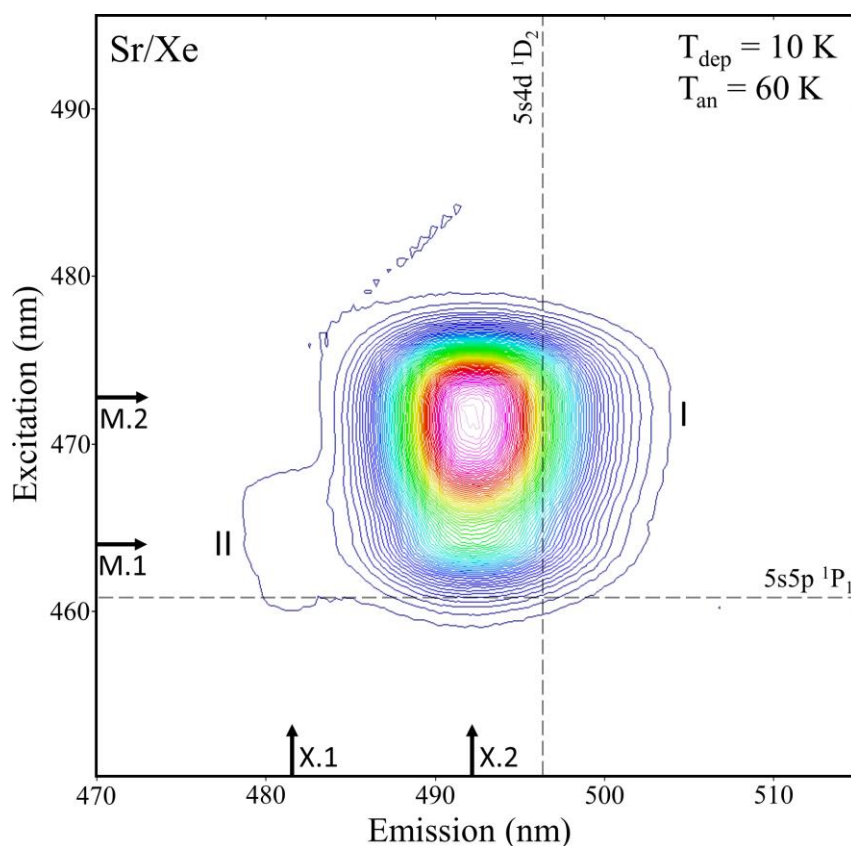

Figure V.2　　**2D-EE spectrum recorded following sample deposition at 10 K and annealing to 60 K. The optical density (OD) of this sample was measured to be 0.13 at 460 nm. The gas phase position[4] of the resonance $(5s5p)\ ^1P_1 \leftarrow (5s^2)\ ^1S_0$ transition of Sr is shown in excitation, represented by a dashed horizontal line. Whereas the $(5s4d)\ ^1D_2 \leftarrow (5s^2)\ ^1S_0$ transition is shown as a vertical line intersecting the emission axis.**

The excitation scans obtained by taking vertical slices through Figure I.1 at X.1 and X.2 are shown overlaid onto the annealed $(5s5p)\ ^1P_1$ absorption profile of Sr/Xe in

---

[a] A comparison of the 2D-EE spectra shows that band I of Figure I.1 is equivalent to band III in Figure V.1

Figure V.3. The 'blue' site excitation spectrum (X.1) directly overlaps the dominant absorption band and shows a partially resolved Jahn-Teller (JT) threefold splitting pattern with peaks at 460.8, 463.3 and 466.1 nm. The 'green' site excitation band is centred at 469.7 nm and overlaps the lower energy absorption shoulder. As both excitation scans account for all of the annealed $(5s5p)\ ^1P_1 \leftarrow (5s^2)\ ^1S_0$ absorption features, it can be stated that two thermally stable sites of isolation exist of Sr/Xe. The photophysical properties of each site will now be presented in detail.
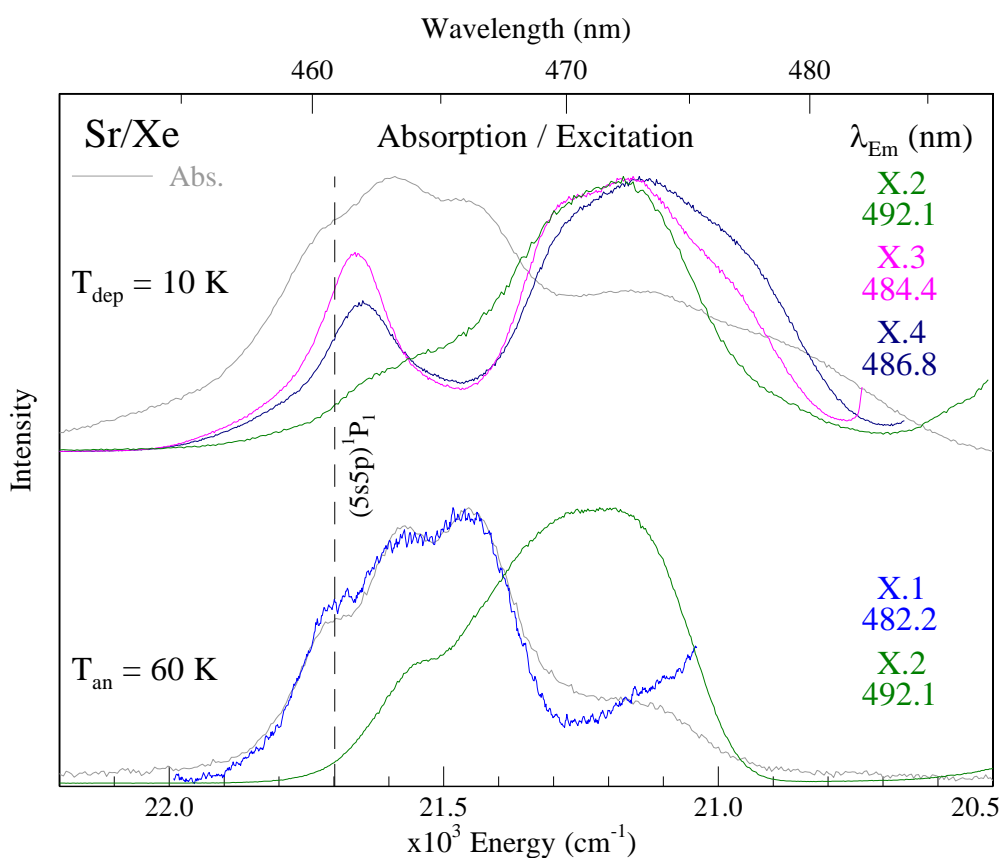

Figure V.3   **Sr/Xe absorption (grey) and excitation spectra (coloured), recorded monitoring the emission features in the 490 nm spectral region. The top traces were obtained following deposition at 10 K, whereas the bottom traces originate from a sample annealed to 60K. The gas phase position[4] of the resonance $(5s5p)\ ^1P_1 \leftarrow (5s^2)\ ^1S_0$ transition of Sr is shown as a dashed vertical line.**

V.2.I.I.A   Blue site

Emission and excitation spectra recorded of the blue site are presented in Figure V.4. The JT excitation band is centred at 463.3 nm and exhibits a matrix red-shift of -144 cm^{-1} from the gas phase resonance (5s5p) $^1P_1 \leftarrow$ (5s^2) $^1S_0$ transition. A lineshape analysis for the excitation spectrum is presented in Figure V.113 of Appendix V.I. Three Gaussian curves of equal bandwidth (146 cm^{-1}) provide an excellent fit of the threefold split band.
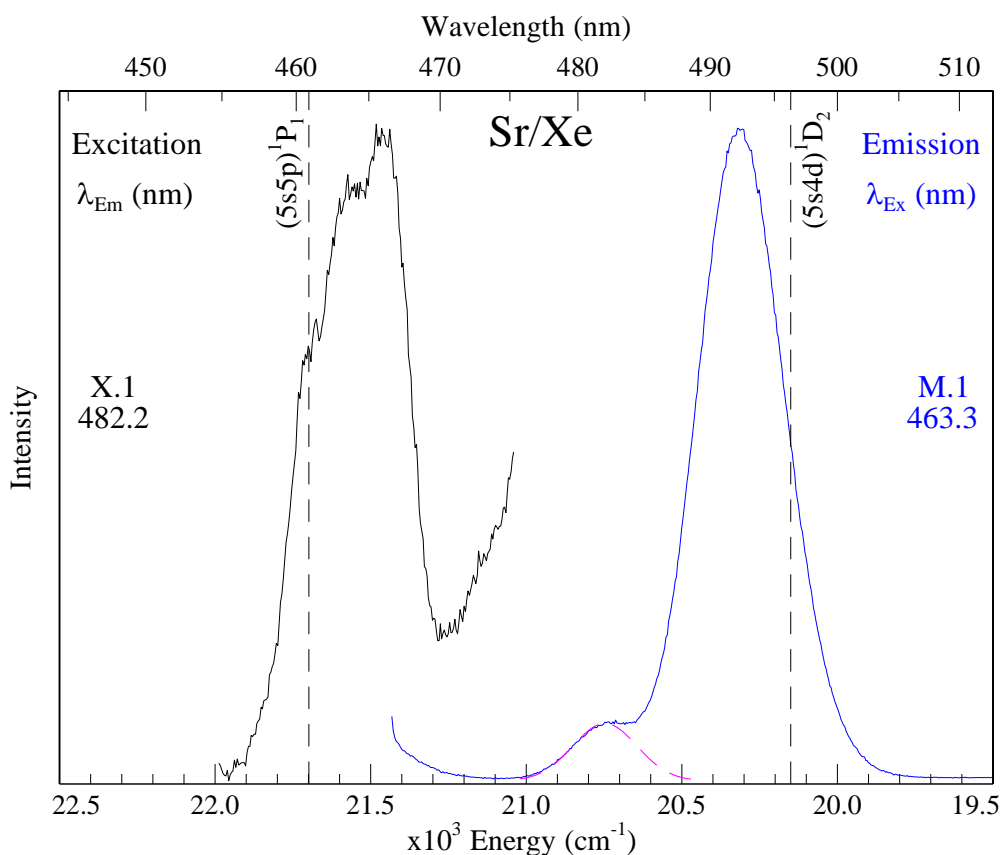

Figure V.4   **Excitation (black) and emission (blue) spectra recorded for the Sr/Xe blue site of isolation, following sample annealing to 60 K. The gas phase[4] positions of the (5s5p) $^1P_1$ and (5s4d) $^1D_2$ states of atomic Sr are shown by dashed vertical lines. The Gaussian fit of the blue site emission is represented by the dashed pink trace.**

Irradiation of the central JT component produces two emission features in this region. The dominant band at 492 nm corresponds to the green site and the weaker band at 482.2 nm is attributed to emission of the blue site. A Gaussian fit (dashed pink line) allowed the bandwidth (fwhm) of the latter to be extracted - its value is 258 cm^{-1}. A Stokes shift of 846 cm^{-1} is determined from the centres of the excitation and emission bands. Assignment of the blue site emission to a particular electronic transition of

atomic Sr is challenging due to the presence of two ($^1P_1$ and $^1D_2$) atomic states in this region, which are shown as dashed vertical lines in Figure V.4. A matrix red-shift of -960 cm^{-1} is determined from the gas phase (5s5p) $^1P_1$ state whereas a matrix blue-shift of +588 cm^{-1} is extracted from the gas phase position of the (5s4d) $^1D_2$ state.
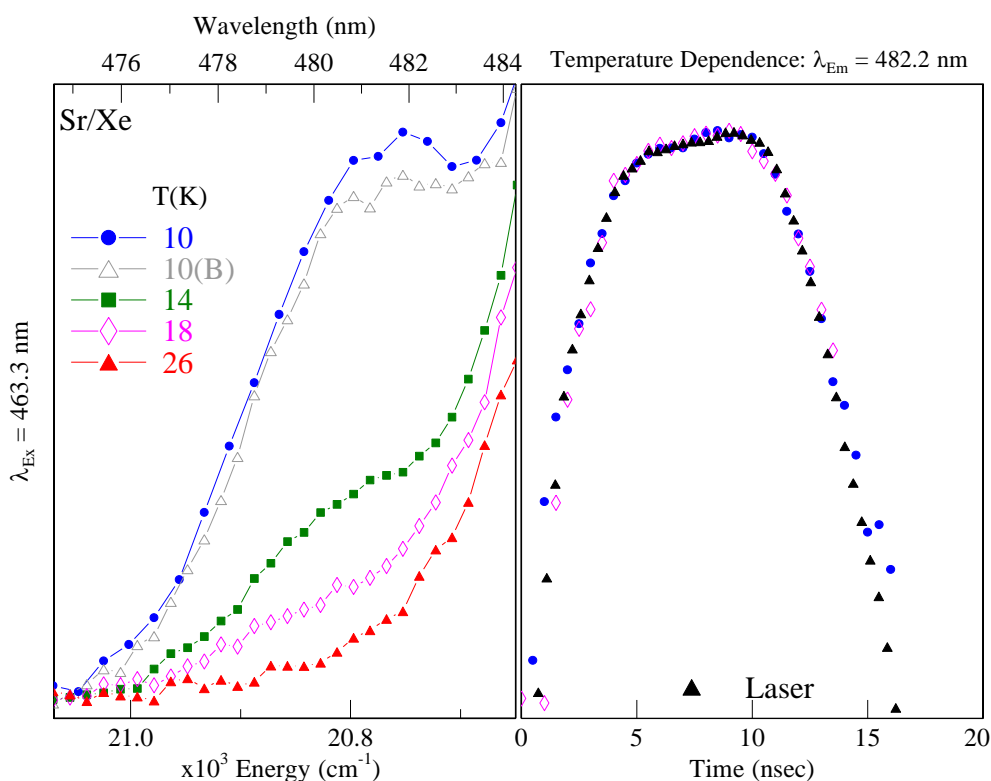

Figure V.5   The left panel shows the temperature dependence of the Sr/Xe blue site emission band at 481.5 nm, recorded over the range 10 – 26 K. The grey trace, denoted 10(B), represents the emission intensity recorded back at 10 K after this investigation. The right panel presents the temperature dependence of the decay curves, recorded at 10 and 18 K, overlaid onto the laser profile (black triangles). The lifetime of the blue site emission is very short (< 1 ns) as it matches the temporal profile of the laser.

In an attempt to resolve this complication, time-resolved emission spectra were recorded. The extracted decay slices obtained at 10 and 18 K are presented in the right panel of Figure V.5 and show a temporal profile which exactly matches that of the laser (represented by the black triangles). At 10 K, the lifetime of this transition is very short (< 1 ns) and cannot be resolved from the Nd:YAG laser pulse. Thus, the radiative lifetime for the blue site emission at 482.2 nm could not be obtained. However a tentative assigned to the resonance (5s5p) $^1P_1 \rightarrow$ (5s^2) $^1S_0$ transition of Sr is made based on the short (< 1 ns) lifetime observed at 10 K. The parity-forbidden (5s5p) $^1D_2 \rightarrow$ (5s^2)

^{1}S$_0$ transition is expected to be longer lived, as will be discussed in Section V.3.III. The spectral scans presented in the left panel of Figure V.5 show that the emission intensity is greatly reduced between 10 and 14 K, and all but vanishes above 18 K. This process is almost completely[b] reversible and indicates that a non-radiative relaxation pathway is highly efficient at quenching the emission of Sr atoms isolated at the blue site in Xe.

V.2.I.I.B   Green site

The luminescence of the green site of isolation is presented in Figure V.6. The excitation band is centred at 469.7 nm and red-shifted from the (5s5p) ^{1}P$_1$ ← (5s^2) ^{1}S$_0$ transition by -408 cm^{-1}. A lineshape analysis conducted for this scan is presented in Figure V.114 of Appendix V.I. A total of five Gaussian curves are required to fit the observed features.
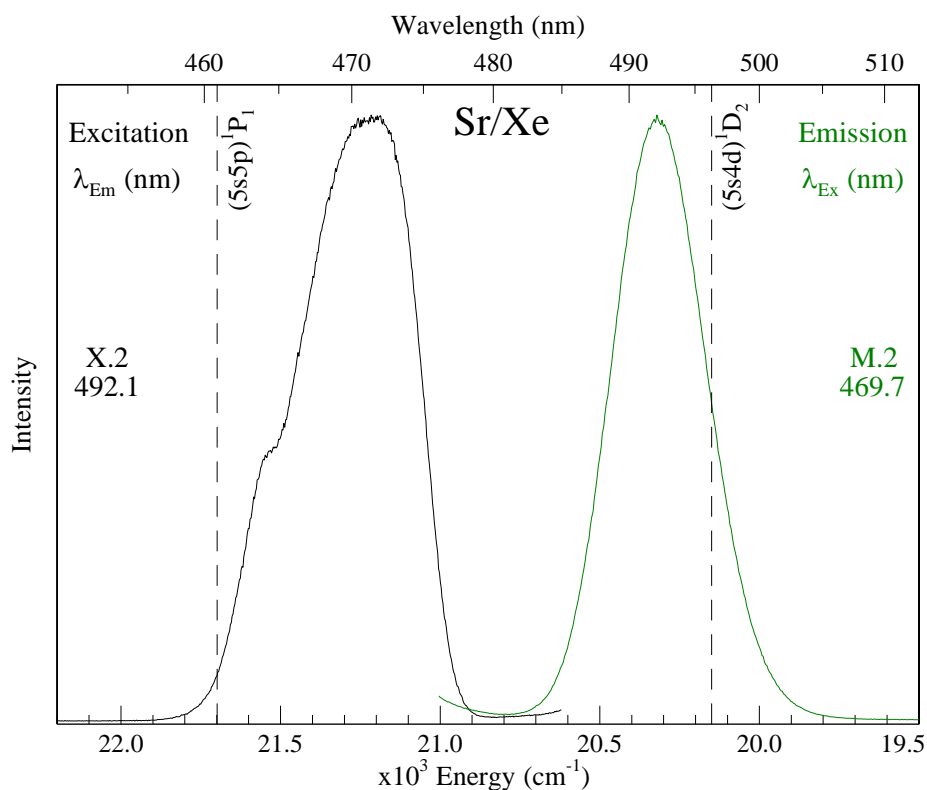

Figure V.6   **Excitation (black) and emission (green) spectra recorded for the Sr/Xe green site of isolation, after annealing to 60 K. The gas phase[4] positions of the (5s5p) ^{1}P$_1$ and (5s4d) ^{1}D$_2$ states of atomic Sr are shown by dashed vertical lines.**

---

[b] A small amount of the blue site emission intensity is permanently lost due to sample bleaching or site interconversion. These effects have also been observed for all three Ba/RG (RG = Ar, Kr and Xe) systems, but are much less significant for the Sr/RG systems.

The two highest energy components at approx. 464 and 467 nm account for some spectral overlap with the blue site. The three lower energy Gaussians peaks (3 - 5), each displaying a bandwidth of 141 cm^{-1}, represent the 'true' green site absorption band and are suggestive of an unresolved JT threefold split. Based on this analysis, if the JT peaks were resolved, they would occur at 469.7, 472.1 and 474.2 nm.

An intense emission feature at 492.1 nm is produced with photoexcitation of the green site absorption. The emission is characterised by a fwhm of 343 cm^{-1} and is Stokes shifted by 861 cm^{-1}, as measured from the central fit component at 472.1 nm. The emission decay profile, recorded with pulsed laser excitation at 472.0 nm, is presented in Figure V.7. A single exponential function employing a decay time of 2.0 ns provides a very good fit of the data.


Sr/Xe - Decay profile $\lambda_{Em.}$ = 492.1 nm at 10 K
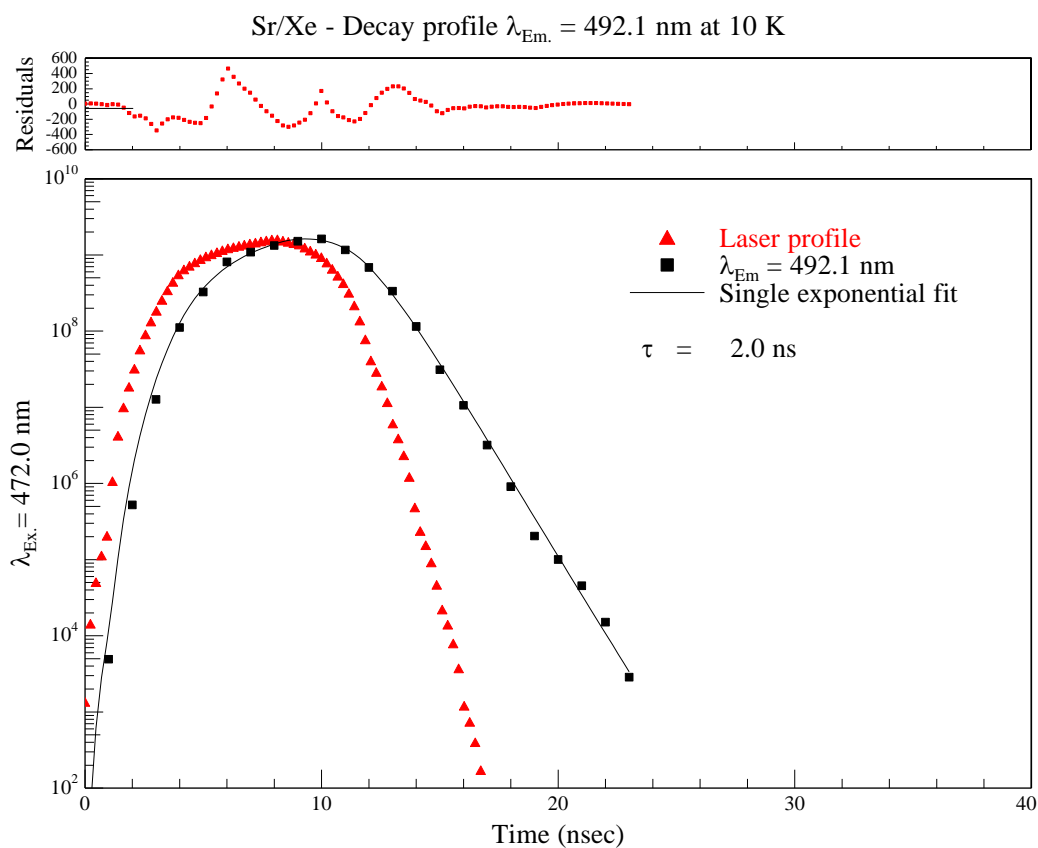
Figure V.7   **Decay profile of the Sr/Xe green site emission band at 492.1 nm, produced by site-selective laser excitation at 472.0 nm. An excited state decay time of 2.0 ns is obtained at 10 K with a single exponential trial function, which included a re-convolution with the time profile of the Nd:YAG laser.**

The spectral and temporal scans made at elevated temperatures are presented in Figure V.8. Inspection of the right panel shows that the observed lifetime is constant

over the small range of 10 – 11 K. The value of 2.0 ns is therefore tentatively assigned as the radiative decay time for the green site emission band. Applying the effective field correction[5,6] using Equation IV.2 (Chapter IV), yields an excited state lifetime of 5.9 ns. This value is in good agreement with the gas phase lifetime[4] (4.98 ns) of the resonance Sr: $(5s5p)$ $^1P_1 \leftrightarrow (5s^2)$ $^1S_0$ atomic transition, allowing an assignment to be made. Inspection of Figure V.6 shows that, as a result of the large Stokes shift, the green site $(5s5p)$ $^1P_1$ emission band overlaps the gas phase position of the $(5s4d)$ $^1D_2$ state.
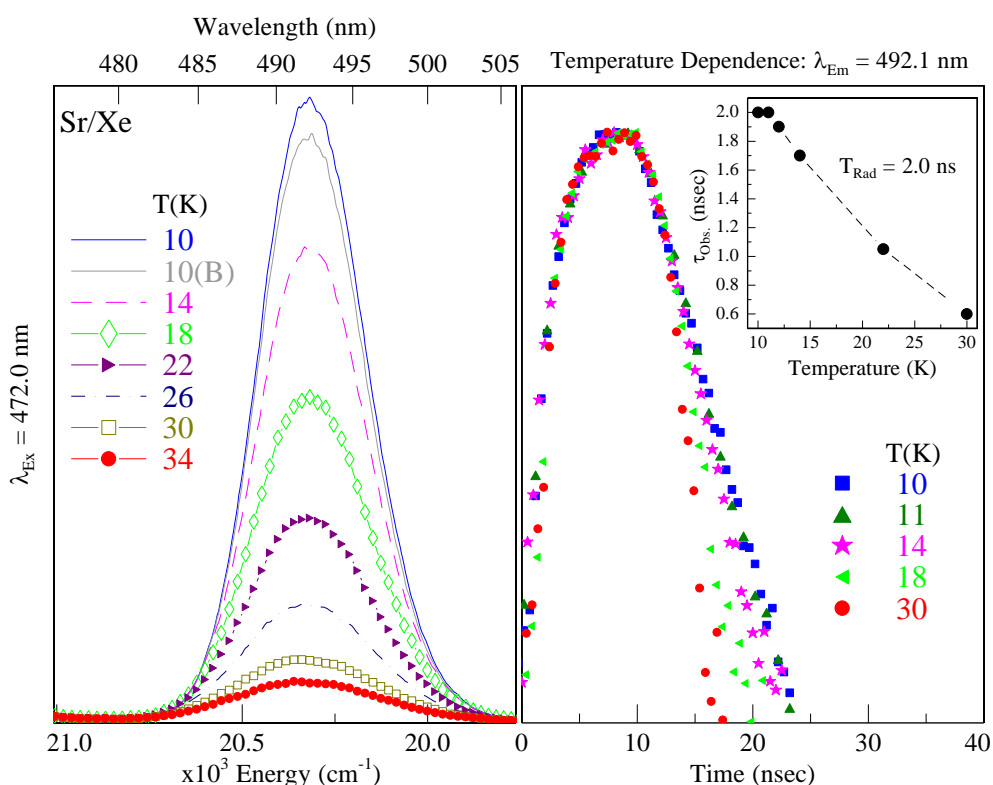

Figure V.8   **The left panel shows the temperature dependence of the Sr/Xe green site emission band at 492.1 nm, recorded over the range 10 – 34 K. The right panel presents the temperature dependence of the decay curves, recorded between 10 and 30 K. The lifetime of the green site emission becomes less than 1 ns above temperatures of 24 K.**

Above 11 K, the decay profiles become significantly shorter. For example, a lifetime of ~1 ns is observed at 24 K. An examination of the spectral scans provided in the left panel of Figure V.8 shows that a dramatic decrease in the emission intensity occurs over the range 10 – 34 K. A more detailed investigation of this trend is provided by the emission integrated areas, which are collected in Table V.1. For instance, at 34 K, the integrated area is reduced to 5 % of its initial 10 K value. This effect is almost

completely reversible. Scans made back at 10 K show that over 95 % of the emission is restored. Similar to the Sr/Xe blue site, a non-radiative relaxation pathway is competing efficiently with the resonance (5s5p) $^1P_1$ emission of atomic Sr, when isolated at the green site. However in the green site, it is effective only at higher temperatures.

Table V.1 **The integrated area of the Sr/Xe green site emission (491.2 nm) measured as a function of temperature (in Kelvin). The 10 K emission band was normalised and the intensities of the higher temperature scans were scaled relative to this. The integration was evaluated over the spectral range 20800 – 19750 cm^{-1}. The rightmost column shows the integrated area of each scan expressed as a percentage of the integrated area for the original 10 K scan.**

Range :	20800 – 19750 cm^{-1}	
Temp (K)	Integrated Area	%
10	349	100
14	276	79
18	197	57
22	130	37
26	78	22
30	45	13
34	28	8
38	17	5
Back to 10	330	95

V.2.II Sr/Xe full range emission

The 490 nm luminescence features of Sr/Xe, presented in the previous section, revealed the existence of two thermally stable trapping sites for Sr in this host. Full range emission scans, produced with site-selective irradiation of the (5s6p) $^1P_1$ absorptions/excitation bands, are presented in Figure V.9. In addition to the bands assigned to the resonance (5s5p) $^1P_1 \rightarrow$ (5s^2) $^1S_0$ atomic transition, two lower energy emission features are observed in the near-IR spectral region (~770 nm). These will now be presented in detail.
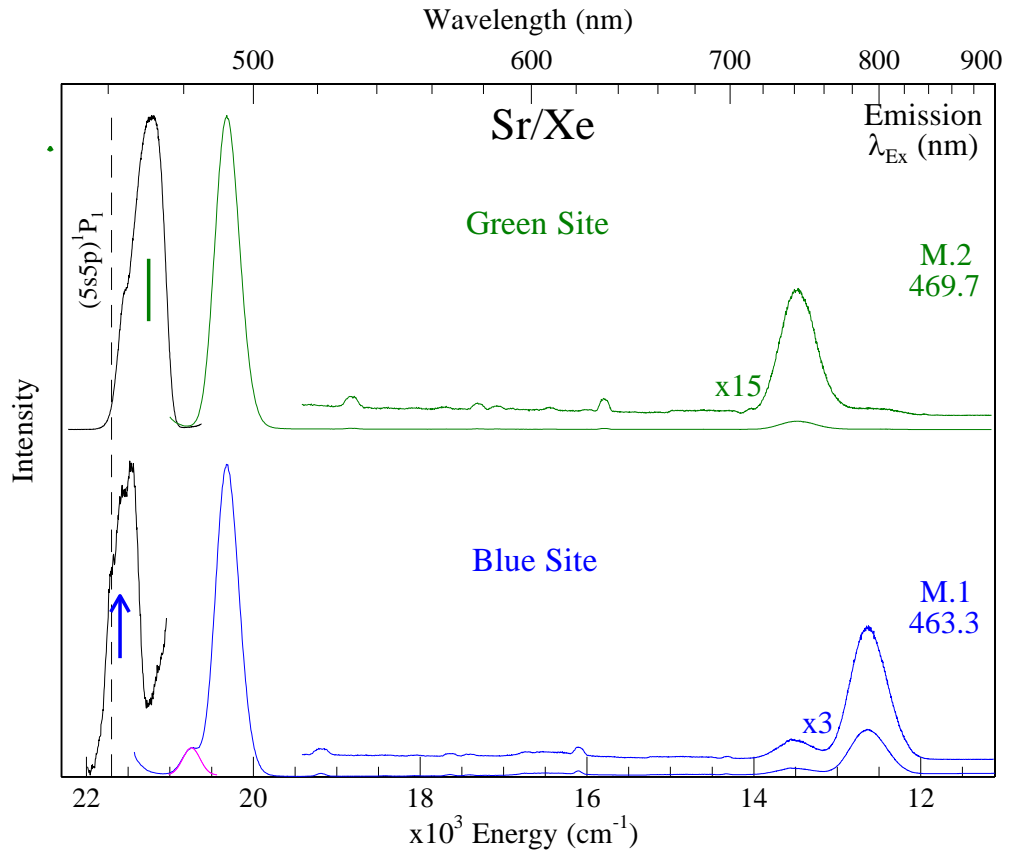
Figure V.9 **Excitation (black) and full range emission spectra (coloured) recorded for Sr/Xe following sample annealing to 60 K. The gas phase position[4] of the resonance $(5s5p)\ ^1P_1 \leftarrow (5s^2)\ ^1S_0$ transition of Sr is shown as a dashed vertical line. A Gaussian fit of the blue site $(5s5p)\ ^1P_1$ emission is represented by the solid pink line.**

V.2.II.I $\lambda_{em} \approx 770$ nm

The 2D-EE plot of an annealed (60 K) Sr/Xe sample is presented in Figure V.10. The spectrum was obtained by monitoring the lower energy emission bands at approx. 770 nm whilst scanning in the region of the $(5s6p)\ ^1P_1$ absorption profile. The two main features, denoted I and II, are centred at 791.2/463.3 and 740.5/469.7 nm (emission/excitation) respectively. The excitation (X.1, X.2) and emission (M.1, M.2) slices obtained from this spectrum are presented in left and right panels of Figure V.11 respectively. The blue and green site excitation bands are equivalent to those obtained from the $^1P_1$ emission features. Interestingly, the blue site emission occurs to lower energy than the green site in this region − in contrast to the visible (∼ 490 nm) emission bands.
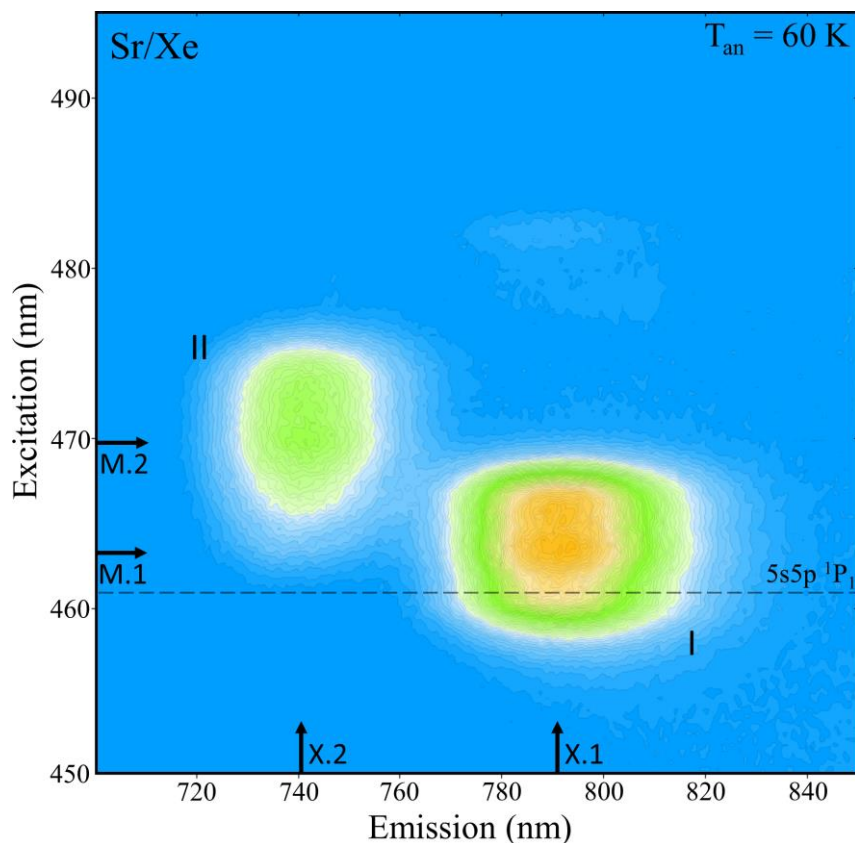
Figure V.10   Sr/Xe 2D-EE spectrum, recorded in the 770 nm spectral region, following sample deposition at 10 K and annealing to 60 K. The gas phase position[4] of the resonance $(5s5p)$ $^1P_1 \leftarrow (5s^2)$ $^1S_0$ transition of Sr is shown in excitation, represented by a dashed horizontal line.
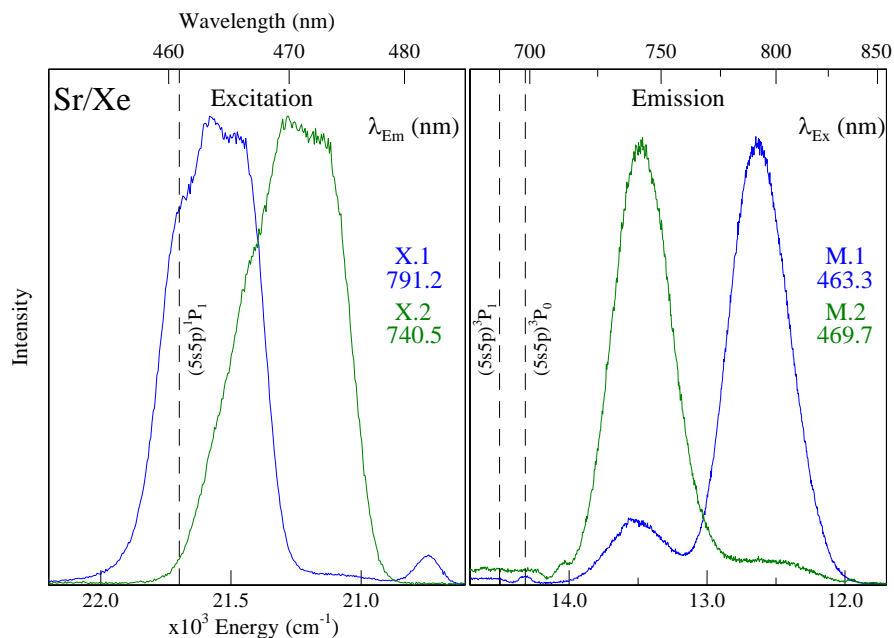

Figure V.11   Left Panel: Blue and green site excitation spectra recorded monitoring the lowest energy Sr/Xe emission bands. Right Panel: emission spectra produced with site-selective excitation of the $(5s5p)$ $^1P_1$ features. In emission, the nearest atomic states, $(5s5p)$ $^3P_1$ and $(5s5p)$ $^3P_0$, are shown by dashed vertical lines.

Examination of the right panel of Figure V.11 reveals that the (5s5p) ^3P_J manifolds of atomic Sr are in close proximity. For comparative purposes, the gas phase positions of (5s5p) $^3P_1$ and (5s5p) $^3P_0$ states are shown as dashed vertical lines. The photophysical and temporal properties of the near-IR emissions will now be presented with the aim of assigning each to a particular electronic state of the Sr atom.

V.2.II.I.A   Blue site

Inspection of Figure V.9 shows that the emission band at 791.2 nm dominates the blue site luminescence of Sr/Xe. Indeed, this feature is more intense and broader (fwhm = 516 cm^{-1}) than the $^1P_1$ emission band at 482.2 nm. A decay profile recorded at 10 K, using a pulsed laser excitation source (Nd:YAG) in combination with multi-channel scaling, is presented in Figure V.12. The decay was well fit with a double exponential function, employing decay times (τ_1 and τ_2) of 17.3 and 163.5 µs, with the respective amplitudes (A_1 and A_2) of 410 and 677.

Sr/Xe - Decay profile $\lambda_{Em.}$ = 791.2 nm at 10.0 K

— — - Data
——— Double exponential Fit (Range 2 to 500 µs)
τ_1 = 17.327 µs A_1 =   410
τ_2 = 163.49 µs A_2 =   677
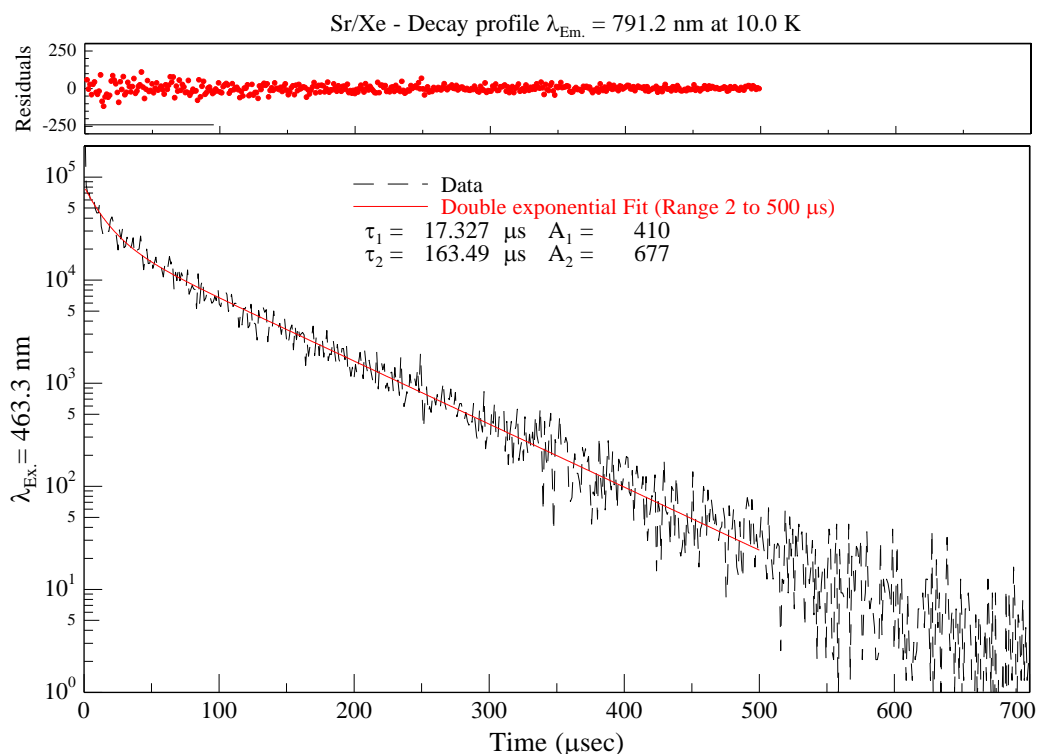
Figure V.12   **Decay profile of the Sr/Xe blue site emission band at 791.2 nm, produced by site-selective laser excitation at 463.3 nm and recorded using the multi-channel scaling technique, as outlined in Chapter II. The residuals present the difference between the double exponential fit and the recorded decay. The error or standard deviation associated with each time component is: $\sigma\tau_1$ = ± 1.3 µs and $\sigma\tau_2$ = ± 2.5 µs.**

The spectral and temporal scans recorded at elevated temperatures are presented in the left and right panels of Figure V.13 respectively. In addition, the resultant fit parameters obtained at each temperature are collected in Table V.2. The observed decay times show little or no change from 10 to 12 K, indicating that the radiative lifetime of the emission has been identified. Correcting the values obtained at 10 K for the effective field[5,6] of the matrix yields excited state lifetimes of 51.0 and 482.0 µs. The shorter component is the same order of magnitude as the gas phase lifetime[4] (21.3 µs) for the Sr: $(5s5p) \, ^3P_1 \rightarrow (5s^2) \, ^1S_0$ atomic transition. An assignment to this transition is therefore proposed. When the sample temperature exceeds 12 K, both decay times of the double exponential fit shorten and the corresponding amplitudes decrease. Inspection of the left panel of Figure V.13 demonstrates that the blue site emission is reduced in intensity, broadened in width and blue-shifted with increasing sample temperature. This effect is reversible indicating that a non-radiative process is competing with the Sr/Xe blue site emission at 791.2 nm.
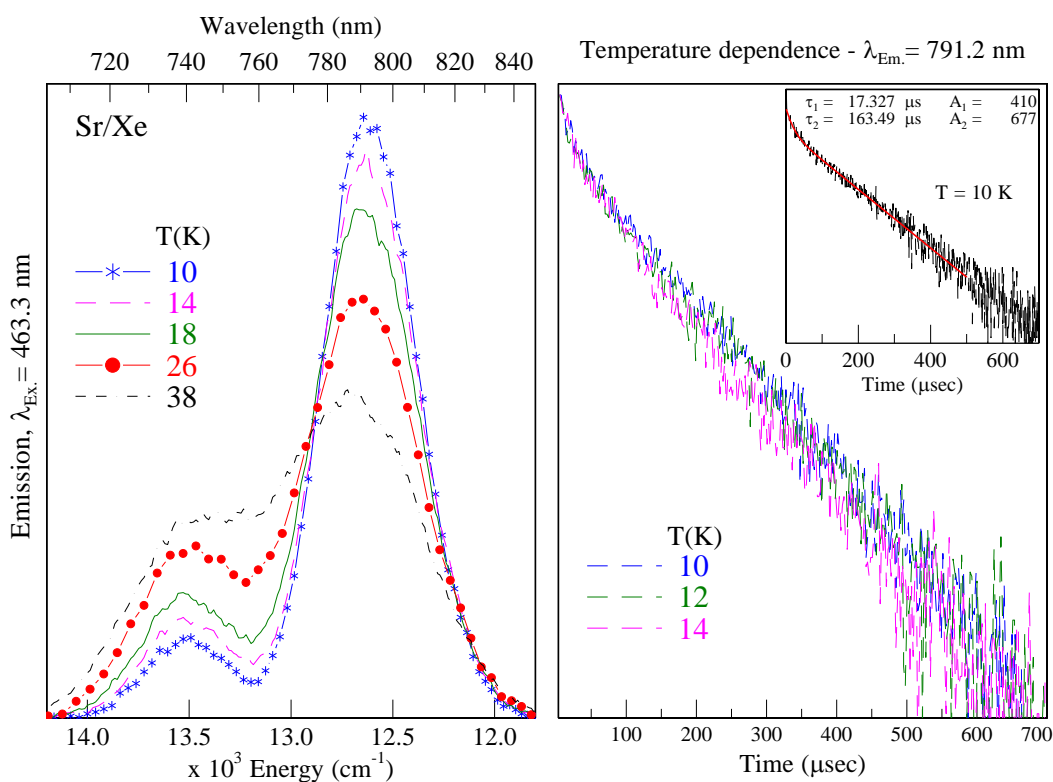

Figure V.13   **The left panel shows the temperature dependence of the Sr/Xe blue site emission band at 791.2 nm over the range 10 – 38 K. The right panel presents the temperature dependence of the decay curves, recorded between 10 and 14 K. The inset of the right panel shows the fit for the decay recorded at 10 K.**

Table V.2   **Temporal characteristics of the Sr/Xe 791.2 nm emission band, recorded over the temperature range of 10 to 26 K.**

T_s (K)	Fit Range (µs)	A_1	τ_1 (µs)	A_2	τ_2 (µs)
10	2 - 500	410	17.3	677	163.5
12	2 - 500	259	17.5	375	162.9
14	2 - 500	238	16.7	365	143.0
26	2 - 350	138	7.1	258	144.6

V.2.II.I.B   Green site

The green site emission occurs at 740.5 nm and exhibits a bandwidth of 499 cm^{-1}. A decay profile recorded at 10 K for this band is presented in Figure V.14. A double exponential function, employing decay times of 6.2 and 110.5 µs with the respective amplitudes of 392 and 341, provides a very good fit.
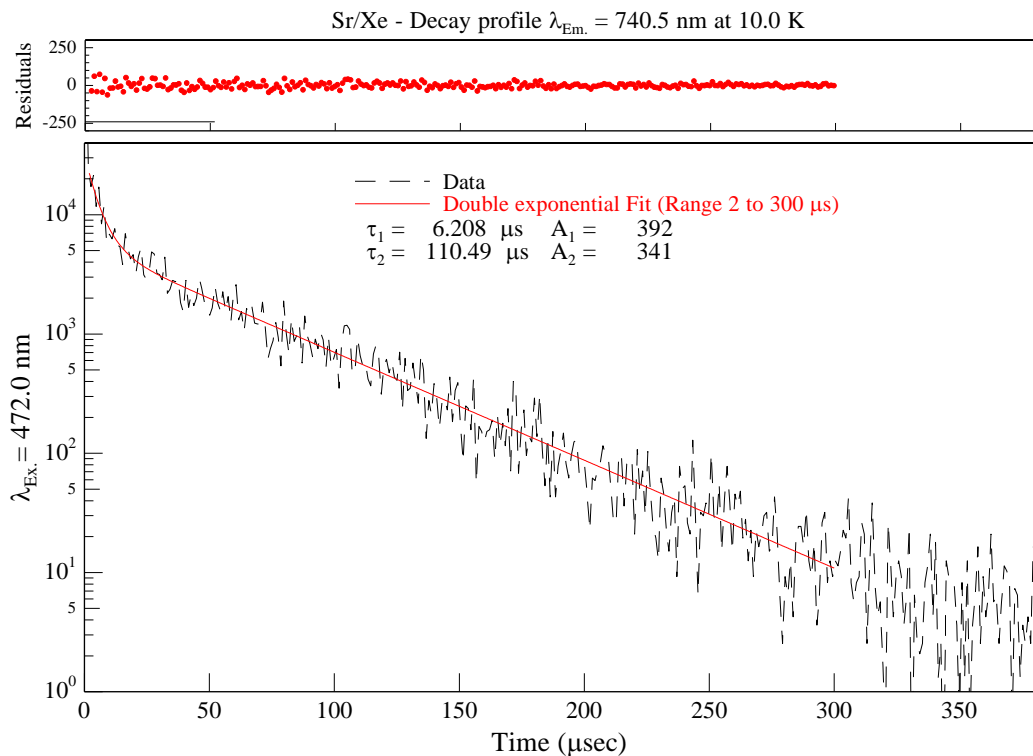
Figure V.14   **Decay profile of the Sr/Xe green site emission band at 740.5 nm, produced by site-selective laser excitation at 472.0 nm and recorded using the multi-channel scaling technique. The residuals present the difference between the double exponential fit and the recorded decay. $\sigma\tau_1 = \pm\ 0.6$ µs and $\sigma\tau_2 = \pm\ 2.5$ µs.**

The temperature dependence of the emission decay profiles is presented in the right panel of Figure V.15. As can be seen, little or no change occurs up to 26 K. Thus, the radiative lifetime of this transition has been recorded. When corrected for the effective

field of the solid, the lifetime values become 18.3 and 325.8 µs. The dominant, shorter component is in excellent agreement with the lifetime of the $(5s5p)\ ^3P_1 \rightarrow (5s^2)\ ^1S_0$ transition of atomic Sr allowing for an assignment to be made.
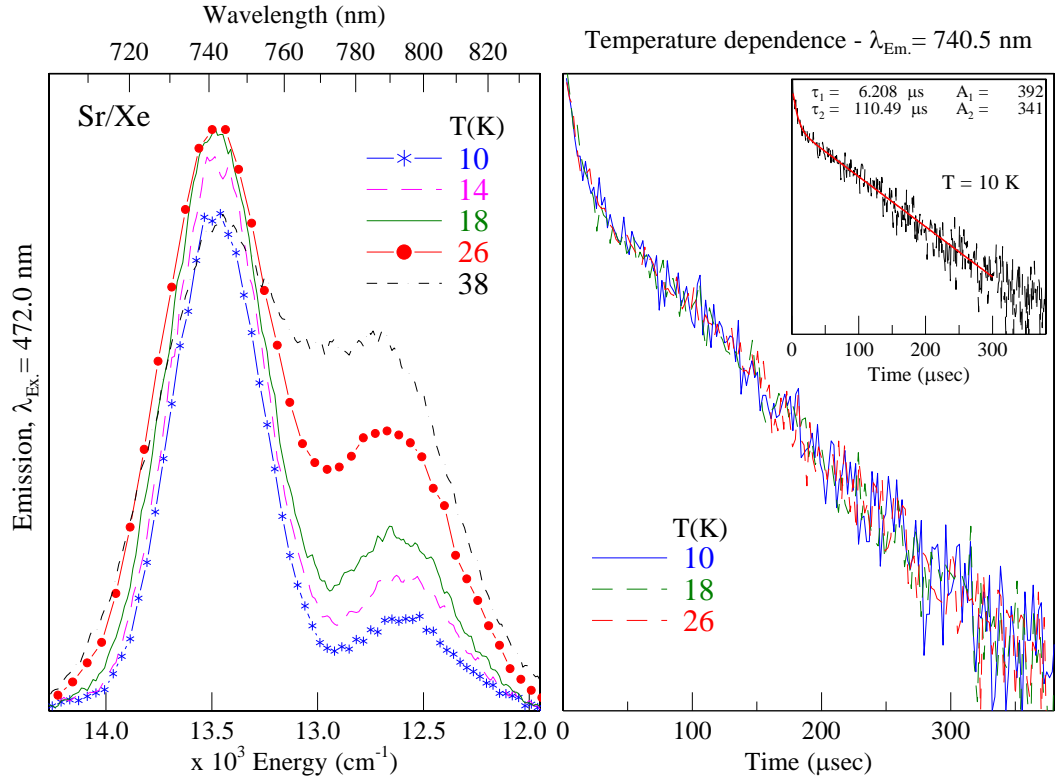

Figure V.15   The left panel shows the temperature dependence of the Sr/Xe green site emission band at 740.5 nm, recorded over the range 10 – 38 K. The right panel presents the temperature dependence of the corresponding decay curves, recorded between 10 and 26 K. The inset of the right panel shows the double exponential fit for the decay recorded at 10 K. It is noteworthy that the blue site emission at 791.2 nm appears to be enhanced at higher temperature. However, a non-radiative step is not the cause of this behaviour. The effect arises due to spectral overlap between the $(5s5p)\ ^1P_1$ absorption profiles of the blue and green sites. As the sample becomes warmer, these profiles become broader and even more overlapped, thereby reducing the site-selectivity of the 472.0 nm excitation wavelength used.

In contrast to the blue site, the spectral scans presented in the right panel of Figure V.15 show that the intensity of 740.5 nm emission increases between 10 and 26 K. Thus, a feeding step from a higher energy state becomes enhanced over this range. Recalling that the intensity and lifetime of the green site emission band at 492.1 nm dramatically decreases at higher temperatures, it is likely that the enhancement of the 740.5 nm feature arises due to an efficient population transfer from the upper $(5s5p)\ ^1P_1$ excited state. However, between 26 and 38 K, the emission intensity actually decreases.

Although not presented, the decays recorded above 26 K become shorter. This behaviour suggests that a non-radiative relaxation pathway to a lower energy level (probably the ground state) has become active over this temperature range and competes with the emission from the $^3P_1$ level. In summary, it appears that two effects lead to the observed temperature dependence. 1. Enhancement of a feeding step from a higher energy excited state, which occurs between 10 and 26 K. 2. A depopulation of the $^3P_1$ state to a lower level by some non-radiative process – this effect becomes significant between 26 and 38 K.

V.2.III   Sr/Xe (5s5p $^1P_1$) luminescence summary

A summary of the luminescence of Sr atoms isolated in the two thermally stable sites in solid Xe is presented in Figure V.16. Dashed vertical lines represent the gas phase position of the assigned electronic transitions. Each trapping site for Sr produced two emission features which occurred at 482.2 and 791.2 nm for the blue site and 492.1 and 740.5 nm for the green site. The higher energy bands were tentatively assigned to the resonance (5s5p) $^1P_1 \rightarrow$ (5s^2) $^1S_0$ electronic transition of atomic Sr, whereas the lower energy bands were assigned to the spin-forbidden (5s5p) $^3P_1 \rightarrow$ (5s^2) $^1S_0$ transition. The spectral and temporal characteristics of these emissions are presented in Table V.3 along with their state assignments. These assignments were made based on each feature's proximity to the corresponding transition in the gas phase and on the lifetime measurements.
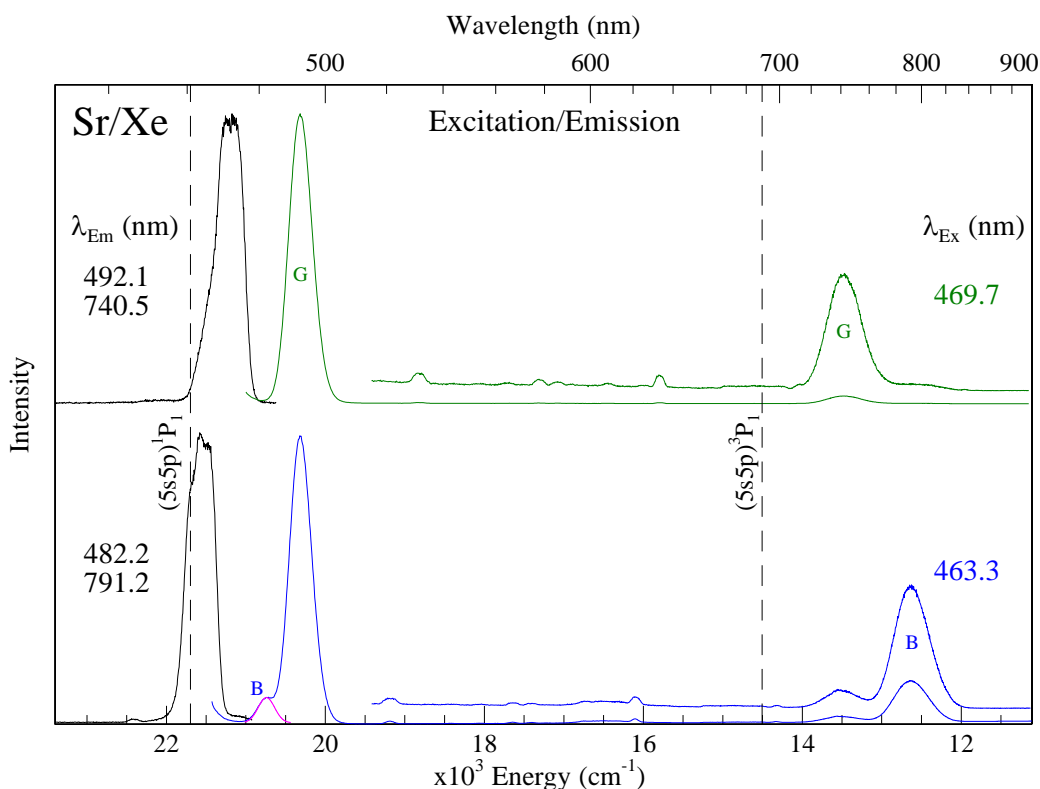
Figure V.16 **A summary of the excitation and emission features arising from the isolation of atomic Sr in the two thermally stable sites of solid Xe. The gas phase positions[4] of the assigned (5s5p) $^1P_1 \to$ (5s^2) $^1S_0$ and (5s5p) $^3P_1 \to$ (5s^2) $^1S_0$ transitions are represented by the dashed vertical lines. A Gaussian fit of the blue site (5s5p) $^1P_1$ emission is represented by the solid pink line.**

Table V.3 **The photophysical characteristics of the thermally stable, site-specific emission features of Sr/Xe, which were obtained with (5s5p) $^1P_1$ excitation. The spectral positions are quoted in both nanometres (nm) and wavenumber (cm^{-1}) units. δ represents the gas phase to matrix frequency shifts, given in wavenumber units. The bandwidth (full width at half maximum, fwhm) is denoted by the symbol Δ and is also expressed in units of wavenumber. The observed lifetimes, recorded in the matrix at 10 K, are listed in the rightmost column.**

Gas Phase[4]	Sr/Xe Site	λ_{em} (nm)	ν (cm^{-1})	δ (cm^{-1})	Δ (cm^{-1})	τ_{obs}
(5s5p)$^1P_1 \to$ (5s5p)$^1S_0$	Blue	482.2	20738	-960	258	< 1 ns
ν = 21698.5 cm^{-1}	Green	492.1	20321	-1377	343	2 ns
τ = 4.98 ns						
(5s5p)$^3P_1 \to$ (5s5p)$^1S_0$	Blue	791.2	12639	-1865	516	17.3 / 163.5 μs
ν = 14505.3 cm^{-1}	Green	740.5	13504	-1000	499	6.2 / 110.5 μs
τ = 21.3 μs						

V.2.IV   Sr/Kr

V.2.IV.I $\lambda_{em} \approx 475$ nm

The 2D-EE spectrum of an annealed Sr/Kr sample is presented in Figure V.17. A cursory inspection reveals that the luminescence of Sr in this host is complex, exhibiting numerous overlapping features, the most prominent of which are labelled I – VII. It is apparent that multiple thermally stable sites of isolation exist for Sr/Kr, even after annealing to 40 K. Further complicating matters, the emission bands in this region occur directly between the $^1P_1$ and $^1D_2$ atomic states, as illustrated by the dashed vertical lines in Figure V.17.
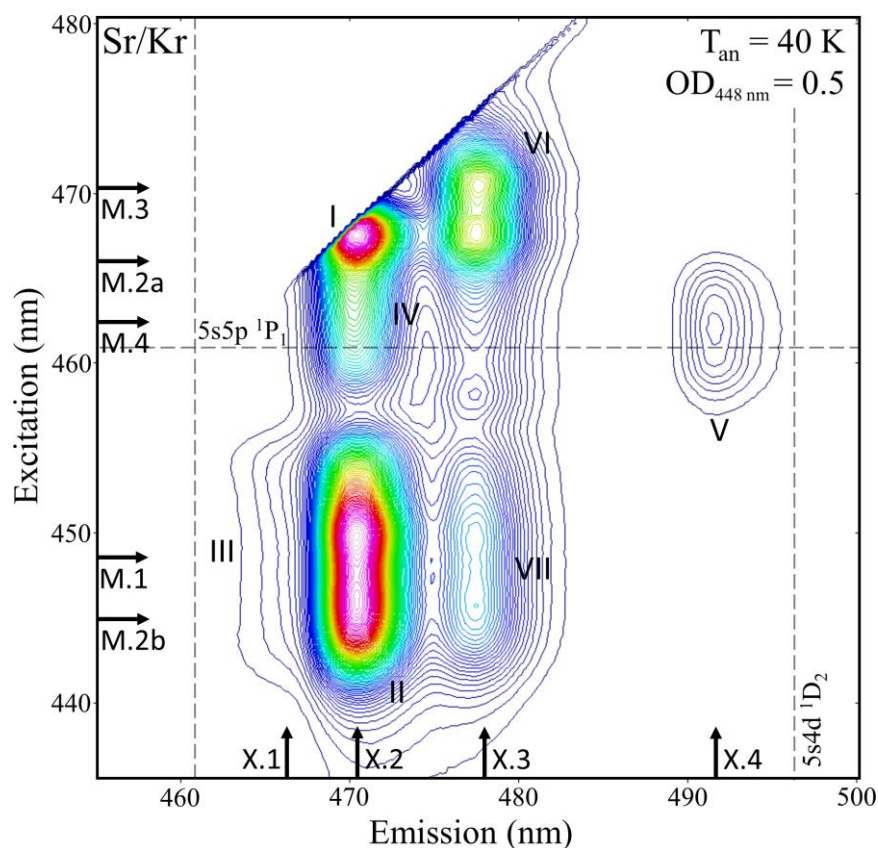
Figure V.17   **2D-EE spectrum of Sr/Kr recorded following sample deposition at 10 K and annealing to 40 K. The optical density (OD) of this sample was measured to be 0.5 at 448 nm. The gas phase position[4] of the resonance (5s5p) $^1P_1 \leftarrow$ (5s^2) $^1S_0$ transition of Sr is shown in emission and excitation. The (5s4d) $^1D_2 \leftarrow$ (5s^2) $^1S_0$ transition is shown in emission only.**

Although the spectrum shown was obtained from a low flux sample, with a low absorption OD (0.5 at 448 nm), the number of emitting sites means that some of the 2D

features are inevitably affected by re-absorption. In an attempt to simplify the situation, a 2D-EE scan was also recorded for a sample with a very low OD of 0.06 at 448 nm. As shown in Figure V.18, this spectrum is simpler as the re-absorbed components are absent. A comparison of the excitation slices (X.1 – X.4) obtained from the two samples is presented in Figure V.19[c].
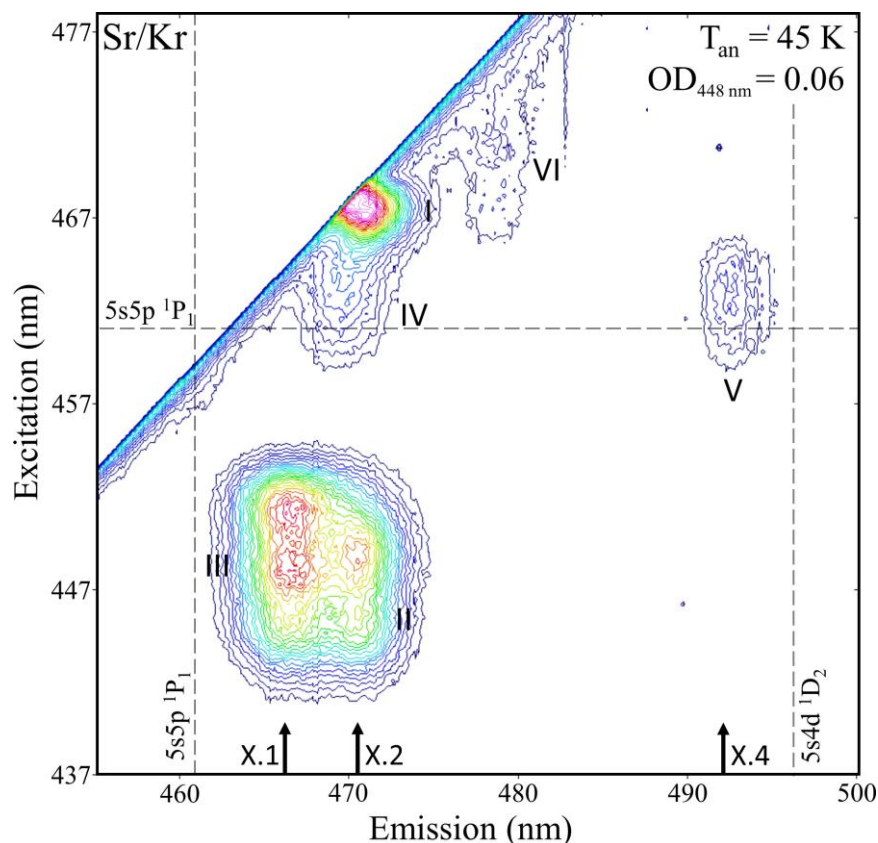

Figure V.18 **2D-EE spectrum of Sr/Kr recorded following sample deposition at 10 K and annealing to a higher temperature of 45 K. The optical density (OD) of this sample was very low, with a value of 0.06 at 448 nm. The gas phase position[4] of the resonance (5s5p) $^1P_1$ ← (5s^2) $^1S_0$ transition of Sr is shown in emission and excitation and the (5s4d) $^1D_2$ ← (5s^2) $^1S_0$ transition is shown in emission only.**

The X.1 excitation scans, shown in blue, are characterised by a fully resolved JT threefold splitting pattern with peaks at 446.2, 448.6 and 451.7 nm. This 'blue site' JT band (III) directly overlaps the dominant absorption feature. Contrasting this, the X.2 scans clearly show an asymmetric threefold split (2+1) composed of a higher energy doublet with peaks at 445.5 and 449.3 (band II) and a lower energy singlet at

---

[c] An X.3 slice, taken from the 2D-EE spectrum (Figure V.18) with a very low OD, is not presented in Figure V.19 because the signal to noise ratio is too low for feature VI in this scan.

467.3 nm (band I). This absorption/excitation structure arises from the occupation of the 'violet' trapping site in solid Kr.

The X.2 scan also reveals the presence of a weak band (IV) at 462.4 nm, occurring to the blue of the violet site singlet. Photoexcitation at this wavelength produces two emission features. The band centred at 470.4 nm directly overlaps the emission of the violet site, which occurs at 470.6 nm.
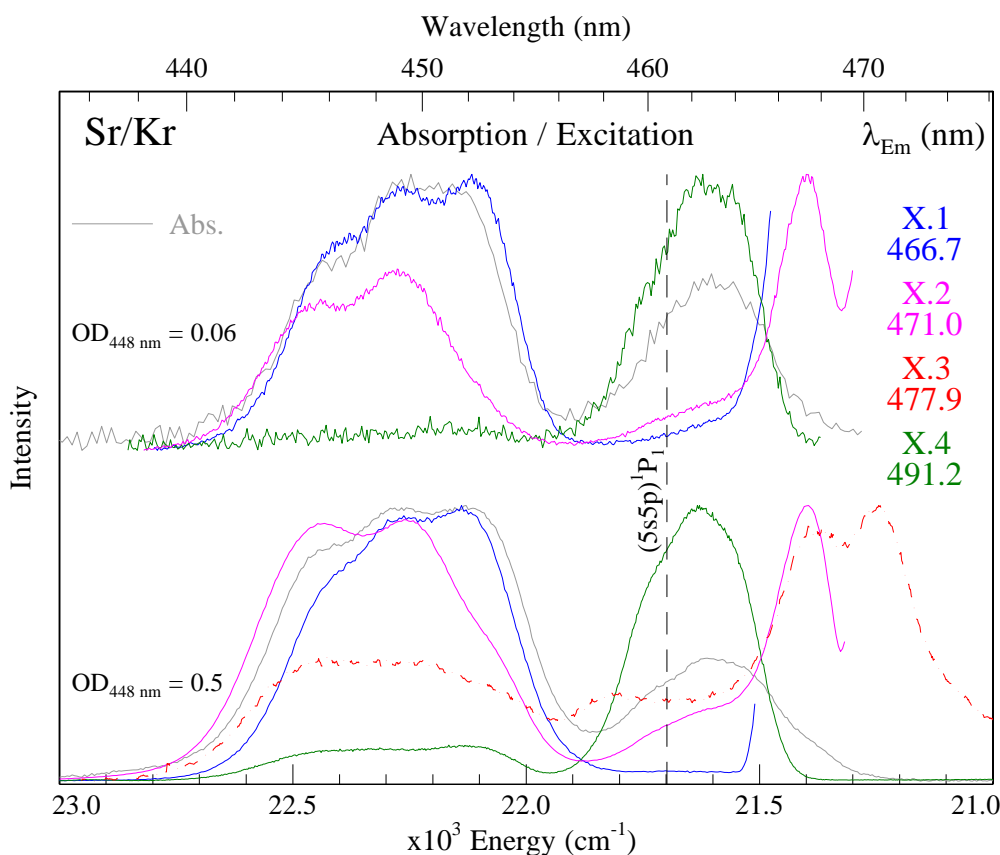
Figure V.19   **Sr/Kr absorption (grey) and excitation spectra (coloured), recorded monitoring the emission features in the 475 and 490 nm spectral regions. The top traces originate from a sample, annealed to 45 K, and characterised by an extremely low absorption OD of 0.06 at 448 nm. The lower traces represent a more absorbing sample with an OD of 0.5 at 448 nm – this deposit was annealed to 40 K. The gas phase position[4] of the resonance (5s5p) $^1P_1 \leftarrow$ (5s^2) $^1S_0$ transition of Sr is shown as a dashed vertical line.**

However the emission band (V) at 491.2 nm is far removed from the rest of the luminescent species and lies very close to the (5s4d) $^1D_2$ atomic state. The excitation scan (X.4) recorded monitoring the lower energy emission, shown in green, is much more discriminating and clearly demonstrates the existence of a distinct site of isolation – the 'green' site. The green site excitation profile overlaps the gas phase (5s5p) $^1P_1 \leftarrow$

$(5s^2)$ $^1S_0$ line and displays a partially resolved threefold split with peaks at 460.5, 462.4 and 464.4 nm. The excitation scan (X.3) of the weak 'red' site of isolation is shown as a dashed red line in the bottom of Figure V.19. This excitation profile is characterised by a doublet structure with peaks at 467.1 and 469.9 nm and a red shoulder at 474.3 nm.

The photophysical properties of the four sites of isolation will now be presented. Although the weakly absorbing Sr/Kr sample yields the simplest luminescence, the poorer S/N ratio precludes the use of this sample in temperature and lifetime investigations. Thus the majority of the emission data now presented was obtained from the more absorbing sample.

V.2.IV.I.A   Blue site

The excitation and emission scans recorded for the blue site of isolation are shown in Figure V.20. The Jahn-Teller excitation band, centred at 448.6 nm, is blue-shifted from the gas phase $(5s5p)$ $^1P_1 \leftarrow (5s^2)$ $^1S_0$ transition by +593 cm^{-1}. A lineshape analysis of this feature is presented in Figure V.115 of Appendix V.I. Three Gaussian curves of equal width (179 cm^{-1}) provide a satisfactory fit. The emission scan (M.1) presented in Figure V.20 was obtained with photoexcitation at 448.6 nm. Atoms isolated in the violet site are also excited at this wavelength. Thus, the emission scan is dominated by an intense violet site band at 470.6 nm. A lineshape analysis of the M.1 profile allows the details of the blue site emission (dashed pink line) to be extracted. Thus, Sr atoms trapped in the blue site emit at 466.7 nm. This emission appears as a resolved shoulder to the blue of the violet site band and is characterised by a bandwidth of 203 cm^{-1} and a Stokes shift of 865 cm^{-1}.
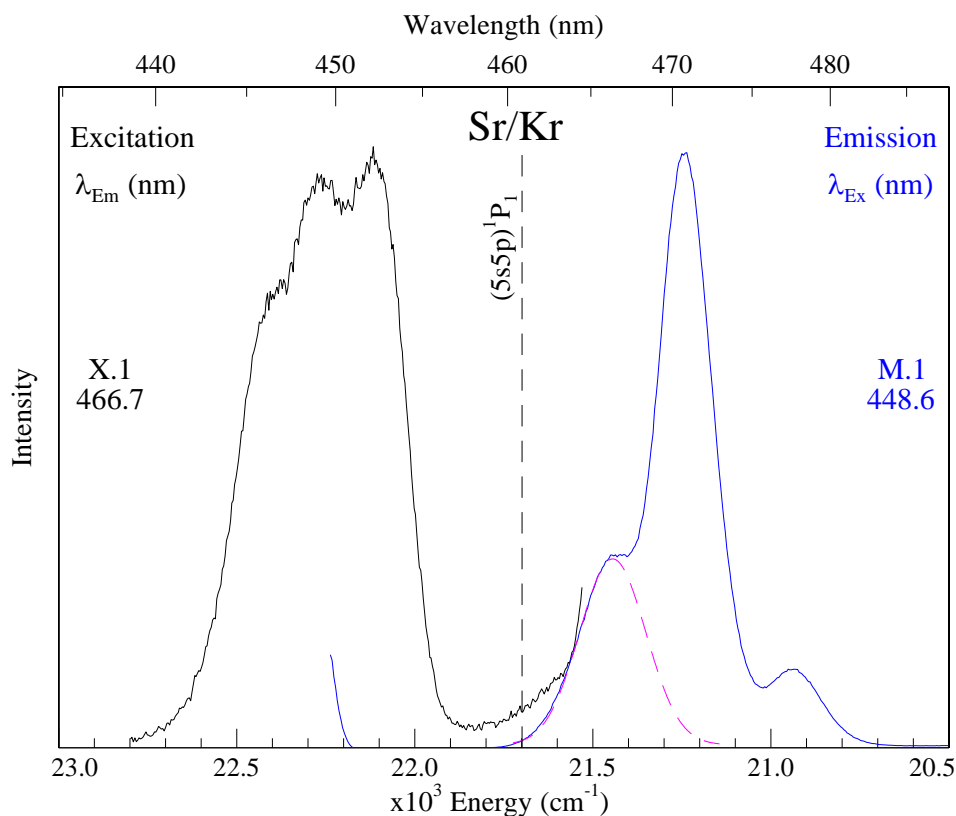
Figure V.20   **Excitation (black) and emission (blue) spectra recorded for the Sr/Kr blue site of isolation, following sample annealing to 45 K. The excitation scan shown was obtained from the weakly absorbing Kr sample because this was the more resolved profile. The gas phase[4] position of the (5s5p) $^1P_1$ state is shown by a dashed vertical line. The Gaussian fit of the blue site emission is represented by the dashed pink line.**

The emission decay profile recorded at 10 K is presented in Figure V.21. The data was well fit with a single exponential function, employing a decay time of 2.6 ns. The temporal profiles recorded over a range of temperatures are presented in the right panel of Figure V.22 and show no change between 10 and 12 K. This implies that the true radiative lifetime has been identified. Applying the effective field correction yields an excited state lifetime of 6.7 ns, allowing a confident assignment to the (5s5p) $^1P_1 \rightarrow$ $(5s^2)$ $^1S_0$ transition of atomic Sr to be made. Above 12 K, the lifetime becomes shortened and a value of 2.3 ns is observed at 30 K. The emission spectral scans recorded over the same temperature range are shown in the left panel of Figure V.22. This study reveals that a gradual decrease in the band intensity occurs as the sample temperature is raised. The temperature effects observed for both the spectral and temporal scans are reversible, implying that a non-radiative relaxation pathway competes with the resonance emission of Sr, when isolated at the blue site in Kr.

Sr/Kr - Decay profile $\lambda_{Em.}$ = 466.7 nm at 10 K
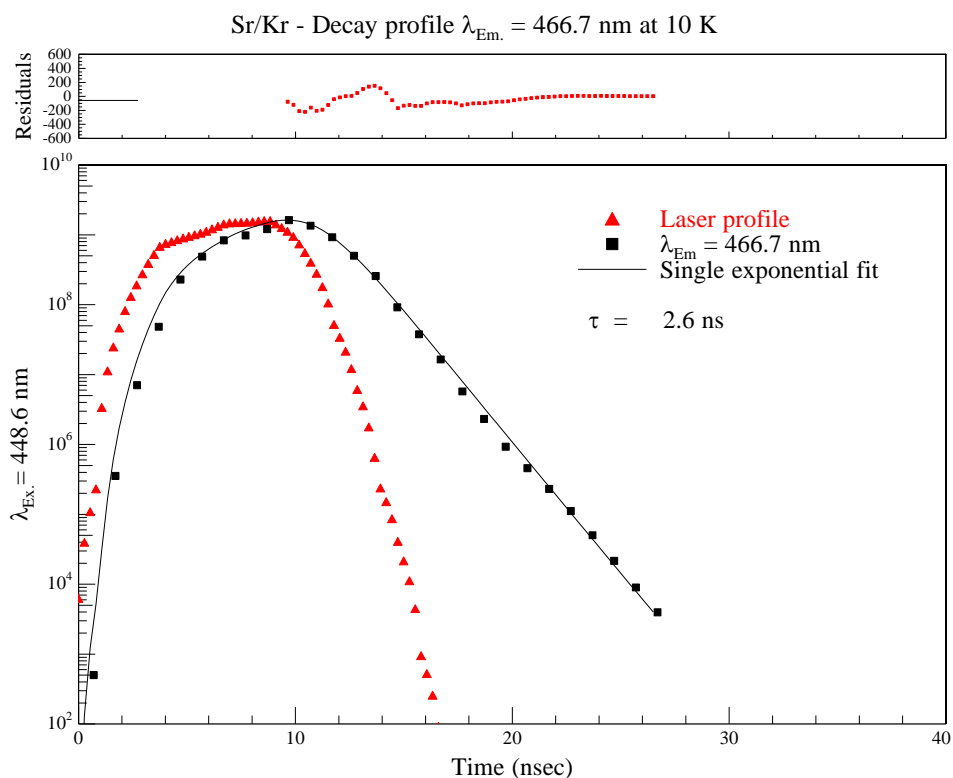
Figure V.21 Decay profile of the Sr/Kr blue site emission band at 466.7 nm, produced by laser excitation at 448.6 nm. An excited state decay time of 2.6 ns is obtained at 10 K with a single exponential trial function.
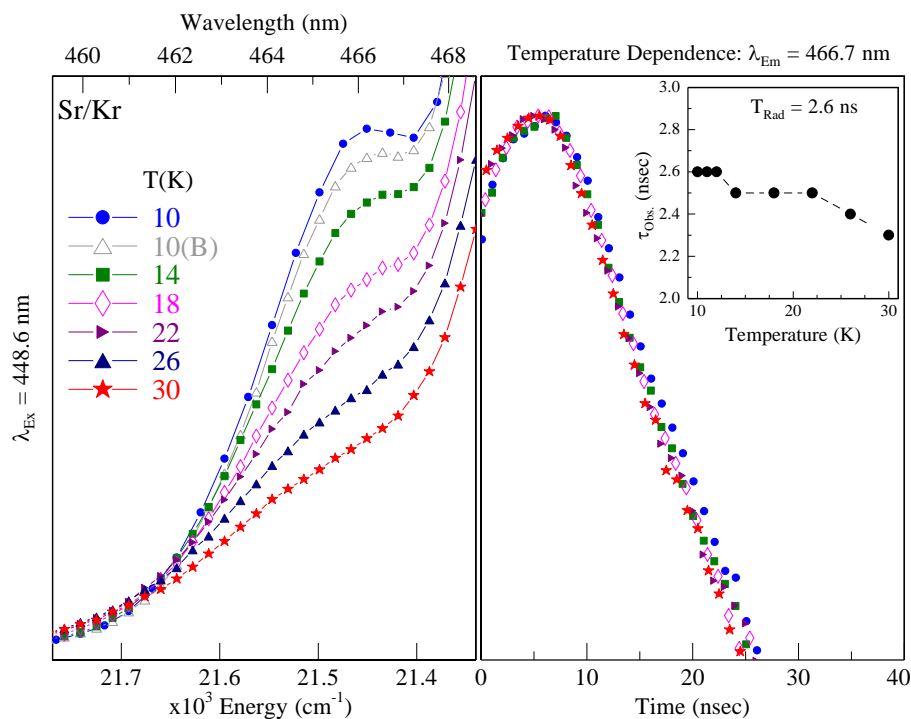
Figure V.22 The left panel shows the temperature dependence of the Sr/Kr blue site emission band at 466.7 nm, recorded over the range 10 – 30 K. The right panel presents the temperature dependence of the corresponding decay curves. The lifetime of the blue site emission is shortened above 12 K.

V.2.IV.I.B   Violet site

The luminescence of the violet trapping site is presented in Figure V.23. The excitation profile is characterised by an asymmetric threefold splitting pattern. The doublet structure is blue-shifted with respect to the gas phase (5s5p) $^1P_1 \leftarrow$ (5s^2) $^1S_0$ line with values of +748 and +744 cm^{-1} evaluated for each peak. In contrast, the singlet exhibits a matrix red-shift of -299 cm^{-1}.
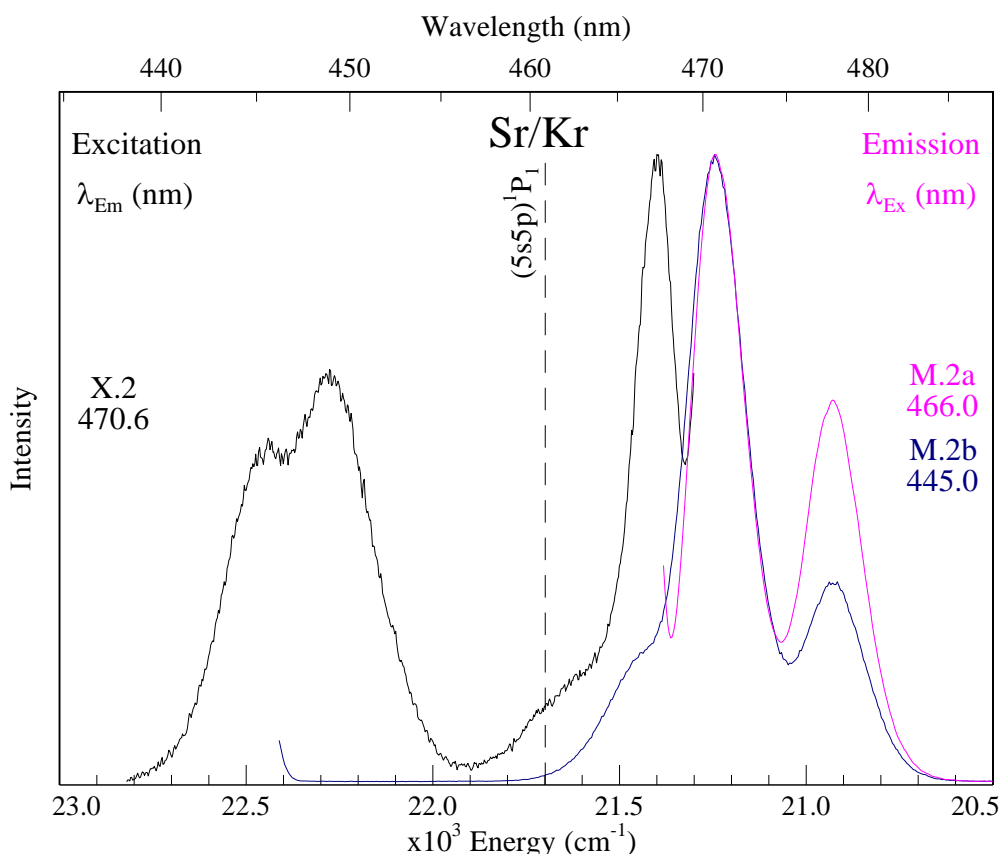
**Figure V.23   Excitation (black) and emission (coloured) spectra recorded for the Sr/Kr violet site of isolation, following sample annealing to 45 K. The excitation scan shown was obtained from the weakly absorbing Kr sample to minimise the contributions from re-absorption. The gas phase[4] position of the (5s5p) $^1P_1$ state is shown by a dashed vertical line.**

The lineshape fit of the 470.6 nm excitation profile is presented in Figure V.116. The two Gaussian curves, labelled 1 and 2 (fwhm = 212 cm^{-1}), account for the resolved peaks of the doublet structure. The singlet is represented by one component, displaying a narrower bandwidth of 139 cm^{-1}.

Photoexcitation of the violet site absorption/excitation peaks produces a bright emission band centred at 470.6 nm exhibiting a fwhm of 184 cm^{-1}, red-shifted with

respect to the (5s5p) $^1P_1$ line by -449 cm^{-1}. The two scans shown in Figure V.23 are obtained by taking horizontal slices through the 2D-EE plot (Figure V.17) at the excitation positions M.2a and M.2b. The decay profile recorded for the 470.6 nm band at 10 K is presented in Figure V.24. A single exponential function with a decay time of 2.8 ns yields a good fit of the time-resolved data.
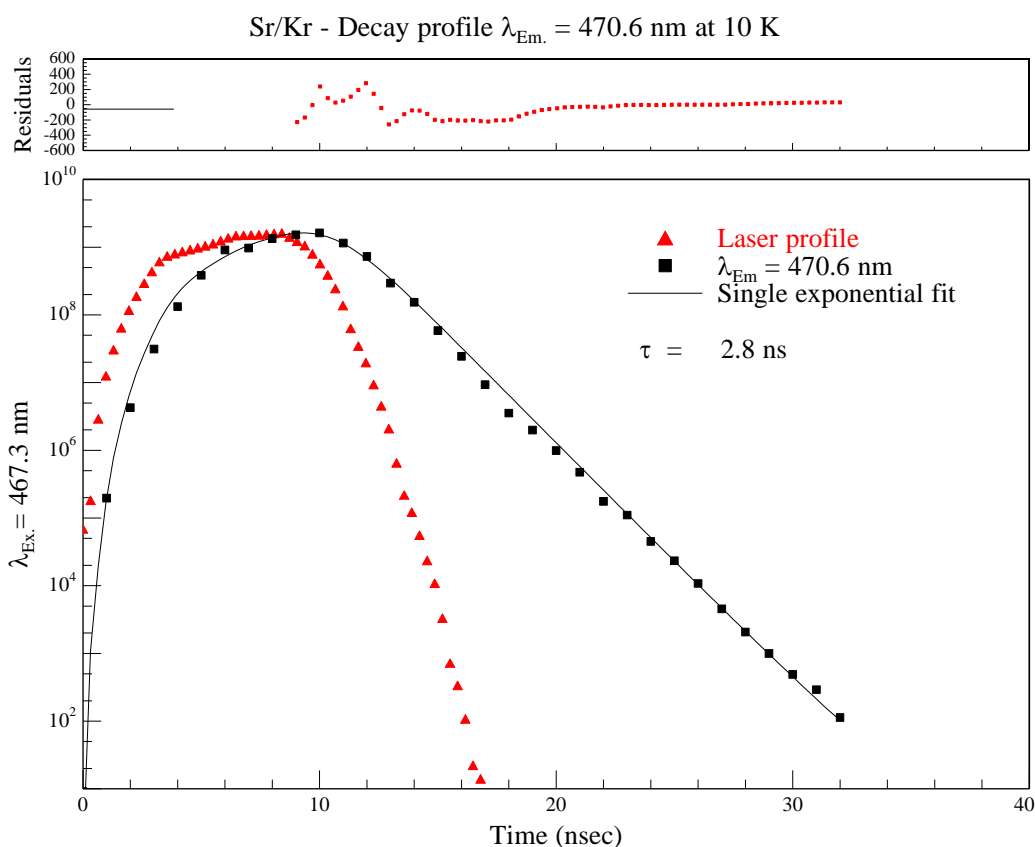
Figure V.24   **Decay profile of the Sr/Kr violet site emission band at 470.6 nm, produced by site-selective laser excitation at 467.3 nm. An excited state decay time of 2.8 ns is obtained at 10 K with a single exponential trial function.**

Inspection of the right panel of Figure V.25 demonstrates that this 2.8 ns decay time represents the radiative lifetime of the violet site emission as the decay profiles do not change between 10 and 30 K. An excited state lifetime of 7.2 ns is obtained by applying the effective field correction. This emission is thereby assigned as resonance (5s5p) $^1P_1 \rightarrow$ (5s^2) $^1S_0$ fluorescence. The invariance of the (5s5p) $^1P_1$ state lifetime to the sample temperature suggests that non-radiative relaxation pathways do not significantly affect the emission of Sr when isolated in the violet site. Conversely, the emission spectral scans presented in the left of Figure V.25 do show a marked temperature dependence. The integrated areas, recorded at each temperature, are

collected in Table V.4. Examination of these values reveals that the overall area is constant from 10 to 14 K – the intensity decrease is compensated by a broadening of the emission bandwidth. At 18 K, the area has been reduced to 83 % of the initial value and is further reduced to 52 % at 30 K. Site interconversion or bleaching effects are likely not responsible for this behaviour because 96 % of the initial emission area is restored following the temperature study.
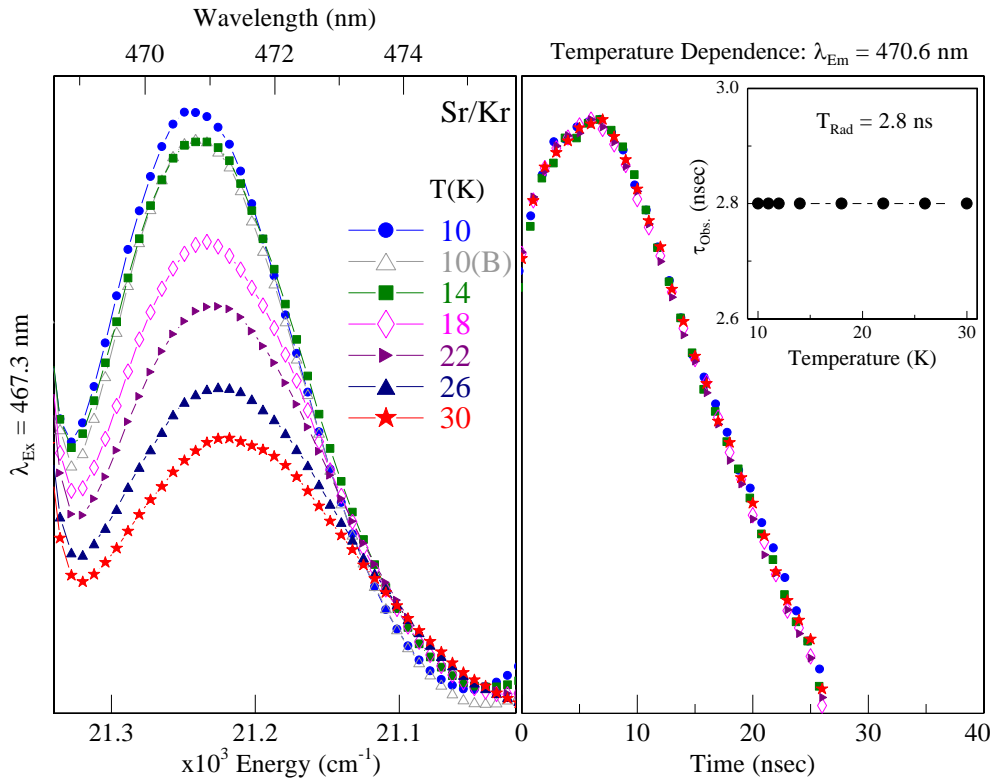
Figure V.25   **The left panel shows the temperature dependence of the Sr/Kr violet site emission band at 470.6 nm recorded over the range 10 – 30 K. The right panel presents the temperature dependence of the corresponding decay curves.**

A possible explanation for this result may be deduced by considering the Ba/Xe violet site excitation spectrum, which was recorded at 35 K and presented in Figure IV.50 of Chapter IV. As the sample temperature increased, the maximum of the Ba/Xe violet site singlet was significantly red-shifted. A similar effect on the Sr/Kr violet site excitation features would account for the reduction of the 470.6 nm emission intensity. As the temperature increases, the maximum of the singlet band is red-shifted away from the 467.3 nm excitation wavelength of the light source, thereby reducing the intensity.

Table V.4   **The integrated area of the Sr/Kr violet site emission (470.6 nm) measured as a function of temperature (in Kelvin). As the emission scans were multi-featured, Gaussian fits were used to extract the integrated areas specific to the violet site. The 10 K scan was normalised and the intensities of the higher temperature scans were scaled relative to this. The integration was evaluated over the spectral range 21000 – 21400 cm⁻¹. The rightmost column shows the integrated area of each scan expressed as a percentage of the integrated area for the original 10 K scan.**

Range :	$21000 – 21400$ cm⁻¹	
Temp (K)	Integrated Area	%
10	144	100
14	144	100
18	120	83
22	108	75
26	87	60
30	75	52
Back to 10	119	96

V.2.IV.I.C   Green site

Emission and excitation spectra recorded for the green site of isolation are presented in Figure V.26. The excitation band is centred at 462.4 nm, overlapping the gas phase $(5s5p)\ ^1P_1 \leftarrow (5s^2)\ ^1S_0$ line of Sr, with a small matrix red-shift of -72 cm⁻¹ evaluated from the band centre. The lineshape analysis conducted on this profile is presented Figure V.117 of Appendix V.I. Three Gaussian functions, each exhibiting a bandwidth of 132 cm⁻¹, accurately reproduce the excitation spectrum.

Two green site emission bands occur in this region, both of which can be obtained by taking a horizontal slice through the 2D-EE spectrum presented in Figure V.17, at the excitation position M.4. The higher energy band is centred 470.4 nm and is characterised by a fwhm of 179 cm⁻¹ and a Stokes shift of 368 cm⁻¹. This emission is strongly overlapped by that of the violet site, however a spectral distinction can be made with site-selective excitation. Indeed, a careful inspection of either Figure V.17 or Figure V.18 (2D-EE spectra) shows that green and violet site emissions are spectrally distinct, with the green site band slightly narrower and blue-shifted relative to the more intense violet site band.

Wavelength (nm)
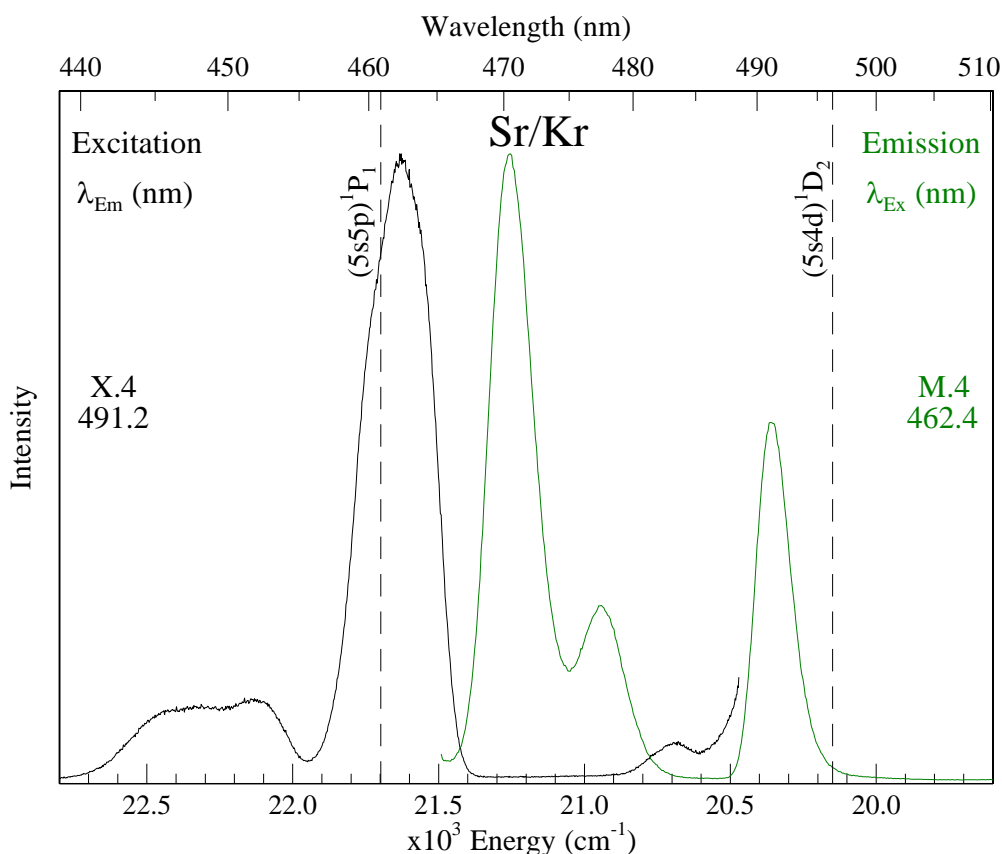
Figure V.26 Excitation (black) and emission (green) spectra recorded for the Sr/Kr green site of isolation, following sample annealing to 45 K. The gas phase[4] positions of the (5s5p) $^1P_1$ and (5s4d) $^1D_2$ states of atomic Sr are shown by dashed vertical lines.

The decay profile of the 470.4 nm emission, recorded at 10 K with excitation at 462.4 nm, is presented in Figure V.27. A single exponential function with a decay time of 3.0 ns accurately fits the decay portion of the data. The decay curves recorded over a range of temperatures are presented in the right panel of Figure V.28. The lifetime of this emission band is constant between 10 and 14 K, so the 3.0 ns value measured at 10 K is identified as the radiative lifetime. Correcting for the effective field of the Kr matrix yields an excited state lifetime of 7.8 ns. This emission band is therefore assigned to the fully allowed (5s5p) $^1P_1 \rightarrow$ (5s^2) $^1S_0$ transition of atomic Sr. Above 14 K, the lifetime values begin to shorten and a value of 2.3 ns is observed at 30 K. Inspection of the spectral scans shown in the right pane of Figure V.28 demonstrates that the emission intensity is greatly diminished with increasing sample temperature. This effect is reversible indicating that a non-radiative relaxation process is activated above 14 K and reduces both the lifetime and intensity of this feature.

Sr/Kr - Decay profile $\lambda_{Em.}$ = 470.4 nm at 10 K
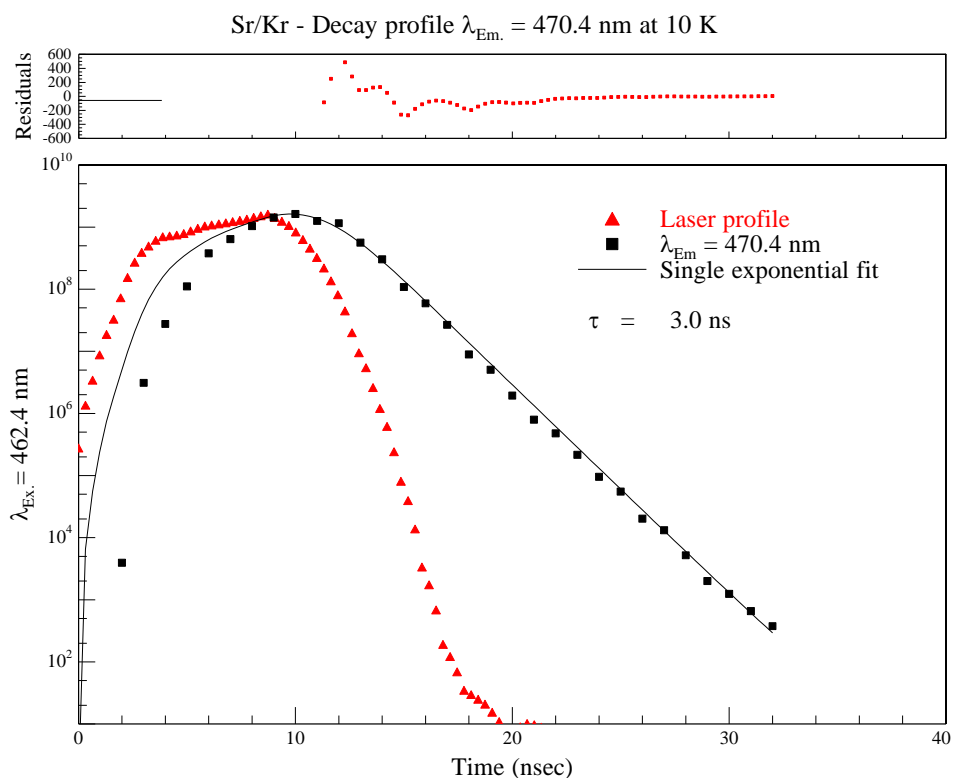
Figure V.27   **Decay profile of the Sr/Kr green site emission band at 470.4 nm, produced by site-selective laser excitation at 462.4 nm. An excited state decay time of 3.0 ns is obtained at 10 K with a single exponential trial function.**

Wavelength (nm)

Temperature Dependence: λ_{Em} = 470.4 nm
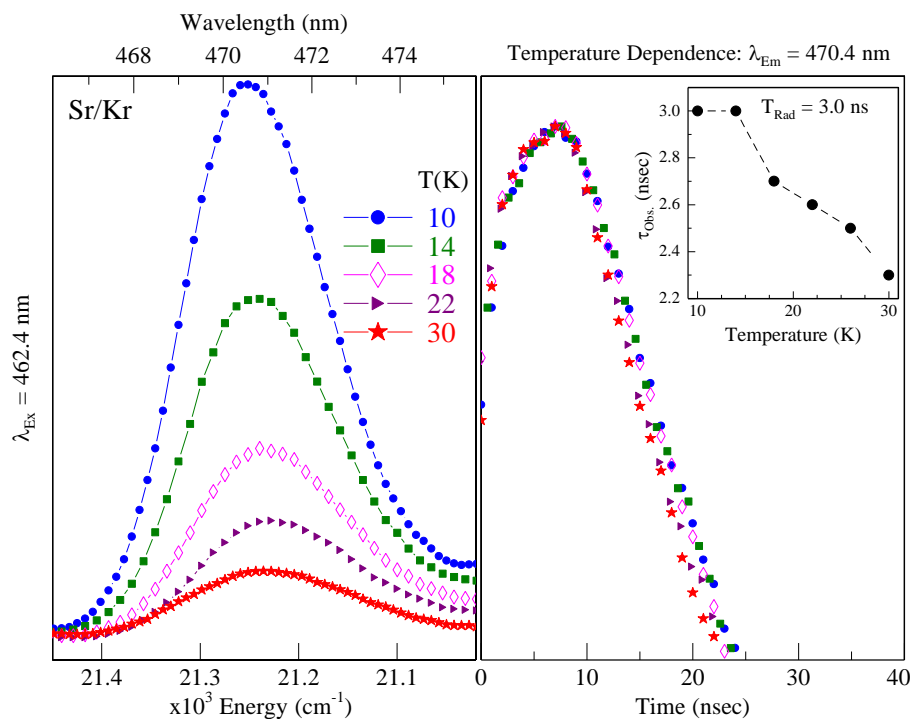
Figure V.28   **The left panel shows the temperature dependence of the Sr/Kr green site emission band at 470.4 nm over the range 10 – 30 K. The right panel presents the temperature dependence of the corresponding decay curves. The lifetime of the blue site emission is shortened at temperatures above 14 K.**

The lower energy green site emission occurring in this region is centred at 491.2 nm. This feature exhibits a narrower bandwidth of 137 cm^{-1} and a greater Stokes shift of 1268 cm^{-1}. Examination of Figure V.26 shows that this band is situated in close proximity to the (5s4d) $^1D_2$ state of Sr which occurs at 496.3 nm in the gas phase[4]. The decay profile, recorded at 10 K with site-selective laser excitation, is shown in Figure V.29. The temporal data is well fit with a single exponential function, employing a decay time of 55.8 ns. The decay curves recorded at higher temperatures are presented in the right panel of Figure V.30. As can be seen, the lifetime is very dependent on the temperature and shortens dramatically between 10 and 12 K.
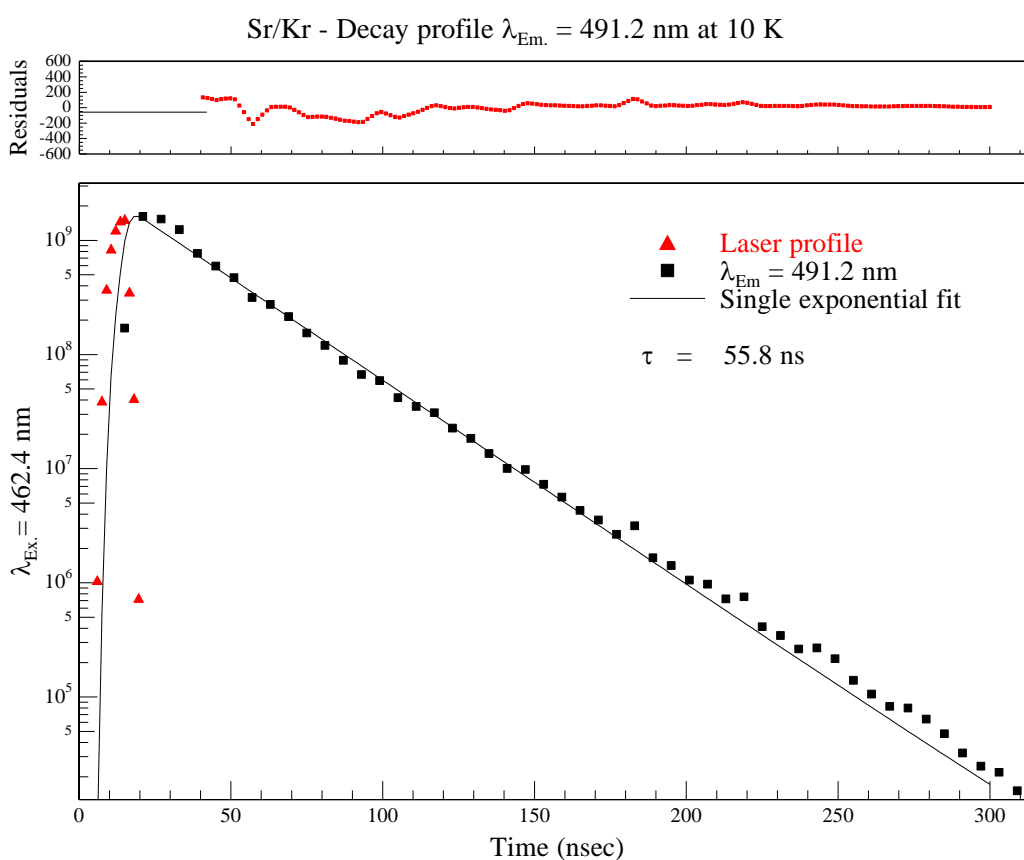

Figure V.29   **Decay profile of the Sr/Kr green site emission band at 491.2 nm, produced by site-selective laser excitation at 462.4 nm. An excited state decay time of 55.8 ns is obtained at 10 K with a single exponential trial function.**

The left panel displays the spectral scans recorded between 10 and 18 K. The emission integrated area is greatly reduced between 10 and 14 K and is completely lost above 18 K. A non-radiative relaxation pathway is competing very efficiently with the 491.2 nm emission and the radiative lifetime has not be identified, even at the low temperature of 10 K. Inspection of Figure V.26 reveals the presence of a weaker excitation band at

483.2 nm which also produces emission at 491.2 nm. Direct laser irradiation of this band yields an excited state lifetime value of 41 ns at 10 K. Unfortunately this value is severely shortened at higher temperatures and the emission band disappears above 14 K. Thus, the radiative lifetime is also not identified with excitation at 483 nm. Nonetheless, a tentative assignment is made to the parity-forbidden (5s4d) $^1D_2 \rightarrow (5s^2)$ $^1S_0$ transition of atomic Sr, based on the observation of narrow emission (491.2 nm) and excitation (483.2 nm) bands which are slightly shifted from the gas phase position of this excited state.
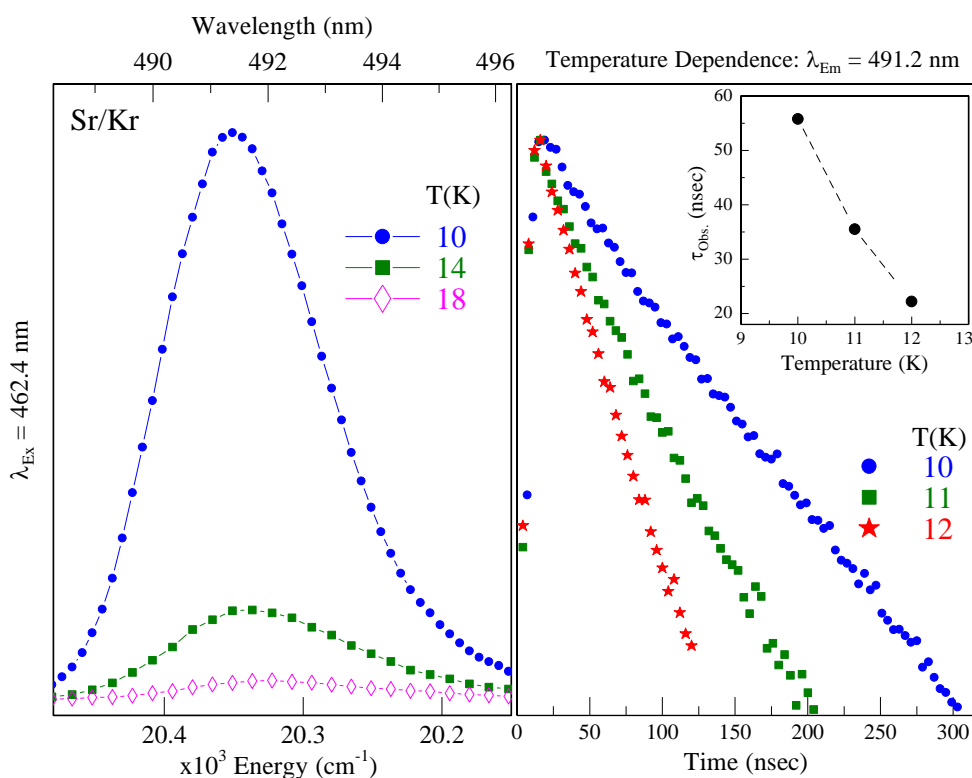
Figure V.30   **The left panel shows the temperature dependence of the Sr/Kr green site emission band at 491.2 nm over the range 10 – 18 K. The right panel presents the temperature dependence of the decay curves recorded between 10 and 12 K.**

V.2.IV.I.D   Red site

Emission and excitation spectra recorded for the relatively weak red site of isolation are presented in Figure V.31. Of the four site-specific emission bands recorded for Sr/Kr, the red site emission is reduced the most with matrix annealing. It is therefore labelled as a partially stable site of isolation and a comparison of the 2D-EE plots presented in Section V.2.IV.I demonstrates that it is greatly reduced between the annealing temperatures of 40 and 45 K. The excitation spectrum is complex and shows intensity across the entire Sr/Kr (5s5p) $^1P_1$ absorption range owing to the effect of re-

absorption. However the lowest energy structures, specifically the peaks at 467.1 and 469.9 nm and a weaker shoulder at 474.3 nm, are proposed to be the 'true' red site absorption profile. A lineshape fit of this portion of the excitation profile is presented in Figure V.118 of Appendix V.I. Three Gaussian curves of near equal bandwidth adequately reproduce the observed splitting pattern. A matrix red-shift of -417 cm^{-1} is determined from the central peak of the threefold split structure.
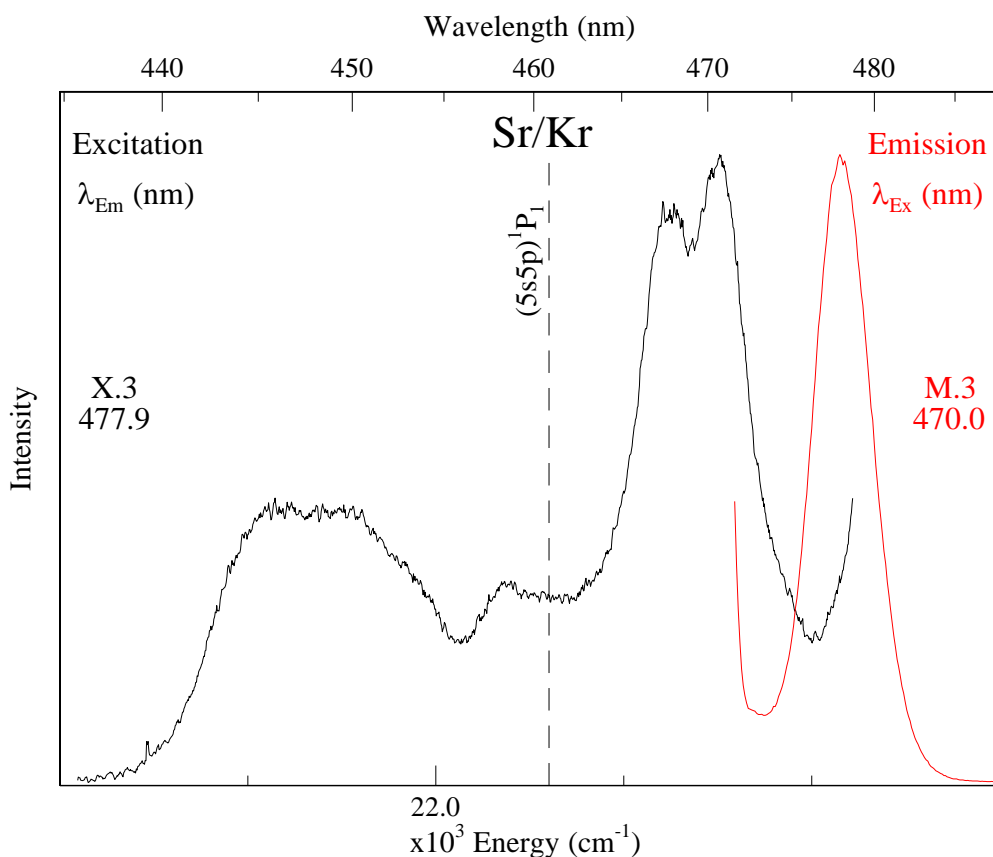
Figure V.31 **Excitation (black) and emission (red) spectra recorded for the Sr/Kr red site of isolation, following sample annealing to 40 K. The gas phase[4] position of the (5s5p) $^1P_1$ state is shown by a dashed vertical line.**

Photoexcitation of the red site absorptions produces an emission band centred at 477.9 nm, displaying a fwhm of 179 cm^{-1}. The emission scan shown in Figure V.31 is equivalent to a horizontal slice through Figure V.17 at M.3. A Stokes shift of 356 cm^{-1} is evaluated from the emission/excitation band centres. A decay profile for this feature, recorded at 10 K with laser excitation at 470.2 nm, is presented in Figure V.32. A lifetime of 2.6 ns is extracted from a single exponential fit of the decay slices. The temperature dependence of the temporal and spectral scans are shown in the right and

left panels of Figure V.33, respectively. The decay profile does not change between 10 and 14 K. Thus the true radiative lifetime has been identified (2.6 ns) corresponding to 6.7 ns when corrected for the field of the surrounding Kr environment. The red site emission at 477.9 nm is confidently assigned to the (5s5p) $^1P_1 \rightarrow$ (5s^2) $^1S_0$ transition of atomic Sr. For temperatures above 14 K, a non-radiative relaxation pathway becomes active, as evidenced by the decrease in both the emission intensity and lifetime values (see the inset of the right panel, Figure V.33).

Sr/Kr - Decay profile $\lambda_{Em.}$ = 477.9 nm at 10 K
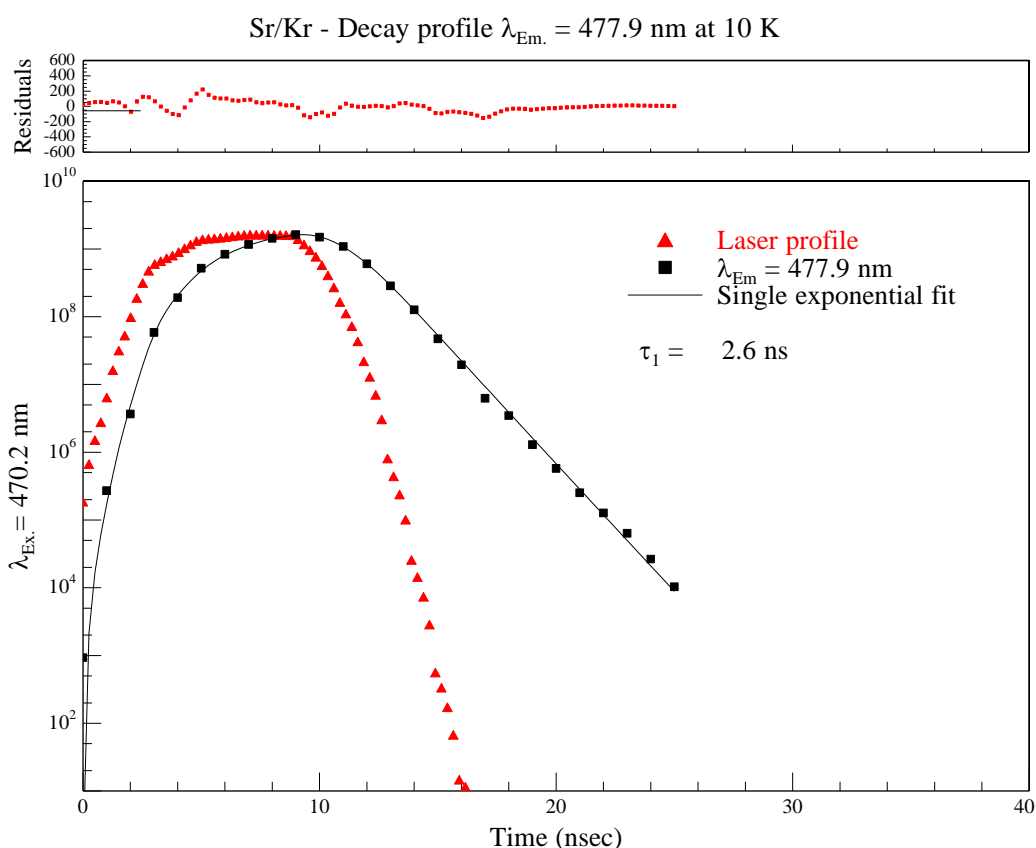
Figure V.32 **Decay profile of the Sr/Kr red site emission band at 477.9 nm, produced by site-selective laser excitation at 470.2 nm. An excited state decay time of 2.6 ns is obtained at 10 K with a single exponential trial function.**
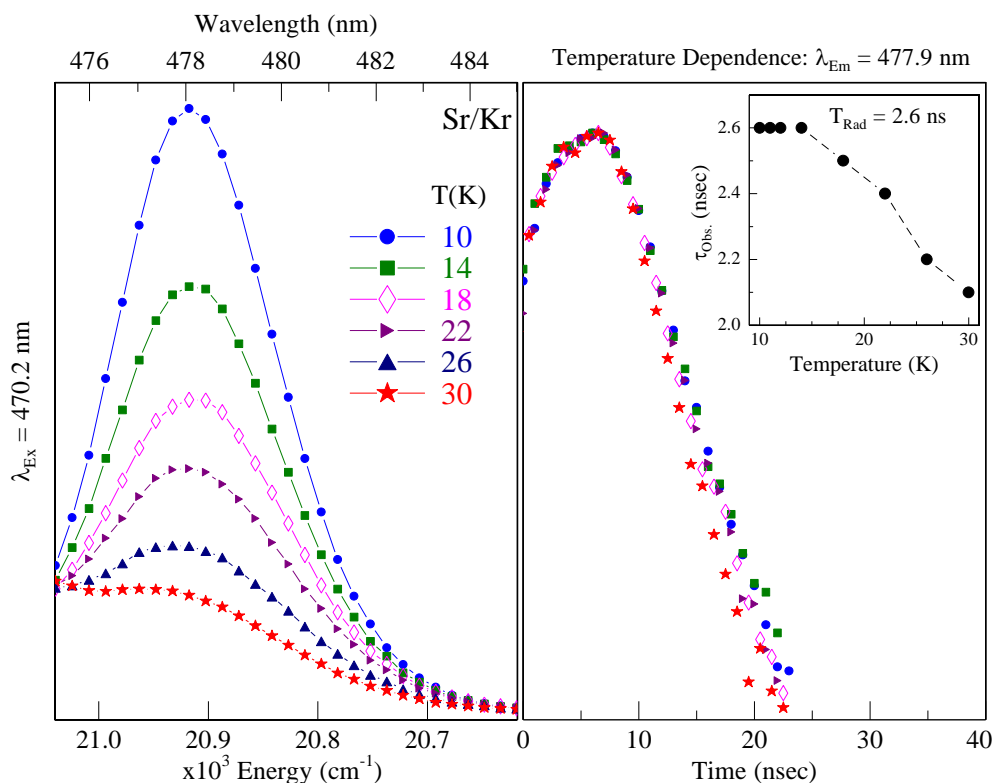
Figure V.33   **The left panel shows the temperature dependence of the Sr/Kr red site emission band at 477.9 nm recorded over the range 10 – 30 K. The right panel presents the temperature dependence of the corresponding decay curves.**

V.2.V Sr/Kr full range emission

The luminescence recorded in the 475 nm spectral region revealed the presence of three thermally stable sites (blue, green and violet) and one partially stable site (red) of isolation for atomic Sr in an annealed Kr matrix. The full range emission scans produced with site-selective excitation of the (5s5p) $^1P_1$ absorption features are presented in Figure V.34. The scans shown for the blue, green and violet sites were obtained from a sample annealed to 45 K. However, to improve the S/N ratio, the red site scan was taken from a sample annealed to 40 K. In addition to the (5s5p) $^1P_1$ band at 466.7 nm, excitation of the blue site JT profile produces emission bands at 575.3 and 727.9 nm. The green site of isolation exhibits the most intense lower energy emission out of the four sites, which is located at 691.7 nm. Excitation of the partially stable red absorption bands at ~ 470 nm yields a very weak emission at 705.4 nm.

In contrast, the violet trapping site does not exhibit any unique lower energy emission bands. The asymmetric band located at 691.7 nm in the violet site scan is

actually a combination of the green site and red site emission features and occurs due to the significant spectral overlap between the absorption peaks of these sites.
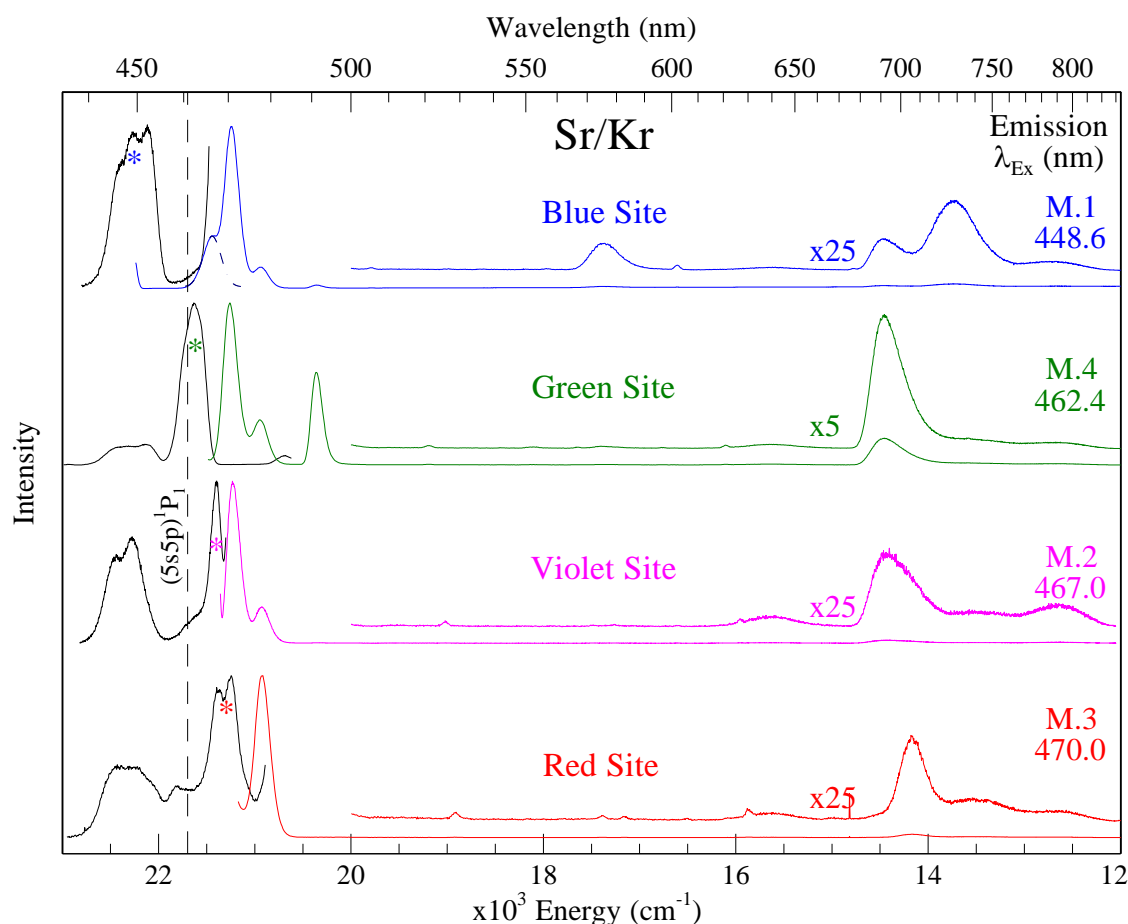
Figure V.34 **Excitation (black) and full range PMT emission spectra (coloured) recorded for Sr/Kr following sample annealing to 45 K. To improve the S/N ratio, the red site emission spectrum was obtained from a sample annealed to the lower temperature of 40 K. The gas phase position[4] of the resonance $(5s5p)\ ^1P_1 \leftarrow (5s^2)\ ^1S_0$ transition of Sr is shown as a dashed vertical line. The asterisks mark the excitation wavelength used to produce each emission scan. A Gaussian fit of the blue site $(5s5p)\ ^1P_1$ emission is represented by the dashed blue line (top traces).**

The photophysical and temporal properties of these lower energy emission features will now be presented, with the main goal being to assign each to a specific electronic transition of Sr.

V.2.V.I   λ_{em} ≈ 575 nm

V.2.V.I.A   Blue site

The blue site emission band centred at 575.3 nm is presented in Figure V.35. The nearby (5s4d) ^3D_J states of atomic Sr are shown by dashed vertical lines.
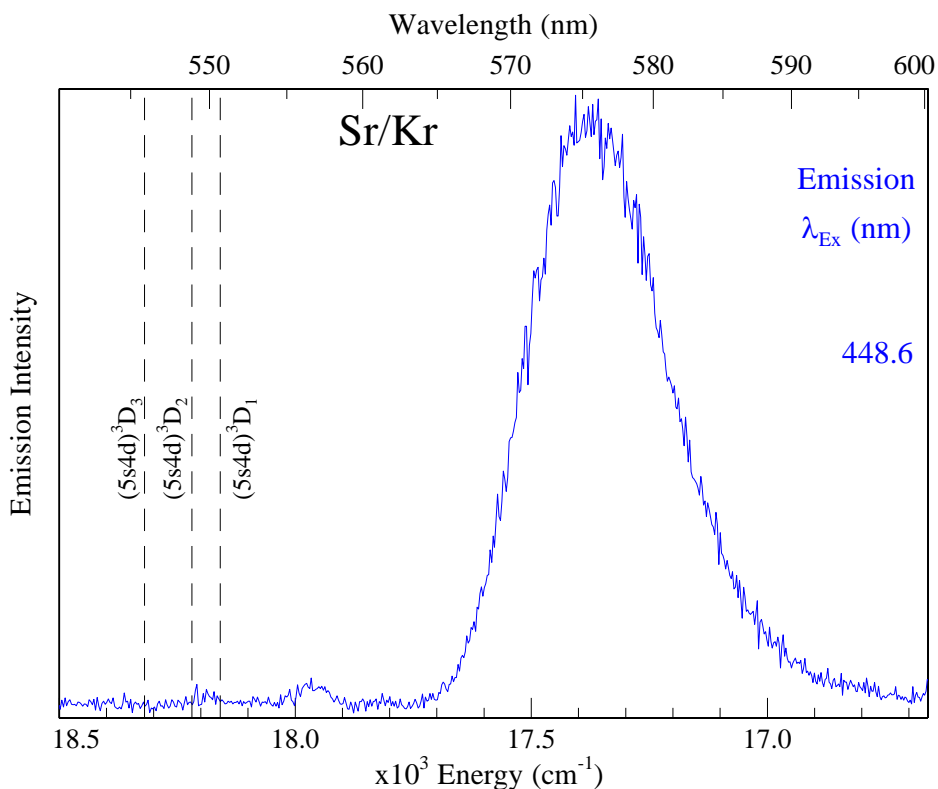
Figure V.35   **Emission spectrum recorded in the 575 nm region with excitation of the blue site at 448.6 nm. The gas phase[4] positions of the (5s4d) ^3D_J states of atomic Sr are shown by dashed vertical lines. The data shown was obtained from a Sr/Kr sample which was annealed to 45 K.**

The emission band is characterised by a fwhm of 370 cm^{-1} and is Stokes shifted from the centre of the JT excitation band by 4909 cm^{-1}. A decay profile, recorded at 10 K using multi-channel scaling, is presented in Figure V.36. A double exponential fit, employing decay times of 1.4 and 0.5 µs with the respective amplitudes of 837 and 685, accurately describes the decay data.
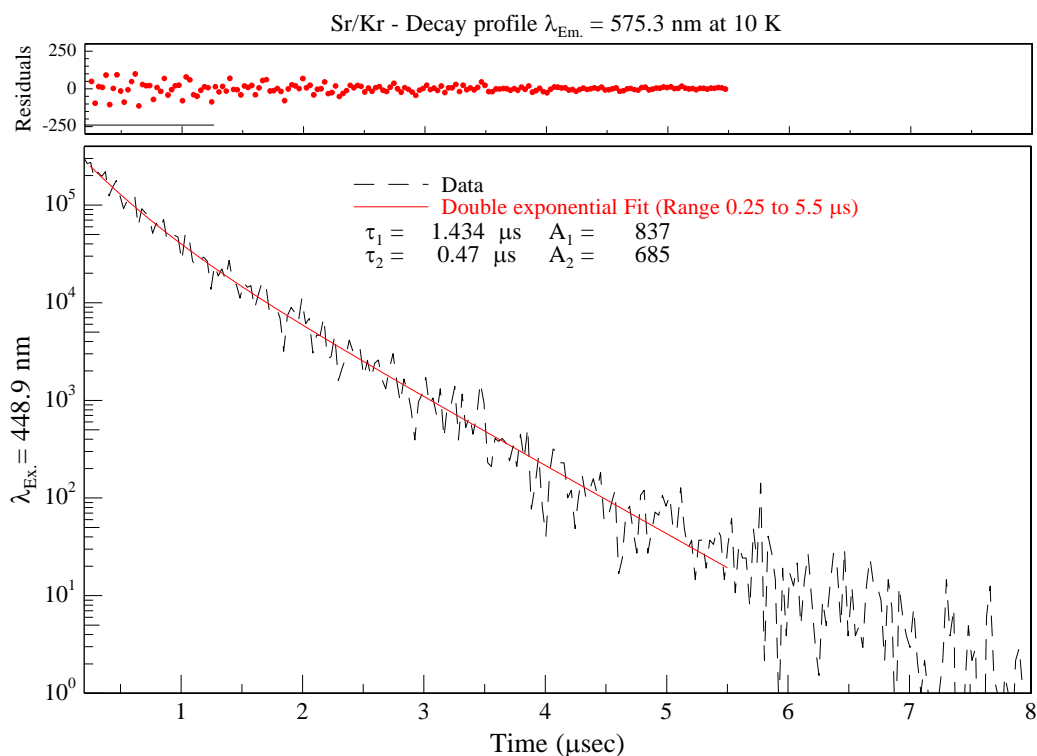
Figure V.36   **Decay profile of the Sr/Kr blue site emission band at 575.3 nm, produced by site-selective laser excitation at 448.9 nm and recorded using the multi-channel scaling technique. The residuals present the difference between the double exponential fit and the recorded decay. $\sigma\tau_1 = \pm 0.1$ µs and $\sigma\tau_2 = \pm 0.1$ µs.**

The temperature dependence of the decay profiles, presented in the right panel of Figure V.37 and collected in Table V.5, reveals that the true radiative lifetime has been obtained because the decay times do not change between 10 and 14 K. Correction for the effective field of the solid yields excited state lifetime values of 3.7 and 1.2 µs. Based on these relatively long-lived values and in the absence of any other atomic levels in this spectral region, the emission band at 575.3 nm is assigned to the (5s4d) $^3D_1 \rightarrow$ (5s^2) $^1S_0$ transition of atomic Sr, exhibiting a matrix red-shift of -777 cm^{-1}. Because the (5s4d) $^3D_J \leftrightarrow$ (5s^2) $^1S_0$ transitions are forbidden in the gas phase, a direct comparison with experimental data cannot be made. Therefore, a conclusive assignment is not possible at the present time. Above 14 K, both lifetime components shorten and the emission spectral scans (left panel of Figure V.37) show a marked decrease in intensity. This behaviour implies that a non-radiative relaxation channel becomes active when the sample temperature is increased.
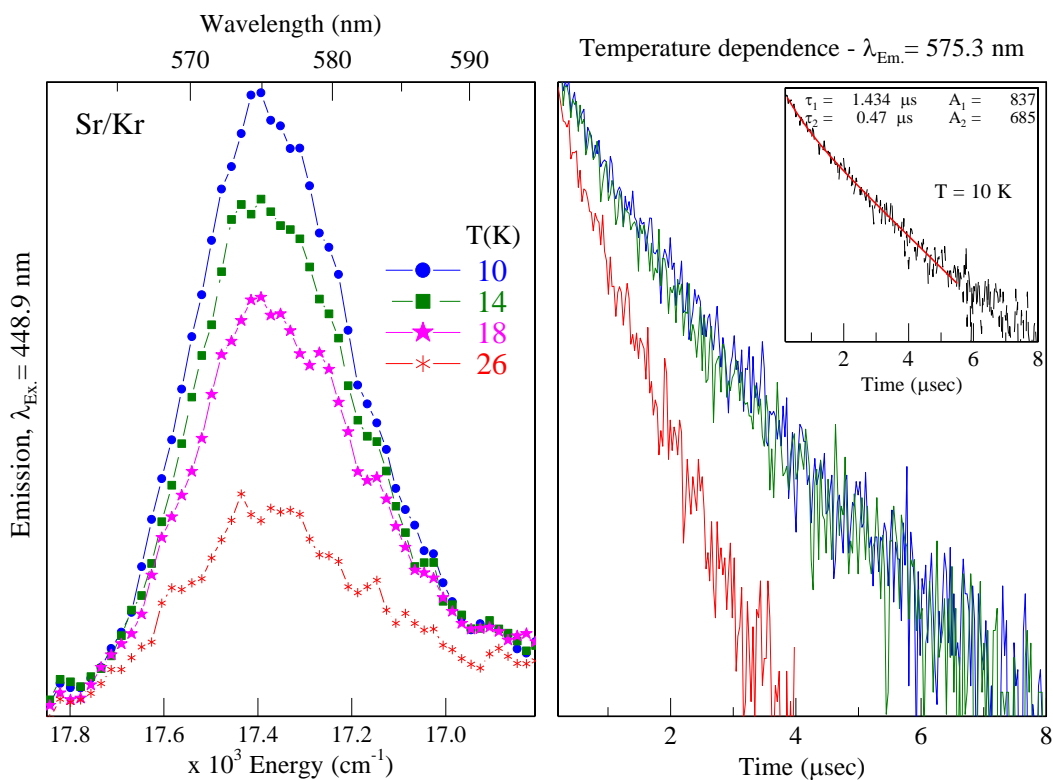
Figure V.37 The left panel shows the temperature dependence of the Sr/Kr blue site emission band at 575.3 nm over the range 10 – 26 K. The right panel presents the temperature dependence of the corresponding decay curves. The inset of the right panel shows the fit for the decay recorded at 10 K.

Table V.5 Temporal characteristics of the Sr/Kr 575.3 nm emission band, recorded over the temperature range of 10 to 26 K.

T_s (K)	Fit Range (µs)	A_1	τ_1 (µs)	A_2	τ_2 (µs)
10	0.25 – 5.5	837	1.4	685	0.47
14	0.25 – 5.5	772	1.4	646	0.47
18	0.3 – 5.0	726	1.2	644	0.26
26	0.3 – 5.0	1082	0.7	1153	0.17

V.2.V.II $\quad \lambda_{em} \approx 710$ nm

An overview of the 710 nm luminescence of an annealed (45 K) Sr/Kr sample is provided by the 2D-EE spectrum in Figure V.38. The main features, labelled I and II, are centred at 691.7/462.4 and 727.9/448.6 nm (emission/excitation) and correspond the green and blue sites of isolation respectively. Band III corresponds to the red site luminescence and is extremely weak in samples annealed to 45 K.
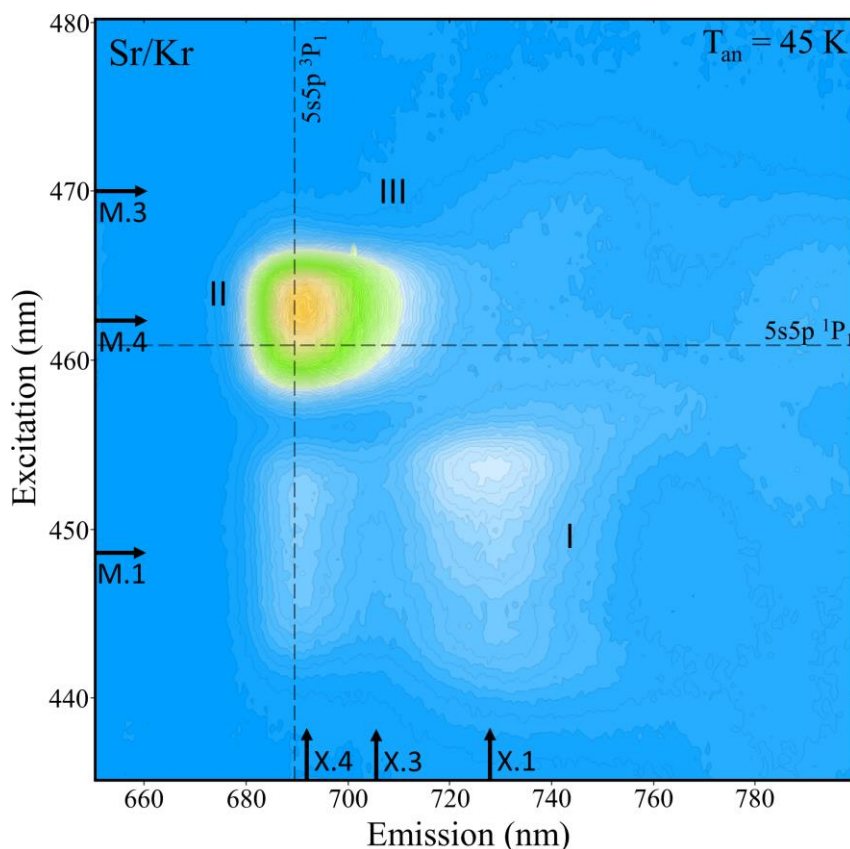
Figure V.38   **Sr/Kr 2D-EE spectrum, recorded in the 710 nm spectral region, following sample deposition at 10 K and annealing to 45 K. The gas phase position[4] of the resonance $(5s5p)$ $^1P_1 \leftarrow (5s^2)$ $^1S_0$ transition of Sr is shown in excitation, represented by a dashed horizontal line. The gas phase position of $(5s5p)$ $^3P_1 \leftarrow (5s^2)$ $^1S_0$ is shown in emission by a dashed vertical line.**

The emission (M.1, M.3 and M.4) and excitation slices (X.1, X.3 and X.4)[d] taken from this plot are presented in Figure V.39. An examination of this figure shows that the 710 nm emission bands are situated close to the $(5s5p)$ ^3P_J states of atomic Sr. Similar to Sr/Xe, the blue site emission band occurs to lower energy than the green site in this

---

[d] The labelling scheme employed for the emission and excitation slices is consistent with the scheme used for the 475 nm region. For example, the slices for the green site are denoted as M.4 and X.4 in both spectral regions.

spectral region and the red site emission is situated between these two features. In contrast to Sr/Xe, the excitation spectra recorded monitoring the 710 nm emission bands are not as resolved as those extracted from the 475 nm features. In particular, the blue site excitation spectrum presented in Figure V.39 is broader when compared to its $^1P_1$ counterpart.
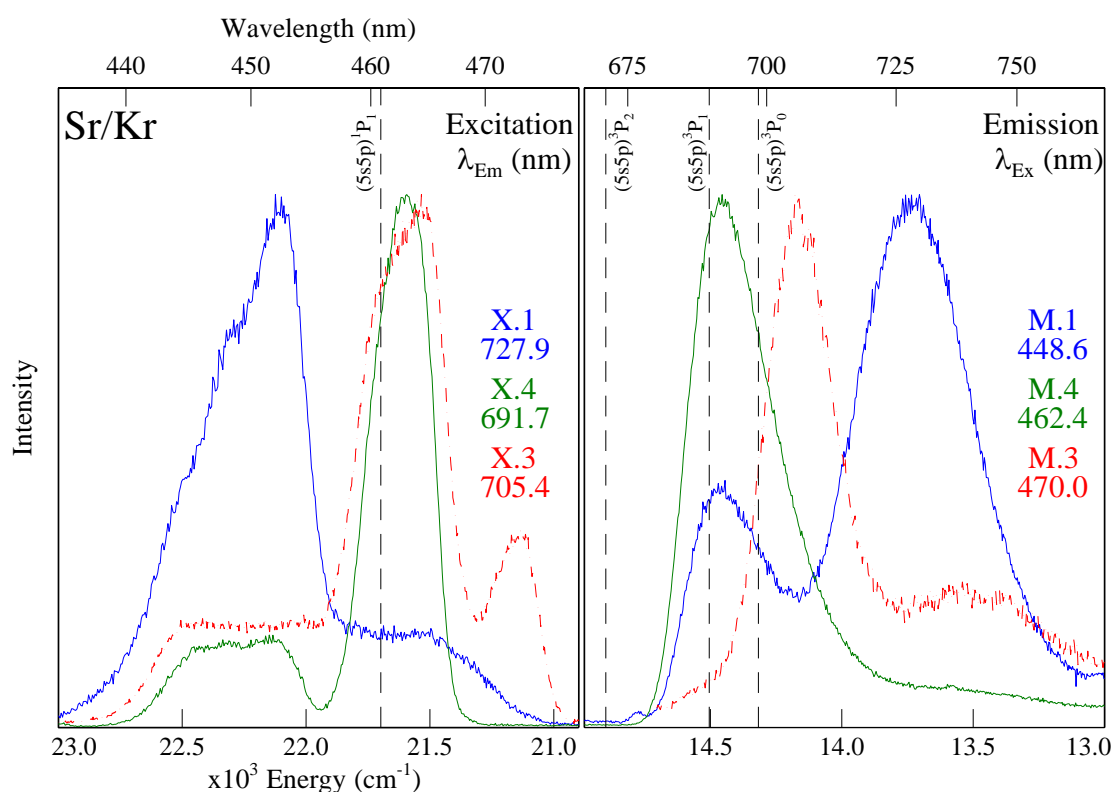
Figure V.39   **Left Panel: blue, green and red site excitation spectra recorded monitoring the lowest energy Sr/Kr emission bands. Right Panel: emission spectra produced with site-selective excitation of the (5s5p) $^1P_1$ features. In emission, the nearby atomic (5s5p) ^3P_J states are shown by dashed vertical lines. The blue and green site scans were acquired from a Sr/Kr sample deposited at 10 K and annealed to 45 K. The red site luminescence was obtained from a sample annealed to 40 K.**

V.2.V.II.A   Blue site

The blue site emission centred at 727.9 nm exhibits a fwhm of 539 cm^{-1}. The 10 K decay profile recorded for this band is presented in Figure V.40 and is satisfactorily fit with a double exponential function. The dominant component consists of a decay time of 6.3 μs with an amplitude value of 6097. The minor component consists of a longer, 70.8 μs, decay time and an amplitude value of 1767. The temperature dependence of the spectral and temporal scans are presented in the left and right panels of Figure V.41, respectively. Inspection of the right panel shows that the overall decay becomes shorter,

even over the small temperature range of 10 to 12 K. The temporal characteristics extracted from the least squares fit of each decay are collected in Table V.6. Examination of these values reveals that the observed shortening is due to the minor component of the double exponential function - the dominant decay time (6.3 µs) shows little or no change between 10 and 14 K. Thus, 6.3 µs is provisionally assigned as the true radiative lifetime.
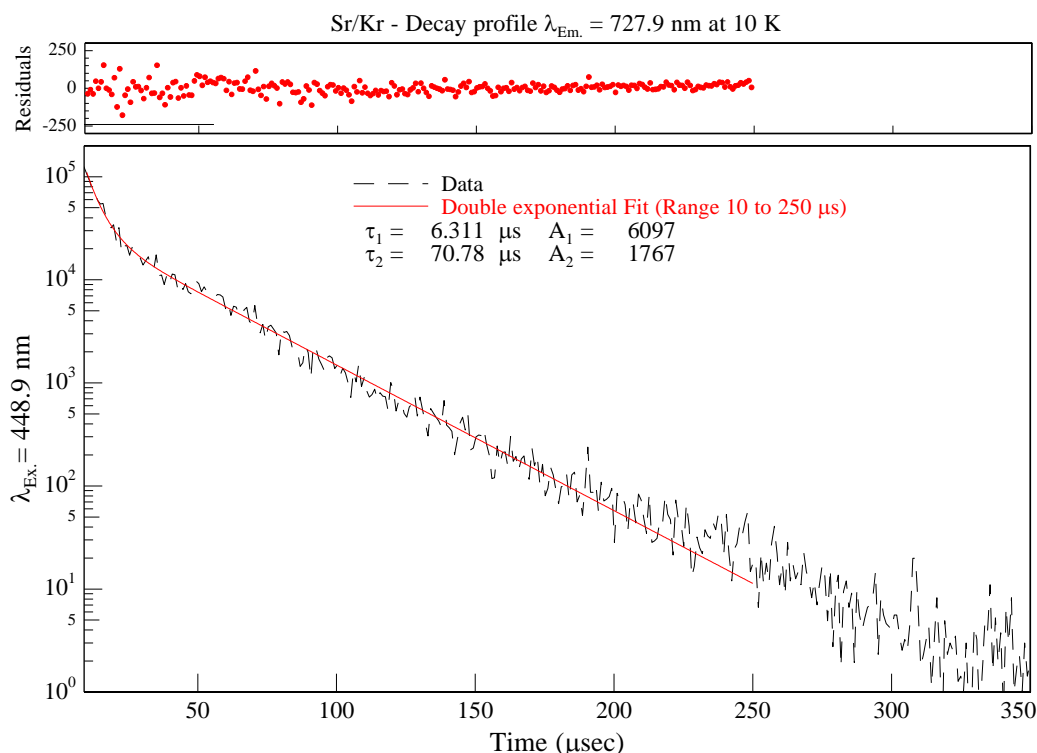
Figure V.40 **Decay profile of the Sr/Kr blue site emission band at 727.9 nm, produced by site-selective laser excitation at 448.9 nm and recorded using the multi-channel scaler. $\sigma\tau_1 = \pm 0.3$ µs and $\sigma\tau_2 = \pm 1.1$ µs.**

Table V.6 **Temporal characteristics of the Sr/Kr 727.9 nm emission band, recorded over the temperature range of 10 to 26 K.**

T_s (K)	Fit Range (µs)	A_1	τ_1 (µs)	A_2	τ_2 (µs)
10	10 – 250	6097	6.3	1767	70.8
12	10 – 200	1842	6.3	643	54.5
14	10 – 200	2303	6.2	578	58.6
26	10 – 150	5052	4.7	898	44.5
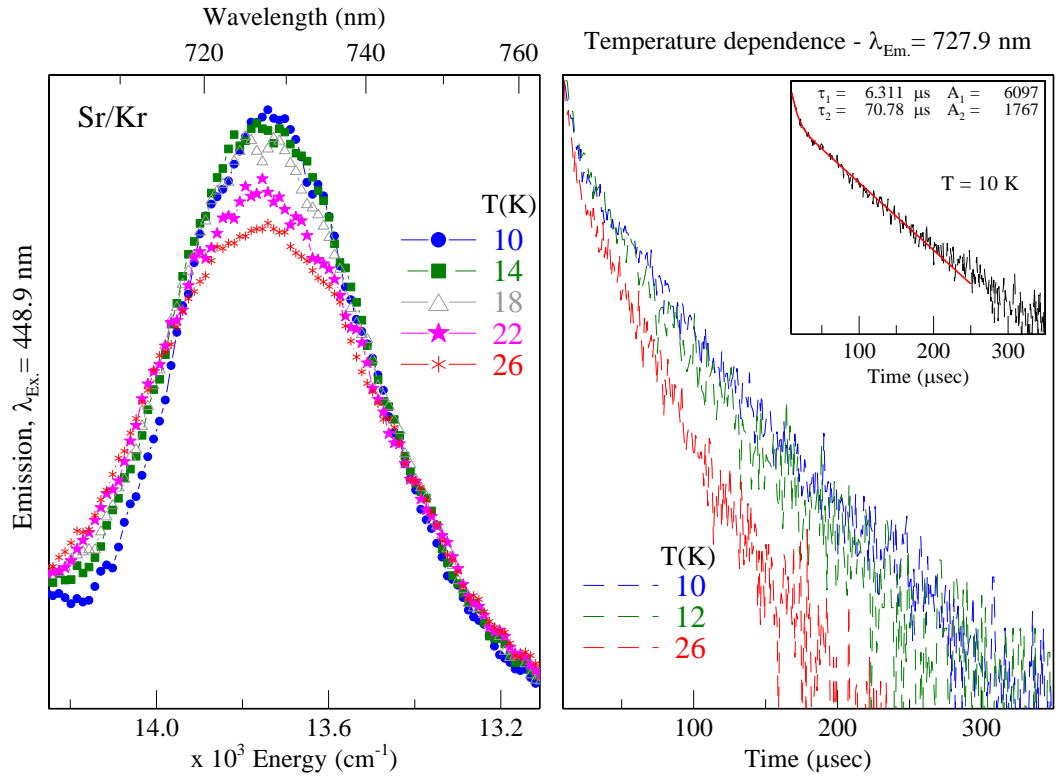
Figure V.41   **The left panel shows the temperature dependence of the Sr/Kr blue site emission band at 727.9 nm recorded over the range 10 – 26 K. The right panel presents the temperature dependence of the corresponding decay curves, recorded at 10, 12 and 26 K. The inset of the right panel shows the double exponential fit for the decay recorded at 10 K.**

Correcting for the effective field of the solid yields an excited state lifetime value of 16.3 µs, in good agreement with the gas phase lifetime[4] (21.3 µs) for the Sr: $(5s5p)\ ^3P_1 \rightarrow (5s^2)\ ^1S_0$ atomic transition. The blue site emission band at 727.9 nm is therefore assigned to this transition. The spectral scans provided in the right of Figure V.41 show that the emission intensity decreases by only a small amount over the temperature range investigated. In addition, the emission is noticeably broadened and slightly blue-shifted at elevated temperatures. Between 14 and 26 K, both lifetime components become shorter, indicating that a non-radiative relaxation pathway is competing with emission from this state.

V.2.V.II.B   Green site

The emission band, produced by Sr atoms isolated in the green site, is centred at 691.7 nm. A decay profile measured for this emission feature is presented in Figure V.42 and is well fit with a triple exponential function. Decay times of 8.7, 213.1 and 833.0 µs

are extracted from the fit, along with the respective amplitudes of 1151, 568 and 774. The temperature dependence of the spectral and temporal scans are presented in Figure V.43. As can be seen in the right panel, the decay profiles exhibit a dramatic shortening from 10 to 26 K. A triple exponential function was fitted to the decay at each temperature, the results of which are collated in Table V.7. Inspection of these values shows that the dominant component (τ_1) changes very little from 10 to 22 K.
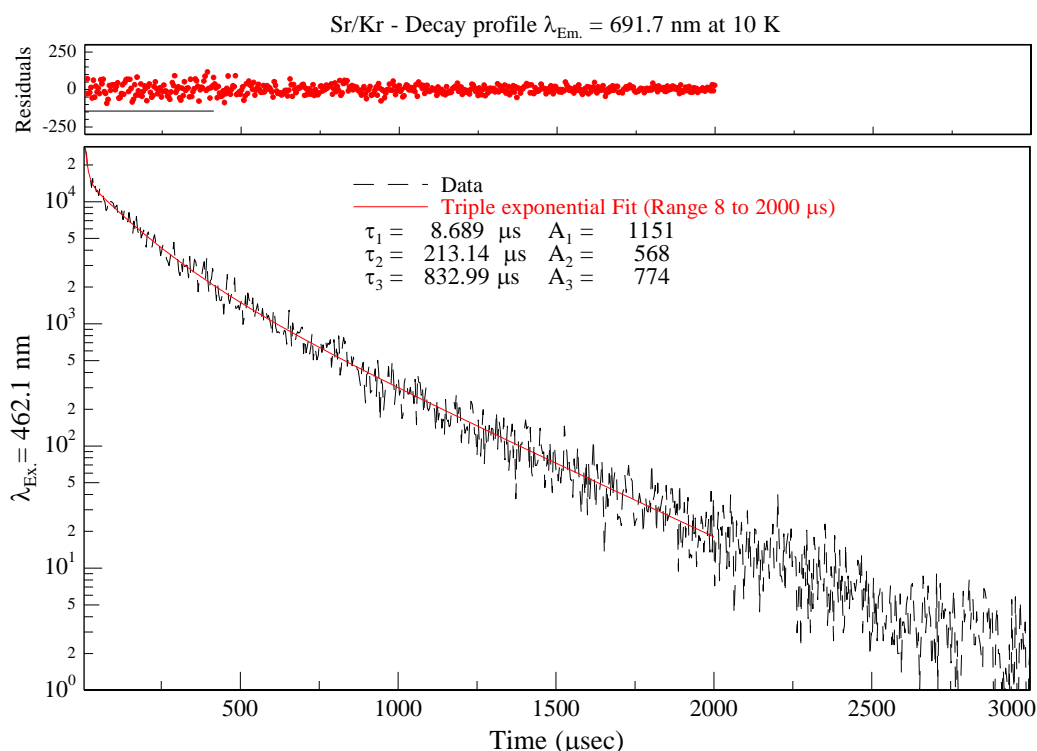

Figure V.42 **Decay profile of the Sr/Kr green site emission band at 691.7 nm, produced by site-selective laser excitation at 462.1 nm and recorded using the multi-channel scaler. $\sigma\tau_1 = \pm 1.4$ µs, $\sigma\tau_2 = \pm 10.6$ µs and $\sigma\tau_3 = \pm 28.4$ µs.**

As with the Sr/Kr blue site emission band, it is proposed that the shorter and dominant component of the fit represents the radiative lifetime. Correcting this value for the effective field of the solid leads to an excited state lifetime of 22.5 µs, in excellent agreement with the gas phase lifetime for the $(5s5p)\,^3P_1 \to (5s^2)\,^1S_0$ transition of atomic Sr. Based on this evidence, the Sr/Kr emission band at 691.7 nm is assigned to this electronic transition.

In contrast to τ_1, the minor components of the decay (τ_2 and τ_3) are shortened at higher temperatures and, in particular, the amplitude of the third component is vastly reduced. Examination of the spectral scans shown in the left panel of Figure V.43

reveals that the emission intensity gradually decreases and the band centre is slightly shifted to lower energies, as the sample becomes warmer. The temperature dependence of the temporal and spectral scans suggests that a non-radiative relaxation to a lower electronic state competes with the emission from this level.
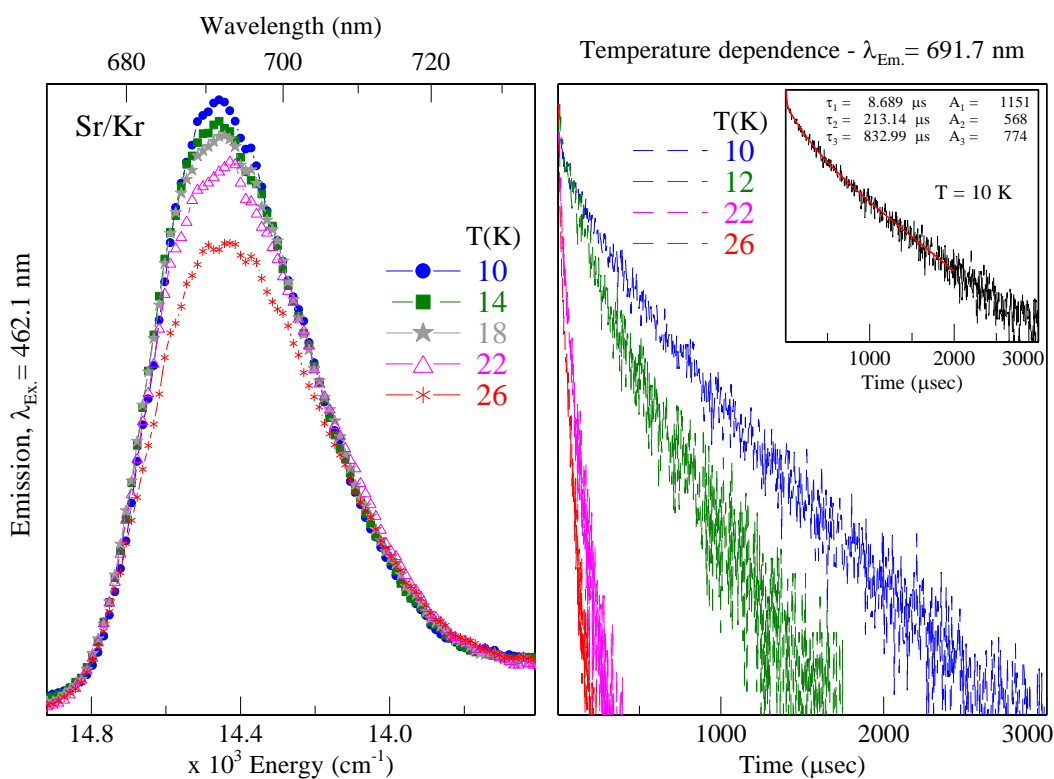

Figure V.43   The left panel shows the temperature dependence of the Sr/Kr green site emission band at 691.7 nm recorded over the range 10 – 26K. The right panel presents the temperature dependence of the corresponding decay curves, recorded at 10, 14, 18 and 26 K. The inset of the right panel shows the double exponential fit for the decay recorded at 10 K.

Table V.7   Temporal characteristics of the Sr/Kr 691.7 nm emission band, recorded over the temperature range of 10 to 26 K.

T_s (K)	Fit Range (µs)	A_1	τ_1 (µs)	A_2	τ_2 (µs)	A_3	τ_3 (µs)
10	8 – 2000	1151	8.7	568	213.1	774	833.0
12	8 – 1500	362	9.0	326	151.0	230	548.6
22	8 – 400	812	7.4	539	60.3	57	200.3
26	8 – 300	1492	6.7	835	48.0	48	154.9

V.2.V.II.C   Red site

The emission from the red site of isolation occurs at 705.4 nm and is characterised by a fwhm of 292 cm^{-1}. The decay profile of this feature is presented in Figure V.44. A triple exponential function is required to accurately fit the data. The three components are 22.1, 145.6 and 424.3 µs with amplitudes of 663, 746 and 458 respectively.
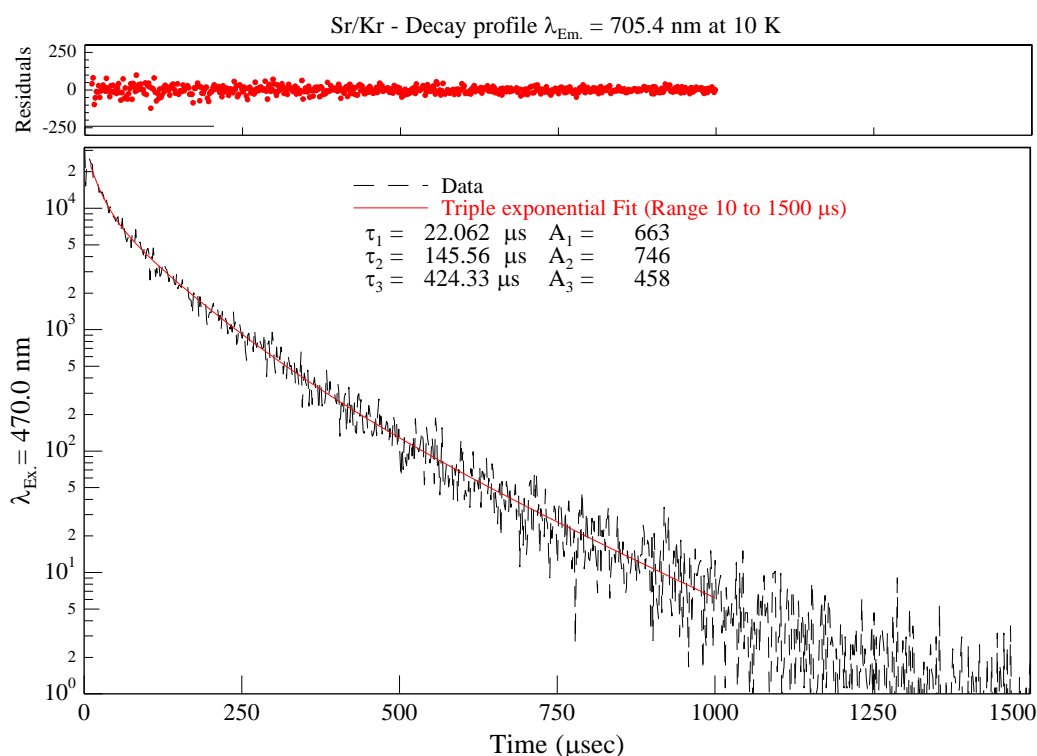

Figure V.44   **Decay profile of the Sr/Kr red site emission band at 705.4 nm, produced by site-selective laser excitation at 470.0 nm and recorded using the multi-channel scaler. στ₁ = ± 2.1 µs, στ₂ = ± 21.8 µs and στ₃ = ± 56.5 µs.**

A temperature dependence study of the emission decay curves is presented in the right panel of Figure V.45 and the results of the least squares fit for each temperature are collected in Table V.8. The decay profiles are very temperature dependent and become much shorter over the range of 10 to 18 K. Inspection of the fit parameters listed in Table V.8 shows that all time components are reduced over this range. Thus, the radiative lifetime has not been identified for this emission band and a definitive assignment to an electronic state of atomic Sr cannot be made. The shortest time component (τ_1) becomes dominant at higher temperatures. The contribution of the longest component (τ_3) is greatly reduced between 10 and 14 K and is completely absent at 18 K – a similar effect was observed for the green site of isolation.

The decrease in all time components, even over the small 10 to 12 K range suggests that a non-radiative relaxation to a lower level is quenching the red site emission. The temperature dependence of the spectral emission scans are shown in the left panel of Figure V.45. The emission intensity exhibits a decrease between 10 and 18 K. However this effect is not fully reversible as over 50 % of the emission intensity is permanently lost due to the instability of the red site. Thus, more definitive statements regarding the relaxation dynamics of this emission feature are not possible.
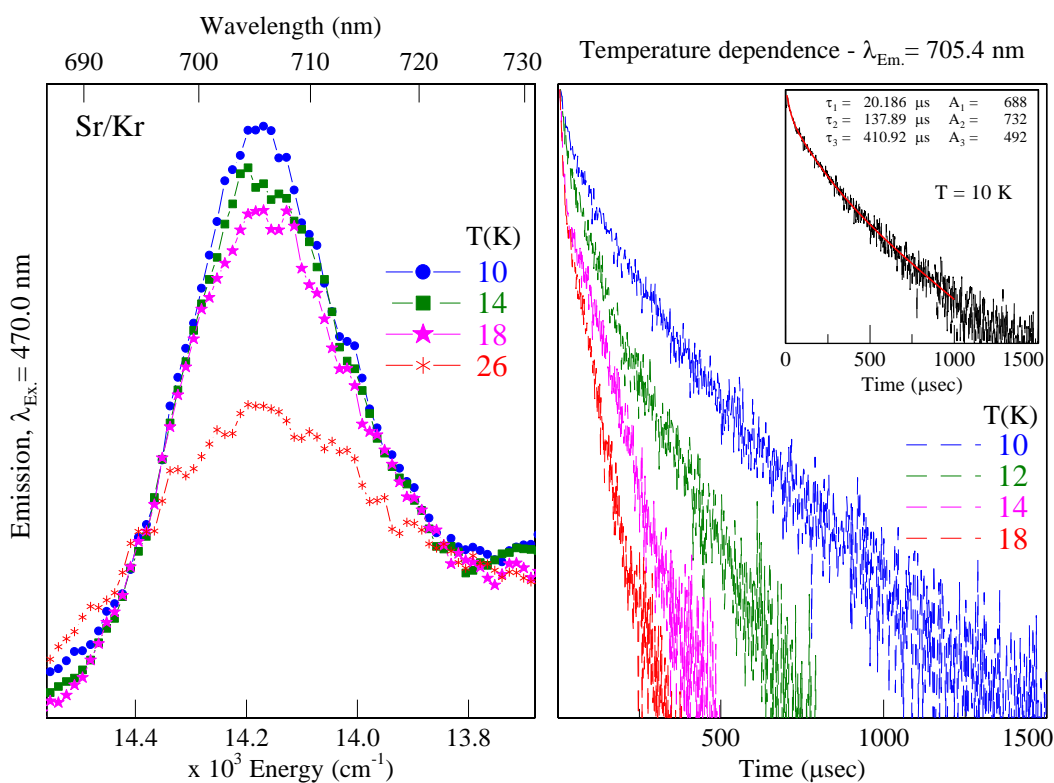

Figure V.45   The left panel shows the temperature dependence of the Sr/Kr red site emission band at 704.5 nm recorded over the range 10 – 26K. The right panel presents the temperature dependence of the decay curves, recorded at 10, 12, 14 and 218 K. The inset of the right panel shows the triple exponential fit for the decay recorded at 10 K.

Table V.8   Temporal characteristics of the Sr/Kr 705.4 nm emission band, recorded over the temperature range of 10 to 26 K.

T_s (K)	Fit Range (μs)	A_1	τ_1 (μs)	A_2	τ_2 (μs)	A_3	τ_3 (μs)
10	10 – 1500	663	22.1	746	145.6	458	424.3
12	10 – 750	743	12.1	892	75.6	431	269.9
14	10 – 400	3349	7.4	1188	120.7	49	125.2
18	10 – 300	6599	5.8	1802	75.9	-	-

V.2.VI   Sr/Kr (5s5p $^1P_1$) luminescence summary

A summary of the Sr/Kr luminescence is presented in Figure V.46. Dashed vertical lines represent the gas phase positions of the (5s5p) $^1P_1$, (5s4d) $^1D_2$, (5s4d) $^3D_1$ and (5s5p) $^3P_1$ excited states of atomic Sr.
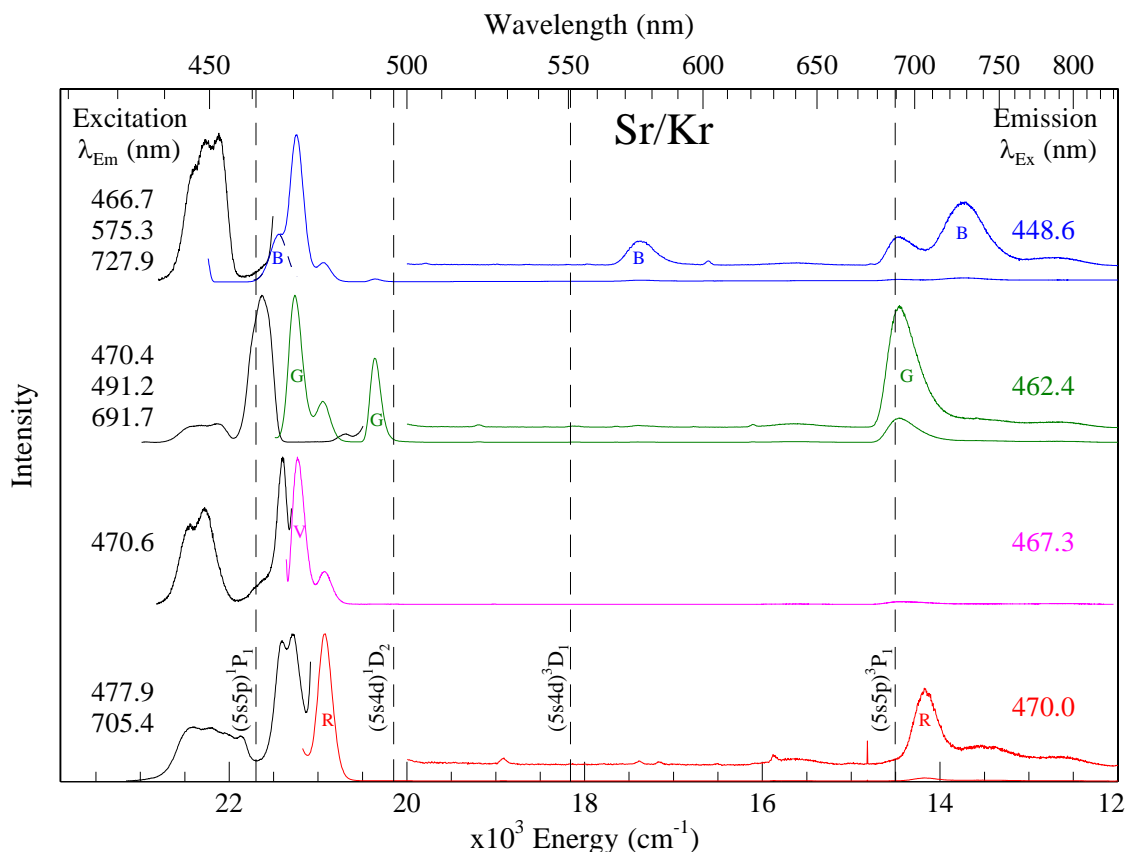
Figure V.46   **A summary of the excitation and emission features arising from the isolation of atomic Sr in the three thermally and one partially stable sites of solid Kr. The gas phase positions[4] of the (5s5p) $^1P_1$, (5s4d) $^1D_2$, (5s4d) $^3D_1$ and (5s5p) $^3P_1$ excited states are shown as dashed vertical lines. A Gaussian fit of the blue site (5s5p) $^1P_1$ emission is represented by the dashed blue line (top traces).**

The blue and green sites each produce three emission bands. For the blue site, the features at 466.7 and 727.9 were assigned to the (5s5p) $^1P_1 \rightarrow$ (5s^2) $^1S_0$ and (5s5p) $^3P_1 \rightarrow$ (5s^2) $^1S_0$ transitions respectively and an assignment to the (5s5p) $^3D_1 \rightarrow$ (5s^2) $^1S_0$ transition was proposed for the 575.3 nm feature. The green site emission bands located at 470.4 and 691.7 were assigned to the (5s5p) $^1P_1 \rightarrow$ (5s^2) $^1S_0$ and (5s5p) $^3P_1 \rightarrow$ (5s^2) $^1S_0$ transitions respectively. Although the radiative lifetime of the 491.2 nm emission was not identified, this emission was tentatively assigned to the parity-forbidden (5s4d) $^1D_2 \rightarrow$ (5s^2) $^1S_0$ transition. Emission bands at 470.6 and 477.9 were identified for the

violet and red sites of isolation respectively, both of which were assigned as resonance $(5s5p)$ $^1P_1 \rightarrow (5s^2)$ $^1S_0$ atomic fluorescence. The red site also shows a weak emission band at 705.4 nm, which could not be definitively assigned to an electronic transition of Sr because the radiative lifetime was not recorded. However, based on the spectral position and lifetime values recorded at 10 K, this band probably arises from the $(5s5p)$ $^3P_1$ state. Interestingly, Sr atoms isolated in the violet site do not emit from the low-lying triplet states. The photophysical and temporal characteristics of the Sr/Kr emission bands are summarised in Table V.9 along with the state assignments (where possible).

Table V.9   **The photophysical characteristics of the thermally stable and site-specific emission features of Sr/Kr, which were obtained with $(5s5p)$ $^1P_1$ excitation. The spectral positions are quoted in both nanometres (nm) and wavenumber (cm^{-1}) units. δ represents the gas phase to matrix frequency shifts, given in wavenumber units. The bandwidth (full width at half maximum, fwhm) is denoted by the symbol Δ and is also expressed in units of wavenumber. The observed lifetimes, recorded in the matrix at 10 K, are listed in the rightmost column.**

Gas Phase	Sr/Kr Site	λ_{em} (nm)	ν (cm^{-1})	δ (cm^{-1})	Δ (cm^{-1})	τ_{obs} at 10 K
$(5s5p)^1P_1 \rightarrow (5s5p)^1S_0$	Blue	466.7	21427	-271	203	2.6 ns
$\nu = 21698.45$ cm^{-1}	Green	470.4	21259	-440	180	3.0 ns
$\tau = 4.98$ ns	Violet	470.6	21249	-449	184	2.8 ns
	Red	477.9	20925	-774	179	2.6 ns
$(5s5p)^3P_1 \rightarrow (5s5p)^1S_0$	Blue	727.9	13738	-766	539	6.3 / 70.8 μs
$\nu = 14504.33$ cm^{-1}	Green	691.7	14457	-47	387	8.7 / 213.1 / 833.0 μs
$\tau = 21.3$ μs						
$(5s5p)^3D_1 \rightarrow (5s5p)^1S_0$	Blue	575.3	17382	-777	370	1.4 / 0.5 μs
$\nu = 18159.04$ cm^{-1}						
$\tau = $ n/a						
$(5s5p)^1D_2 \rightarrow (5s5p)^1S_0$	Green	491.2	20358	209	137	55.8 ns
$\nu = 18159.04$ cm^{-1}						
$\tau = 19.6 \pm 6$ ms^{7,8}						
Unassigned Bands	Red	705.4	14176	-	292	22.1 / 145.6 / 424.3 μs

V.2.VII   Sr/Ar

V.2.VII.I $\lambda_{em} \approx 460$ nm

The 2D-EE spectrum of Sr/Ar, recorded following sample deposition at 10 K and annealing to 28 K, is presented in Figure V.47. Six prominent luminescence bands are observed, which are labelled $1 - VI$. Akin to Sr/Kr, numerous thermally stable sites of isolation exist for Sr in an annealed Ar matrix. The excitation slices $X.1 - X.3$ are shown overlaid onto the annealed (5s5p) $^1P_1$ absorption profile of Sr/Ar in the bottom of Figure V.49.
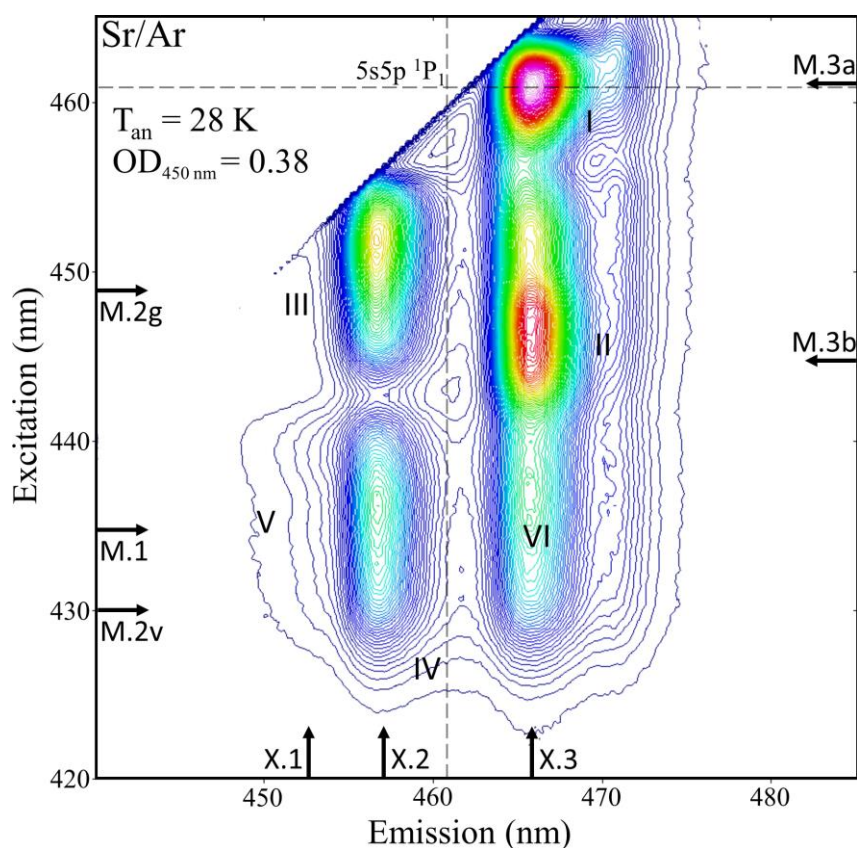
Figure V.47   **2D-EE spectrum of Sr/Ar recorded following sample deposition at 10 K and annealing to 28 K. The optical density (OD) of this sample was measured to be 0.38 at 450 nm. The gas phase position[4] of the resonance (5s5p) $^1P_1 \leftarrow$ (5s^2) $^1S_0$ transition of Sr is shown in emission and excitation.**

For comparative purposes, a 2D-EE scan obtained from a very weakly absorbing (OD < 0.1 at 450 nm) Sr/Ar sample is presented in Figure V.48. The sample in question was deposited at 10 K and annealed to the slightly higher temperature of 30 K. Inspection

of this plot shows that luminescence is much simpler at lower metal loadings, in particular band VI is completely absent and may be classed as a re-absorbed feature. The five remaining bands (I-V) are more clearly identifiable. The excitation slices extracted from this 2D-EE plot are presented in the top of Figure V.49 and are a truer reflection of the 'real' absorption bands associated with each site of isolation.
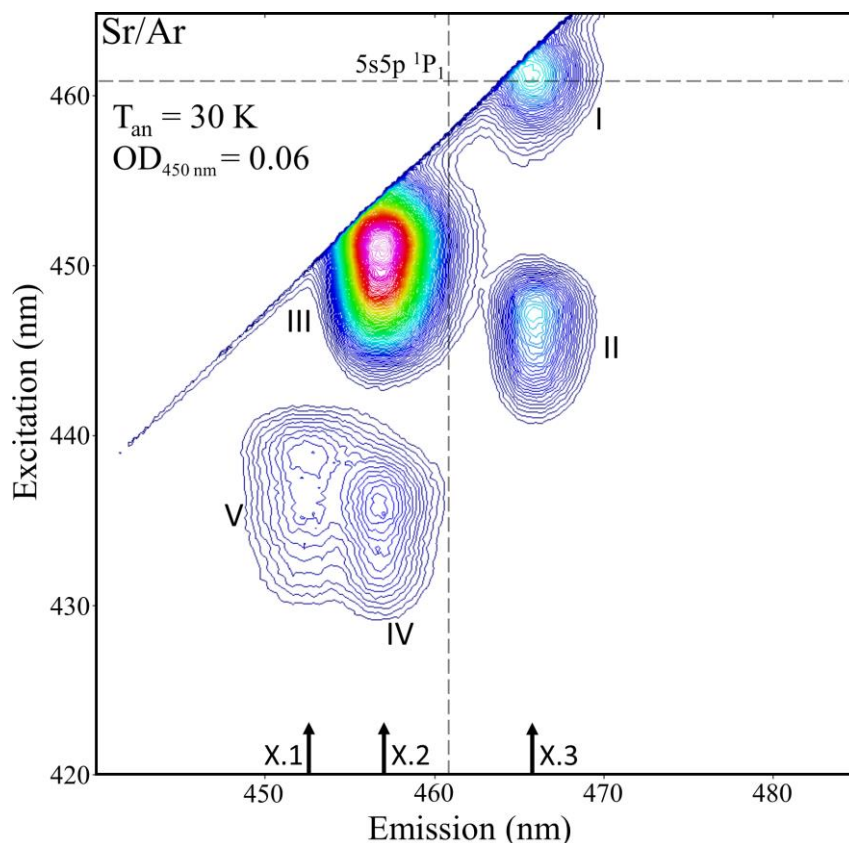
Figure V.48   **2D-EE spectrum of Sr/Ar recorded following sample deposition at 10 K and annealing to 30 K. The optical density (OD) of this sample was very low, with a value of 0.06 at 450 nm. The gas phase position[4] of the resonance (5s5p) $^1P_1 \leftarrow$ (5s^2) $^1S_0$ transition of Sr is shown in emission and excitation.**

The 'blue' site excitation scan (X.1) consists of a band (V) centred at 434.8 nm which is characterised by a fully resolved Jahn-Teller threefold splitting. The excitation slice, X.2, is composed of two main features: a doublet (IV) with peaks at 431.7 and 436.2 nm and a broad, lower energy band (III) located at ~ 450 nm. This trace consists of contributions from two distinct sites of isolation, namely the 'violet' and 'green' sites. Band III mostly represents the absorption of the dominant green trapping site and directly overlaps the strongest (5s5p) $^1P_1$ absorption feature. The violet site exhibits an asymmetric (2+1) threefold splitting pattern. While the higher energy doublet (IV) is

clearly visible, the remaining lower energy singlet cannot be extracted from the excitation spectrum alone, as it is strongly overlapped by the broad and intense green site absorption band (III). Thus, a lineshape analysis will be used in the following sections to allow the absorption features of both sites to be deconvoluted. An excitation profile for the 'R1' site[e] of isolation is labelled X.3 and shown as a red continuous line in Figure V.49. The spectrum consists of two features.
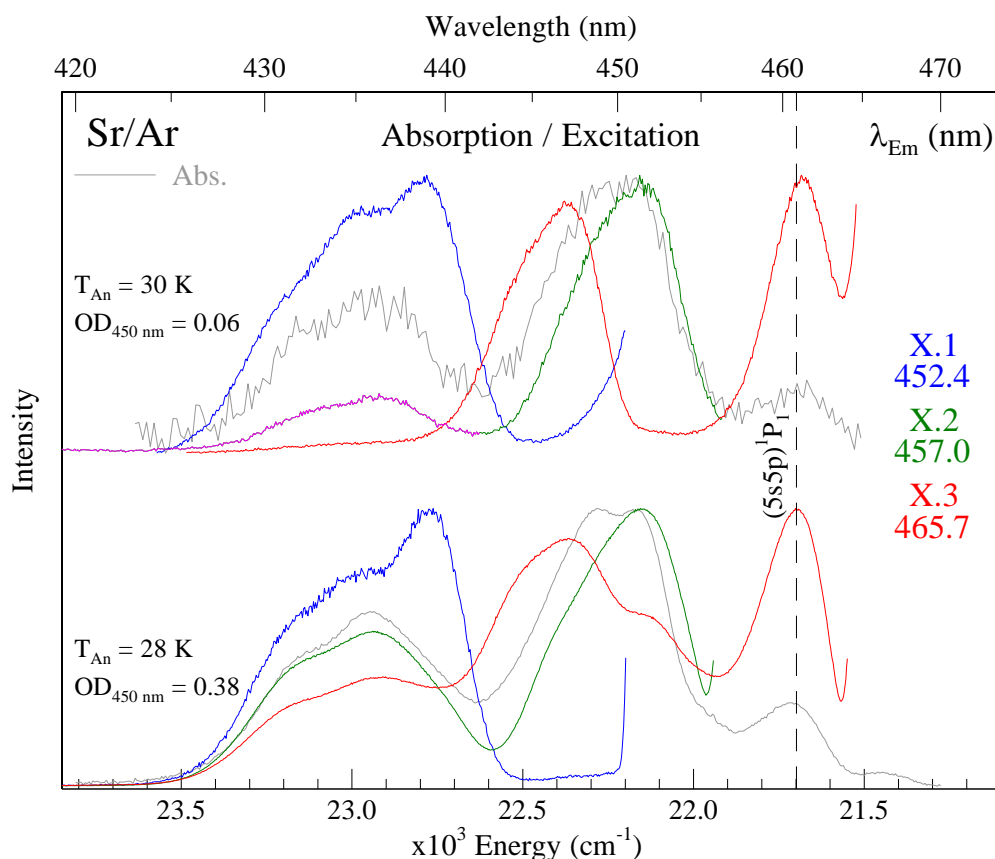
Figure V.49   **Sr/Ar absorption (grey) and excitation spectra (coloured), recorded monitoring the emission features in the 460 nm spectral region. Two samples are represented. The top traces originate from a sample annealed to 30 K and by a characterised by an extremely low absorption OD of 0.06 at 450 nm. The lower traces represent a more absorbing sample with an OD of 0.5 at 448 nm. This sample was annealed to 28 K. The gas phase position[4] of the resonance (5s5p) $^1P_1$ ← (5s²) $^1S_0$ transition of Sr is shown as a dashed vertical line.**

The lowest energy excitation band (I) is located at 461.2 nm and directly overlaps the gas phase (5s5p) $^1P_1$ ← (5s²) $^1S_0$ line. The higher energy component is broader and displays a maximum at 447.3 nm (II), with a hint of a higher energy shoulder at 444.7

---

[e] 'R1' stands for primary red trapping site. This notation is used to distinguish from a secondary red site of isolation (R2) which will presented ahead in Section V.2.VIII.

nm. In summary, four thermally stable trapping sites exist for Sr in an annealed Ar matrix. The photophysical properties of each will now be described in detail.

V.2.VII.I.A   Blue site

Emission and excitation spectra recorded for the blue site of isolation, are presented Figure V.50. The JT excitation band is centred at 434.8 nm, exhibiting a matrix blue-shift of +1301 cm^{-1}. The lineshape analysis conducted for this scan is shown in Figure V.119 of Appendix V.I. Three Gaussian curves of equal width (247 cm^{-1}) are required to reproduce the observed profile.
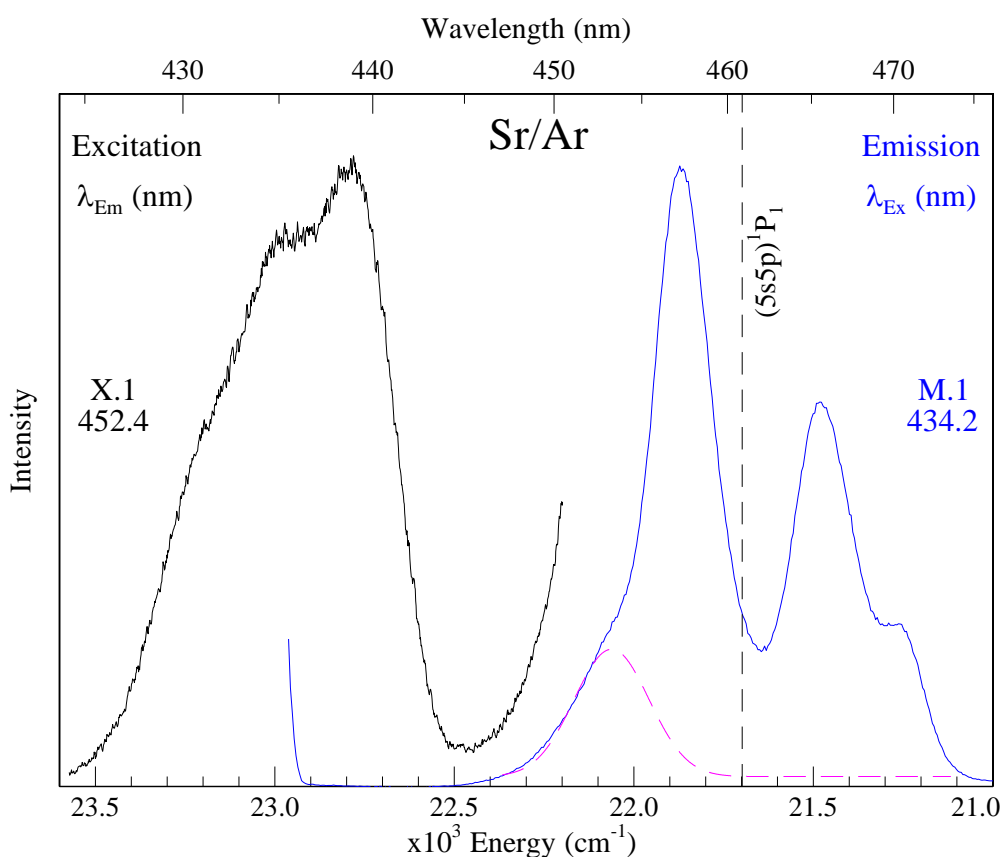
Figure V.50   **Excitation (black) and emission (blue) spectra recorded for the Sr/Ar blue site of isolation, following sample annealing to 28 K. The excitation scan shown was obtained from the weakly absorbing Ar sample because this was the more resolved profile. The gas phase[4] position of the (5s5p) $^1P_1$ state is shown by a dashed vertical line. The Gaussian fit of the blue site emission is represented by the dashed pink line.**

The emission for this site is located at 452.4 nm and can be obtained by taking a horizontal slice through the 2D-EE plot (Figure V.47) at M.1. A Stokes shift of 895

cm^{-1} is evaluated from the excitation/emission band centres. A bandwidth of 186 cm^{-1} is obtained from a lineshape analysis of the entire emission scan presented in Figure V.50. For clarity, the Gaussian peak specific to the blue site emission is represented by the dashed pink line.

An emission decay profile recorded at 10 K is presented in Figure V.51. A single exponential function, with a decay time of 2.8 ns, provides a very good fit of the data points.

Sr/Ar - Decay profile $\lambda_{Em.}$ = 452.4 nm at 10 K
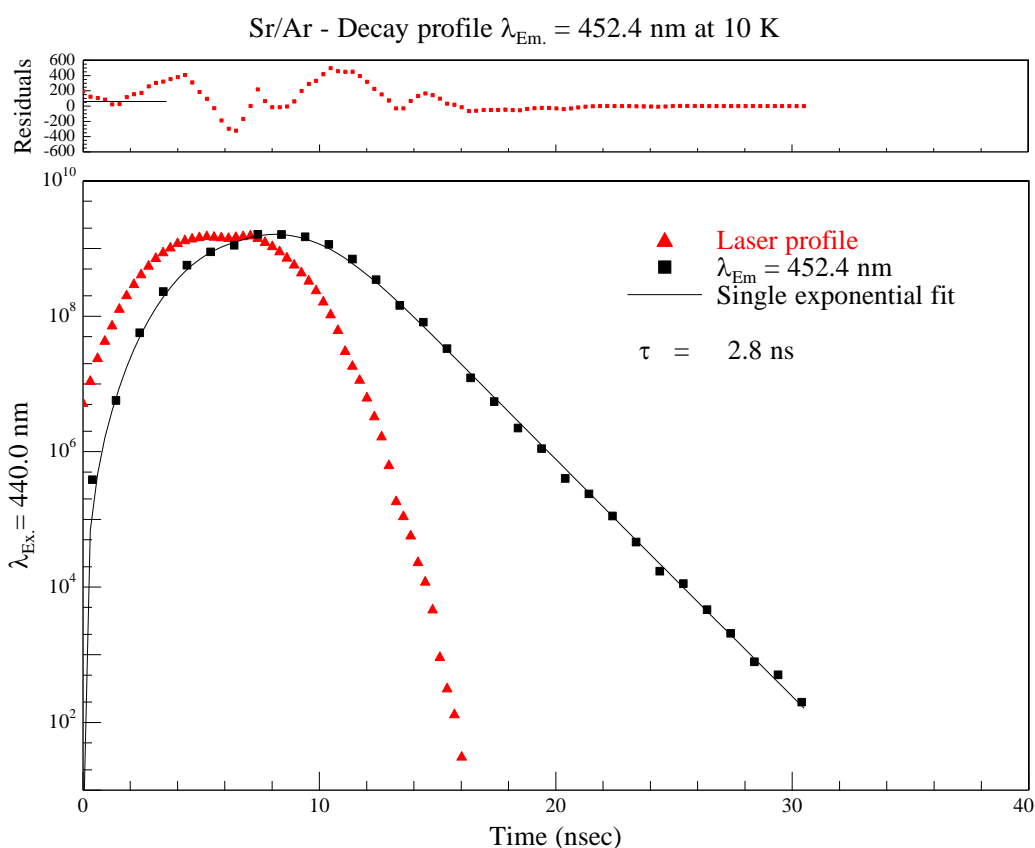
Figure V.51   **Decay profile of the Sr/Ar blue site emission band at 452.4 nm, produced by laser excitation at 440.0 nm. An excited state decay time of 2.8 ns is obtained at 10 K with a single exponential trial function.**

The temperature dependence of the temporal and spectral scans are presented in the right and left panels of Figure V.52, respectively. The lifetime values do not change between 10 and 26 K, thus the true radiative lifetime of 2.8 ns has been identified. Applying the effective field correction gives an excited state lifetime of 5.8 ns. The favourable comparison of this corrected lifetime value with that of the gas phase (5s5p) $^1P_1 \rightarrow$ (5s^2) $^1S_0$ transition[4] allows an assured assignment to be made. Inspection of the spectral scans shown in Figure V.52 reveals that the emission intensity also shows very

little change from 10 to 18 K. In contrast to the blue sites in Kr and Xe, it appears that non-radiative relaxation pathways are not competing significantly with the blue site (5s5p) $^1P_1$ emission in solid Ar.
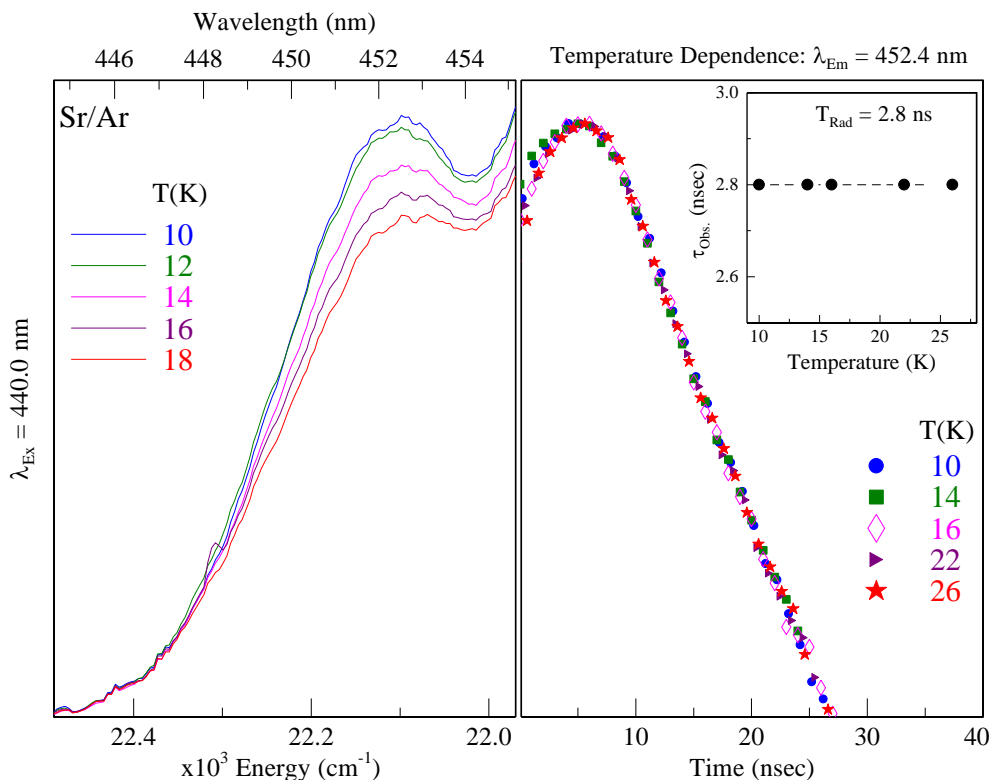
Figure V.52 **The left panel shows the temperature dependence of the Sr/Ar blue site emission band at 452.4 nm over the range 10 – 18 K. The right panel presents the temperature dependence of the decay curves from 10 to 26 K.**

V.2.VII.I.B   Violet site

Emission and excitation spectra recorded for the violet site of isolation are presented in Figure V.53. Extracting the luminescence features specific to this site was quite challenging because unlike Ba/Ar, the emission bands of the green and violet sites of Sr/Ar are fully coincident. Consequently, the emission wavelength cannot be tuned to favour the contribution of the violet site over the green site in excitation. Therefore, the excitation spectrum (X.2) presented by the black trace in Figure V.53 will also be shown in the next section (V.2.VII.I.C) for the green site. A lineshape analysis for this profile is presented in Figure V.120 of Appendix V.I. A total of six Gaussian peaks were required to satisfactorily fit the scan and account for the two sites (green and violet) of isolation.
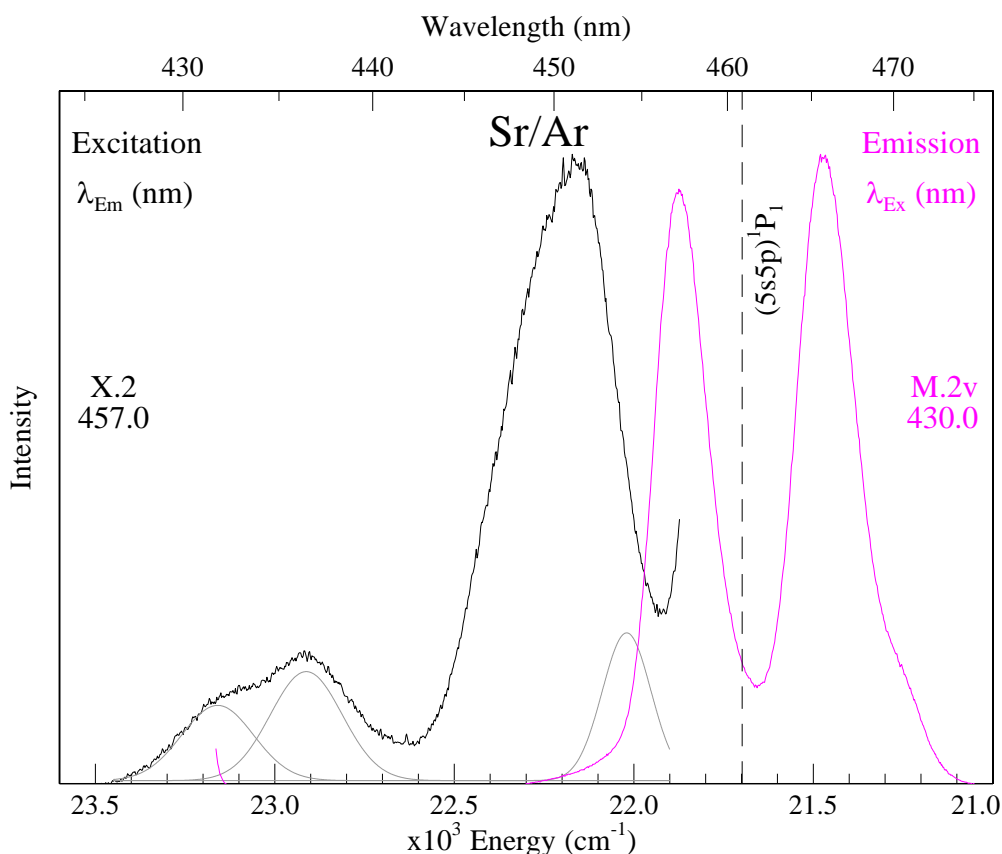
Figure V.53   Excitation (black/blue) and emission (pink) spectra recorded for the Sr/Ar violet site of isolation, following sample annealing to 28 K. The excitation scan shown was obtained from the weakly absorbing Ar sample. The gas phase[4] position of the (5s5p) $^1P_1$ state of atomic Sr is shown by a dashed vertical line. The three Gaussian curves representing the violet site absorptions are shown in grey.

The three Gaussian components, labelled $1 - 3$, represent the violet absorptions. For clarity, these fitted peaks are also presented in Figure V.53 (grey curves) and highlight the portion of the excitation scan which pertains to violet site. As can be seen, this trapping environment for Sr produces an asymmetric threefold (2+1) split in absorption/excitation. The higher energy doublet is accounted for by two Gaussian curves of equal width (fwhm = 235 cm^{-1}). Matrix blue-shifts of +1466 and +1227 are measured for each peak of the doublet. The position of the lower energy singlet has been revealed by the fit and occurs at 454.1 nm, exhibiting a narrower bandwidth of 141 cm^{-1}. A smaller matrix blue-shift of 323 cm^{-1} is observed for this feature.

The emission scan shown in Figure V.53 corresponds to a horizontal slice through Figure V.47 at the excitation value denoted M.4. The violet site emission band is centred at 457.0 nm and displays a fwhm of 184 cm^{-1}, slightly narrower than that of the green site. Large Stokes shifts of 1282 and 1043 cm^{-1} are evaluated from the

emission centroid to each peak of the excitation doublet. In contrast, a much smaller Stokes shift of 140 cm^{-1} exists for the lower energy singlet.

Time-resolved decay curves were difficult to ascertain for the violet site. Selecting a wavelength which excites the lower energy singlet would concurrently excite atoms in the green site - excitation wavelengths corresponding the higher energy doublet must be used. However, irradiation of either doublet component simultaneously excites Sr atoms in the blue site. The blue site emission, which occurs at 452.4 nm, directly overlaps the green site excitation band. If the sample is too absorbing, the decay profile of the violet site emission will contain a contribution from the re-absorbed blue site fluorescence.
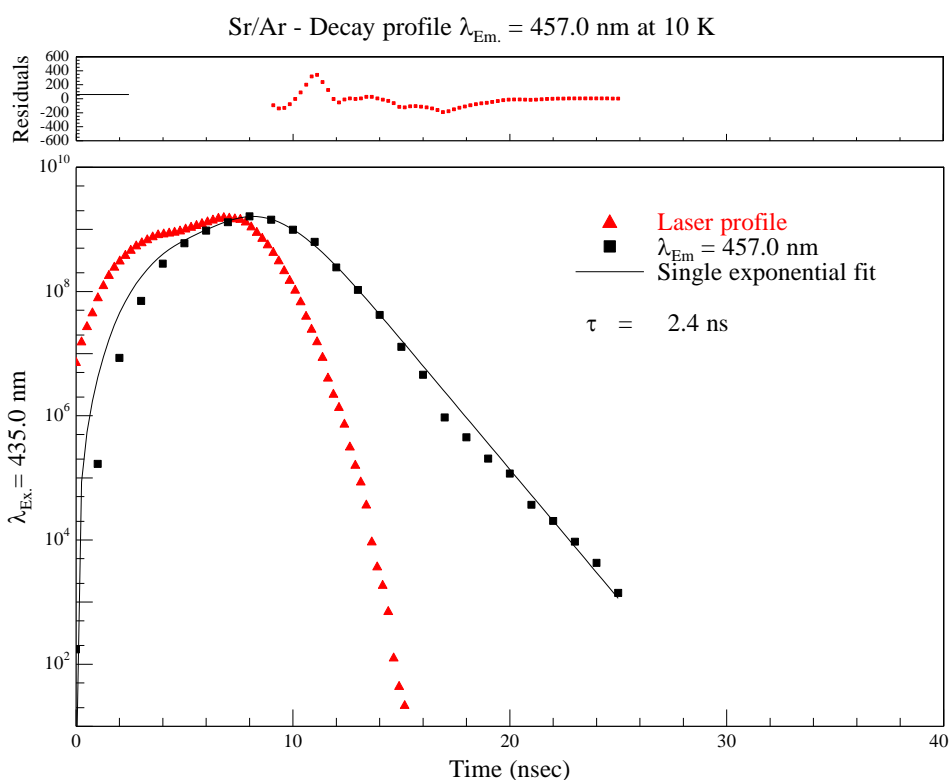
Figure V.54   **Decay profile of the Sr/Ar violet site emission band at 457.0 nm, produced by laser excitation at 435.0 nm. An excited state lifetime of 2.4 ns is obtained at 10 K with a single exponential trial function.**

To overcome this issue, the violet site decay profile presented in Figure V.54 was obtained from the very weakly absorbing sample, despite the poorer S/N ratio. Inspection of this plot reveals that a single exponential function, with a 2.4 ns decay time, accurately matches the slope of the decay points. The temperature dependence of the spectral and temporal scans are presented in the left and right panels of Figure V.55

respectively. The recorded decays show little or no change from 10 to 18 K and the 457.0 nm emission band shows only a minor intensity decrease over this range. The radiative lifetime is therefore identified as 2.4 ns. An excited state lifetime of 4.9 ns is obtained following application of the effective field equation, allowing confident assigned of this band to the resonance $(5s5p)\,^1P_1 \rightarrow (5s^2)\,^1S_0$ transition[4] of atomic Sr.
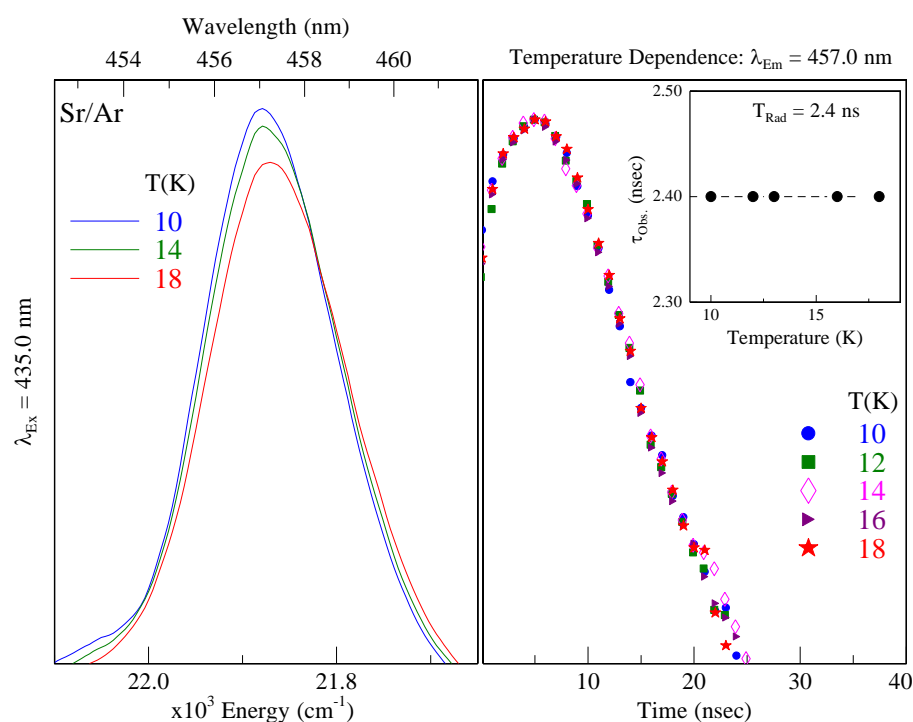
Figure V.55   The left panel shows the temperature dependence of the Sr/Ar violet site emission band at 457.0 nm over the range 10 – 18 K. The right panel presents the temperature dependence of the corresponding decay curves.

V.2.VII.I.C   Green site

The emission and excitation spectra recorded for the green site of isolation are presented in Figure V.56. The excitation band is centred at 448.9 nm and exhibits a matrix blue-shift of +578 cm^{-1}. A lineshape analysis of this feature is presented in Figure V.120. The three Gaussian curves, labelled 4 – 6, represent the green site absorption profile. Each component exhibits a fwhm of 139 cm^{-1}. For convenience, the Gaussian curves are shown in Figure V.56 (grey traces), overlapping the X.2 scan.

The emission spectrum presented in Figure V.56 (green trace) corresponds to a horizontal slice through the 2D-EE plot (Figure V.47) at M.2g. Two intense features are observed, however, the highest energy band at 457.0 nm originates from Sr atoms

trapped in the green site. This emission is characterised by a linewidth of 202 cm^{-1} and a Stokes shift of 395 cm^{-1}.
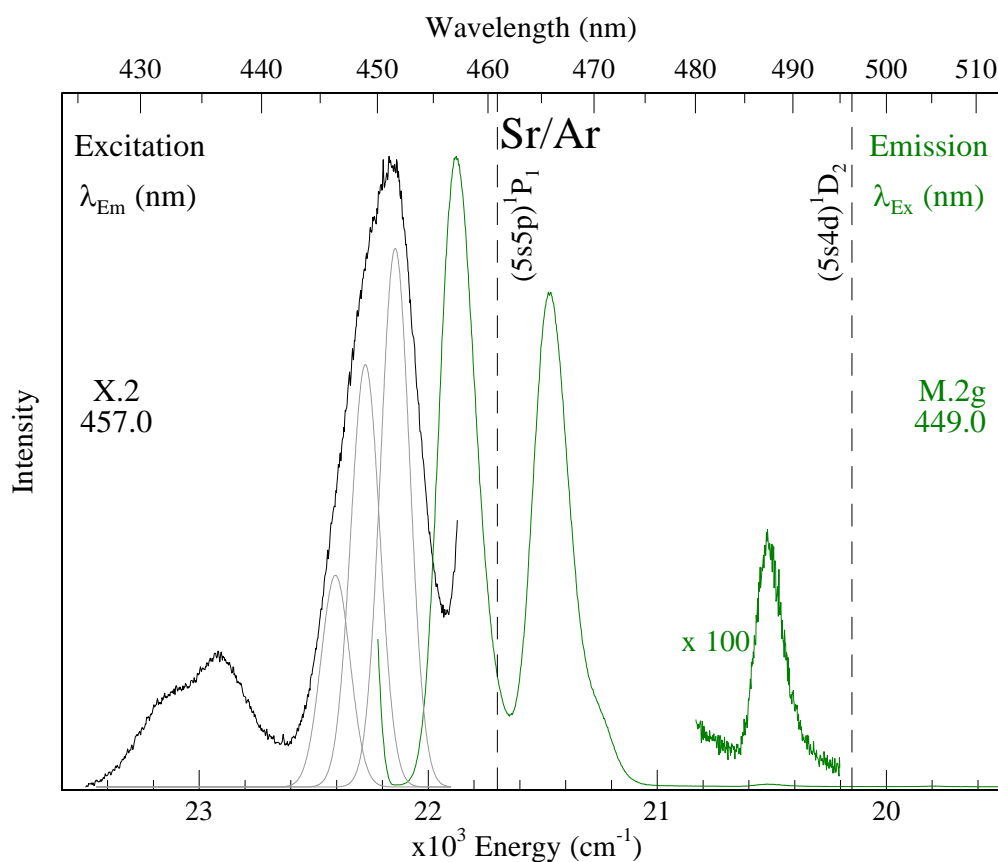

Figure V.56   **Excitation (black) and emission (green) spectra recorded for the Sr/Ar green site of isolation, following sample annealing to 28 K. The excitation scan shown was obtained from the weakly absorbing Ar sample because this profile was not 'contaminated' by re-absorbed bands. The gas phase[4] positions of the (5s5p) ^{1}P$_1$ and (5s4d) ^{1}D$_2$ states of atomic Sr are shown by dashed vertical lines. The three Gaussian curves representing the green site absorption band are shown in grey.**

A decay profile, recorded at 10 K with laser excitation at 451.0 nm, is shown in Figure V.57 and the temperature dependence of both the spectral and temporal scans are presented in the left and right panels of Figure V.58 respectively. A single exponential trial function, employing a decay time of 3.0 ns, provides a good fit of the temporal profile. This value does not change between 10 and 18 K, indicating that the true radiative lifetime has been identified. An excited state lifetime of 6.2 ns is obtained when the observed value (3.0 ns) is corrected for the effective field of the Ar matrix. Accordingly, the 457.0 nm emission band is assigned to the resonance (5s5p) ^{1}P$_1 \rightarrow$ (5s^2) ^{1}S$_0$ transition[4] of atomic Sr. Above 18 K, the lifetime becomes shorter. The spectral scans shown in the left panel of Figure V.58 show a reversible decrease in

intensity, broadening in width and red-shift in position as the temperature increases. A non-radiative relaxation pathway competes with the emission of Sr isolated in the green site. This process becomes active above 18 K, as evidenced by the temporal scans.
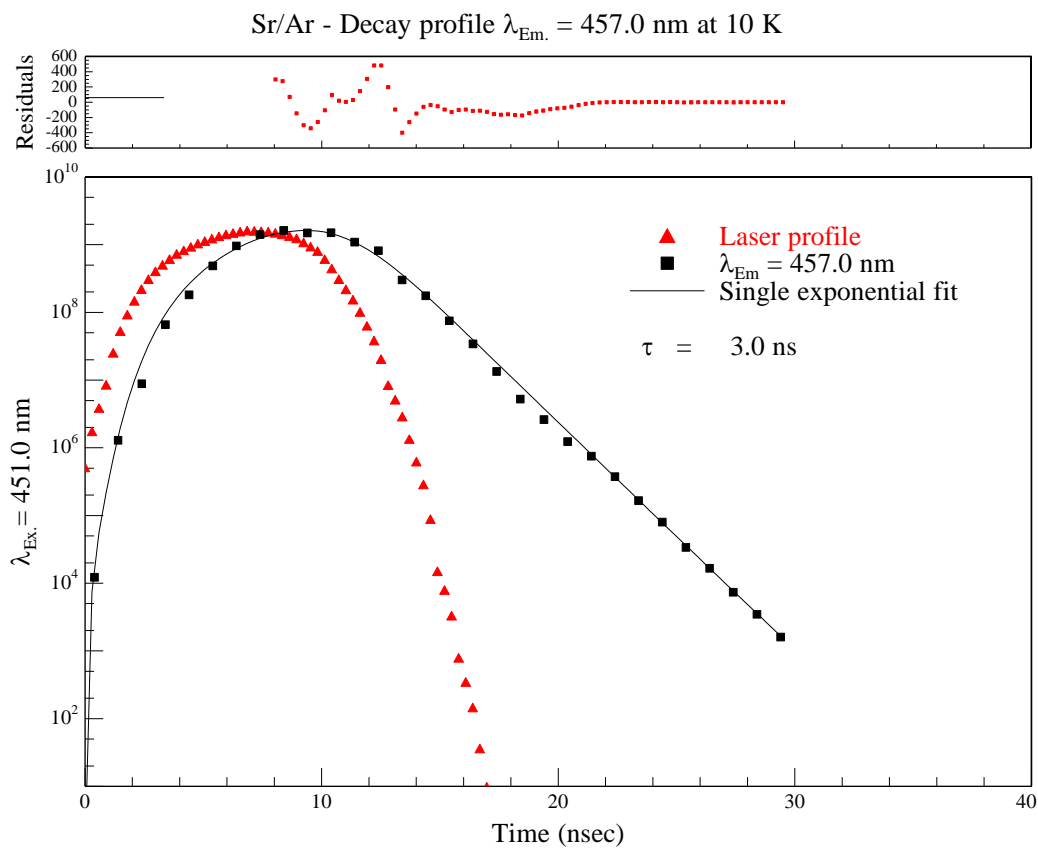

Figure V.57   **Decay profile of the Sr/Ar green site emission band at 457.0 nm, produced by laser excitation at 451.0 nm. An excited state lifetime of 3.0 ns is obtained at 10 K with a single exponential trial function.**
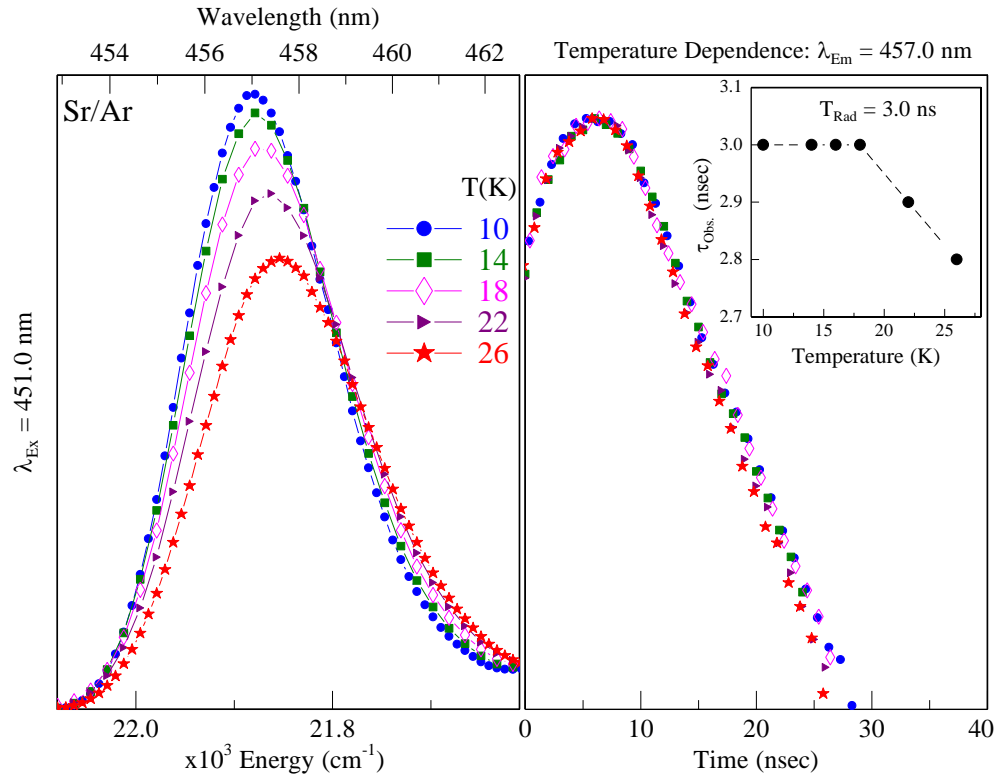
Figure V.58 **The left panel shows the temperature dependence of the Sr/Ar green site emission band at 457.0 nm over the range 10 – 26 K. The right panel presents the temperature dependence of the corresponding decay curves. The lifetime of the green site emission is shortened at temperatures above 18 K.**

Similar to Sr/Kr, a lower energy emission band occurring close to the (5s4d) $^1D_2$ atomic state is observed for the green site of Sr/Ar. Inspection of Figure V.56 reveals that this band is centred at 487.3 nm and is quite narrow, exhibiting a fwhm of 131 cm^{-1}. In addition, it can be seen that the intensity is far weaker in Ar. Consequently, accurate time-resolved decays could not be obtained with laser excitation of the green site absorption at 451.0 nm. However, the excitation spectrum (not shown) recorded monitoring this emission feature reveals the presence of a weak band at approx. 481 nm. An acceptable decay profile was obtained by exciting into this band and a decay time of ~64 ns[f] was obtained from a single exponential fit. As was the case for Sr/Kr, the radiative lifetime could not be identified because the 487.3 nm emission vanishes at temperatures above 10 K. Despite this, a tentative assignment is made to the parity-forbidden (5s4d) $^1D_2 \rightarrow$ (5s^2) $^1S_0$ of atomic Sr. This assignment is based on the

---

[f] This value is similar to that obtained for the equivalent Sr/Kr emission band (~41 ns), which was recorded with direct laser excitation of the absorption at 483 nm.

observation of narrow emission/excitation features which are situated close in energy to the (5s4d) $^1D_2$ state.

V.2.VII.I.D Red (R1) site

The luminescence (emission and excitation) spectra of the R1 trapping site is shown in Figure V.59. The excitation profile consists of two main components. A lineshape analysis conducted for this spectrum is presented in Figure V.121 of Appendix V.I. The highest energy band was well reproduced by two Gaussian curves, each exhibiting a spectral width of 203 cm^{-1}. The lower energy band was fit with a single, slightly broader Gaussian function (fwhm = 221 cm^{-1}).
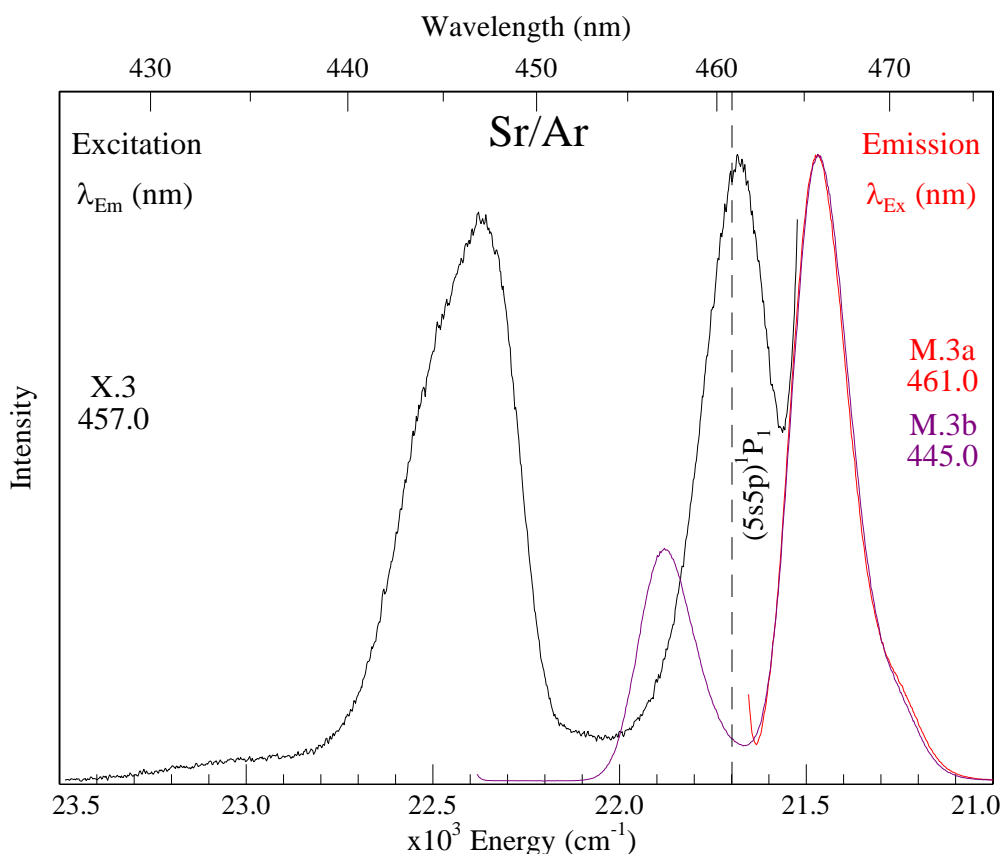

Figure V.59   **Excitation (black) and emission (red/purple) spectra recorded for the Sr/Ar red site (R1) of isolation, following sample annealing to 28 K. The excitation scan shown was obtained from the weakly absorbing Ar sample because this profile was not 'contaminated' by re-absorbed bands. The gas phase[4] position of the (5s5p) $^1P_1$ state of atomic Sr is shown by a dashed vertical line.**

It can therefore be stated that Sr atoms isolated in the red site of solid Ar produce an asymmetric (2+1) threefold splitting pattern in absorption. The peaks of the higher energy doublet are partially resolved and occur at 444.7 and 447.3 nm, exhibiting the

respective matrix blue-shifts of +789 and 658 cm^{-1}. The lower energy singlet is centred at 461.2 nm is slightly red-shifted with respect to the (5s5p) $^1P_1 \leftarrow$ (5s^2) $^1S_0$ line by -16 cm^{-1}.

Irradiation of any red site absorption peak produces an emission band at 465.7 nm which is characterised by a bandwidth of 180 cm^{-1}. Stokes shifts of 1014, 883 and 210 cm^{-1} are calculated from the centre of this emission to each of the three absorption peaks. The red and purple scans, shown in Figure V.59, correspond to horizontal slices through the 2D-EE plot (Figure V.47) at M.3a and M.3b respectively.
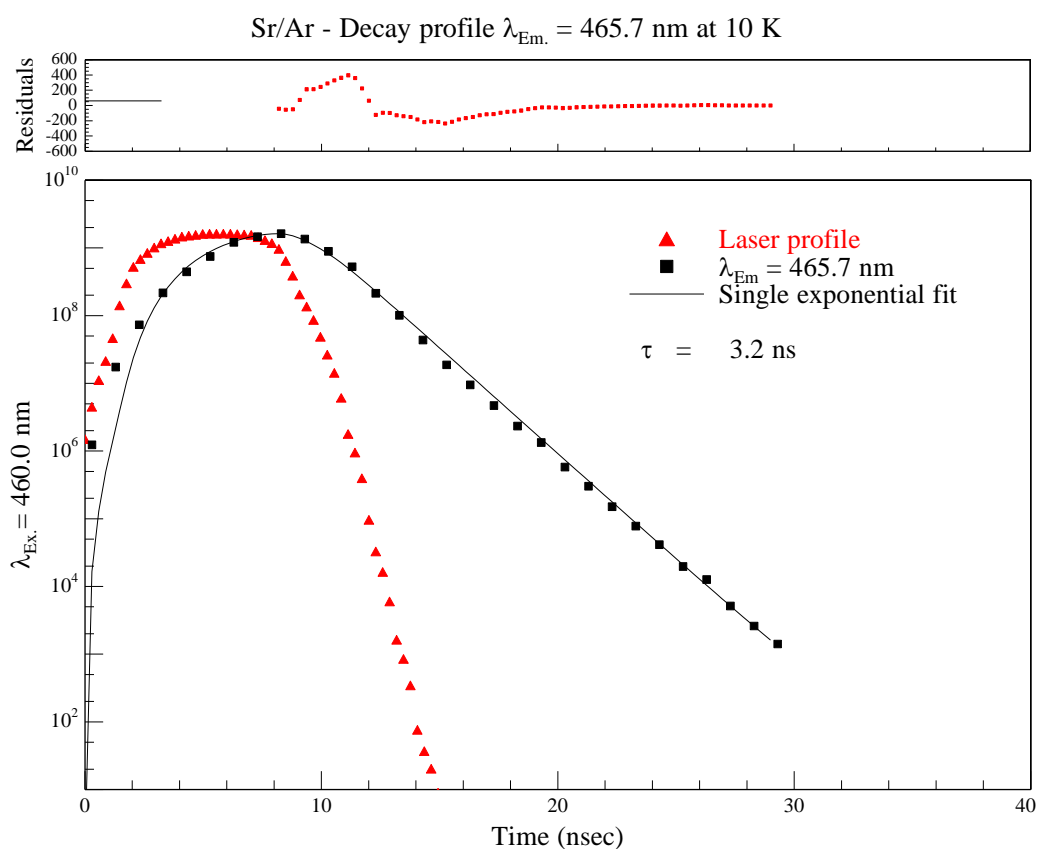

Figure V.60   **Decay profile of the Sr/Ar red site emission band at 465.7 nm, produced by laser excitation at 460.0 nm. An excited state lifetime of 3.2 ns is obtained at 10 K with a single exponential trial function.**

The decay profile for this emission is presented in Figure V.60 and is accurately described by a single exponential function, using a decay time of 3.2 ns. The temperature dependence of the temporal scans are provided in the right panel of Figure V.61. As can be seen, the decays exhibit no change between 10 and 18 K. Thus, the radiative lifetime has been identified. Correcting for the effective field of the Ar host

yields an excited state lifetime of 6.6 ns. Consequently, the 465.7 nm emission is assigned to the fully-allowed $(5s5p)$ $^1P_1 \rightarrow (5s^2)$ $^1S_0$ transition[4] of atomic Sr. The spectral scans presented in the left panel of Figure V.61 display a marked decrease in intensity above 18 K. Coupling this behaviour with the observed shortening of the lifetime values between 18 and 22 K indicates that a non-radiative transition competes with the R1 site emission over this temperature range.
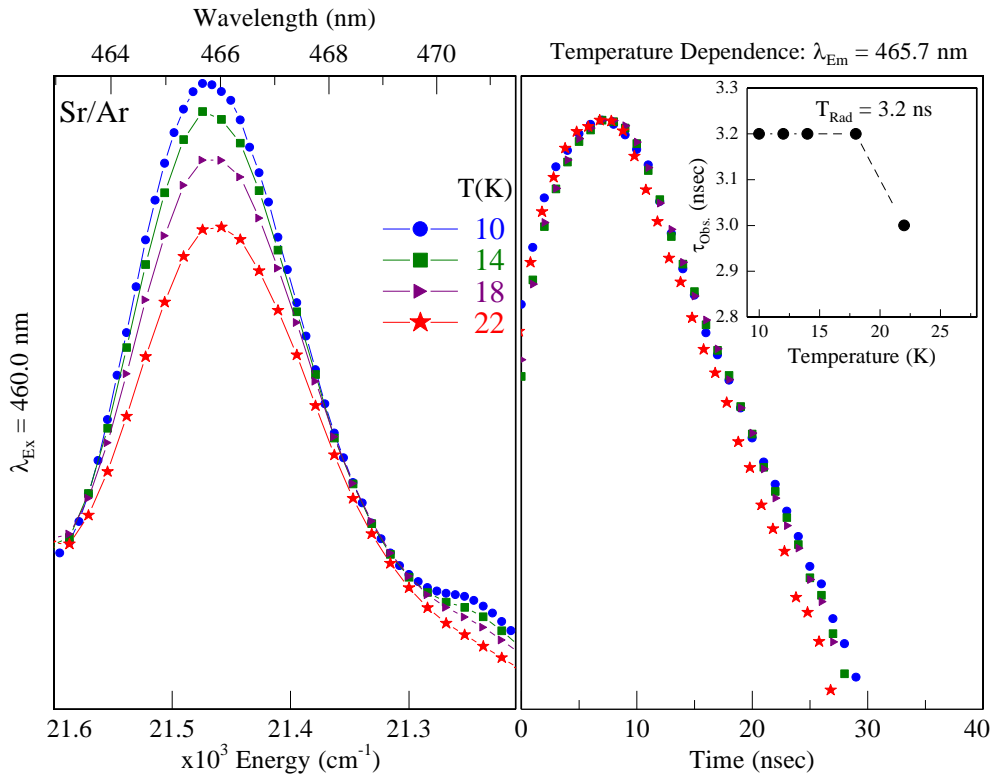
Figure V.61   **The left panel shows the temperature dependence of the Sr/Ar R1 site emission band at 465.7 nm over the range 10 – 22 K. The right panel presents the temperature dependence of the corresponding decay curves.**

V.2.VIII Sr/Ar full range emission

The 460 nm luminescence revealed the presence of four thermally stable trapping sites for atomic Sr in an annealed Ar matrix. The full range emission scans, produced with site-selective excitation, are presented in Figure V.62. In addition to the resonance $^1P_1$ emission bands, three emission features are observed at 676.1, 691.9 and 722.2 nm – occurring in the region of the ^3P_J atomic manifolds.
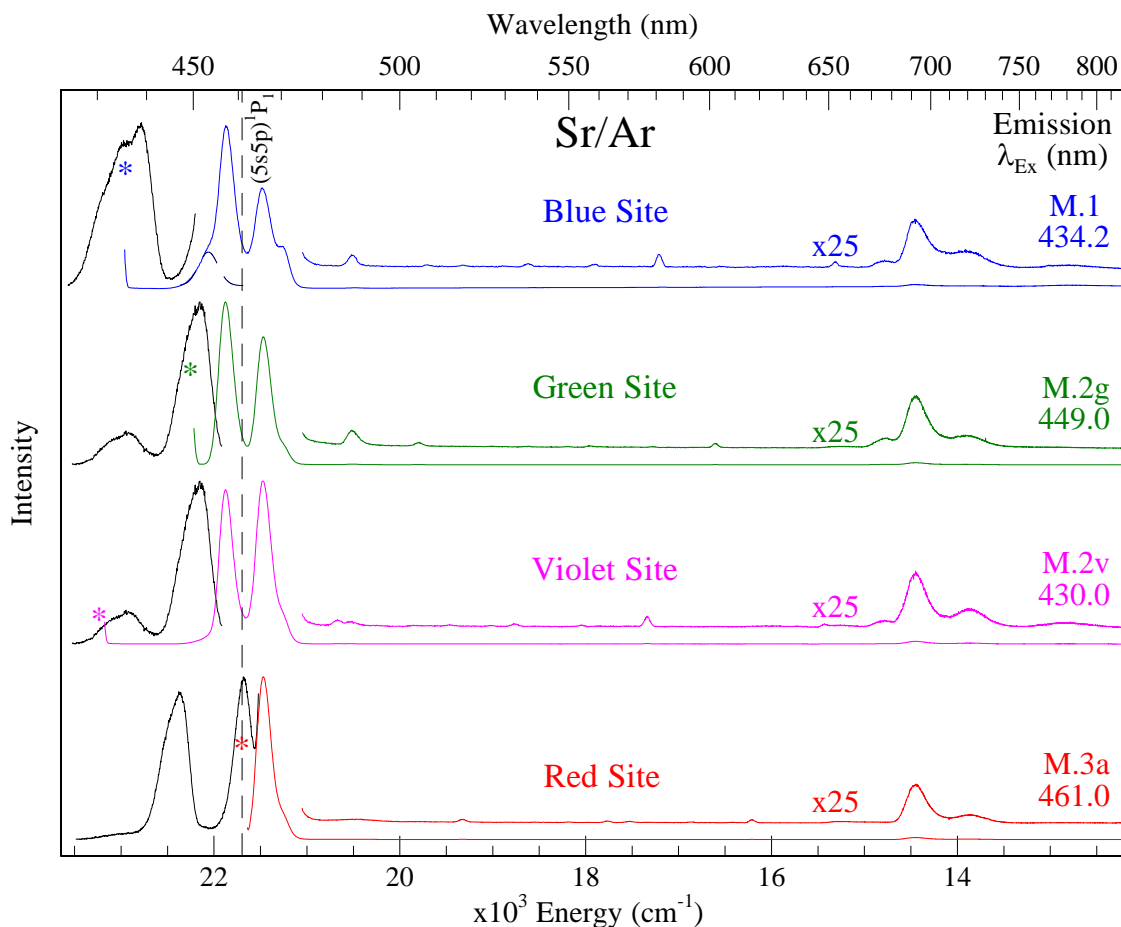
Figure V.62   **Excitation (black) and full range emission spectra (coloured) recorded for Sr/Ar following sample annealing to 28 K. The gas phase position[4] of the resonance (5s5p) $^1P_1 \leftarrow$ (5s^2) $^1S_0$ transition of Sr is shown as a dashed vertical line. The asterisks mark the excitation wavelength used to produce each emission scan. A Gaussian fit of the blue site (5s5p) $^1P_1$ emission is represented by the dashed blue line (top traces).**

Inspection of this plot shows that the relative intensity of these bands do no vary much with the excitation wavelength, which complicates the assignment of each to one of the specific sites of isolation. A comparison of the excitation spectra recorded monitoring these near-IR bands with those extracted from the $^1P_1$ luminescence will be presented

in the following section, in a bid to identify the Sr/Ar site of isolation giving rise to each feature. Following site attributions, the photophysical and temporal properties will be examined and state assignments will be made.

V.2.VIII.I $\lambda_{em} \approx 700$ nm

The 2D-EE spectrum of an annealed Sr/Ar sample, recorded in the 700 nm spectral region, is presented in Figure V.63. The 691.6 nm emission feature (I) dominates the luminescence in this region. A vertical excitation slice[g] at this emission wavelength (X.4) is shown in the bottom of Figure V.64.
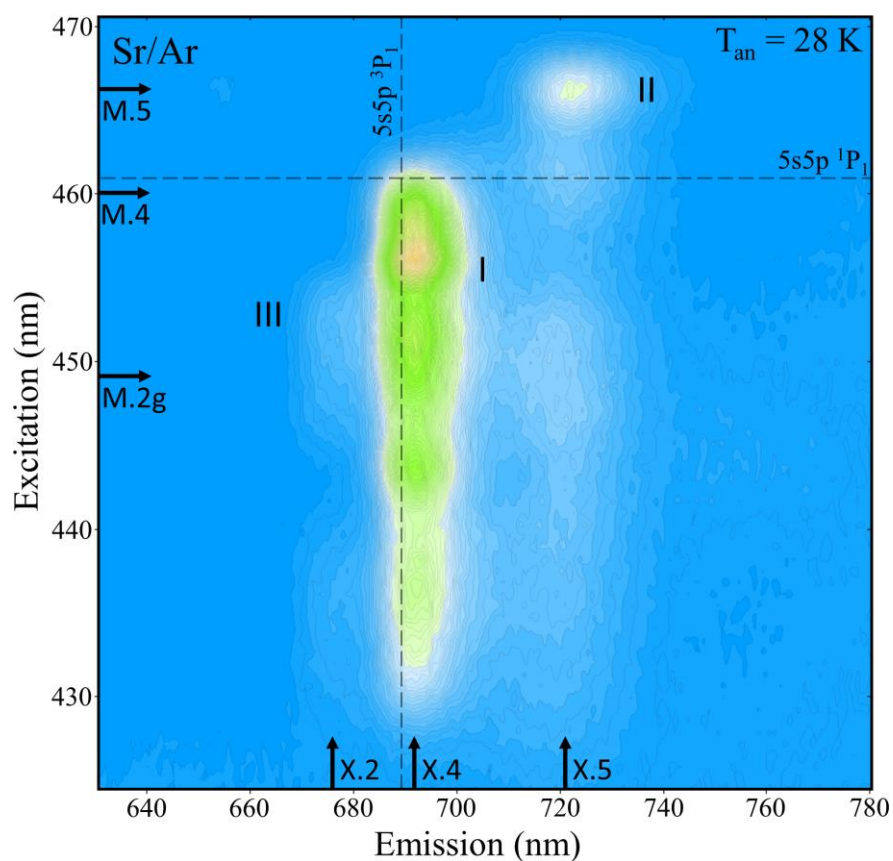
Figure V.63   **Sr/Ar 2D-EE spectrum, recorded in the 700 nm spectral region, following sample deposition at 10 K and annealing to 28 K. The gas phase position[4] of the resonance (5s5p) $^1P_1 \leftarrow$ (5s^2) $^1S_0$ transition of Sr is shown in excitation, represented by a dashed horizontal line. In emission, the gas phase position of (5s5p) $^3P_1 \leftarrow$ (5s^2) $^1S_0$ transition is shown by a dashed vertical line.**

---

[g] The labelling scheme employed for the emission and excitation slices is consistent with the scheme used for the 460nm region. For example, the slices for the green site are denoted as M.2g and X.2 in both spectral regions.

Excitation slices (X.5 and X.2) of the weaker features (II and III) are also presented in the bottom of this plot. A comparison of these scans with those obtained monitoring the 475 nm emission bands reveals a number of important points regarding the origin of the 700 nm features. Firstly, the lowest energy emission at 722.2 nm corresponds to the remnants of a thermally unstable (T.U.) site of isolation. The grey excitation profile shown in the top of Figure V.64 was obtained by monitoring the emission at 470.5 nm[h] and consists of two main peaks at 462.3 and 466.2 nm.
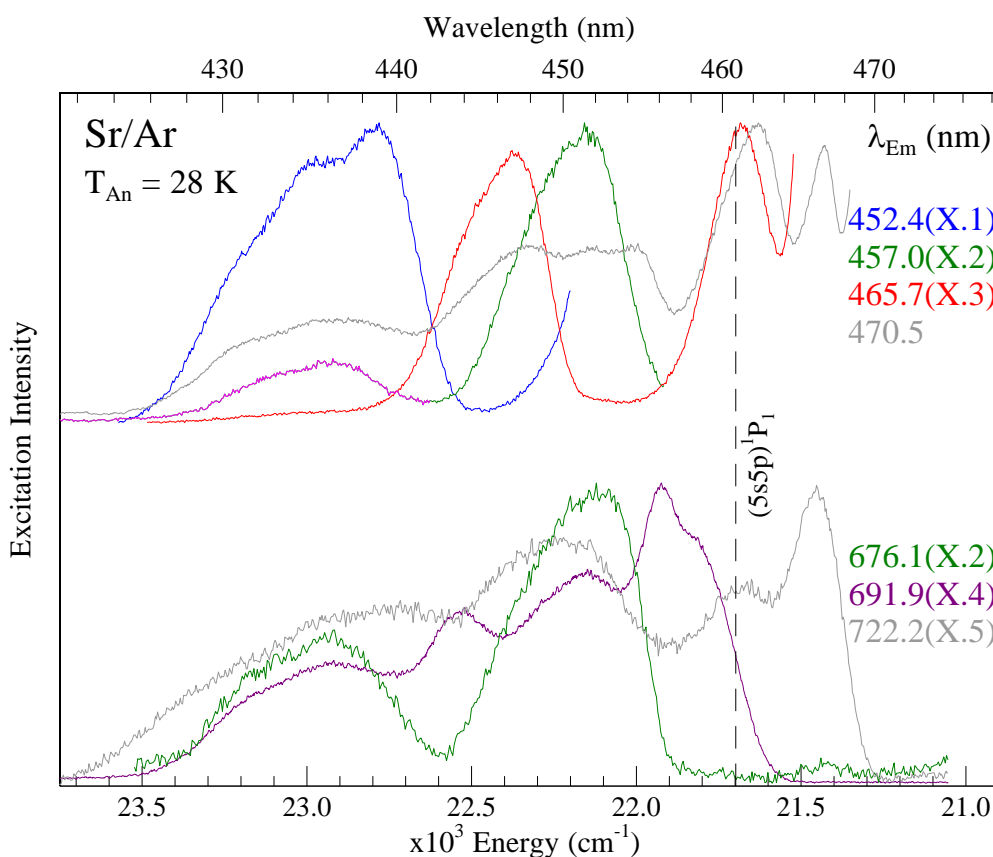
Figure V.64   **A comparison of the excitation spectra recorded monitoring the $^1P_1$ emission bands (top traces) versus those obtained from the near-IR emission bands ~ 700 nm (lower traces). The grey excitation spectra represent a thermally unstable site of isolation. The gas phase position[4] of the resonance (5s5p) $^1P_1 \leftarrow$ (5s^2) $^1S_0$ transition of Sr is shown as a dashed vertical line.**

The most prominent features of the two grey excitation profiles (top and bottom) match quite well, indicating that same, thermally unstable, site of isolation is responsible for the emission bands at 470.5 and 722.2 nm. Secondly, the very weak emission at 676.1

---

[h] This band was not discussed in the Section V.2.VII.I as it can be fully removed with annealing to temperatures of 30 K or more.

corresponds to the green site of isolation. A comparison of the green traces in Figure V.64 reveals a clear resemblance, with the most dominant component in both centred at ~450 nm, i.e. the green site absorption band. Finally, the excitation profile recorded for the 691.6 nm emission does not have a (5s5p) $^1P_1$ counterpart and must correspond to a new, unique 'red' site of isolation. This will be referred to as the R2 trapping site. The main R2 absorptions occur as a doublet with peaks at 456.2 and 458.5 nm. There may be a third absorption component associated with this site (e.g. the peak located at 443.8 nm), but it is difficult to be certain because the excitation profile extends across the entire (5s5p) $^1P_1$ range due to re-absorption effects.

A close-up view of the 700 nm emission bands is presented in Figure V.65. For comparative purposes, the gas phase positions of the atomic (5s5p) ^3P_J manifolds are represented by dashed vertical lines.
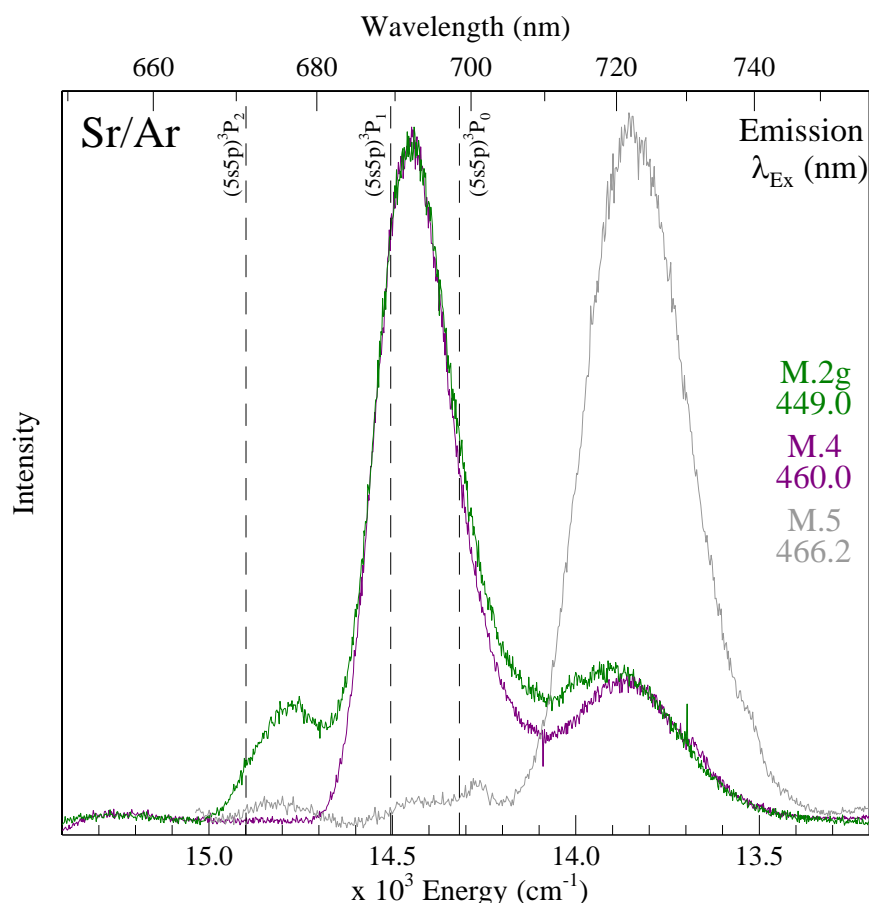
Figure V.65   **Normalised emission spectra produced with site-selective excitation of the (5s5p) $^1P_1$ features. The green, purple and grey scans were obtained with irradiation of the green, R2 and T.U. sites of isolation respectively. The atomic (5s5p) ^3P_J states are shown by dashed vertical lines.**

The spectra shown correspond to horizontal slices through the 2D-EE plot (Figure V.63) at excitation values denoted by M.2g, M.4 and M.5. The following section aims to identify the excited state from which the two most stable emission features arise.

V.2.VIII.I.A   Green site

The green site emission is centred at 676.1 nm and is characterised by a bandwidth of 239 cm^{-1}. A decay profile for this feature is presented in Figure V.66 and is well fit with a double exponential function, employing decay times of 8.0 and 115.0 µs with amplitudes of 573 and 676 respectively.
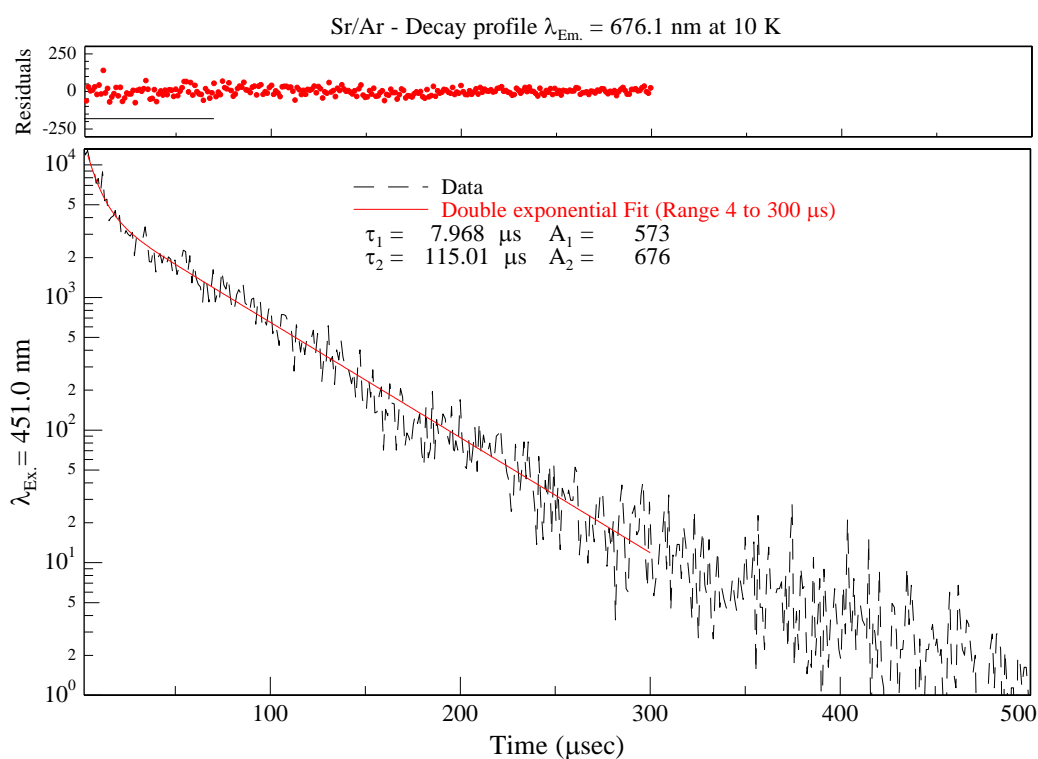
Figure V.66   **Decay profile of the Sr/Ar green site emission band at 676.1 nm, produced by site-selective laser excitation at 451.0 nm and recorded using the multi-channel scaling technique. $\sigma\tau_1 = \pm 0.7$ µs and $\sigma\tau_2 = \pm 2.0$ µs.**

The temperature dependence of the decays are presented in the right panel of Figure V.67 and the results of each fit are collected in Table V.10. The temporal attributes show little or no change between 10 and 12 K, indicating that the true radiative lifetime has been identified. Applying the effective field correction produces excited state decay times of 16.4 and 236.2 µs. As the shorter component (τ_1) is in very good agreement with the gas phase lifetime of the (5s5p) $^3P_1$ excited state, assignment to the spin-

forbidden $(5s5p)\ ^3P_1 \rightarrow (5s^2)\ ^1S_0$ atomic transition is made. Inspection of the spectral scans shown in the left panel of Figure V.67 reveals that the green site emission intensity increases as the sample temperature is raised. This implies that a feeding step to the $(5s5p)\ ^3P_1$ state has become enhanced. While the shorter decay time (τ_1) remains constant from 10 to 26 K, the longer time component (τ_2) is somewhat reduced over this range.
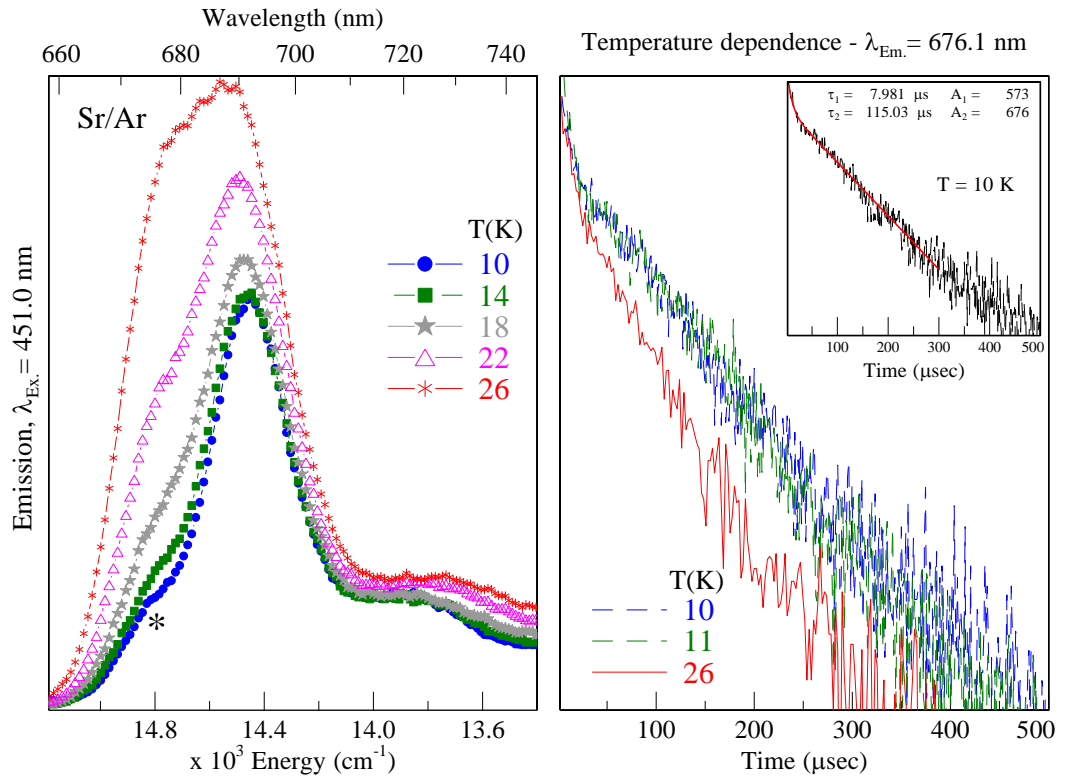
Figure V.67   The left panel shows the temperature dependence of the Sr/Ar green site emission band at 676.1 nm (denoted by a *) recorded over the range 10 – 26 K. The right panel presents the temperature dependence of the decay curves, recorded at 10, 11 and 26 K. The inset of the right panel shows the double exponential fit for the decay recorded at 10 K.

Table V.10   Temporal characteristics of the Sr/Ar 676.1 nm emission band, recorded over the temperature range of 10 to 26 K.

T_s (K)	Fit Range (μs)	A_1	τ_1 (μs)	A_2	τ_2 (μs)
10	4 – 300	573	8.0	676	115.0
11	4 – 300	890	7.9	604	116.8
12	4 – 300	2430	8.0	1277	117.5
26	3 – 200	335	8.2	372	75.8

V.2.VIII.I.B   Red (R2) site

The R2 site emission band, located at 691.9 nm, exhibits a fwhm of 239 cm^{-1}. The decay profile recorded for this feature at 10 K is presented in Figure V.68. A triple exponential function is required to accurately fit the data. The three time components are 9.6, 86.2 and 529.1 µs and the amplitude values are 1327, 1681 and 356 respectively.
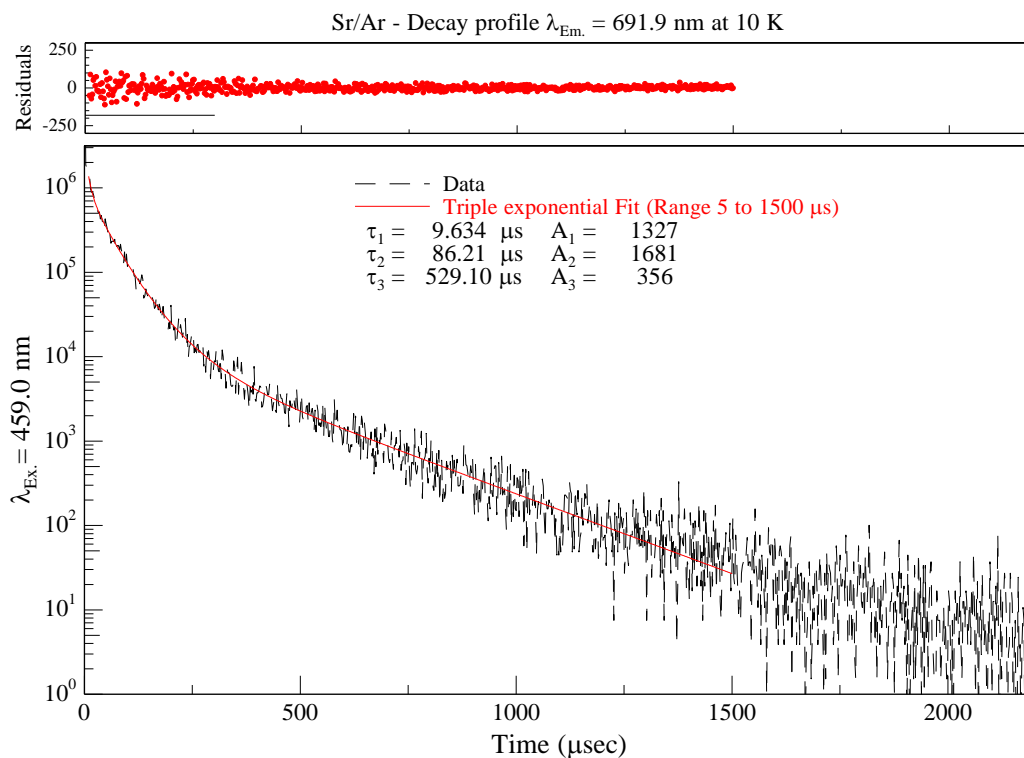
Figure V.68   **Decay profile of the Sr/Ar R2 site emission band at 691.9 nm, produced by site-selective laser excitation at 459.0 nm and recorded using the multi-channel scaling technique. στ1 = ± 0.8 µs, στ2 = ± 1.6 µs and στ3 = ± 15.6 µs.**

The temperature dependence of the temporal scans is presented in the right panel of Figure V.69 and the results of the fit at each temperature are collected in Table V.11. The dominant components of the fit (τ_1 and τ_2) are relatively constant over the range of 10 to 12 K, implying that the radiative lifetime of the transition has been obtained. Applying the effective field correction to the decay times measured at 10 K yields excited state lifetimes of 19.8 and 177.1 µs. The shorter component agrees very well with the gas phase lifetime of the Sr: (5s5p) $^3P_1 \rightarrow$ (5s^2) $^1S_0$ transition, allowing for an assignment to be made. Overall, the decay profiles show a strong temperature dependence and are shortened dramatically over the range 10 to 22 K. This effect

appears to be related to the minor component (τ_3), which becomes less significant (in amplitude) as the temperature increases and is completely absent from the decays recorded at temperatures above 14 K.
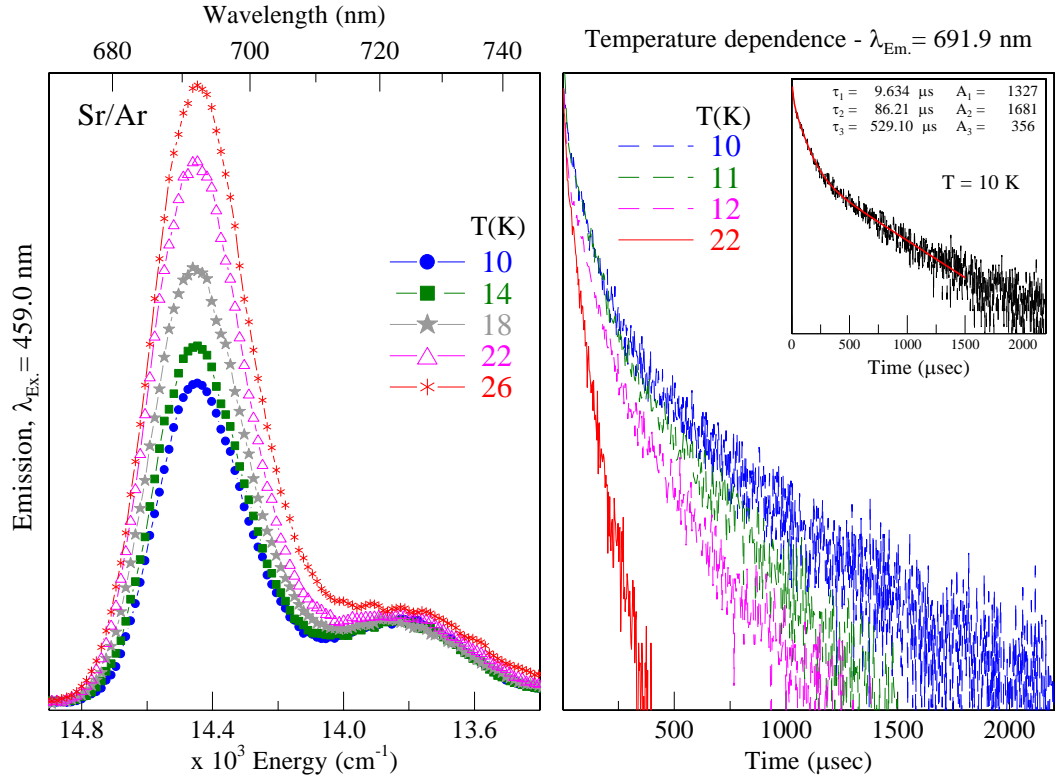
Figure V.69   The left panel shows the temperature dependence of the Sr/Ar R2 site emission band at 691.9 nm recorded over the range 10 – 26 K. The right panel presents the temperature dependence of the decay curves, recorded at 10, 11, 12 and 22 K. The inset of the right panel shows the double exponential fit for the decay recorded at 10 K.

Table V.11   Temporal characteristics of the Sr/Ar 691.9 nm emission band, recorded over the temperature range of 10 to 22 K.

T_s (K)	Fit Range (μs)	A_1	τ_1 (μs)	A_2	τ_2 (μs)	A_3	τ_3 (μs)
10	5 – 1500	1327	9.6	1681	86.2	356	529.1
11	5 – 1300	2044	9.7	1040	112.9	246	564.5
12	5 – 1000	2015	9.5	1296	93.8	227	399.9
18	5 – 300	3669	6.3	1208	83.9	-	-
22	5 – 200	988	8.1	840	59.4	-	-

V.2.IX   Sr/Ar (5s5p $^1P_1$) luminescence summary

A summary of the Sr/Ar luminescence is presented in Figure V.70. Four thermally stable sites of isolation (blue, green, violet and R1) were found from the 2D-EE spectra recorded with the emission wavelength centred at 460 nm. The true radiative lifetime was identified for each site - nanosecond values were observed in all cases. Accordingly, the 460 nm emission bands were confidently assigned to the resonance $(5s5p)\ ^1P_1 \rightarrow (5s^2)\ ^1S_0$ transition of atomic Sr. In addition, a narrow green site band was observed at 487.3 nm and was tentatively assigned as $(5s4d)\ ^1D_2 \rightarrow (5s^2)\ ^1S_0$ emission.
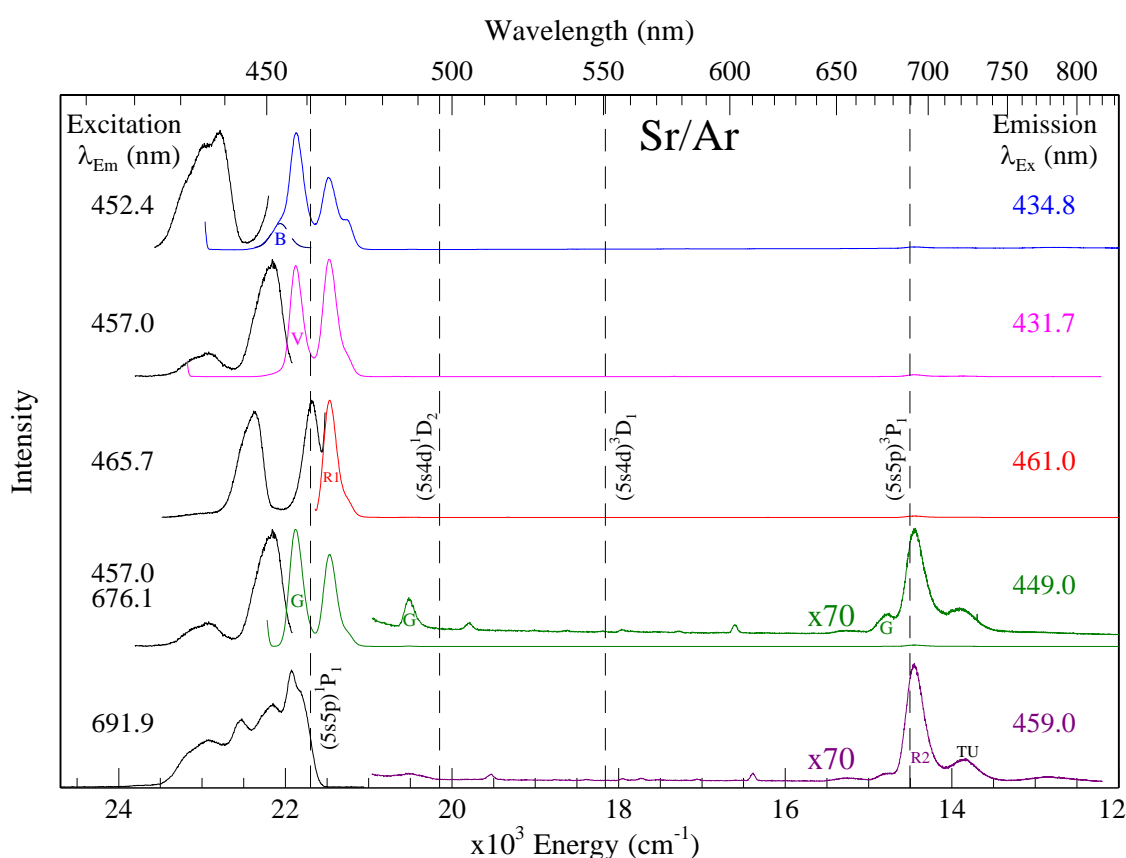
Figure V.70   **A summary of the excitation and emission features arising from the isolation of atomic Sr in the five thermally stable sites of solid Ar. The gas phase positions[4] of the (5s5p) $^1P_1$, (5s4d) $^1D_2$, (5s4d) $^3D_1$ and (5s5p) $^3P_1$ excited states are shown as dashed vertical lines. A Gaussian fit of the blue site (5s5p) $^1P_1$ emission is represented by the dashed blue line (top traces).**

Lower energy emission bands, occurring near the (5s5p) ^3P_J atomic levels, were also observed for Sr/Ar. The excitation spectra recorded of these bands showed that a distinct Ar trapping site gave rise to each emission. The weak band at 676.1 nm was attributed to the green site of isolation and the emission at 722.2 nm was assigned to a

thermally unstable site, which was not fully removed with annealing to 28 K. The excitation profile, recorded of the dominant emission in this region, did not match any of the existing $^1P_1$ excitation features. As a result, this band was attributed to a secondary 'red' site of isolation, labelled R2. The radiative lifetimes of the two thermally stable near-IR features were identified. Comparable to the other Sr/RG systems investigated, the lower energy emission bands exhibited multi-exponential decays. The shortest decay component of each band was 8.0 and 9.6 μs, for the green and R2 site emission respectively. Based on these values, a tentative assignment to the $(5s5p)\,^3P_1 \rightarrow (5s^2)\,^1S_0$ transition of atomic Sr was made.

Overall, the proportion of excited Sr ($^1P_1$) atoms reaching the $^3P_1$ state in Ar is significantly smaller when compared to Kr and Xe. Indeed, the blue, violet and R1 sites did not demonstrate any $(5s5p)\,^3P_1$ emission, even at elevated temperatures. The green site yielded a very weak $^3P_1$ band at 10 K and this could be enhanced with increasing the sample temperature (at least up to 26 K). It is very interesting that R2 site does not emit from the $(5s5p)\,^1P_1$ excited state and could only be identified from the $^3P_1$ emission it produces. Clearly the efficiency of the $(5s5p)\,^1P_1 \rightarrow (5s5p)\,^3P_1$ population transfer is very high for Sr atoms located in this site of isolation. The photophysical and temporal characteristics of the observed Sr/Ar emission bands are collected in Table V.12 along with the state assignments.

Table V.12 **The photophysical characteristics of the thermally stable and site-specific emission features of Sr/Ar, which were obtained with (5s5p) $^1P_1$ excitation. The spectral positions are quoted in both nanometres (nm) and wavenumber (cm^{-1}) units. δ represents the gas phase to matrix frequency shifts, given in wavenumber units. The bandwidth (full width at half maximum, fwhm) is denoted by the symbol Δ and is also expressed in units of wavenumber. The observed lifetimes, recorded in the matrix at 10 K, are listed in the rightmost column**

Gas Phase	Sr/Ar Site	λ_{em} (nm)	ν (cm^{-1})	δ (cm^{-1})	Δ (cm^{-1})	τ_{obs} at 10 K
(5s5p)^{1}P$_1 \rightarrow$ (5s5p)^{1}S$_0$	Blue	452.4	22104	406	186	2.8 ns
ν = 21698.45 cm^{-1}	Green	457.0	21882	183	202	3.0 ns
τ = 4.98 ns	Violet	457.0	21882	183	184	2.4 ns
	R1	465.7	21473	-225	180	3.2 ns
(5s5p)^{1}D$_2 \rightarrow$ (5s5p)^{1}S$_0$	Green	487.3	20521	372	131	64 ns
ν = 18159.04 cm^{-1}						
(5s5p)^{3}P$_1 \rightarrow$ (5s5p)^{1}S$_0$	Green	676.1	14791	286	174	8.0 / 115.0 μs
ν = 14504.33 cm^{-1}	R2	691.9	14453	-51	239	9.6 / 86.2 / 529.1 μs
τ = 21.3 μs						

V.3 Sr/RG (5s5p $^1P_1$) discussion and conclusions

V.3.I Site association

A summary of the excitation spectra recorded for atomic Sr isolated in Ar, Kr and Xe is presented in Figure V.71. Annealed Sr/Xe samples represent the simplest situation, with the occurrence of two sites of isolation which are labelled as 'blue' and 'green'.
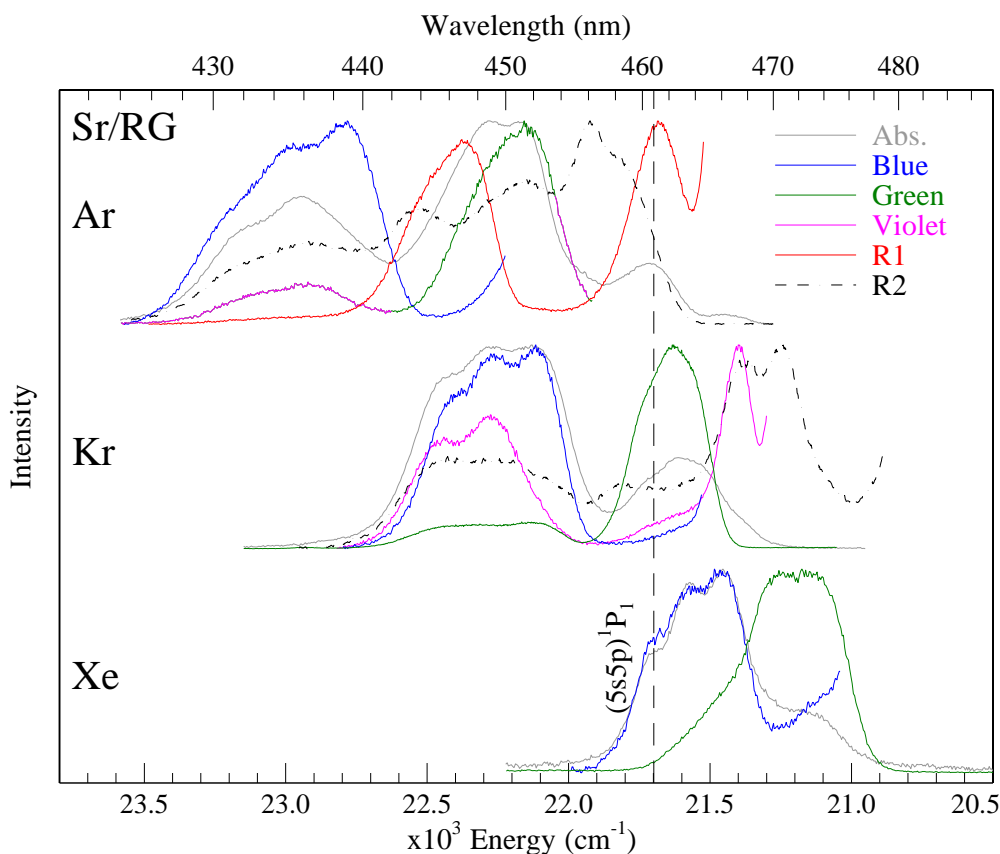
Figure V.71 **A summary of the Sr/RG site-specific excitation spectra recorded in the region of the dominant (5s5p) $^1P_1 \leftarrow$ (5s^2) $^1S_0$ transition of Sr at 10 K, following sample annealing.**

Blue and green sites were also identified for Sr isolated in annealed Ar and Kr matrices. The polarisability model (see Chapter IV) of Laursen and Cartland[9] is applied to these two Sr/RG sites, the results of which are presented in Figure V.72. The gas phase to matrix frequency shift is calculated from each of the blue site threefold components.
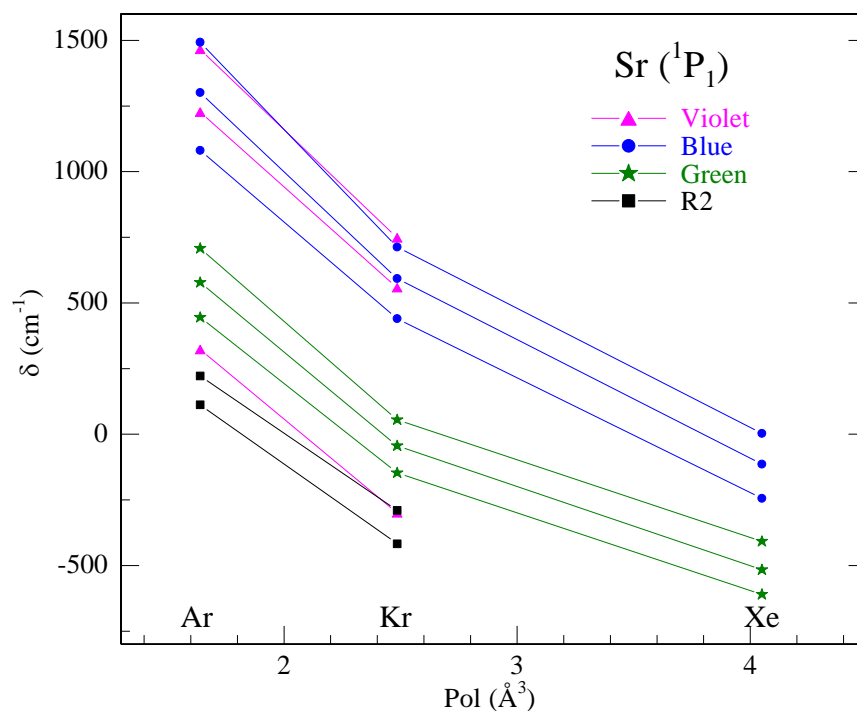
Figure V.72   A plot of the gas phase to matrix frequency shifts (δ cm^{-1}), observed for each absorption component of the violet, blue and green sites which were identified using the (5s5p) $^1P_1$ ← (5s^2) $^1S_0$ transition of atomic Sr, versus the RG host polarizabilities. The three components plotted for the green site in each host were obtained from Gaussian fits of the excitation bands.

As the green site excitation spectra are broad and featureless, the results of the Gaussian lineshape fits are used to extract the three JT components. This analysis demonstrates a correspondence between the sites of a given 'colour' in all three hosts. For example, the dominant site in Xe, which shows a Jahn-Teller (JT) splitting, is associated with the dominant JT band observed in Kr and the threefold split band in Ar. Thus, each site 'colour' represents a particular type of trapping environment for atomic Sr in the rare gas solids.

In contrast to Sr/Xe, additional thermally stable sites were found in the lighter hosts, Ar and Kr. For Sr/Kr, a clear asymmetric threefold (2+1) excitation band was observed, arising due to the occupation of the 'violet' trapping site. Although masked by the more dominant blue and green site absorptions, an equivalent violet site excitation profile was identified for Sr in Ar – in this case a lineshape analysis was required to extract the lower energy singlet band. The polarizability model can only be applied to two RG hosts because a violet site was not observed for Sr/Xe. Nonetheless, the gas phase to matrix frequency shift calculated from each of the asymmetric threefold peaks is plotted against the RG polarizability in Figure V.72 (pink triangles

connected by a solid pink line). The slope of the line from Ar to Kr is very similar for each component implying that the same kind of trapping site is occupied in both hosts, viz. the violet site.

The remaining sites of isolation in Ar and Kr are more challenging to interpret. Two 'red' sites of isolation exist for Sr in Ar. The excitation profile for the R1 (primary red) site, represented by the red trace in Figure V.71, was obtained by monitoring the resonance $(5s5p)\ ^1P_1 \rightarrow (5s^2)\ ^1S_0$ emission at 465.7 nm. Similar to the violet site, the absorption/excitation spectrum of Sr atoms trapped at this location is characterised by an asymmetric threefold $(2+1)$ splitting pattern. In contrast, the R2 site of isolation does not show any $(5s5p)\ ^1P_1$ emission and the excitation profile, shown by the black dashed trace in the top of Figure V.71, was obtained from the $(5s5p)\ ^3P_1$ emission band at 691.9 nm. A single, partially stable red site exists for Sr in Kr and the excitation scan for this site is represented by black dashed trace in the middle of Figure V.71.

It is proposed that the secondary red (R2) site in Ar corresponds to the single red site of isolation in Kr – both excitation profiles are comparable, exhibiting a dominant doublet structure with a lower energy shoulder. Moreover, these features are red-shifted with respect to the absorptions of the higher energy sites by a similar amount. In Figure V.72, the gas phase to matrix frequency shift calculated from each resolved doublet peak is plotted against the RG polarizability. Indeed, the slope of the line (black squares connected by a solid black line) from Ar to Kr is the same for each component and is similar to the slopes observed for the other RG trapping sites. This site will be referred to as R2 hereafter. Finally, it appears that the R1 trapping site exists solely in Ar and has no thermally stable counterpart in the heavier RG hosts. The photophysical properties of the site-specific absorption/excitation are collected in Table V.13 for the three RG hosts.

V.3.II   Blue site

A summary of the blue site luminescence in the three Sr/RG systems is presented in Figure V.73 and the photophysical properties are collected in Table V.13 (excitation) and Table V.14 (emission). Inspection of Figure V.73 demonstrates that the blue site of isolation must be one of high (cubic) symmetry (O_h or T_d) since resolved (Jahn-Teller) threefold split absorption/excitation bands (black traces) are observed in each RG solid.
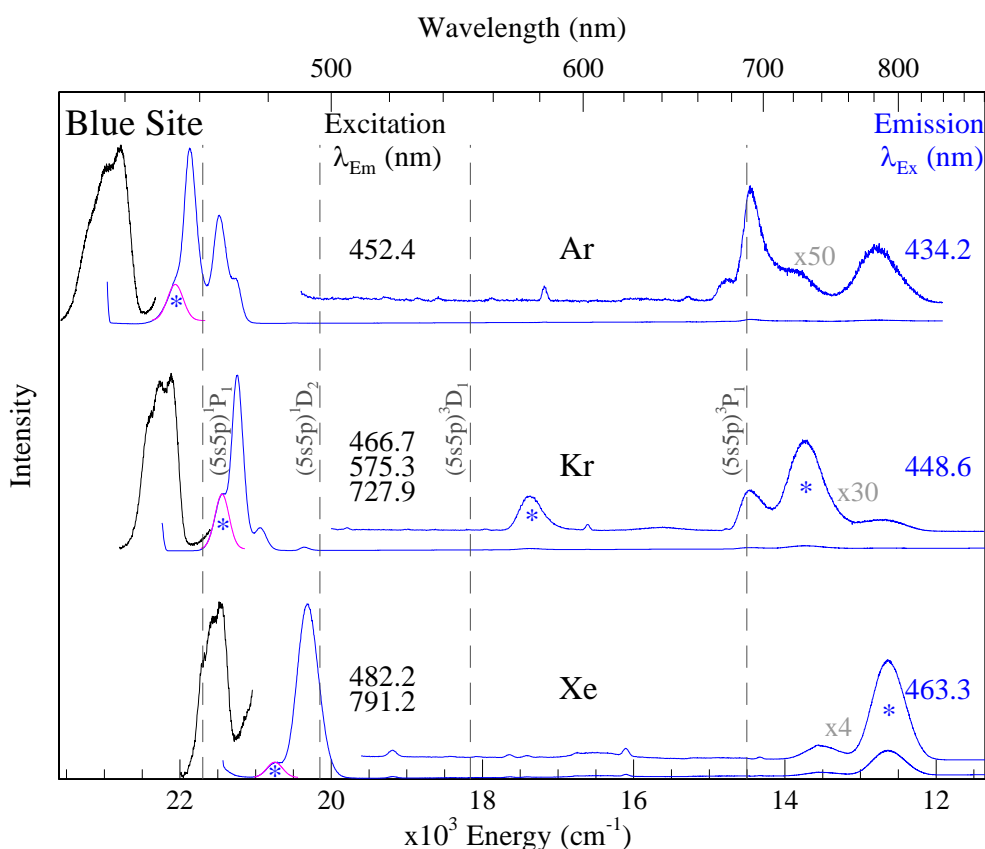
Figure V.73   **Excitation (black) and emission (blue) spectra recorded for the Sr/RG blue site of isolation, following sample annealing to 28, 45 and 60 K for Ar, Kr and Xe respectively. The gas phase positions[4] of the (5s5p) $^1P_1$, (5s4d) $^1D_2$, (5s4d) $^3D_1$ and (5s5p) $^3P_1$ excited states are shown as dashed vertical lines. The emission bands originating from Sr atoms trapped in the blue site of each RG host are indicated by an asterisk '*'. The Gaussian fits of the blue site (5s5p) $^1P_1$ emissions are represented by the solid pink lines.**

A lineshape analysis was conducted for the these bands and revealed the average width of three JT components is 247, 179 and 146 cm^{-1} for Ar, Kr and Xe respectively (see Appendix V.I).

Table V.13 **Photophysical characteristics of the thermally stable Sr/RG sites of isolation as revealed by the (5s5p) $^1P_1 \leftarrow$ $^1S_0$ (5s^2) excitation spectroscopy. δ represents the gas phase to RG matrix shift (given in units of wavenumber) calculated from the gas phase value[4] for this transition at 460.9 nm or 21698.452 cm^{-1}. *Component extracted from Gaussian fit.**

Sr/RG Site	Component	λ_{ex} (nm)	ν (cm^{-1})	δ (cm^{-1})
Ar	1	431.7	23164	1466
Violet	2	436.2	22925	1227
	3*	454.1	22022	323
	1	431.2	23191	1493
Blue	2	434.8	22999	1301
	3	439	22779	1081
	1*	446.3	22406	708
Green	2*	448.9	22277	578
	3*	451.6	22143	445
Red (R2)	1	456.2	21920	222
	2	458.5	21810	112
	1	444.7	22487	789
Red (R1)	2	447.3	22356	658
	3	461.2	21683	-16
Kr	1	445.5	22447	748
Violet	2	449.3	22257	558
	3	467.3	21400	-299
	1	446.2	22411	713
Blue	2	448.6	22292	593
	3	451.7	22139	440
	1*	459.7	21753	55
Green	2*	461.8	21654	-44
	3*	464	21552	-147
	1	467.1	21409	-290
Red	2	469.9	21281	-417
	3	474.3	21084	-615
Xe	1	460.8	21701	3
Blue	2	463.3	21584	-114
	3	466.1	21455	-244
	1*	469.7	21290	-408
Green	2*	472.1	21182	-516
	3*	474.2	21088	-610

Examination of Figure V.73 reveals that a progressive red-shift to lower energy is observed for the (5s5p) $^1P_1$ excitation (absorption) bands, as one moves to a heavier, more polarisable RG hosts (i.e. from Ar to Kr to Xe). The matrix-shift is related to the strength of the short-range M-RG repulsive interaction in the excited P state and strongly depends on the size of the vacancy[10]. In the blue site of isolation, values of +1301, +593 and -144 cm^{-1} are calculated from the band centres for Ar, Kr and Xe respectively. Clearly the excited 5p orbitals of the Sr atom experience the greatest confinement, and hence repulsive interaction, when located at this site in Ar. In contrast, the net interaction[i] is slightly attractive for the blue site in Xe. We can infer that Xe possesses a larger blue site cavity than Ar – this is directly related to the greater *fcc* lattice parameter of solid Xe.

Table V.14 The photophysical properties of the Sr/RG blue site, obtained with (5s5p) $^1P_1$ excitation. The emission spectral positions are quoted in both nanometres (nm) and wavenumber (cm^{-1}) units. δ represents the gas phase to matrix frequency shifts, given in wavenumber units. The Stokes shift (S.S.) is computed from the centre of the JT excitation band to the centre of the emission feature. The bandwidth (full width at half maximum, fwhm) is denoted by the symbol Δ and is also expressed in units of wavenumber. *Bandwidth obtained from a Gaussian lineshape fit.

Transition	Host	λ_{em} (nm)	ν (cm^{-1})	δ (cm^{-1})	S.S (cm^{-1})	Δν (cm^{-1})
(5s5p)$^1P_1 \rightarrow$ (5s5p)$^1S_0$	Ar	452.4	22104	406	895	186*
	Kr	466.7	21427	-271	865	203*
	Xe	482.2	20738	-960	846	258*
(5s5p)$^3P_1 \rightarrow$ (5s5p)$^1S_0$	Ar	-	-	-	-	-
	Kr	727.9	13738	-766	8553	539
	Xe	791.2	12639	-1865	8945	516
(5s4d)$^3D_1 \rightarrow$ (5s5p)$^1S_0$	Kr	575.3	17382	-777	4909	370

The full range emission scans are depicted by the solid blue traces in Figure V.73. The spectra shown are quite complex, especially for Ar and Kr, owing to re-absorption effects. The blue site emission band occurs within the broad (5s5p) $^1P_1$ absorption profiles in the lighter RG hosts. As a consequence, the lower energy trapping

---

[i] Using simple 1:1 Sr-RG diatomics as a model, the 'net' interaction may be described as the sum of contributions from the repulsive Σ and attractive Π molecular orbitals. The contribution of the former becomes enhanced, owing to the Pauli Exclusion Principle, at shorter internuclear separations - such distances occur in smaller RG vacancies. The latter becomes more significant with increasing RG polarizability.

sites are indirectly excited, giving rise to numerous emission bands. Analysis of the 2D-EE spectra recorded of these features, in particular the excitation slices, allowed for conclusive site assignments to be made. For clarity, the emission bands specific to the blue site are marked with an asterisk. As can be seen, the luminescence of this site strongly depends on the RG host. For Ar, only a single feature exists at 452.4 nm which was assigned to the resonance $(5s5p)$ $^1P_1 \rightarrow (5s^2)$ $^1S_0$ atomic transition. In contrast, two bands are observed for Sr/Xe. Although the radiative lifetime could not be obtained, the weaker 482.2 nm feature was tentatively assigned as resonance $(5s5p)$ $^1P_1 \rightarrow (5s^2)$ $^1S_0$ emission. The dominant, lower energy band at 791.2 nm was assigned to the spin-forbidden $(5s5p)$ $^3P_1 \rightarrow (5s^2)$ $^1S_0$ transition of atomic Sr. In addition to the assigned $^1P_1$ and $^3P_1$ emission bands at 466.7 and 727.9 nm respectively, Sr/Kr exhibits a third feature at 575.3 nm. Based on the relatively long radiative lifetimes (1.4/0.5 μs) and spectral location, this emission was proposed to correspond to the $(5s4d)$ $^3D_1 \rightarrow (5s^2)$ $^1S_0$ transition. However, in the absence of a gas phase lifetime to compare with, a definitive assignment was not possible.

Akin to the $(5s5p)$ $^1P_1$ absorption bands, the $(5s5p)$ $^1P_1$ and $(5s5p)$ $^3P_1$ emission features are shifted to longer wavelengths with increasing RG mass. The gas-phase-to-matrix shifts listed in Table V.14 highlight this trend. For instance, the blue site $(5s5p)$ $^1P_1$ emission bands exhibit matrix shifts of 406, -271 and -960 cm^{-1} in Ar, Kr and Xe respectively. The corresponding values for the $^3P_1$ bands are larger, with red-shifts of -766 and -1865 cm^{-1} observed respectively for Kr and Xe. Also evident in Table V.14 is the greater spectral widths of the $^3P_1$ emission bands when compared to the $^1P_1$ bands. This behaviour indicates that a greater excited state stabilisation occurs for the $^3P_1$ state than for the $^1P_1$ state. Such an effect can be qualitatively explained by the 1:1 M-RG excited state PECs. As these are not known for the Sr-RG complexes, the existing Ca-RG determinations will be used. This is reasonable since the lowest excited states of both metal atoms exhibit the same energy ordering. Theoretical determinations by Czuchaj *et al.*[11] revealed that, for a given RG atom, the (Ca ^3P + RG) $^3\Pi$ molecular state is more attractive than the (Ca ^1P + RG) $^1\Pi$ state and the equilibrium bond lengths of the triplet states are up to 0.7 Å shorter. This effect was also confirmed for Ca-Ar by the pseudopotential calculations of Breckenridge and co-workers[12].

V.3.III Green site

A summary of the green site luminescence in the three Sr/RG systems presented in Figure V.74 and the photophysical properties are collected in Table V.13 (excitation) and Table V.15 (emission). In a given host, the (5s5p) $^1P_1$ absorption band of this site is narrower than that of the blue site and exhibits, at most, only a partially resolved threefold splitting pattern. The observed bandwidths are tentatively attributed to the dynamic JT effect, which lifts the degeneracy of the excited 5p orbitals of Sr. A lineshape analysis conducted allowed the average width of the three JT components to be extracted – values of 149, 132 and 141 cm^{-1} were obtained for RG = Ar, Kr and Xe respectively.
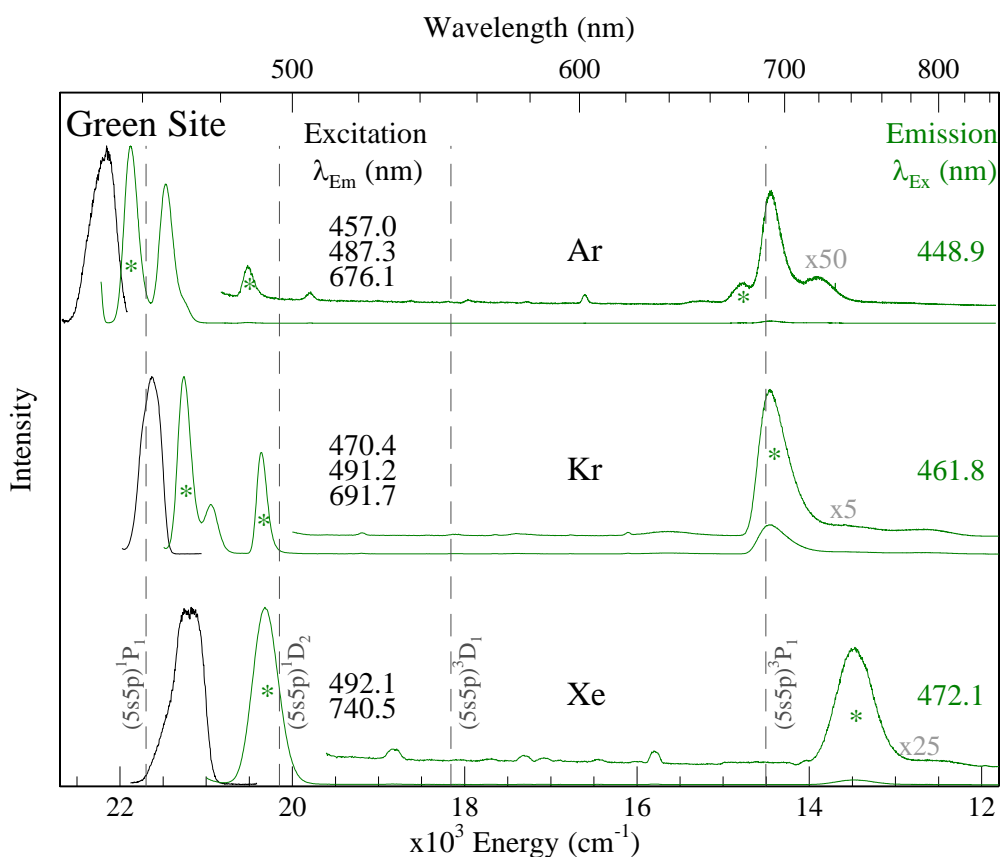
Figure V.74   **Excitation (black) and emission (green) spectra recorded for the Sr/RG green site of isolation, following sample annealing to 28, 45 and 60 K for Ar, Kr and Xe respectively. The gas phase positions[4] of the (5s5p) $^1P_1$, (5s4d) $^1D_2$, (5s4d) $^3D_1$ and (5s5p) $^3P_1$ excited states are shown as dashed vertical lines. The emission bands originating from Sr atoms trapped in this site are indicated by an asterisk '*'.**

Comparing the relative positions of the green and blue site excitation bands in a given host reveals that the green site is a larger vacancy than the blue site. The excited (5s5p)

$^1P_1$ Sr atom experiences a smaller repulsive interaction in Ar and a greater overall attractive interaction in Kr and Xe matrices, when trapped in this void.

The emission bands specific to the green site are marked with an asterisk in Figure V.74. Xe represents the simplest host, with the occurrence of two main features at 492.1 and 740.5 nm. The highest energy band overlaps the gas phase position of the $(5s4d)\ ^1D_2$ state. However the large bandwidth and nanosecond lifetime value allowed this feature to be assigned as resonance $(5s5p)\ ^1P_1 \rightarrow (5s^2)\ ^1S_0$ emission. In contrast, the lowest energy band exhibited a much longer (µs) radiative decay and, as a result, was assigned to the spin forbidden $(5s5p)\ ^3P_1 \rightarrow (5s^2)\ ^1S_0$ transition of atomic Sr. Similar to Xe, green site excitation in Ar (Kr) yields a higher energy $(5s5p)\ ^1P_1$ emission band at 457.0 (470.4) nm and a near-IR $(5s5p)\ ^3P_1$ band at 676.1 (691.7) nm. As was the case for the blue site, Sr/Kr exhibits a third intense emission band which is located at 491.2 nm. An equivalent green site emission was observed in Ar at 487.3 nm – although the intensity is far weaker in this host. Excited state lifetime values recorded of these bands at 10 K were within the range of 40 – 65 ns. However, the temporal decay curves showed a strong temperature dependence and the 10 K decay times are not radiative – the true radiative lifetimes may be longer.

Table V.15 **The photophysical properties of the Sr/RG green site, obtained with $(5s5p)\ ^1P_1$ excitation. The emission spectral positions are quoted in both nanometres (nm) and wavenumber (cm^{-1}) units. δ represents the gas phase to matrix frequency shifts, given in wavenumber units. The Stokes shift (S.S.) is computed from the centre of the excitation band to the centre of the emission feature. The bandwidth (full width at half maximum, fwhm) is denoted by the symbol Δ and is also expressed in units of wavenumber. *Bandwidth obtained from a Gaussian lineshape fit. #The matrix shifts for the unassigned emissions were computed from the nearest electronic state: $(5s4d)\ ^1D_2$.**

Transition	Host	λ_{em} (nm)	ν (cm^{-1})	δ (cm^{-1})	S.S (cm^{-1})	$\Delta\nu$ (cm^{-1})
$(5s5p)^1P_1 \rightarrow (5s5p)^1S_0$	Ar	457.0	21882	183	395	202
	Kr	470.4	21259	-440	396	180
	Xe	492.1	20321	-1377	861	343
$(5s5p)^3P_1 \rightarrow (5s5p)^1S_0$	Ar	676.1	14791	286	7486	239*
	Kr	691.7	14457	-47	7197	387
	Xe	740.5	13504	-1000	7678	499
$(5s5p)^1D_2 \rightarrow (5s5p)^1S_0$	Ar	487.3	20521	372#	1755	131
	Kr	491.2	20358	209#	1296	137

These features were provisionally assigned to the parity-forbidden (5s4d) $^1D_2 \rightarrow$ (5s^2) $^1S_0$ transition of atomic Sr. Indeed their spectral location, coupled with their narrow bandwidths (fwhm = 131 and 137 cm^{-1} for Ar and Kr respectively), are suggestive of a 'classical' D $\leftrightarrow$ S type transition[10]. The gas phase (5s4d) $^1D_2 \rightarrow$ (5s^2) $^1S_0$ lifetime has been determined from the emission spectrum of a Sr hollow-cathode lamp[7,8]. A value of 19.6 ±6 ms was obtained, which is in good agreement with a number of theoretical studies[7,13,14]. However, we know this transition will become enhanced in a matrix environment because the D $\leftarrow$ S absorption bands of Sr were easily identified in all three hosts (see Chapter III). A greater D $\leftrightarrow$ S transition probability was also observed for matrix-isolated atomic Mn[15], where the gas phase lifetimes were shortened by up to three orders of magnitude.

The photo-physical properties of the blue and green site (5s5p) $^1P_1$ emission bands are summarised in Table V.14 and V.15, respectively. A comparison of the two sites reveals an interesting effect. The Stokes shifts recorded for the blue site are relatively large and occur within a small range – values of 895, 865 and 846 cm^{-1} are observed for Ar, Kr and Xe respectively. Conversely, the Stokes shifts observed for the green site exhibit an unusual trend. Near-identical values of 395 and 396 cm^{-1} are evaluated for Ar and Kr – smaller than those of the blue site. However, the green site emission in Xe is Stokes shifted by more than twice as much, with a value 861 cm^{-1}. Moreover, the bandwidth of this 491.1 nm feature (343 cm^{-1}) is larger than any other (5s5p) $^1P_1 \rightarrow {}^1S_0$ (5s^2) emission. Indeed the green site exhibits a greater Stoke shift and bandwidth than even the blue site in the same host. The observed behaviour can be explained by two effects: 1. The strength of the Sr($^1P_1$)-RG interaction and 2. The size of the vacancy.

When compared to the green site in the lighter RGs, the larger bandwidth and Stokes shift in Xe can be mostly accounted for by the first effect. Considering the theoretical[11,12] PECs for the Ca·RG diatomics offers some insight. The key point of note is the substantial increase in the binding energies of the $^1\Pi$ potential energy curves, which correlate to the Ca($^1P_1$) + RG asymptote, with increasing rare gas mass (D$_e$ = 130, 216 and 337 cm^{-1} for RG = Ar, Kr and Xe). If the same trend holds for the Sr($^1P_1$)-RG interactions, then a greater degree of stabilisation can be expected for excited Sr($^1P_1$) atom when trapped in Xe. On the other hand, the size of the vacancy explains the photophysical characteristics observed for the blue and green site in Xe. In contrast

to the cramped blue site, the excited $Sr(^1P_1)$ atom has a greater freedom to explore the PES and reach a more stable, lower energy configuration, when isolated in the more voluminous green vacancy.

V.3.IV   R2 site

Figure V.75 summarises the luminescence of the R2 trapping site. This site was found to be thermally stable in Ar and partially stable in Kr, where it is greatly reduced between annealing temperatures of 40 and 45 K. The true excitation features of the R2 site are not easy to interpret as their scans extend across the full (5s5p) $^1P_1$ absorption range and contain contributions from numerous matrix sites. The most intense portion of each corresponds to a doublet structure plus a partially resolved lower energy shoulder – these are proposed as the 'true' R2 site absorptions.
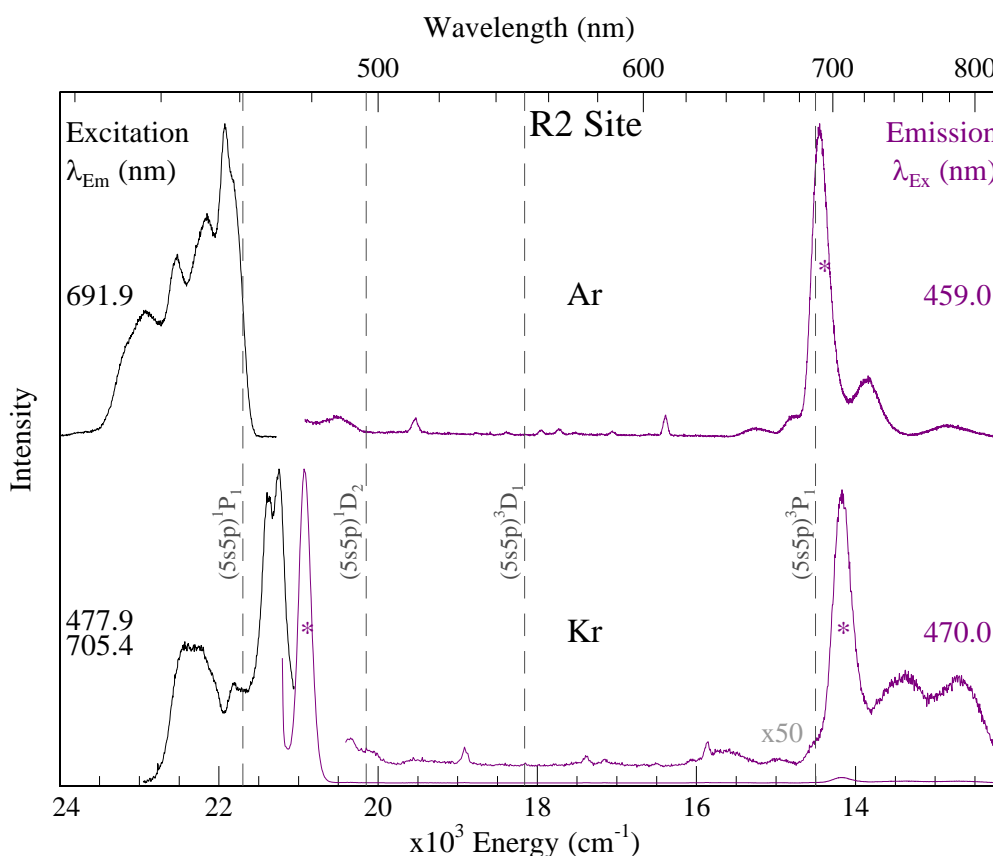
**Figure V.75**   **Excitation (black) and emission (purple) spectra recorded for the Sr/RG R2 site of isolation, following sample annealing to 28, 45 and 60 K for Ar, Kr and Xe respectively. The gas phase positions[4] of the (5s5p) $^1P_1$, (5s4d) $^1D_2$, (5s4d) $^3D_1$ and (5s5p) $^3P_1$ excited states are shown as dashed vertical lines. The emission bands originating from Sr atoms trapped in this site are indicated by an asterisk '*'.**

It is clear that the absorption/excitation splitting patterns are not caused by the JT effect and probably arise from the occupation of larger RG vacancies which are characterised by a lower symmetry.

Inspection of Figure V.75 reveals that the luminescence of this site is very host dependent. For Sr/Kr, two R2 emission bands are observed: one at 477.9 nm which was assigned as resonance $(5s5p)\ ^1P_1 \rightarrow\ ^1S_0\ (5s^2)$ fluorescence and one at 705.4 nm which is likely $(5s5p)\ ^3P_1$ state phosphorescence[j]. In contrast, the R2 site in Ar does not exhibit any $(5s5p)\ ^1P_1 \rightarrow\ ^1S_0\ (5s^2)$ emission and could only be identified by the $(5s5p)\ ^3P_1$ emission band it produces at 691.9 nm. This behaviour points to a 100 % efficient $^1P_1 \rightarrow\ ^3P_1$ population transfer rate for this site in Ar.

Table V.16 **The photophysical properties of the Sr/RG R2 site, obtained with $(5s5p)\ ^1P_1$ excitation. The emission spectral positions are quoted in both nanometres (nm) and wavenumber (cm^{-1}) units. δ represents the gas phase to matrix frequency shifts, given in wavenumber units. The Stokes shift (S.S.) is computed from the lowest energy component of the doublet structure in excitation. The bandwidth (full width at half maximum, fwhm) is denoted by the symbol Δ and is also expressed in units of wavenumber. *Bandwidth obtained from a Gaussian lineshape fit.**

Transition	Host	λ_{em} (nm)	ν (cm^{-1})	δ (cm^{-1})	S.S (cm^{-1})	$\Delta\nu$ (cm^{-1})
$(5s5p)^1P_1 \rightarrow (5s5p)^1S_0$	Kr	477.9	20925	-774	356	179
$(5s5p)^3P_1 \rightarrow (5s5p)^1S_0$	Ar	691.9	14453	-51	7357	239*
	Kr	705.4	14176	-328	7105	292

V.3.V   Violet and R1 sites

Figure V.76 presents a comparison of the Sr/RG trapping sites which give rise to an asymmetric threefold (2+1) splitting pattern in absorption/excitation. The top traces correspond to the violet site luminescence in Ar and Kr, whereas the bottom traces represent the luminescence of the red (R1) site in Ar. For clarity, the excitation scans shown for the violet site have been corrected for the presence of the strongly overlapping green site. This was done using the results of the Gaussian lineshape fits (see Figure V.116 and Figure V.120). The excited Sr ($^1P_1$) atom is subjected to two distinct interactions, when isolated in such vacancies. For the violet cavity, the splitting between the doublet and singlet feature is substantial - values of 1024 and 952 cm^{-1} are

---

[j] A conclusive assignment could not be made because the radiative lifetime was not identified.

determined (from the lowest energy singlet to the centre of the doublet) in Ar and Kr. The R1 site in Ar exhibits a somewhat smaller splitting of 741 cm^{-1} and the higher energy doublet is not as resolved, although a Gaussian lineshape demonstrates that two components are required to accurately reproduce the bandshape.
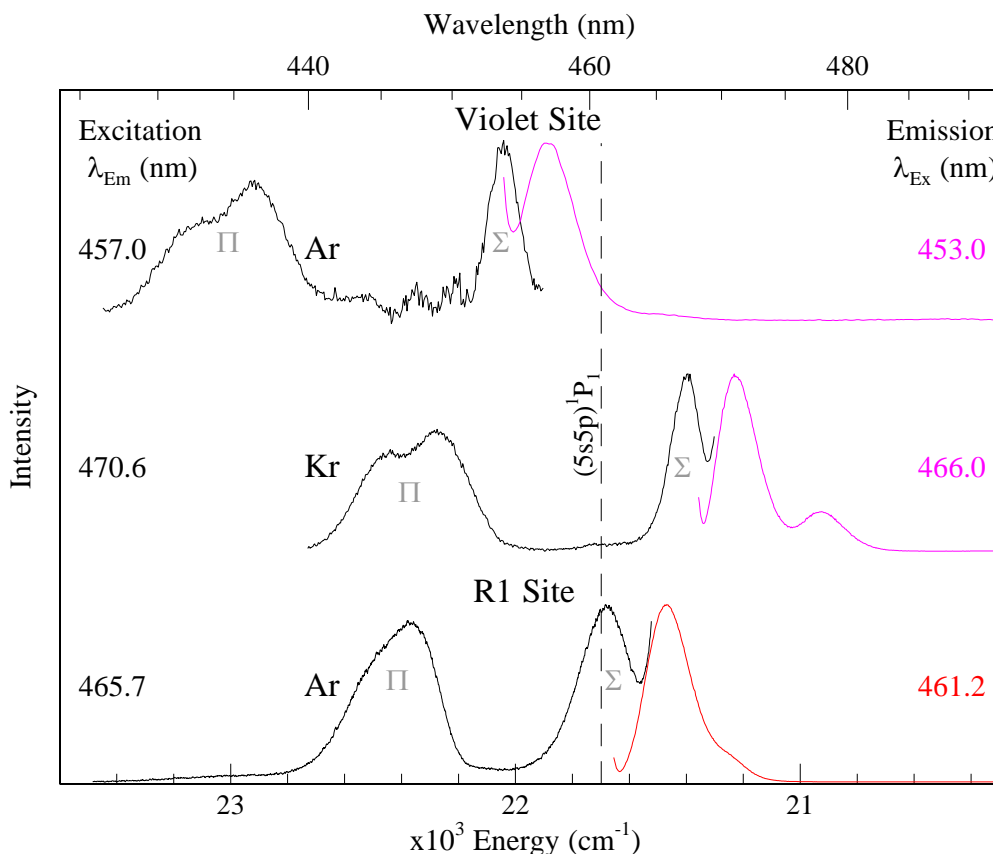
Figure V.76   **Top traces: Excitation (black) and emission (pink) spectra recorded for the violet site of isolation in Ar and Kr. Bottom trace: Excitation (black) and emission (red) spectra recorded for the red (R1) site of isolation in Ar. The data presented was obtained from annealed samples: T_{an} = 28 and 45 K for Ar and Kr respectively. The gas phase position[4] of the resonance (5s5p) $^1P_1 \leftarrow$ (5s^2) $^1S_0$ transition of Sr is shown as a dashed vertical line. The green site absorptions have been removed from the violet site excitation profiles using the results of the Gaussian fits.**

Similar excitation features were observed for the Ba/RG systems (see Chapter IV) and were attributed to the occupation of cylindrical voids[16,17] within the RG solids. The same model trapping site may be used to interpret the Sr/RG data. The key point is the orientation of the $5p_x$, $5p_y$ and $5p_z$ orbitals of the excited Sr atom in relation to the anisotropic RG environment. In such a site, two of the p orbitals (p_x and p_y) are perpendicular to the long axis of the cylinder and point towards one or more RG atoms (Π configuration). In this arrangement, the electrons in the $5p_{x,y}$ orbitals involved experience a large repulsive interaction. The interaction seems to be slightly different

for each orbital (p_x and p_y), as evidenced by the non-degenerate Π doublet observed in absorption. Contrasting this, the remaining p_z orbital, is collinear with the long axis of the cylinder (Σ configuration) and points towards mostly empty space. Thus, repulsive interactions with the host atoms are not as significant for this configuration. Indeed, inspection of Figure V.76 shows that the Σ-bands, recorded for the violet site in Kr and the R1 site in Ar, actually lie to the red of the (5s5p) $^1P_1 \leftarrow$ (5s^2) $^1S_0$ line.

As was the case for the equivalent Ba/RG sites, a fast, non-radiative relaxation must occur to the lowest energy Σ configuration because only a single emission band is observed in each case. Examination of Table V.17 shows that the magnitude of the Stokes shifts strongly depends on the configuration accessed in absorption. For example, the shifts evaluated for the violet site range from 1282 to 140 and 1197 to150 cm^{-1} for Ar and Kr respectively. A less extensive range of 1014 to 210 cm^{-1} exists for the R1 site. Combining this characteristic with a smaller Σ - Π energy gap suggests a weaker overall interaction of the excited Sr atom at this site in comparison to the violet site. As with Ba/Ar, a larger cylindrical cavity is proposed for the R1 trapping site of Sr/Ar.

Table V.17   **Resonance (5s5p) $^1P_1 \rightarrow$ $^1S_0$ (5s^2) emission features recorded for the Violet and R1 sites of isolation. The emission spectral positions are quoted in both nanometres (nm) and wavenumber (cm^{-1}) units. δ represents the gas phase to matrix frequency shifts, given in wavenumber units. The Stokes shift (S.S.) is computed from each peak of the asymmetric threefold absorption profile to the centre of the emission band. The bandwidth (full width at half maximum, fwhm) is denoted by the symbol Δ and is also expressed in units of wavenumber.**

Site	Host	λ_{ex} (nm)	λ_{em} (nm)	ν (cm^{-1})	δ (cm^{-1})	S.S (cm^{-1})	$\Delta\nu$ (cm^{-1})
Violet	Ar	431.7 436.2 454.1	457.0	21882	183	1282 1043 140	184
	Kr	445.5 449.3 467.3	470.6	21249	-449	1197 1007 150	184
R1	Ar	444.7 447.3 461.2	465.7	21473	-225	1014 883 210	180

V.3.VI Temporal analysis and temperature dependence

V.3.VI.I (5s5p) $^1P_1 \rightarrow$ $^1S_0$ (5s^2) Emission

In all three Sr/RG systems, direct irradiation of the (5s5p) $^1P_1$ absorptions produced site-specific and intense emission bands, which occurred in the $450 - 500$ nm spectral region. Time-resolved emission spectra (TRES) were recorded for each feature using pulsed laser excitation and iCCD detection. The decay profiles extracted were well fitted with single exponential functions, allowing the excited state lifetimes to be determined. These values are collected in Table V.18
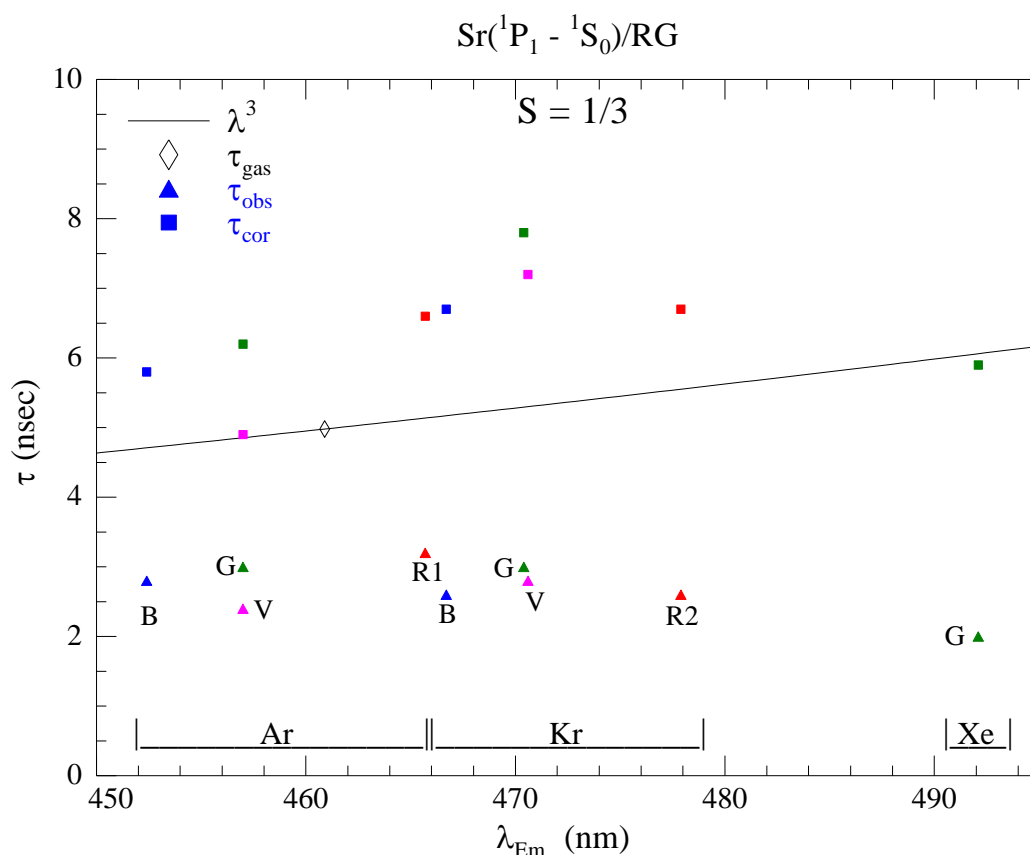
Figure V.77   **A comparison of the lifetimes record at 10 K for the thermally stable Sr: (5s5p) $^1P_1 \rightarrow$ $^1S_0$ (5s^2) emission features in Ar, Kr and Xe and a λ^3 extrapolation of the gas phase lifetime[4] for this transition of atomic Ba. The uncorrected lifetime values are given by filled triangles whereas the values corrected for the effective field of the host are denoted by the filled squares.**

With the exception of the two sites in solid Xe, all temporal scans were found to be invariant over a temperature range of at least 2 K[k]. Thus the radiative lifetimes were

---

[k] Not including the very narrow emission bands observed in Kr and Ar in the $487 - 492$ nm region.

identified for all of the emission bands in Ar and Kr. The decay time observed for the green site emission in Xe did not change between 10 and 11 K and is tentatively assigned as the radiative lifetime. In most cases, short nanosecond lifetimes allowed these bands to be confidently assigned as resonance (5s5p) $^1P_1 \to {}^1S_0$ (5s^2) atomic fluorescence.

In Figure V.77, the matrix lifetimes are plotted along with a λ^3 extrapolation of the gas phase[4] lifetime (4.98 ns). As expected, the directly observed matrix values are all less than the gas phase extrapolation. The effective field of the matrix is accounted for by applying Equation IV.2. As was discussed in Chapter IV, the *s* term in this formula, referred to as the 'shape' parameter, relates to the symmetry of the site accommodating the guest atom (*s* = 1/3 for a spherical cavity). Similar to the analysis done for the Ba/RG systems, a number of different values for *s* were investigated, the results of which are collected in Table V.18. The lifetimes corrected using *s* = 1/3 are in best agreement with the λ^3 gas phase extrapolation presented in Figure IV.49. This was also the case for the Ba/RG time-resolved data.

Table V.18   **A summary of the observed and corrected (5s5p) $^1P_1 \to {}^1S_0$ (5s^2) emission lifetimes for each site of isolation, in all three RG systems. The effective field correction was made with Equation IV.2 given in Chapter IV. The effect of increasing temperature on the emission integrated areas are listed in Column A. Whereas, the temperature dependence of the observed lifetimes are collected in Column B – the temperature at which the decay curves begin to shorten is also provided. The extent of this dependence is colour coded: Green = little or no change, blue = a small but noticeable change and red = a large temperature dependence over the range investigated. *The decay time obtained for the green site in Xe is tentatively assigned as the radiative lifetime.**

RG	Site	τ_{obs} (ns)	τ_{rad} ?	A) Integrated Area v Temp.	B) τ_{obs} v Temp.	τ_{cor} (ns): S= 0	τ_{cor} (ns): S= 1/3	τ_{cor} (ns): S= 1/2	τ_{cor} (ns): S= 1
Ar	Violet	2.4	✓	→	→	3.2	4.9	6.0	9.6
	Blue	2.8	✓	↓	→	3.7	5.8	6.9	11.2
	Green	3	✓	↓	↓ > 18 K	4.0	6.2	7.4	12.0
	R1	4.9	✓	↓	↓ > 18 K	6.5	10.1	12.2	19.6
Kr	Violet	2.8	✓	↓	→	4.0	7.2	9.2	16.6
	Blue	2.6	✓	↓	↓ > 12 K	3.7	6.7	8.6	15.4
	Green	3	✓	↓	↓ > 14 K	4.3	7.8	9.9	17.8
	R2	2.6	✓	↓	↓ > 14 K	3.7	6.7	8.6	15.4
Xe	Green	2	✓*	↓	↓ < 11 K	3.0	5.9	7.7	14.7
	Blue	< 1	✗	↓	↓ < 10 K	-	-	-	-

Table V.18 summarises the behaviour of the (5s5p) $^1P_1 \rightarrow {}^1S_0$ (5s^2) emission features with increasing sample temperature. Inspection of Column A reveals that the integrated areas of most bands are reduced as the temperature is raised. Matrix sites which are highlighted in red exhibit the greatest temperature dependence. In contrast to Ba, this behaviour is reversible for the thermally stable sites of isolation - bleaching or site-interconversion effects are not as significant for Sr. Thus, the loss of emission intensity must correspond to the activation of alternate relaxation channels for the excited metal atom. Moreover, an examination of Column B reveals that most of the recorded lifetimes shorten at elevated temperatures, which is a clear indication of competing non-radiative processes. Within a given RG host, the activation temperature for these processes show a slight dependence on the site of isolation. However, it is clear that the role of the host is the dominant factor. The atomic emission bands recorded in Xe exhibit the greatest overall temperature dependence. Indeed, the radiative lifetime of the blue site could not be identified at 10 K and only a tentative assignment was possible for the green site. From the luminescence measurements presented in the preceding sections, it is apparent that following excitation to the (5s5p) $^1P_1$ state, a population transfer occurs to the lower lying (5s5p) ^3P_J levels. This is most evident for the blue site in Xe, where the dominant emission band occurs in the vicinity of these excited state manifolds.

V.3.VI.II   Population Transfer: (5s5p) $^1P_1 \rightarrow$ (5s5p) ^3P_J

An illustration of the possible relaxation pathways available to atomic Sr once excited into its (5s5p) $^1P_1$ (and indeed the (5s4d) $^1D_2$) state is presented in Figure V.78. The simplest model is that the population of the excited (5s5p) $^1P_1$ state is transferred to the lower lying (5s5p) ^3P_J levels through radiative cascading – such a relaxation channel is represented by the green arrows in Figure V.78. However, this cannot account for the strong host dependence described in the previous section. A viable explanation may be obtained from a number of existing gas phase experiments. In 1992, Gallagher *et al.*[8] examined the collisional energy transfer between the excited Sr($^1P_1$) atom and the rare gases (RG = He − Xe). More recently (2004), these experiments were revisited by Castano and co-workers[18,19]. Both bodies of work revealed a clear trend: the excited (5s5p) $^1P_1$ population of Sr is transferred exclusively to the (5s4d) ^3D_J states via

collisions with the RG atoms. The same is also true of the (5s4d) $^1D_2$ excited state. The propensity for $^1P_1 \rightarrow {}^3D_J$ energy transfer was reflected by the large collisional branching ratios measured for this transition (0.295, 0.31 and 0.34 for Ar, Kr and Xe respectively).
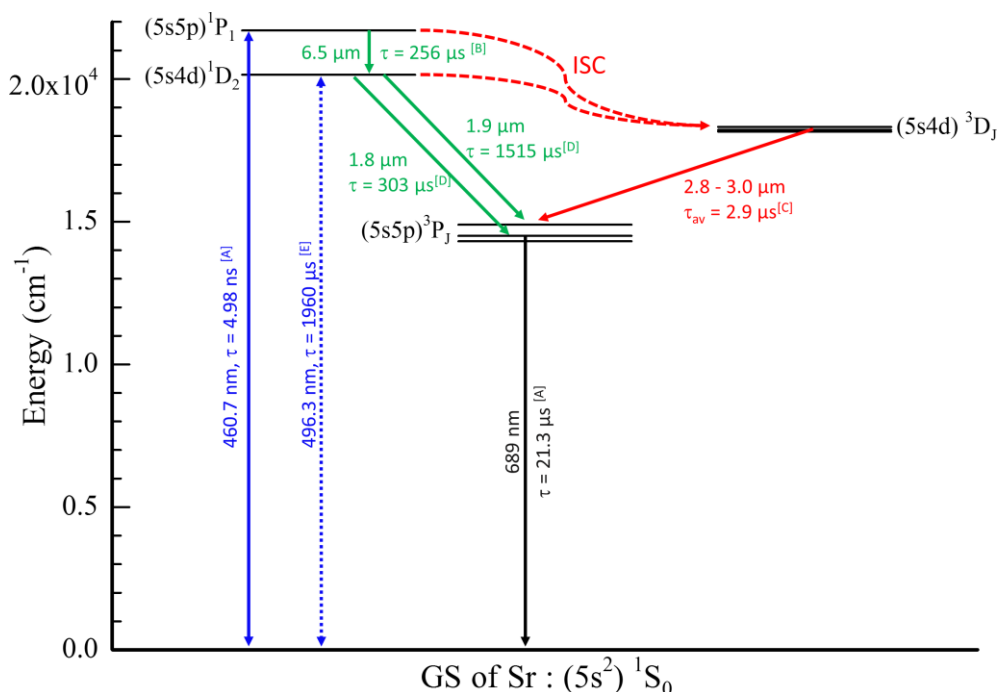

Figure V.78   **A schematic of possible relaxation channels available to atomic Sr once excited into its (5s5p) $^1P_1$ or (5s4d) $^1D_2$ state. Many of these transitions are strongly forbidden in the gas phase. The oscillator strengths which are known come from, in most cases, combined experimental and theoretical studies. A: NIST[4], B: Weiss et al.[20] (experiment), C: Gallagher et al.[21] or Castano and co-workers[18,19] (Sr-RG collisions), D: Bauschlicher/Partridge[13,22] (theory), E: Gallagher et al.[7] (experiment and theory).**

Following non-radiative transfer, the ^3D_J states are de-populated by radiative transitions to the ^3P_J levels, which in turn emit back to the ground state. The two step relaxation pathway just described is represented by the red arrows in Figure V.78.

A similar deactivation of the excited Ca($^1P_1$) atom by collisions with the rare gases was also observed by Breckenridge and Merrow[23]. The explanation for such a process was based on an earlier model, which accurately described singlet-to-triplet transfer within M-RG (M = Cd, Zn and Mg) van der Waals complexes[24]. For Ca, the non-radiative (4s4p) $^1P_1 \rightarrow$ (4s3d) ^3D_J transition was attributed to a crossing between the attractive Ca-RG $^1\Pi$ state potential energy curve (PEC) arising from the (4s4p) $^1P_1$ atomic asymptote with the repulsive Ca-RG $^3\Sigma$ curve originating from the (4s3d) ^3D asymptotes. More recently, ground and excited state calculations[11,12] of the 1:1 Ca-RG

complexes confirm the existence of this crossing. Indeed, it was shown that the repulsive (4s3d) $^3\Sigma$ curve crosses all higher excited states except for (4s4p) $^1\Sigma$.

The low-lying excited states of Ca and Sr are ordered in the same manner. A similar curve crossing may occur for the Sr-RG diatomics, unfortunately, accurate excited state PECs are not available for these complexes. Nonetheless, extension of this model to the RG solids may explain why the Sr ^3P emission bands are so bright in Xe, rivalling the intensity of the resonance $^1P_1$ features. Inspection of Figure V.78 shows that the population of the Sr: (5s5p) ^3P_J manifolds depends on the rate of $^1P_1 \rightarrow {}^3D_J$ intersystem crossing (ISC). The efficiency of this transition is expected to be greatest in solid Xe owing to the external heavy atom effect - the Sr-RG (5s5p) $^1\Pi$ states become more bound and the (5s4d) $^3\Sigma$ state become more repulsive with increasing host polarizability[10,24]. A comparable result was documented for Ba in Chapter IV. The (6s6p) $^1P_1$ emission bands exhibited the greatest temperature dependence when this metal atom was trapped in Xe. A non-radiative $^1P_1 \rightarrow {}^3P_2$ transition, caused by a $^1\Pi$ - $^3\Sigma$ curve crossing, was proposed to interpret this behaviour. For Ba, the route is more direct because the repulsive $^3\Sigma$ curve originates from the (6s6p) $^3P_2$ atomic asymptote. Whereas for Sr, $^1P_1 \rightarrow {}^3P_J$ transfer may be composed of two steps: ISC to the ^3D_J levels, followed by radiative decay to the ^3P_J manifolds.

V.3.VI.III   (5s5p) $^3P_1 \rightarrow {}^1S_0$ (5s^2) Emission

In contrast to the resonance (5s5p) $^1P_1$ emission bands, the decay profiles recorded of the lowest energy Sr/RG features are long-lived ($\tau > 1$ µs) and multi-featured. Double and triple exponential functions were required to fit the data - the extracted time components are collected in Table V.19. It is possible that the complex decays reflect the $^1P_1 \rightarrow {}^3P_J$ relaxation dynamics, which may involve a combination of radiative and non-radiative steps. As a consequence, assignment of these phosphorescent bands to a particular ^3P_J electronic state of Sr was not as straightforward. The key question is: which time component represents the true radiative decay of the excited state?

Throughout this Chapter, the Sr/RG emission bands in the vicinity of the (5s5p) ^3P_J levels were assigned to the (5s5p) $^3P_1 \rightarrow {}^1S_0$ (5s^2) atomic transition. These assignments were based on the shortest temporal component of each decay. Inspection of Table V.19 shows that, aside from the R2 site in Kr, the observed τ_1 values do not

change over a minimum temperature range of $10 - 12$ K and can be provisionally assigned as the radiative lifetimes. Applying the effective field formula ($s = 1/3$) yields excited lifetime values which range from $16.3 - 51$ µs.

Table V.19 **A summary of the observed and corrected (5s5p) $^3P_1 \rightarrow {}^1S_0$ (5s^2) emission lifetime values. The effective field correction was made with Equation IV.2 (see Chapter IV). The column labelled 'τ_{rad}' assesses each time component of the multi-exponential fits – lifetimes (τ) which were found to be independent of temperature over the range of at least $10 - 12$ K are marked with a tick '✓'. The temperature above which each decay component becomes shorter, is also listed. The right-most column describes the reversible behaviour of the emission intensity with increasing temperature.**

RG	Site	λ_{em} (nm)	Observed / Corrected ($s = 1/3$)			τ_{rad}?			Intensity v Temp
			τ_1 (µs)	τ_2 (µs)	τ_3 (µs)	τ_1	τ_2	τ_3	
Ar	Green	676.1	8 / 16.4	116 / 238.3	-	✓ ?	✓ >14K	-	↑
	R2	691.9	9.6 / 19.7	86.2 / 177.1	564.5 / 1159.6	✓ >12K	✓ >12K	✗ >11K	↑
Kr	Blue	727.9	6.3 / 16.3	70.8 / 183.3	-	✓ >14K	✗ >10K	-	↓
	Green	691.7	8.7 / 22.5	213.1 / 551.6	833 / 2156.3	✓ >14K	✗ >10K	✗ >10K	↓
	R2	705.4	22.1 / 57.2	145.6 / 376.9	424.3 / 1098.4	✗ >10K	✗ >10K	✗ >10K	↓
Xe	Blue	791.2	17 / 51.0	163.49 / 482.0	-	✓ >12K	✓ >12K	-	↓
	Green	740.5	6.2 / 18.3	110.5 / 325.8	-	✓ >26K	✓ >26K	-	↑,↓

These values are in agreement with the gas phase lifetime of the (5s5p) $^3P_1 \rightarrow {}^1S_0$ (5s^2) transition, which is reported[4] as 21.3 µs. Moreover, the transitions from the remaining ^3P_J (J = 2,0) levels to the ground state are strongly forbidden. Lifetimes of ~140 and ~520 seconds have been recorded in optical lattice[25] and magneto-optical trap (MOT)[26] experiments, for the $^3P_0$ and $^3P_2$ states, respectively.

The temperature dependence of the $^3P_1$ emission bands was investigated and the results are collected in Table V.19. The behaviour observed may be summarised as follows: For Kr, all of the $^3P_1$ emissions are reduced as the sample temperature is raised from $10 - 30$ K. The opposite behaviour is observed for Ar, where these bands are all enhanced at elevated temperatures. Xe is even more complex: The green site emission initially increases from $10 - 26$ K and subsequently decreases with further warming. On the other hand, the blue site intensity diminishes at all temperatures above 10 K. It is likely that two effects compete to produce the varied temperature dependence observed for the phosphorescence bands. The first is the efficiency of the $^1P_1 \rightarrow {}^3P_J$ population transfer, which may consist of two rate determining steps – assuming the gas phase model discussed in the previous section is correct. If the $^3P_1$ emission

intensity increases as a function of temperature, then this relaxation pathway has become enhanced. On the other hand, if the emission is reduced and a change in the lifetime is not observed, then at least one of the transfer steps has become less efficient with increasing temperatures. The second effect becomes apparent once the temporal characteristics are examined. The decay times recorded for each band are all eventually shortened; the temperature at which this occurs depends on the host and the site. Thus, a non-radiative relaxation to a lower state, i.e. the ground state, must be directly competing with emission from the $^3P_1$ level.

V.4 Sr/RG (5s5p $^1D_2$) Luminescence

In Chapter III, the absorption spectroscopy of atomic Sr isolated in annealed rare gas (RG = Ar, Kr and Xe) matrices was characterised by two main features: 1. an intense $(5s5p)\ ^1P_1 \leftarrow\ ^1S_0\ (5s^2)$ absorption profile centred at ~455 nm and 2. a weaker series of bands at approx. 500 nm[1]. The latter were assigned to the parity-forbidden $(5s4d)\ ^1D_2 \leftarrow\ ^1S_0\ (5s^2)$ transition. A detailed analysis of the $(5s5p)\ ^1P_1$ luminescence of Sr in each host solid was presented in Section V.2. To further characterise these Sr/RG systems, the luminescence obtained with direct excitation of the $(5s4d)\ ^1D_2$ absorption profiles will now be presented.

V.4.I Sr/Xe

Photoexcitation of the $(5s4d)\ ^1D_2$ absorption bands of Sr/Xe produces emission features only in the region of the $(5s5p)\ ^3P_J$ manifolds ~770 nm. Thus, the efficiency of $^1D_2 \rightarrow\ ^3P_J$ population transfer must be very high as direct $(5s4d)\ ^1D_2 \rightarrow\ ^1S_0\ (5s^2)$ emission is completely quenched in this host. A comparable behaviour was observed and described in the previous sections with excitation of $(5s5p)\ ^1P_1$ absorptions.

V.4.I.I $\lambda_{em} \approx 770$ nm

The 2D-EE spectrum of Sr/Xe, recorded over an excitation range which covers both the $(5s5p)\ ^1P_1$ and $(5s4d)\ ^1D_2$ absorption bands $(440 - 540$ nm), is presented in Figure V.79. In Section V.2.II.I, the two dominant excitation features, which occur in the region of the Sr: $(5s5p)\ ^1P_1$ state, were assigned to the blue (B) and green (G) sites of isolation. Conversely, a single luminescence band (I) prevails in the vicinity of the $(5s4d)\ ^1D_2$ state. Inspection of Figure V.79 demonstrates that this feature, which is located at 791.2/512.4 nm (emission/excitation), originates from the blue site of isolation. A vertical slice through the plot at 740.5 nm (the assigned green site $^3P_1$ emission) reveals the presence of excitation components at 504.6 (II) and 526.6 nm (III) – these bands represent the $(5s4d)\ ^1D_2 \leftarrow\ ^1S_0\ (5s^2)$ absorption of Sr trapped in the green site of solid Xe. Consistent with the absorption spectra presented in Chapter III,

---

[1] Absorption values observed for Sr/Kr.

the green site (5s4d) $^1D_2$ luminescence is far weaker than the blue site. The spectral and temporal properties of the observed near-IR emissions will now be presented.
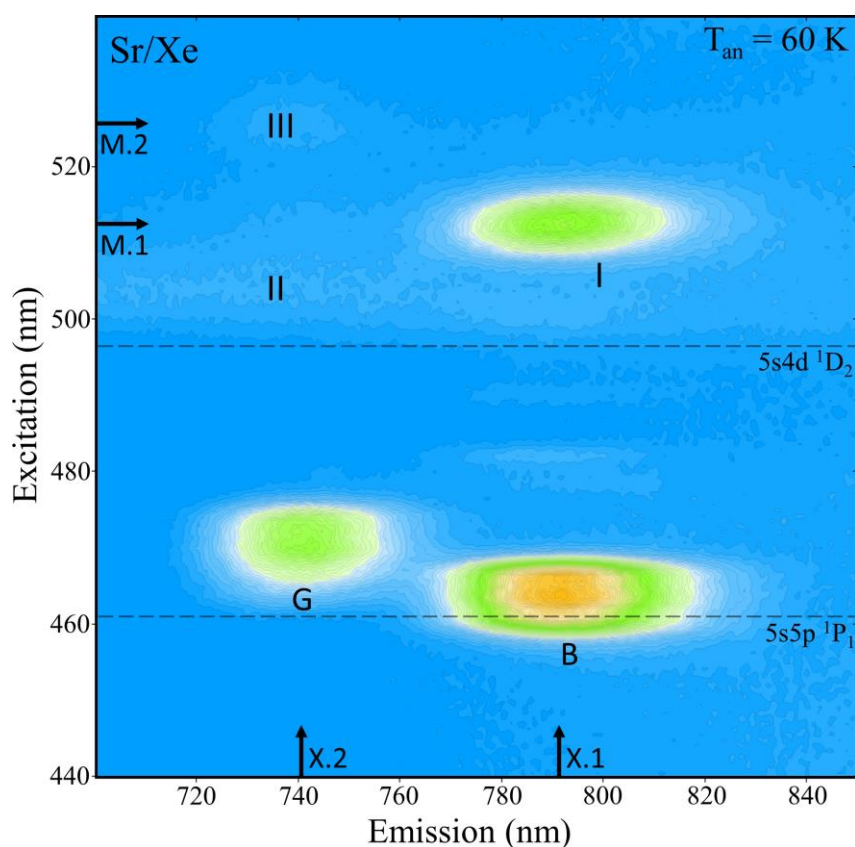

Figure V.79   Sr/Xe 2D-EE spectrum, recorded in the 770 nm spectral region, following sample deposition at 10 K and annealing to 60 K. The gas phase positions[4] of the (5s5p) $^1P_1$ and (5s4d) $^1D_2$ states of atomic Sr are shown in excitation, represented by the dashed horizontal lines.

V.4.I.I.A   Blue site

A summary of the blue site luminescence of Sr/Xe is presented in Figure V.80. The (5s4d) $^1D_2 \leftarrow {}^1S_0$ (5s^2) absorption of atomic Sr trapped in this site consists of a single, unstructured band at 512.4 nm, red-shifted with respect to the gas phase[4] value by -634 cm^{-1}. A lineshape analysis of this feature is provided in Figure V.122 of Appendix V.I (lower traces). In contrast to the blue site (5s5p) $^1P_1$ absorption profile, the (5s4d) $^1D_2$ bandshape is well fit by a single Gaussian function, exhibiting a linewidth of 267 cm^{-1}. A high resolution laser excitation scan^m, recorded in the region of (5s4d) $^1D_2$ band by monitoring the emission at 791.2 nm, is also presented in Figure V.122 of Appendix

---

^{m} The dye material, Coumarin 500, was pumped with the 2ω of the Nd:YAG laser, thereby producing tuneable laser radiation in this region (485 – 530 nm).

V.I (top trace). This technique did not reveal the presence of any unresolved absorption components.
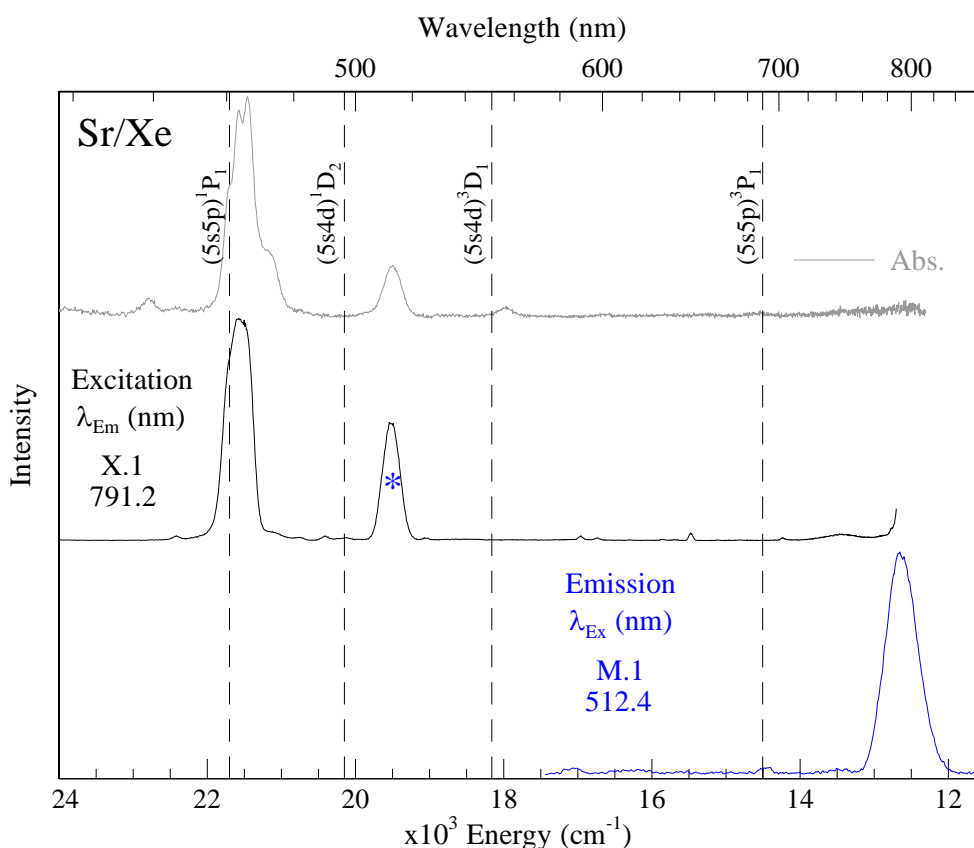

Figure V.80   **Absorption (grey), excitation (black) and emission (blue) spectra recorded for the Sr/Xe blue site of isolation, following sample annealing to 60 K. The gas phase[4] positions of the (5s5p) $^1P_1$, (5s4d) $^1D_2$, (5s4d) $^3D_1$ and (5s5p) $^3P_1$ states of atomic Sr are shown by dashed vertical lines.**

Photoexcitation of either the (5s5p) $^1P_1$ JT band at 463.3 nm or the (5s4d) $^1D_2$ band at 512.4 nm produces the same emission feature at 791.2 nm. Excited state lifetime measurements were made using the multi-channel scaling technique. A decay profile for this emission, obtained with laser excitation at 512.0 nm is presented in Figure V.81. A double exponential function, employing decay time/amplitude values of 5.1 µs/1154 and 65.1 µs /1122, accurately describes the decay profile. The temperature dependence of the decays was investigated over the range 10 - 26 K. As shown in the right panel of Figure V.82, the slope of the decay remains constant indicating that the true radiative lifetime has been obtained.
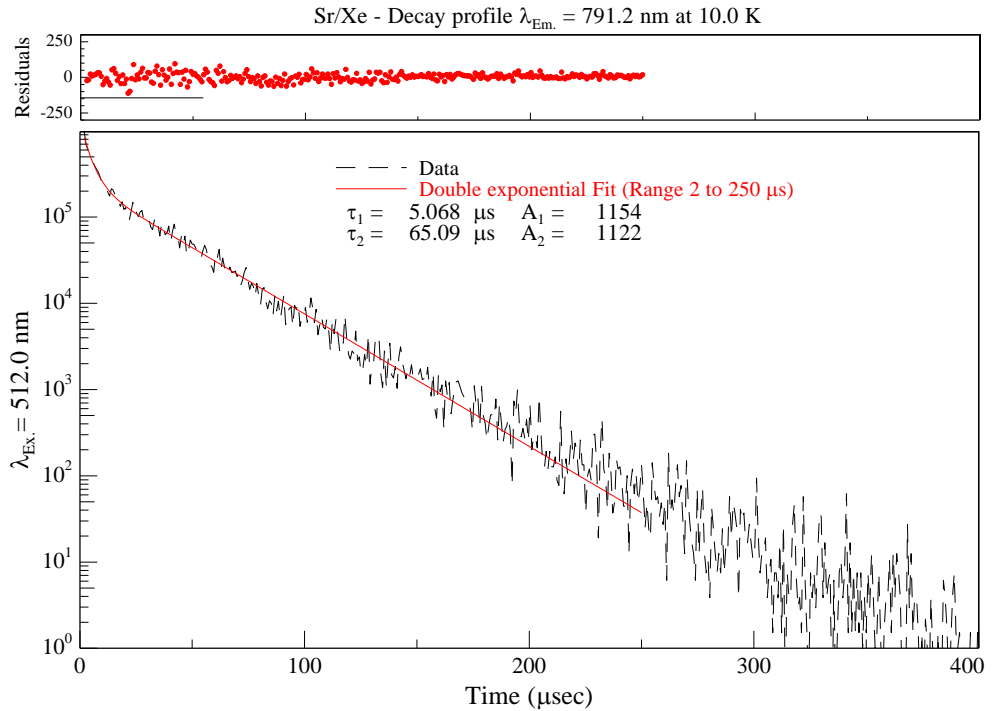
Figure V.81   Decay profile of the Sr/Xe blue site emission band at 791.2 nm, produced by site-selective laser excitation at 512.0 nm and recorded using the multi-channel scaling technique, as outlined in Chapter II. The residuals present the difference between the double exponential fit and the recorded decay. $\sigma\tau_1 = \pm 0.3$ µs and $\sigma\tau_2 = \pm 0.8$ µs.
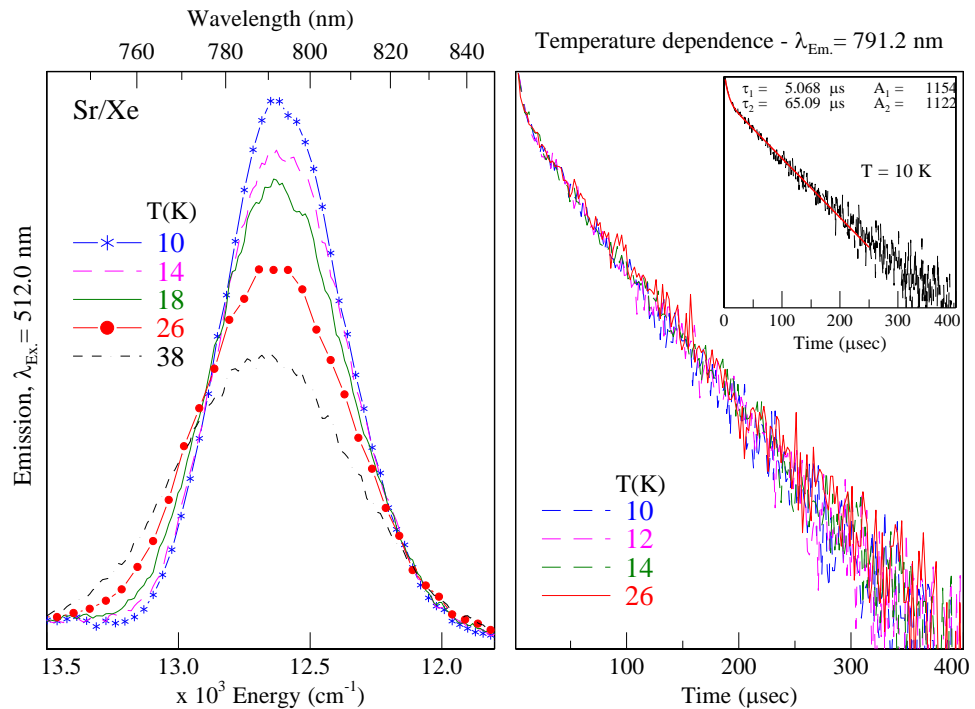
**Figure V.82**   The left panel shows the temperature dependence of the Sr/Xe blue site emission band at 791.2 nm over the range 10 – 38 K. The right panel presents the temperature dependence of the decay curves, recorded between 10 and 26 K. The inset of the right panel shows the fit for the decay recorded at 10 K. The data presented in this plot was produced with photoexcitation of the $^1D_2$ absorption band at 512 nm.

Excited state lifetimes of 15.0 and 191.9 µs are obtained upon application of the effective field correction. These values are noticeably shorter than those obtained when the (5s5p) $^1P_1$ excited state is pumped. Nonetheless, assignment to the (5s5p) $^3P_1 \rightarrow$ ($5s^2$) $^1S_0$ transition of atomic Sr is made based on the favourable comparison of the shorter and dominant decay component with the gas phase lifetime[4] (21.3 µs) of this transition. The temperature dependence of the spectral emission scans are presented in left-side of Figure V.82. A reversible decrease in intensity, broadening in width and blue-shift of the band maximum occurs with increasing sample temperature. As the decays show no change, this is likely caused by the weakening of a feeding step to the (5s5p) $^3P_1$ excited state.

V.4.I.I.B   Green site

The excitation and emission spectra recorded for the green site of isolation are presented in Figure V.83. The green site (5s4d) $^1D_2$ absorptions occur at 504.6 and 526.6 nm, red-shifted with respect to the gas phase transition energy by -332 and -1160 cm^{-1} respectively. A lineshape analysis is presented in Figure V.123 of Appendix V.I. A total of three Gaussian functions are required to reproduce the multi-featured profile.
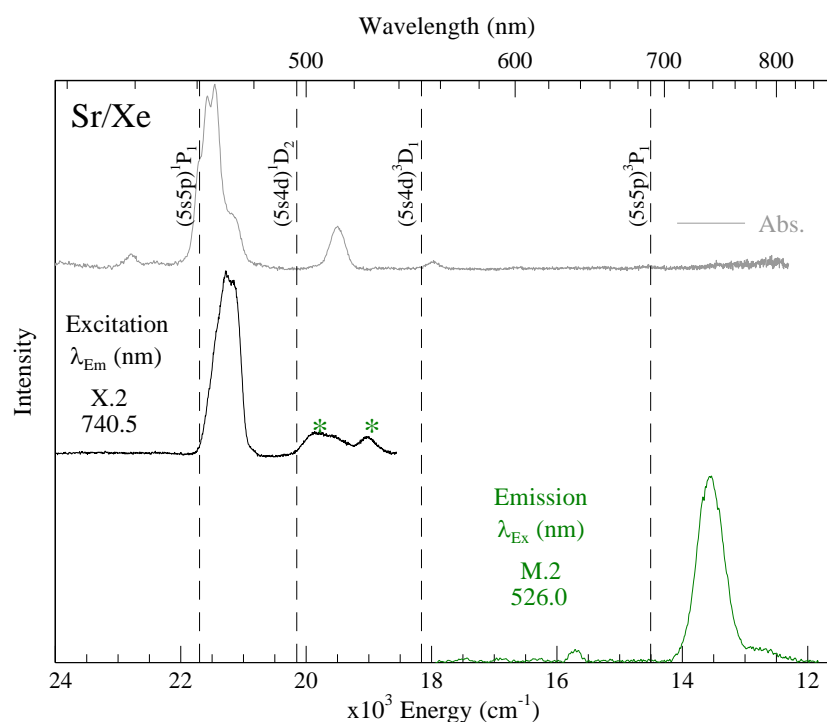
**Figure V.83**   **Absorption (grey), excitation (black) and emission (green) spectra recorded for the Sr/Xe green site of isolation, following sample annealing to 60 K. The gas phase[4] positions of the (5s5p) $^1P_1$, (5s4d) $^1D_2$, (5s4d) $^3D_1$ and (5s5p) $^3P_1$ states of atomic Sr are shown by dashed vertical lines. The most site-selective excitation peaks are marked with an asterisk.**
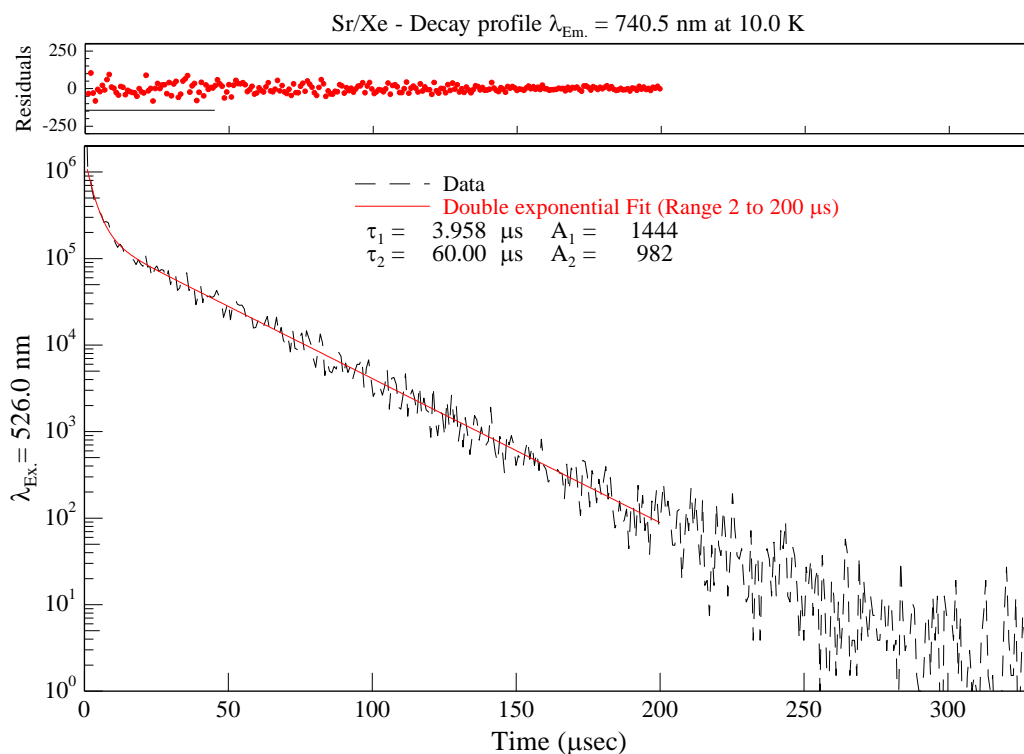
Figure V.84   **Decay profile of the Sr/Xe green site emission band at 740.5 nm, produced by site-selective laser excitation at 526.0 nm and recorded using the multi-channel scaling technique. The residuals present the difference between the double exponential fit and the recorded decay. $\sigma\tau_1 = \pm\,0.2\ \mu s$ and $\sigma\tau_2 = \pm\,0.9\ \mu s$.**

Irradiation of either the $(5s5p)\ ^1P_1$ or $(5s4d)\ ^1D_2$ absorption bands yields an identical, green site emission at 740.5 nm – although the intensity is much weaker when the $^1D_2$ manifold is pumped. The temporal profile of this feature, obtained with laser excitation at 526 nm, is presented in Figure V.84. The decay is well fit by a double exponential function, employing decay times of 4.0 and 60 µs with amplitudes of 1444 and 982 respectively. These lifetime values do not change up to 26 K, as illustrated by the temperature dependence study in the right panel of Figure V.85. Thus, the true radiative lifetimes have been identified and applying the effective field correction produces excited state lifetimes of 11.8 and 176.9 µs. The shorter, dominant component of the double exponential decay is in good agreement with the gas phase lifetime[4] recorded for the $(5s5p)\ ^3P_1 \rightarrow (5s^2)\ ^1S_0$ transition of atomic Sr. Accordingly, the band at 740.5 nm is assigned as $(5s5p)\ ^3P_1$ emission. Similar to the blue site, the emission spectral scans (see left panel of Figure V.85) display a reversible temperature dependence. The temporal decays do not show such a dependence, inferring that an intermediate step to the $(5s5p)\ ^3P_1$ excited state becomes less efficient at higher temperatures.
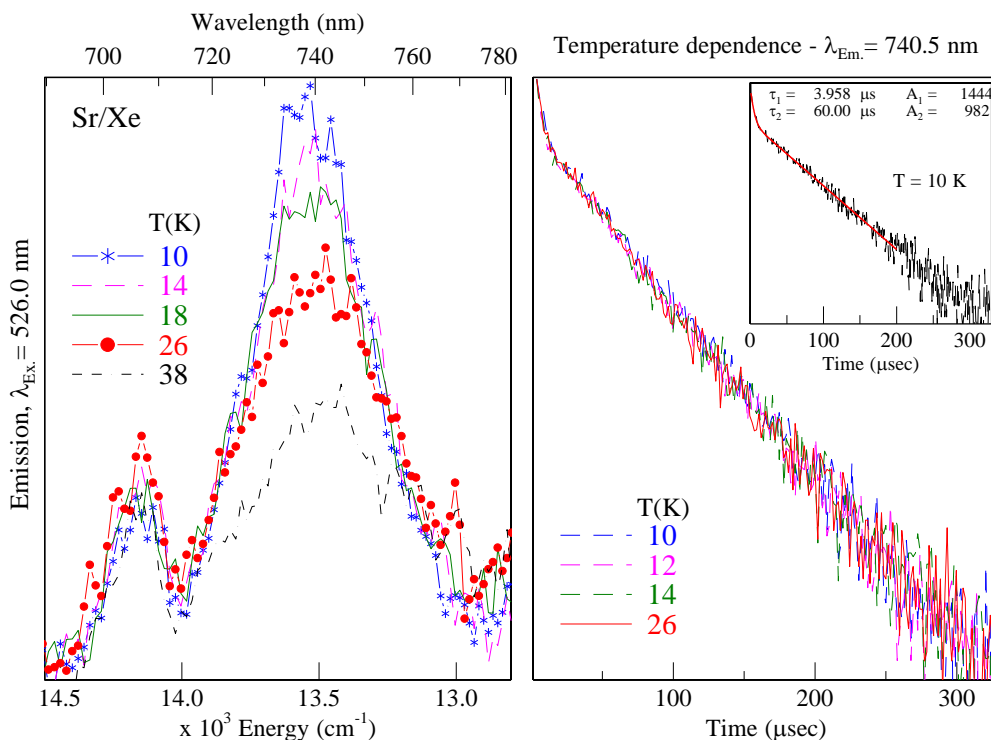
Figure V.85 The left panel shows the temperature dependence of the Sr/Xe green site emission band at 740.5 nm over the range 10 – 38 K. The right panel presents the temperature dependence of the decay curves, recorded between 10 and 26 K. The inset of the right panel shows the fit for the decay recorded at 10 K. The data presented in this plot was produced with photoexcitation of the $^1D_2$ absorption band at 526.

V.4.II Sr/Kr

Photoexcitation of the (5s4d) $^1D_2$ absorption bands of Sr/Kr yields emission features in three distinct spectral regions, corresponding to the (5s4d) $^1D_2$, (5s4d) $^3D_1$ and (5s5p) $^3P_1$ excited states. It will be shown that the excited states observed in emission strongly depend on the site occupied by the Sr atom. Such a site dependence was also found for the (5s5p) $^1P_1$ luminescence (see Section V.2.IV).

V.4.II.I $\lambda_{em} \approx$ 490 and 710 nm

The 2D-EE spectrum of Sr/Kr, recorded by scanning the excitation monochromator over the 435 – 520 nm range, with the emission monochromator centred at 730 nm, is presented in Figure V.86. Inspection of this plot reveals that the (5s5p) $^3P_1$ emission features are more resolved when produced with (5s4d) $^1D_2$ excitation. This probably

arises because of weaker electron-phonon coupling in the (5s4d) $^1D_2$ excited state, which results in narrower (5s4d) $^1D_2 \leftarrow {}^1S_0$ (5s^2) absorption bands. Thus, a greater degree of site-selectivity is achieved with (5s4d) $^1D_2$ excitation. The two most prominent $^1D_2$ luminescence features are centred at 688.4/494.6 (I) and 730.0/505.4 nm (II). A comparison with the (5s5p) $^1P_1$ bands reveals that these can be assigned to the green (I) and blue (II) sites of isolation, respectively.
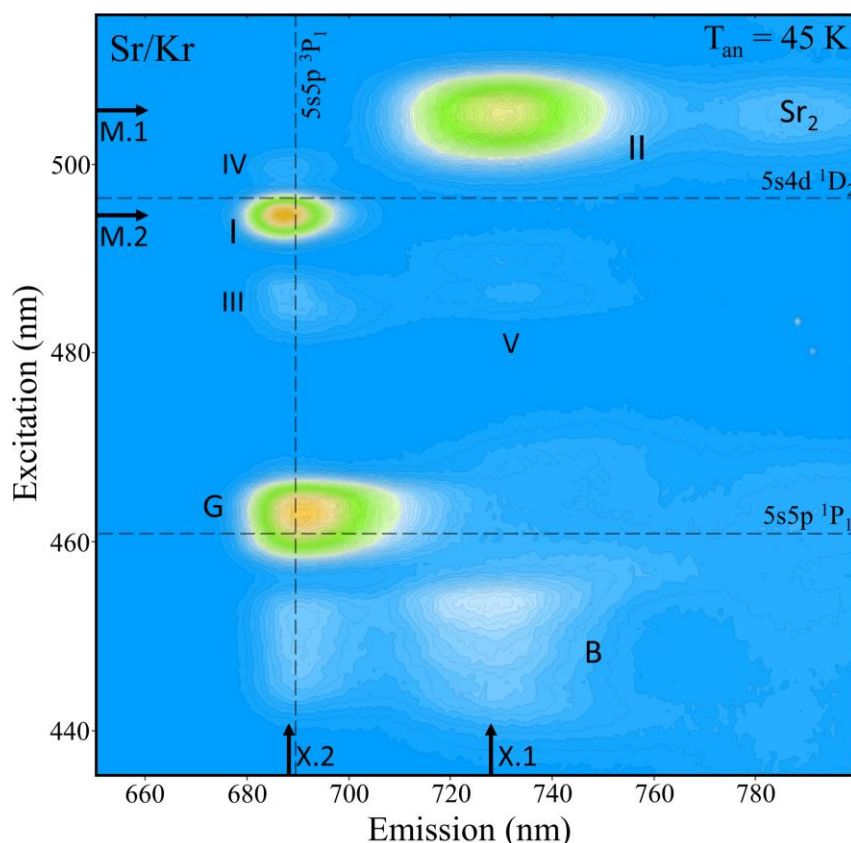
Figure V.86   **Sr/Kr 2D-EE spectrum, recorded in the 710 nm spectral region, following sample deposition at 10 K and annealing to 45 K. The gas phase positions[4] of the (5s5p) $^1P_1$ and (5s4d) $^1D_2$ states of atomic Sr are shown in excitation, represented by the dashed horizontal lines.**

In addition, a number of weaker 'satellite' features are also observable in this region. The bands labelled III and IV share a common emission wavelength (~688 nm) with band I and likely correspond to (5s4d) $^1D_2$ absorptions of the green site. Similarly, feature V may be associated with the blue site. However, conclusive site assignments of these weak features is challenging. With the exception of the absorption at ~483 nm (band III)[n], excitation of the remaining $^1D_2$ absorption peaks does not yield resonance

---

[n] See Section V.4.II.I.B.

(5s4d) $^1D_2$ emission. Thus, the excitation slices (X.1 and X.2) presented ahead are really 'action' spectra, as it is the $^3P_1$ emission bands that are being monitored.

V.4.II.I.A   Blue site

A summary of the blue site luminescence is presented in Figure V.87. The main (5s4d) $^1D_2$ excitation band (II) for this site is situated at 505.4 nm and is characterised by a fwhm of 250 cm^{-1}. A matrix red-shift of -363 cm^{-1} is evaluated from the band centre.
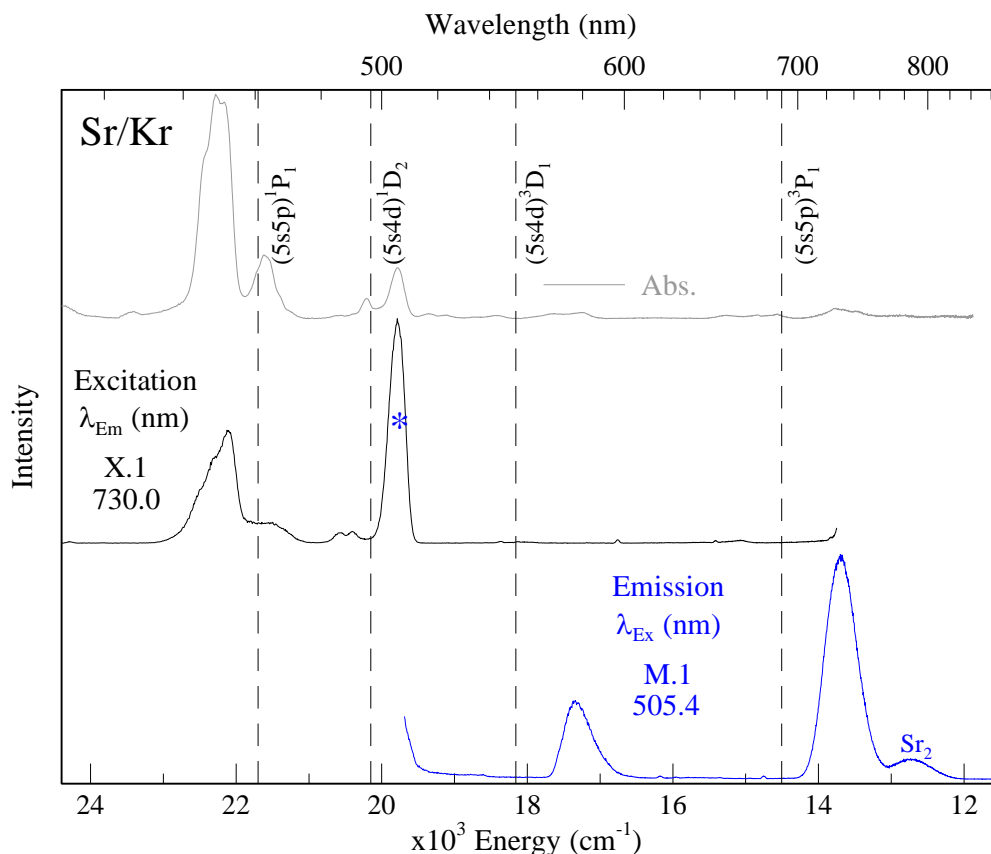
Figure V.87   **Absorption (grey/top), excitation (black/middle) and emission (blue/bottom) spectra recorded for the Sr/Kr blue site of isolation, following sample annealing to 45 K. The gas phase[4] positions of the (5s5p) $^1P_1$, (5s4d) $^1D_2$, (5s4d) $^3D_1$ and (5s5p) $^3P_1$ states of atomic Sr are shown by dashed vertical lines.**

The lineshape analysis of the 505.4 nm excitation feature is presented in Figure V.124 of Appendix V.I. Two Gaussian curves, exhibiting bandwidths of 221 and 177 cm^{-1} are required to faithfully re-produce the asymmetric bandshape. A high resolution laser excitation scan, recorded monitoring the 730.0 nm emission band, is presented in the top of Figure V.124. Similar to the blue site in Xe, the laser scan did not reveal the presence of any unresolved components in the lower resolution monochromator scan.

Photoexcitation at 505.4 nm produces emission bands at 576.7 and 730.0 nm. The higher energy feature will be discussed ahead in Section V.4.II.II. The lowest energy emission is situated to the red of the (5s5p) $^3P_1$ line and displays a fwhm of 503 cm^{-1}. An emission decay profile recorded at 10 K is presented in Figure V.88. The temporal profile was fit with double exponential function. Decay times of 7.4 and 58.9 µs, with amplitudes of 2369 and 1125 respectively, are extracted from the least squares fit.

Sr/Kr - Decay profile $\lambda_{Em.}$ = 730.0 nm at 10 K
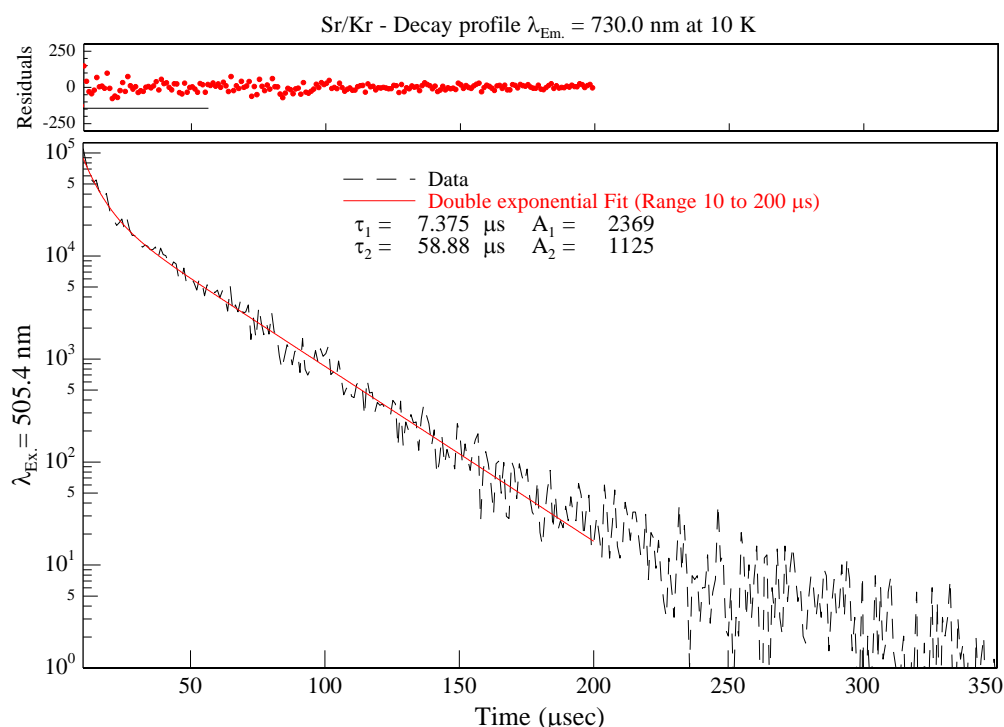
Figure V.88 **Decay profile of the Sr/Kr blue site emission band at 730.0 nm, produced by site-selective laser excitation at 505.4 nm and recorded using the multi-channel scaling technique. $\sigma\tau_1 = \pm 0.5$ µs and $\sigma\tau_2 = \pm 1.2$ µs.**

The temperature dependence of the temporal scans are presented in the right panel of Figure V.89. The decay profiles clearly exhibit a temperature dependence, even over the small range of 10 to 12 K. Inspection of the fit parameters collected in Table V.20 shows that this dependence is caused by a shortening of the minor decay component (τ_2). In contrast, the dominant component (τ_1) shows little or no change between 10 and 18 K and is therefore assigned as the radiative lifetime. An excited state lifetime of 19.2 µs is obtained following application the effective field formula. Accordingly, the 730.0 nm emission is assigned as (5s5p) $^3P_1 \rightarrow$ (5s^2) $^1S_0$ phosphorescence. The spectral scans are also dependent on the sample temperature - as

can be seen in the left panel of Figure V.89. In going from 10 to 34 K, the emission loses intensity, broadens in width and blue-shifts in position. Examination of the temporal characteristics listed in Table V.20 reveals that all of the decay components become shorter above 18 K. This implies that a non-radiative relaxation pathway reduces the population of Sr atoms in the (5s5p) $^3P_1$ excited state, when the sample temperature exceeds 18 K.
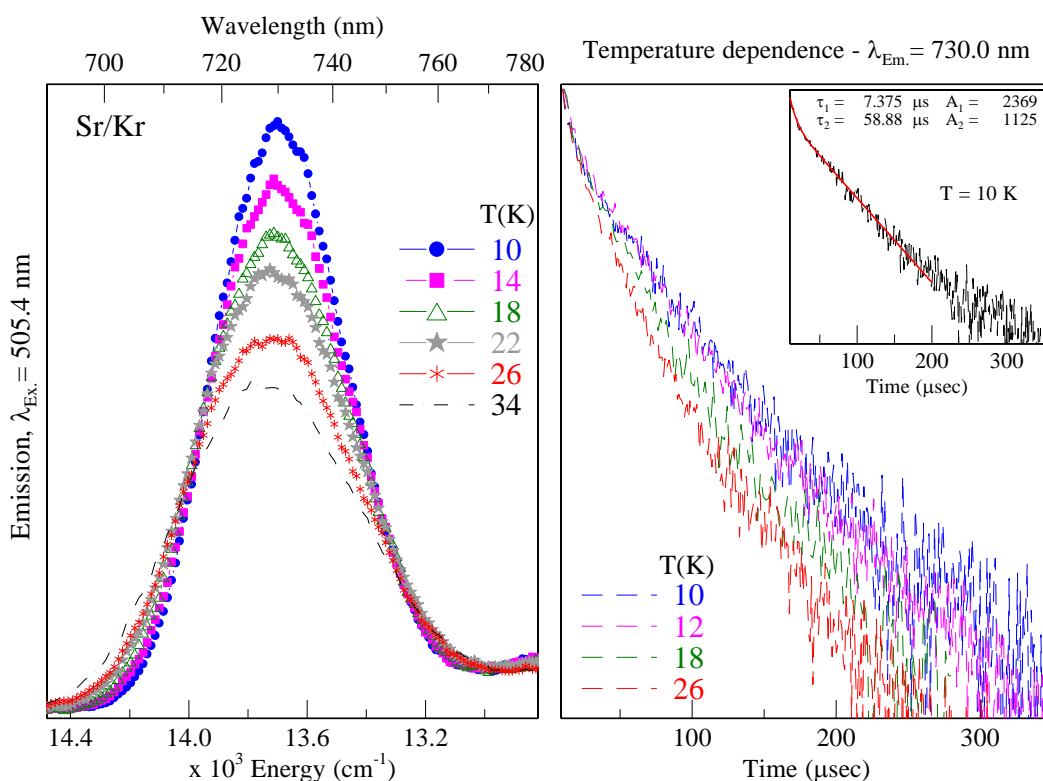
Figure V.89   **The left panel shows the temperature dependence of the Sr/Kr blue site emission band at 730.0 nm over the range 10 – 38 K. The right panel presents the temperature dependence of the decay curves, recorded between 10 and 26 K. The inset of the right panel shows the fit for the decay recorded at 10 K. The data presented in this plot was produced with photoexcitation of the $^1D_2$ absorption band at 505.4 nm.**

Table V.20   **Temporal characteristics of the Sr/Kr 730.0 nm emission band, recorded over the temperature range of 10 to 30 K.**

T_s (K)	Fit Range (µs)	A_1	τ_1 (µs)	A_2	τ_2 (µs)
10	10 – 200	2369	7.4	1125	58.9
12	10 – 200	6168	7.8	3016	53.5
14	10 – 200	2507	8.4	1228	49.6
18	10 – 150	1850	7.6	951	43.0
26	10 – 150	8913	6.3	3702	36.7
30	10 – 150	3651	5.6	1647	34.3

V.4.II.I.B   Green site

Long range emission and excitation spectra recorded for the green site of isolation are presented in Figure V.90. The dominant (5s4d) $^1D_2$ excitation feature occurs at 494.6 nm and overlaps the gas phase line – a small blue-shift of +69 cm^{-1} is measured from the band centre.
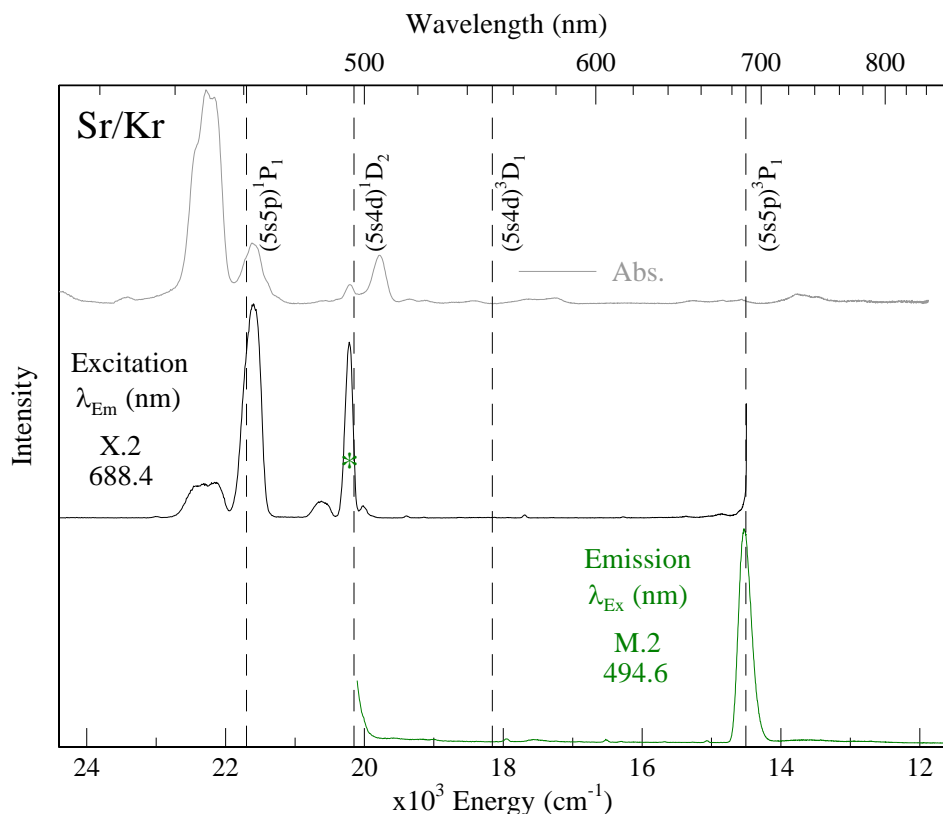
Figure V.90   **Absorption (grey/top), excitation (black/middle) and emission (green/bottom) spectra recorded for the Sr/Kr green site of isolation, following sample annealing to 45 K. The gas phase[4] positions of the (5s5p) $^1P_1$, (5s4d) $^1D_2$, (5s4d) $^3D_1$ and (5s5p) $^3P_1$ states of atomic Sr are shown by dashed vertical lines.**

The bandshape is asymmetric and quite narrow (fwhm of 127 cm^{-1}). Two Gaussian curves are required to fit the observed profile, as can be seen in Figure V.125 of Appendix V.I. Moreover, a high resolution laser excitation scan recorded of this band (see the top trace of Figure V.125) revealed the presence of two distinct components, centred at 494.3 and 495.1 nm. Weaker absorptions at 483.3 (III) and 499.9 nm (IV) surround the main peak. It was mentioned at the outset that these features were difficult to assign to a particular site of isolation. However, band (III) must be a green site absorption. As shown in the left panel of Figure V.91, excitation at 483 nm produces the distinctively narrow green site (5s4d) $^1D_2 \rightarrow$ (5s^2) $^1S_0$ emission at 491.2 nm.
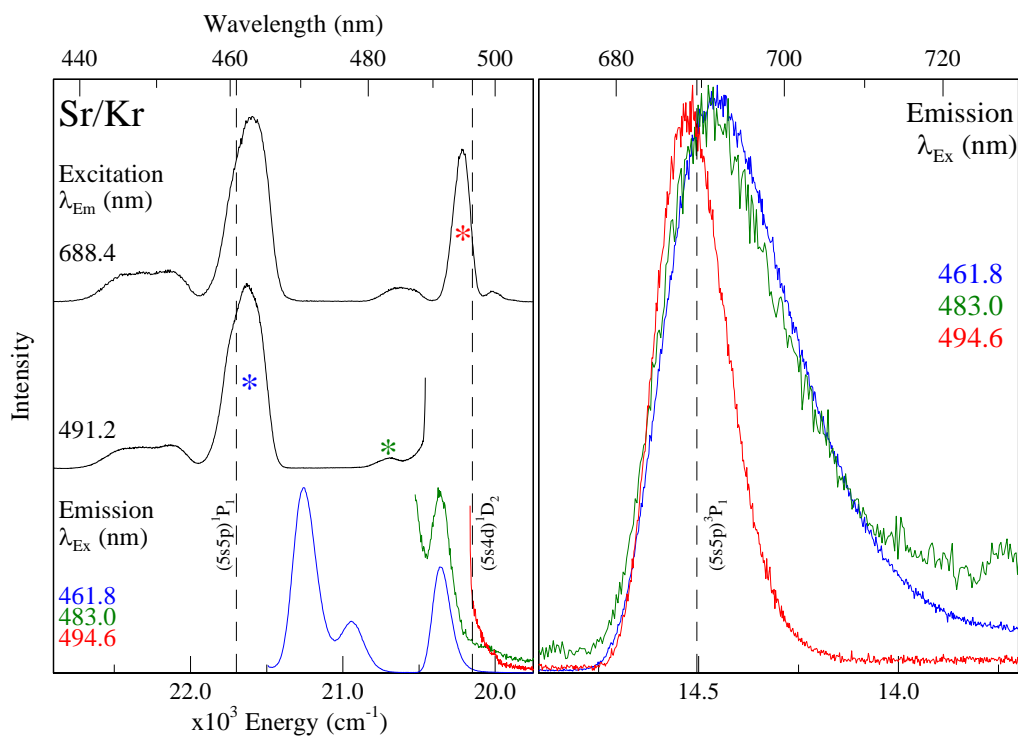
Figure V.91   **Left Panel: Excitation (black) and emission (coloured) spectra recorded for the green site of isolation, in the region of the (5s5p) $^1P_1$ and (5s4d) $^1D_2$ atomic states. The excitation wavelength used to produce each emission spectrum is indicated with a coloured star. Right Panel: Green site emission spectra recorded in the (5s5p) $^3P_1$ region.**

Photo-irradiation of the green site $^1P_1$ absorption also produces this narrow emission (blue trace), as was discussed in Section V.3.III.

It is noteworthy that the photophysical properties of the green site $^3P_1$ emission seem to depend on the excitation wavelength. For example, when the (5s4d) $^1D_2$ absorption band at 494.6 nm is irradiated, an emission is produced at 688.4 nm and is characterised by a spectral width of 210 cm^{-1}. Conversely, excitation at 461.8 ($^1P_1$) or 483.0 nm ($^1D_2$) produces a broader emission (fwhm = 387 cm^{-1}) centred at 691.7 nm, exhibiting a tail to longer wavelengths. This effect can be clearly seen in the right panel of Figure V.91 and the explanation is quite simple. The R2 trapping site is concurrently[o] excited when the two higher energy excitation wavelengths are used and, as was shown

---

[o]   This occurs both directly and indirectly. When the green site 461.8 ($^1P_1$) band is excited, a $^1P_1$ emission is produced at 470.4 nm. This emission overlaps the R2 site $^1P_1$ absorption band and is competitively re-absorbed, indirectly yielding R2 emission at 705.4 nm. In contrast, the green site $^1D_2$ absorption ~485 nm coincides with the $^1D_2$ absorption of the R2 site – this is more evident samples annealed to a lower temperature where the R2 site is more prevalent. For clarity, an excitation scan recorded of the 705.4 nm R2 emission in Kr will be presented ahead in Section V.5.

in Section V.3.IV, this site emits at 705.4 nm. Thus, true site-selectivity is available only with $^1D_2$ excitation at 494.6 nm.

An emission decay profile, recorded at 10 K with laser excitation at 494.6 nm, is presented in Figure V.92. A triple exponential function, employing decay times of 7.1, 327.7 and 833.2 µs with the amplitudes of 4024, 1374 and 235 respectively, was required to account for the complex decay kinetics.

Sr/Kr - Decay profile $\lambda_{Em.}$ = 688.4 nm at 10 K
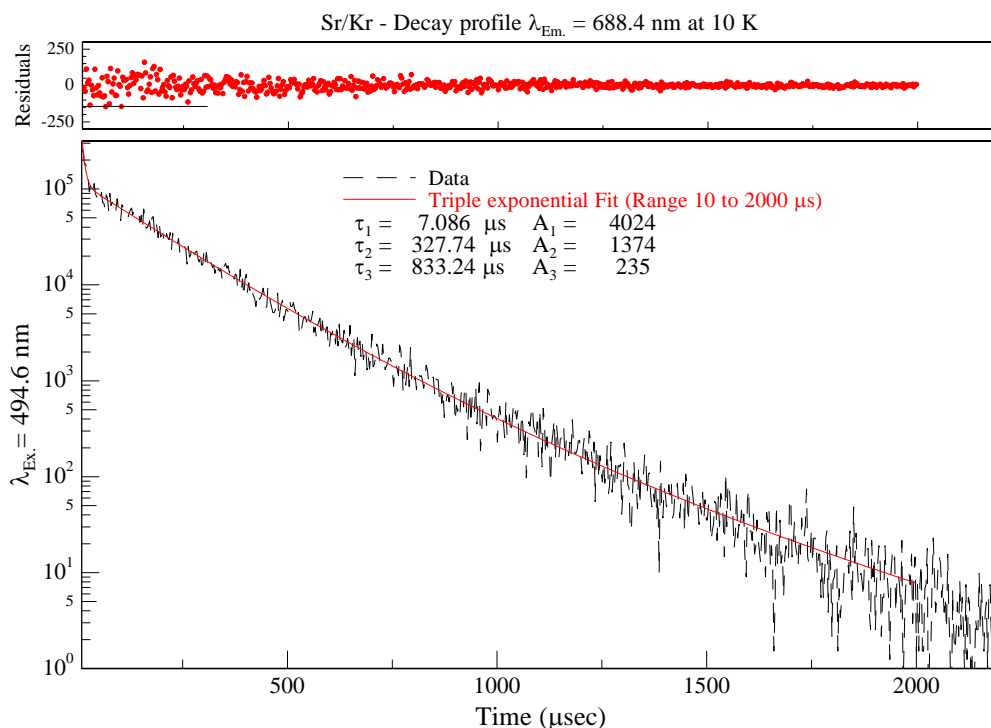
Figure V.92   **Decay profile of the Sr/Kr green site emission band 688.4 nm, produced by site-selective laser excitation at 494.6 nm and recorded using the multi-channel scaling technique. $\sigma\tau_1 = \pm 0.6$ µs, $\sigma\tau_2 = \pm 19.7$ µs and $\sigma\tau_3 = \pm 231.3$ µs.**

The temperature dependence of the temporal and spectral scans are presented in the right and left panels of Figure V.93 respectively. The decay curves are very temperature dependent, as revealed by a cursory inspection of the right panel of this plot. A multi-exponential function was fitted at each temperature, the results of which are collated in Table V.21. Inspection of these values shows that the dominant component (τ_1) changes very little from 10 to 12 K and is identified as the radiative lifetime. Correcting for the effective field of the host produces an excited state lifetime of 18.4 µs, thereby allowing assignment of the 688.4 nm emission band to the spin-forbidden (5s5p) $^3P_1 \rightarrow$ (5s^2) $^1S_0$ transition of atomic Sr.
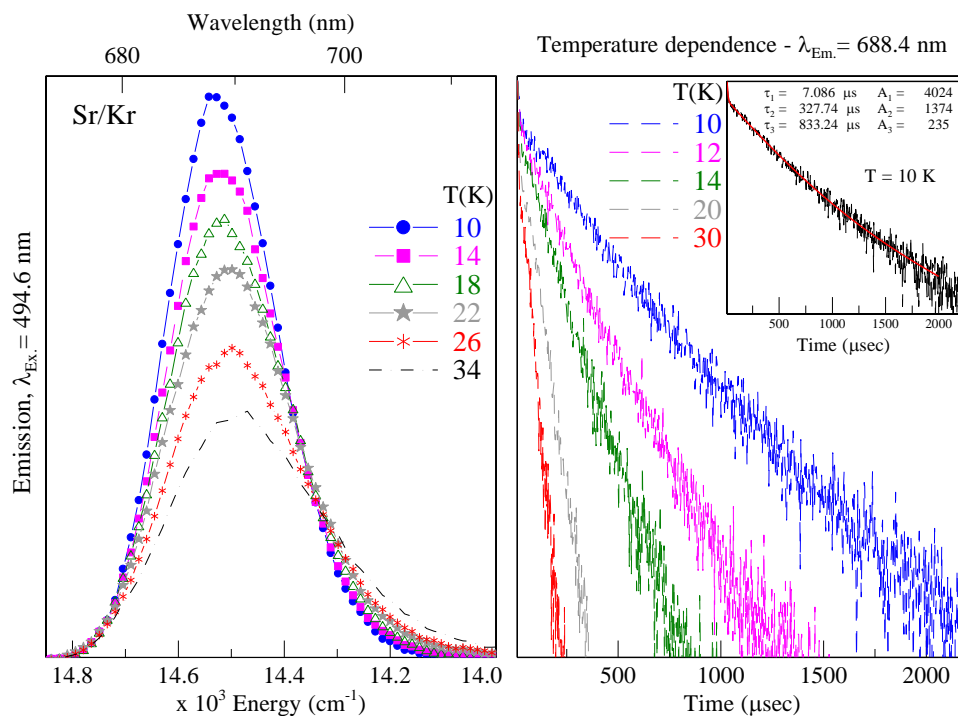
Figure V.93 The left panel shows the temperature dependence of the Sr/Kr green site emission band at 688.4 nm over the range 10 – 38 K. The right panel presents the temperature dependence of the decay curves, recorded between 10 and 30 K. The inset of the right panel shows the fit for the decay recorded at 10 K. The data presented in this plot was produced with photoexcitation of the $^1D_2$ absorption band at 494.6 nm.

In contrast to τ_1, the minor components of the decay (τ_2 and τ_3) are shortened at temperatures above 12 K. In addition, the temporal scans recorded at temperatures exceeding 14 K all exhibit double exponential decays because the amplitude of the third component is vastly reduced. Examination of the spectral scans shown in the left panel of Figure V.93 reveals that the emission intensity gradually decreases as the sample becomes warmer. The fully reversible temperature dependence observed for both the temporal and spectral scans suggests that $^3P_1$ emission is being quenched by a competing relaxation pathway. It is possible that the population of this state is non-radiatively transferred back to the ground state. This process becomes more efficient with increasing sample temperature.

Table V.21   **Temporal characteristics of the Sr/Kr 688.4 nm emission band, recorded over the temperature range of 10 to 30 K.**

T_s (K)	Fit Range (µs)	A_1	τ_1 (µs)	A_2	τ_2 (µs)	A_3	τ_3 (µs)
10	10 – 2000	4024	7.1	1374	327.7	235	833.2
12	10 – 1200	3768	8.0	1584	191.2	316	424.7
14	10 – 800	5912	6.4	1602	161.1	-	-
20	5 – 400	7314	6.3	1504	89.3	-	-
30	5 – 170	11856	5.0	1401	57.2	-	-

V.4.II.II $\lambda_{em} \approx 575$ nm

V.4.II.II.A   Blue site

The emission spectrum produced with excitation of the blue site (5s4d) $^1D_2$ absorption band is represented by the red trace in Figure V.94.
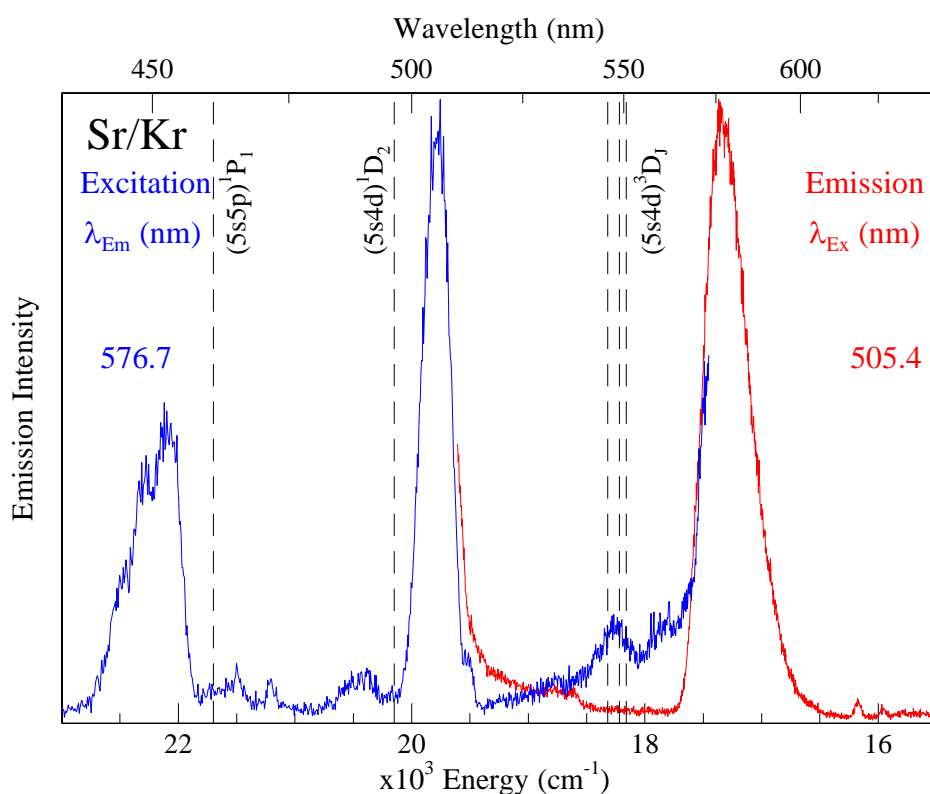
Figure V.94   **Excitation (blue) and emission (red) spectra recorded for the Sr/Kr blue site of isolation. The gas phase positions[4] of the (5s5p) $^1P_1$, (5s4d) $^1D_2$, and (5s4d) ^3D_J excited states are shown as dashed vertical lines.**

In addition to the (5s5p) $^3P_1$ emission band at 730.0 nm, a higher energy emission[p] occurs at 576.6 nm and is characterised by a Stokes shift of 2446 cm^{-1} and a matrix red-shift of -819 cm^{-1} (when evaluated from the position of the $^3D_1$ atomic state). The excitation scan recorded monitoring the intensity of this feature is shown in blue. Examination of this spectrum allows the emission at 576.6 nm to be confidently assigned to the blue site of isolation since the characteristic (5s5p) $^1P_1$ and (5s4d) $^1D_2$ absorptions are clearly evident at 448.6 and 505.4 nm respectively.

An emission decay curve recorded at 10K is presented in Figure V.95. The profile was well fit with a double exponential function employing decay times of 0.65 and 1.5 µs with amplitudes of 1873 and 591 respectively.
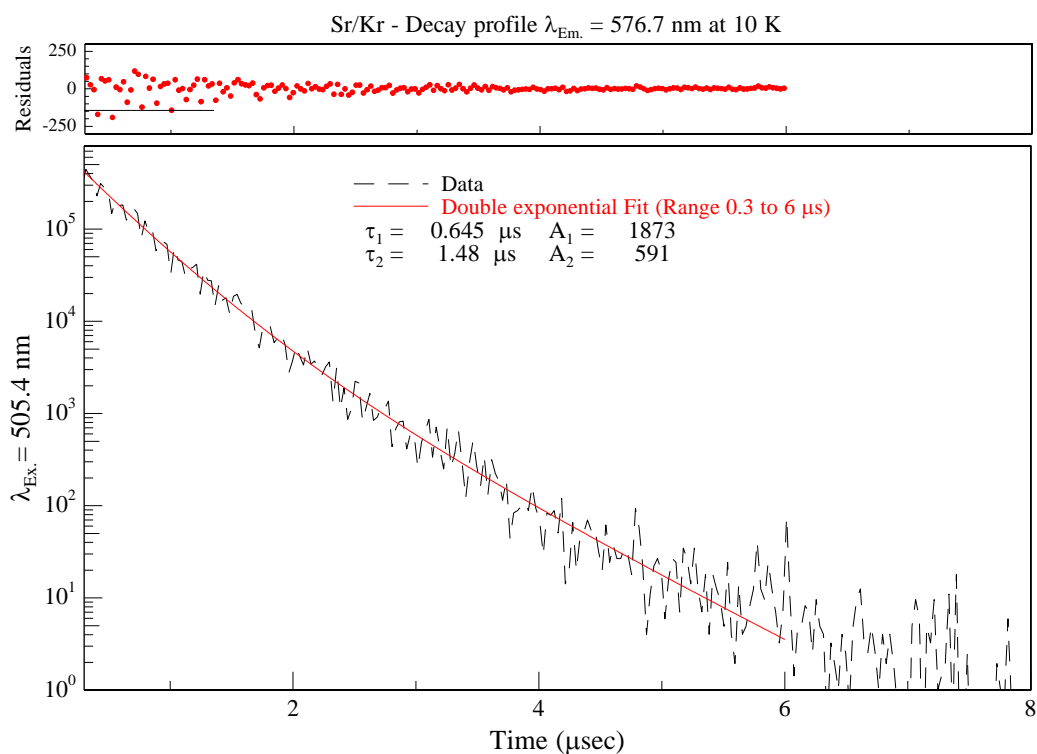
Figure V.95   **Decay profile of the Sr/Kr blue site emission band at 576.7 nm, produced by site-selective laser excitation at 505.4 nm and recorded using multi-channel scaling. $\sigma\tau_1 = \pm 0.1$ µs and $\sigma\tau_2 = \pm 0.4$ µs.**

Time resolved scans made at elevated temperatures are presented in the right panel of Figure V.96. In addition, the results of the least squares fit at each temperature are collected in Table V.22. The decays show little or no change between 10 and 12 K, so

---

[p] This emission band was presented in Section V.2.V.I.A as it is also produced with (5s5p) $^1P_1$ excitation.

the radiative lifetime has been identified. Applying the effective field correction yields excited state lifetimes of 1.7 and 3.8 μs – very similar to the values obtained with (5s5p) $^1P_1$ excitation (see Section V.2.V.I.A). An assignment to the forbidden (5s4d) $^3D_1 \rightarrow$ (5s^2) $^1S_0$ transition of atomic Sr is proposed. The excitation scan in Figure V.94 reveals the presence of weak absorptions ~547.5 nm which directly overlap the (5s4d) ^3D_J manifolds. These were not investigated with direct laser excitation in the present study. Nonetheless, the observation of absorption features in this region bolsters the assignment of the 576.6 nm band as (5s4d) $^3D_1 \rightarrow$ (5s^2) $^1S_0$ phosphorescence.
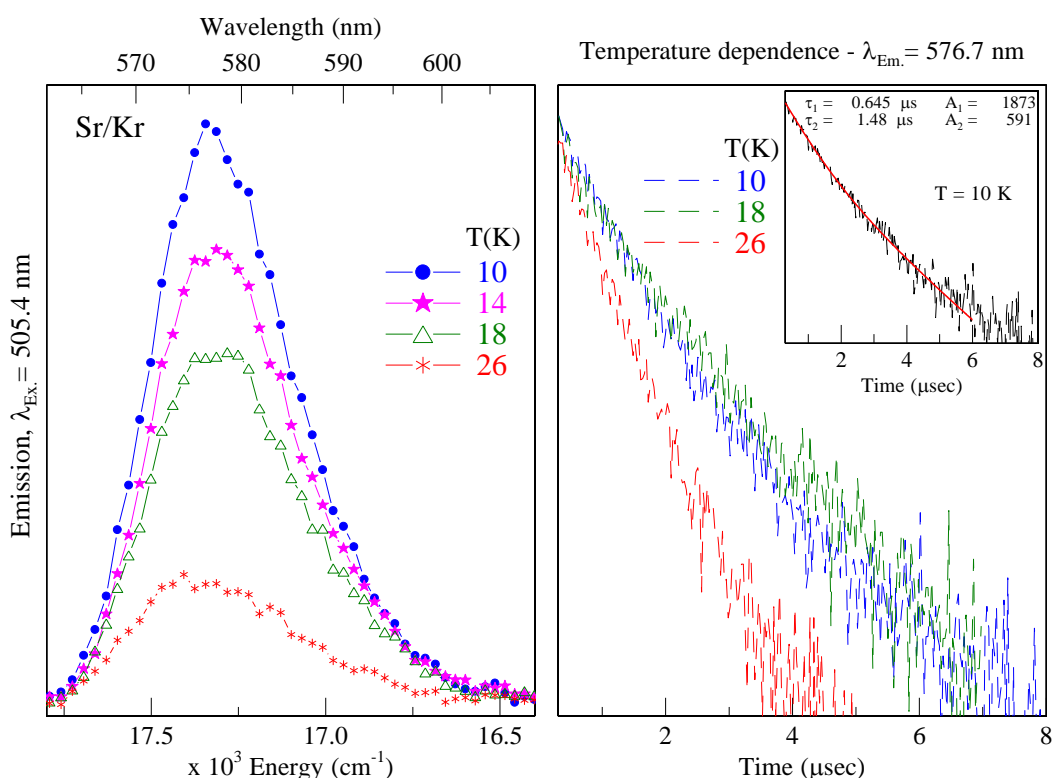
Figure V.96   The left panel shows the temperature dependence of the Sr/Kr blue site emission band at 575.3 nm over the range 10 – 26 K. The right panel presents the temperature dependence of the corresponding decay curves. The inset of the right panel shows the fit for the decay recorded at 10 K.

Emission scans were also recorded over a range of temperatures. As shown in Figure V.96, the intensity is markedly reduced with increasing temperature. In addition, all of the decay times become shorter between 12 and 18 K. Combining this behaviour with the temperature dependence observed for the temporal scans, indicates that a non-radiative relaxation process is competing with the emission from this level and becomes active between 12 and 18 K.

Table V.22   **Temporal characteristics of the Sr/Kr 576.7 nm emission band, recorded over the temperature range of 10 to 26 K.**

T_s (K)	Fit Range (μs)	A_1	τ_1 (μs)	A_2	τ_2 (μs)
10	0.3 – 6.0	1873	0.645	591	1.48
12	0.3 – 6.0	861	0.640	393	1.70
18	0.3 – 6.0	776	0.390	808	1.36
26	0.3 – 6.0	1666	0.329	1643	0.74

V.4.III   Sr/Ar

Similar to Sr/Kr, photoexcitation of the (5s4d) $^1D_2$ absorption bands of Sr/Ar yields emission features in three distinct spectral regions, which pertain to the (5s4d) $^1D_2$, (5s4d) $^3D_1$ and (5s5p) $^3P_1$ excited states. As was the case for the for the (5s5p) $^1P_1$ luminescence, the excited states observed in emission strongly depend on the site of isolation. In addition, a comparison of the (5s4d) $^1D_2$ and (5s5p) $^1P_1$ luminescence will show that, for the blue site, the lower lying triplet states can only be observed with (5s4d) $^1D_2$ excitation.

V.4.III.I $\lambda_{em} \approx$ 490 and 700 nm

The 2D-EE spectrum of Sr/Ar, recorded monitoring the near-IR emission bands at approximately 700 nm, is presented in Figure V.97. In excitation, the scan extends over both (5s5p) $^1P_1$ and (5s4d) $^1D_2$ absorption features (425 – 510 nm) that were identified in Chapter III. Inspection of this plot reveals that the near-IR emissions are quite dependent on the excited state accessed. While a single band dominates with (5s5p) $^1P_1$ excitation, five cleanly resolved features are identifiable with (5s4d) $^1D_2$ excitation – these are labelled I - IV. Based on their location in emission, the dominant feature (I) at 676.1/491.3 nm (emission/excitation) and the weaker band (IV) at 676.1/480.6 nm are assigned to the green site of isolation. Similar to the other two hosts, it appears that the green site (5s4d) $^1D_2$ profile in Ar is multi-featured. Likewise, bands III and V which are located at 691.9/483.5 and 691.9/490.4 nm are attributed to the occupation of the R2 trapping site.

Closer scrutiny of Figure V.97 reveals that band II, centred at 699.6/500.1 nm, has no clear (5s5p) $^1P_1$ counterpart. Despite this, an assignment to the blue site of isolation is made, based on a comparison with the equivalent 2D-EE spectra recorded

in the heavier hosts. This behaviour signifies that the $^1D_2 \rightarrow {}^3P_J$ relaxation pathway is more efficient than the $^1P_1 \rightarrow {}^3P_J$ channel, when Sr atoms are isolated in this vacancy. Indeed, a blue site (5s5p) $^3P_1$ emission could not be identified with excitation of the Jahn-Teller band (see Section V.2.VIII) at 434.8nm.
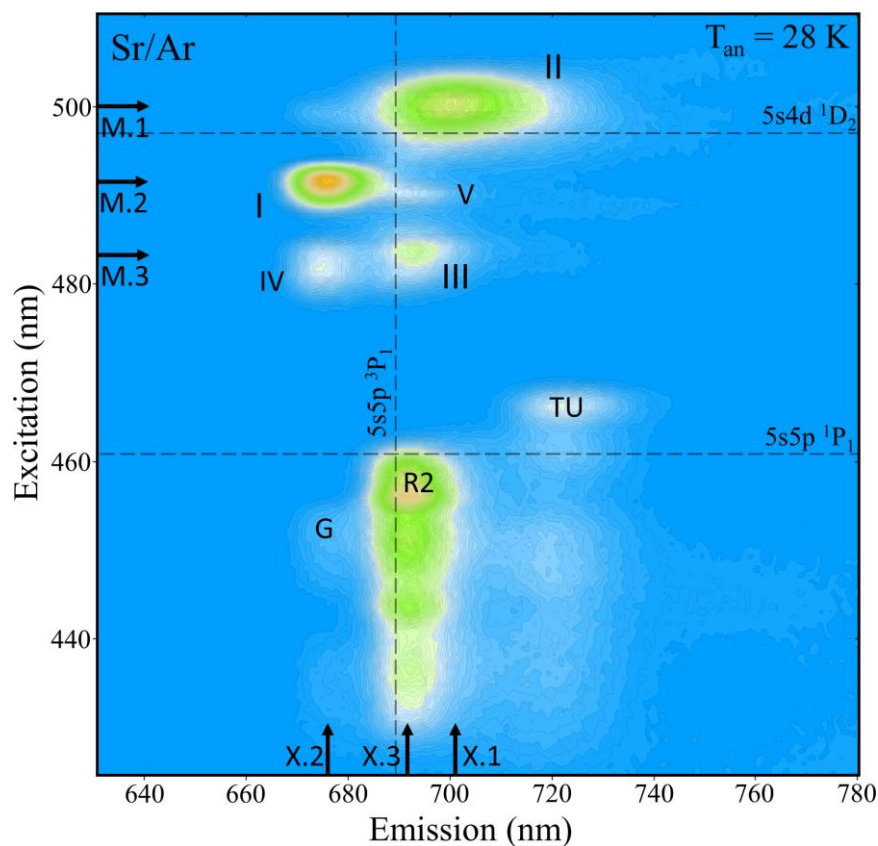
Figure V.97   Sr/Ar 2D-EE spectrum, recorded in the 700 nm spectral region, following sample deposition at 10 K and annealing to 28 K. The gas phase positions[4] of the (5s5p) $^1P_1$ and (5s4d) $^1D_2$ states of atomic Sr are shown in excitation, represented by the dashed horizontal lines.

The same behaviour is also observed for the green site, thus, the (5s5p) $^3P_1$ emission is far more intense when Sr atoms are promoted to the (5s4d) $^1D_2$ manifold. This is evident when the two excitation regions are compared (band I versus band G).

V.4.III.I.A   Blue site

A summary of the blue site luminescence is provided in Figure V.98. The excitation band is centred at 500.1 nm and is characterised by a linewidth of 244 cm^{-1}. A matrix red-shift of -154 cm^{-1} is measured from the band centre to the position of the gas phase (5s4d) $^1D_2 \leftarrow {}^1S_0$ (5s^2) transition. A lineshape analysis for this feature is presented in

Figure V.126 of Appendix V.I. Two Gaussian functions are required to re-produce the asymmetric shape.
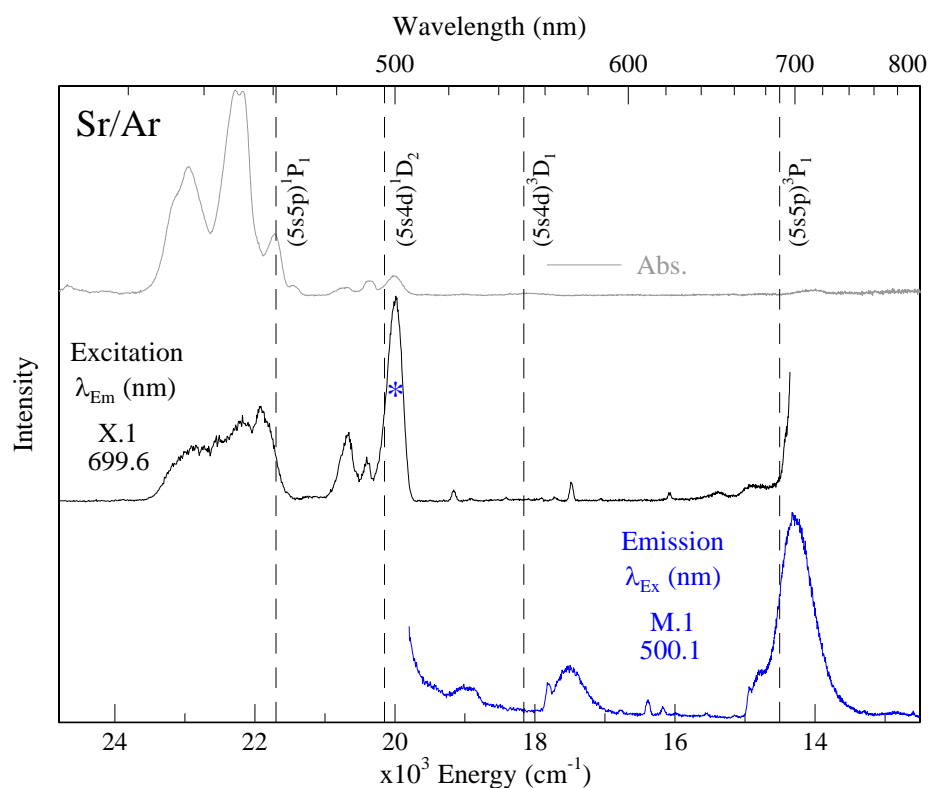
Figure V.98 **Absorption (grey/top), excitation (black/middle) and emission (blue/bottom) spectra recorded for the Sr/Ar blue site of isolation, following sample annealing to 28 K. The gas phase[4] positions of the (5s5p) $^1P_1$, (5s4d) $^1D_2$, (5s4d) $^3D_1$ and (5s5p) $^3P_1$ states of atomic Sr are shown by dashed vertical lines**

As with the other RG hosts, high resolution laser scans of the blue site absorption did not reveal the presence unresolved structures (see top trace of Figure V.126).

Photoexcitation at 500.1 nm produces an emission band at 699.6 nm which is characterised by a fwhm of 561 cm^{-1} and matrix red-shift of -210 cm^{-1} (evaluated from the position of $^3P_1$ level). A decay curve recorded for this feature is shown in Figure V.99. The profile is well fit with a double exponential function. From this, decay times of 11.5 and 109.3 µs (amplitudes = 624 and 828 respectively) are obtained. The temporal scans recorded over a range of temperatures are presented in the right-side of Figure V.100 and the results of the fits are collected in Table V.23. Inspection of these data shows that the shortest component of the decay does not change between 10 and 12 K. Thus, 11.5 µs is identified as the radiative lifetime.
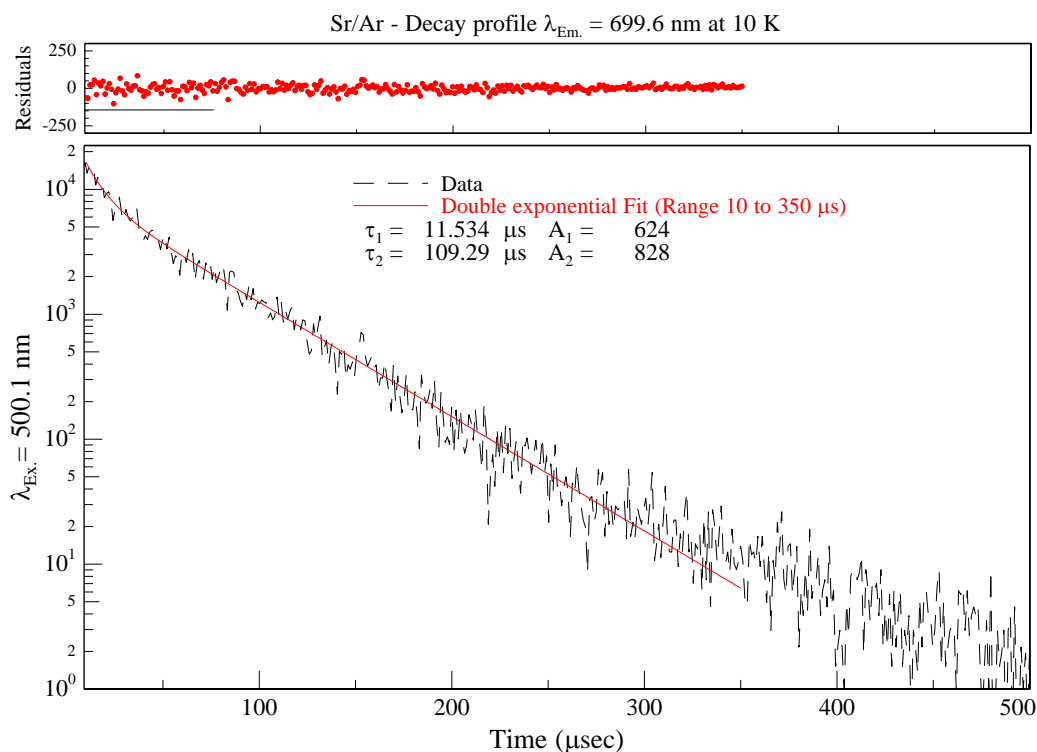
Figure V.99   **Decay profile of the Sr/Ar blue site emission band at 699.6 nm, produced by site-selective laser excitation at 500.1 nm and recorded using the multi-channel scaling technique. $\sigma\tau_1 = \pm\ 0.7\ \mu s$ and $\sigma\tau_2 = \pm\ 1.5\ \mu s$.**

Application of the effective field equation produces an excited state lifetime of 23.6 μs, which is in agreement with the known gas phase lifetime[4] (21.3 μs) of the (5s5p) $^3P_1$ $\rightarrow$ (5s^2) $^1S_0$ transition. Consequently, the 699.6 nm emission band is assigned to this transition. Above 12 K, all decay components become shorter. The temperature dependence of the emission band is presented in the left panel of Figure V.100 - It is reduced in intensity, broadened in width and blue-shifted in position, with increasing temperature. The behaviour observed for both spectral and temporal scans is reversible. From this, we can infer that a non-radiative relaxation pathway is competing with the emission from this state.
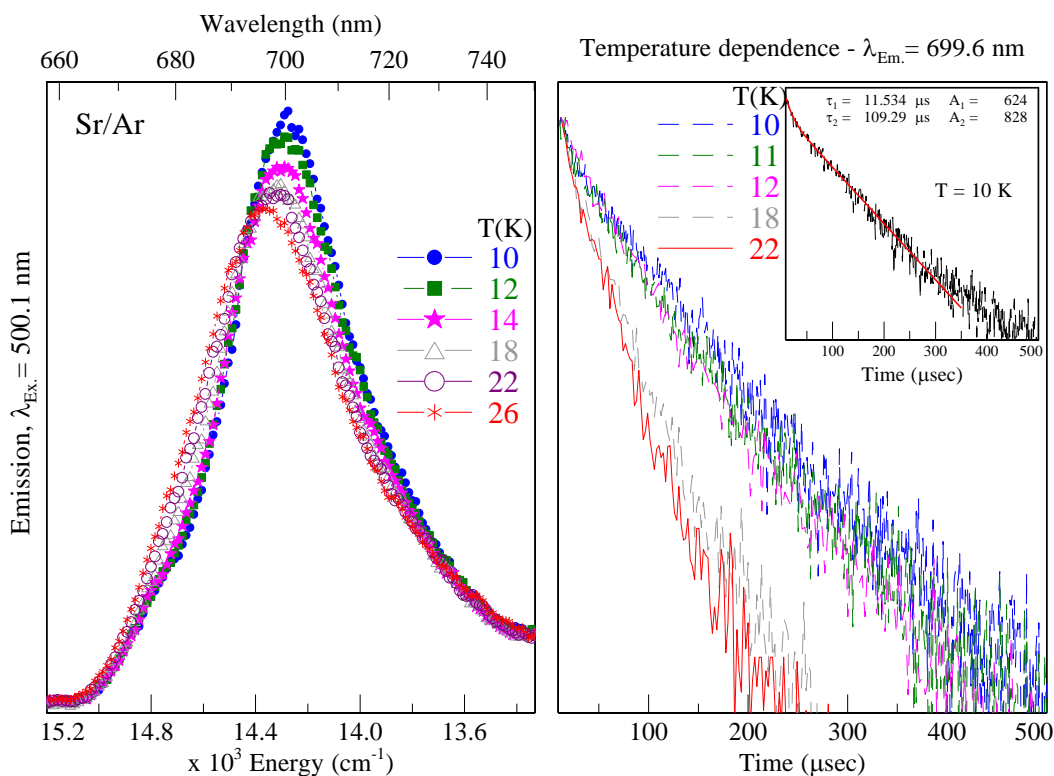
Figure V.100   The left panel shows the temperature dependence of the Sr/Ar blue site emission band at 699.6 nm over the range 10 – 26 K. The right panel presents the temperature dependence of the decay curves, recorded between 10 and 22 K. The inset of the right panel shows the fit for the decay recorded at 10 K. The data presented in this plot was produced with photoexcitation of the $^1D_2$ absorption band at 500.1 nm.

Table V.23   Temporal characteristics of the Sr/Ar 699.6 nm emission band, recorded over the temperature range of 10 to 22 K.

T_s (K)	Fit Range (μs)	A_1	τ_1 (μs)	A_2	τ_2 (μs)
10	10 – 350	624	11.5	828	109.3
11	10 – 350	1080	11.3	1296	94.5
12	10 – 350	628	14.8	740	88.9
18	10 – 200	1011	8.2	965	52.2
22	10 – 150	1310	5.8	956	42.8

V.4.III.I.B   Green site

Emission and excitation spectra recorded for the green site of isolation are presented in Figure V.101. The dominant absorption/excitation band is centred at 491.3 nm, blue-shifted from the gas phase position of the (5s4d) $^1D_2$ state by +204 cm^{-1}. A narrow linewidth of 151 cm^{-1} is recorded for this feature.
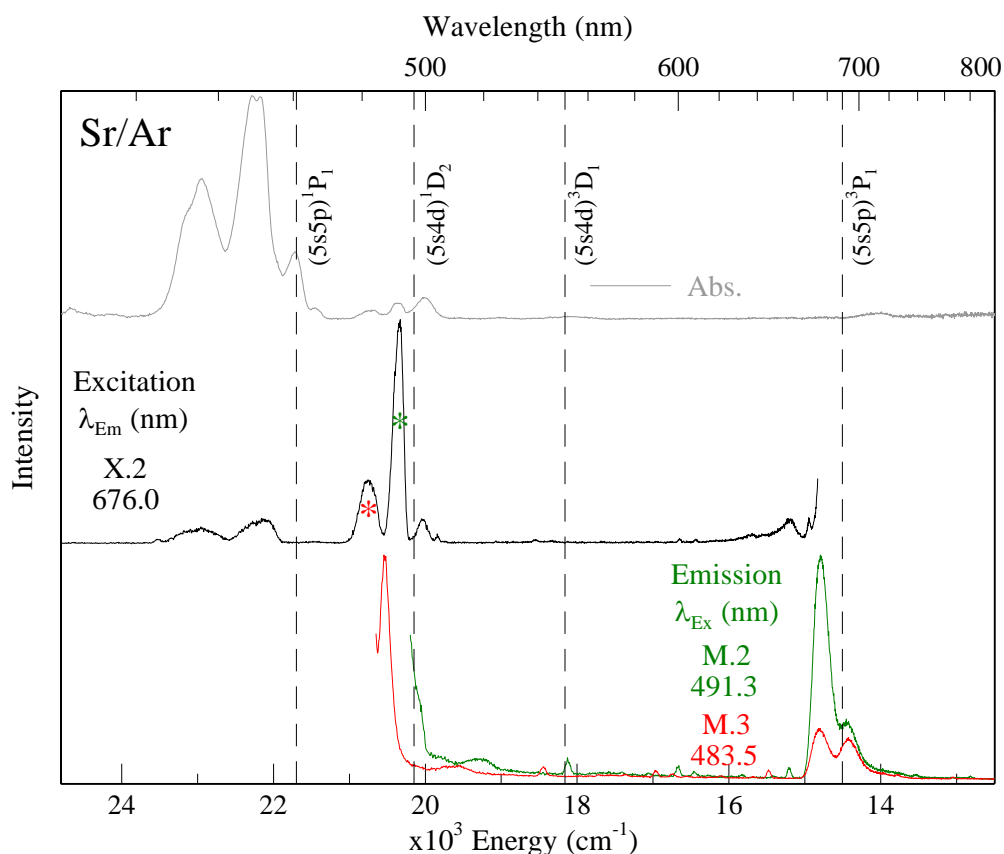
Figure V.101   Absorption (grey/top), excitation (black/middle) and emission (blue/bottom) spectra recorded for the Sr/Ar green site of isolation, following sample annealing to 28 K. The gas phase[4] positions of the (5s5p) $^1P_1$, (5s4d) $^1D_2$, (5s4d) $^3D_1$ and (5s5p) $^3P_1$ states of atomic Sr are shown by dashed vertical lines

The weaker green site absorption is centred at 480.6 nm, blue-shifted with respect to the (5s4d) $^1D_2$ atomic level by 658 cm^{-1}. As with the equivalent band in Kr, excitation of this feature produces a sharp resonance (5s4d) $^1D_2 \rightarrow$ (5s^2) $^1S_0$ emission at 487.3 nm, as illustrated by the red trace in Figure V.101. In addition, two emissions are observed in (5s5p) $^3P_1$ region with excitation at this wavelength. The more intense band of the pair is centred at 676.0 nm and represents the green site emission. Whereas the remaining band at 693.2 nm is associated with the R2 trapping site – the luminescence of this site will be discussed in Section V.4.III.I.C.

     A lineshape analysis of the dominant excitation band is presented in the bottom of Figure V.102 – two Gaussian functions are required to account for the asymmetric profile. Similar to the green site of Kr, a high resolution laser excitation scan revealed the presence of an unresolved component. As illustrated by the top trace of Figure V.102, a sharp (fwhm $\approx$ 6 cm^{-1}) zero-phonon line (ZPL) exists at 493.05 nm. This feature was not identifiable in any of the lamp excitation scans. The observation of such

a structure indicates that the electron-phonon coupling is quite weak in both the ground $^1S_0$ and excited $^1D_2$ states of Sr, when isolated at this site in Ar.
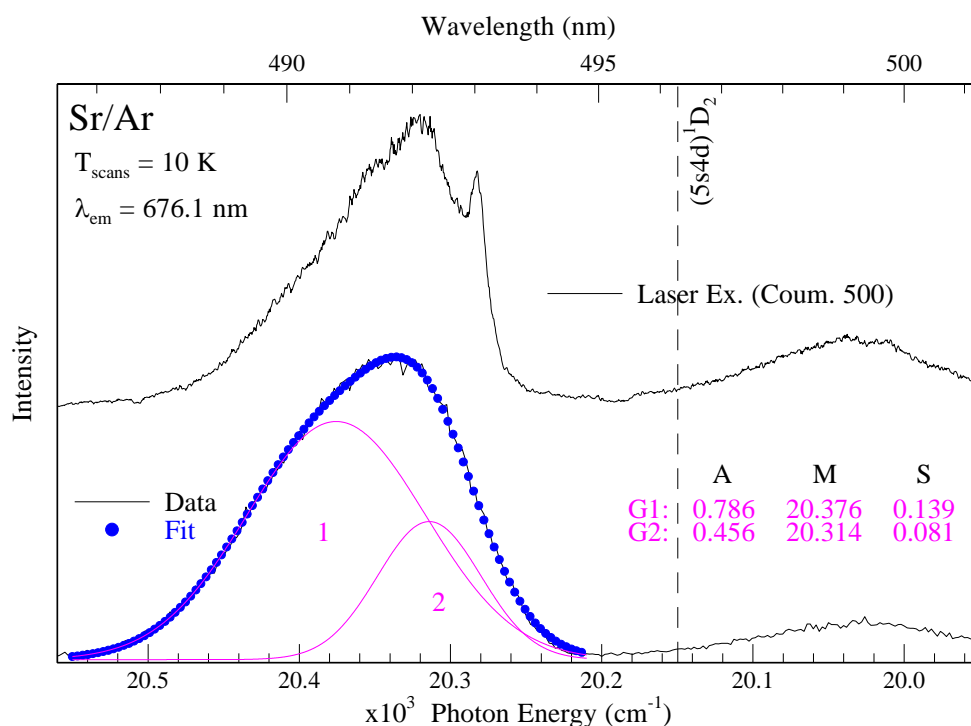
Figure V.102 **Bottom traces: A lineshape analysis of the Sr/Ar green site $^1D_2$ excitation band. Two Gaussian curves provide a good fit of the profile. The symbols a, m and s are explained in Figure IV.52. During the fit, all of the Gaussian parameters were allowed to vary. $\sigma_{M1} = \pm 10.0$ cm^{-1} and $\sigma_{M2} = \pm 3.1$ cm^{-1}. Top trace: Laser excitation scan obtained by monitoring the intensity of the 676.1 nm emission. Coumarin 500 was the dye material used for this scan. The laser spectrum was not corrected for the intensity distribution of the dye.**

Photoexcitation at 491.3 nm produces an emission band at 676.1 nm (fwhm = 234 cm^{-1}) which is blue-shifted with respect to the $^3P_1$ level by +151 cm^{-1}. The decay curve recorded for this band at 10 K is presented in Figure V.103. A double exponential function, employing decay times of 407 and 1278 μs with amplitudes of 332 and 768 respectively, adequately fits the data. The temperature dependence of the temporal and spectral scans are presented in the right and left panels of Figure V.104. In addition, the results of the least squares fit at each temperature are collected in Table V.24. Examining these data shows that a non-radiative relaxation process significantly depletes the population of this level, as evidenced by the shortening of all decay components, even over the small temperature range of 10 to 12 K. As a consequence, the radiative lifetime of this emission could not be identified. However, this emission was already assigned as (5s5p) $^3P_1$ phosphorescence in Section V.2.VIII.I.A. It is

noteworthy that, in contrast to all of the other emission bands recorded in this spectra region, a shorter (< 10 µs) time component was not observed for this emission.
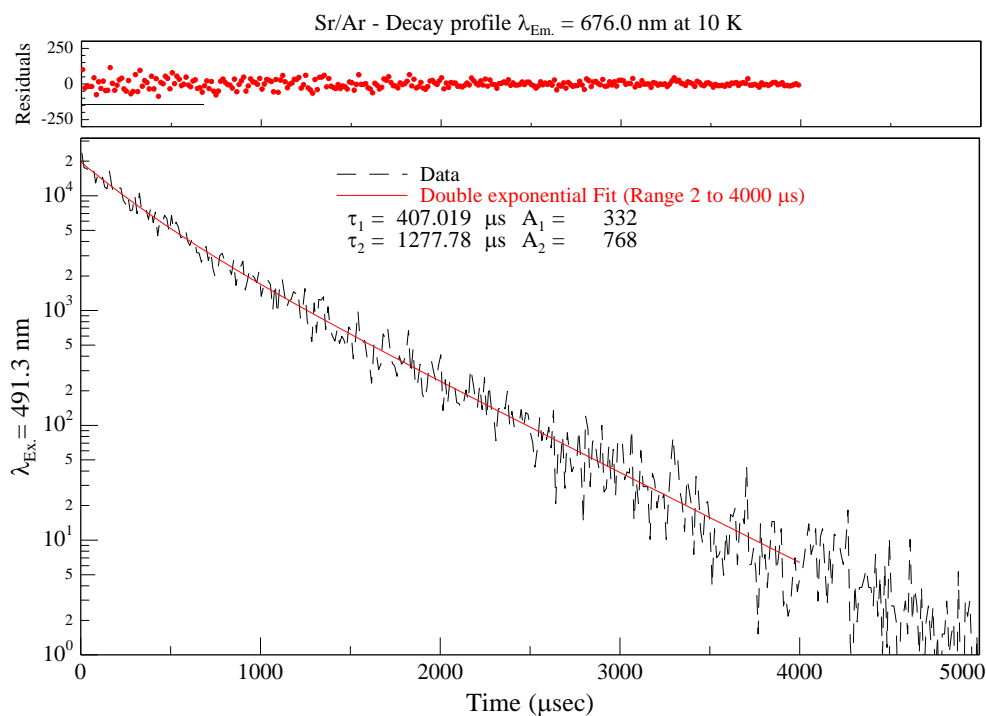
Figure V.103 Decay profile of the Sr/Ar green site emission band 676.0 nm, produced by site-selective laser excitation at 491.3 nm and recorded using the multi-channel scaling technique. $\sigma\tau_1 = \pm 77.1$ µs and $\sigma\tau_2 = \pm 63.0$ µs.

Table V.24 Temporal characteristics of the Sr/Ar 676.0 nm emission band, recorded over the temperature range of 10 to 30 K.

T_s (K)	Fit Range (µs)	A_1	τ_1 (µs)	A_2	τ_2 (µs)
10	2 – 4000	322	407.0	768	1277.8
11	10 – 3000	335	302.0	606	941.6
12	10 – 1800	336	154.5	826	603.7
14	10 – 1200	1307	69.2	1794	318.9
18	10 – 600	1613	56.5	1136	163.5
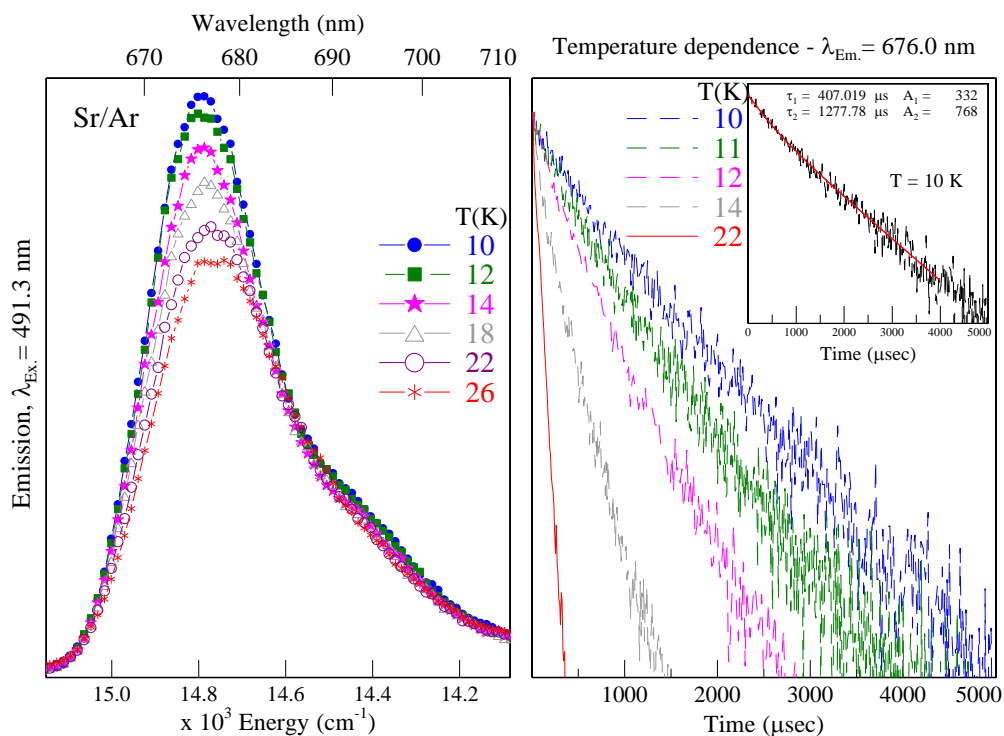
Figure V.104 **The left panel shows the temperature dependence of the Sr/Ar green site emission band at 676.0 nm over the range 10 – 26 K. The right panel presents the temperature dependence of the decay curves, recorded between 10 and 22 K. The inset of the right panel shows the fit for the decay recorded at 10 K. The data presented in this plot was produced with photoexcitation of the $^1D_2$ absorption band at 491.3 nm.**

V.4.III.I.C   R2 site

The luminescence of the R2 site is summarised in Figure V.105. As with the green site, the R2 absorption profile consists of two components: 1. a dominant band centred at 483. 5 exhibiting a matrix blue-shift of +533 cm^{-1} and 2. a weaker peak at 490.4 nm which exhibits a smaller blue-shift of +242 cm^{-1}. Photoexcitation of either component produces both green and R2 site emission bands at 676.1 and 693.2 nm, respectively. This occurs due to spectral overlap between the (5s4d) $^1D_2$ absorption features of these sites. The R2 emission is characterised by a fwhm of 304 cm^{-1} and is red-shifted from the gas phase position of the (5s5p) $^3P_1 \rightarrow$ (5s^2) $^1S_0$ transition by -78 cm^{-1}. A decay profile recorded for this band at 10 K is presented in the left panel of Figure V.106. A triple exponential function, employing decay times/amplitudes of 9.2 µs/1722, 208.0 µs /1919 and 907.2 µs /253, adequately fits the decay profile.
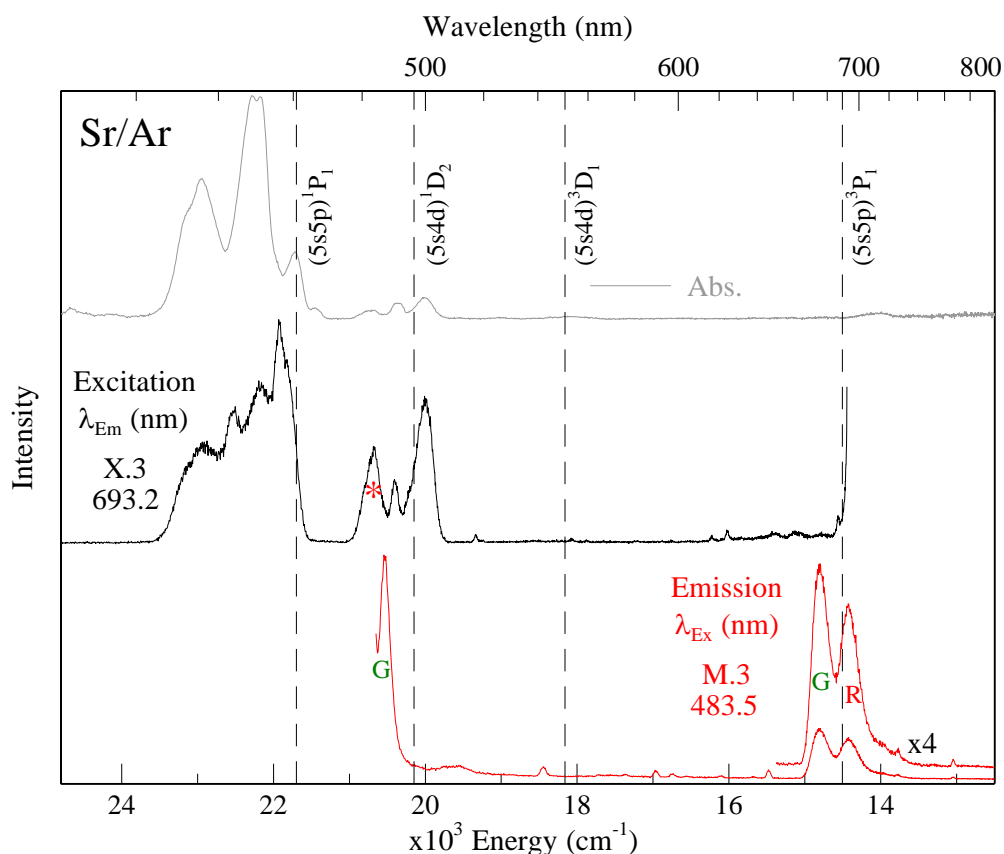
Figure V.105   **Absorption (grey/top), excitation (black/middle) and emission (blue/bottom) spectra recorded for the Sr/Ar R2 site of isolation, following sample annealing to 28 K. The gas phase[4] positions of the (5s5p) $^1P_1$, (5s4d) $^1D_2$, (5s4d) $^3D_1$ and (5s5p) $^3P_1$ states of atomic Sr are shown by dashed vertical lines**

The temperature dependence of this decay profile was not investigated with direct $^1D_2$ excitation. Nonetheless, this emission was already assigned as (5s5p) $^3P_1 \rightarrow (5s^2)\ ^1S_0$ phosphorescence in Section V.2.VIII.I.B. The spectral scans recorded over a range of temperatures are shown in the right panel of Figure V.106. As the two emission bands occurring in this region are extensively overlapped, the integrated area was measured for the entire scan. The area under the curve was observed to increase with the temperature. This behaviour is attributed to the enhancement of the R2 site emission because the green site band was previously shown to diminish at elevated temperatures. Thus, for the R2 site, a non-radiative feeding step to the (5s5p) $^3P_1$ level becomes more efficient over the range of 10 to 26 K.
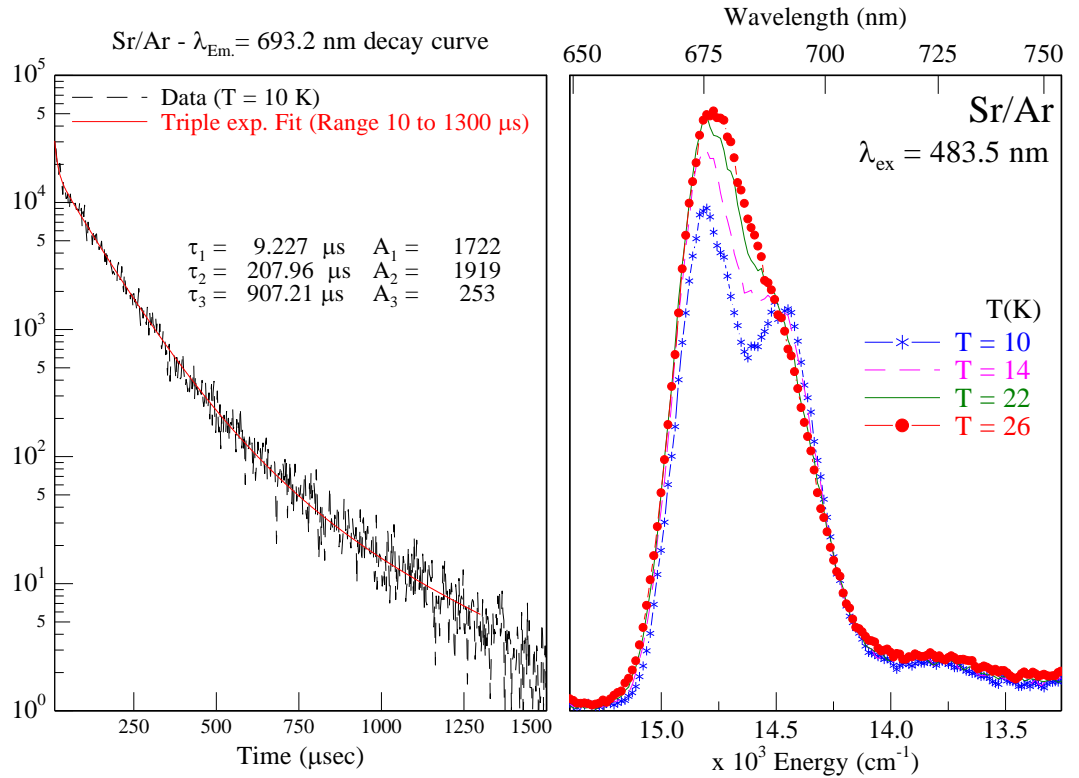
Figure V.106 **Left Panel: Decay profile of the Sr/Ar R2 site emission band 693.2 nm, produced by site-selective laser excitation at 483.5 nm and recorded using the multi-channel scaling technique. $\sigma\tau_1 = \pm 1.3$ μs, $\sigma\tau_2 = \pm 8.6$ μs and $\sigma\tau_3 = \pm 165.3$ μs. Right Panel: The temperature dependence of the R2 site emission recorded over the range 10 – 26 K.**

V.4.III.II $\lambda_{em} \approx 570$ nm

V.4.III.II.A Blue site

Excitation of the blue site (5s4d) $^1D_2$ band at 500.1 nm produces a weak emission at 570.9 nm, as was shown in Figure V.98. An expanded view of this region is presented in Figure V.107. This emission is characterised by a fwhm of 514 cm^{-1} and is red-shifted with respect to the (5s4d) $^3D_1$ atomic state by -643 cm^{-1}. An emission decay is presented in Figure V.108 and was adequately fit with a double exponential function. From this, decay times of 0.7 and 1.9 μs with the respective amplitudes of 1274 and 630, were extracted. In an attempt to assign the radiative lifetime of this emission, decays were recorded at elevated temperatures. These are presented in the right-hand side of Figure V.109 and the temporal characteristics are listed in Table V.25. The decay times show little or no change between 10 and 14 K. Thus, the radiative lifetime has been identified and excited state lifetimes of 1.5 and 3.9 μs are obtained following application of the

effective field correction. Similar to the 576.6 nm emission of Sr/Kr, assignment is made to the forbidden $(5s4d)\ ^3D_1 \rightarrow (5s^2)\ ^1S_0$ transition of atomic Sr.
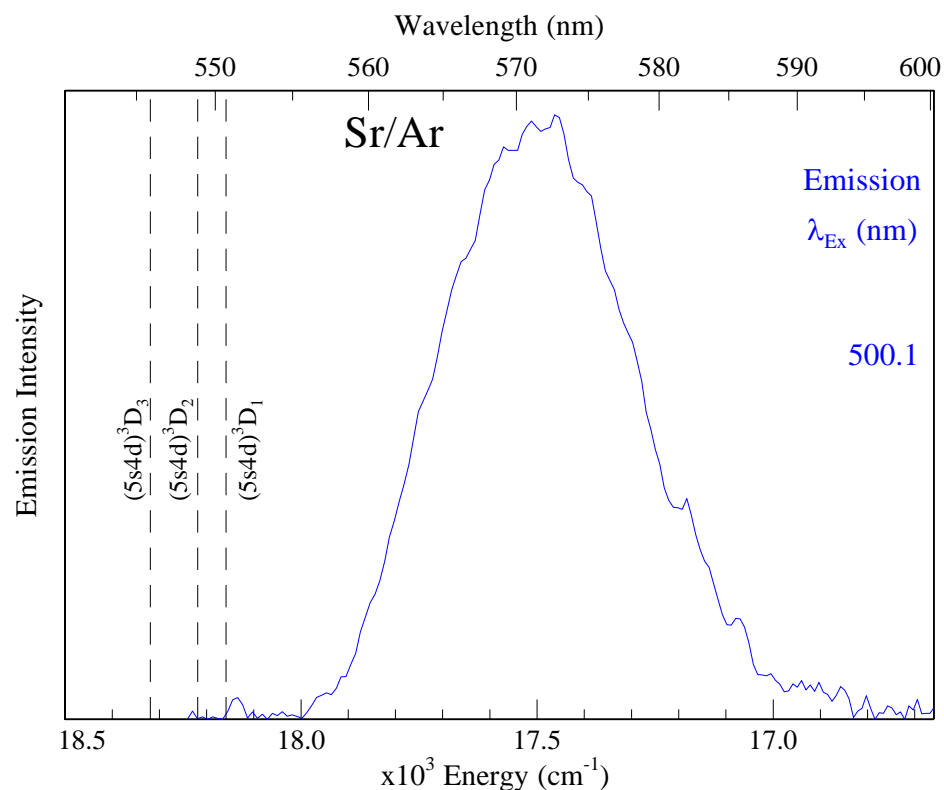
Figure V.107 Emission spectrum recorded in the 570 nm region with excitation of the blue site at 500.1 nm. The gas phase[4] positions of the $(5s4d)\ ^3D_J$ states of atomic Sr are shown by dashed vertical lines. The data shown was obtained from a Sr/Ar sample which was annealed to 28 K.

The temperature dependence of the spectral scans are shown in the left panel of Figure V.109. The emission intensity decreases with temperature. In addition, the decay curves are shortened above 14 K. Both of these effects indicate that a non-radiative relaxation pathway quenches the blue site emission. This process is enhanced at elevated temperatures.

Table V.25 Temporal characteristics of the Sr/Ar 570.9 nm emission band, recorded over the temperature range of 10 to 26 K.

T_s (K)	Fit Range (μs)	A_1	τ_1 (μs)	A_2	τ_2 (μs)
10	0.3 – 7.0	1274	0.72	630	1.90
12	0.3 – 7.0	1309	0.80	418	2.03
14	0.3 – 7.0	704	0.74	188	1.99
18	0.3 – 4.0	729	0.56	598	1.26
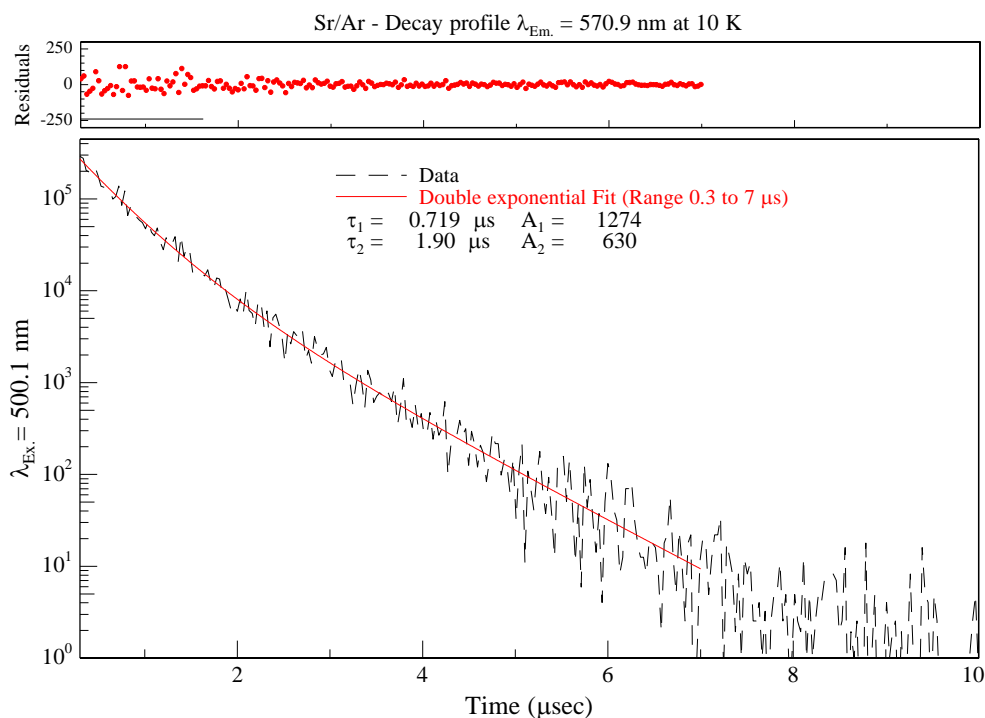
**Figure V.108**   Decay profile of the Sr/Ar blue site emission band at 570.9nm, produced by site-selective laser excitation at 500.1 nm and recorded using multi-channel scaling. $\sigma\tau_1 = \pm 0.1$ μs and $\sigma\tau_2 = \pm 0.2$ μs.
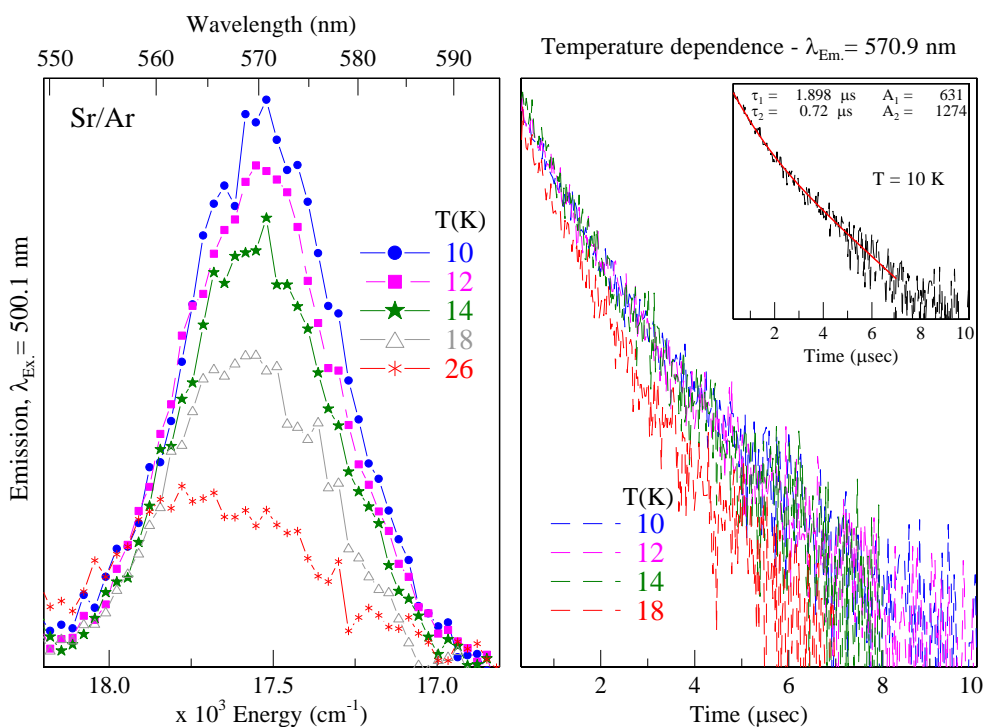
Figure V.109   The left panel shows the temperature dependence of the Sr/Ar blue site emission band at 570.9 nm recorded over the range 10 – 26 K. The right panel presents the temperature dependence of the decay curves, recorded between 10 and 18 K. The inset of the right panel shows the fit for the decay recorded at 10 K. The data presented in this plot was produced with photoexcitation of the $^1D_2$ absorption band at 500.1 nm

V.5   Sr/RG (5s5p $^1D_2$) discussion and conclusions

A summary of the (5s4d) $^1D_2$ luminescence is presented in Figure V.110 and the emission photophysical properties and state assignments are collected in Table V.26. Excitation of the blue site (5s4d) $^1D_2$ bands produces broad emission ~575 nm in Ar and Kr matrices – these were assigned to the (5s4d) $^3D_1 \rightarrow$ (5s^2) $^1S_0$ transition of atomic Sr. The lowest energy emissions observed in this study occurred in the near-IR region and were all assigned as (5s5p) $^3P_1 \rightarrow$ (5s^2) $^1S_0$ phosphorescence.
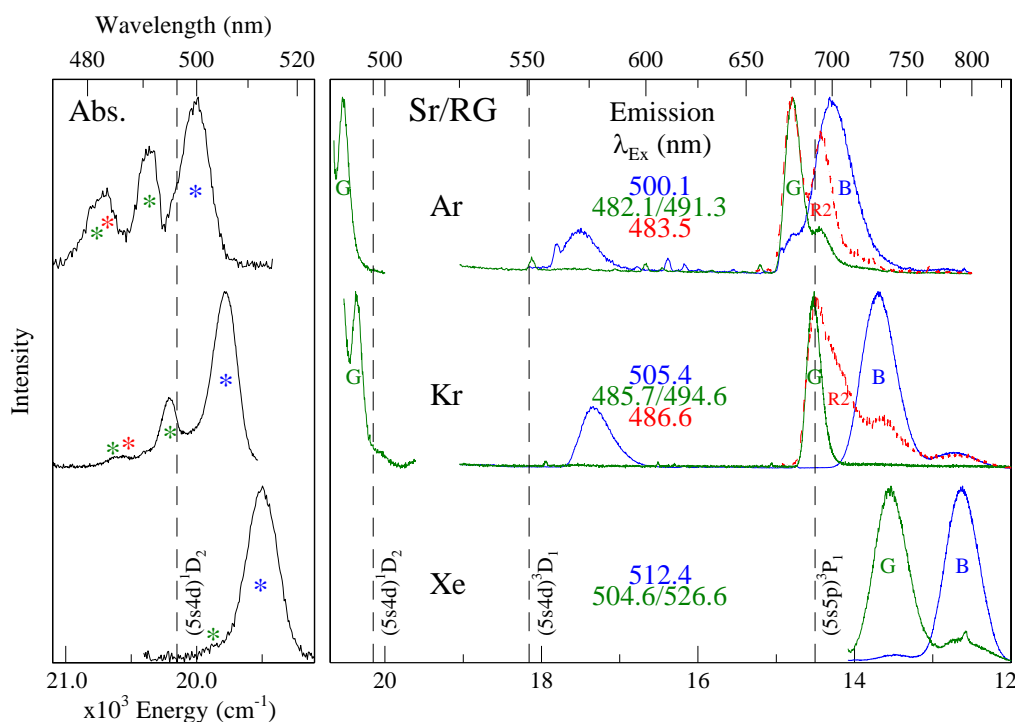
Figure V.110   **Left Panel: (5s4d) $^1D_2$ absorption spectra recorded for Sr isolated in the RG solids (RG = Ar, Kr and Xe). The samples were annealed to 28, 45 and 60 K for Ar, Kr and Xe respectively. The coloured asterisks indicate the excitation wavelength used to produce the emission scans shown in the right panel. Right Panel: Emission scans obtained with excitation of the (5s4d) $^1D_2$ absorption bands. Note, the emission spectrum shown for the R2 site in Kr (red trace) was obtained from a sample annealed to the lower temperature of 38 K. The gas phase[4] positions of the (5s4d) $^1D_2$, (5s4d) $^3D_1$ and (5s5p) $^3P_1$ states of atomic Sr are shown by dashed vertical lines**

Resonance (5s4d) $^1D_2 \rightarrow$ (5s^2) $^1S_0$ emission was observed only for Sr atoms isolated in the green sites of Ar and Kr matrices. High resolution laser excitation and emission scans, recorded of this parity-forbidden transition, are presented in Figure V.111. As was discussed in Section V.3.III, these (5s4d) $^1D_2$ emission bands are characterised by narrow, asymmetric bandwidths and are both blue-shifted with respected to the gas

phase energy. Moreover, a 'mirror' symmetry almost exists between the excitation and emission bands. Coupling this observation with the small Stokes shifts of 286 and 333 cm^{-1}, that are evaluated in Ar and Kr respectively, implies that the equilibrium configuration of the Sr/RG centre is nearly the same in the ground ($^1S_0$) and excited ($^1D_2$) state.
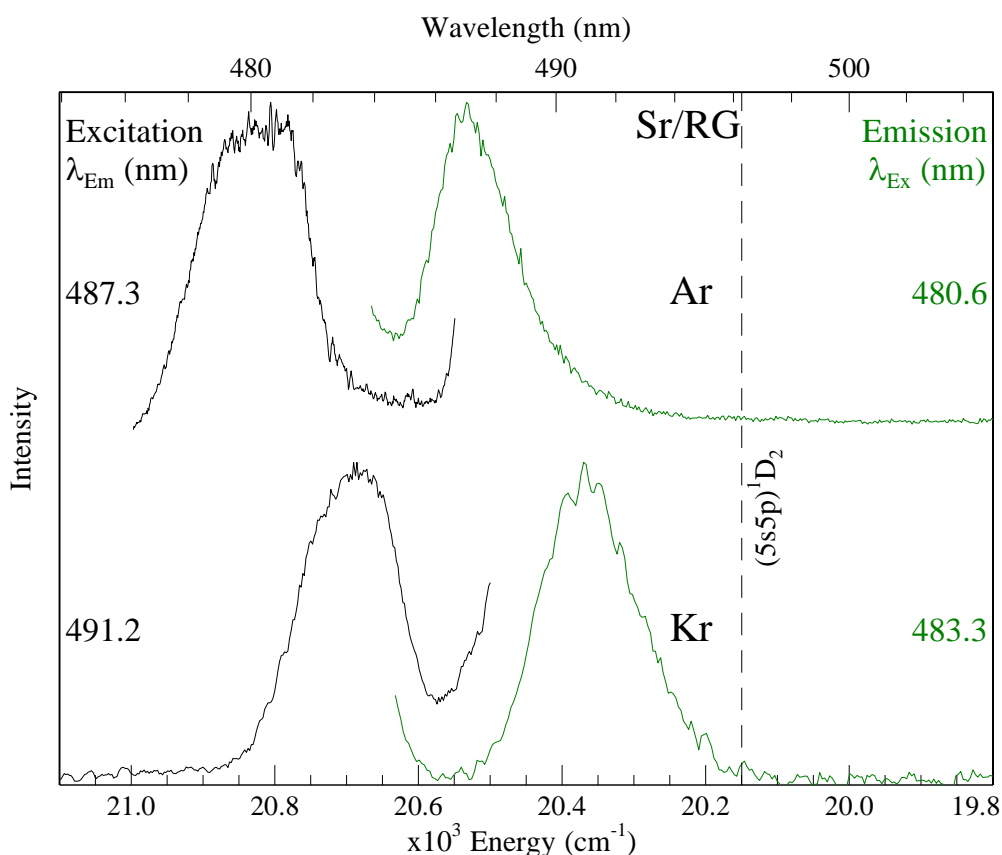
Figure V.111   **High resolution laser excitation (black) and emission (green) spectra recorded for the green site of isolation in Ar and Kr matrices. These features represent the only (5s4d) $^1D_2$ state emission bands observed in this study.**

It is interesting to note that, for the blue site, (5s4d) $^3D_1$ or (5s5p) $^3P_1$ emission was not observed with (5s5p) $^1P_1$ excitation in Ar. This behaviour can be explained by invoking the population transfer model described in Section V.3.VI.II. The $^1P_1 \rightarrow {}^3D_J$ intersystem crossing (ISC) was shown to be weak for Ar. For instance, the blue site (5s5p) $^1P_1$ emission showed little or no temperature dependence, indicating that the population of this state was directly and radiatively transferred back to the ground state. As a result, emission was not observed from the low-lying triplet states. Conversely, resonance emission was not identified with irradiation of the blue site (5s4d) $^1D_2$

absorption bands. From this we can infer that $^1D_2 \rightarrow {}^3D_J$ intersystem crossing is much more efficient for the blue site in Ar.

Table V.26 The photophysical properties of the Sr/RG sites of isolation, obtained with (5s4d) $^1D_2$ excitation. The emission spectral positions are quoted in both nanometres (nm) and wavenumber (cm^{-1}) units. δ represents the gas phase to matrix frequency shifts, given in wavenumber units. The bandwidth (full width at half maximum, fwhm) is denoted by the symbol Δ and is also expressed in units of wavenumber. *Bandwidth obtained from a Gaussian lineshape fit.

Gas Phase[4]	Site	Host	λ_{em} (nm)	ν (cm^{-1})	δ (cm^{-1})	$\Delta\nu$ (cm^{-1})
$(5s5p)^3P_1 \rightarrow (5s5p)^1S_0$	Blue	Ar	699.6	14294	-210	561
$\nu = 14504.33$ cm^{-1}		Kr	730.0	13699	-806	503
		Xe	791.2	12639	-1865	503
	Green	Ar	676.1	14791	286	234
		Kr	688.4	14526	22	210
		Xe	740.5	13504	-1000	499
	R2	Ar	693.2	14426	-78	304*
		Kr	705.4	14176	-328	393*
$(5s5p)^3D_1 \rightarrow (5s5p)^1S_0$	Blue	Ar	570.9	17516	-643	514
$\nu = 18159.04$ cm^{-1}		Kr	576.7	17340	-819	427
$(5s4d)^1D_2 \rightarrow (5s5p)^1S_0$	Green	Ar	487.3	20521	372	131
$\nu = 20149.69$ cm^{-1}		Kr	491.2	20358	209	137

The magnitude of the matrix shifts observed for the (5s5p) $^3P_1$ phosphorescent bands in Xe is much greater than in the lighter hosts. This trend is best highlighted by considering the energy difference between the emissions of a given site. Taking the blue site as an example: a difference of +596 cm^{-1} exists between the band centres in Ar and Kr, while the difference between Kr and Xe is almost twice as large, with a value of +1060 cm^{-1}. A similar trend was also observed for the features of the green site. Thus, a greater degree of stabilisation occurs in the (5s5p) $^3P_1$ excited state of Sr atoms, when isolated in Xe matrices. Referring to the theoretical[11,12] Ca-RG PECs offers some insight into this behaviour. It was shown that the $^3\Pi$ potential energy curves, which correlate to the Ca(^3P) + RG asymptote, become more deeply bound with increasing rare gas mass (D_e = 158, 268 and 441 cm^{-1} for RG = Ar, Kr and Xe). If a similar trends holds for the excited states of the Sr-RG diatomics, then a larger attractive interaction would be expected for the excited Sr($^3P_1$) atom with Xe. In the solid state environment, this results in a greater displacement of the excited state

surface minimum with respect to that of the ground state, leading to broad and red-shifted emission.

Figure V.112 presents a comparison of the (5s5p) $^1P_1$ and (5s4d) $^1D_2$ excitation spectra recorded for each Sr/RG system. The (5s5p) $^1P_1$ scans (left panel) were obtained by monitoring the resonance (5s5p) $^1P_1 \rightarrow$ (5s^2) $^1S_0$ emission bands[q].
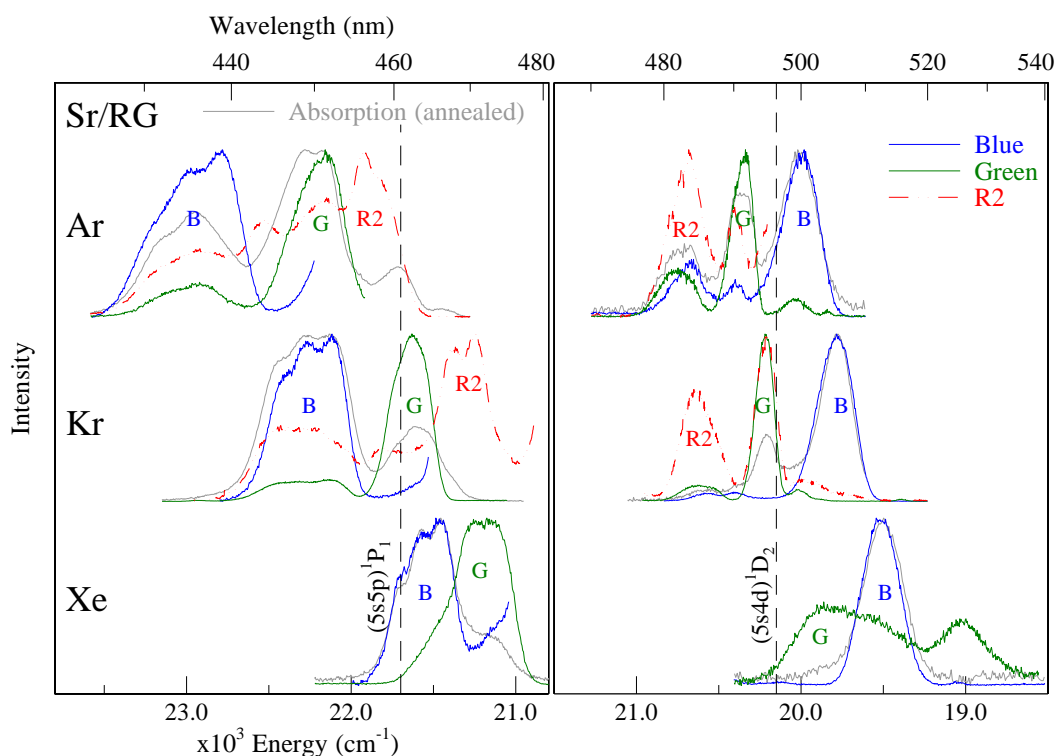
Figure V.112   **Left Panel: Site specific excitation spectra recorded by monitoring the resonance (5s5p) $^1P_1$ emission bands. A scan for the R2 site in Ar was obtained by monitoring the (5s5p) $^3P_1$ emission. Right Panel: Site specific excitation spectra recorded by monitoring the (5s5p) $^3P_1$ emission bands. The gas phase[4] positions of the (5s4d) $^1D_2$ and (5s5p) $^1P_1$ states of atomic Sr are shown by dashed vertical lines. In both panels, the annealed absorption spectra are represented by the solid grey traces.**

Out of necessity, the (5s4d) $^1D_2$ excitation scans (right panel) were recorded monitoring the intensity of the (5s5p) $^3P_1$ emission features – the photophysical properties of these absorption/excitation bands are collected in Table V.27. A comparison of both spectral regions reveals that the (5s4d) $^1D_2$ absorptions are narrower than the (5s5p) $^1P_1$ bands. In addition, a progressive red-shift is observed for the features of both excited states in going from Ar – Xe, however, a smaller overall shift exists on the $^1D_2$ bands. This effect is rationalised by considering the 5s4d electronic configuration of the $^1D_2$ excited state.

---

[q] Except for the R2 site which only exhibits $^3P_1$ emission.

The 4d orbitals occupied are spatially enclosed within the larger 5s orbital and are therefore shielded, to an extent, from the surrounding RG environment.

Table V.27   (5s5p) $^1D_1$ excitation features obtained by monitoring the (5s5p) $^3P_1 \rightarrow$ (5s^2) $^1S_0$ emission bands in each RG host. δ represents the gas phase to RG matrix shift (given in units of wavenumber) calculated from the gas phase value[4] for this transition at 689.4 nm or 14898.545 cm^{-1}.

Host	Site	λ_{ex} (nm)	ν (cm^{-1})	δ (cm^{-1})
Ar	Blue	500.1	19996	-154
	Green	480.6	20807	658
		491.3	20354	204
	R2	483.5	20683	533
		490.4	20392	242
Kr	Blue	505.4	19786	-363
	Green	483.3	20691	541
		491.3	20354	204
	Red	486.6	20551	401
Xe	Blue	526.6	18990	-1160
	Green	504.6	19818	-332

In Chapter III, it was shown that annealing of freshly deposited Sr/RG matrix samples had a pronounced effect on the absorption spectra in that the red features present on the (5s5p) $^1P_1 \leftarrow$ (5s^2) $^1S_0$ resonance transitions are removed. In contrast, the blue features are removed on the (5s4d) $^1D_2 \leftarrow$ (5s^2) $^1S_0$ transition. The same behaviour was observed in the MCD study[3] of Miller *et al.* which showed that the $^1P_1$ A-terms were a 'mirror image' of the $^1D_2$ A-terms. Following a careful analysis of the Sr/RG (5s5p) $^1P_1$ and (5s4d) $^1D_2$ luminescence, an explanation for this effect can now be provided. The excitation scans presented in Figure V.112 allow the absorption profiles to be deconvoluted into site-specific features. As can be seen, the 'mirroring' effect is actually a consequence of the site occupancy. For example, the highest energy (5s5p) $^1P_1$ features and the lowest energy (5s4d) $^1D_2$ bands correspond to the same, compact site of isolation, i.e. the blue site. Similarly, the (5s5p) $^1P_1$ absorption of the larger R2 vacancy is shifted to lower energies, whereas the (5s4d) $^1D_2$ absorption of this site is shifted to higher energies. Thus, the annealing effect observed in Chapter III is simply related to the removal of large, thermally unstable vacancies. It is very interesting that when trapped in the smaller vacancies, such as the blue site, the excited Sr($^1P_1$)

experiences a net repulsive interaction[r] with the RG host. Conversely, a net attractive interaction occurs with $^1D_2$ atom. However, in the larger vacancies, the opposite is true. Thus, for the R2 site, the Sr($^1P_1$)-RG interaction is attractive and the Sr($^1D_2$)-RG interaction is repulsive. Molecular dynamics simulations would be required to fully unravel this intriguing site and state dependence.

V.6   Summary

This chapter has presented a detailed analysis of the luminescence produced with both (5s5p) $^1P_1$ and (5s4d) $^1D_2$ excitation of Sr isolated in the RG solids – Ar, Kr and Xe. Resonance (5s5p) $^1P_1$ emission bands, characterised by short nanosecond lifetimes, are observed in each host. The 2D-EE spectra recorded of these features revealed a myriad of distinct and thermally stable sites of isolation for Sr. Two thermally stable sites are identified in Xe, while three (plus one partially stable) are found in Kr. The lightest host, Ar, is the most complex and exhibits a total of five thermally stable vacancies. Similar to Ba, the excitation spectra recorded for these sites display a variety of patterns, ranging from the classic Jahn-Teller threefold split to asymmetric threefold (2+1) patterns and broad, unstructured bands. From this we can infer that the trapping of Sr atoms occurs in both cubo-octahedral, crystalline sites and in sites of lower symmetry, such as those found at grain boundaries. This is a profound consequence of the large ground state bond lengths which characterise the Sr-RG diatomics (see Chapter VI).

In contrast to Ba, the lower lying excited states of Sr are accessible with the detection system used in the current experimental set-up and were investigated in this study. The production of emission from these levels was found to depend on 1. the RG host, 2. the site of isolation and 3. the excited state initially accessed in absorption ($^1P_1$ versus $^1D_2$). The host dependence was clearly observable for the resonance (5s5p) $^1P_1$ bands. For instance, the radiative lifetime of the blue site was not identified in Xe, even at the minimum attainable temperature of 10 K. Conversely, the same site in Ar showed little or no temperature dependence. A $^1P_1 \rightarrow {}^3D_J$ intersystem crossing was the mechanism proposed to explain this behaviour and the enhancement of this transition in solid Xe probably arises from the external heavy atom effect[10,24]. Accurate Sr-RG

---

[r] This repulsive interaction is counteracted by the RG polarizability, which increases from Ar to Xe.

excited state potentials would be required to interpret the relaxation dynamics which occur following promotion of Sr to either the (5s5p) $^1P_1$ or (5s4d) $^1D_2$ excited states.

The luminescence features observed in this study were assigned based on their spectral (such as location, bandwidth etc.) and temporal characteristics. Emission bands associated with the (5s4d) $^1D_2$, (5s4d) $^3D_1$ and (5s5p) $^3P_1$ excited states have been observed. In general the (5s4d) $^1D_2 \rightarrow$ (5s^2) $^1S_0$ features are spectrally narrow and slightly blue-shifted from the gas phase. This is typical of classical D $\rightarrow$ S type transitions. Contrasting this, the (5s4d) $^3D_1$ and (5s5p) $^3P_1$ phosphorescence bands are broad and exhibit quite large matrix shifts. Overall, the temporal scans recorded for the triplet excited states are long-lived (> 1 µs) and complex; double or triple exponential functions were required to accurately fit the decay profiles. This may well be a reflection of the excited state relaxation processes leading to the observed emission.

References

1   J. C. Miller, and L. Andrews, J. Chem. Phys. **69**, 936 (1978).
2   J. C. Miller, B. S. Ault, and L. Andrews, J. Chem. Phys. **67**, 2478 (1977).
3   J. C. Miller, R. L. Mowery, E. R. Krausz, S. M. Jacobs, H. W. Kim, P. N. Schatz, and L. Andrews, J. Chem. Phys. **74**, 6349 (1981).
4   A. Kramida, Y. Ralchenko, J. Reader, and NIST ASD Team. NIST Atomic Spectra Database (ver. 5.2). Available at: http://physics.nist.gov/asd [2015, October]. National Institute of Standards and Technology, Gaithersburg, MD.
5   T. i. Shibuya, J. Chem. Phys. **78**, 5175 (1983).
6   R. L. Fulton, J. Chem. Phys. **61**, 4141 (1974).
7   H. G. C. Werij, C. H. Greene, C. E. Theodosiou, and A. Gallagher, Phys. Rev. A **46**, 1248 (1992).
8   H. G. C. Werij, M. Harris, J. Cooper, A. Gallagher, and J. F. Kelly, Phys. Rev. A **43**, 2237 (1991).
9   S. L. Laursen, and H. E. Cartland, J. Chem. Phys. **95**, 4751 (1991).
10   C. Crepin-Gilbert, and A. Tramer, Int. Rev. Phys. Chem. **18**, 485 (1999).
11   E. Czuchaj, M. Krośnicki, and H. Stoll, Chem. Phys. **292**, 101 (2003).
12   F. Spiegelman, L. Maron, W. H. Breckenridge, J.-M. Mestdagh, and J.-P. Visticot, J. Chem. Phys. **117**, 7534 (2002).
13   J. C. W. Bauschlicher, S. R. Langhoff, and H. Partridge, Journal of Physics B: Atomic and Molecular Physics **18**, 1523 (1985).
14   N. Vaeck, M. Godefroid, and J. r. E. Hansen, Phys. Rev. A **38**, 2830 (1988).
15   M. A. Collier, M. C. Ryan, and J. G. McCaffrey, J. Chem. Phys. **123**, 044508 (2005).
16   J. A. Boatz, and M. E. Fajardo, J. Chem. Phys. **101**, 3472 (1994).
17   J. Douady, S. Awali, L. Poisson, B. Soep, J. M. Mestdagh, and B. Gervais, The Journal of Physical Chemistry A **119**, 6074 (2015).

[18]   C. Redondo, M. N. Sánchez Rayo, P. Ecija, D. Husain, and F. Castaño, Chem. Phys. Lett. **392**, 116 (2004).

[19]   C. Redondo, M. N. Sanchez Rayo, J. A. Fernandez, D. Husain, and F. Castano, PCCP **6**, 391 (2004).

[20]   L. Hunter, W. Walker, and D. Weiss, Phys. Rev. Lett. **56**, 823 (1986).

[21]   D. Miller, L. You, J. Cooper, and A. Gallagher, Phys. Rev. A **46**, 1303 (1992).

[22]   J. C. W. Bauschlicher, S. R. Langhoff, R. L. Jaffe, and H. Partridge, Journal of Physics B: Atomic and Molecular Physics **17**, L427 (1984).

[23]   W. Breckenridge, and C. N. Merrow, J. Chem. Phys. **88**, 2320 (1988).

[24]   W. Breckenridge, Int. Rev. Phys. Chem. **13**, 291 (1994).

[25]   T. Zelevinsky, M. Boyd, A. Ludlow, S. Foreman, S. Blatt, T. Ido, and J. Ye, in *TCP 2006* (Springer, 2007), pp. 411.

[26]   M. Yasuda, and H. Katori, Phys. Rev. Lett. **92**, 153004 (2004).

Appendix V.I
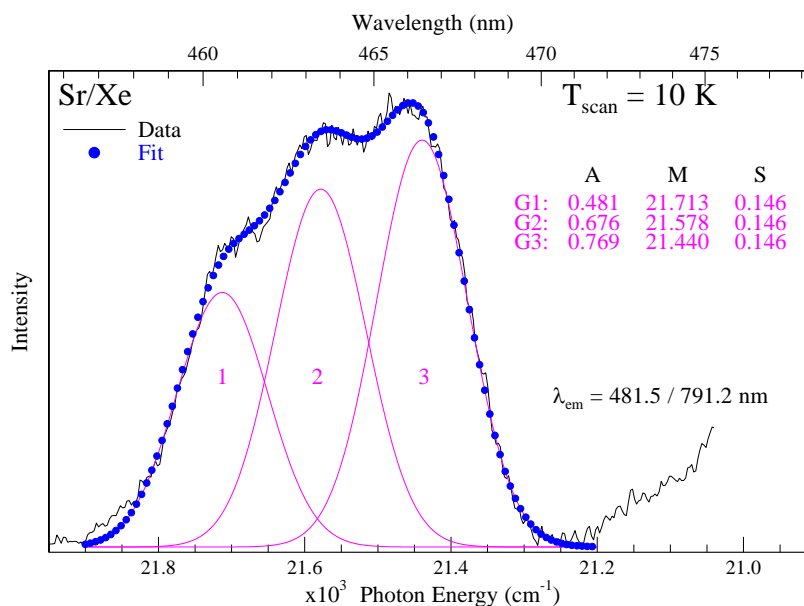
Figure V.113   **A lineshape analysis of the blue site excitation spectrum of Sr/Xe. Three Gaussian curves (see Equation II.2) were required to provide an adequate fit of the scan. The symbols *A*, *M* and *S* denote the intensity, location and bandwidth of each component, where *M* and *S* are in units of 1 x 10^3 cm^{-1}. During the fit, the widths of each composite Gaussian curve were equal and held constant, while the intensities and positions were allowed to vary. The best overall fit, which minimised the root mean variance, was obtained using peak widths of 146 cm^{-1}. The error (standard deviation) associated with each peak position is: $\sigma_{M1} = \pm 2.9$ cm^{-1}, $\sigma_{M2} = \pm 3.0$ cm^{-1} and $\sigma_{M3} = \pm 1.7$ cm^{-1}.**
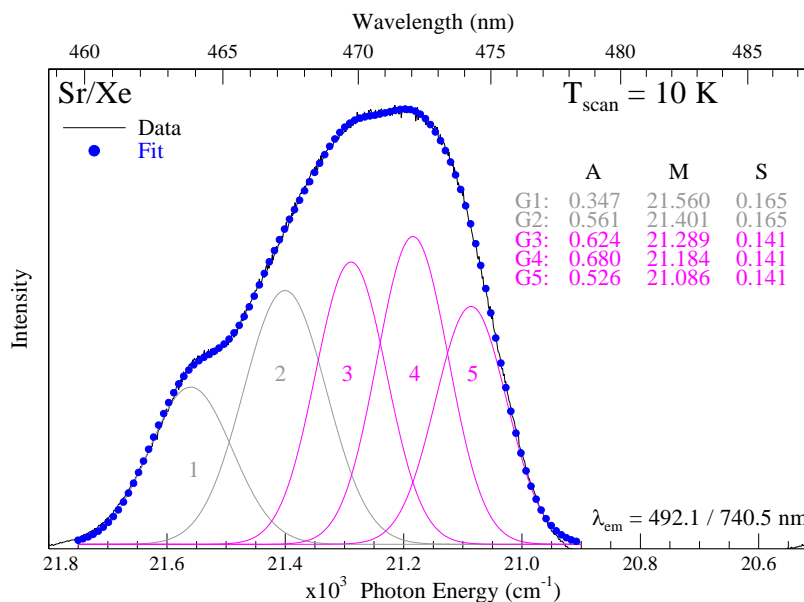
Figure V.114   **A lineshape analysis of the green site excitation spectrum of Sr/Xe. Five Gaussian curves were required to provide an adequate fit of the scan. During the fit, the widths of each composite Gaussian curve were held constant, while the intensities and positions were allowed to vary. $\sigma_{M1} = \pm 1.8$ cm^{-1}, $\sigma_{M2} = \pm 3.2$ cm^{-1}, $\sigma_{M3} = \pm 4.0$ cm^{-1}, $\sigma_{M4} = \pm 3.7$ cm^{-1} and $\sigma_{M5} = \pm 1.9$ cm^{-1}.**
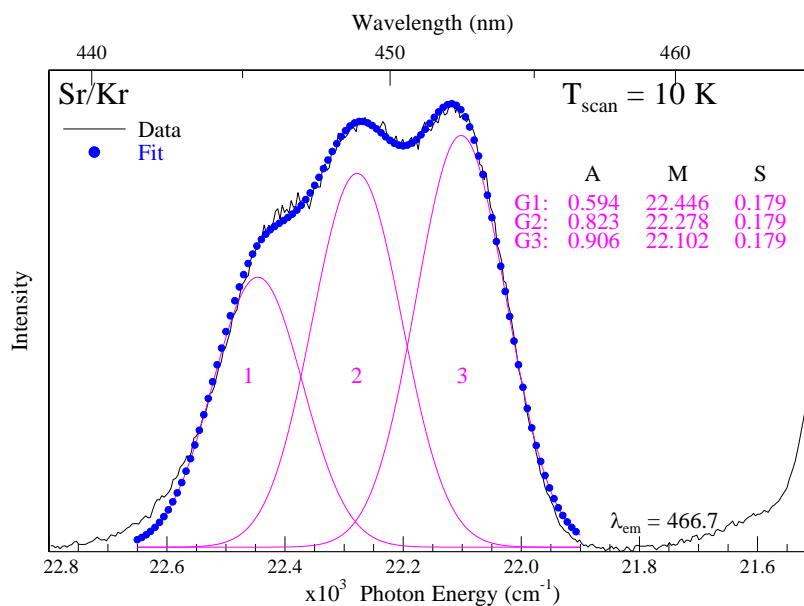
Figure V.115 **A lineshape analysis of the Sr/Kr blue site excitation spectrum. Three Gaussian curves were provide a good of the scan. During the fit, the widths of each composite Gaussian curve were held constant, while the intensities and positions were allowed to vary. $\sigma_{M1} = \pm 5.8$ cm^{-1}, $\sigma_{M2} = \pm 3.9$ cm^{-1} and $\sigma_{M3} = \pm 5.6$ cm^{-1}.**
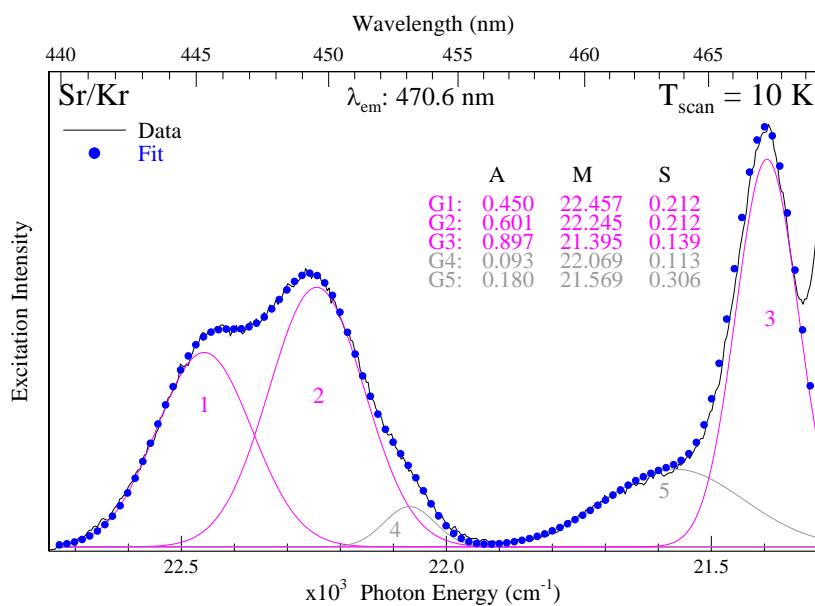
Figure V.116 **A lineshape analysis of the Sr/Kr violet site excitation spectrum. Five Gaussian curves were required to provide a good fit of the scan. During the fit, the widths of the three pink Gaussian curves (1 – 3) were held constant, while the intensities and positions were allowed to vary. All of the parameters of the remaining two Gaussians (4 and 5 – shown in grey) were allowed to vary. $\sigma_{M1} = \pm 3.4$ cm^{-1}, $\sigma_{M2} = \pm 3.2$ cm^{-1}, $\sigma_{M3} = \pm 2.1$ cm^{-1}, $\sigma_{M4} = \pm 9.8$ cm^{-1} and $\sigma_{M5} = \pm 8.7$ cm^{-1}.**
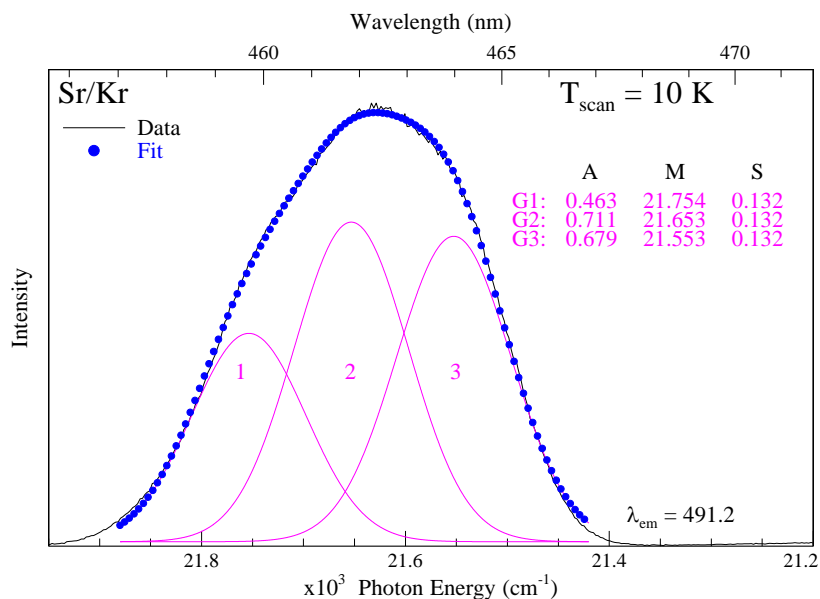
Figure V.117 A lineshape analysis of the Sr/Kr green site excitation spectrum. Three Gaussian curves were required to provide an adequate fit of the scan. During the fit, the widths of each composite Gaussian curve were held constant, while the intensities and positions were allowed to vary. $\sigma_{M1} = \pm 5.7$ cm^{-1}, $\sigma_{M2} = \pm 7.2$ cm^{-1} and $\sigma_{M3} = \pm 3.9$ cm^{-1}.
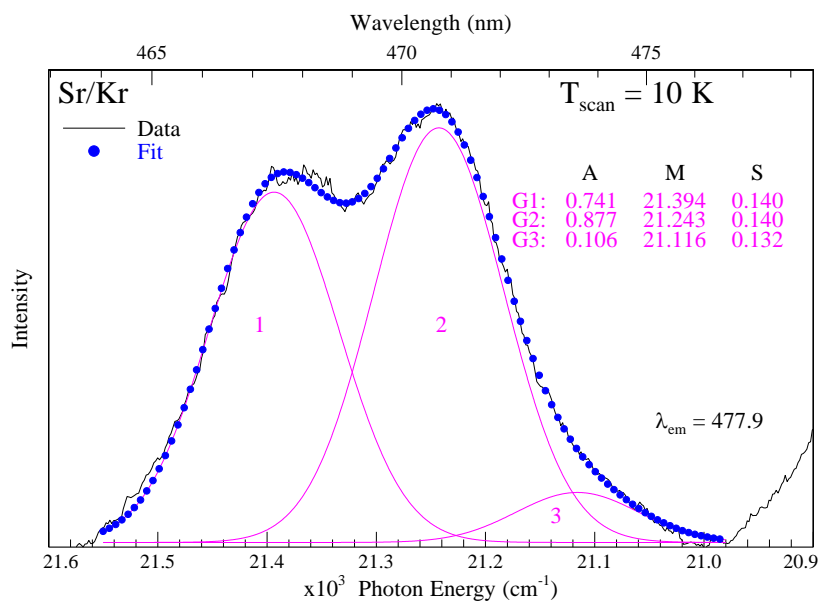
Figure V.118 A lineshape analysis of the Sr/Kr red site excitation spectrum. Three Gaussian curves were required to provide an adequate fit of the scan. During the fit, the widths of each composite Gaussian curve were held constant, while the intensities and positions were allowed to vary. $\sigma_{M1} = \pm 1.1$ cm^{-1}, $\sigma_{M2} = \pm 1.5$ cm^{-1} and $\sigma_{M3} = \pm 8.9$ cm^{-1}.
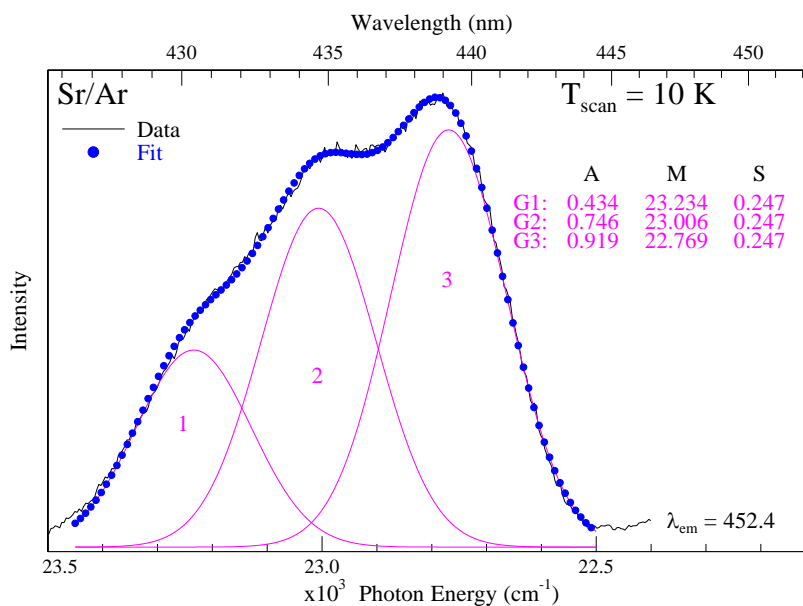
Figure V.119   A lineshape analysis of the Sr/Ar blue site excitation spectrum. Three Gaussian curves were required to provide an adequate fit of the scan. During the fit, the widths of each composite Gaussian curve were held constant, while the intensities and positions were allowed to vary. $\sigma_{M1} = \pm 1.1$ cm^{-1}, $\sigma_{M2} = \pm 2.5$ cm^{-1} and $\sigma_{M3} = \pm 1.4$ cm^{-1}.
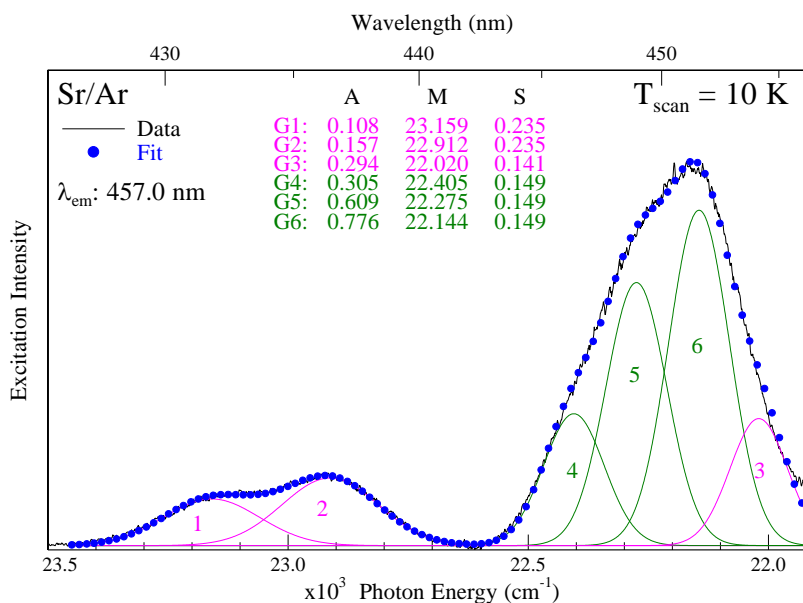
Figure V.120   A lineshape analysis of the Sr/Ar green and violet sites excitation spectrum. A total of six Gaussian curves were required to provide an adequate fit of the scan. During the fit, the widths of each composite Gaussian curve were held constant, while the intensities and positions were allowed to vary. The components labelled 1, 2 and 3 (shown in pink) represent the violet site of isolation and the curves labelled 4, 5 and 6 (shown in green) account for the green site of isolation. $\sigma_{M1} = \pm 4.4$ cm^{-1}, $\sigma_{M2} = \pm 3.0$ cm^{-1}, $\sigma_{M3} = \pm 5.1$ cm^{-1}, $\sigma_{M4} = \pm 1.8$ cm^{-1}, $\sigma_{M5} = \pm 1.6$ cm^{-1} and $\sigma_{M6} = \pm 1.0$ cm^{-1}.
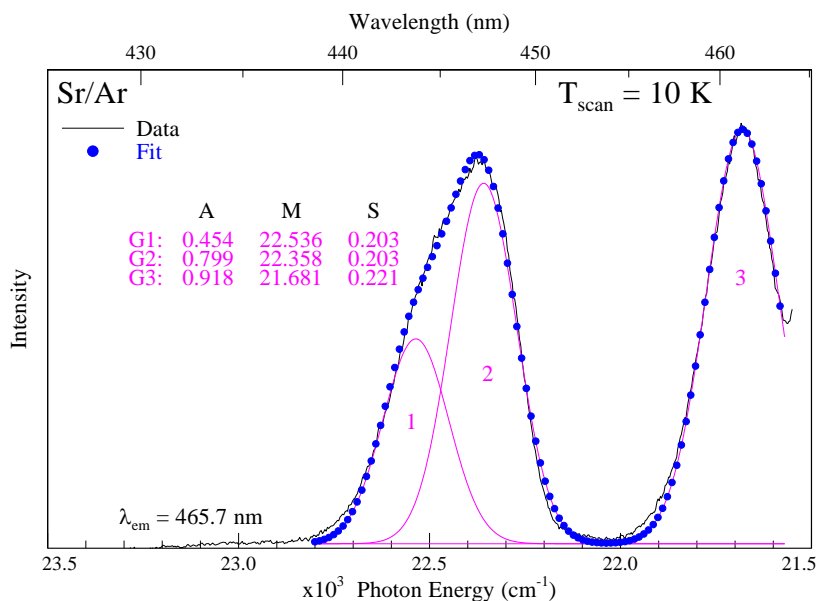
**Figure V.121** **A lineshape analysis of the Sr/Ar red site excitation spectrum. Three Gaussian curves were required to provide an adequate fit of the observed structure. During the fit, the widths of each composite Gaussian curve were held constant, while the intensities and positions were allowed to vary. $\sigma_{M1} = \pm 1.3$ cm^{-1}, $\sigma_{M2} = \pm 0.7$ cm^{-1} and $\sigma_{M3} = \pm 0.4$ cm^{-1}.**
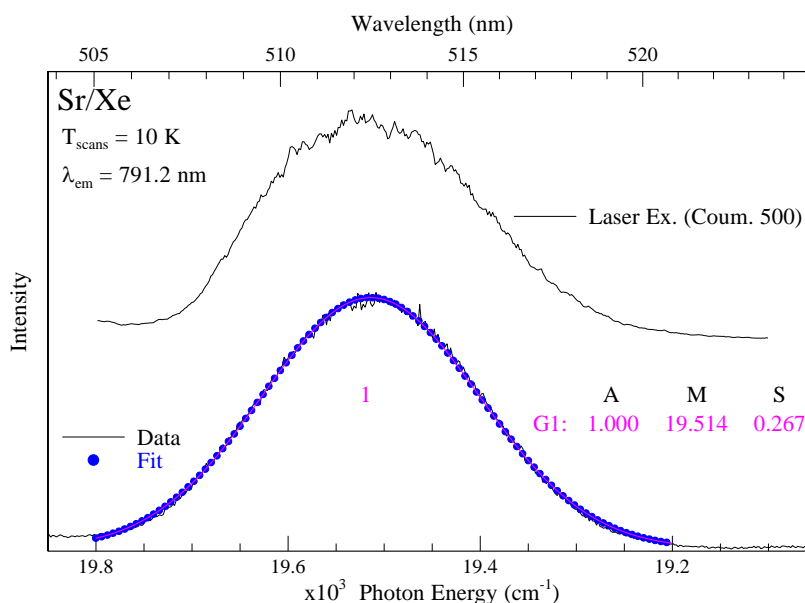
Figure V.122 **Bottom traces: A lineshape analysis of the Sr/Xe $^1D_2$ blue site excitation spectrum. A single Gaussian curve provides an adequate fit of the observed band. During the fit, all of the Gaussian parameters were allowed to vary. $\sigma_{M1} = \pm 0.5$ cm^{-1}. Top trace: Laser excitation scan obtained by monitoring the intensity of the 791.2 nm emission. Coumarin 500 was the dye material used for this scan. The laser spectrum was not corrected for the intensity distribution of the dye.**
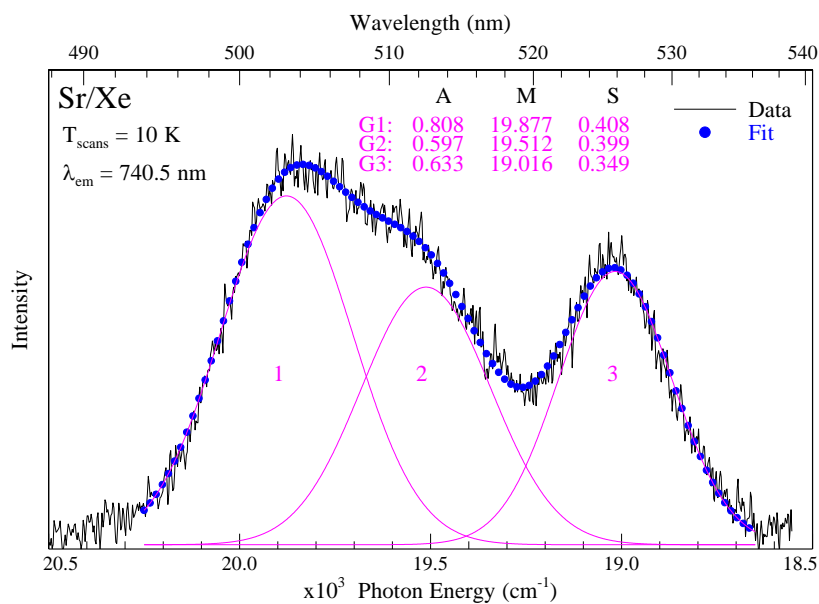
Figure V.123   A lineshape analysis of the Sr/Xe $^1D_2$ green site excitation spectrum. Three single Gaussian curve provides an adequate fit of the observed bandshape. During the fit, all of the Gaussian parameters were allowed to vary. $\sigma_{M1} = \pm\ 7.1\ cm^{-1}$, $\sigma_{M2} = \pm\ 8.5\ cm^{-1}$ and $\sigma_{M3} = \pm\ 2.1\ cm^{-1}$.
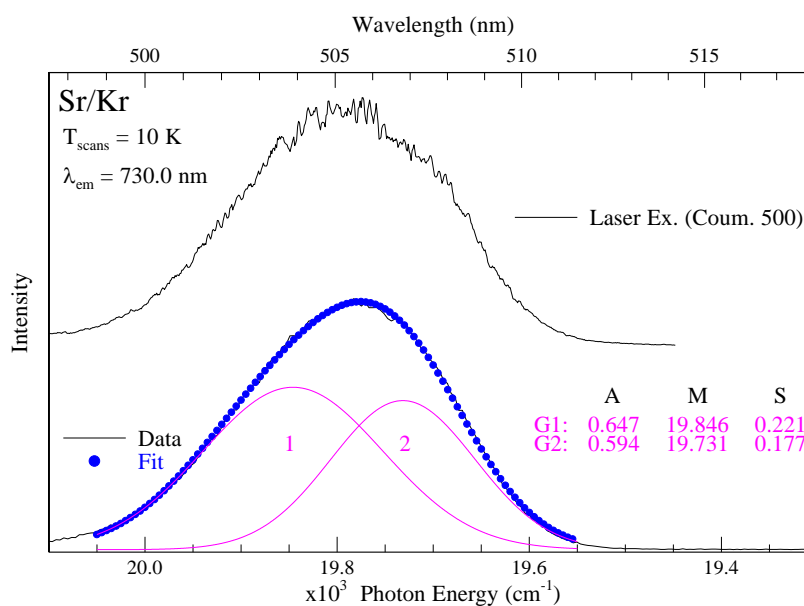

Figure V.124   Bottom traces: A lineshape analysis of the Sr/Kr $^1D_2$ blue site excitation spectrum. Two Gaussian curves provide a good fit of the observed bandshape. During the fit, all of the Gaussian parameters were allowed to vary. $\sigma_{M1} = \pm\ 12.7\ cm^{-1}$ and $\sigma_{M2} = \pm\ 5.7\ cm^{-1}$. Top trace: Laser excitation scan obtained by monitoring the intensity of the 730.0 nm emission. Coumarin 500 was the dye material used for this scan. The laser spectrum was not corrected for the intensity distribution of the dye.
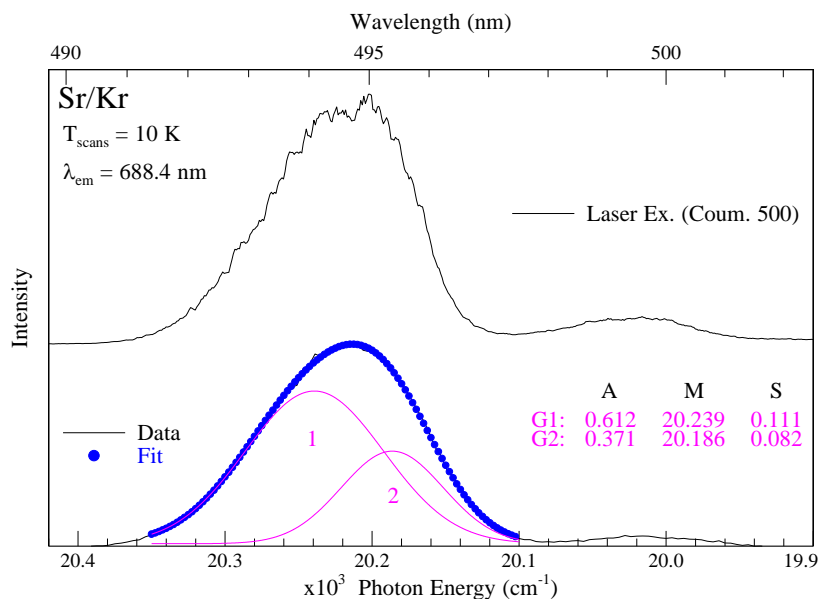
Figure V.125 Bottom traces: A lineshape analysis of the Sr/Kr $^1D_2$ green site excitation spectrum. Two Gaussian curves provide a good fit of the observed bandshape. During the fit, all of the Gaussian parameters were allowed to vary. $\sigma_{M1} = \pm$ 19.7 cm^{-1} and $\sigma_{M2} = \pm$ 15.4 cm^{-1}. Top trace: Laser excitation scan obtained by monitoring the intensity of the 688.4 nm emission.
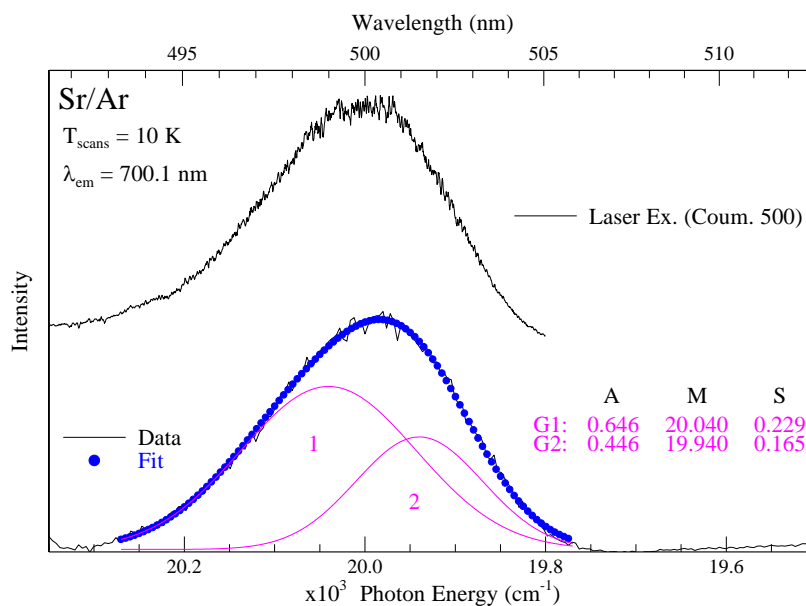
Figure V.126 Bottom traces: A lineshape analysis of the Sr/Ar $^1D_2$ blue site excitation spectrum. Two Gaussian curves provide a good fit of the observed bandshape. During the fit, all of the Gaussian parameters were allowed to vary. $\sigma_{M1} = \pm$ 16.9 cm^{-1} and $\sigma_{M2} = \pm$ 15.5 cm^{-1}. Top trace: Laser excitation scan obtained by monitoring the intensity of the 700.1 nm emission.

Chapter VI

M·RG ground state potential energy curves:

Analysing the site occupancy of the alkaline earths in solid RG matrices

VI.1 Introduction

The preceding chapters described the spectroscopy of matrix-isolated alkaline earth atoms, Ba and Sr. A characteristic common to both metal atoms was the observation of numerous, thermally stable sites of isolation in the three rare gas hosts (RG=Ar, Kr and Xe). As it is the local environment of the guest atom which governs the photophysical properties, knowledge of the matrix trapping sites is highly desirable. A long term goal is to interpret the data collected in this thesis using molecular dynamic simulations of the M/RG systems. Such theoretical studies could be used to gain information, for example, on the matrix vacancies formed upon deposition or on the excited state dynamics which lead to the observed luminescence. However, the necessary requirements for such a study are accurate ground and excited state potential energy curves (PECs), to describe the 1:1 M·RG interactions. A model of the metal doped matrices can then be built using these pair-potentials. Unfortunately, studies reporting reliable PECs for these systems are quite sparse and the existing data is fragmented, with many different levels of theory used. Thus, the goals of this chapter are:

1. Obtain high quality ground state interaction potentials for the 1:1 M·RG complexes (M=Ca, Sr, Ba and RG = Ar, Kr, Xe), which are treated within a consistent theoretical framework.

2. Use these potentials, in combination with the matrix spectra presented in the previous chapters, as a first step in interpreting the ground state site occupancy of Sr and Ba atoms trapped in the RG solids.

Two contrasting theoretical methods will be investigated. Firstly, the Tang-Toennies (TT) analytical function will be used to model the ground state potentials for the M·RG diatomics. This approach was pursued because of the low computational costs involved. In addition, the derivatives of this function can be easily calculated – a

property that would be very useful if larger M/RG systems were to be simulated. Secondly, the ground state M·RG interactions will be computed at the coupled-cluster (CC) level of theory involving single, double and non-iterative triple (CCSD(T)) excitations. For a long time the CCSD(T) method has been considered the 'gold standard' of computational chemistry and, when coupled with extensive correlation consistent basis sets, it is particularly adept at describing non-covalent interactions. Thus, a comparison of the *ab initio* curves with the potentials generated using the analytic TT function will allow the usefulness of the latter to be assessed.

VI.2   Methods

VI.2.I   Tang-Toennies (TT)

In 1983, Tang and Toennies obtained[1] a simple universal expression for the well region of an atom-atom van der Waals potential, by adding the Born-Mayer repulsive term (a) to a damped dispersion potential (b). The ground state potential energy curves of Ca·RG, Sr·RG and Ba·RG (RG = Ar, Kr and Xe) dimers were determined, in the present study, using the Tang-Toennies (TT) function[1] (Equations. VI.1 and VI.2). The potential energy $V(R)$ depends on the variable, R (internuclear separation), and on five key parameters – the Born-Mayer[2,3] coefficients, A and b, and the three leading dispersion coefficients, C_6, C_8 and C_{10}.

$$V(R) = \overbrace{Ae^{-bR}}^{a} - \overbrace{\sum_{n=3}^{n_{max}} f_{2n}(bR)\frac{C_{2n}}{R^{2n}}}^{b} \qquad \text{Eq. (VI.1)}$$

where

$$f_{2n}(bR) = 1 - e^{-bR}\sum_{k=0}^{2n}\frac{(bR)^k}{k!} \qquad \text{Eq. (VI.2)}$$

In 2009, Yang *et al.*[4] showed that if these five coefficients were known for the homonuclear diatomics, Ca_2 and RG_2, applying the correct combining rules[5] allowed determination of the corresponding parameters for the heteronuclear Ca·RG dimers. Following this approach, model potentials were generated for the five Ca·RG diatomics, RG= He, Ne, Ar, Kr and Xe. Shortly afterwards, the 1:1 Sr·RG[6] complexes

were computed by Yin *et al.* in a similar fashion. Correct modelling of the heteronuclear diatomics therefore crucially depends on obtaining accurate parameters for the homonuclear dimers.

The three most important dispersion coefficients (C_6, C_8 and C_{10}) for the group II metal dimers (Be - Ba)[7] and for the rare gas dimers[8,9] can be obtained from accurate *ab initio* calculations. Thus, two unknown parameters remain, namely, *A* and *b*. However, if the experimental spectroscopic constants (R_e and D_e) are available, *A* and *b* can be extracted by fitting these constants with the reduced form of the model potential (including the *ab initio* dispersion coefficients). In 2002, Tang and Toennies[10] demonstrated this for the 21 possible combinations of homonuclear and heteronuclear rare gas pairs and the necessary parameters were obtained for each combination. The five parameters for Ca_2 and Sr_2 were acquired in the same way, by fitting the reduced form of the model potential to the experimentally determined bond lengths and dissociation energies[11,12]. Armed with these data, the five parameters of the M·RG (M = Ca, Sr) dimers can be computed.

In contrast to Ca and Sr dimer, much less experimental data exists for Ba dimer. The only spectroscopic information available is the fundamental vibrational frequency (ω_e) which was measured[13] to be 33.2 cm^{-1}. Despite this restriction, Li *et al.* showed[14] that the ground state of Ba_2 could be accurately described by the Tang-Toennies model. In this work, the authors used the corresponding states principle and the available spectroscopic data[13], to derive an equilibrium bond length and dissociation energy for Ba_2. The underlying assumption was that the reduced potential of Ba_2 is the same as, or at least very similar to, that of Sr_2. This technique yielded a binding energy of 1198 cm^{-1} and an equilibrium distance of 5.169 Å, which compare favourably to high level MRCI calculations of the Ba_2[15] (D_e = 1122 cm^{-1}, R_e = 5.22 Å). Combining these empirical R_e and D_e values with the *ab initio* dispersion coefficients once again allowed *A* and *b* to be extracted from the reduced form of the Tang-Toennies equation. Thus the five key parameters for Ba_2 are available and with the appropriate combining steps, model potentials can also be derived for the heteronuclear Ba·RG pairs.

In the present study, Tang-Toennies potential energy curves for nine Ca·RG, Sr·RG and Ba·RG diatomics have been generated. The combining method used is described in detail for the Sr·RG diatomics[6] – a synopsis of this method will now be presented. Firstly, the heteronuclear *A* and *b* values were obtained using the Equations. VI.3 and VI.4:

$$A_{ij} = \left[A_i A_j \right]^{\frac{1}{2}} \qquad\qquad \text{Eq. (VI.3)}$$

$$b_{ij} = 2 \frac{b_i b_j}{b_i + b_j} \qquad\qquad \text{Eq. (VI.4)}$$

The indices i and j specify the potential parameters for the RG_2 and M_2 diatomics respectively. The two Born-Mayer (A and b) values for the RG dimers (Ar_2, Kr_2, Xe_2) were obtained, as described above, and can be found in Ref. 10. For Ca_2, Sr_2 and Ba_2, these values were taken from Refs. 4, 6 and 14 respectively. Next the three effective energies Ω_1, Ω_2 and Ω_3 were computed for each homonuclear dimer with the following equations:

$$\Omega_1 = \frac{4}{3} \left(\frac{C_6}{\left(\alpha_1 \right)^2} \right) \qquad\qquad \text{Eq. (VI.5)}$$

$$\Omega_2 = \frac{2 C_8 \Omega_1}{15 \alpha_1 \alpha_2 \Omega_1 - 2 C_8} \qquad\qquad \text{Eq. (VI.6)}$$

$$\Omega_3 = \frac{C(1,3) \Omega_1}{7 \alpha_1 \alpha_3 \Omega_1 - C(1,3)} \qquad\qquad \text{Eq. (VI.7)}$$

where

$$C(1,3) = \frac{1}{2} \left[C_{10} - \frac{35}{4} \left(\alpha_1 \right)^2 \Omega_2 \right] \qquad\qquad \text{Eq. (VI.8)}$$

In these equations, α_1, α_2 and α_3 are the atomic polarizabilities and C_6, C_8 and C_{10} are the homonuclear dispersion coefficients. For the three RG dimers α_1^i and C_6^i were obtained from the work of Kumar and Meath[8] and α_2^i, α_3^i, C_8^i and C_{10}^i were computed by Thakkar *et al.*[9]. The atomic polarizabilities (α_1^j, α_2^j and α_3^j) for Ca, Sr and Ba, and the leading C_6^j, C_8^j and C_{10}^j dispersion coefficients for Ca_2, Sr_2 and Ba_2 were calculated by Porsev and Derevianko[7]. Using this information, the heteronuclear C_6^{ij}, C_8^{ij} and C_{10}^{ij}

coefficients were then calculated with the combining formulae, given by Equations VI.9 – VI.11:

$$C^6 = C^{ij}(1,1)$$

Eq. (VI.9)

$$C^8 = C^{ij}(1,2) + C^{ij}(2,1)$$

Eq. (VI.10)

$$C^{10} = C^{ij}(1,3) + C^{ij}(2,2) + C^{ij}(3,1)$$

Eq. (VI.11)

where

$$C^{ij}(1,1) = \frac{3}{2}\left[\frac{\alpha_1^i \alpha_1^j \Omega_1^i \Omega_1^j}{\Omega_1^i + \Omega_1^j}\right]$$

Eq. (VI.12)

$$C^{ij}(1,2) = \frac{15}{4}\left[\frac{\alpha_1^i \alpha_2^j \Omega_1^i \Omega_2^j}{\Omega_1^i + \Omega_2^j}\right]$$

Eq. (VI.13)

$$C^{ij}(1,3) = 7\left[\frac{\alpha_1^i \alpha_3^j \Omega_1^i \Omega_3^j}{\Omega_1^i + \Omega_3^j}\right]$$

Eq. (VI.14)

and

$$C^{ij}(2,2) = \frac{35}{2}\left[\frac{\alpha_1^i \alpha_2^j \Omega_2^i \Omega_2^j}{\Omega_2^i + \Omega_2^j}\right]$$

Eq. (VI.15)

Here $C^{ij}(1,1)$, $C^{ij}(1,2)$, $C^{ij}(2,2)$ and $C^{ij}(1,3)$ represent the dipole-dipole, dipole-quadrupole, quadrupole-quadrupole and dipole-octupole interactions, respectively. The calculated effective energies for the homonuclear diatomics $(\Omega_1, \Omega_2, \Omega_3)$ and all of the necessary parameters are collected in Table VI.6 of Appendix VI.I. The resultant C_6, C_8 and C_{10} coefficients and the A and b parameters of

Ca·RG, Sr·RG and Ba·RG diatomics are listed in Table VI.1. It must be highlighted that the values obtained in this study for the Ca·RG diatomics are markedly different from those presented in Ref. 4. In Yang *et al.*'s work, *ab initio*[16] values were used for the C_6, C_8 and C_{10} coefficients of the Ca·RG dimers instead of generating them with the combining rules. Ultimately we wish to compare the analytical Tang-Toennies potentials to those determined by high level CCSD(T) calculations. For consistency, all of the heteronuclear parameters were calculated with the combining rules. The M·RG model potentials presented hereafter were obtained with the five parameters of Table VI.1 and by summing the Tang-Toennies series (Equations. 1 and 2) to $n_{max} = 5$. For convenience, a summary of the method just described is provided by the flow chart in Figure VI.1.

Table VI.1   **The five parameters required to generate the Tang-Toennies model potentials for each M·RG heteronuclear diatomic. All values are expressed in atomic units (a.u.).**

System	C_6	C_8	C_{10}	A	b
Ca-Ar	254.793	17317.0	1199181	145.3427	1.3390
Kr	378.814	26911.3	1941069	153.2927	1.3008
Xe	595.666	45745.0	3540414	163.9186	1.2530
Sr-Ar	297.250	22652.1	1803544	182.9521	1.3129
Kr	442.619	35098.9	2886440	192.9592	1.2761
Xe	697.561	59346.7	5172122	206.3347	1.2301
Ba-Ar	370.883	30462.1	2840928	280.8395	1.3007
Kr	552.970	47285.2	4506636	296.2009	1.2647
Xe	873.102	80070.6	7960822	316.7329	1.2194
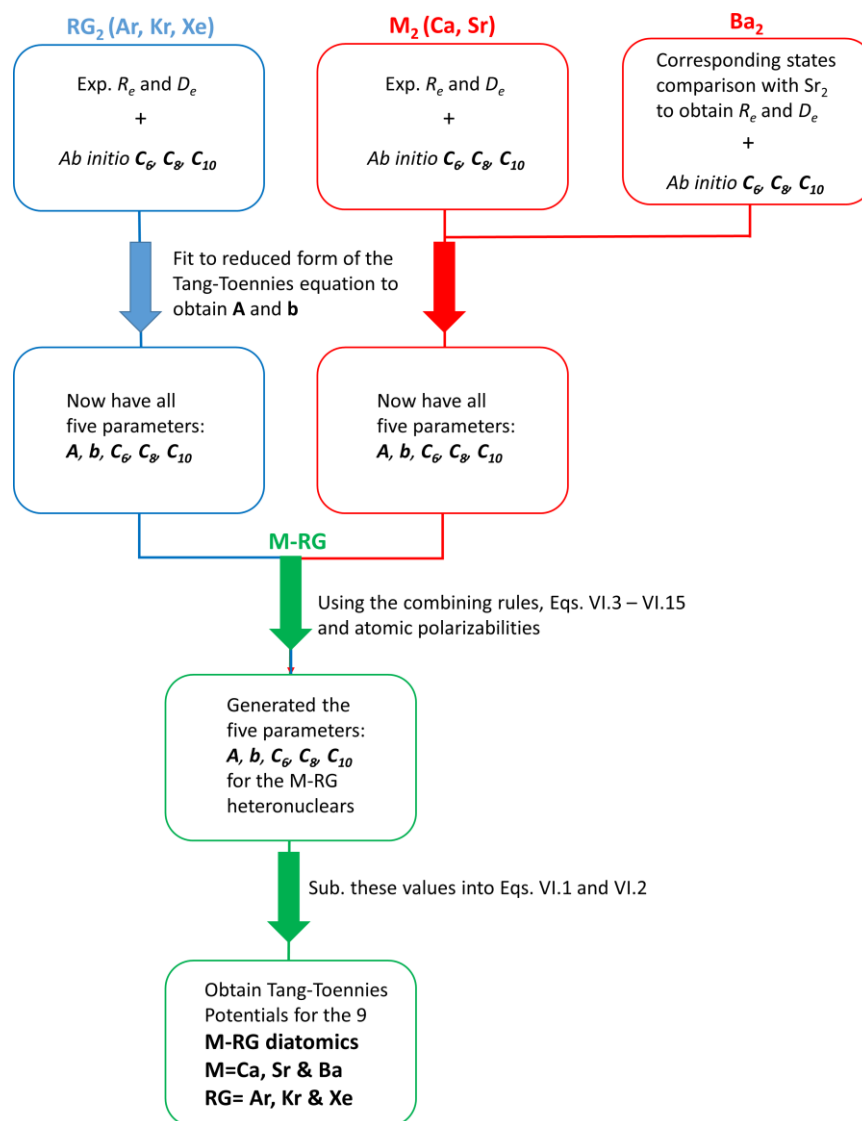
Figure VI.1   **A summary of the method used to generate the Tang-Toennies ground state pair-potentials for the nine M·RG diatomics; M = Ca, Sr, Ba and RG = Ar, Kr and Xe.**

VI.2.II   CCSD(T)

The coupled-cluster (CC) theory was introduced in 1960[17] to calculate nuclear binding energies in nuclei that could be treated, in the first approximation, by a single configuration of neutrons or protons. The concept of CC theory relies on the exponential formulation of the wave operator and its expansion into clusters of excitation operators. Accordingly, CC methods are size-extensive (the energy scales properly with the size of a system) and the convergence of the CC energy toward the full configuration interaction (FCI) value is faster compared to other methods with the same asymptotic scaling with respect to system size[18]. The CCSD(T) method stands out among all CC approximations for its excellent accuracy to computational cost ratio

– hence the "gold standard" label. It is characterised by an iterative inclusion of single and double excitations and a perturbative (4th-order and one term from the fifth order) inclusion of triple excitations.

The CCSD(T) method is very suitable for the calculation of ground state energies and for the properties of systems with single reference character. It also yields highly accurate binding energies and geometries for van der Waals complexes, provided large enough basis sets are used on each atom[18-21]. With this caveat, the CCSD(T) approach can be quite computationally demanding for molecules containing atoms with a high atomic number (large number of electrons). For instance, the inclusion of single and double excitations in the CC scheme, i.e., CCSD, leads to equations with numerous terms, from which the most computationally demanding scale as $\sim N_o^2 N_v^4$ and $\sim N_o^3 N_v^3$ (N_o stands for the number of correlated occupied orbitals and N_v the number of active virtual orbitals). The overall scaling of a CCSD iteration is usually dominated by one of these terms, depending on the N_o/N_v ratio. In addition, the scaling of the perturbative triples calculation is by an order of magnitude steeper, i.e., $N_o^3 N_v^4$ – this often represents the bottleneck of CCSD(T) calculations on larger systems. Thus, a CCSD(T) calculation is far more expensive than the Tang-Toennies approach, which can be carried out with relative ease using Microsoft Excel and standard plotting programs (e.g. Genplot).

In this study, ground state potential energy curves were calculated for the Ba·RG, Sr·RG and Ca·RG (RG = Ar, Kr and Xe) diatomics at the CCSD(T) level of theory with a restricted Hartree-Fock reference wavefunction. These computations were implemented using the NWChem-6.5 (revision 26243-4) quantum chemistry package[22] running on a PC workstation (AMD64 quad-core 2.8 GHz processor) with the Linux Mint-17.1 (Cinnamon) operating system. The standard correlation consistent aug-cc-pVQZ basis set[23-25] was employed for Ar and Kr atoms. The heaviest rare gas, Xe, was represented by the aug-cc-pVQZ-PP basis set with a small core, fully relativistic ECP28MDF effective core potential (ECP)[26,27]. For atomic Ca, Sr and Ba the aug-cc-pVQZ-PP basis set[28,29] was used in conjunction with the respective relativistic ECP10MDF, ECP28MDF and ECP46MDF effective core potentials[30]. All the electrons of Ar and Kr were correlated, as were all of the non-ECP electrons of Xe, Ca, Sr and Ba. The Boys and Bernardi[31,32] counterpoise correction was computed at each point to account for basis set superposition error (BSSE). The potential energy curves were generated by cubic spline interpolation of the single point energy values.

Binding energies were determined by taking the energy difference between the minima with the values existing at 50 Å, taken to be the asymptotic limit. The single point energy values were computed in steps of 0.1 Å in the range from 3.5 – 6 Å. This was done in order to accurately describe the repulsive wall and minimum of the potential energy curves. As the long range portion of the curve changes more gradually, steps of 0.2 Å and 0.5 Å were adopted and sufficiently accurate in the ranges from 6 – 8 Å and 8 – 9 Å respectively.

VI.3   Results

VI.3.I   Tang-Toennies (TT)

The M·RG ground state interaction potentials, modelled using the Tang-Toennies approach, are presented in Figure VI.2 and the extracted spectroscopic constants are collated in Table VI.2. Inspection of these values demonstrates that the M·RG diatomics are all weakly bound with dissociation energies in the range of 59.6 – 141.2 cm^{-1} and long equilibrium bond lengths, each in excess of 5 Å. These values are typical of van der Waals type interactions. The alkaline earth atoms and the rare gas atoms exhibit spherically symmetric grounds states due to both having closed shell electronic configurations and, consequently, their interaction is dominated by dispersion. As expected, the potentials become more deeply bound as the mass of the RG increases; this is in line with the increasing polarizability of the RG atom. The spectroscopic constants obtained for the Sr·RG complexes are identical to those produced by Yin *et al*[6], thereby confirming that this study has accurately replicated their model potentials.
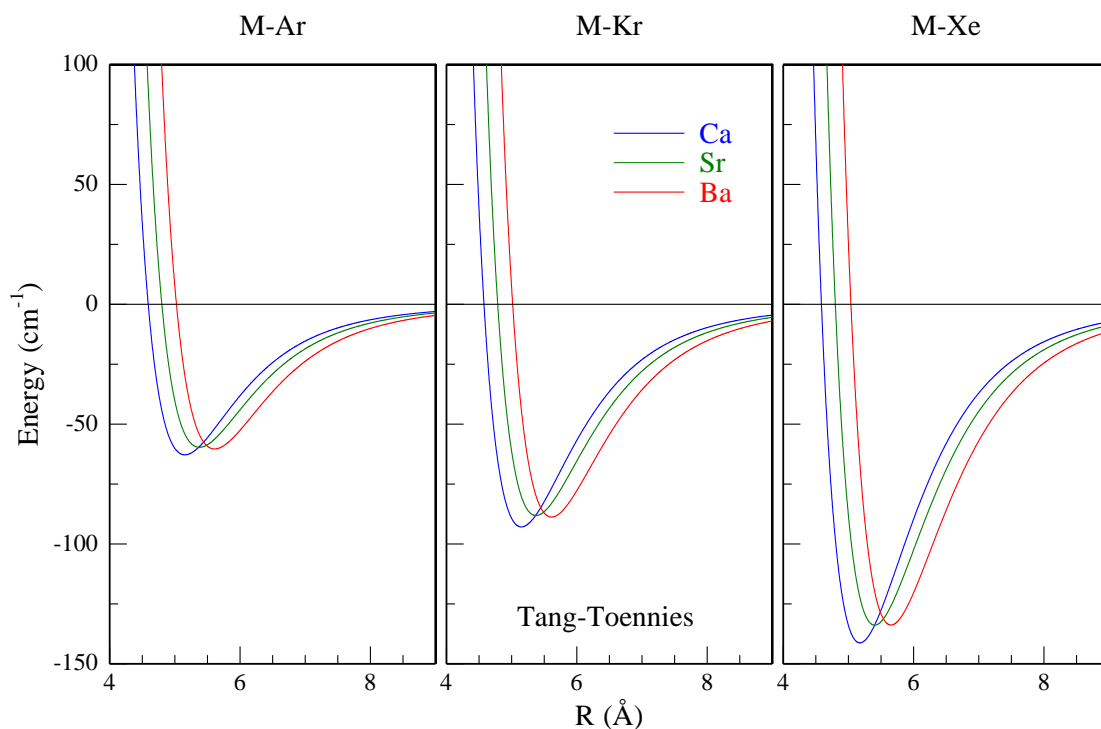
Figure VI.2   Ground state M·RG (M = Ca, Sr and Ba; RG = Ar, Kr and Xe) potential energy curves generated using the Tang-Toennies model and appropriate combining rules, as described in Section VI.2.I.

Unsurprisingly, the constants obtained for the Ca·RG dimers are different to those reported by Yang and co-workers[4] – the model potentials generated in the current study using the combing rules are less bound, with a larger internuclear separation, than those obtained using the *ab initio* dispersion coefficients in Ref. 4 (see Section VI.2.I). To the best of my knowledge, Tang-Toennies model potentials for the Ba·RG complexes have not appeared in the literature thus far, and are presented for the first time in this work.

Table VI.2   Ground state M·RG spectroscopic constants obtained from the Tang-Toennies model potentials, which are shown in Figure VI.2.

System	R_e (cm^{-1})	D_e (cm^{-1})
Ca-Ar	5.16	62.8
Kr	5.15	92.9
Xe	5.18	141.2
Sr-Ar	5.38	59.6
Kr	5.38	88.1
Xe	5.40	133.8
Ba-Ar	5.61	60.3
Kr	5.61	88.7
Xe	5.65	133.8

VI.3.II   CCSD(T)

The ground state potential energy curves calculated at the CCSD(T) level of theory with the basis sets specified in the Section VI.2.II are presented in the three panels of Figure VI.3. The computed equilibrium bond length (R_e) and dissociation energy (D_e) of the nine M·RG diatomics are collected in Table VI.3. Inspection of these values reveals long bond lengths in the range 5.15 to 5.62 Å for all the diatomics. For a given metal atom M, there is very little variation in the bond lengths for the three rare gases studied. For example, the equilibrium bond lengths for Ca·Ar, Ca·Kr and Ca·Xe were determined to be 5.16, 5.15 and 5.17 Å respectively. In the Sr·RG series all the bond lengths are around 5.3 Å. The Ba·RG series reveals a different situation where the Ba·Xe complex has the shortest bond length, 5.55 Å, while the Ba·Ar complex is the longest at 5.62 Å. This behaviour is related to the competition between the RG polarizability and the electron repulsion arising from the physical size of the metal atom (number of electrons).
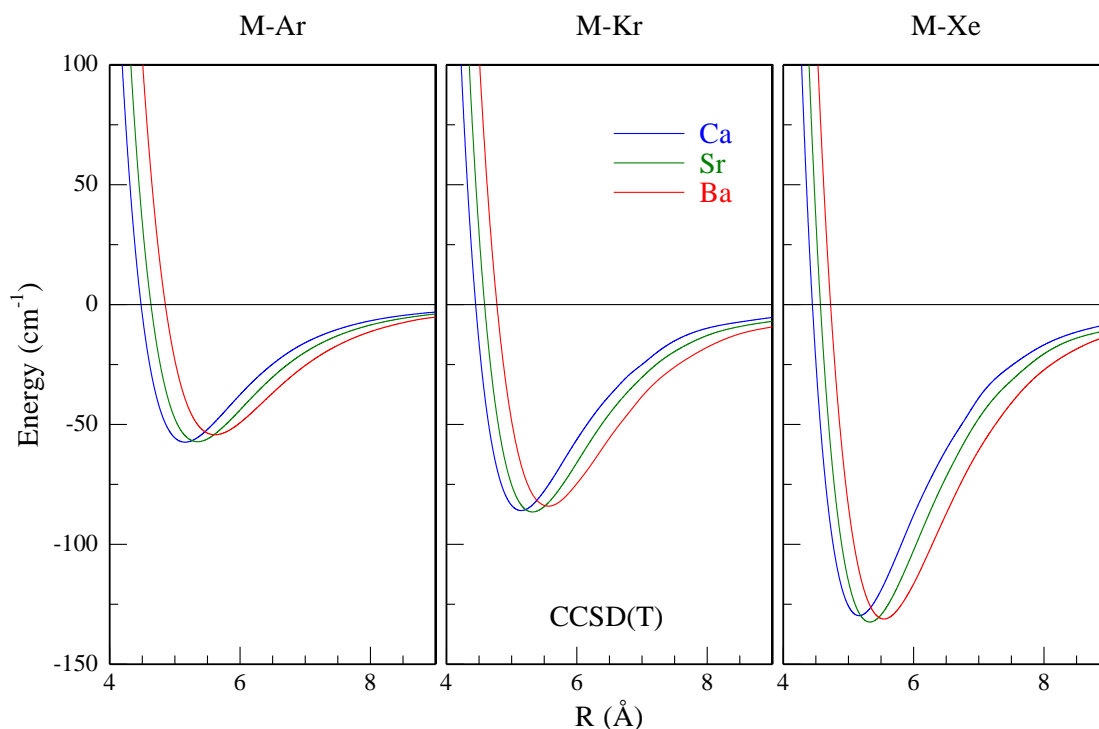
Figure VI.3   **Ground state M·RG (M = Ca, Sr and Ba; RG = Ar, Kr and Xe) potential energy curves calculated at the CCSD(T) level of theory using the aug-cc-pVQZ basis sets, as described in Section VI.2.II.**

For Ba·Xe, the repulsive forces are somewhat counteracted by the increased polarizability, leading to a shorter equilibrium bond length for this pair. In contrast, the

binding energies vary quite strongly between the rare gases – for Ca·RG values of 57, 86 and 130 cm^{-1} are found for RG=Ar, Kr and Xe respectively. A similar observation was made for the Tang-Toennies potentials and is simply related to the increasing polarizability of the rare gas partner. For a given RG gas atom the binding energies are fairly independent of the metal atom with M·Ar, M·Kr and M·Xe values existing in the small range from 54.2 – 57.3, 84.0 – 86.5 and 129.7 – 132.3 cm^{-1} respectively.

Table VI.3   **Ground state M·RG spectroscopic constants extracted from ab initio CCSD(T) determinations of the 1:1 potential energy curves shown in Figure VI.3.**

System	R_e (cm^{-1})	D_e (cm^{-1})
Ca-Ar	5.16	57.3
Kr	5.15	85.9
Xe	5.17	129.7
Sr-Ar	5.35	57.2
Kr	5.32	86.5
Xe	5.33	132.3
Ba-Ar	5.62	54.2
Kr	5.57	84.0
Xe	5.55	131.1

VI.3.III   TT and CCSD(T): Comparison

In this section, the M·RG potential energy curves obtained using the Tang-Toennies and coupled-cluster methods are compared – they are also compared with existing experimental and theoretical determinations. Inspection of Table VI.4 reveals that the spectroscopic constants obtained with these two distinct methods are in very good agreement, especially for the Sr·RG dimers. This is remarkable considering the empirical nature of the TT function. Figure VI.4 presents a comparison of the potential shapes, for a selection[a] of M·RG complexes. The strength and weakness of the empirical method can be gleaned from this plot. It is clear that the TT model potentials provide an excellent description the long-range portion of the PECs. However, the performance on the repulsive inner wall is quite poor and gets worse for the heavier atoms. Thus, Ba·Xe is worse than Ca·Ar. This behaviour originates from the TT formalism itself. The long-range portion is very reliable because the dispersion coefficients are computed using the well-established combining rules[5]. Conversely, the

---

[a] A comparison of the remaining complexes is provided in Figures VI.9 – VI.11 of Appendix VI.1

repulsive part is describe using a simple Born-Mayer potential which is added to the attractive potential. Tang *et al.*[6] concede that the combining rules for the Born-Mayer parameters aren't nearly as accurate. This is very evident from a comparison with the high level CCSD(T) results shown in Figure VI.4.
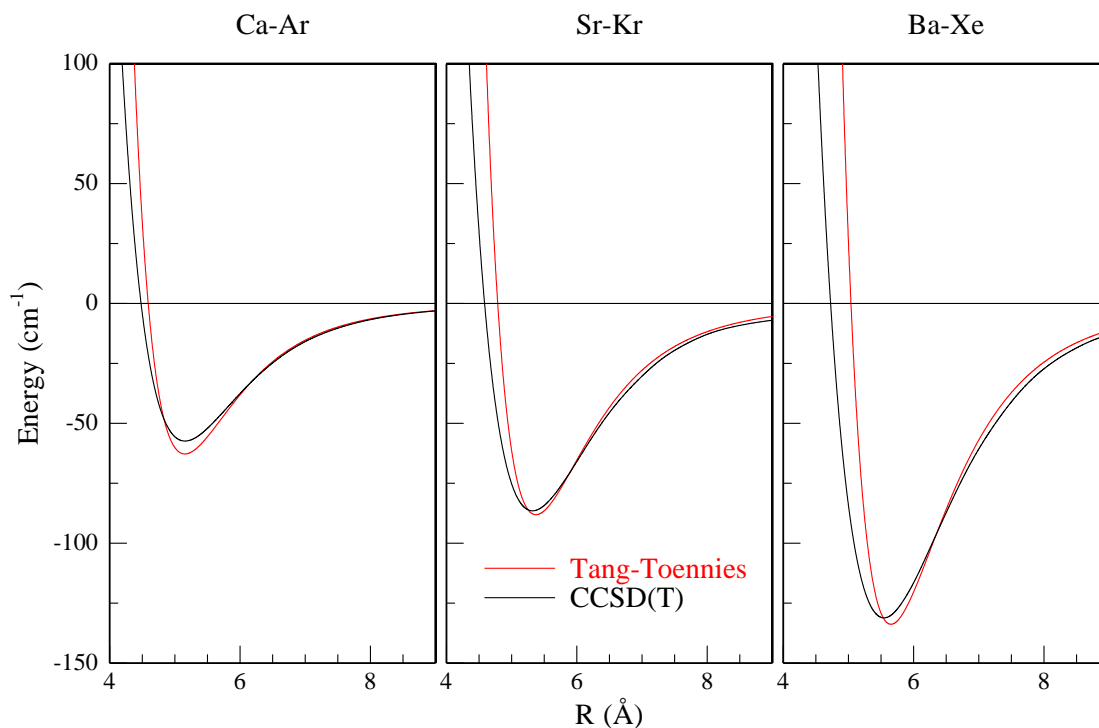
Figure VI.4   **A comparison of the CCSD(T) (black) and Tang-Toennies (red) ground state potential energy curves made for a selection of M·RG systems.**

In contrast to the corresponding metal (M_2) and rare gas (RG_2) homonuclear diatomics, very little experimental data is available concerning the interaction potentials of the mixed M·RG diatomics. The only spectroscopic constants derived from experiment comes from the work of Breckenridge[33] and co-workers. In their study, laser excitation spectra were recorded for Ca·Ar, Sr·Ar and Ba·Ar, which were formed in a supersonic jet. Ground state well depths of 62 ± 10 and 68 ± 15 cm^{-1} were obtained from a Birge-Sponer extrapolation for Ca·Ar and Sr·Ar respectively. However, a similar analysis for Ba·Ar was not possible because the excitation spectrum of this complex was of poorer quality. The experimental binding energy obtained for Ca·Ar is in very good agreement with the current CCSD(T) result. While the agreement for Sr·Ar is less favourable, the present *ab initio* dissociation energy lies within the

quoted experimental error. Unfortunately, experimentally determined ground state bond lengths are currently not available for the M·RG dimers.

Theoretical investigations of the nine M·RG diatomics are also quite limited. The 1:1 Ca·Ar complex is the most studied of these systems and has been treated at varying levels of theory, ranging from *ab initio* methods such as CCSD(T)[34], Møller–Plesset (MP2)[35], configuration interaction (CI)[36] and multi-configurational self-consistent-field theory (MCSCF)[37] to an empirical method such as the Tang-Toennies (TT)[4] model potential. However, only two of these studies[4,34] extend to Ca·Kr and Ca·Xe. The most relevant comparison that can be made is with the work of Czuchaj *et al.*[34], who computed the ground state Ca·RG PECs using a combined pseudopotential/CCSD(T) approach. R_e (Å)/D_e (cm^{-1}) values of 5.09/61.9, 5.05/97.5 and 5.17/131.4 were calculated for Ca·Ar, Ca·Kr and Ca·Xe respectively, which as shown in Table I.1, are in agreement with the present determinations.

Conversely, much less theoretical effort has been directed at the heavier M·RG complexes (M = Sr and Ba). It turns out the most extensive study of the Sr·RG diatomics was conducted by Tang *et al.*[6] – the TT model potentials have been reproduced in this study. To the best of my knowledge, only the Sr·Ar molecule has been studied using an *ab initio* method. An MCSCF calculation was carried out by Zhu *et al.*[37] for this system, yielding a comparable ground state dissociation energy of 63.5 cm^{-1}, but a longer equilibrium bond length of 6.2 Å. The Ba·RG 1:1 complexes have been studied by Czuchaj and co-workers[38]. The CI/pseudopotential calculations they conducted yielded ground state R_e (Å)/D_e (cm^{-1}) values of 5.56/73.0, 5.72/80 and 5.93/101 for Ba·Ar, Ba·Kr and Ba·Xe respectively. In this case, the equilibrium bond lengths are systematically longer than the current coupled-cluster values and, aside from Ba·Ar, their potentials are more weakly bound. More recent computations have been conducted for Ba·Ar[39] and Ba·Xe[40] using a similar theoretical approach. While the ground state spectroscopic constants obtained for Ba·Ar (R_e = 5.36 Å and D_e = 72.7 cm^{-1}) are quite close to the original work of Czuchaj and co-workers[38], the updated Ba·Xe potential of Abdessalem *et al.*[40] is too deeply bound (R_e = 5.11 Å and D_e = 427 cm^{-1}).

Table VI.4 **A comparison of the present CCSD(T) and Tang-Toennies (TT) M·RG spectroscopic constants with existing theoretical and experimental data. The equilibrium bond lengths, R_e, are quoted in units of Angstrom (Å) and the dissociation energies, D_e, are given in wavenumber units (cm^{-1}). For each system, the top numbers highlighted in red represent the current CCSD(T) values. Likewise, the values listed second from the top and highlighted in blue are the current Tang-Toennies determinations. a) CCSD(T) + PP2[34] b) MP2 + pVQZ quality basis sets[35]. c) Tang-Toennies Ca·RG Model Potential[4] . d) Tang-Toennies Sr·RG Model Potential[6]. e) CI + Pseudopotential[38]. f) CI + Pseudopotential + Core Polarization Operators[40] (CPP). g) CI + Pseudopotential + CPP. h) Experimental Supersonic Jet[33]. i) CI + Pseudopotential + CPP[36]. j) MRCI + Pseudopotential[37].**

System	R_e (Å)	D_e (cm^{-1})
Ca-Ar	**5.16**	**57.3**
	5.16	**62.8**
	5.09[a]	61.9[a]
	4.995[b]	81.1[b]
	5.10[c]	72.7[c]
		62 ± 10[h]
	4.86[i]	$D_0 = 87$[i]
	5.9[j]	72.6[j]
Kr	**5.15**	**85.9**
	5.15	**92.9**
	5.05[a]	97.5[a]
	5.11[c]	102.7[c]
Xe	**5.17**	**129.7**
	5.18	**141.2**
	5.17[a]	131.4[a]
	5.15[c]	152.2[c]
Sr-Ar	**5.35**	**57.2**
	5.38[d]	**59.6**[d]
		68 ± 15[h]
	6.2[j]	63.5[j]
Kr	**5.32**	**86.5**
	5.38[d]	**88.1**[d]
Xe	**5.33**	**132.3**
	5.40[d]	**133.8**[d]
Ba-Ar	**5.62**	**54.2**
	5.61	**60.3**
	5.56[e]	73[e]
	5.36[g]	72.7[g]
Kr	**5.57**	**84.0**
	5.61	**88.7**
	5.72[e]	80[e]
Xe	**5.55**	**131.1**
	5.65	**133.8**
	5.93[e]	101[e]
	5.11[f]	427[f]

VI.3.IV   Summary

The ground state PECs for the 1:1 M·RG complexes (M= Ca, Sr, Ba; RG = Ar, Kr, Xe), have been computed using two theoretical methods. Good agreement was found between the spectroscopic parameters obtained at the Tang-Toennies and CCSD(T) levels of theory. Overall, both models predicted the M·RG dimers to be weakly bound (< 140 cm^{-1}) with long (< 5 Å) equilibrium bond lengths. If the isolation of these metal atoms, which exhibit large van der Waals radii, occurs within cramped vacancies of RG solids, then a correct description of the repulsive portion of the PEC is essential. Thus, the poor performance of the TT function at describing the inner repulsive walls precludes the use of this method in analysing the site occupancy of the M/RG systems. Consequently, in the following sections the site occupancy will be interpreted only using the more reliable *ab initio* results.

VI.4   M/RG site occupancy

As was discussed in the Chapter I, the alkaline earth atoms all exist in spherically symmetric S ground states. Thus, the isolation of these metal atoms would be expected to occur in 'cubic' sites of the close packed *fcc* rare gas lattices. If this is the case, then the guest-host ground state interaction is isotropic and the site occupancy may be analysed with a straight-forward comparison of the M·RG and RG$_2$ potential energy curves. Such a comparison is presented in Figure VI.5. In this plot, the RG$_2$ potentials were generated with Morse functions[b] using the parameters[41] D_e = 99.545, 138.4, 196.24 (cm^{-1}), R_e = 3.7565, 4.017, 4.3634 (Å) and β_e = 1.40218, 1.604, 1.509 (Å^{-1}) for Ar$_2$, Kr$_2$ and Xe$_2$ respectively.

A feature immediately evident is the pronounced mismatches which exist between the M·RG potentials (coloured traces) and those of the corresponding rare gas dimers (RG$_2$), shown by the black traces. Thus, the binding energies of the rare gas dimers are all greater than the heteronuclear diatomics, but more significantly for site occupancy, the M·RG potentials all have their minima at nuclear separations greatly in excess of the rare gas dimers. This latter characteristic has profound implications on the possible sites occupied by the heavy alkaline earth metal atoms in the solid rare

---

[b] See equations VI.16 – VI.19 of Appendix VI.I.

gases. The sizes of the cubic vacancies in the sRG's capable of accommodating the spherical ground state $^1S_0$ metal atoms are indicated by the vertical grey lines. The energetics determined from the calculated M·RG potentials for single vacancy (SV) and multi-vacancy (tetravacancy (TV), hexavacancy (HV) and cubo-octahedral (CO) substitutional) site occupancies are provided in Table VI.5.
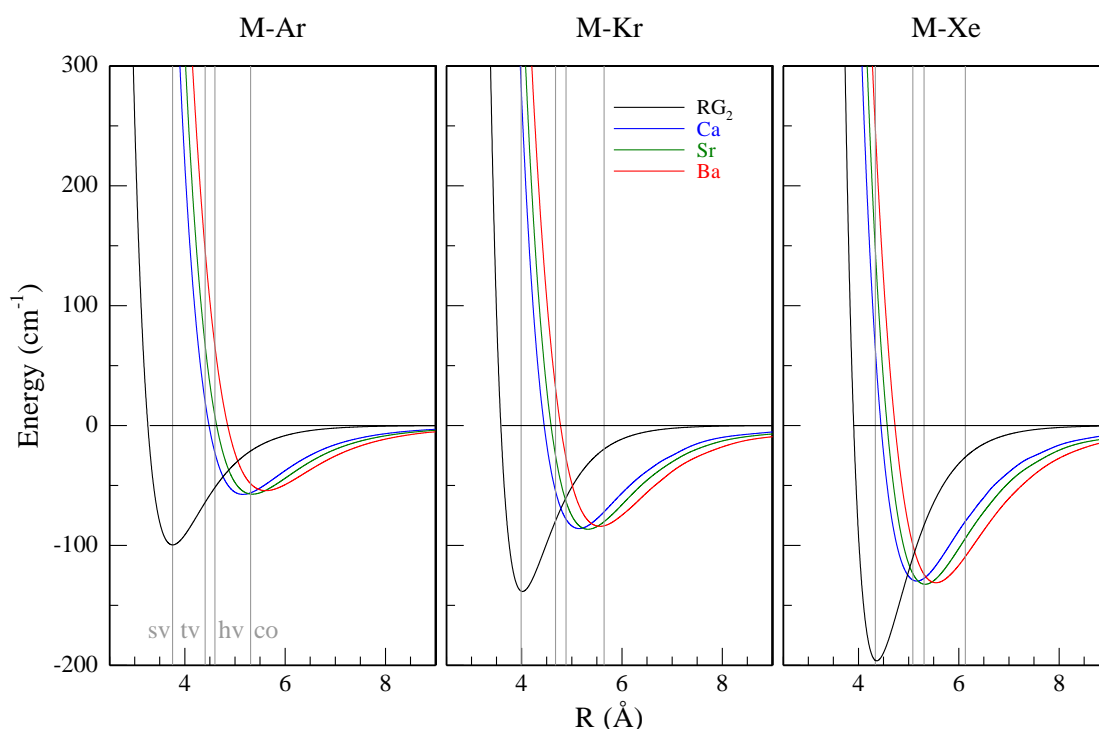
Figure VI.5   **A comparison of the three rare gas (RG₂) dimer potentials (black curves) with those calculated with the coupled-cluster method for the nine M·RG diatomics (coloured curves). The grey vertical lines show the sizes of the cubic sites in the solid rare gases considered to accommodate a spherical guest atom. The energies of the M·RG interactions at these sites are provided in Table VI.5.**

From the numbers listed there, none of the M/RG matrix systems would be expected to have SV occupancy with the possible exception of Ca/Xe which only has a very slight (64 cm^{-1}) repulsive interaction. For all the other M/RG systems tetra-vacancy (TV) site occupancy would be predicted with the exception of Ba/Ar. In this system attractive M-Ar interactions are only experienced in the large cubo-octahedral (CO) substitutional site which involves the removal of a central Ar atom and 12 of its nearest neighbours. Although, even for Ba/Ar, smaller sites such as a HV may be occupied because of the requirement for lattice stabilisation.

However, site assignments are not possible based solely on the application of the M·RG ground state PECs to the matrix systems, as the values listed in Table VI.5

reveal the possibility of numerous energetically viable sites for Sr and Ba. Therefore, the valuable information obtained from the spectroscopic (absorption and luminescence) interrogation of these M/RG solids, will now be used to strengthen any site assignments. Of the three hosts, Xe should be most adept at trapping these large metal atoms. Indeed this behaviour was observed in the luminescence chapters (IV and V), where the least number of sites were identified for Sr and Ba in Xe. Thus, a M/Xe case study will now be undertaken, where a comparison of the site-specific excitation spectra recorded for these two atoms will be presented.

Table VI.5 **A summary of the M-RG energies at the distances that exist by placing the metal atom in single vacancy (SV), tetravacancy (TV), hexavacancy (HV) and cubo-octahedral (CO) substitutional sites of the solid rare gas lattices. These distances are represented in Figure VI.5 by the vertical grey lines for the *fcc* Ar, Kr and Xe lattices and were computed using Equations I.1 – I.7, which were presented and described in Chapter I.**

		Energies of the matrix sites (cm^{-1})			
M	**RG**	**SV**	**TV**	**HV**	**CO**
Ca	**Ar**	454.9	20.0	-22.3	-56.1
	Kr	282.6	-54.5	-78.0	-72.0
	Xe	64.3	-128.8	-127.4	-79.8
Sr	**Ar**	583.3	67.3	8.3	-57.1
	Kr	392.2	-24.7	-63.1	-80.1
	Xe	147.3	-123.4	-132.3	-94.1
Ba	**Ar**	695	146.5	66.8	-48.5
	Kr	504	31.7	-26.9	-83.7
	Xe	248.6	-99.3	-124.1	-109.3

VI.4.I M/Xe

The absorption and excitation profiles, recorded for atomic Sr and Ba isolated in annealed Xe matrices, are presented in Figure VI.6. For comparative purposes, the spectra have been zeroed with respect to the gas phase positions of the resonance ns^1np^1 $^1P_1 \leftarrow ns^2\,^1S_0$ transitions (n=5 and 6 for Sr and Ba, respectively). For each metal atom, the dominant absorption feature is characterised by Jahn-Teller (JT) threefold splitting pattern, indicative of a highly symmetric (cubic) trapping site. The corresponding

excitation traces (shown in blue) also display this pattern and indeed, for Ba, the excitation scan is more resolved.

Absorption/Excitation
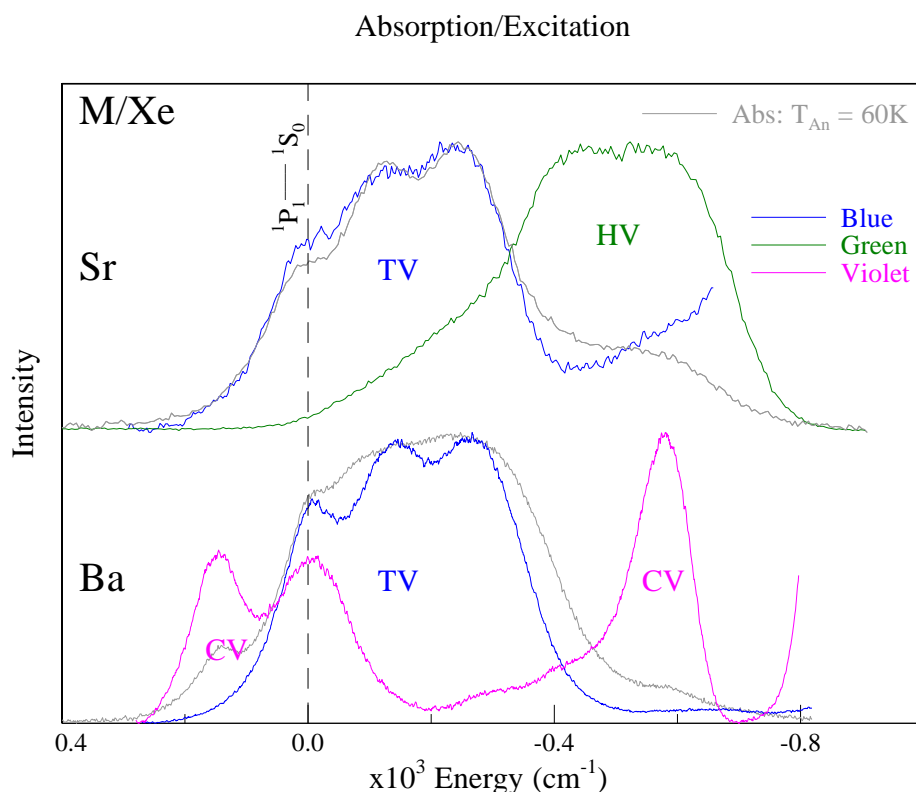
Figure VI.6   A comparison of the absorption (grey) and excitation (coloured) recorded for two M/Xe systems examined in this study. Both samples were annealed to 60 K. To facilitate comparison the spectra have been zeroed around the gas phase positions of the resonance $ns^1np^1\ {}^1P_1 \leftarrow ns^2\ {}^1S_0$ transitions (n = 5 & 6 for Sr and Ba) at 21698.452 and 18060.261 cm^{-1} respectively.

The JT bands are quite similar for the two metals and are shifted from the gas phase by approximately the same amount, which is an indication of a comparable ground and excited state guest-host interaction. In both systems, these profiles were labelled as the blue site of isolation and it is clear from the comparison that the same vacancy is occupied by both alkaline earths. Inspection of the site energetics collected in Table VI.5 rules out a single vacancy, as was discussed in the previous section. Thus, the blue site of isolation for Sr and Ba in solid Xe is tentatively assigned as a tetra-vacancy (TV) – the next larger cubic site available.

In contrast to the primary site of isolation, a strong dissimilarity exists between the excitation profiles of the secondary sites. This behaviour points to the occupation of different vacancies for Sr and Ba. For Sr/Xe, the green site excitation scan (green trace) is broad and red-shifted with respect to the blue site, indicating that the atom is

occupying a larger vacancy. The lineshape fits conducted in Chapter V suggested that this feature may be an unresolved JT band – three Gaussian components were required to reproduce the dominant portion of the scan. Based on this evidence, a site of cubic symmetry may be considered. An examination of the values collected in Table VI.5 reveals that ground state Sr atoms should be stabilised in a hexa-vacancy (HV) trapping site in solid Xe. Consequently, a tentative assignment to this cavity is made.

The secondary (violet) site for Ba in Xe is not one of cubic symmetry because the excitation profile (pink trace) is characterised by the asymmetric (2+1) splitting pattern. As was discussed in Chapter IV, this behaviour results from an anisotropic interaction of the excited $Ba(^1P_1)$ atom with the rare gas host. Such an interaction would occur if the ground state atom was isolated in a vacancy of lower symmetry, in which a strongly preferred direction exists - like a cylindrical void (CV). A provisional assignment to this type of cavity is therefore proposed. The high annealing threshold (> 60 K) implies that the vacancy is quite stable and may occur within the bulk crystal[42] or at a grain boundary[43], as suggested by simulations conducted for the matrix isolated alkali metals.

It is evident that the theoretical approach used in this chapter cannot account for the differing secondary site preferences of Sr and Ba in Xe matrices. Inspection of the site energetics listed in Table VI.5 suggests that a hexa-vacancy should also be occupied by Ba, which is in conflict with the experimental data. However, this model doesn't take into account properties of the solid, such as the lattice stabilisation energy, which can significantly affect the population of a given site. It may be that the cylindrical void is stabilised by the presence of the larger Ba atom, which exhibits more spatially extensive valence s and p orbitals than Sr. Perhaps this site requires fewer RG atoms to be replaced and is therefore more thermodynamically favourable than the 6-atom HV site. More conclusive statements about the site structures are, however, not possible in the absence of molecular dynamics simulations.

VI.4.II   M/RG

The same analysis is now extended to the lighter RG hosts. Comparisons of the site-specific excitation scans are provided for Kr and Ar in Figure VI.7 and VI.8 respectively. The major point of note is the increasing number of thermally stable sites which are occupied in going from Xe to Ar. This reflects the smaller sites sizes

available in the lighter solids – thus a wider range of trapping sites become are required for these large metal atoms. Despite the increased complexity, tentative site assignment may still be made, using the simplest host Xe as a starting point.

Absorption/Excitation
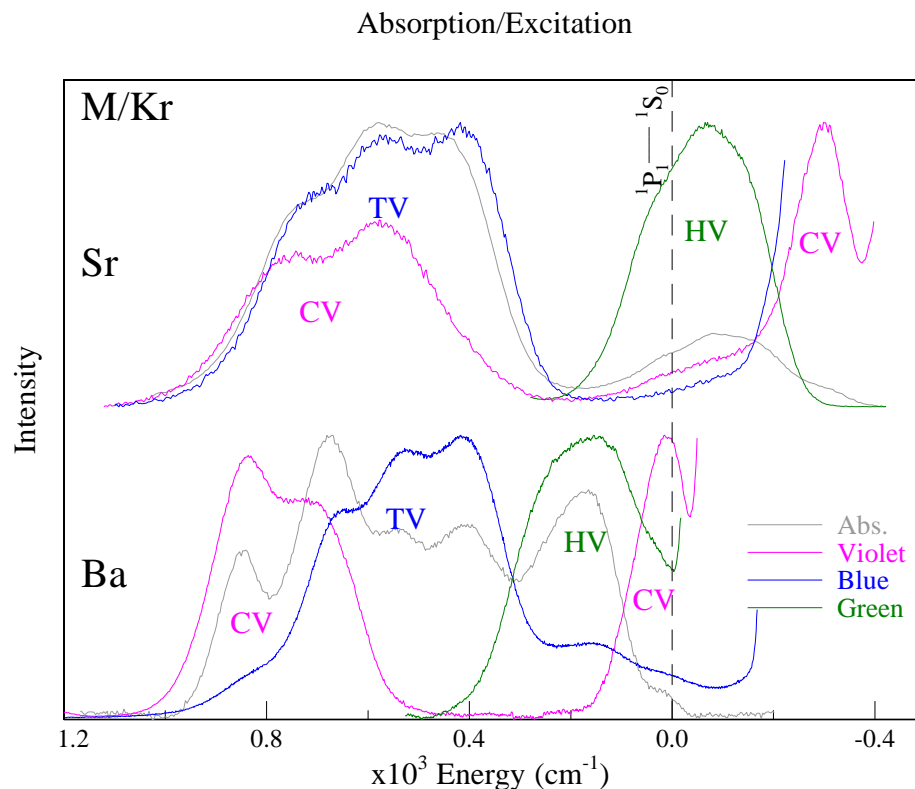
Figure VI.7 **A comparison of the absorption (grey) and excitation (coloured) spectra recorded for annealed Sr/Kr and Ba/Kr systems. Both were annealed to 45 K. The spectra have been zeroed around the gas phase positions of the resonance $ns^1np^1\ ^1P_1 \leftarrow ns^2\ ^1S_0$ transitions.**

In the Chapters IV and V, a plot of RG polarisability versus shift from the gas phase allowed association of certain site types occupied by these metal atoms[44]. Using this model and with consideration of the theoretical PECs, the following site assignments are made: The blue sites of isolation occupied by Sr and Ba in all three RG solids are tentatively assigned as TVs. Similarly, the green sites identified for both alkaline earths are provisionally assigned as HVs. These assignments are labelled in Figures VI.6 – VI.8.

Inspection of the comparison made for Kr in Figure VI.7 reveals an interesting difference between the absorptions of the TV and HV sites. Thus, the central positions of the TV bands recorded for Sr and Ba are approximately equal. In contrast, the HV absorption profile recorded for Ba is significantly blue-shifted with respect to Sr. The

observed matrix shifts depend both on the size of the vacancy and the size of the metal atom.
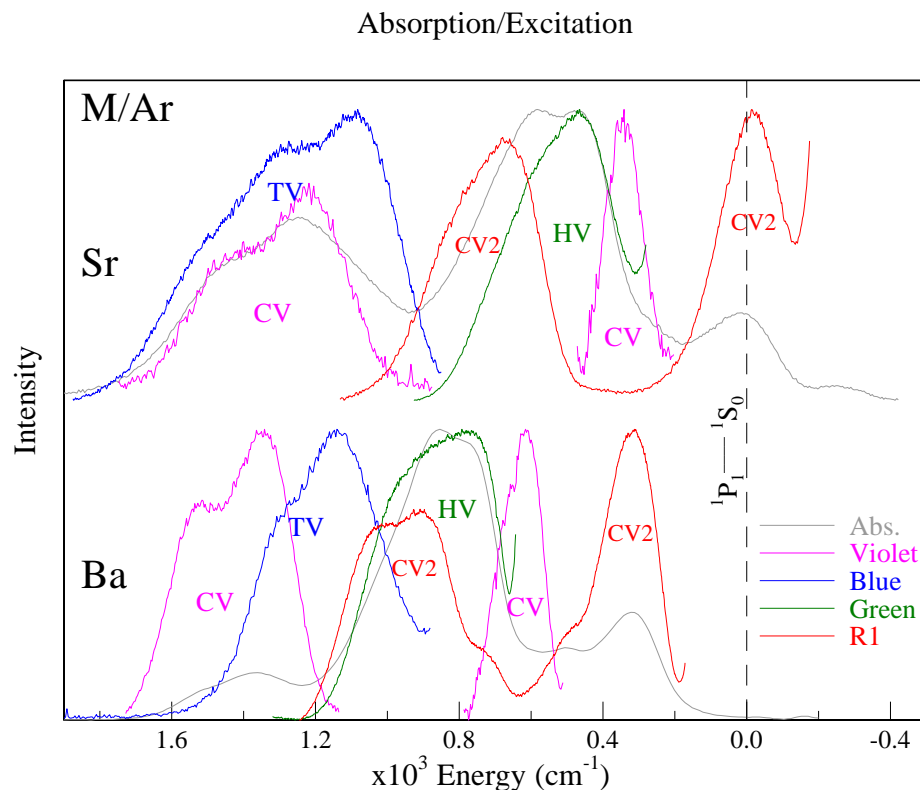

Figure VI.8   **A comparison of the absorption (grey) and excitation (coloured) spectra recorded for annealed Sr/Ar and Ba/Ar systems. Both were annealed to 30 K. The spectra have been zeroed around the gas phase positions of the resonance ns^1np^1 $^1P_1 \leftarrow ns^2$ $^1S_0$ transitions.**

The hexa-vacancy in Kr can easily accommodate a Sr atom with minimum perturbation, as revealed by the absorption band of this site which directly overlaps the gas phase line. In contrast, the larger van der Waals radius of Ba results in a greater repulsive guest-host interaction at this location, leading to a blue-shift. However, when isolated in the smaller tetra-vacancy site, both metal atoms are very confined and significantly perturb the host RG lattice. In this instance, the larger size of Ba does not result in greater matrix shift, but instead is manifested by the preferential occupation of more spacious vacancies.

An examination of Figures VI.6 - VI.8 reveals that for a given site of isolation, the Ba/RG absorptions are consistently narrower than their Sr/RG counterpart. This is especially evident in the M/Ar and M/Kr systems which are shown in Figures VI.7 and VI.8, respectively. Based on the very similar van der Waals interactions (R_e and D_e values) identified in the CC calculations between these metals and a given rare gas, this

behaviour is simply related to the greater mass of atomic Ba compared with Sr. As a result, the effective phonon frequency coupling in the Ba/RG systems has a lower value than the Sr/RG systems. This in turn produces narrower absorption bands as the electron-phonon coupling determines the lineshapes of the transitions in the solid state spectra.

Although this approach can't account for the occupation of non-cubic sites, trends evident from a comparison of the two guest atoms allow for some comments to be made. An examination of the spectra recorded in Ar and Kr matrices reveals that the violet sites (pink traces) likely correspond to the same type of trapping environment for Sr and Ba, i.e. a cylindrically shaped void. This is evident as the scans recorded for each M/RG system exhibit the characteristic asymmetric (2+1) threefold splitting pattern. Similar to the behaviour observed for the HV sites, the violet peaks of Ba are all blue-shifted with respect to those of Sr. A comparison may also be made for the excitation features of the R1 trapping site (red traces) recorded for Sr and Ba in Ar. The striking spectroscopic resemblance again suggests that the same type of vacancy is being occupied by both metal atoms. The absorption splitting patterns are indicative of a cylindrical-type void. However, from the relative spectral location of the profiles, we can infer that this is a more spacious cavity than the violet site – hence the label CV2 is used.

VI.5   Conclusions

Ground state potential energy curves were computed for the 1:1 M·RG complexes (M=Ca, Sr, Ba and RG = Ar, Kr, Xe), using empirical (Tang-Toennies) and *ab initio* (CCSD(T)) approaches. Both methods revealed long bond lengths (> 5 Å) and shallow bound regions (<142 cm^{-1}) for the nine M·RG diatomics. Although the spectroscopic constants (R_e and D_e) computed by both methods were in good agreement, the shapes of the potentials were found to differ in a significant way. The short range portion of the TT potentials were too repulsive, when compared with the same region of the CCSD(T) potentials. For large metal atoms such as Sr or Ba, the repulsive interaction will play a key role in determining the sites of isolation accessible in a rare gas solid. Therefore the more reliable coupled-cluster results were used to interpret the site occupancy.

A simple comparison of the M·RG and RG$_2$ potential energy curves allowed for comments to be made regarding the occupancy within cubic sites. Combining this theoretical approach with the site-specific excitation spectra recorded for the alkaline earth atoms in annealed RG matrices allowed for tentative site assignments to be made. Thus, the 'blue' sites of isolation for Sr and Ba were assigned as tetra-vacancies (TV). Similarly, the 'green' sites were provisionally assigned as hexa-vacancies (HV). Although the approach presented in this chapter is limited to highly symmetric (cubo-octahedral) sites, the trends evident from a comparison of the two guest atoms allowed for comments to be made regarding the non-cubic voids. It was proposed that the 'violet' site represents the same type of trapping environment for both Sr and Ba atoms in the sRG's and a similar conclusion was drawn for the R1 trapping site in Ar.

In summary, the results presented in this chapter should serve as a solid starting point for any future molecular dynamics simulation of these M/RG systems. Moreover, recreating the experimental observation of trapping in both cubic and non-cubic sites of isolation will prove to be a rigorous test for any theoretical model. Indeed, Sr and Ba are the first spherically symmetric ground state metal atoms, studied by the Maynooth Group[45-47], which demonstrate a clear preference for occupancy in vacancies of non-cubic symmetry. These cylindrical sites have been proposed in the Monte Carlo study of Fajardo *et al.*[42] and the molecular dynamics simulations conducted by Gervais *et al.*[43] suggested that they may exist as small grain boundary cavities. They have also been observed in the absorption/excitation spectra recorded of the P ← S transitions of Cd atoms isolated in annealed ethane matrices[48]. In this system, the singlet − doublet (Σ-Π) energy gap was much greater (~2400 cm^{-1}) due to a stronger interaction of the excited metal atom (P state) with the molecular host.

References

[1] K. Tang, and J. P. Toennies, J. Chem. Phys. **80**, 3726 (1984).

[2] M. Born, and J. E. Mayer, Z. Phys. **75**, 1 (1932).

[3] A. A. Abrahamson, Phys. Rev. **178**, 76 (1969).

[4] D. D. Yang, P. Li, and K. T. Tang, J. Chem. Phys. **131**, 154301 (2009).

[5] K. Tang, and J. P. Toennies, Zeitschrift für Physik D Atoms, Molecules and Clusters **1**, 91 (1986).

[6] G. P. Yin, P. Li, and K. T. Tang, J. Chem. Phys. **132**, 074303 (2010).

[7] S. G. Porsev, and A. Derevianko, Journal of Experimental and Theoretical Physics **102**, 195 (2006).

[8] A. Kumar, and W. J. Meath, Mol. Phys. **54**, 823 (1985).

[9] A. J. Thakkar, H. Hettema, and P. E. S. Wormer, J. Chem. Phys. **97**, 3252 (1992).

[10] K. T. Tang, and J. P. Toennies, J. Chem. Phys. **118**, 4976 (2003).

[11] O. Allard, A. Pashov, H. Knöckel, and E. Tiemann, Phys. Rev. A **66**, 042503 (2002).

[12] A. Stein, H. Knöckel, and E. Tiemann, Phys. Rev. A **78**, 042508 (2008).

[13] M. A. Lebeault, J. Viallon, V. V. Boutou, and J. Chevaleyre, J. Mol. Spectrosc. **192**, 179 (1998).

[14] P. Li, J. Ren, N. Niu, and K. T. Tang, J. Phys. Chem. A **115**, 6927 (2011).

[15] A. V. Mitin, Russian Journal of Physical Chemistry A **83**, 1160 (2009).

[16] J. Mitroy, and J. Y. Zhang, J. Chem. Phys. **128**, 134305 (2008).

[17] F. Coester, and H. Kümmel, Nucl. Phys. **17**, 477 (1960).

[18] K. E. Riley, M. Pitoňák, P. Jurečka, and P. Hobza, Chem. Rev. **110**, 5023 (2010).

[19] T. Helgaker, P. Jorgensen, and J. Olsen, *Molecular electronic-structure theory* (John Wiley & Sons, 2014).

[20] R. J. Bartlett, and M. Musiał, Rev. Mod. Phys. **79**, 291 (2007).

[21] J. Řezáč, L. Šimová, and P. Hobza, Journal of Chemical Theory and Computation **9**, 364 (2013).

[22] M. Valiev *et al.*, Comput. Phys. Commun. **181**, 1477 (2010).

[23] D. E. Woon, and T. H. Dunning Jr, J. Chem. Phys. **98**, 1358 (1993).

[24] A. K. Wilson, D. E. Woon, K. A. Peterson, and T. H. Dunning Jr, J. Chem. Phys. **110**, 7667 (1999).

[25] T. H. Dunning Jr, K. A. Peterson, and A. K. Wilson, J. Chem. Phys. **114**, 9244 (2001).

[26] K. A. Peterson, D. Figgen, E. Goll, H. Stoll, and M. Dolg, J. Chem. Phys. **119**, 11113 (2003).

[27] EMSL Basis Set Exchange (v1.2.2). Available at: https://bse.pnl.gov/bse/portal

[28] H. Li *et al.*, Mol. Phys. **111**, 2292 (2013).

[29] Correlation Consistent Basis Sets for Ca, Sr, Ba, and Ra. Available at: http://tyr0.chem.wsu.edu/~kipeters/basissets/alkali-pp.html

[30] I. S. Lim, H. Stoll, and P. Schwerdtfeger, J. Chem. Phys. **124**, 034107 (2006).

[31] S. F. Boys, and F. Bernardi, Mol. Phys. **100**, 65 (2002).

[32] S. l. Simon, M. Duran, and J. J. Dannenberg, J. Chem. Phys. **105**, 11024 (1996).

[33] A. Kowalski, D. J. Funk, and W. H. Breckenridge, Chem. Phys. Lett. **132**, 263 (1986).

[34] E. Czuchaj, M. Krośnicki, and H. Stoll, Chem. Phys. **292**, 101 (2003).

[35] K. N. Kirschner, J. Chem. Phys. **112**, 10228 (2000).

[36] F. Spiegelman, L. Maron, W. H. Breckenridge, J.-M. Mestdagh, and J.-P. Visticot, J. Chem. Phys. **117**, 7534 (2002).

[37] R.-S. Zhu, K.-L. Han, J.-H. Huang, J.-P. Zhan, and G.-Z. He, Bull. Chem. Soc. Jpn. **71**, 2051 (1998).

[38] E. Czuchaj, F. Rebentrost, H. Stoll, and H. Preuss, Theor. Chem. Acc. **100**, 117 (1998).

[39] K. Issa, R. Dardouri, and B. Oujia, Journal of Surfaces and Interfaces of Materials **1**, 15 (2013).

[40] K. Abdessalem, L. Mejrissi, N. Issaoui, B. Oujia, and F. X. Gadea, J. Phys. Chem. A **117**, 8925 (2013).

[41] W. Breckenridge, Int. Rev. Phys. Chem. **13**, 291 (1994).

[42] J. A. Boatz, and M. E. Fajardo, J. Chem. Phys. **101**, 3472 (1994).

[43] E. Jacquet, D. Zanuttini, J. Douady, E. Giglio, and B. Gervais, J. Chem. Phys. **135**, 174503 (2011).

[44] S. L. Laursen, and H. E. Cartland, J. Chem. Phys. **95**, 4751 (1991).

[45] M. A. Collier, and J. G. McCaffrey, J. Chem. Phys. **122**, 54503 (2005).

[46] O. Byrne, and J. G. McCaffrey, J. Chem. Phys. **134**, 124501 (2011).

[47] M. Ryan, M. Collier, P. d. Pujo, C. Crépin, and J. G. McCaffrey, J. Phys. Chem. A **114**, 3011 (2009).

[48] B. Healy, *PhD Thesis: Experimental and Theoretical Analysis of the Spectroscopy of Atomic Cadmium Isolated in Low Temperature Solids.* (Maynooth University, Maynooth, Co. Kildare, Ireland, 2001).

Appendix VI.I

Table VI.6 **Homonuclear (M₂ or RG₂) diatomic parameters which were inputted into the combining rules formula (Eqs. 8 – 14) to generate the five key Tang-Toennies variables for the mixed (heteronuclear) M·RG complexes. All values are expressed in atomic units (a.u.).**

System	C_6	C_8	C_{10}	A	b	α_1	α_2	α_3	Ω_1	Ω_2	Ω_3
Sr-Sr (j)	3103	379000	4.22×10^7	44.73	0.9699	202	4630	1.06×10^5	0.101	0.116	0.205
Ba-Ba(j)	5160	772000	1.01×10^8	105.4	0.9567	272.1	8900	2.06×10^5	0.093	0.078	0.170
Ar-Ar (i)	64.3	1623	4.91×10^4	748.3	2.031	11.08	51.86	531.3	0.698	0.817	0.751
Kr-Kr (i)	129.6	4187	1.56×10^5	832.4	1.865	16.79	99.296	1272.64	0.613	0.738	0.615
Xe-Xe (i)	285.9	12810	6.20×10^5	951.8	1.681	27.16	223.29	3640.6	0.517	0.619	0.494

The functional form of the Morse Potential $V(R)$ is as follow:

$$V(R) = D_e(1 - e^{-\beta_e(R-R_e)})^2 \qquad \text{Eq. (VI.16)}$$

where

$$\beta_e = \left(\frac{2\pi^2 c \mu_{AB}}{D_e h} \right)^{\frac{1}{2}} \omega_e \qquad \text{Eq. (VI.17)}$$

$$\beta_e = 0.12177881 \left(\frac{\mu_{AB}}{D_e} \right)^{\frac{1}{2}} \omega_e \qquad \text{Eq.}$$

(VI.18)

Here ω_e, D_e and R_e represent the fundamental frequency, dissociation energy and equilibrium bond length, respectively. These parameters may be obtained from experiment. The reduced mass is given by:

$$\mu_{AB} = \frac{m_A m_B}{m_A + m_B} \qquad \text{Eq. (VI.19)}$$

where *m* is the mass of the atom. Atomic units (a.u.) are used throughout.
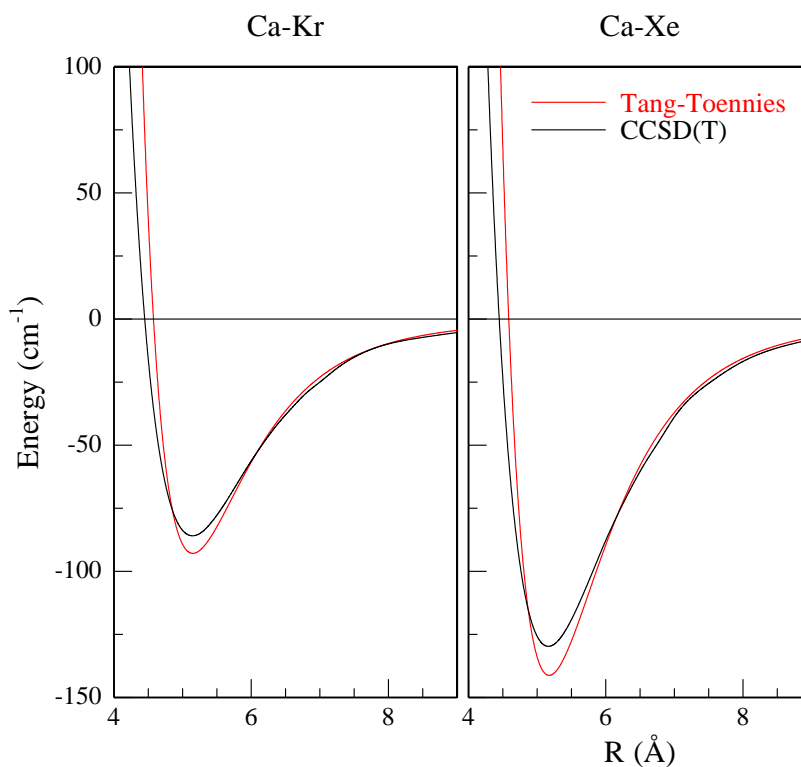
Figure VI.9   **A comparison of the CCSD(T) (black) and Tang-Toennies (red) ground state potential energy curves made for the Ca-Kr and Ca-Xe systems.**
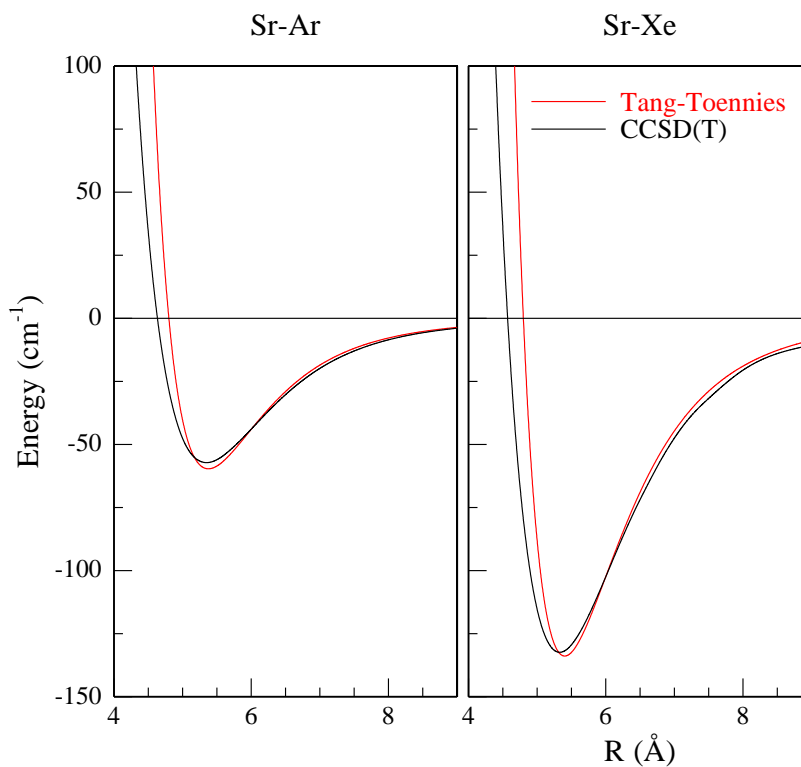
Figure VI.10   **A comparison of the CCSD(T) (black) and Tang-Toennies (red) ground state potential energy curves made for the Sr-Ar and Sr-Xe systems.**
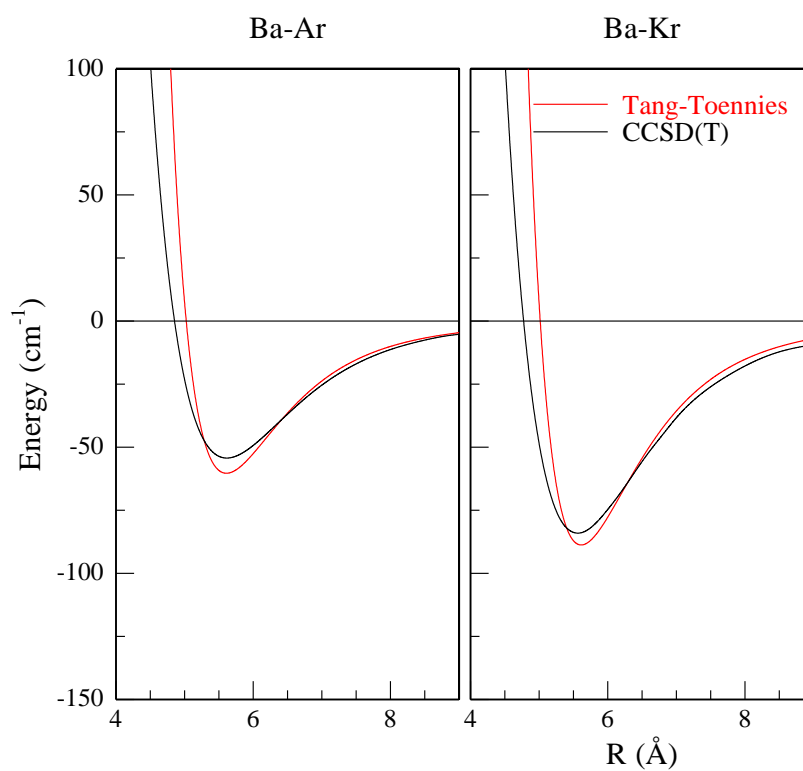
**Figure VI.11**   **A comparison of the CCSD(T) (black) and Tang-Toennies (red) ground state potential energy curves made for the Ba-Ar and Ba-Kr systems.**

Chapter VII
Conclusions

The work presented in this thesis describes a spectroscopic investigation of Sr/RG and Ba/RG solids (RG = Ar, Kr and Xe). The salient findings of this endeavour will now summarised. Firstly, the Sr impurity identified in sources of Ba metal is discussed - this important result provided the initial impetus to study matrix-isolated Sr, in addition to Ba. Secondly, a comparison of the photophysical properties of the metal dimers, Sr_2 and Ba_2, isolated in the three rare gas hosts is provided. Thirdly, an overview of the UV/Vis absorption and luminescence, recorded for well isolated Ba and Sr atoms, is presented. Finally, the ground state potential energy curves computed for the M·RG diatomics are discussed, as are the site assignments proposed for each M/RG system.

VII.1 Sr impurity in sources of Ba metal

The first absorption spectra recorded of Ba/RG solids were complex − in addition to the strong (6s6p) $^1P_1 \leftarrow$ (6s^2) $^1S_0$ resonance transition of Ba at approx. 550 nm, a number of bands were also observed at 460 nm. Because of their spectral positions, these bands were thought initially to be Ba ions isolated on deposition. Atomic Ba exhibits a relatively low first ionisation threshold[1] (5.21 eV) and it was suspected that the cation was being produced during vaporisation via e-bombardment. To investigate this possibility, a low energy thermal source (dispenser) was constructed and replaced the e-gun. However, it was found that the dispenser samples actually contained more Ba 'ions' than those deposited with e-gun vaporisation of the metal. Because of this nonsensical result, checks were made of the purity of Ba sources and it was discovered that Sr is a small (~ 0.8 %) but persistent impurity in Ba metal. Motivated by this finding, pure Sr/RG samples were deposited and UV/Vis absorption spectra were recorded to characterise these solids. A comparison of the Sr/Xe and Ba/Xe absorption spectra demonstrated, conclusively, that the 460 nm absorption bands identified in the spectra of Ba/RG samples originated from matrix-isolated atomic Sr. A systematic study of the vaporisation conditions was conducted to minimise the amount of Sr deposited in the Ba/RG matrix samples. This study revealed that Ba/RG samples

largely free of Sr could be formed with e-bombardment, provided the metal flux was kept small during the deposition (i.e. using a low e-beam current).

VII.2 Metal dimers isolated in rare gas solids (M$_2$/RG)

Concentration studies were conducted for the M/RG systems primarily to identify the deposition conditions which lead to the most atomic samples, but also to allow investigation and characterisation of matrix-isolated metal dimers (M$_2$). It was found that depositing at 10 K, under conditions of low metal loading, produced matrices composed almost exclusively of well-isolated metal atoms (M). Conversely, depositing on a 'warm' sample window, even with a low metal flux, significantly increased the yield of metal dimers (M$_2$). This effect was attributed to the enhanced mobility of the guest atoms upon arrival at the surface of the growing matrix sample.

Absorption spectra recorded of Ba/RG samples, deposited at high temperature, revealed the presence of additional non-atomic features – these were attributed to Ba dimer based on the low metal fluxes used. The absorptions of Ba$_2$ occurred in the vicinity of the (6s6p) $^1P_1 \leftarrow$ (6s^2) $^1S_0$ resonance transition of the atom (490 – 610 nm) and in the near-IR region, where a broad, unstructured band (I) was observed at 747 nm (value in Ar). Similarly, concentration studies allowed identification of the dimer absorptions in the spectra of Sr/RG samples. The observed growth patterns revealed the features at 406 (III), 550 (II) and 708 nm (I) to be absorptions of Sr$_2$ (values in Ar). In stark contrast to Ba dimer, the near-IR absorption of Sr dimer exhibited resolved vibrational structure. From a comparison with existing theoretical[2,3], matrix[4,5] and gas phase[6,7] studies, the lowest energy M$_2$ band (I) was assigned to a fully allowed $^1\Sigma_u^+ \leftarrow$ X $^1\Sigma_g$ molecular transition. Further deconvolution of atomic and dimer absorption bands was achieved with the assistance of full range excitation spectra, which were recorded monitoring the emission of Ba$_2$ and Sr$_2$ in each RG matrix.

Photoexcitation into the visible absorption bands of Ba$_2$ produced emission at 580.9, 617.4 and 676.8 nm in Ar, Kr and Xe respectively – this is the first time the luminescence of Ba$_2$/RG solids has been reported. Interestingly, the Stokes shifts evaluated for each band ranged from 375 cm^{-1} in Ar to 1721 cm^{-1} in Xe, indicating a stronger interaction between the excited metal dimer and the heaviest host. Moreover, radiative lifetimes of 6 ns were recorded for the features in Ar and Kr, while the value

in Xe was longer, in the region of 9 ns. These short nanosecond lifetimes are indicative of a fully allowed molecular transition. Emission scans were made beyond 850 nm in all three RGs but additional, lower energy dimer emission was not observed in these low flux/high temperature samples. Furthermore, direct excitation of the broad, near-IR absorption did not yield any emission out to the limit of our detection, which is around 900 nm.

Unlike Ba, photoexcitation into the lowest energy absorption band (I) of Sr dimer gave rise to resonance emission at 780, 785 and 787 nm in Ar, Kr and Xe, respectively. An excited state radiative lifetime of 15 ns was recorded for the dimer fluorescence in Ar, thereby supporting assignment to a fully allowed $^1\Sigma_u^+ \leftarrow X\, ^1\Sigma_g$ molecular transition. Additionally, a high resolution laser excitation scan was recorded for the near-IR absorption by monitoring the intensity of the 780 nm emission in Ar. The vibronic structure present in excitation was far more resolved than in the absorption scan and an average splitting of 63.7 cm^{-1} was extracted – the vibrational spacing of the excited $^1\Sigma_u^+$ state involved in the transition.

Overall, the luminescence of the metal dimer absorption bands of Ba and Sr revealed very different behaviour. Resonance fluorescence was observed for the lowest energy transition of Sr$_2$ while this transition was completely quenched in Ba$_2$. This behaviour is consistent with the absence of vibrational structure on the Ba$_2$ absorption band (I) – indicating lifetime broadening arising from efficient relaxation to lower lying molecular states of the dimer. The density of molecular states in this spectral region is much greater for Ba$_2$ than for Sr$_2$ due to the large number of atomic ^{1}D and ^{3}D asymptotes, which exist for the former and are absent in the latter. The population of the $^1\Sigma_u^+$ state of Ba$_2$ must be non-radiatively transferred to one of these lower energy molecular states and hence emission was not found in the near-IR region. Moreover, the excitation/emission features that were observed in the visible spectral region (580 – 680 nm) for matrix-isolated Ba$_2$ must correspond to different, higher energy excited states of the dimer. A theoretical study of Ba$_2$, which examines the molecular states dissociating to atomic asymptotes above the (6s6p) ^{1}P$_1$ level, would greatly assist the interpretation of the observed Ba$_2$/RG luminescence.

VII.3   Metal atoms isolated in rare gas solids (M/RG)

VII.3.I Ba/RG: absorption and luminescence

UV/Vis absorption spectra were recorded of dilute Ba/RG samples, deposited at 10 K. In each host solid (Ar, Kr and Xe), atomic bands were observed in two distinct spectral regions. The dominant absorption features occurred in the visible, centred at ~ 547 nm (in Kr) and were assigned to the (6s6p) $^1P_1 \leftarrow {}^1S_0$ (6s^2) transition of Ba, based on their proximity to the gas phase line. Weaker near-UV atomic bands were also identified in each host and are reported for the first time. These features were most prominent in Ar matrices and their spectral location, coupled with an analysis of the absorption integrated areas, allowed state assignments to be made. Thus, the doublet centred at 318 nm was assigned to the two electron (5d6p) $^1P_1 \leftarrow {}^1S_0$ (6s^2) atomic transition – this was also observed in Kr and Xe matrices at 326 and 336 nm respectively. The weaker, higher energy bands at 295 and 270 nm, only identified in solid Ar, were tentatively assigned to the (6s7p) $^1P_1 \leftarrow {}^1S_0$ (6s^2) and (6s8p) $^1P_1 \leftarrow {}^1S_0$ (6s^2) transitions, respectively.

A comparison of the visible (6s6p) $^1P_1$ and UV (5d6p) $^1P_1$ absorption profiles revealed an interesting effect of the solid state environment. A progressive red-shift was observed for both transitions in going from Ar – Xe – a result of the increasing rare gas polarizability. However, the (5d6p) $^1P_1$ absorptions are all blue-shifted with respect to the gas phase, with matrix shifts of approx. 2892, 2121 and 1208 cm^{-1} evaluated in Ar, Kr and Xe, respectively. Conversely, the (6s6p) $^1P_1$ absorption profiles are located to the blue of the gas phase line in Ar (+855 cm^{-1}) and Kr (+536 cm^{-1}) matrices, and to the red in Xe (-130 cm^{-1}). The larger matrix blue-shifts present on the UV bands may be explained by the fact they involve a two electron transition – the excited [Xe]5d6p electronic configuration is accessed from the [Xe]6s^2 ground state. The presence of two electrons in the excited state therefore leads to an appreciably larger repulsive guest-host interaction.

The intense (6s6p) $^1P_1 \leftarrow {}^1S_0$ (6s^2) absorption band was used to probe the site-occupancy of Ba in each host solid. Broad and complex (6s6p) $^1P_1$ profiles were observed on deposition, indicating that multiple sites of isolation were occupied in each RG solid. The absorption bands exhibited significant changes with matrix annealing to 28, 38 and 60 K, for Ar, Kr and Xe respectively. This behaviour reflected the removal

of thermally labile sites for Ba, which were populated during vapour deposition at 10 K. In general, the lowest energy Ba: (6s6p) $^1P_1$ features were most amenable to reduction/removal and probably correspond to the trapping of Ba at defect sites or large grain boundary voids. Although simpler, the remaining structured absorption bands suggested the existence of multiple thermally stable sites of isolation for Ba in all three solid RG's.

Photoexcitation of the annealed Ba/RG (6s6p) $^1P_1$ absorption bands produced intense emissions in the visible spectral region. Based on their proximity to the gas phase line and short nanosecond lifetimes, assignment to the fully allowed (6s6p) $^1P_1$ $\rightarrow$ (6s^2) $^1S_0$ transition of atomic Ba was made. Furthermore, scans made out to 900 nm did not reveal any lower energy features – only resonance (6s6p) $^1P_1$ fluorescence was observed. Despite the existence of only a single electronic transition, multiple site occupancy for Ba resulted in the observation of numerous distinct P $\rightarrow$ S emission bands, many of which were strongly overlapping. Thus, the luminescence of Ba/RG solids was quite challenging to interpret. To identify and resolve the site-specific features, extensive use was made of two dimensional – excitation and emission (2D-EE) spectra. Indeed, these spectra proved vital in allowing the complex site occupancy of Ba to be analysed. Moreover, the 2D-EE scans allowed changes to the atomic luminescence to be easily tracked. For example, a comparison of the 2D-EE spectra recorded of high and low flux Ba/Ar deposits, revealed that site-specific emission bands can be completely obscured if the (6s6p) $^1P_1$ absorption coefficient is too high (> 0.5 OD). The original publication by Balling and Wright suffered from this re-absorption phenomenon. The Ba/Ar emission data presented in their work comprised a single band located at ~568 nm. Thus, their sample was too strongly absorbing and the observed emission originated from a single 'red' site.

The excitation slices extracted from the 2D-EE spectra allowed the complex Ba/RG (6s6p) $^1P_1$ absorption profiles to be resolved into site-specific components. The site-occupancy of Ba was found to be far richer than previous metal atom systems studied by Dr. McCaffrey's group at Maynooth – three thermally stable sites were identified in Kr and Xe matrices (violet, blue and green) and five sites were found in Ar (violet, blue, green, R1 and R2). A plot of RG polarisability versus shift from the gas phase allowed association of certain site types occupied by metal atoms in the rare gas solids. This analysis demonstrated a correspondence between sites of a given 'colour' in all three hosts. For instance, the dominant site in Xe, which shows a Jahn-

Teller (JT) splitting, was associated with the JT band observed in Kr and the minor, partially resolved threefold split band in Ar – these represented absorptions of the blue site. The excitation spectra recorded for Ba displayed a variety of patterns, ranging from the classic Jahn-Teller threefold split, to asymmetric threefold (2+1) patterns and broad, unstructured bands. A summary of the site assignments proposed for both Ba and Sr is presented ahead in Section VII.5.

In order to investigate the possibility of non-radiative relaxation pathways competing with the radiative (6s6p) $^1P_1 \rightarrow$ $^1S_0$ (6s^2) fluorescence, time-integrated intensity scans and time-resolved decay profiles were recorded for each emission band over a range of temperatures. Of the three systems studied, the decay profiles and emission bands of Ba/Xe displayed the greatest temperature dependence. The effect was most pronounced for atoms isolated in the blue site, where the radiative lifetime could not be identified, even at the lowest temperature of 10 K. A gas phase[8,9] model was invoked to explain this behaviour. It was proposed that the shortening of the emission lifetimes at elevated temperatures arose from a non-radiative $^1P_1 \rightarrow$ $^3P_2$ transition, facilitated by the molecular Ba-Xe states. A crossing between the attractive Ba-RG $^1\Pi$ state potential energy curve (PEC) dissociating to the (6s6p) $^1P_1$ atomic asymptote and the repulsive Ba-RG $^3\Sigma$ curve originating from the (6s6p) $^3P_2$ asymptote, assists this population transfer[10,11]. The enhanced efficiency of intersystem crossing (ISC) in solid Xe was attributed to the external heavy atom effect. It was also demonstrated that the site of isolation plays a role. For the blue, green and violet sites in Xe, the activation temperatures for ISC were ≤ 10 K, > 13 K and > 24 K respectively. Molecular dynamics simulations of the Ba/RG systems would be required to fully unravel this intriguing host and site dependence.

The spectroscopy of Ba isolated in a solid Xe matrix has recently attracted the attention of the nEXO Collaboration[12], as a possible way of observing the neutrinoless double beta (0νββ) decay of ^{136}Xe. This decay process produces a daughter ion, ^{136}Ba^{++}. The experimental concept of the nEXO project is that following 0νββ decay, the resultant Ba ion is frozen with some surrounding Xe, onto a cold probe. The detection of Ba$^+$ or Ba atoms (following neutralisation) isolated in solid Xe infers that the decay event has occurred. Thus, the strong resonance (6s6p) $^1P_1 \rightarrow$ $^1S_0$ (6s^2) fluorescence of neutral Ba acts as a 'tag' for the 0νββ occurrence. However, the luminescence data reported in this thesis, revealed that the Xe environment can

efficiently induce a non-radiative population transfer out of the Ba:(6s6p) $^1P_1$ excited state to lower energy excited states, most likely (6s6p) $^3P_2$. This effect must be considered in the nEXO studies as it will certainly result in a lower quantum efficiency for atomic emission in Ba/Xe.

VII.3.II Sr/RG: absorption and luminescence

UV/Vis absorption spectra were recorded of highly atomic Sr/RG samples following deposition at 10 K. Although scans were made from 180 - 900 nm, the matrix absorption bands of this metal atom were identified only in the visible region from 420 to 520 nm. The dominant profiles (centred at 457.4 in Kr) were assigned to the fully-allowed (5s5p) $^1P_1 \leftarrow$ $^1S_0$ (5s^2) transition of the atom. In addition, a series of weaker absorption peaks were detected to the red of the (5s5p) $^1P_1$ features (centred at 492.2 nm in Kr), which were assigned to the parity-forbidden (5s4d) $^1D_2 \leftarrow$ $^1S_0$ (5s^2) transition. The Ar, Kr and Xe matrices were subsequently annealed to 30, 45 and 60 K respectively, thereby reducing/removing the thermally unstable sites of isolation and minimising their contribution in absorption.

Photoexcitation of the annealed $^1P_1$ absorption profiles produced intense emission bands centred in the visible spectral region at approx. 475 nm (Kr). These features were characterised by short lifetimes, in the range 3.0 - 6.5 ns. Moreover, the radiative values were identified in most cases, permitting confident assignment to the resonance (5s5p) $^1P_1 \rightarrow$ $^1S_0$ (5s^2) transition. Atomic Sr occupied a myriad of sites in annealed rare gas solids, and this was manifested in the luminescence spectra, where multiple resonance emission bands were observed in each host system. Similar to Ba, 2D-EE spectra were recorded which allowed deconvolution of the strongly overlapped emission bands. Moreover, the excitation spectra extracted from the 2D-EE scans allowed the complex (5s5p) $^1P_1$ absorption profiles to be resolved into site specific components. Two thermally stable sites were identified in Xe (blue and green), while four were found in Kr (violet, blue, green and red/R2). The lightest host, Ar, was the most complex with five thermally stable vacancies detected. Four of these (violet, blue, green and R1) were identified from the (5s5p) $^1P_1$ fluorescence, however, the fifth (R2) was only revealed in an excitation scan recorded of the (5s5p) $^3P_1$ phosphorescence – the R2 site did not produce any resonance (5s5p) $^1P_1$ emission. In addition, a plot of

RG polarisability versus shift from the gas phase allowed a connection to be made between sites of a given 'colour' in all three hosts.

Spectral and temporal scans were recorded over a range of temperatures to investigate the possibility of non-radiative relaxation pathways competing with the (5s5p) $^1P_1$ state fluorescence. These temperature studies revealed a strong host dependence, where the emission integrated areas in Xe were most prone to reduction with increasing sample temperature. Moreover, the radiative lifetime of the blue site could not be identified in this host, even at 10 K, and only a tentative assignment was possible for the green site. In stark contrast, the emission bands in Ar showed little or no change with increasing temperature and the radiative lifetimes were obtained in all cases. To rationalise this behaviour, a model based on existing gas phase studies[13-15] was adopted. These investigations showed that collisions of the excited Sr atom ($^1P_1$ or $^1D_2$) with RG atoms can induce a non-radiative population transfer to the lower lying (5s4d) ^3D_J manifolds. The strong host dependence, revealed in the temperature studies of the (5s5p) $^1P_1$ fluorescence of matrix-isolated Sr, was therefore attributed to a $^1P_1 \rightarrow$ ^3D_J intersystem crossing (ISC). The external heavy atom effect results in a more efficient $^1P_1 \rightarrow$ ^3D_J transition in Xe.

The data presented in Chapter V was not limited to the resonance (5s5p) $^1P_1 \rightarrow$ $^1S_0$ (5s^2) transition. In contrast to Ba, the lower lying excited states of Sr were accessible with the detection system used and a detailed study of the full range luminescence was conducted. In addition to the resonance fluorescence at approx. 475 nm, excitation of the $^1P_1$ and $^1D_2$ absorption profiles produced lower energy emission bands in the range 480 - 800 nm. Each band was firstly assigned to a particular site of isolation. The 2D-EE spectra and long range excitation scans, recorded of these lower-lying emissions, significantly aided this endeavour. State assignment were made based on the observed spectral (location and bandwidth) and temporal characteristics. The emission features located at 490, 575 nm, and 710 nm (values in Kr) were assigned to the (5s4d) $^1D_2$, (5s4d) $^3D_1$ and (5s5p) $^3P_1$ excited states of atomic Sr, respectively.

In summary, the $^1P_1$ and $^1D_2$ state luminescence recorded of Sr/RG solids at 10 K was complex and the photo-physical properties were found to depend on a number of factors, such as: 1. the rare gas host, 2. the excited state initially accessed in absorption ($^1P_1$ or $^1D_2$) and 3. the site of isolation. The steady state, two dimensional and time-resolved luminescence techniques employed in this study allowed these

complexities to be resolved and clearly categorised. A summary is provided in Table VII.1 and a few notable examples of each dependence are discussed.

Table VII.1 The photophysical properties of the Sr/RG systems were found to depend on the host solid, site of isolation and the initial excited state promoted. This table summarises the observations made at 10 K.

Excited state pumped	Host	Site				

Excited state pumped	Host	Site	(5s5p) $^1P_1$	(5s4d) $^1D_2$	(5s4d) $^3D_1$	(5s5p) $^3P_1$
(5s5p) $^1P_1$	Ar	Violet	✓	-	-	-
		Blue	✓	-	-	-
		Green	✓	✓	-	✓
		R1	✓	-	-	-
		R2	-	-	-	✓
	Kr	Violet	✓	-	-	-
		Blue	✓	-	✓	✓
		Green	✓	✓	-	✓
		R2	✓	-	-	✓
	Xe	Blue	✓	-	-	✓
		Green	✓	-	-	✓
(5s4d) $^1D_2$	Ar	Blue	-	-	✓	✓
		Green	-	✓	-	✓
		R2	-	-	-	✓
	Kr	Blue	-	-	✓	✓
		Green	-	✓	-	✓
		R2	-	-	-	✓
	Xe	Blue	-	-	-	✓
		Green	-	-	-	✓

Header spanning: "Excited state observed in emission" spans the four rightmost columns.

1. **Rare gas host:** The temperature study conducted for the visible (5s5p) $^1P_1$ emission features revealed a strong host dependence, which was attributed to a $^1P_1 \rightarrow {}^3D_J$ intersystem crossing (ISC). This non-radiative process is present even at 10 K and significantly affects the P state luminescence. For example, the near-IR (5s5p) $^3P_1$ emission bands identified in Xe and Kr were far more intense than in Ar, indicating that a greater proportion of the $^1P_1$ population reaches the $^3P_1$ level in the heavier RG solids.

2. **Excited state initially accessed:** In contrast to the $^1P_1$ luminescence, resonance $^1D_2$ emission was rarely observed in the RG solids. Direct emission from this state was identified only when Sr atoms were isolated in the green site in Ar and Kr matrices. Moreover, these $^1D_2$ emission bands were very weak – a surprising result considering the intensity of the $(5s4d)\ ^1D_2 \leftarrow\ ^1S_0\ (5s^2)$ transition in absorption. It was therefore concluded that the $^1D_2$ excited state of Sr is rapidly quenched in all three rare gas solids. This behaviour may be associated with a very efficient $^1D_2 \rightarrow$ ^3D_J intersystem crossing (ISC), which is active at 10 K – assuming the gas phase model is correct. Furthermore, the $^1D_2 \rightarrow\ ^3D_J$ transition must be more efficient than the corresponding $^1P_1 \rightarrow\ ^3D_J$ channel. This is best exemplified in the 2D-EE spectrum recorded of the $^3P_1$ phosphorescence bands in Ar, which revealed a striking difference between the $^1P_1$ and $^1D_2$ regions (in excitation). The P state luminescence bands were weak and showed little or no site-selectivity - the R2 site dominated. In contrast, the D state luminescence was much more site-selective, exhibiting cleanly resolved and more intense $^3P_1$ emission bands, which emanated from Sr atoms in the blue, green and R2 vacancies.

3. **Site of isolation:** The site of isolation governs the photophysical properties of the Sr/RG systems and is inextricably linked with the other two dependences. For example, the host dependence of the $^1P_1 \rightarrow\ ^3D_J$ intersystem crossing was most conspicuous for the blue site of isolation. $(5s5p)\ ^3P_1$ emission was not observed in the near-IR for the blue site in Ar, while in Xe, it was the dominant spectral feature. Interestingly, it was observed that $^3D_1$ emission only occurs when Sr atoms are trapped in the blue site, whereas $^1D_2$ emission is unique to the green site.

A proposal of this study is that intersystem crossing mechanisms, namely the $^1P_1,\ ^1D_2 \rightarrow\ ^3D_J$ non-radiative transitions, strongly affect the luminescence of atomic Sr in RG solids. Indeed, it is possible that both the host and excited state dependences discussed above are, to a large extent, a manifestation of intersystem crossing. While the exact mechanisms suggested in this work are supported by gas phase collisional studies[13-15], alternate relaxation pathways cannot be discounted in a matrix environment, where the guest-host atoms are more confined and the interactions are expected to be stronger. Molecular dynamics simulations of the solid state environment, based on accurate 1:1 Sr·RG ground and excited state potentials, would

greatly assist and advance the interpretation of the luminescence observed for Sr/RG systems.

VII.4   Ground state interaction potentials of M·RG diatomics

Novel ground state potential energy curves were computed for the 1:1 M·RG complexes (M=Ca, Sr, Ba and RG = Ar, Kr, Xe), using the empirical Tang-Toennies (TT) and *ab initio* CCSD(T) methods. The latter involved the use of extensive correlation consistent (aug-cc-pVQZ) basis sets[16,17] to describe each atom and, in addition, the core electrons of Ca, Sr, Ba and Xe were replaced with Stuttgart-Cologne effective core potentials[18]. Both methods revealed long bond lengths (> 5 Å) and shallow bound regions (<142 cm^{-1}) for the nine M·RG diatomics. Moreover, the spectroscopic constants (R_e and D_e) obtained from each approach were in good agreement, especially for the Sr·RG diatomics − a remarkable result considering the empirical nature of the Tang-Toennies formula. A comparison with the CCSD(T) potentials showed that the TT model was adequate at describing the long range, attractive portion of the M·RG interaction. However, the poor performance of the TT function at describing the inner repulsive walls precluded the use of this method in analysing the site occupancy of the M/RG systems, where short range, repulsive guest-host interactions are important. Thus, the site occupancy was interpreted using only the CCSD(T) results.

VII.5   M/RG site occupancy

A comparison of the M·RG (*ab initio*) and RG$_2$ (experimental spectroscopic constants fitted to a Morse function) potential energy curves allowed for comments to be made regarding the occupancy of the alkaline earth atoms within cubic sites of the *fcc* rare gas lattices. It was found that the binding energies of the rare gas dimers are all greater than the heteronuclear diatomics but more significantly, the M·RG potentials all have their minima at nuclear separations greatly in excess of the rare gas dimers. The energetics determined from the calculated M·RG potentials, for single vacancy (SV) and multi-vacancy [tetra-vacancy (TV), hexa-vacancy (HV) and cubo-octahedral (CO) substitutional] distances, allowed the most probable M/RG site occupancies to be

assessed. This analysis predicted that Sr or Ba atoms do not occupy SV sites and, because of the required for lattice stabilisation, TV or HV sites are the most likely candidates for accommodating these large metal atoms.

Table VII.2 **A summary of proposed M/RG site assignments. The rightmost column provides a description of the excitation bands observed and possible locations for each vacancy.**

Site	Assignment	Description
Blue	Tetra-vacancy (TV)	Jahn-Teller (JT) threefold split band. This site occurs within the *fcc* lattice
Green	Hexa-vacancy (HV)	Broad with a hint of threefold splitting in some cases - proposed to be unresolved JT bands. This site occurs within the *fcc* lattice.
Violet	Cylindrical void (CV)	Asymmetric threefold (2+1) spitting. Very high annealing threshold - possibly exists as a small cavity at a grain boundary or a multi-atom vacancy with the *fcc* lattice.
R1	Cylindrical void (CV2)	Asymmetric threefold (2+1) spitting, but a smaller Σ-Π energy gap and a less resolved Π doublet suggest a more spacious cavity than CV. Most likely a grain boundary site as evidenced by the relatively low annealing threshold.

Combining the theoretical analysis with the site-specific ($nsnp$) $^1P_1$ excitation spectra recorded in annealed M/RG solids yielded tentative site assignments. The blue site excitation bands were characterised by a Jahn-Teller threefold split, inferring that the metal atoms were trapped in a site of high (cubic) symmetry – accordingly, these were assigned as tetra-vacancies (TV). At best, the excitation bands of the green site of isolation showed hints of a threefold splitting pattern (Sr/Kr). Nonetheless, these profiles were well reproduced with three Gaussian curves of equal width, suggesting that the Jahn-Teller effect contributes to the absorption bandwidths. As a result, the green sites were provisionally assigned as hexa-vacancies (HV).

In stark contrast to the blue and green sites, the P ← S excitation spectra recorded for Sr and Ba atoms isolated in the violet and R1 sites, displayed an asymmetric threefold (2+1) spitting pattern, consisting of a higher energy doublet (Π configuration) and lower energy singlet (Σ configuration). Monte Carlo simulations[16] of Na/Ar demonstrated that sites of lower (non-cubic) symmetry, in which a strongly

preferred direction exists, produce this characteristic pattern in absorption. Accordingly, the violet and R1 trapping sites were tentatively assigned as cylindrically shaped voids (CV). Sr and Ba are the first metal atoms, studied by the Maynooth Group, which show a clear preference for occupancy in vacancies of lower (non-cubic) symmetry. This is a direct consequence of the large 1:1 M·RG ground state bond lengths. A summary of the site assignments proposed in this thesis is provided in Table VII.2.

VII.6 Summary and future work

In conclusion, the study of Sr and Ba atoms isolated in rare gas matrices was a valuable and revealing endeavour. The spectroscopic data reported in this thesis has advanced matrix studies of the alkaline earth atoms and augmented the research conducted by the Maynooth Group on S ground state metal atoms. Moreover, the existing literature on these M/RG systems was sparse and contained many inaccuracies, which have been addressed and corrected. When these experiments began, it was intended that Ba be a stand-alone matrix study, however, the work quickly evolved to include atomic Sr. Fortuitously, the existence of Sr as an impurity in Ba metal has proven to be an asset, since it has allowed a detailed comparison to be made between the spectra of these two, closely-related, but complex matrix systems.

The rare gas solids have provided an ideal environment to isolate and study the metal atoms and homonuclear dimers. The absorption and luminescence of the Sr_2/RG and Ba_2/RG systems has been recorded, providing a partial characterisation of these metal dimers. For example, lifetime values have been obtained for a few of the low-lying excited molecular states, which, to the best of my knowledge, have not been reported in the literature. Matrix embedding of the metal atoms led to numerous, fascinating effects, which were revealed in the absorption and luminescence measurements made. Although the spectra recorded were complex, these systems were extensively characterised and simplified using a combination of steady-state, two-dimensional (2D-EE) and time-resolved spectroscopic techniques. A myriad of thermally stable sites of isolation were identified for both metal atoms in each rare gas host, especially in solid Ar. From the range of $P \leftarrow S$ excitation patterns observed, it was concluded that the Sr and Ba atoms reside in both cubo-octahedral, crystalline sites

on one hand and in non-crystalline sites on the other – a significant departure from many of the S ground state metal atoms studied by the Dr. McCaffrey's group at Maynooth. State-of-the-art CCSD(T) computations of the 1:1 M·RG ground state potentials were presented, which greatly aided the analysis of the metal atom site occupancy. Moreover, it was demonstrated that the site of isolation critically governs the excited state guest/host interactions and the photophysical properties observed for these metal atom systems.

An important extension of this work would be to conduct molecular dynamic simulations of the M/RG systems. Such theoretical studies could be used to gain information, for example, on the matrix vacancies formed upon deposition or on the excited state dynamics leading to the observed luminescence. However, these simulations rely on the availability of 1:1 M·RG interaction potentials, either derived experimentally or from *ab initio* computations. While accurate 1:1 M·RG ground state potentials were computed in this study at the CCSD(T) level of theory, the excited states of these M·RG dimers are, unfortunately, not well known.

Future experiments may entail the co-condensation of vaporised Sr or Ba with a host mixture containing an excess of Ar and small amounts of reactive molecules (CH_4, CO, CF_4 or N_2). Thus, the reaction products that are produced on deposition or with photolysis could be isolated and characterised. In fact, some of these studies are already underway and preliminary results show that Ba and Sr atoms react with CO on deposition and with N_2 following promotion of the metal to the $nsnp$ $^1P_1$ excited state.

A spectroscopic investigation of M/ethane matrices may provide further insights into the cylindrical voids identified for Sr and Ba in rare gas solids. Unlike the rare gases, cylindrically shaped cavities are intrinsic to packing structure of solid ethane. As a result, the characteristic threefold (2+1) spitting pattern was previously observed on the P $\leftarrow$ S transition of atomic Cd isolated in this host[19]. However, the singlet – doublet (Σ-Π) energy gap is expected to be much greater for Sr and Ba in this molecular matrix, due to a stronger interaction of the excited metal atom (P state) with the molecular host.

References

[1]   W. M. Haynes, *CRC handbook of chemistry and physics* (CRC press, 2014).

[2]   N. Boutassetta, A. Allouche, and M. Aubert-Frécon, Phys. Rev. A **53**, 3845 (1996).

[3]   A. R. Allouche, M. Aubert-Frécon, G. Nicolas, and F. Spiegelmann, Chem. Phys. **200**, 63 (1995).

[4]   J. C. Miller, B. S. Ault, and L. Andrews, J. Chem. Phys. **67**, 2478 (1977).

[5]   J. C. Miller, and L. Andrews, J. Chem. Phys. **69**, 936 (1978).

[6]   A. Stein, H. Knöckel, and E. Tiemann, The European Physical Journal D **64**, 227 (2011).

[7]   M. A. Lebeault, J. Viallon, V. V. Boutou, and J. Chevaleyre, J. Mol. Spectrosc. **192**, 179 (1998).

[8]   W. H. Breckenridge, and C. N. Merrow, J. Chem. Phys. **88**, 2329 (1988).

[9]   W. Breckenridge, Int. Rev. Phys. Chem. **13**, 291 (1994).

[10]   E. Czuchaj, F. Rebentrost, H. Stoll, and H. Preuss, Theor. Chem. Acc. **100**, 117 (1998).

[11]   K. Abdessalem, L. Mejrissi, N. Issaoui, B. Oujia, and F. X. Gadea, J. Phys. Chem. A **117**, 8925 (2013).

[12]   E. X. O. C. n *et al.*, Phys. Rev. A **91**, 022505 (2015).

[13]   C. Redondo, M. N. Sanchez Rayo, J. A. Fernandez, D. Husain, and F. Castano, PCCP **6**, 391 (2004).

[14]   C. Redondo, M. N. Sánchez Rayo, P. Ecija, D. Husain, and F. Castaño, Chem. Phys. Lett. **392**, 116 (2004).

[15]   D. Miller, L. You, J. Cooper, and A. Gallagher, Phys. Rev. A **46**, 1303 (1992).

[16]   K. A. Peterson, D. Figgen, E. Goll, H. Stoll, and M. Dolg, J. Chem. Phys. **119**, 11113 (2003).

[17]   H. Li *et al.*, Mol. Phys. **111**, 2292 (2013).

[18]   EMSL Basis Set Exchange (v1.2.2). Available at: https://bse.pnl.gov/bse/portal

[19]   B. Healy, *PhD Thesis: Experimental and Theoretical Analysis of the Spectroscopy of Atomic Cadmium Isolated in Low Temperature Solids.* (Maynooth University, Maynooth, Co. Kildare, Ireland, 2001).